FORCE AND WAKE CHARACTERISTICS OF ROAD VEHICLES AND SIMPLE BLUFF BODIES NEAR TO GROUND WITH AN EXAMINATION OF THE LOADS ON ROAD VEHICLES IN PROXIMITY TO OTHERS.

Jeffrey Peter Howell

Ph.D Thesis

The City University
Department of Aeronautics

September 1977

CONTENTS

LIST OF ILLUSTRATIONS AND TABLES

FIGURES

38. Effect of yaw on lift curve slope.
39. Total lift on saloon 1 model at 2^{o} incidence.
40. Simple vehicle dynamics model.
41. Front suspension model.
42. Effect of block position on ground board pressure distribution.
43. Pressure distribution on ground under block 2N at incidence.
44. Influence of span and edge radius on ground pressure distribution.
45. Ground board pressure distribution - effect of length and camber
46. " " " " - passenger cars.
47. Saloon 1 - effect of incidence and yaw on the ground board pressures
48. Ground board pressure distributions for Saloon 1 and Can-Am racing car.
49. Velocity profiles in approaching boundary layer and underbody gap-block 2N.
50. Boundary layer velocity profiles - block 2.
51. " " " " - block 9C.
52. Trailing edge velocity profiles - block 2N.
53. " " " " - $Z_o/t = 0.25$
54. Boundary layer velocity profiles - saloon 1.
55. Development of ground board boundary layer displacement thickness.
56. Boundary layer growth with various simulations of ground.
57. Wake profiles.
58. Boundary layer at g.b. centre.
59. Effect of a thickened boundary layer on car lift.
60. Extrapolation to zero b.l. thickness at front wheels.
61. Suggestion for design of static ground board upstream of model.
62. Wake traverses - free stream.
63. Decay of maximum velocity deficit, free stream.
64. Wake half widths - free stream.
65. Base pressure - free stream.
66. Determination of bubble length - free stream.
67. Frequency spectra - free stream - block 2N.
68. " " " " - blocks 1N, 3N.
69. Wake traverses - block 2N near yo ground.
70. Wake traverses - blocks 1N, 3N.
71. Effect of ground proximity on wake decay.
72. Increase in bubble length arising from ground proximity
73. Wake traverses - block 2NS.
74. Block 2NS - contours e/E_{∞} , E/E_{∞} .
75. Pitot contours.
76. Base pressures - block 2N, zero incidence

77. Frequency spectra.

78. Development of trailing vortex sheet.

79. Modifications to profile and velocity deficit.

80. Pitot contours - free stream.

81. Pitot contours - block 2N in ground proximity.

82. Pitot contours - blocks 1N, 3N.

83. Path of minimum total head.

84. Base pressures - block 2N at incidence.

85. Traverses through position of minimum total head.

86. " " " " " " "

87. Frequency spectra - block 2N.

88. Pitot contours - block 9C.

89. Path of minimum total head for cambered block 9C.

90. Wake traverses - block 9C

91. Frequency spectra - block 9C.

92. Path and velocity of a vortex in a corner.

93. Pitot contours obtained from Kiel probe measurements showing separation regions.

94. Pitot contours - saloon 1

95. " " - saloon 3

96. " " - fastback 1

97. " " - fastback 2

98 " " - fastback 3

99. " " - estate 1

100. " " - saloon 1 at yaw

101. " " - fastback 4, estate 1.

102. " " - small lorry model.

103. " " - Can-Am racing car.

104. Traverses through position of total head minimum using hot wire anemometer contours E/E_∞ , e/E_∞ .

105. Traverses through position of total head minimum using yaw probe.

106. Transverse velocity vectors - saloon 1

107. Rotating vane measurements - saloon 1.

108. Decay in maximum rotating speed of vane.

109. Wake centre-line traverses - saloon 1

110. " " " " - fastback 2.

111. Downwash on wake centre-line.

112. Wake centre-line traverses - estate 1

113. Transverse velocities - estate 1

114. Centre line traverse - Can-Am

115. Can-Am car - downwash and transverse velocities

116. Near wake centre-line traverses - passenger cars.

117. Flow over boot and trailing edge - saloons 1,2,3.

118. Frequency spectra - estate 1.

119. " " - fastbacks 2,3.

120. " " - fastback 1, saloon 1.

121. " " - saloon 1.

122. " " - saloon 1 centre line.

123. Reverse flow 'bubble' shapes.

124. Vortex paths as defined by four techniques.

125. Flows adjacent to the ground.

126. Vortex in a corner.

127. Vortex in a corner with superimposed corner flow.

128. Decay of rotational velocities in a trailing vortex.

129. Decay of axial flow in vortices.

130. Velocity of vortex sheet.

131. Relation between lift and the higher frequency peak.

132. Modification to boot design of a typical small car.

133. Influence of Reynolds No. for vehicle shapes used in overtaking experiment.

134. Force variations during overtaking manoeuvre
Long lorry and saloon

135. Short lorry and saloon.

136. Effect of Reynolds' No. and repeatability on the side force of saloon near medium length lorry.

137. Increase in lift and pitching moment for saloon in proximity to short lorry.

138. Lift sensitivity to incidence for saloon 1 in priximity to short lorry.

139. Pitot contours - Large lorry (short length).

140. Wake traverses - large lorry.

141. Representation of lorry by 2-D step.

142. Comparison between theory and experiment, saloon.

143. Forces on Can-Am racing car in proximity to another.

144. Force variations with offset.

145. Effect of vehicle proximity on sensitivity to incidence.

146. Rear axle lift on cars at yaw.

147. Suggestion for rear light cluster design to reduce dirt accumulation.

TABLES

ACKNOWLEDGEMENTS.

I am extremely grateful to Professor G. [redacted] and the Department of Aeronautics, The City University, for allowing me to perform the work included in this thesis.

I acknowledge the joint supervision of Mr. A. Scibor-Rylski and Professor R. Cox and I am thankful for useful discussions with other members of the department, especially Mr. D. Sykes who latterly acted supervisor.

To Mr. D. [redacted], Mr. J. [redacted] and all the technicians I am indebted for their continuous support and help.

I am obliged to my mother-in-law, Mrs E. [redacted] for typing the manuscript.

Finally, but most important, I apologise sincerely to [redacted], my wife, and [redacted], my son, for the neglect they have suffered over the past years.

DECLARATION

This thesis may be copied in full or in part without further reference to the author at the discretion of the University Librarian (provided that only single copies are made and used for study purposes) subject to the normal conditions of acknowledgement.

ABSTRACT

A considerable degree of driving discomfort can be experienced when driving a vehicle in the wake of others. This is especially true in either wet or dusty conditions when both forward and rearward vision becomes obscured. This thesis reports a wind tunnel investigation of the wake characteristics of typical road vehicles and a series of basic rectangular blocks, with and without camber. They are tested through a range of yaw while the influence of incidence on the blocks is studied. The use of static ground simulation is justified and the alternatives discussed. Prior to obtaining wake measurements the force characteristics of the various bodies in ground proximity are determined. Hot wire anemometer and pressure probes are used to derive velocity profiles, turbulence intensities, decay rates and periodic effects in the wake. Two distinct types of vortex wake are obtained, depending on whether the lift is generated by the influence of camber or incidence. Finally consideration is given to the problems created for the drivers of road vehicles by the wake and to ways in which these can be alleviated by design of the vehicle.

NOTATION

a	constant
A	model frontal area (max)
A^1	local cross section area
b	Model span, vortex spacing
B	solid blockage ratio
c	damping
c_f	skin friction coefficient
C	constant
Cp	pressure coefficient
Cp_b	base pressure coefficient
Cx	drag force coefficient
Cy	side " "
Cz	lift " "
Cl	rolling moment "
CM	pitching " "
CN	yawing " "
CZ_1	effective lift coefficient $(Cz - (Cz)_{C_x min})$
d^1	spacing between shear layers
D	model width (overtaking data)
e	r.m.s. voltage output
E	d.c. voltage
h	height of vortex
h^1	step height
H	form factor
H_1	wind tunnel height
H_2	" " width
I	moment of inertia
k	constant, suspension stiffness
l	length, wheelbase
l (m)	Thwaites function
L	car length (overtaking data)
L,M,N	moments
m	vehicle mass
n	frequency (H_z)
n^1	rotating vane speed (r.p.m.)
P	pressure
q	pitch rate
R	Reynolds' number
s	Laplace operator

S	Strouhal number
t	thickness (max)
t^1	thickness (base), uniformising variable
u,v,w	disturbance velocities
U.V.W	mean velocity components
Uc	critical vehicle speed
Um	$U_\infty \ (1-Cpb)^{\frac{1}{2}}$
V^1	Volume
w, W^1	complex potential
x	distance aft of ground board leading edge
x,y,z	displacements
X,Y,Z	forces
Z_o	ground clearance
α	incidence
β	yaw
δ	boundary layer thickness
δ^*	displacement thickness
Δ	increment
ϵ	blockage correction
λ	wavelength
$\Phi(n)$	spectrum function such that $\left(\frac{e}{E_\infty}\right)^2 = \int_{-\infty}^{\infty} n\Phi(n)\, d(\log n)$
ϕ, ψ	velocity, stream potentials
θ	momentum thickness, polar coordinate
τ	flow correction constant
Γ	vortex strength
ν	kinematic viscosity
ρ	density
ω_n	natural frequency
Ω	complex variable

Suffices

1	front suspension
2	rear "
F	front wheels
R	rear wheels
C	car
L	lorry
b	bubble
v	vortex
$\frac{1}{2}$	half width
∞	free stream

INTRODUCTION

In 1895, some years before the Wright brothers were to perform their wind tunnel aerofoil tests, a wind channel was used to investigate the aerodynamic resistance to motion of a model railway train. The history of ground vehicle aerodynamics is therefore a long one although it is only recently that the field has once again been considered of primary importance. This level of interest is predominantly a reflection on the speed of travel. The world's land speed record now stands at 1000 km/h. Future high speed ground transportation vehicles are expected to reach speeds of 500 km/h should current research programmes succeed and present generation high speed rail systems exceed 200 km/h in operations. Speeds above 300 km/h are maintained by modern racing cars which are capable of 400 km/h under favourable conditions. For conventional road vehicles, sustained high speed motorway driving at a speed of more than 150 km/h is possible in most countries while even under present restrictions the 110 km/h limit has not discouraged the attention, which increasingly over the past few years, has been paid to road vehicle aerodynamics

Most aspects of aerodynamics relevant to road vehicle design have been explored, although the vehicle has almost invariably been considered in isolation. As the motion of a body through a real fluid gives rise to a wake flow a road vehicle is very rarely completely outside the influence of another. In addition to generating a drag force, the presence of a wake is responsible for a number of unpleasant features which reduce driving comfort. Under adverse weather conditions, such as rain, the vehicle which generates the wake can suffer from reduced rearward vision due to the separating shear layers at the base entraining water particles, thrown up by the tyres from the road, which then become deposited on the rear screen. Those water droplets which remain in the wake obstruct the forward vision from vehicles travelling downstream. Even under ideal weather conditions a vehicle can produce considerable disturbance on another within its wake. This is especially true where the upstream vehicle is considerably larger than the downstream one.

This thesis examines the wake flows of typical road vehicles. In common with most ground vehicles the body shapes are moderately bluff which implies that the flow separates at a base which is comparable in

area to the maximum frontal area of the body and that any prior separations tend to reattach. Comparisons have therefore been made with the wakes of simple rectangular blocks, for which variations in geometry, ground clearance, incidence and camber are readily separated and easily performed.

A review of previous studies of the aerodynamic characteristics of various types of ground vehicle is given in Appendix 'A'. In Chapter 1 the wind tunnel facilities and models tested are described and the limitations imposed by the wind tunnel boundaries are considered. The force characteristics of the various models are shown in Chapter 2, while the influence of the bodies on the ground is the subject of Chapter 3. Chapter 4 presents the wake flow measurements. Finally in Chapter 5, the influence of a wake on other vehicles is discussed.

1. WIND TUNNEL TECHNIQUES

1.1 Introduction

The wind tunnel has been the most widely used tool for obtaining aerodynamic data on vehicles near to ground, but it is subject to certain limitations. Various methods have been employed to simulate the ground and these are briefly discussed. The wind tunnel and models to be used in this investigation are described and the errors imposed by the tunnel walls are examined.

1.2 Ground Simulation

A variety of techniques have been employed in the past to simulate the ground plane in a wind tunnel. These are fully described in Appendix B but the most common methods are shown in Figure 1. It is usual practice for a flat plate to represent the ground. The board is usually mounted clear of the tunnel floor and the model is located such that it has a ground clearance equal to the local boundary layer displacement thickness. The advantage of this arrangement is its simplicity. It is inexpensive, easy to make and install, but it suffers the disadvantage of incorrect flow boundary conditions on the ground. In the case of a vehicle moving in still air the ground is stationary relative to the external flow, whereas in the wind tunnel the ground and vehicle are both stationary in a moving stream. A boundary layer therefore grows on the ground which is unrepresentative of the real situation. The tunnel floor may be used to represent the ground but this suffers from an even thicker boundary layer.

This boundary layer can be eliminated if an image model technique is employed. The plane of symmetry then represents the ground surface, but the relative velocity of the imaginary boundary is then neither zero nor has the free stream value. Absolute symmetry is required and the setting up procedure is complex.

The only way to obtain the correct boundary conditions at the ground is by use of a moving ground plane, where a flat flexible belt moves at tunnel speed. This is a costly and complex arrangement and requires considerable time for both setting up and in operation. Although this approach gives the theoretically correct boundary conditions, the evidence available, as discussed fully in Appendix B, shows that this technique in fact gives rise to considerably greater errors than does the simpler static ground plane method.

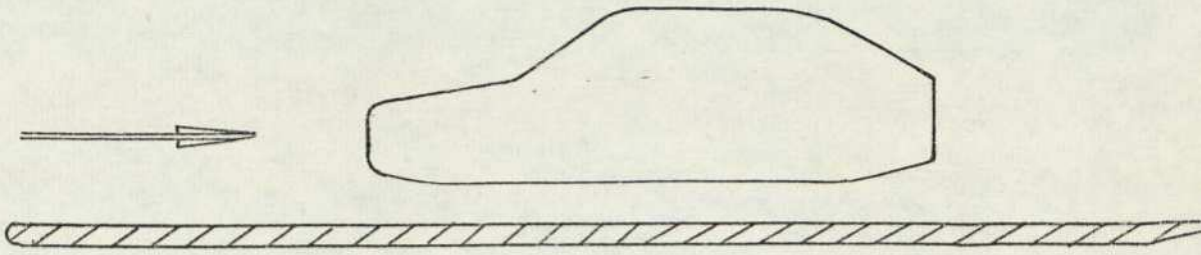

(a) FIXED PLATE

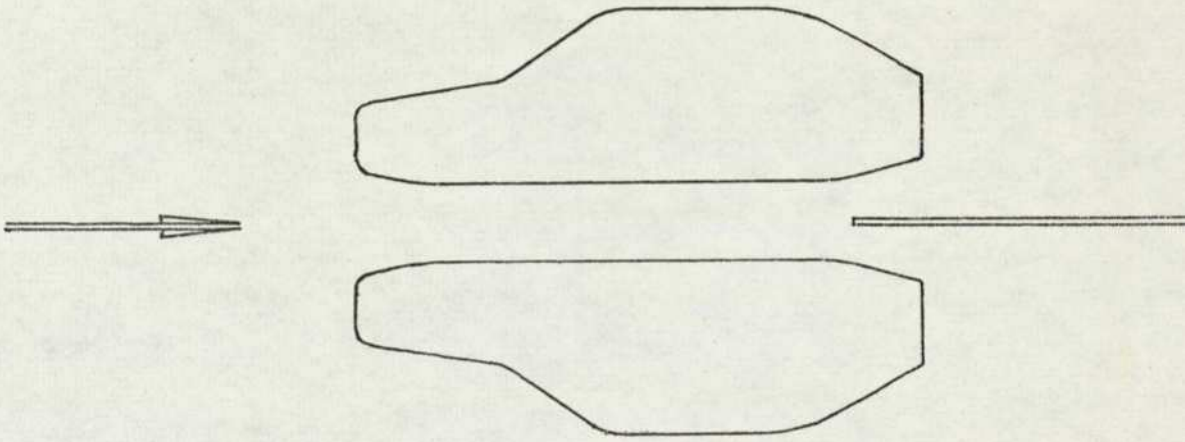

(b) MIRROR IMAGE

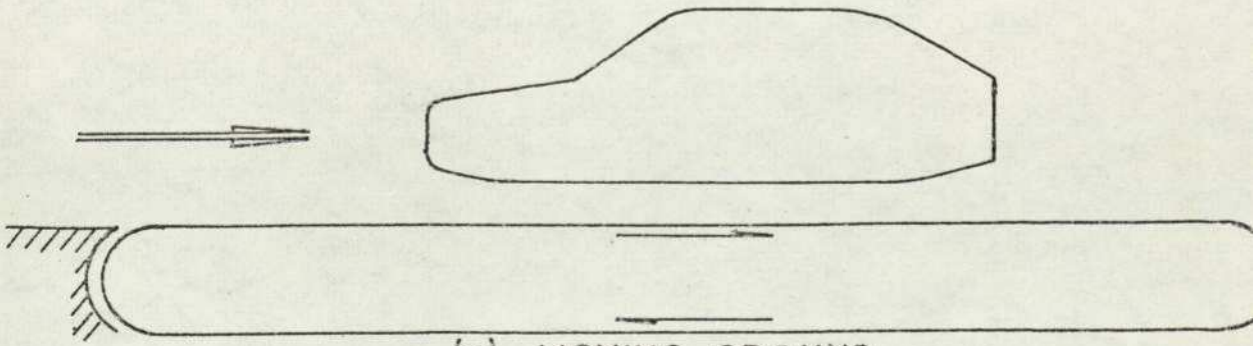

(c) MOVING GROUND

FIG.1 BASIC GROUND SIMULATION TECHNIQUES

Consequently all the experimental data that follows was obtained using a static ground plane, and in the light of subsequent measurements the problem of ground representation is re-examined in Chapter 3.

1.3 Wind Tunnel and Models

1.3.1 Wind Tunnel

The wind tunnel used for all the experiments was the T3 tunnel of the Department of Aeronautics, The City University. It is a closed return type with an octagonal working section 1.14 m wide by 0.93 m high and 1.53 m long. Figure 2 is a cross section of the working area showing the fixed ground board in position. The ground board has a thickness of 0.015 m, is of wooden construction and was mounted 0.2 m above the floor of the working section. This provides an area above the ground plane of 0.75 m^2. The ground spanned the tunnel and was the full length of the working section; it was fitted with a semi-circular leading edge and a straight tapered trailing edge. Twenty pressure tappings were distributed along the length of the ground board upper surface with the front tapping, 0.08 m aft of the leading edge, being duplicated on the lower surface. Equalising of the two leading edge pressures, implying that the flow onto the ground plane was parallel to the surface, was accomplished by adjusting the angle of a flat plate mounted to the tunnel floor at the mid length of the working section. This operation was performed from outside the tunnel. The influence of any model on the circulation around the ground board plus model could therefore be accounted for.

Also shown in Figure 2 is the traversing gear which had to be made for carrying the various probes. It enabled a complete range of vertical and lateral traverses, across a typical wake to be performed at any given longitudinal station in the working section. The principle requirements of the design were, minimum frontal area, the location of all components except the probe itself to be outside of a typical wake boundary, and the complete operation had to be performed from outside the tunnel. Furthermore it had to be constructed with sufficient rigidity that models could be mounted to it for the experiments on interference effects between vehicles. The longitudinal station was set by clamping the runners to the square section rails which ran the length of the working section. Lateral positioning was by rotation of the screw bar which passed through a captive slider to which was attached the vertical traversing arrangement. This was performed manually from the tunnel roof, with a removeable shaft

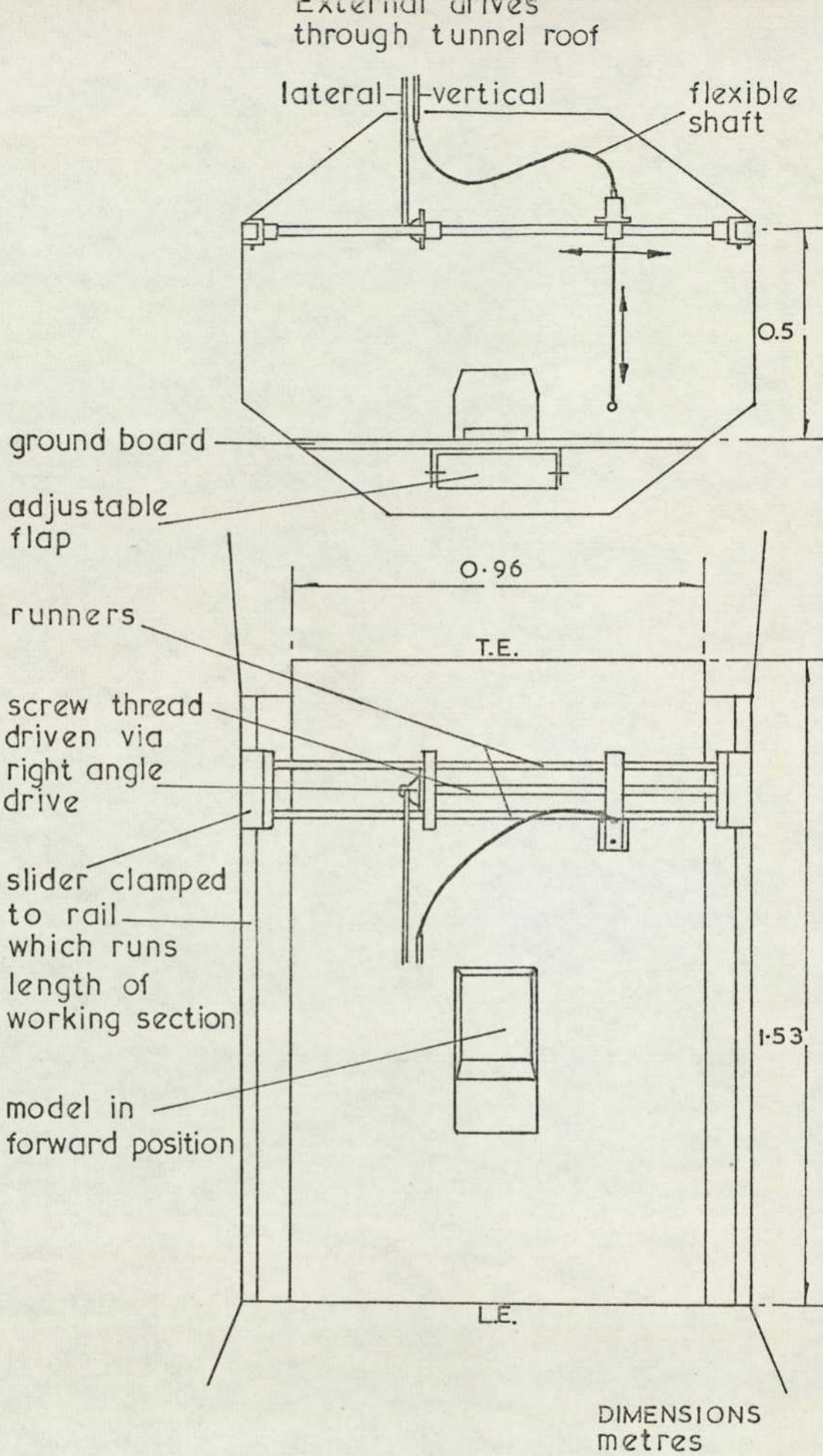

FIG.2 WIND TUNNEL WORKING SECTION

connecting through a right angle drive. The lateral position was recorded by a revolution counter mounted on the screw bar. The vertical traversing was obtained from a vertical rack driven manually, via a series of gears, by a flexible drive which, again, passed out through the tunnel roof. The probes were mounted on an extension fixed to the lower end of the rack. Vertical position was recorded from a revolution counter driven by the flexible shaft.

The traverse gear gave up to 0.6m lateral movement and 0.2m vertical motion. It had a total frontal area less than $0.02m^2$. To avoid positioning errors arising from backlash in the gears the traverses were always performed in one direction, the zero being set at a stop.

1.3.2 Wind tunnel calibration

The wind tunnel working section was calibrated in the absence of any models but with the ground plane fitted. The velocity distribution was measured at three longitudinal stations in the working section using a standard pitot static probe, and with the tunnel speed nominally 30 m/s. The contours of equal velocity are shown in Figure 3. The turbulence intensity was also measured at the three stations, using a constant temperature hot-wire anemometer, mounted 0.1 m above the ground board. It was found to be always less than 0.6%.

The static pressure distribution along the upper surface of the ground plane is shown in Figure 4. A pitot rake was used to measure the boundary layer growth along the ground board at various speeds. The results are plotted, as a function of Reynolds number, and distance downstream from the leading edge of the ground, in Figure 5 (a). The boundary layer thickness δ, has been taken as the height at which the velocity is 99% of the free stream value. The growth of the boundary layer thickness fits the expression

$$\delta = 0.385 \times R_x^{-0.2} \qquad (1.1)$$

where R_x is the Reynolds number based on the distance aft of the ground leading edge. This is very close to the theoretical zero pressure gradient growth of a power law boundary layer with exponent seven. The spanwise variation in boundary layer thickness is shown in Figure 5b. All stations show a thickening away from the centre line but the effect is most marked near the leading edge.

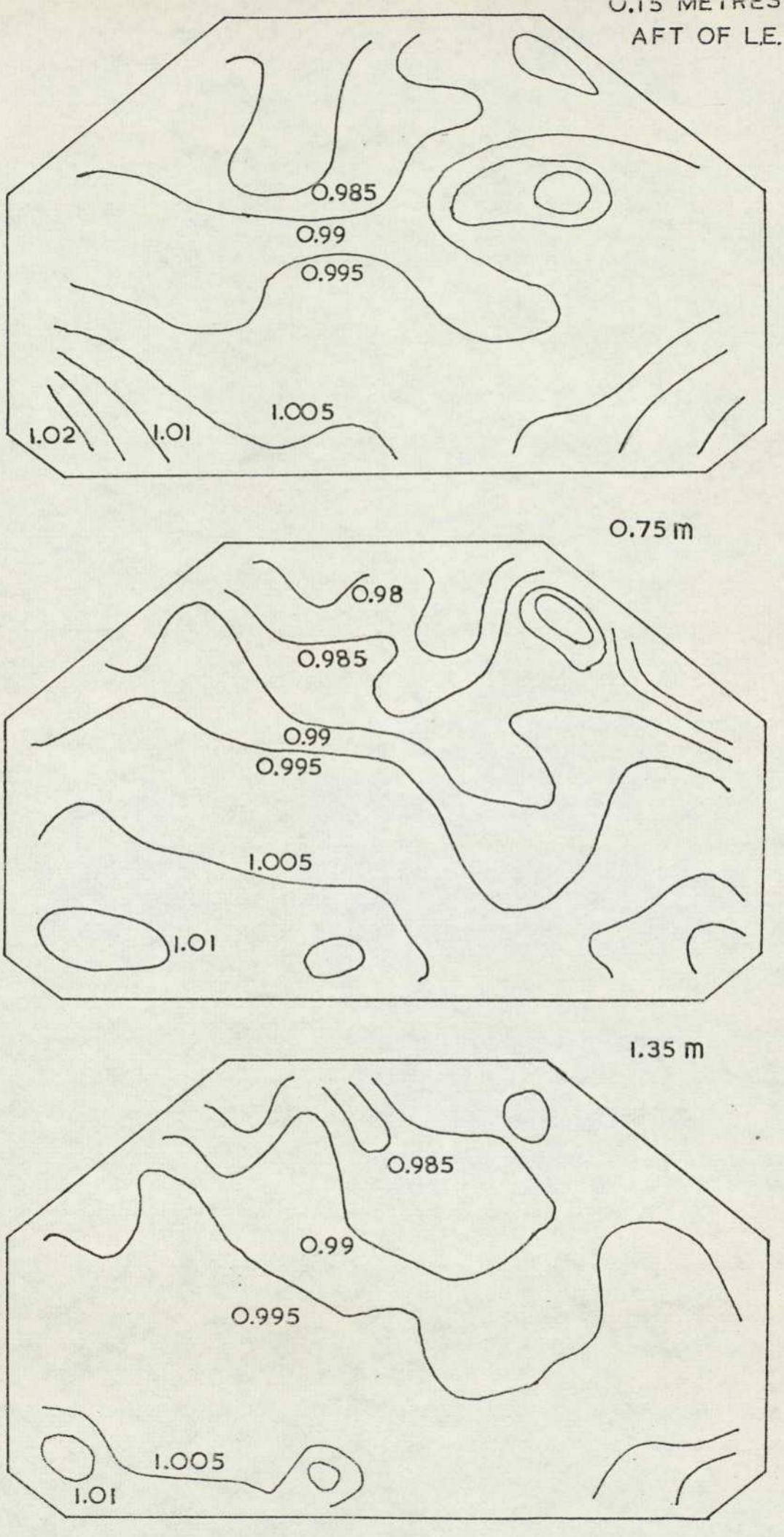

FIG. 3 VELOCITY DISTRIBUTION IN WORKING SECTION

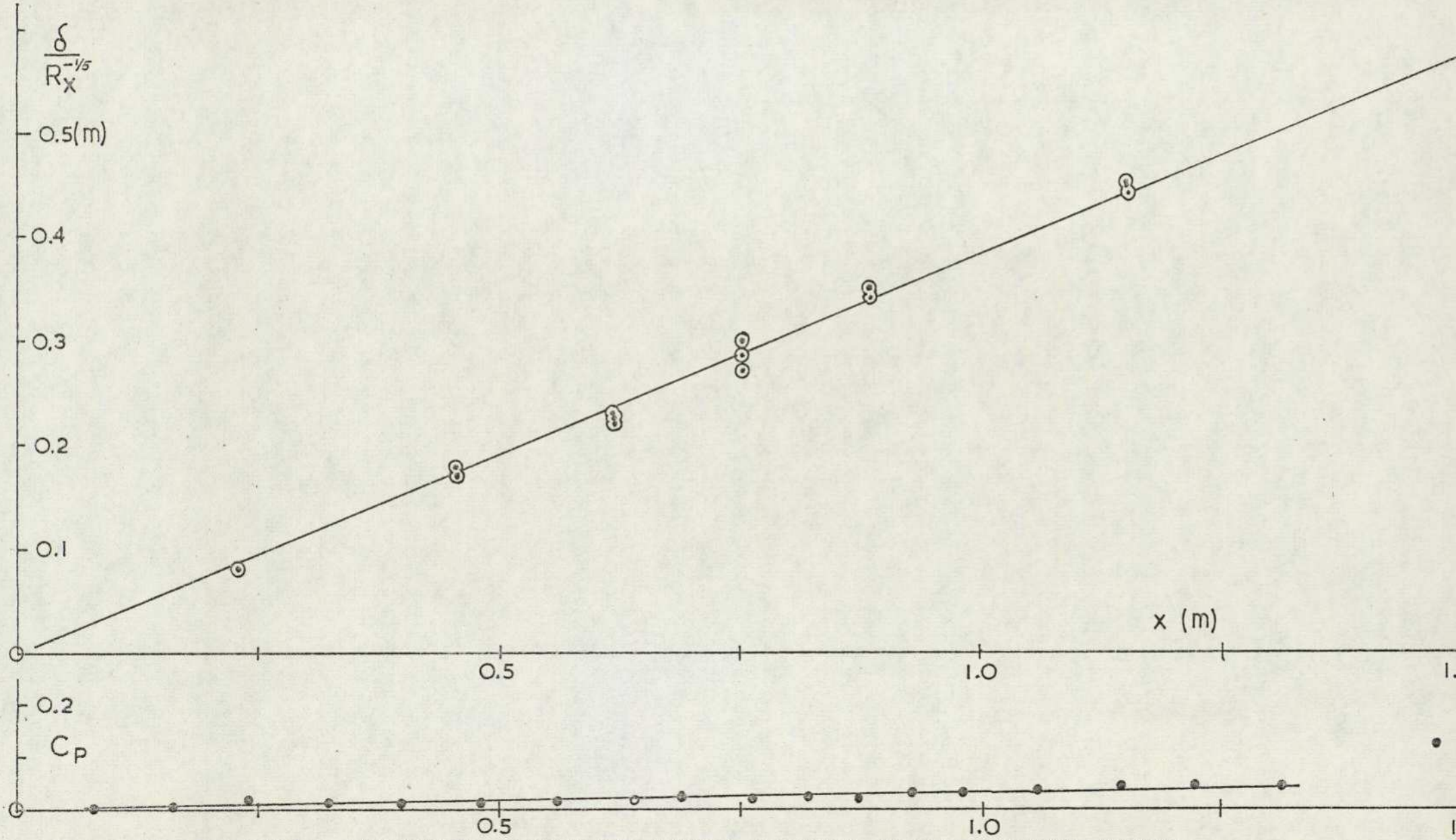

FIG.4 STATIC PRESSURE , BOUNDARY LAYER GROWTH ALONG GROUND BOARD

A two hole 'yaw' probe was mounted on the tunnel centre line at several stations and traversed vertically to a height of 0.25 m. The variation in flow pitch angle is shown in Figure 6. Close to the ground the flow is parallel but demonstrates an increasing downward inclination with height. Variation across the span at the mid length of the ground plane is slight. The flow yaw angle was not directly measured but subsequent data on the lateral force characteristics of model cars shows that the yaw angle on the tunnel centre line varies between 0° close to the leading edge and 1.5° near to the trailing edge of the ground board.

A hot wire anemometer is sensitive to temperature variations in the surrounding fluid. It was expected that the probe would be subjected to a considerable amount of start-stop running and so the temperature variation through a typical run cycle was measured, Figure 7. The increase appeared excessive and a cooling experiment was attempted. Air was blown through the hollow corner vanes immediately upstream of the settling chamber. The effect of this is shown, also in Figure 7, and it can be seen that only a slight reduction in temperature at a given time is realised. It was decided that rather than continuously monitor the tunnel temperature, a temperature compensated hot wire probe would be more suitable. The only disadvantage to such a probe appears to be that it suffers a loss in frequency response above 5 kHz, which is outside the frequency range of interest.

1.3.3 Models

Vehicles which operate close to the ground are almost invariably flat bottomed, or have a lower surface which is predominantly parallel to the ground; they have little or no camber, and are moderately bluff. The latter implies that the separating flow at the base has a cross section comparable with the frontal area of the vehicle. On removing the influence of camber the simplest body having these general characteristics is a rectangular block. A series of these blocks were made for the initial studies and one is shown in Figure 8. The dimensions of the blocks are given in Table 1. The notation used for identifying each block is used throughout the text. To each block could be added a nose block which introduced radiused upper and lower leading edges. The edge radius of curvature is always

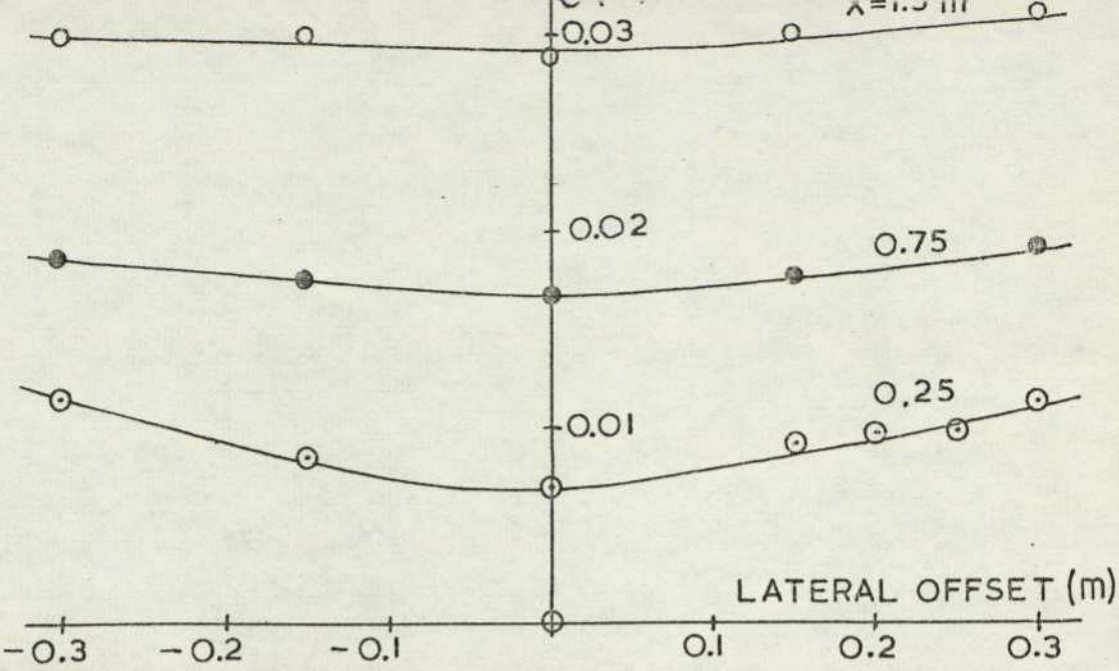

FIG.5 EFFECT OF OFFSET ON B.L. THICKNESS

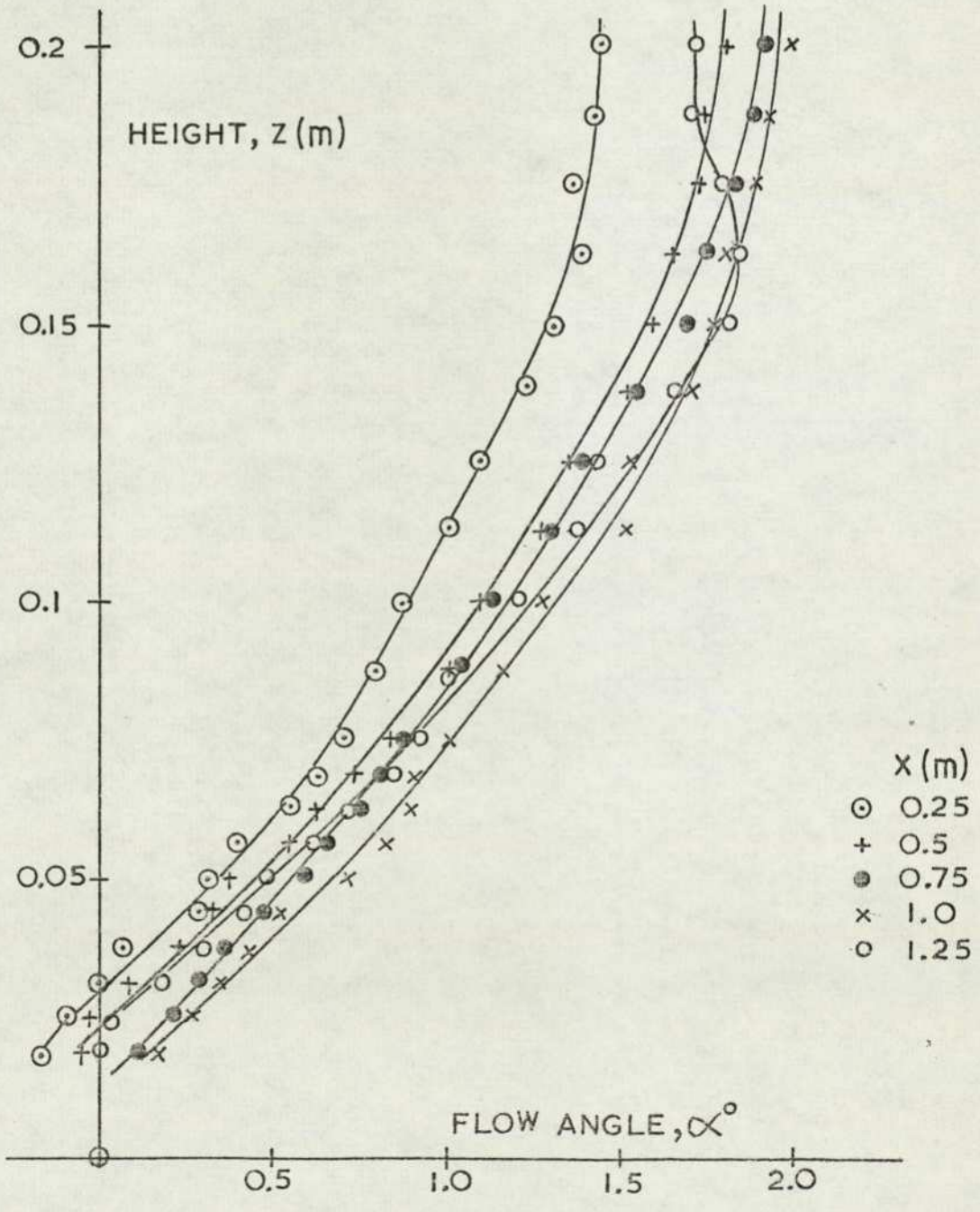

FIG.6 FLOW PITCH ANGLE

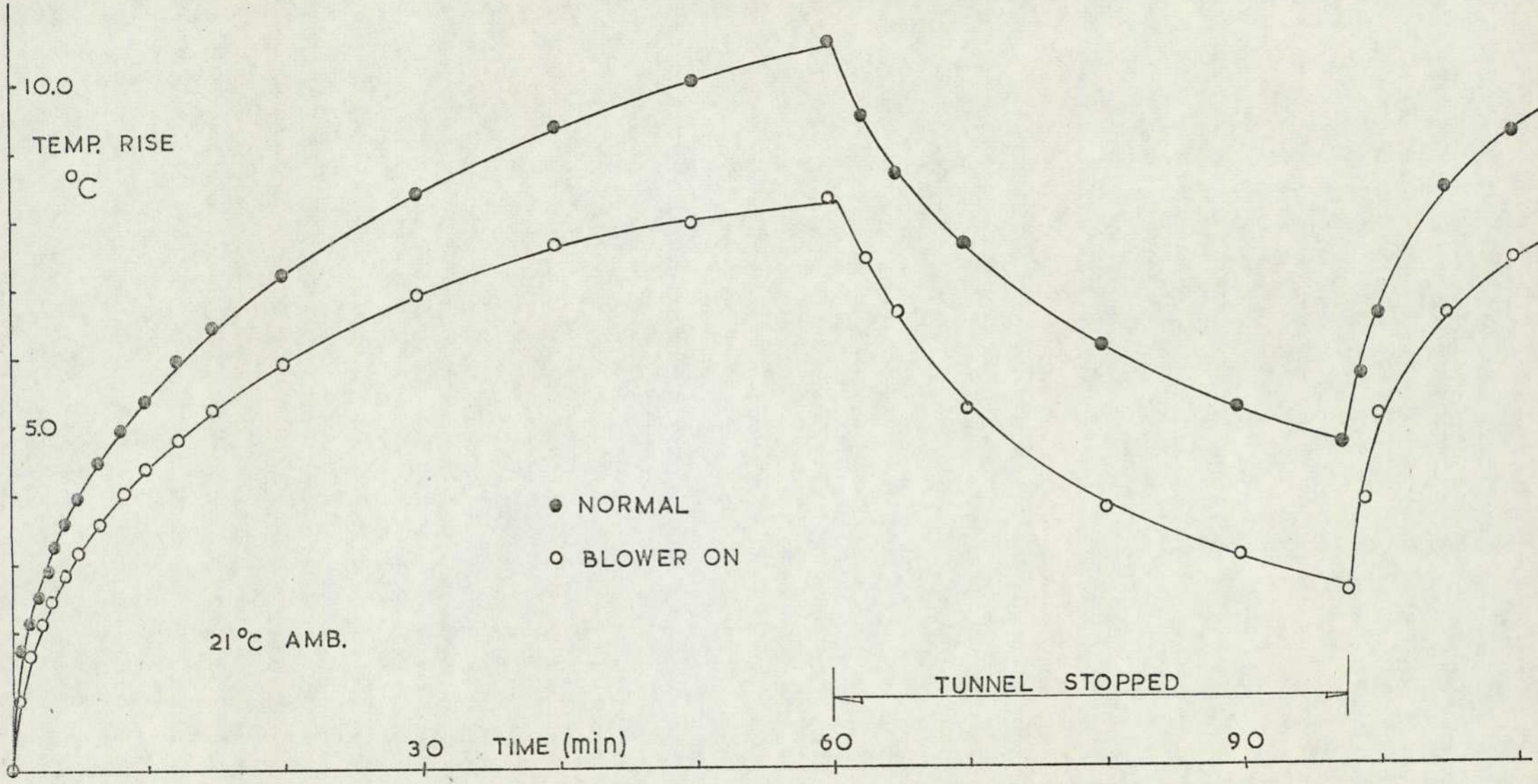

FIG.7 TEMPERATURE RISE IN WIND-TUNNEL T.3.

0.25 t where t is the body thickness, and each block with nose added becomes 25 mm longer. This configuration, the most frequently used is designated by N added to the block number.

TABLE I: Block dimensions (metres)

block	$\frac{1}{}$	b	t	$\frac{b}{1}$	$\frac{b}{t}$
1N	0.3	0.1	0.1	0.33	1.0
2N	"	0.2	"	0.67	2.0
3N	"	0.3	"	1.0	3.0
4N	"	0.2	0.05	0.67	4.0
5N	"	0.2	0.025	0.67	8.0
6N	0.2	0.2	0.1	1.0	2.0
7N	0.4	0.2	"	0.5	2.0
Basic blocks $\frac{1}{}$ - 0.025 blocks NS b + 0.025					
Cambered blocks					
	0.4	0.2	0.15		
	max thickness pos$^{n.}$				
8C	0.25 $\frac{1}{}$				
9C	0.35 $\frac{1}{}$				
10C	0.45 $\frac{1}{}$				
11C	0.6 $\frac{1}{}$				
12	0.41	0.22	0.11	0.53	2.0

NOTE: A fold out sheet showing all the rectangular blocks drawn in Figure 8, but in clearer detail, is on page (336) in Appendix D at the end of this thesis. This should be used in all future reference to the rectangular blocks.

	block 'N'	+	block 'X'	gives	block 'X'N
block 's'	+	"	+	"	"	'X'NS
cambered	" 'y'	+	"	+	" 7	"	"	'y'C

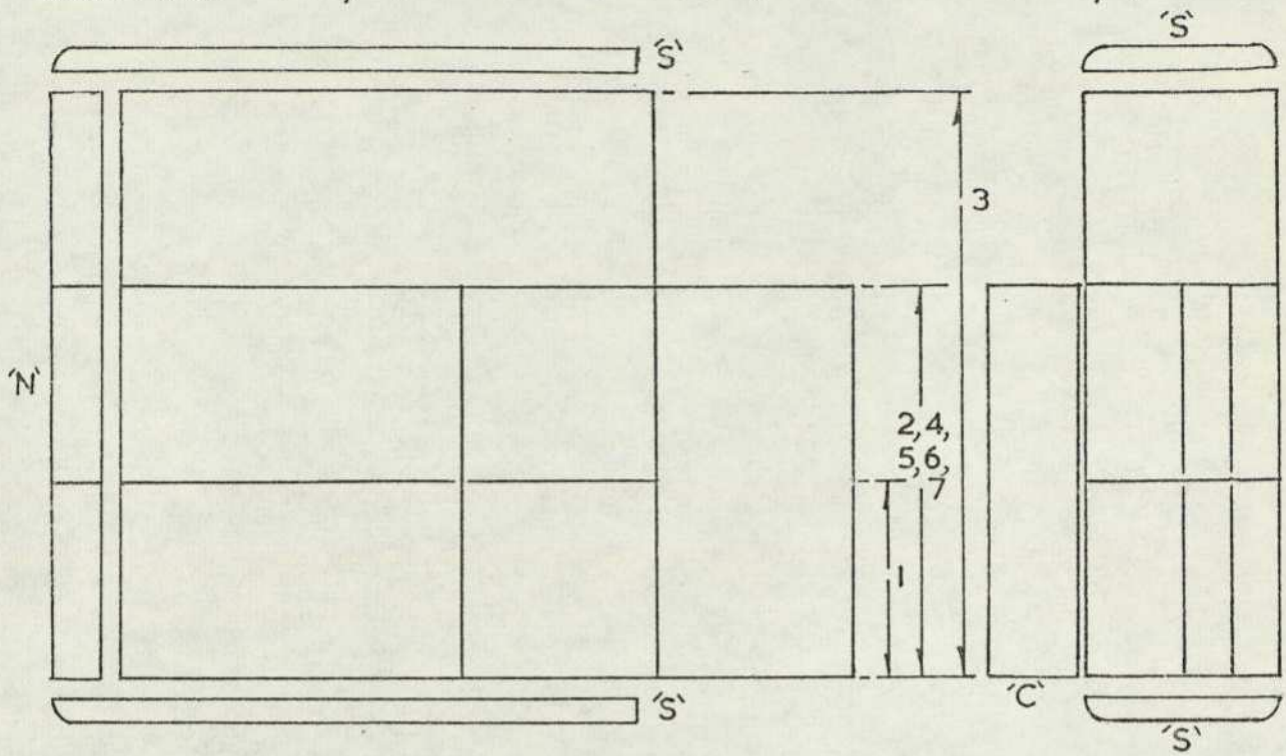

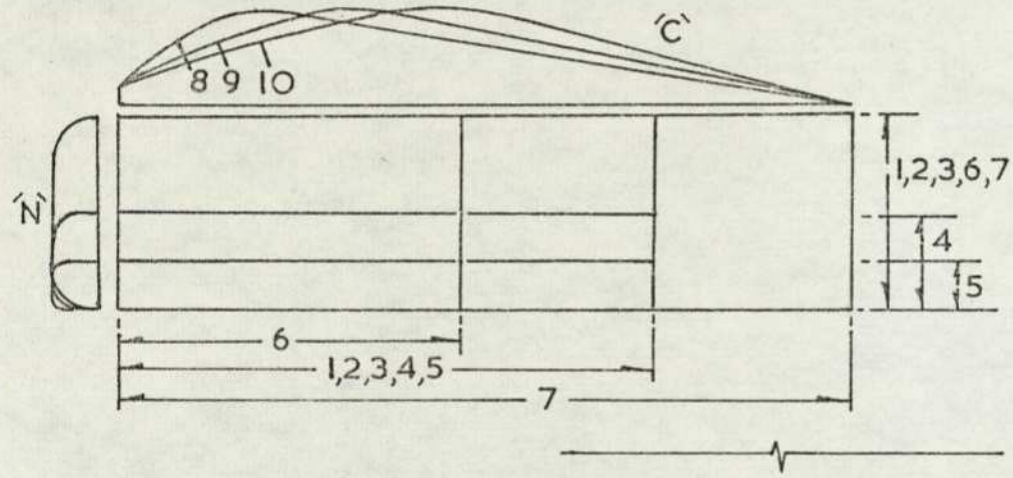

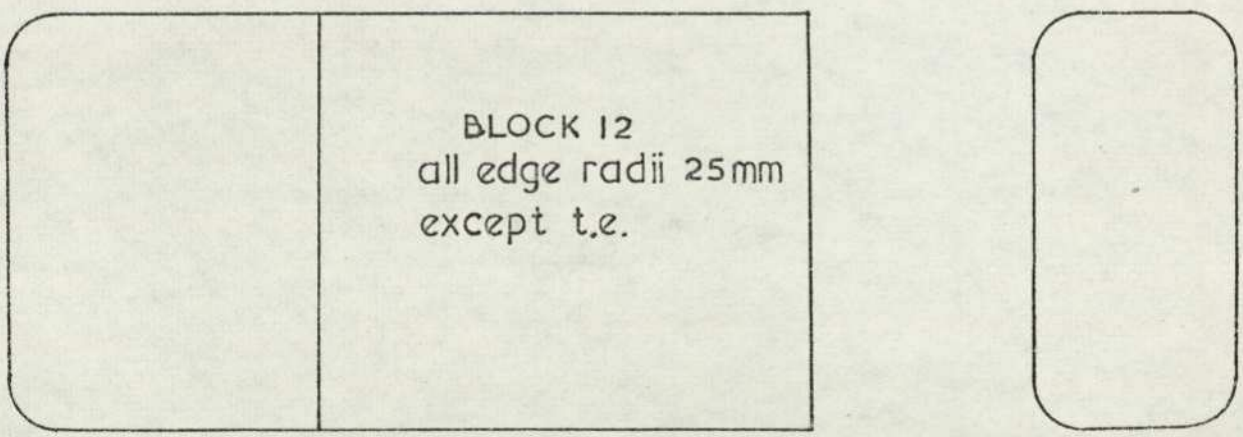

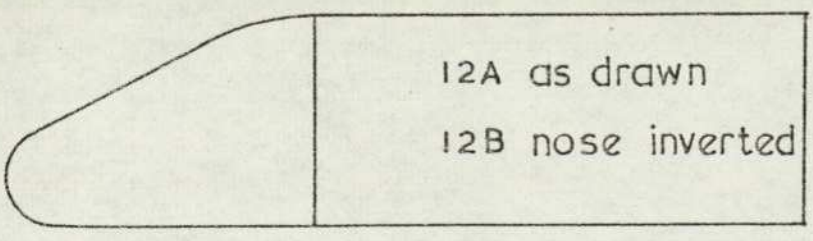

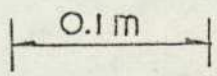

DIMENSIONS:
see Table 1

FIG. 8 RECTANGULAR AND CAMBERED BLOCKS

A transition strip was placed on the vertical face of the nose block at the intersection with the radiused horizontal edges. In addition, for blocks of height 0.1 m, fitted with the nose section, side plates could be attached which increased the overall block width by 25 mm and introduced a radius of curvature of 12.5 mm on all the side edges except those at trailing edge. These blocks are designated by adding NS to the block number. The body having a planform aspect ratio of 0.67 was available in two additional thicknesses giving base aspect ratios of 4.0 and 8.0. These were only used in force measurement tests. Two extra blocks having base aspect ratio of 2.0 were made. These had planform aspect ratios of 0.5 and 1.0 to complement the original with planform aspect ratio of 0.67. For the longer one of these, block 7N, a series of cambered upper surfaces were made, Figure 8, which all gave similar aspect ratios and increased the thickness by 50%. The position of the maximum thickness could be varied between 25% and 60% of the overall length. These cambered blocks are designated by the suffix C. Block 9C was used for wake studies, the remainder only being employed for force measurements.

Three distinct passenger car types have been modelled. These are categorised as saloon, estate, and fastback. A modern trend in vehicle styling is to confuse the distinction between saloon and fastback by reducing the backlight rake angle and increasing the boot slope, but this type has not been considered. As shown in Figure 9 all the car models have a common lower body shape, the variation being almost exclusively above the boot-bonnet line. The models represent approximately one twelfth scale vehicles. All the boot trailing edges were made sharp edged as were the front and rear wings. The sill and bonnet leading edges were given radii of 5 mm and 15 mm respectively. For definition of styling terms reference should be made to Figure 10. On the underside of the lower chasis a number of roughness elements having cross section 3 mm by 6 mm and of varying lengths were attached in an attempt at representing typical underbody components such as suspension members, silencer and axle. No cooling flow was introduced. Transition strips were fitted at the nose along the intersection of the radiused edge and the vertical face. The wheels were made easily removable flush with the lower surface. No effect of wheel arch recesses was allowed for.

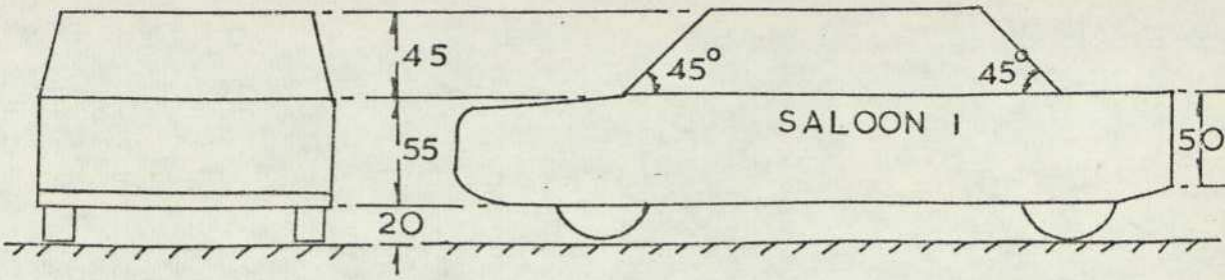

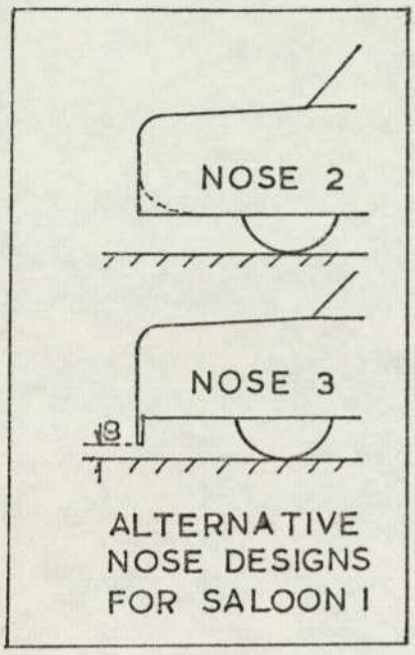

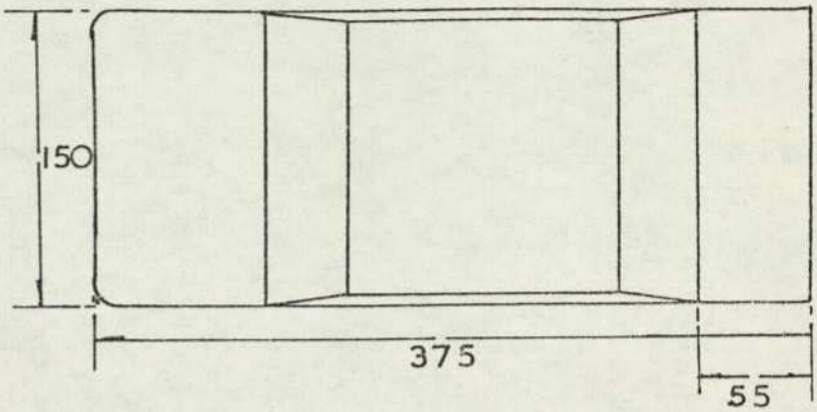

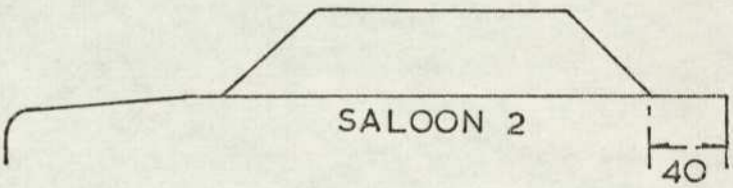

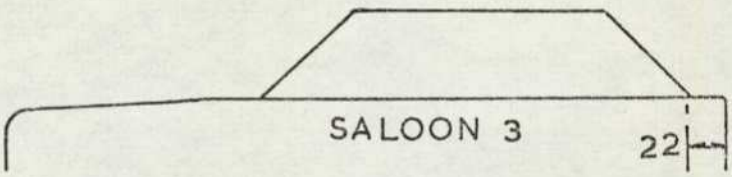

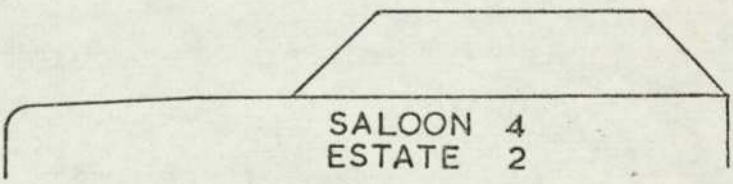

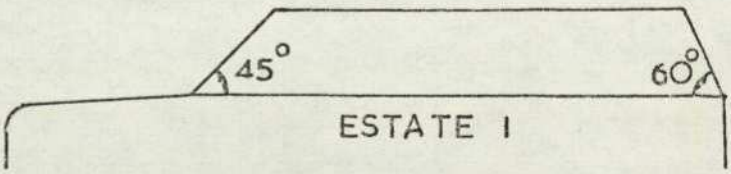

DIMENSIONS
millimetres

FIG.9 PASSENGER CAR MODEL SHAPES

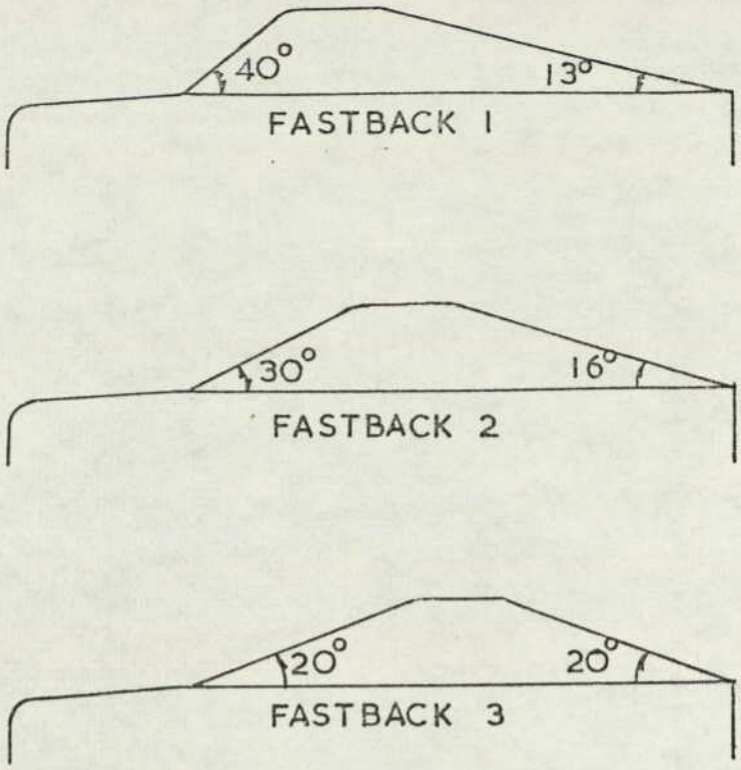

FIG.9(CONT.) FASTBACK MODELS

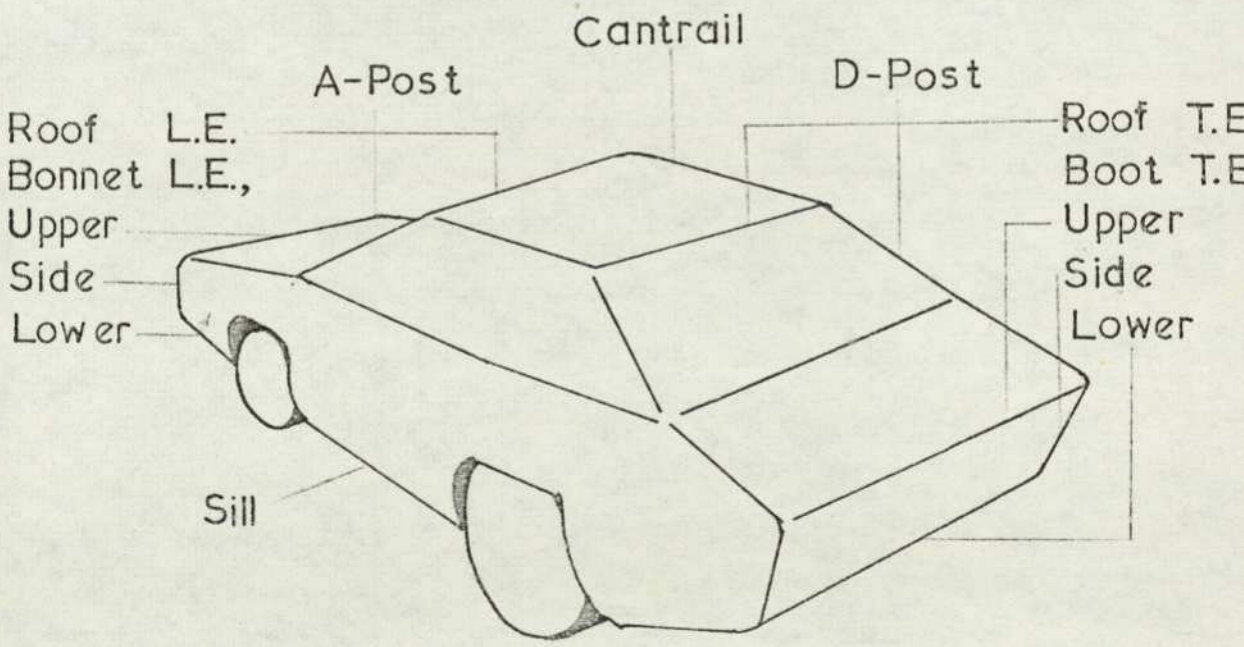

FIG.10 STYLING TERMS

The position of the upper section of the saloon car model was adjustable to give variation in the boot length; these models being designated Saloon 1, 2 and 3 in order of reducing boot length and where Saloon 1 represents the conventional saloon car configuration. By moving this shape completely aft so that no boot is exposed a sporting estate type profile is possible, Estate 2, for comparison with the conventional estate shape, Estate 1. Three fastback models were available giving variable windscreen and backlight slope. All these models have identical principal dimensions of overall length, height and width. The tumble home angle was always 8°. A-posts and D-posts were sharp edged while the cantrail and roof leading and trailing edges were radiused 5mm.

For measurements of interference effects between large and small vehicles three lorry models and three additional car models were built to approximately one twelfth scale. The additional car models were necessary because the internal strain gauge balance used in this experiment required lightweight models of hollow construction. The design of the car models is shown in Figure 11. The upper rear body section is removeable to facilitate changes in body configuration. Three lorries were investigated, having identical cab shape but different container lengths, Figure 11. The cab leading upper and side edges plus the upper longitudinal edges of both lorry and cab were radiused by 10 mm. All other edges were sharp edged. The longest lorry had a pair of rear axles while the other two were fitted with a single one. The rear wheels were mounted to 25 mm square steel tubing running the length of the lorry underside. Only the short model was used in wake measurements. To simulate a lorry at smaller scale for wake measurements at a reasonable distance downstream the rectangular block 1 was fitted with a different nose block of similar width to the block which represented a cab. No further modifications were made to scale the two models.

The variety of racing car configurations is considerable. For this study a type which is known to generate an extreme amount of down-thrust was chosen. As it has fully enclosed bodywork it does not suffer the disturbing effects of wheel rotation. Figure 12 shows the model which typifies the Group 7 Can-Am racing car. It is to the same scale as the other models. All corners were sharp edged except for the curve

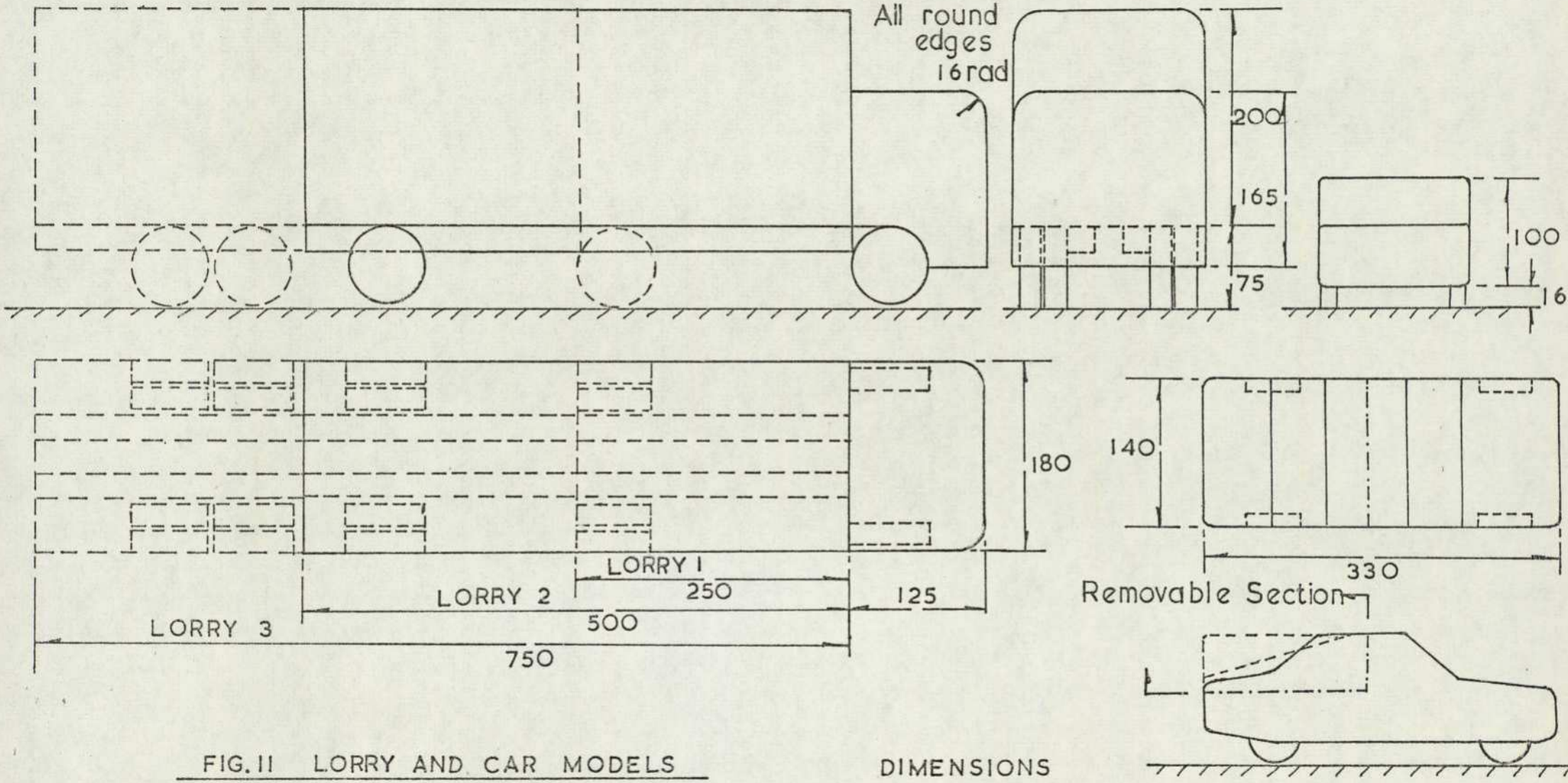

FIG. 11 LORRY AND CAR MODELS
INTERFERENCE TESTS

DIMENSIONS
millimetres

above the front wheel position. The wing was made to approximately Clark Y profile with a thickness to chord ratio of 0.125. No wheels were fitted to the model.

Force measurements were obtained from an overhead balance, except for interference effects data which came from an internal strain gauge balance. The model was mounted on a single strut which was adjustable in length to provide variable ground clearance. In the case of the cambered models a two strut mounting was employed, the model being supported between the struts by an unshielded circular bar, diameter 5 mm. For wake measurements the models were mounted to a strut, 10 mm diameter, which passed through the ground plane and was clamped to a fitting on the underside of the board, giving vertical adjustment. The attitude of the model was adjustable from within the body.

1.4 Wind Tunnel Corrections.

In addition to the problem of ground simulation the flow conditions existing around a model in a wind tunnel differ from those experienced by a body in free air. Spurious forces arise from the confined working section boundaries modifying both magnitude and direction of the flow local to the model.

1.4.1 Static pressure correction.

The presence of a boundary layer growing along the walls of the working section effectively reduces the area of cross section of the jet. This implies that an axial pressure gradient exists which tends to increase the model drag. The effect on normal forces is assumed to be negligible.

For any body the drag coefficient increase, ΔC_x is given by

$$\Delta C_x = \frac{1}{\frac{1}{2}\rho U^2 A} \int_0^l A' \frac{\partial p}{\partial x} \, dx \qquad (1.2)$$

where A is the frontal area of the model, A' is the local area of cross section at x, $\partial p / \partial x$ is the pressure gradient, l is the model length, and U, ρ are free stream velocity and density respectively.

Assuming that $\frac{\partial p}{\partial x}$ is a constant this simplifies to

$$\Delta C_x = \Delta C_p \frac{V'}{Al} \qquad (1.3)$$

where ΔC_p is the change of pressure coefficient over the length of the model and V' is the model volume.

For the rectangular blocks the ratio V'/Al is unity, while for the car models this term is not significantly different, varying between 0.79 for the saloon to 0.87 for the estate cars. The value for ΔC_p is taken from Figure 4.

For all the rectangular blocks

$$\Delta C_x = 0.02$$

For the lorries

$$\Delta C_x = 0.02 - 0.04 \quad \text{depending on length}$$

while for all the car models it is sufficient to take

$$\Delta C_x = 0.017 .$$

1.4.2 Streamline curvature.

The tunnel walls have a restraining influence on the flow curvature around a lifting body. The presence of a ground plane close to the model reduces the change in curvature at the model due to the working section boundaries. This is immediately apparent once the model and its images are replaced by a simple horseshoe vortex system as in Figure 13a. Taking a two dimensional model near to a centrally placed ground plane, for simplicity, and writing $\Delta\alpha$ for the flow angle of incidence correction, then

$$\Delta\alpha = \frac{W}{U} \qquad (1.4)$$

where W is the induced vertical velocity due to all the images outside the tunnel walls (i.e not including the image in the ground plane). The induced velocity arising from the nearest image pairs is given by

$$\Delta W = \frac{\Gamma x}{2\pi}\left[\frac{2}{H_1^2+x^2} - \frac{1}{(H_1+h)^2+x^2} - \frac{1}{(H_1-h)^2+x^2}\right] \qquad (1.5)$$

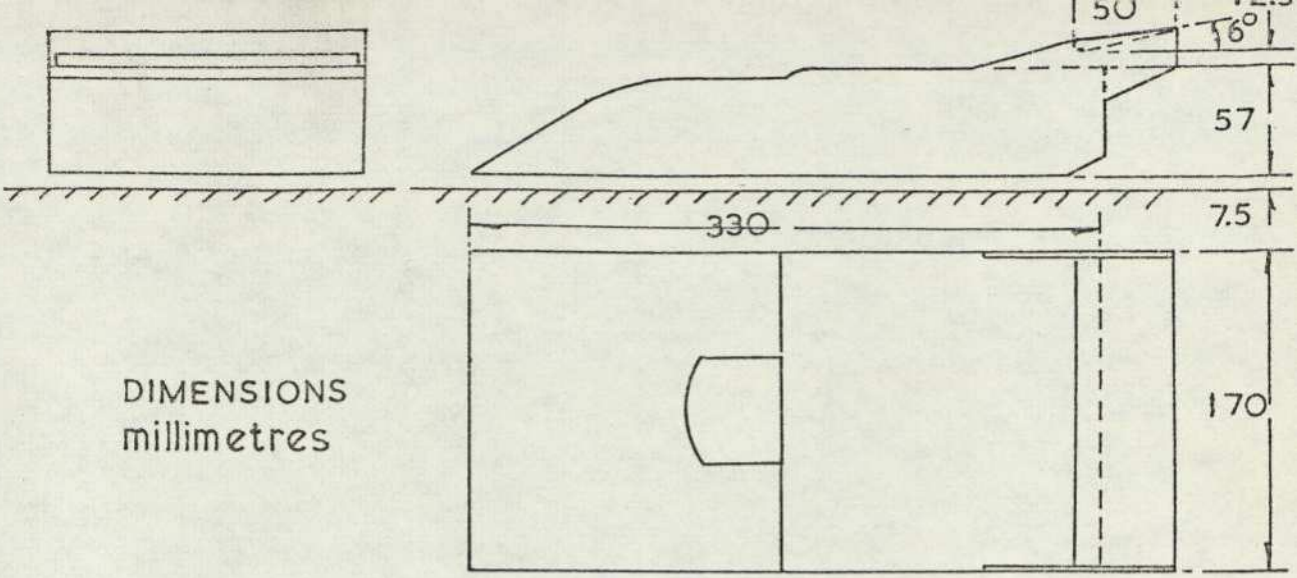

FIG.12 CAN-AM RACING CAR MODEL

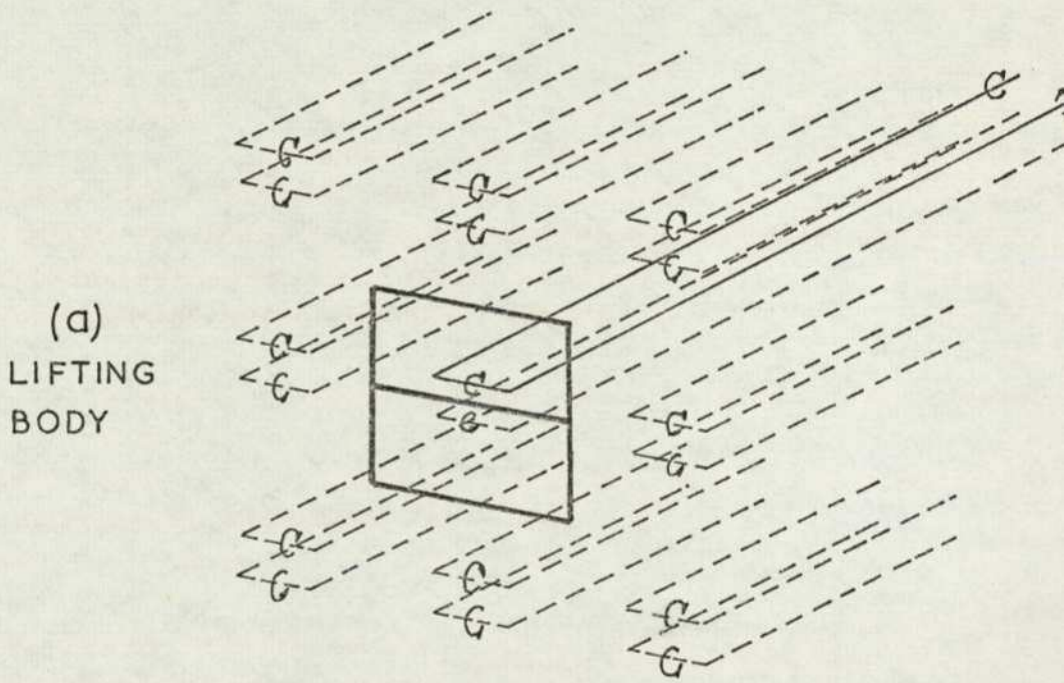

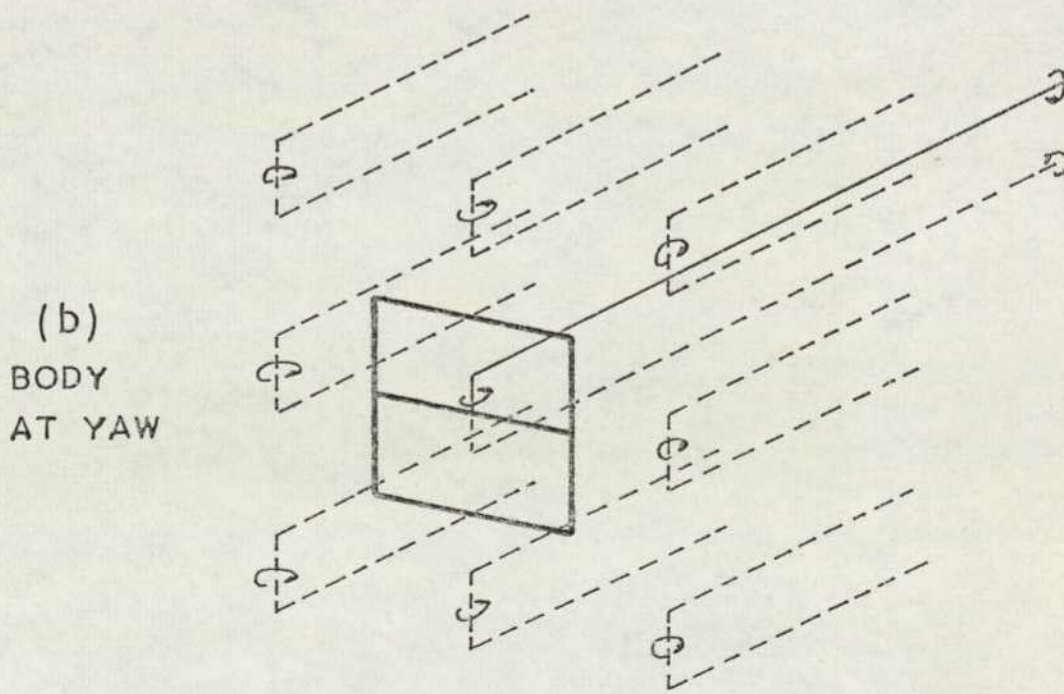

FIG.13 IMAGE SYSTEMS FOR BODIES NEAR TO A GROUND PLANE IN A CLOSED WIND TUNNEL

where Γ is the model vortex strength, for a line vortex situated at a height h above the ground, x is the distance downstream from the vortex position, and H_1 is the tunnel height.

If $h, x \ll H_1$ equation (1.5) can be simplified to

$$\Delta W = -\frac{\Gamma x}{\pi} \frac{3h^2}{H_1^4} \tag{1.6}$$

The induced velocity due to all the external images is then

$$W = -\frac{\Gamma x 3h^2}{\pi H_1^4} \sum_{n=1}^{\infty} \frac{1}{n^4} \triangleq \frac{\Gamma x h^2}{H_1^4} \tag{1.7}$$

For a lifting body, Γ can be replaced from

$$Z = C_z \tfrac{1}{2} \rho U^2 A = \rho U \Gamma b \tag{1.8}$$

where Z is the lift force, b is the span. The flow incidence correction, $\Delta\alpha$ is then given by

$$\Delta\alpha = \frac{1}{2} \frac{h^2}{H_1^4} \frac{Ax}{b} C_z \tag{1.9}$$

Substituting extreme values for ground vehicles;

$$C_z = 1.0$$
$$h/H_1 = 0.1$$
$$A/H_1^2 = 0.025$$

at $x/b = 4.0$

$$\Delta\alpha = 0.5 \times 10^{-3} \text{ rad.}$$

The correction for a horseshoe vortex would be an order of magnitude less and so this is a negligible correction for road vehicle tests and can be ignored.

1.4.3 Downwash correction.

The presence of an infinite array of image horseshoe vortex pairs induces an extra downwash at the plane of the model. It is assumed that the downwash correction arises predominantly from the image vortices in the horizontal plane. The immediately adjacent images induce a downwash velocity, ΔW given by

$$\Delta W = \frac{\Gamma}{\pi}\left[\frac{1}{H+b/2} - \frac{1}{H-b/2} + \frac{2h}{(H-b/2)^2+(2h)^2} - \frac{2h}{(H+b/2)^2+(2h)^2}\right] \qquad (1.10)$$

where H_2 is the tunnel width.

If $h, b \ll H_2$

$$\Delta W = \frac{\Gamma}{2\pi}\left[\frac{4hb}{H_2^3} - \frac{b}{H_2^2}\right] \qquad (1.11)$$

The total downwash, is then

$$W = -\frac{\Gamma}{\pi}\frac{b}{H_2^2}\left[\sum_{n=1}^{\infty}\frac{1}{n^2} - \frac{4h}{H_2}\sum_{n=1}^{\infty}\frac{1}{n^3}\right] \qquad (1.12)$$

Substituting for Γ from equation (1.8)

$$\Delta\alpha = \frac{C_z}{2\pi}\frac{A}{H_2^2}\left[1.645 - \frac{4h}{H_2}1.202\right] \qquad (1.13)$$

which gives $\Delta\alpha = \frac{1}{5}C_z\frac{A}{H_2{}^2}$ for $h/H_2 = 0.07$ (1.14)

where A/H_2 is essentially the solid blockage ratio, B. This gives $\Delta\alpha = 0.005\ C_z$ rad, when B = 0.025, which is negligible for most ground vehicles, which have a low lift coefficient.

1.4.4 Corrections for bodies at yaw.

The ground plane loses its significance when considering corrections for wind tunnel tests on vehicles at yaw because the flow deviations tend to be parallel to the ground surface. For analysis of this case it is convenient to replace the model and its plane image

by a single horseshoe vortex. The corrections then become identical to those for a conventional three dimensional lifting body (see Figure 13b) except that lift is substituted by twice the side force.

From Pope and Harper (1) the boundary induced cross flow angle, denoted here by $\Delta\beta$, is given by

$$\Delta\beta = \frac{V}{U} = k B 2 C_Y (1+\tau) \tag{1.15}$$

where k is a constant for a given tunnel design and varies between 0.10 and 0.15 for a closed jet tunnel depending on cross section shape, B is the ratio of model area to tunnel cross section area except that the 'model' area now includes the image. The term τ is a function of downstream distance. The incremental side force coefficient, is given by

$$\frac{\Delta C_Y}{C_Y} = \frac{-\Delta\beta}{\beta} = -2 k B \frac{\delta C_Y}{\delta \beta} (1+\tau) \tag{1.16}$$

For the models to be tested

$$B = 0.03$$

$$\frac{\delta C_Y}{\delta \beta} \triangleq 5.0$$

and for the tunnel τ will vary between zero at the front wheels and approximately 0.4 at the rear wheels. Denoting the side force at the front wheels by C_{YF} and at the rear wheels by C_{YR}, the corrections become approximately;

$$\Delta C_{YF} = - 0.02 \; C_{YF}$$

$$\Delta C_{YR} = - 0.03 \; C_{YR} \; .$$

At the extreme downstream positions, where $x \sim O(H)$, τ tends to unity and the change in flow direction is given by

$$\Delta\beta = 0.04\beta \tag{1.17}$$

which is not insignificant.

1.4.5 Solid and Wake Blockage corrections.

The stream velocity around a model placed in an enclosed working section is increased by the constraining influence of the wind tunnel walls. This increase in velocity above the reference condition implies that the measured coefficients are in error. If the ratio of incremented velocity to free stream velocity is denoted by ϵ , the corrected coeffecients are given by

$$C_{correct} = \frac{1}{(1+\epsilon)^2} C_{measured} \qquad (1.18)$$

where ϵ is called the blockage correction. In general the blockage includes terms arising from the effects of the body and the wake, although it is common to consider the two together. Numerous derivations of correction terms exist for both streamlined and extremely bluff bodies. Fewer are available for intermediate shapes, representative of road vehicles.

Pope and Harper (1) suggest an empirical correction factor for bodies of unusual shape given by

$$\epsilon = 0.25\ B \qquad (1.19)$$

where the tunnel area represented in B is now the area above the ground plane and assumes prior calibration of the working section with ground installed. Gross and Secksciewski (2) have used this method with satisfactory results and the experiments of Bettes and K elly (3) support its use. Calvert (4) and subsequently Mair (5) compared three existing correction methods for application to blunt based bodies of revolution. The method of Maskell (6) gave the most suitable results for bodies of equivalent fineness ratio to typical road vehicles. Six different correction methods have been investigated by Carr (7) in an experiment using rectangular blocks. It was found that the standard MIRA correction

$$\epsilon = \frac{1}{1 + B} \qquad (1.20)$$

gave the best results.

Sykes (8) independently obtained an almost identical correction factor given by

$$(1+C)^2 = (1+1.9B)^{-1} \qquad (1.21)$$

for similar rectangular bodies. Sykes also showed

that the size of the correction term could be substantially reduced using a simple slotted wall tunnel.

There is a factor of four between the most favoured correction terms. Crude measurements using a pitot-static probe in the vicinity of the lorry model tended to support the argument in favour of the larger correction factor, and so the MIRA expression (1.20) was adopted and applied to all data.

1.5 Conclusions

The use of a fixed ground plane has been justified from the results of previous investigations. These have shown that the use of a moving ground, although more representative of the true boundary conditions, gives results which are significantly in error when compared with tests using a static ground board.

Measurements on the ground plane in the empty tunnel show that the boundary layer growth on the ground is almost identical to that expected for a flat plate.

An analysis of the influence of the tunnel boundaries on flow conditions at the model and in the wake has revealed that for a body at pitch, near to ground, the effect is negligible. This is not true for a yawed vehicle. There is a slight pressure gradient along the working section which introduces a small correction to drag. The blockage effects of a typical model are sufficient to require significant correction. The MIRA blockage correction factor has been adopted.

2. FORCES ON BODIES NEAR TO GROUND

2.1 Introduction

The measurement of aerodynamic loads on bodies in ground proximity has a long history. The data has been mainly derived for wings (see Appendix A) and winglike bodies while little attention has been paid to the problem of bluff or thick bodies near to ground. It was felt that the wake structure would depend on the lift generated by the body and so prior to taking wake measurements the force characteristics of the rectangular blocks at incidence near to ground were determined. This has been extended to cover the effects of pitch angle on typical road vehicle aerodynamic characteristics.

2.1.1 Low aspect ratio bodies

Lift and drag forces and pitching moment measurements for an idealised streamlined uncambered body shape of low aspect ratio (0.365) and large thickness (21%) in ground effect were made by Stollery and Burns (9). Reduction of ground clearance increased lift curve slope while the influence on drag was only significant at negative incidence when separation on the lower surface occurred. The forward shift of the aerodynamic centre and the increase in C_{Mo} with reducing ground clearance suggested the effects were similar to the introduction of negative camber. Provision was made on the model for progressively blunting the trailing edge. In free stream the blunting had negligible effect on lift, but drag increased due to the extra base drag. The aerodynamic centre shifted forwards with blunting but as a ratio of actual length this direction was reversed. The effects of ground proximity were found to be similar to those for the streamlined shape. The body does not represent typical road vehicles because of excessive underbody curvature, very small ground clearances, giving lift forces which are too negative and drag forces which tend to be too low.

A similar type of body having planform aspect ratio, 0.256, was investigated by Carr (10). Variations in thickness, from 9% to 27%, were studied and for the thickest model the camber could be modified to give an essentially flat lower surface. The uncambered models showed that lift curve slope was practically independent of thickness, although non linearities were noticeable with the thinner sections at lowest ground clearances. Thickness was found to have no effect on the induced drag although ground clearance had a strong influence. Results with the cambered models at zero incidence showed a rearward shift of the centre of pressure. The influence of the ground was again found to be similar to an

induced negative camber, although there was little change in the location of the aerodynamic centre. Flow visualisation revealed that streamwise vortices on the side edges tended to suppress underflow separation aft of the minimum ground clearance position. With the model streamlined in planform instead of side elevation, a larger drag was experienced on approaching the ground, side force slope with yaw increased while yawing moments were very small. The same criticism can be levelled against these models as against the earlier one although it should be remembered that the purpose of the testing was to establish links between aerofoil testing and typical vehicles by reduction of the former to aspect ratios typical of the latter.

Waters (11) has investigated lift drag and pitching moment on a 40% thick body with elliptical side profile and planform aspect ratios of 1.0 and 0.58. The bodies could be halved in thickness to give a flat bottomed section. The lift curve slope, as expected, increased with reducing ground clearance, but at very low clearances some geometrics exhibited a reversal in slope. Drag force variation with ground clearance was found to be dependent on the type of body. The full elliptical body and the half ellipse with flat surface uppermose experienced a drag which varied inversely with clearance. Inverting the half body gave a drag reduction with decreasing clearance due possibly to the influence of vortices forming along the salient edges. Reducing the ground clearance also lowered the induced drag.

To represent high speed ground transport vehicles Grunwald (12) has measured the aerodynamic characteristics of a number of slender bodies in ground proximity. Length to width ratios between 5.0 and 10.0 were studied, the ratio depending on the cross section. Most of the testing was done at yaw but the effects of incidence were investigated for the bodies at certain ground clearances, using moving and stationary ground techniques. The lift variation was found to be highly dependent on cross section; a circular section giving the lowest and the semicircular shape with a flat base the largest change in lift due to incidence. The moving ground gave higher results compared to the stationary belt but as the boundary layer on the latter is relatively deep, the results could be unrepresentative. The lift curve slope was also found to increase at yaw.

2.1.2. Effects of pitch on road vehicles.

A vast quantity of literature, has understandable been built up over the years, examining the influence of yaw on road vehicles. Surprisingly little attention has been devoted to the subject of forces arising from flow and attitude changes in the vertical plane. An angle of incidence between a vehicle and the external flow can occur.

for a number of reasons. The wake of a lifting body contains transverse velocities so that when two vehicles are in close proximity the downstream one will experience an effective incidence. Can-Am racing, in America, using cars typically shaped like the model shown in Figure 12, has produced three frightening accidents in which one car following closely behind another has experienced a pitching moment sufficient to turn the vehicle completely over (13). A vehicle in isolation can be subjected to a vertical component of the natural wind, especially where the road passes through a cutting, over an embankment or bridge, or near to a large building. The vehicle will itself adopt a pitch angle when the weight distribution differs from the design value. Janssen and Hucho (14) have shown that allowable weight distributions produce incidence variations exceeding 3.5 degrees. Inertial forces similarly have a pitch effect, which can be greater than $\pm$ 2 degrees under normal braking and acceleration, Ellis (15). A few brief studies of the effects of incidence have been performed, usually dealing with racing cars. Larrabee (16) measured the lift curve slope on a one twentyfifth scale Corvette Coupe and obtained $\delta C_z / \delta \alpha = 4.5$ rad^{-1}. Janssen and Hucho (14) found lift slopes between 2.25/rad and 4.5/rad for three vehicle types, and considerable drag variation was also shown to exist. Simplified models of a saloon car and a sports car were tested by Stafford (17) who found $\delta C_z / \delta \alpha$ values of 5.0 and 4.0 respectively. The lift on a saloon, Can-Am, and a formula 1 car model has been measured by Wright (18). Based on full scale vehicles travelling at 150 m.p.h, the lift per degree was quoted as 100 lbf, 225 lbf and 65 lbf respectively which based on typical frontal areas would give lift slopes of 5.5, 19.0, and 6.0 per radian in each case. Pothoff (19) has shown that the value of $\delta C_z / \delta \alpha$ for a typical sports racing car approaches 6.0/rad with the front wheel lift exceeding this figure and the rear wheel lift decreasing with increasing incidence. A similar type of vehicle tested by Stollery and Burns (9) gave a result 25% higher while a model of Donald Campbell's Bluebird was found to have a lift slope of 6.0/rad. Korff (20) in tests on the Goldenrod land speed record car found that the lift curve slope varied between 0.4/rad and 0.0/rad depending on the nose design although the wheels on the model were not fixed relative to the ground and could have produced spurious results. In some tests on a small racing car the author found that varying the nose profile and the addition of canard wings made negligible difference to the lift curve slope of 4.5/rad, see appendix.

2.2 Force measurements on rectangular blocks at incidence

2.2.1 Reynold's Number effects.

The measurement of forces on rectangular blocks in ground proximity and at incidence was originally undertaken to provide reference data for comparison with the wake studies using similar blocks under identical conditions. This applied to blocks 1N, 2N, 3N, 9C. The results appeared to be of general interest so the range was extended to cover variations such as edge radiusing, thickness ratio, length ratio, and camber.

The models were mounted on a single strut to an overhead balance. The pivot point of the mounting was at the mid-length of the model and was identical in location to the support pivot used for the wake studies. Height variation was obtained by adjusting the strut length. Lift and drag forces and pitching moment were measured, as was the ground board pressure distribution. The axes and notation system employed are shown in Figure 14, with coefficients based on frontal area, and model length. The nominal speed in the working section was always 30 m/s unless stated otherwise and all results have been corrected for blockage effects only using the MIRA system as discussed in Chapter 1, equation (1.20).

The effect of small variation in Reynold's number, based on overall length, on the drag coefficient of various blocks, in free stream, at zero incidence, is shown in Figure 15. The nominal running speed corresponds to a Reynolds number of 0.65×10^6. Considerable reduction in drag coefficient is apparent for all bodies on increasing speed, the rate of change depending on body geometry and slightly less on edge effects. The lower the model span the more critical the Reynold's number problem becomes, although the results seem surprising for these sharp edged bodies which would be expected to show little influence of Reynold's number.

2.2.2 Effect of edge radius.

The effect of an edge radius on the aerodynamic characteristics of blocks 1,2 and 3 in ground proximity was determined. Because of similarities between the results for all three blocks only the data derived for block 2 is presented. The ground clearance as measured at the mid-length was varied from 2.5 mm to 50mm for each block and a reference free stream condition was obtained with the model mounted on the tunnel centre line in the absence of a ground plane. Figure 16

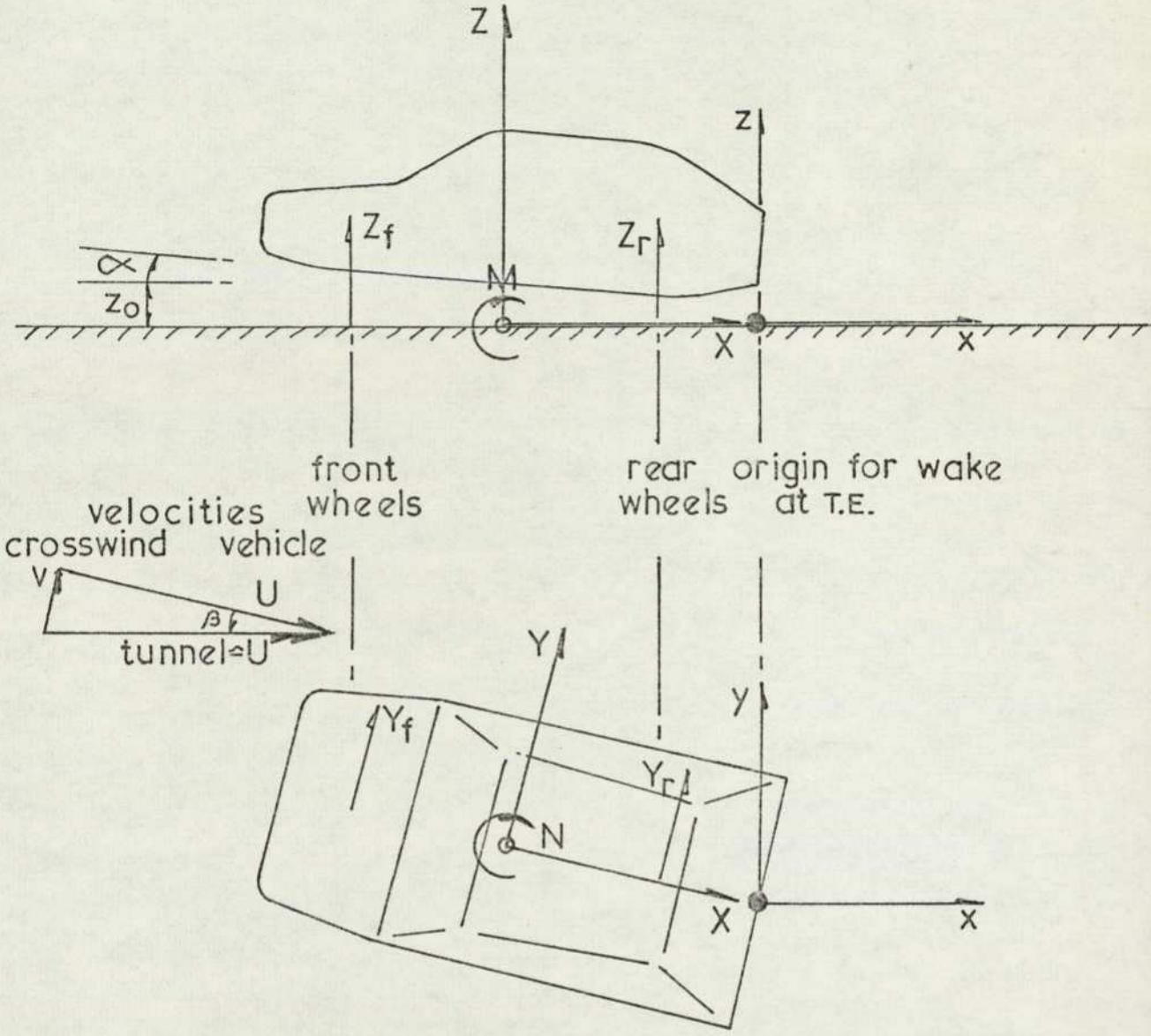

BLOCKS Alternative axis system

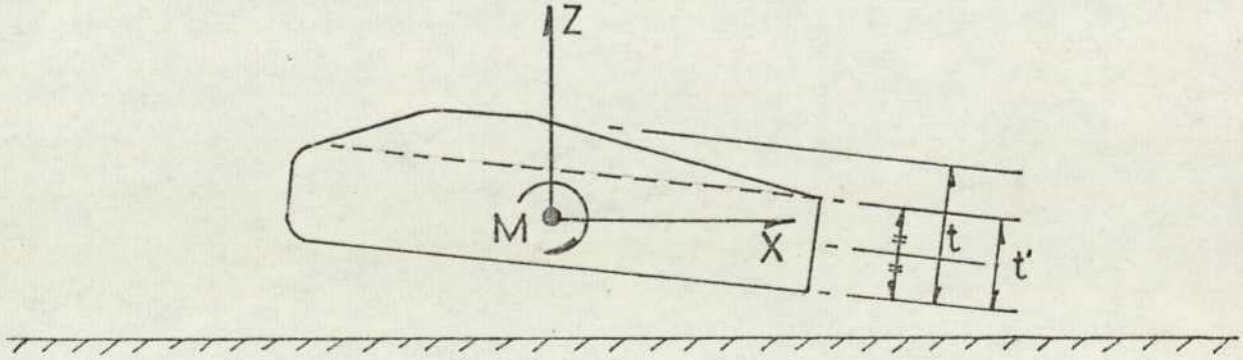

FIG.14 AXIS SYSTEM

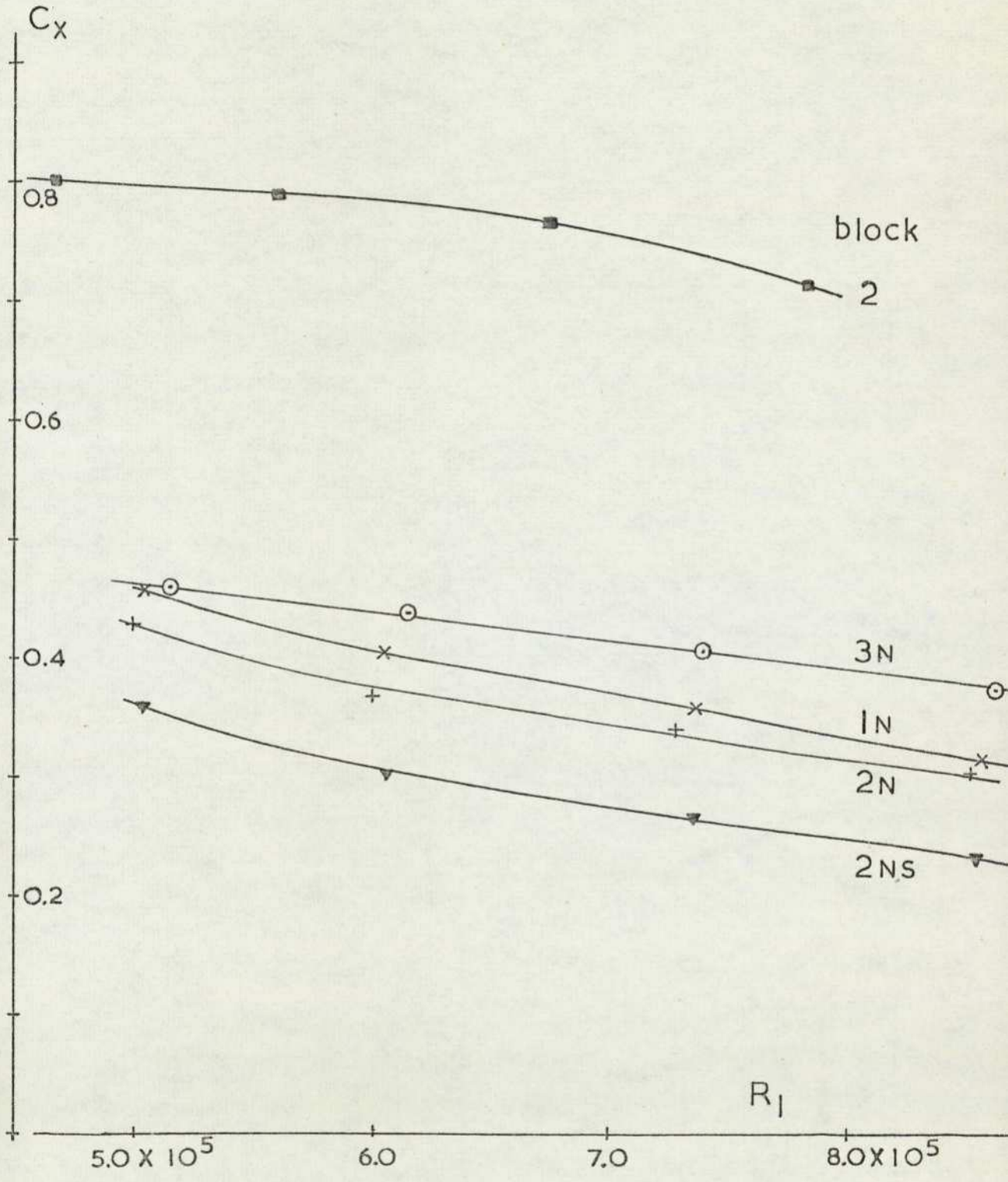

FIG.15 EFFECT OF REYNOLDS' NO. ; FREE STREAM

shows the results of varying incidence and ground clearance, for blocks 2,2N and 2NS, where block 2 is the basic body with all edges sharp; block 2N is fitted with a nose block to give the upper and lower leading edge a radius of 25mm , and block 2NS has additional side plates, increasing the span by 25mm , which give the upper and lower longitudinal and side leading edges a radius of 12.5mm . The trailing edges were always sharp edged.

In figure 16(a) the change of lift with incidence is seen to increase dramatically with reducing ground clearance. A high degree of linearity exists in all cases, although the divergence at higher incidence increases with reducing ground clearance. Changes to the edge conditions appears to have only a very slight effect on the lift especially at positive incidence. At the lowest ground clearance, for which incidence variation was possible, all the blocks show a reversal in the lift slope, which indicates a separation of the flow from the model or the ground. The basic model, 2, behaves similarly at all ground clearances although the effect is less marked as the clearance increases. All models, near the ground, exhibit a slight negative lift at zero incidence, except at the minimum clearance when a positive lift results from the blocking of the flow in the gap between body and ground.

The influence of edge conditions on drag is more noticeable as would be expected, Figure 16 (b). The basic model drag appears to be virtually independent of ground clearance, when in ground proximity, showing the dominating effect of the flow separation, although the free stream case has substantially less drag. Adding the nose reduces drag considerably and introduces a dependence on ground clearance, the drag reducing with increasing clearance. Radiusing the side edges reduces the drag further although the reduction is less, especially at larger clearance. The minimum drag incidence becomes increasingly negative with ground clearance for all tests although the free stream case must obviously be symmetrical. Comparing blocks 2N and 2NS appears to give an additional drag, due to edge effect, which is constant for all incidence but is dependent on ground clearance.

The induced drag can be deduced from Figure 16(c), where the effective lift coefficient, C_{z_1}, plotted, is given by

$$C_{z_1} = (C_z - (C_z)_{C_{x_{min}}})$$

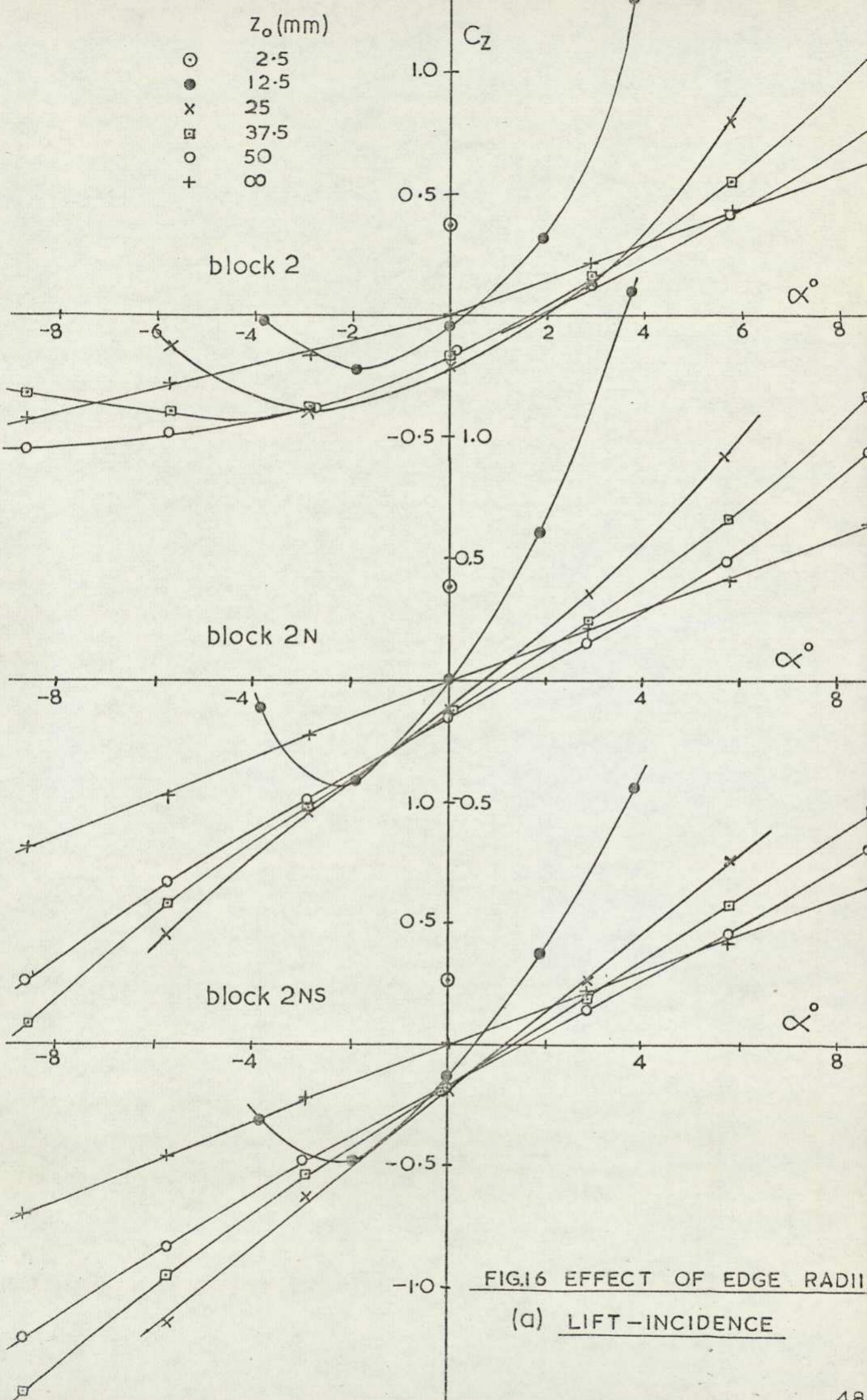

FIG.16 EFFECT OF EDGE RADII

(a) LIFT – INCIDENCE

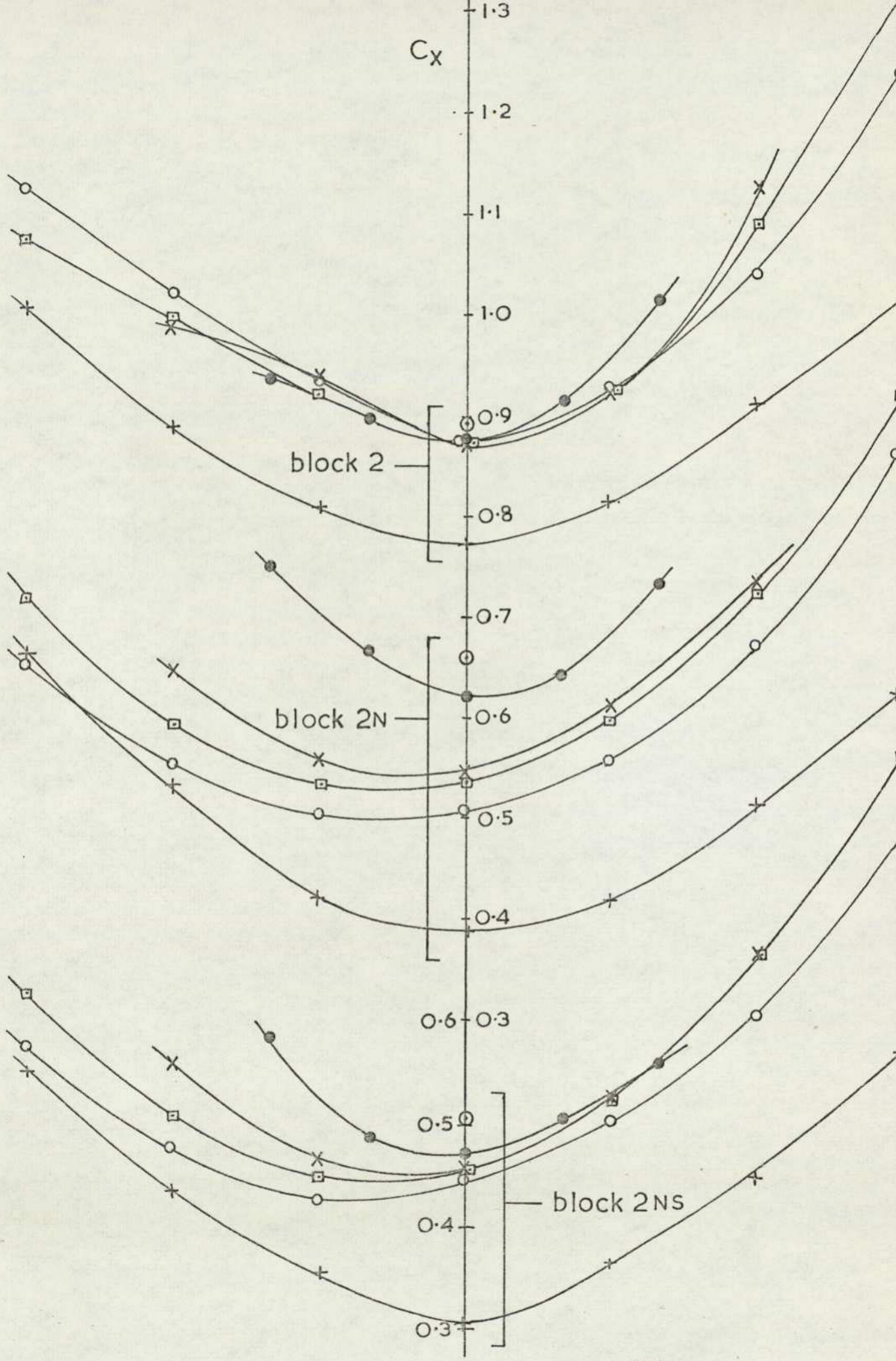

FIG 16(b) DRAG–INCIDENCE

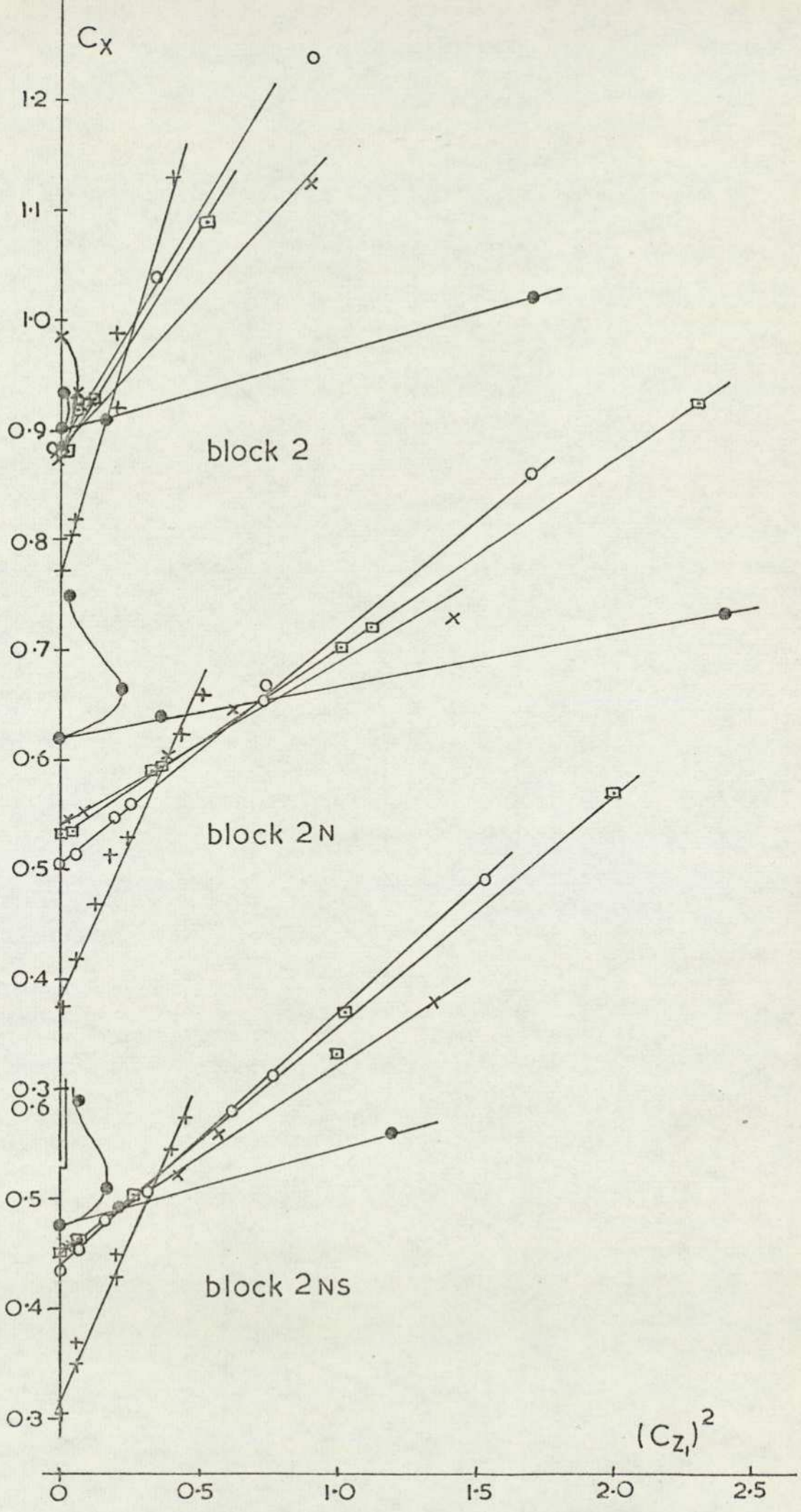

FIG.16(C) INDUCED DRAG

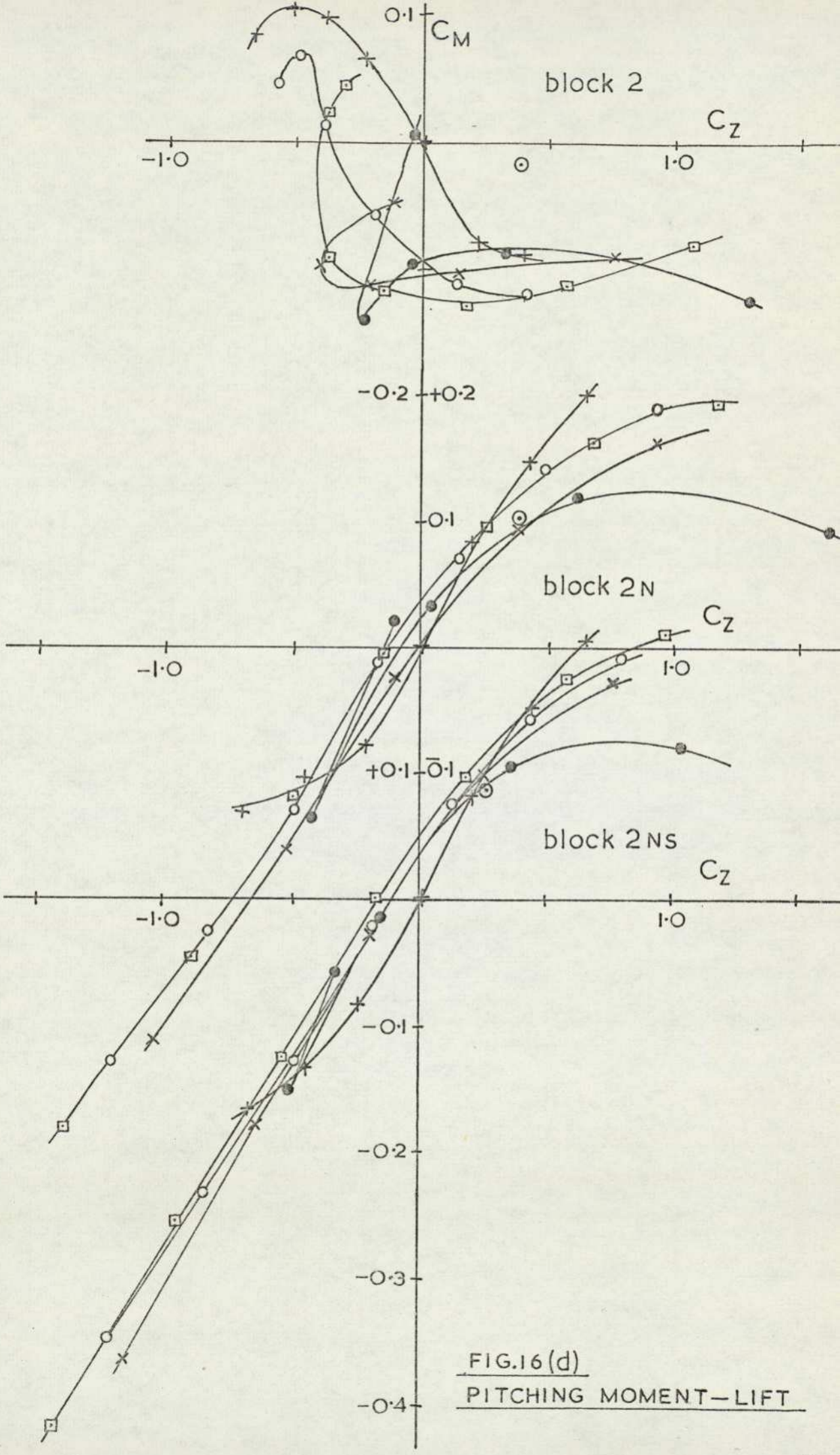

FIG.16(d)

PITCHING MOMENT—LIFT

C_z being the actual lift coefficient and $(C_z)_{Cx\ min}$ is the lift coefficient at the minimum drag incidence. The drag due to lift is reduced with ground clearance. Block 2 experiences approximately twice the induced drag of the other two blocks which differ only slightly. Figure 16 (d) plots the pitching moment versus lift. Ground proximity and variation in the clearance produce very little change in the curve slope, the aerodynamic centre moving aft by 15% of the length between the free stream and the near to ground condition.

2.2.3 Influence of Planform aspect ratio.

The aerodynamic characteristics of Blocks IN and 3N are shown in Figure 17(a)-(d). Comparison with the data for block 2N from Figure 16 gives three different planform aspect ratios from 0.33 to 1.0 with constant thickness to length ratio of 0.33. Increasing the span increased the lift curve slope approximately proportional to span while the zero incidence lift coefficient ramains nearly equal for all three blcoks at a given ground clearance. This is not true at minimum clearance where the lift coefficient increases with span. The curves of drag coefficient against incidence show that in free stream conditions only small differences exist. On reducing the ground clearance the model with the lowest aspect ratio shows considerably greater changes in coefficients than the higher ratios. At the same time the minimum drag incidence changes more rapidly with increasing span. The induced drag curves show similar features to those for the blocks 2. Increasing of the span is seen to noticeably reduce the drag due to lift. The pitching moment characteristics of block 3N are almost identical to those of block 2N. Block IN, however, while demonstrating similar slopes at negative lift, has a considerably greater spread of data at zero and positive lift, although the increase of scale should be noted.

2.2.4 Modifications of thickness to length ratio.

Additional variations in planform aspect ratio were obtained by modifying the length of the models, while maintaining the width to height ratio (base aspect ratio) constant and equal to that of block 2. The planform aspect ratios obtained were 1.0 (block 6N) and 0.5 (block 7N). Figure 18(a)-(d) shows the aerodynamic characteristics of both bodies at incidence and in ground proximity. The longer body experiences a greater degree of non-linearity of lift to incidence, and the underbody flow breaks down at considerably lower incidence. Free stream lift for both bodies is

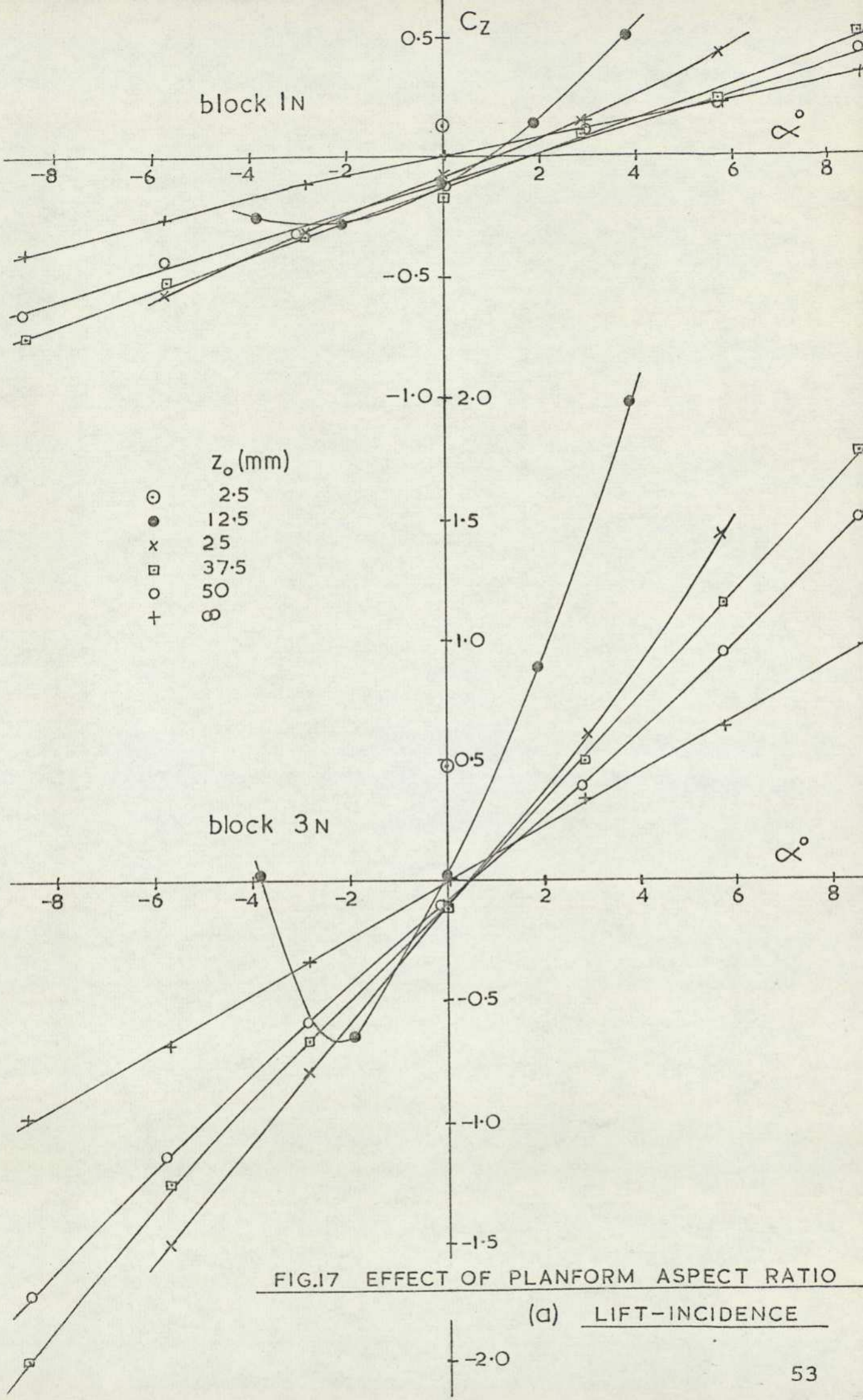

FIG.17 EFFECT OF PLANFORM ASPECT RATIO

(a) LIFT-INCIDENCE

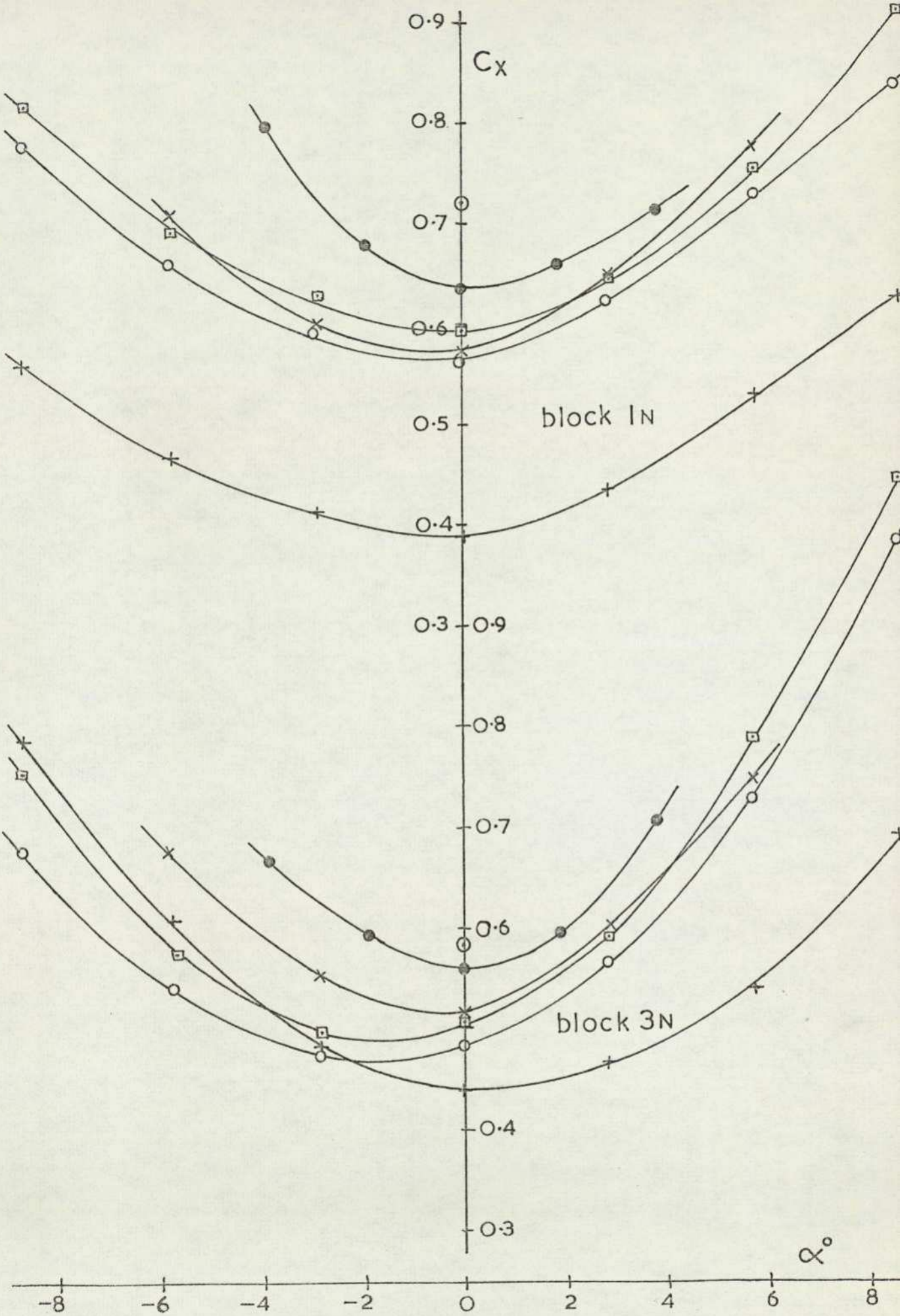

FIG.17 (b) DRAG—INCIDENCE

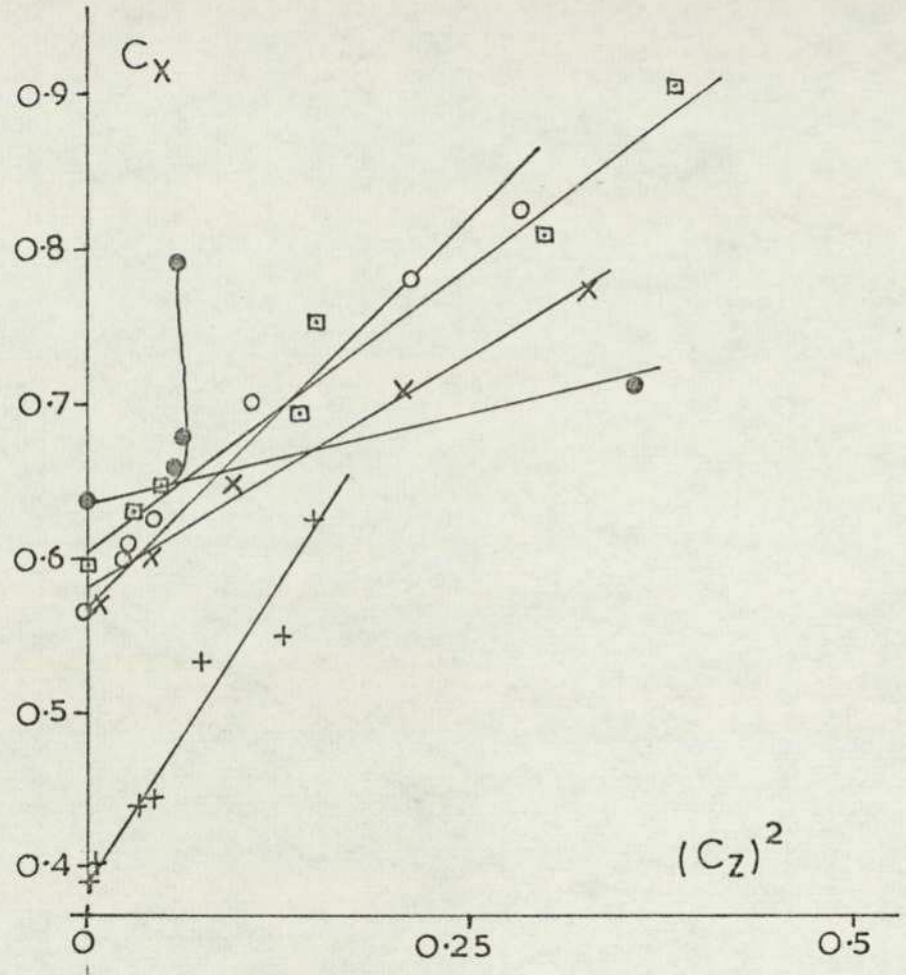

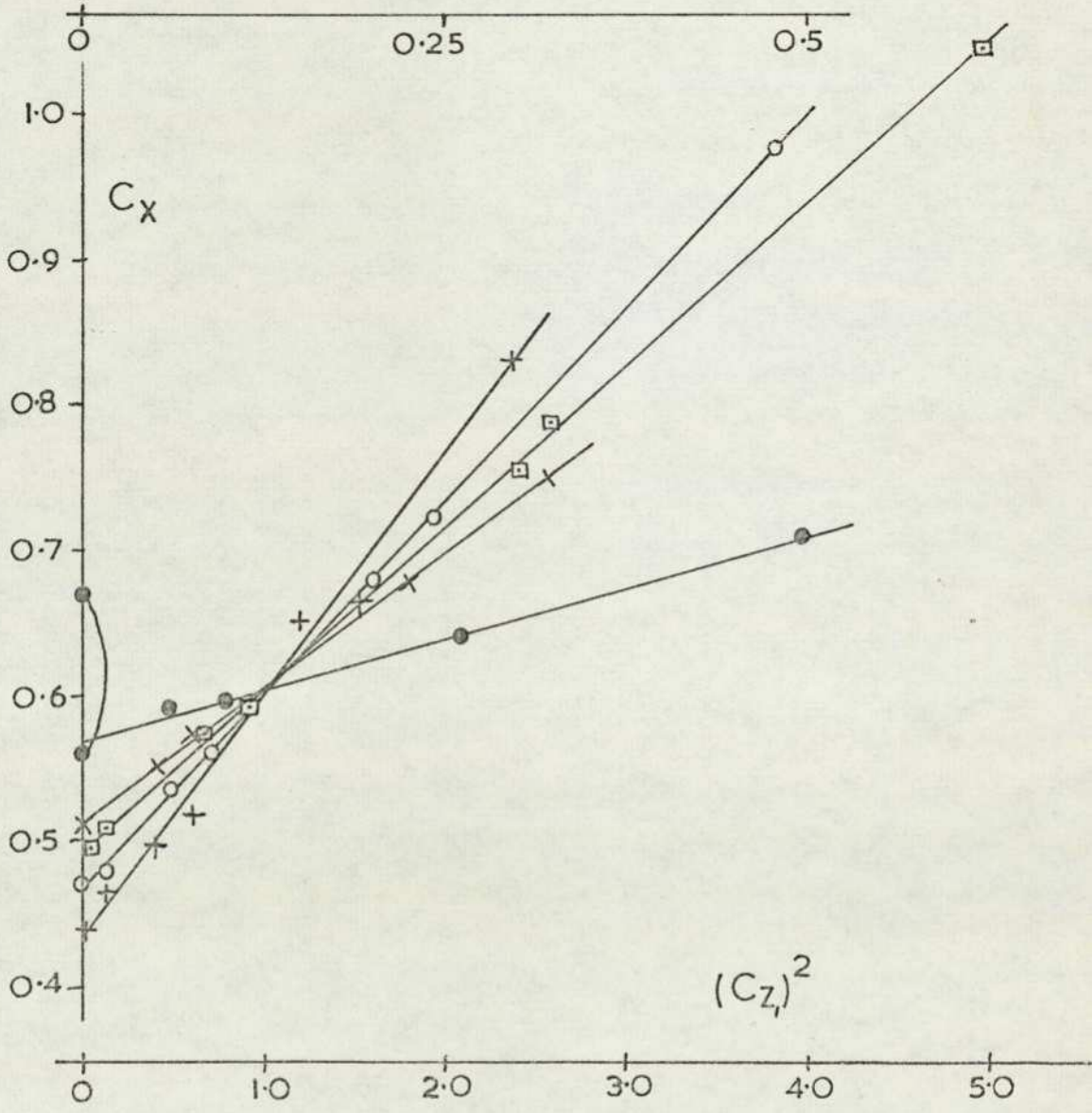

FIG.17(C) INDUCED DRAG

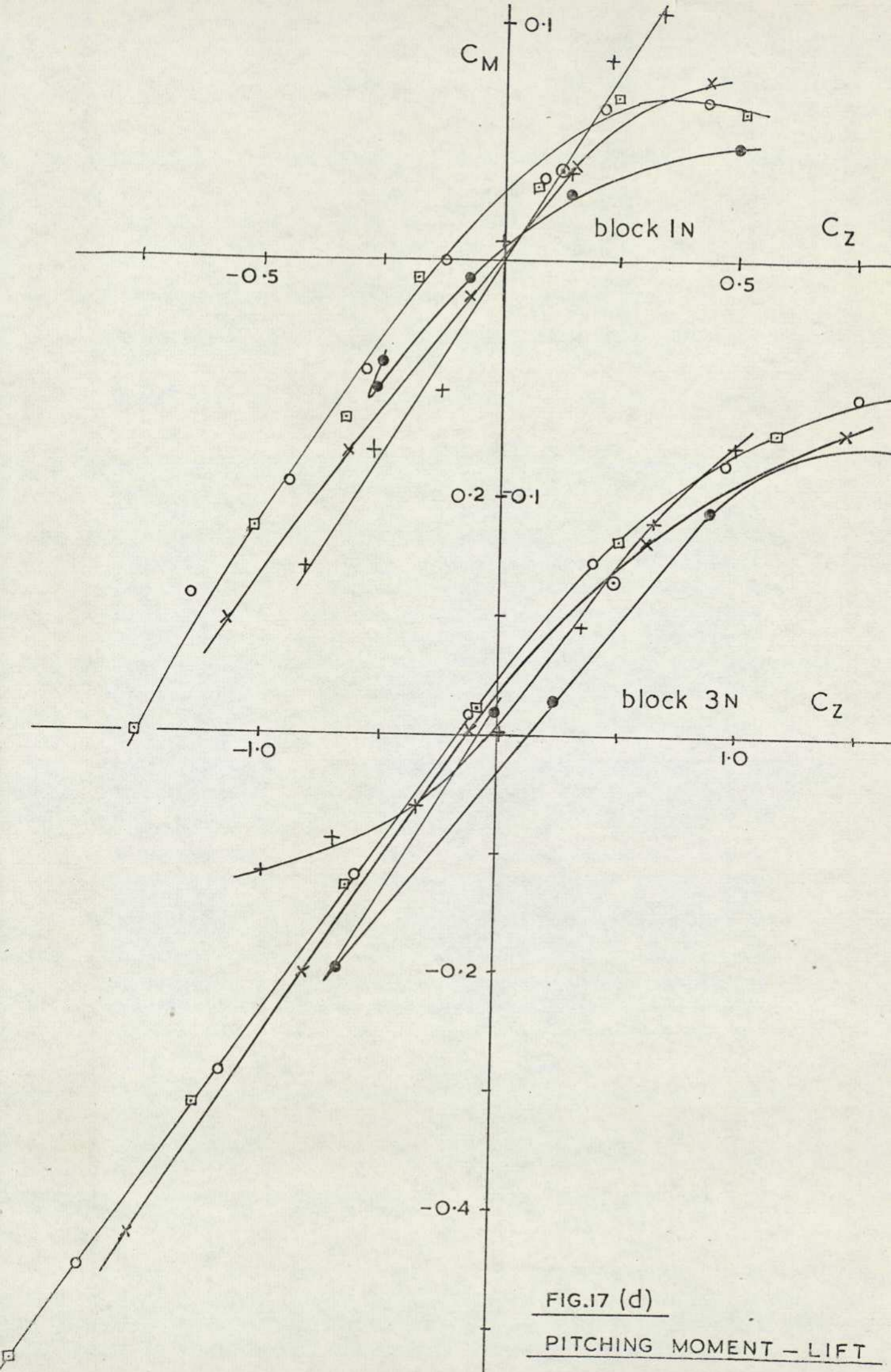

FIG.17 (d)

PITCHING MOMENT – LIFT

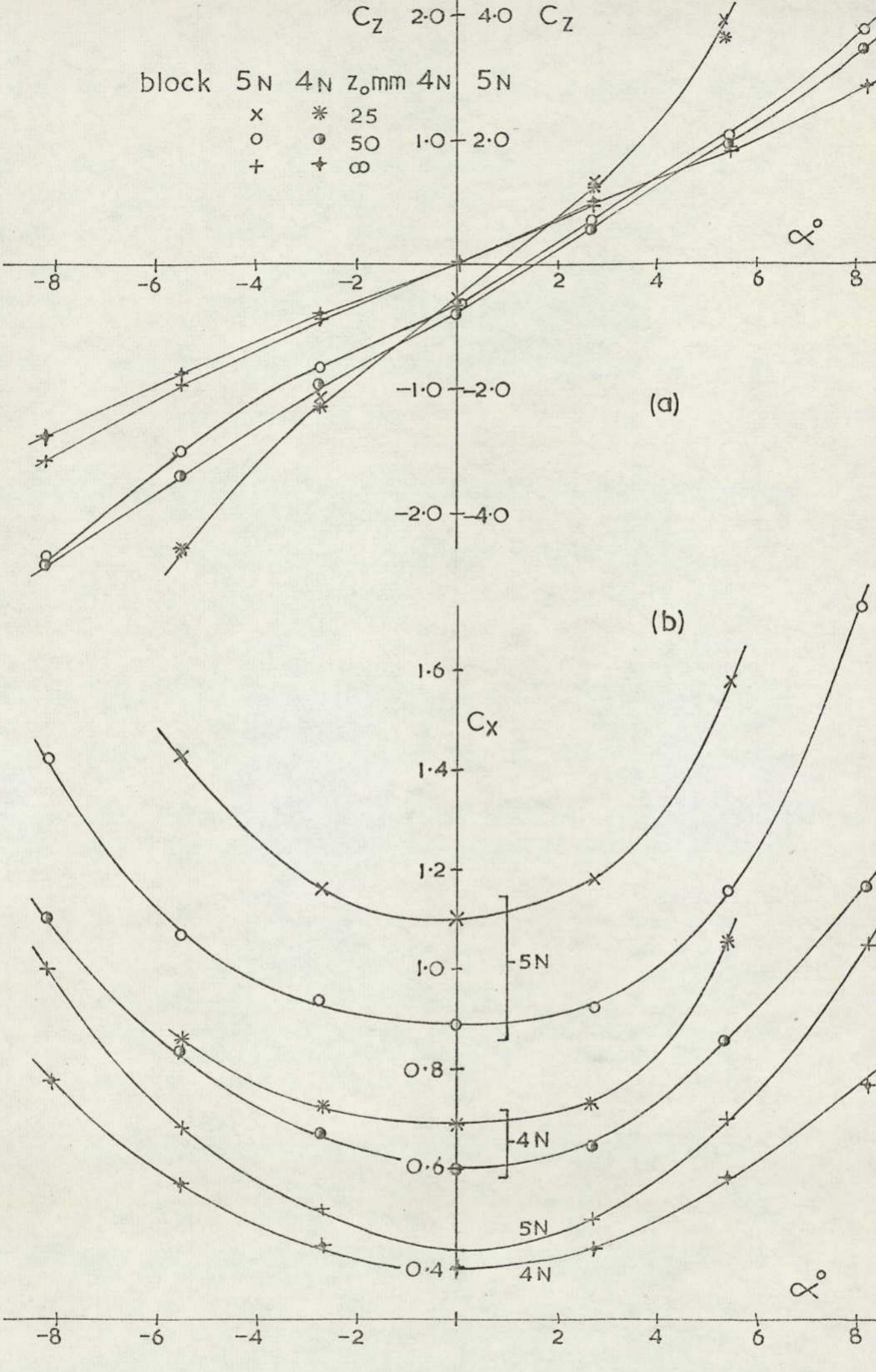

FIG.18 EFFECT OF THICKNESS (a) LIFT-INCIDENCE
(b) DRAG-INCIDENCE

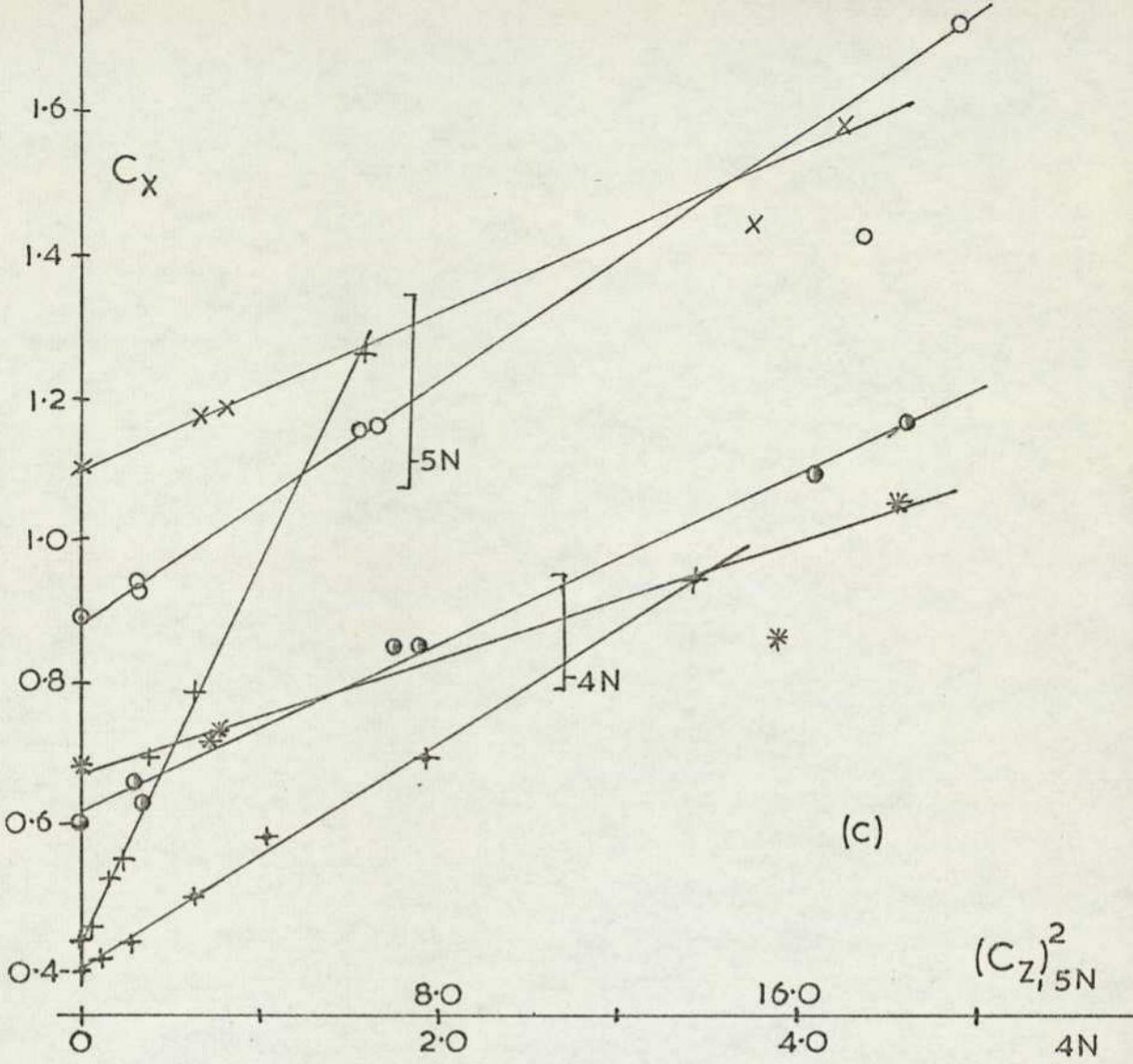

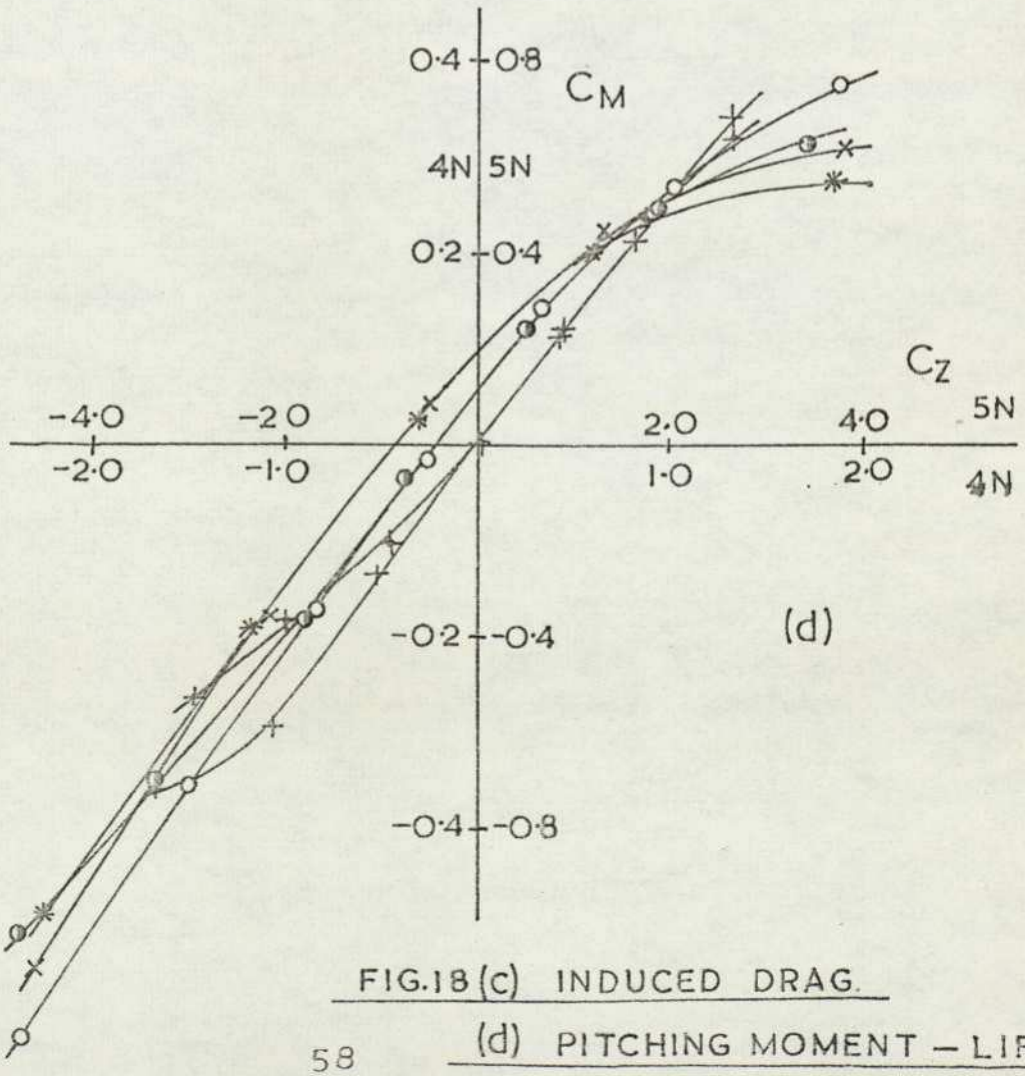

FIG.18(c) INDUCED DRAG.

(d) PITCHING MOMENT — LIFT

identical which is expected from slender body theory, but as the ground is approached the lift curve slope increases with increasing body length. Identical drag measurements are obtained in free stream for both bodies and the same is true at the highest ground clearance tested. At lower clearances, however, the shorter body experiences considerably greater drag coefficient. The minimum drag for block 6N is comparable with that for block 2N although the incidence at which minimum drag occurs appears to be more positive. The induced drag for both cases is similar, although as always, there is a spread of data points, which allow considerable choice for the interpretation of slope. Curves of pitching moment against lift for both blocks give only a limited linear region, the longer body producing non linearity from its earlier proximity to the ground and the shorter body suffering from its lack of length.

Further variation in thickness to length ratio was available by modifying the thickness of the block while maintaining a constant planform aspect ratio, equal to that for block 2N. The two additional blocks investigated had base aspect ratios of 4.0 (block 4N) and 8.0 (block 5N) The lengths were similar to that of block 2N while the edge radius on the upper and lower leading edge remained at 25% of body thickness. Only two ground clearances were studied besides the free stream case and the results are shown in Figure 19 (a)-(d). The lift coefficient increases considerably on reducing thickness, although it can be seen that if the results were based on planform rather than frontal area, the coefficients would then be virtually identical for all three blocks of identical planform. This suggests that in the presence of the ground the effects of thickness are negligible. The drag curves again show very high coefficients of drag on reducing the thickness when in ground proximity although the free stream curves are very similar for all blocks. The lower frontal area exaggerates an almost constant force, arising from the flow through identical gaps between body and ground, into a large additional coefficient. The induced drag curves for the free stream case show a reduced slope on reducing the thickness and at a given ground clearance the slope appears to be reduced by a similar ratio. The pitching moment curves are identical for both bodies, if, as before, the coefficients are based on planform area. Note that as plotted the coefficients are based on frontal area.

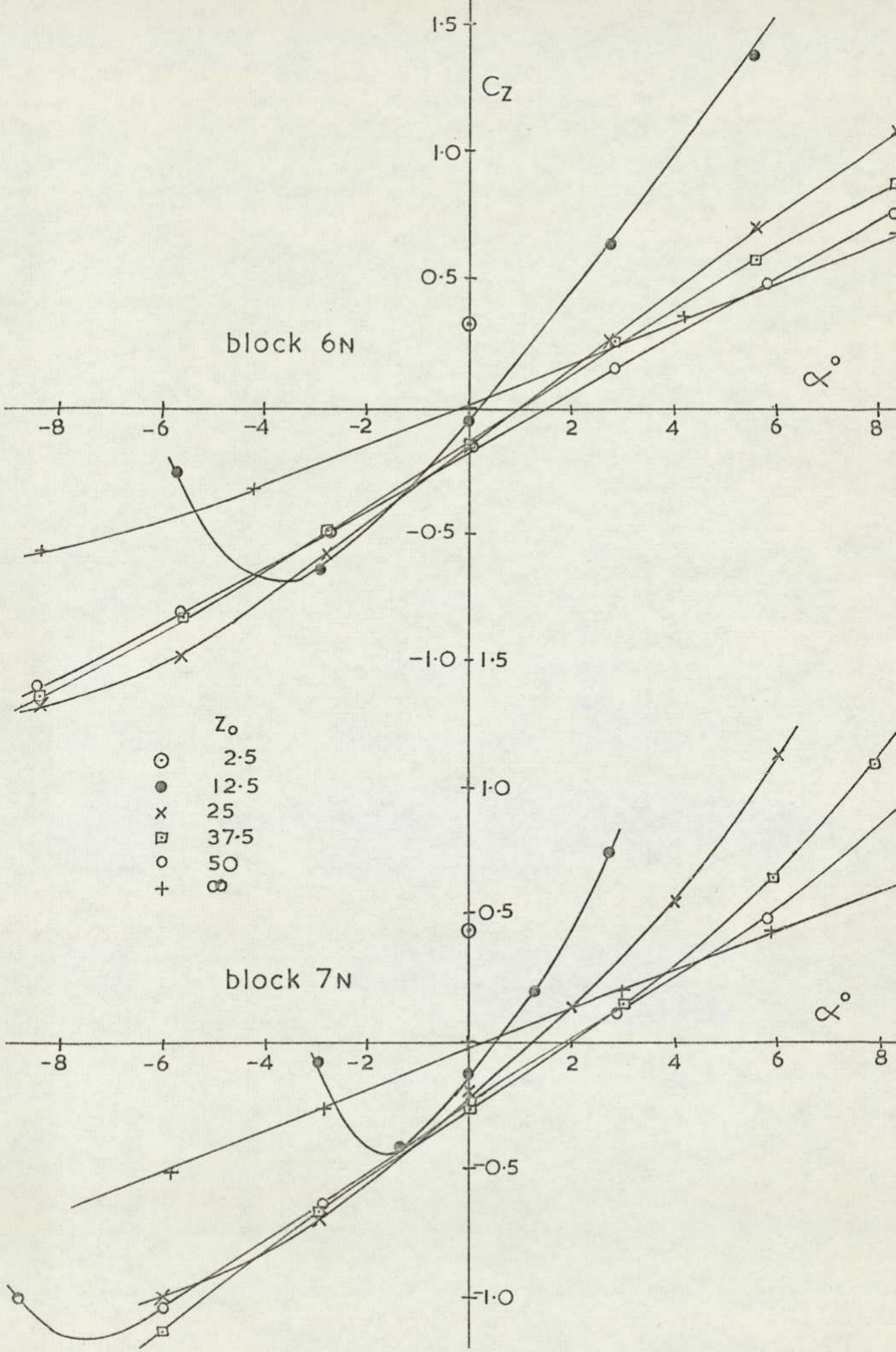

FIG.19 EFFECT OF LENGTH

(a) LIFT-INCIDENCE

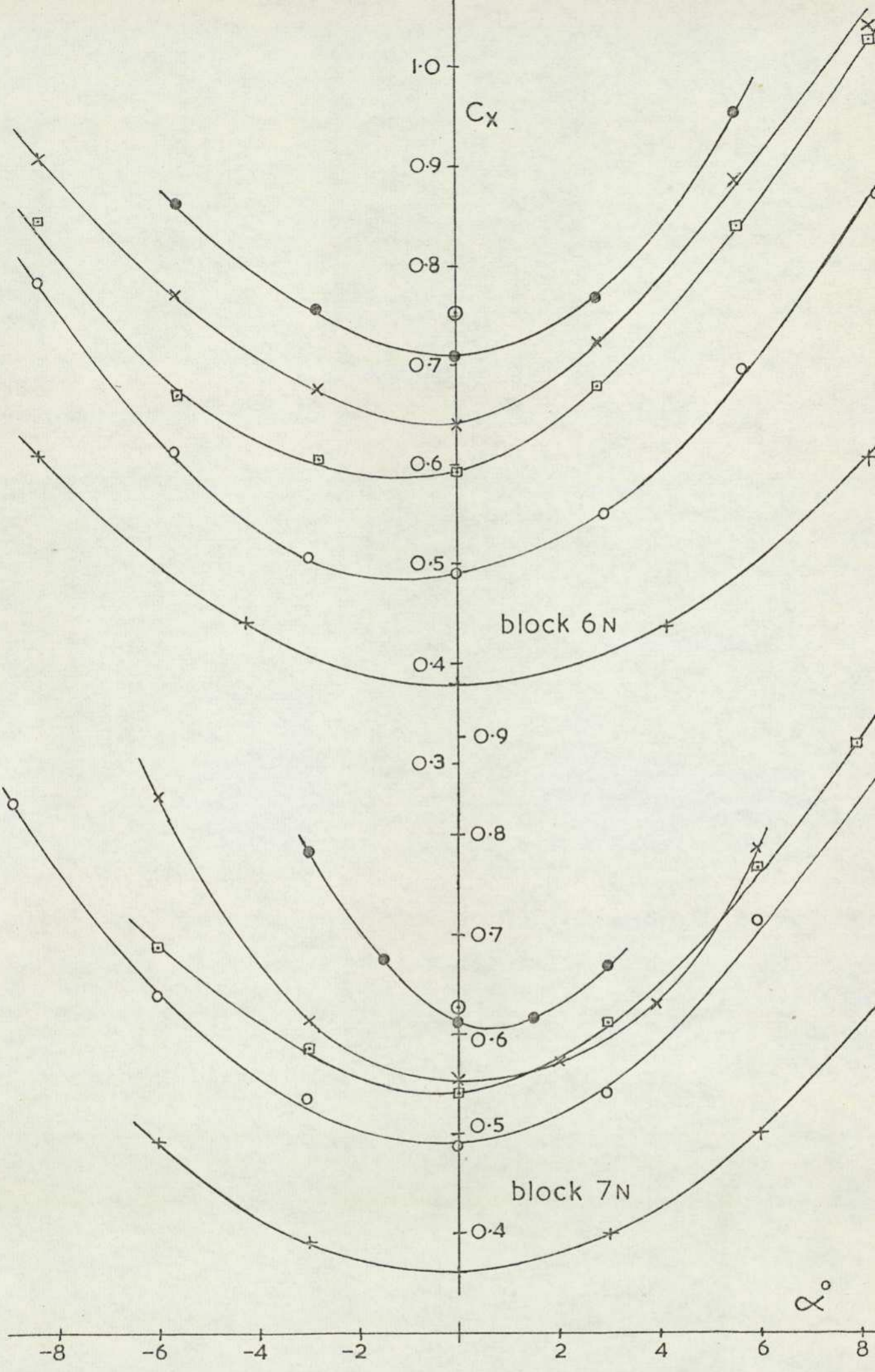

FIG.19(b) DRAG-INCIDENCE

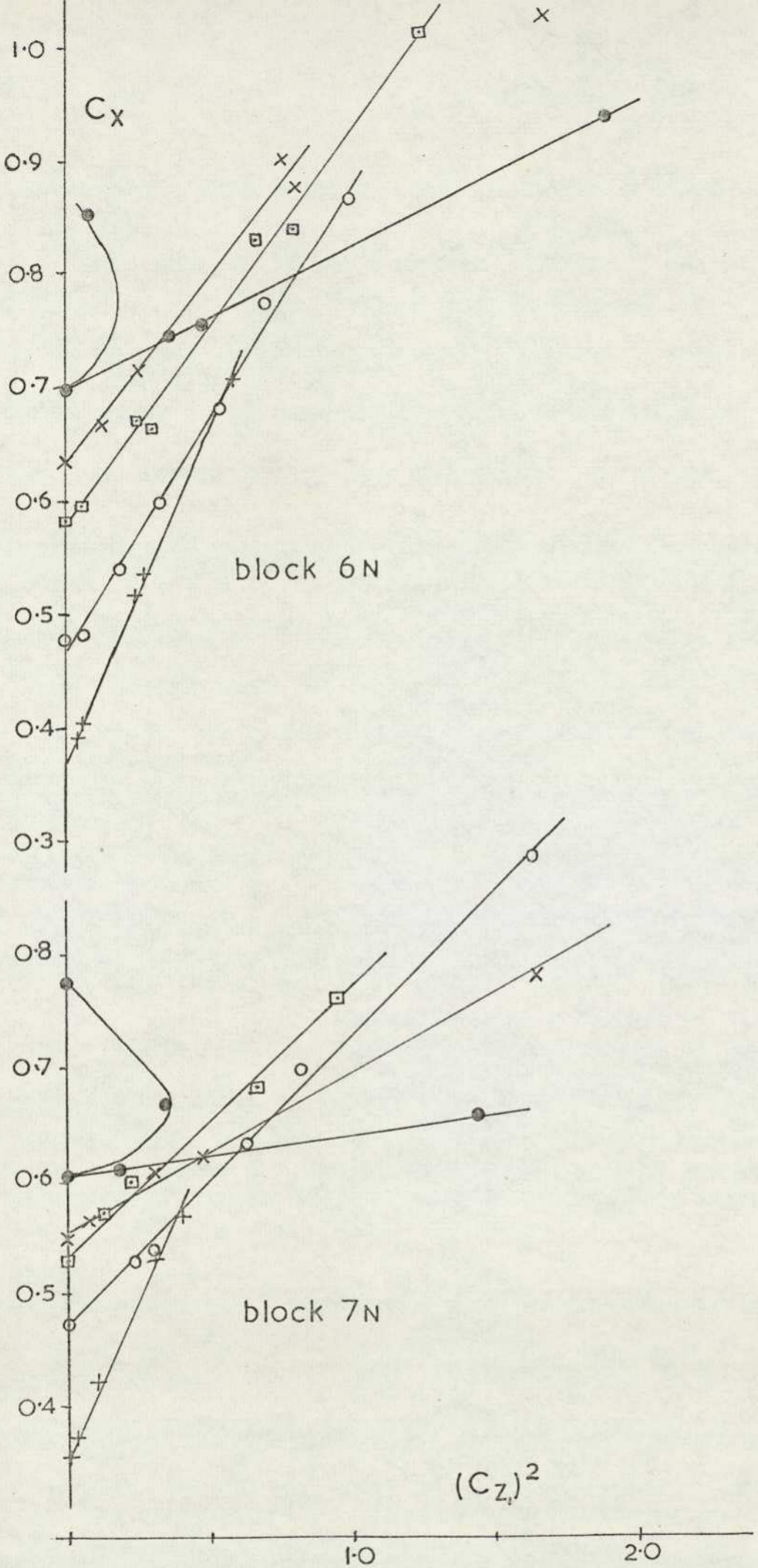

FIG.19 (C) INDUCED DRAG

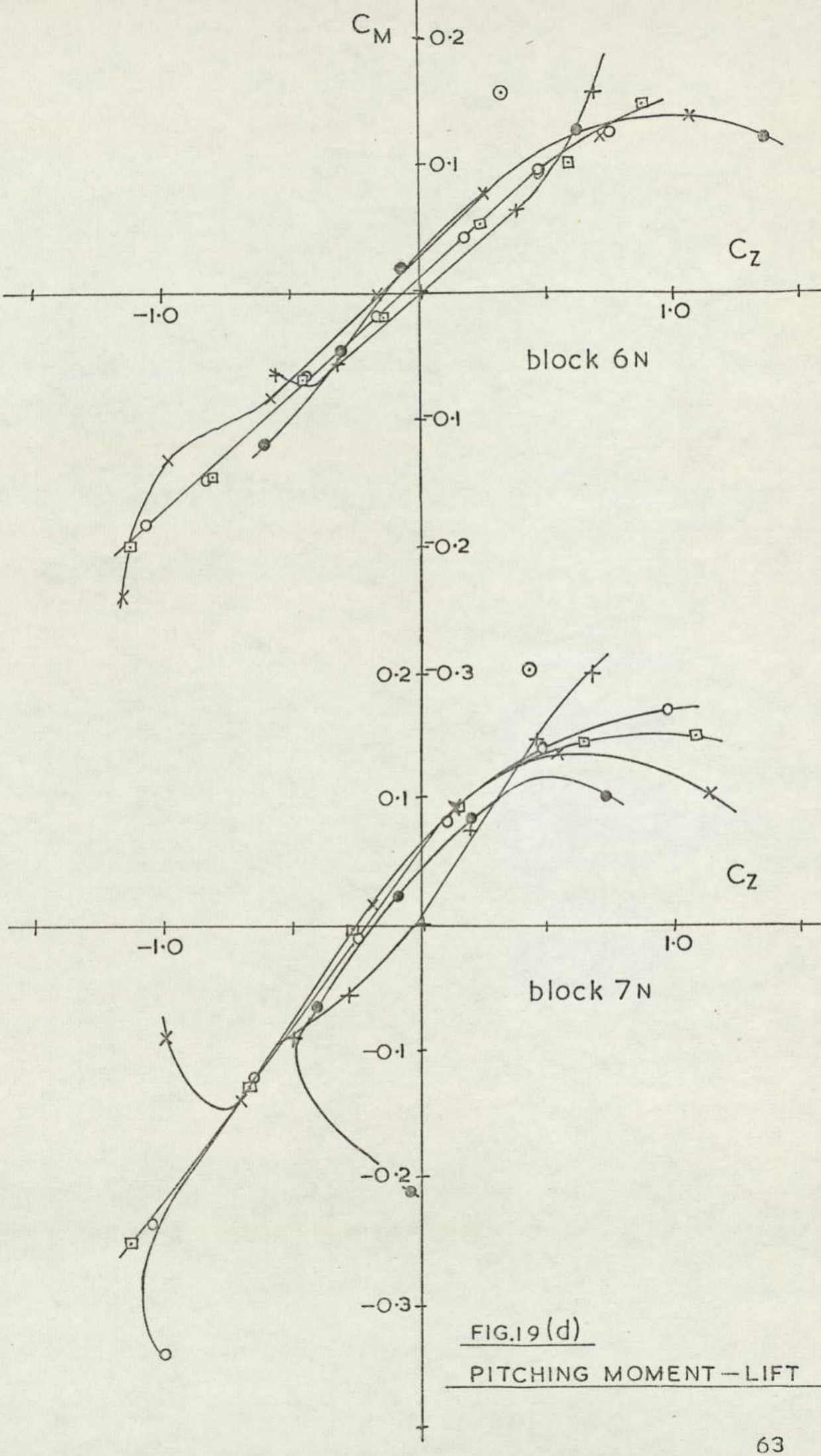

FIG.19(d)

PITCHING MOMENT — LIFT

2.2.5 Effects of camber.

Block 7N was fitted with a curved upper section to produce a cambered body while retaining a flat lower surface. The maximum thickness was increased by 50% and occurred at 35% of model length aft of the nose (block 9C). The trailing edge geometry remained identical to that for block 2N. The aerodynamic characteristics are plotted in Figure 20 (a)-(d). Comparison with Figure 18 shows that near to ground the camber has very little influence on absolute lift values apart from a slight increase in lift. Additional camber profiles were investigated in free stream only and it can be seen that a rearward shift in the maximum thickness position introduces a lift increment and an increased nose down pitching moment. There is negligible effect on drag. In ground proximity the pitching moment characteristics are very similar to those for block 7N apart from a negative pitching moment change. These results tend to confirm the dominating effects of the ground.

An additional cambered model, (block 12C), which had cross section changes in the nose region only and had a flat lower surface, was also investigated, see Figure 21. The model could be inverted to study the effect of a gross change of the flow condition at the leading edge. The lift characteristics are very similar to those of block 2N apart from a marked non linearity at negative incidence and a negative lift increment. Inverting the model only produces a further lift increment due to the curvature of the lower surface and initiates a flow breakdown at an earlier incidence. The two drag curves show an effective incidence shift over most of the incidence range, although a large difference is apparent at the minimum ground clearance. The induced drag curves show similar characteristics for both bodies at all ground clearances studied. The pitching moment slope shows little influence of either shape or ground proximity but the absolute value of the pitching moment differs considerably with shape, the model with the uppermost leading edge having a significantly higher nose up moment.

2.2.6 The Influence of Ground proximity.

To study more closely the effects of ground proximity, plots of essential parameters against ground clearance have been made. The parameters of interest are the lift slope, $\delta C_Z/\delta\alpha$, the zero incidence lift coefficient C_{Z_0}, the minimum drag coefficient, $C_{X_{min}}$, the incidence at which $C_{X_{min}}$ occurs $\alpha|_{C_{X_{min}}}$, and the "efficiency" of the body as a

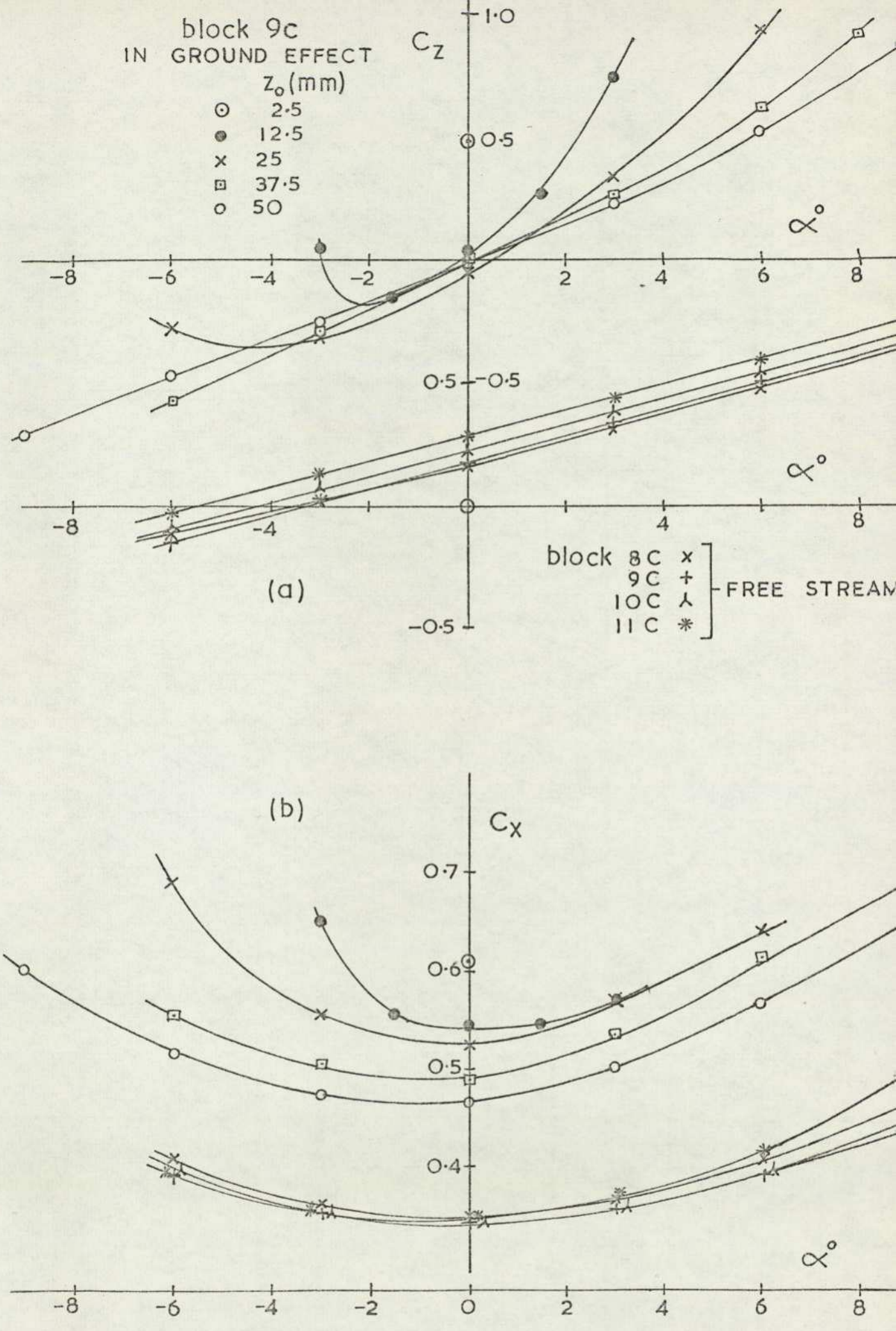

FIG. 20 EFFECT OF CAMBER (a) LIFT — INCIDENCE

(b) DRAG — INCIDENCE

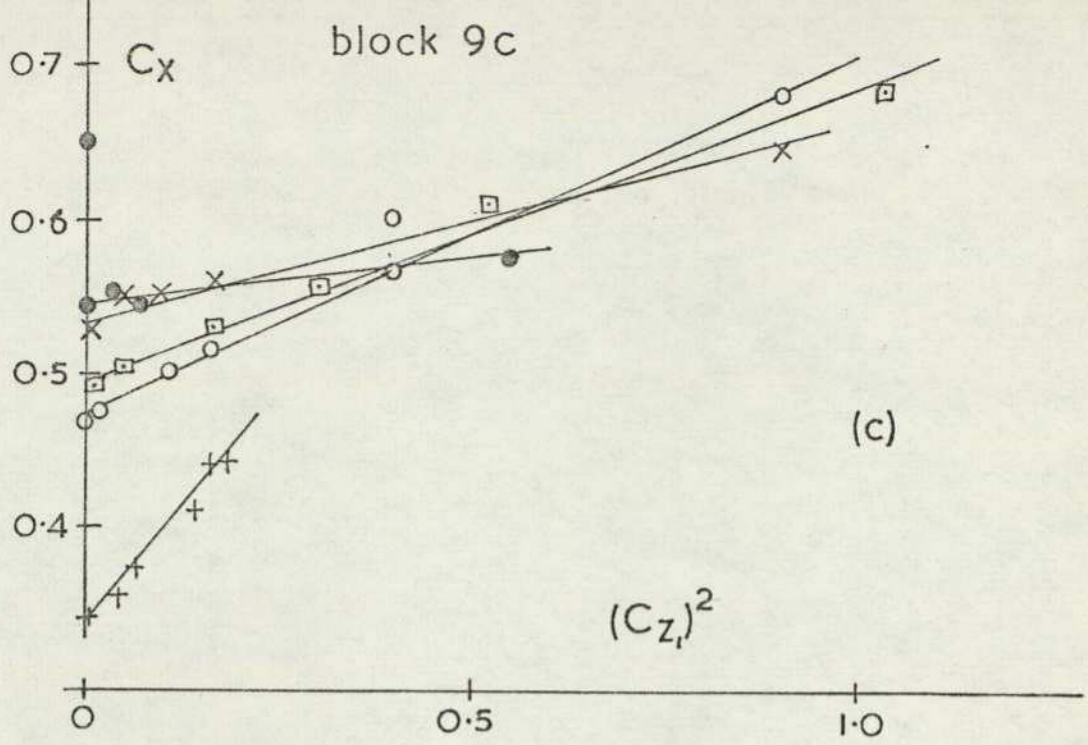

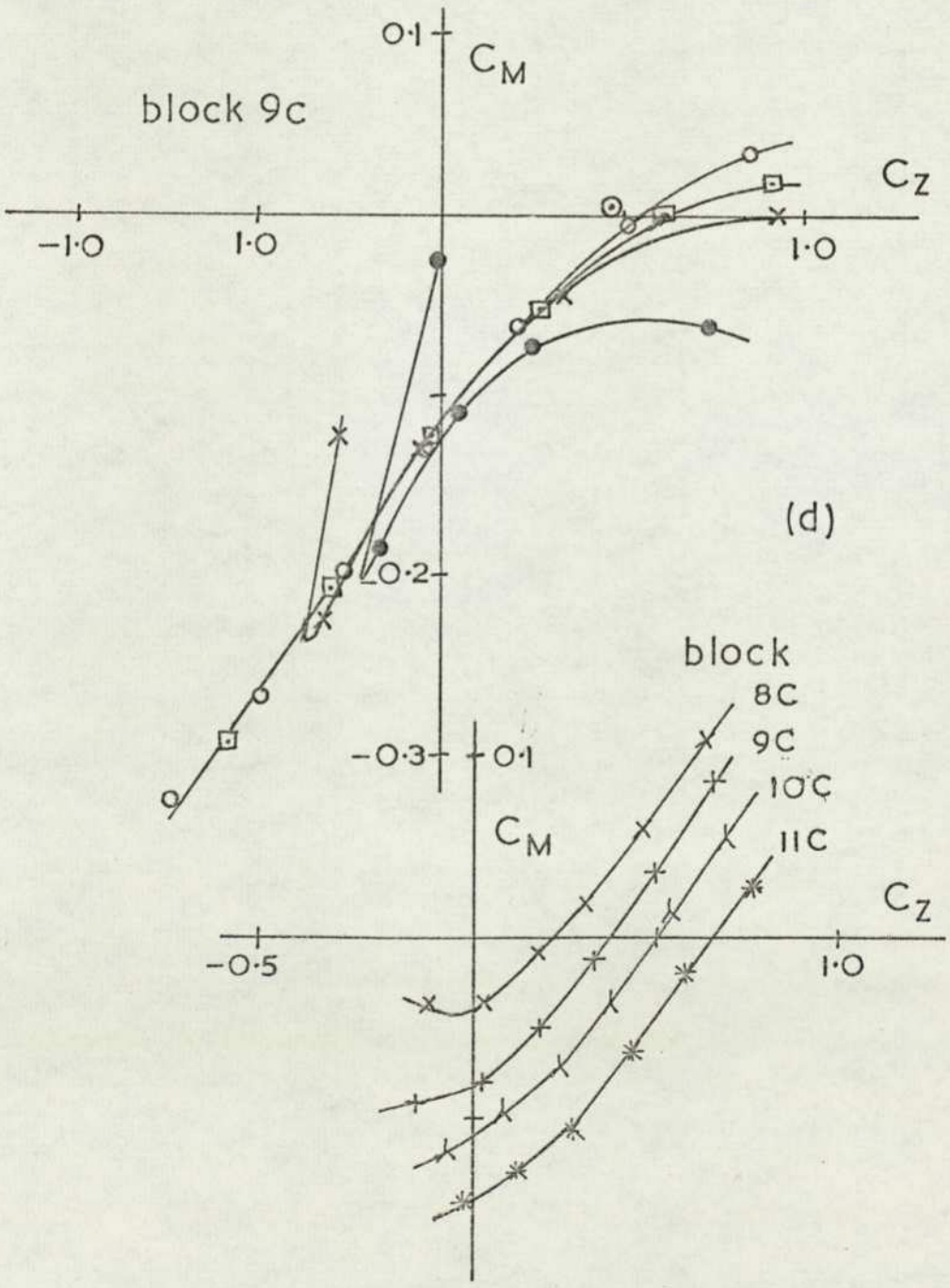

FIG. 20 (c) INDUCED DRAG

(d) PITCHING MOMENT — LIFT

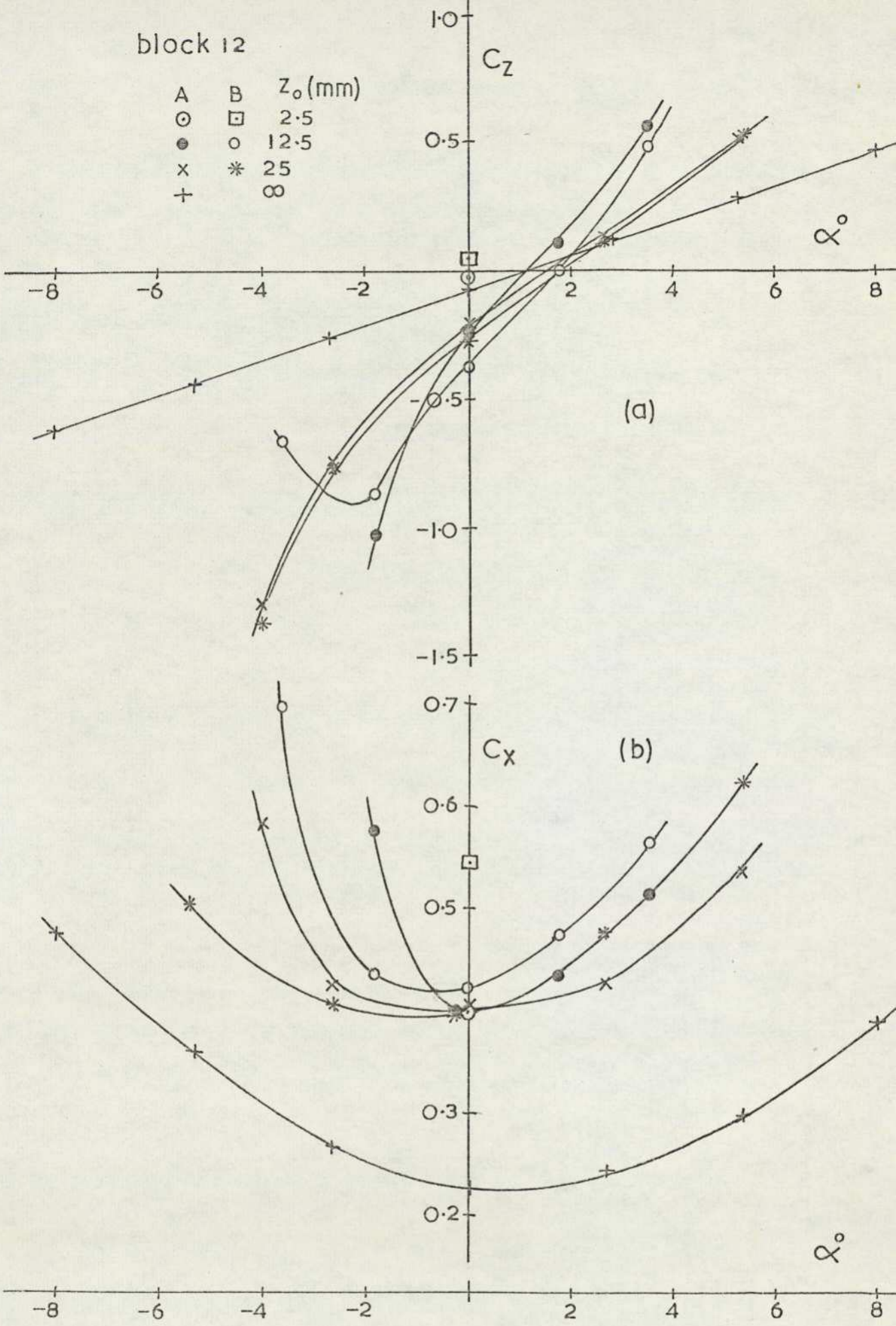

FIG.21 EFFECT OF NOSE SHAPE (a) LIFT–INCIDENCE
(b) DRAG–INCIDENCE

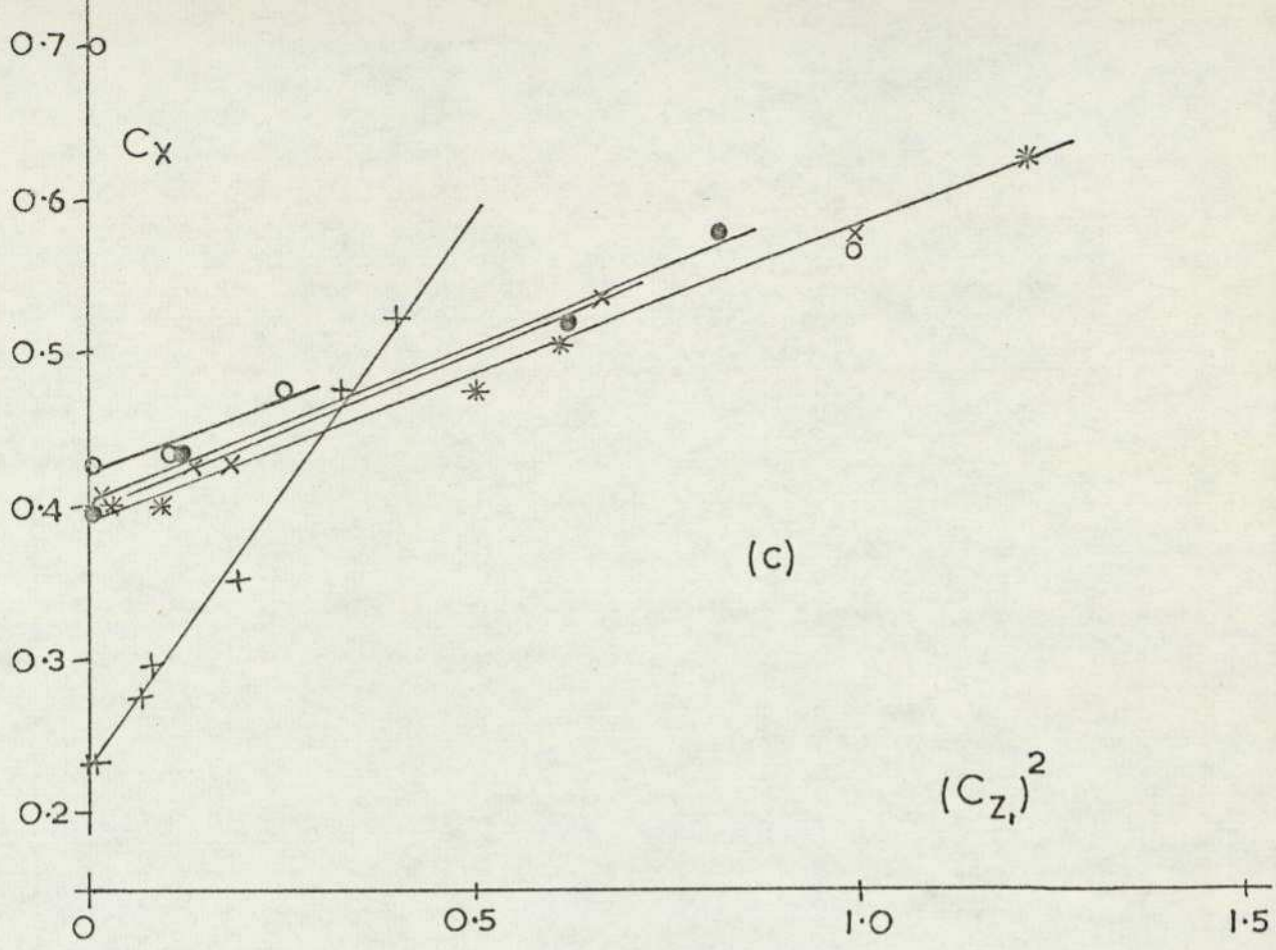

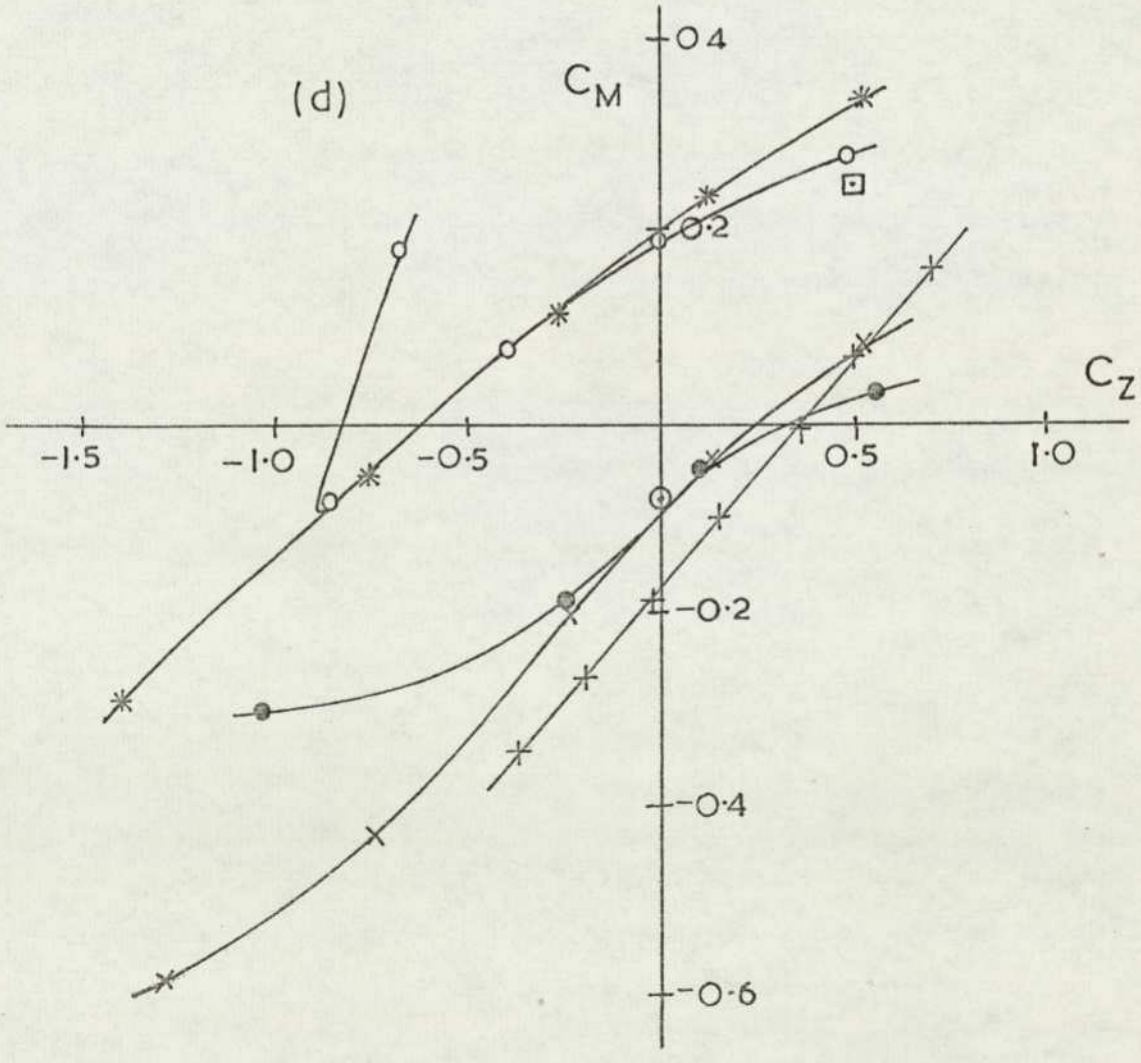

FIG. 21 (c) INDUCED DRAG

(d) PITCHING MOMENT – LIFT

lifting device as measured by $\delta C_x / \delta C_z^2$. The ground clearance has been normalised by the span of (or thickness) the block. In figure 22 (a) these parameters are compared for the three edge conditions. The lift slopes all lie on a straight line, for a given body, when plotted against the inverse of the ground clearance. The basic block 2 shows less change due to the approaching ground, while blocks 2N and 2NS give comparable results. All the lift coefficients at zero incidence lie close to a single curve. The minimum drag coefficient curves show that significant drag changes occur on approaching the ground for block 2N while block 2NS shows a considerably reduced effect and the basic block experiences negligible variation over the range investigated although the presence of the ground obviously has an influence. The plot of $\alpha|_{C_{x\,min}}$ against ground clearance shows that the basic square edged block is not influenced by the ground while the other two blocks experience similar variation of the incidence, which increases negatively over the range of heights investigated. The curves of $\delta C_x / \delta C_z^2$ against ground clearance all show similar trends with an initially linear slope from the origin, the basic block giving the greatest slope. Normalising with respect to the free stream value gives a common curve.

On varying the span, Figure 22(b), the slope of $\delta C_z / \delta \alpha$ against normalised ground clearance remains constant, the absolute value increasing by a fixed amount at a given ground clearance due to the free stream increase. Zero incidence lift coefficient is given by a single curve for all three blocks. The curve of $C_{x\,min}$ against ground clearance shows similar free stream values while the drag coefficient variation near to ground shows similar trends, the magnitude increasing with reducing span. The minimum drag incidence shows almost identical results for all three blocks, while the plots of $\delta C_x / \delta C_z^2$ display the initial linear trend seen earlier with the slope increasing dramatically with reducing base aspect ratio.

Modifying model length while maintaining the base section of block 2N gives lift curve slopes which increase approximately proportional to length when in close ground proximity and are equal in free stream; Figure 22(c). Zero incidence lift is again similar for all blocks. $C_{x\,min}$ is similar to that consistently measured on block 2N. The blocks all show a similar trend for the minimum drag incidence but this time there is a greater spread of results. The induced drag slopes

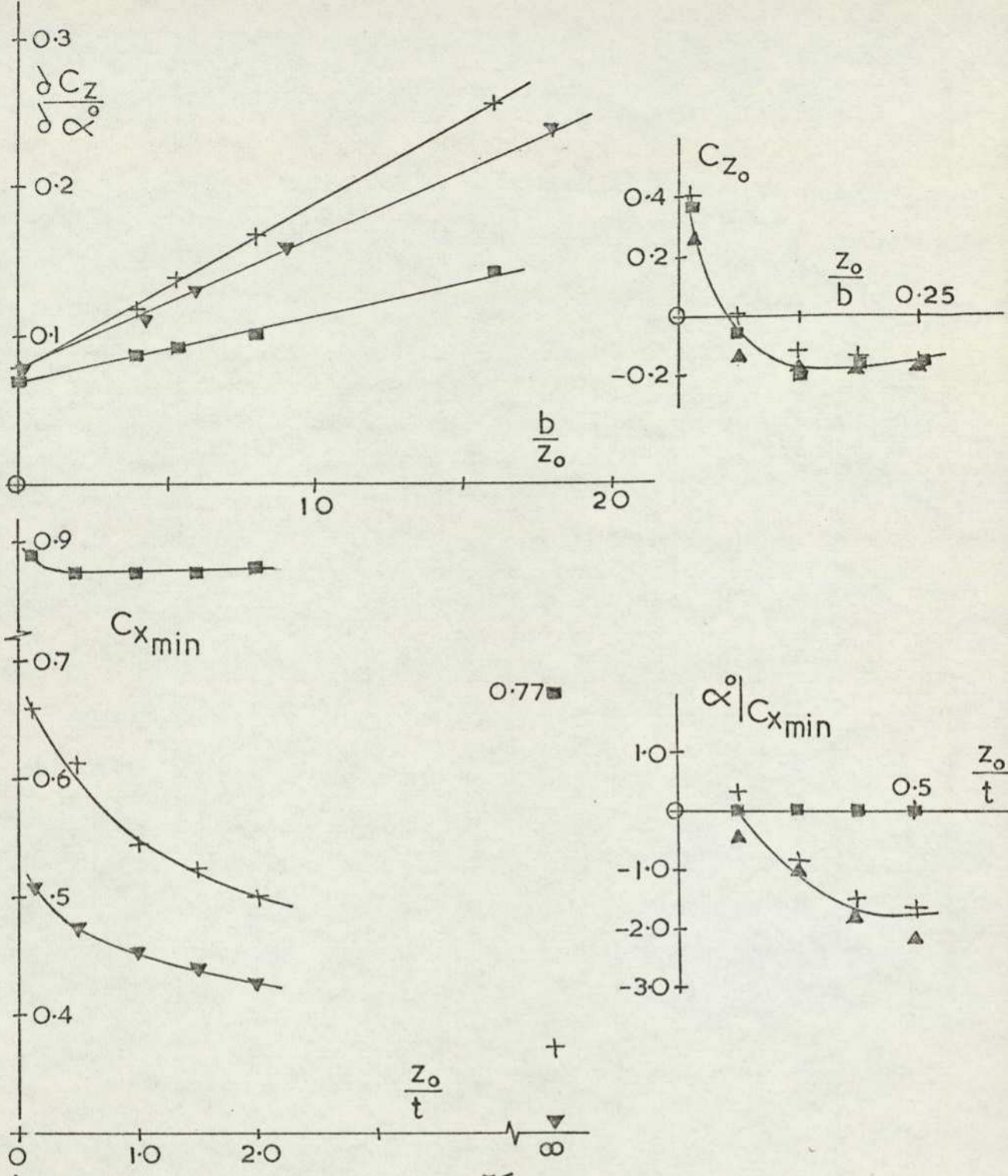

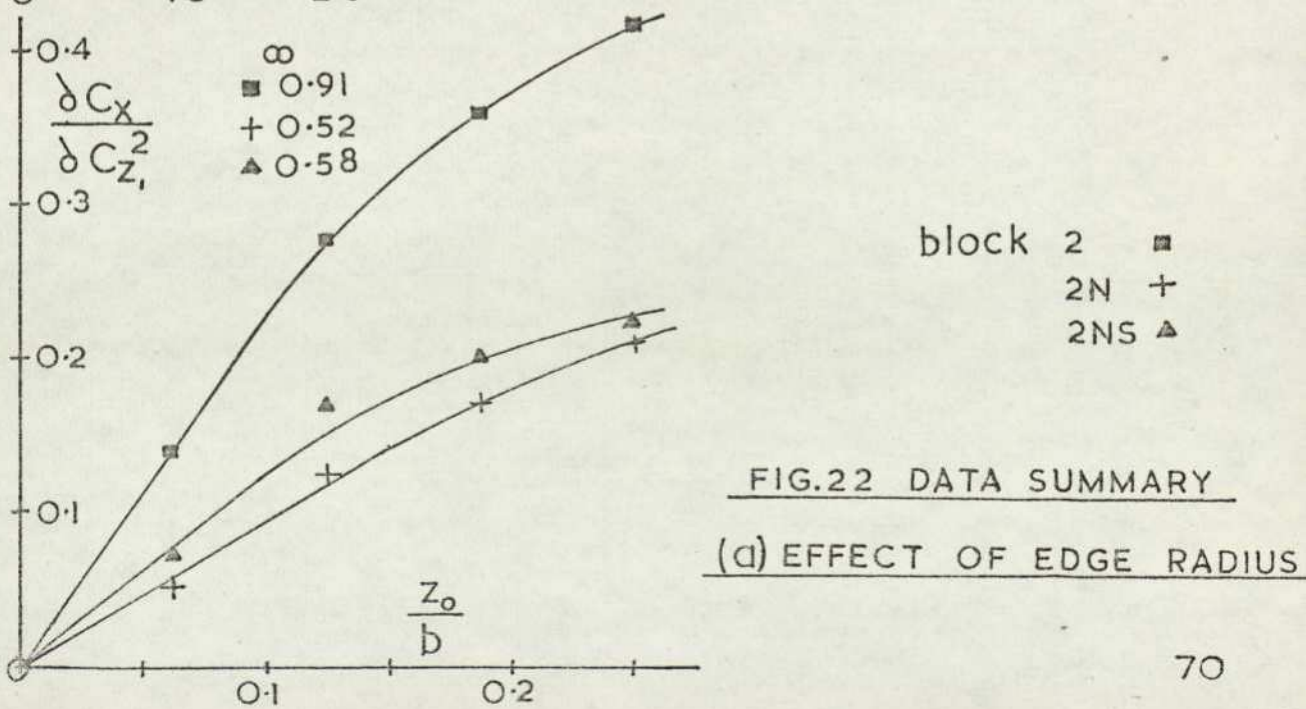

FIG.22 DATA SUMMARY

(d) EFFECT OF EDGE RADIUS

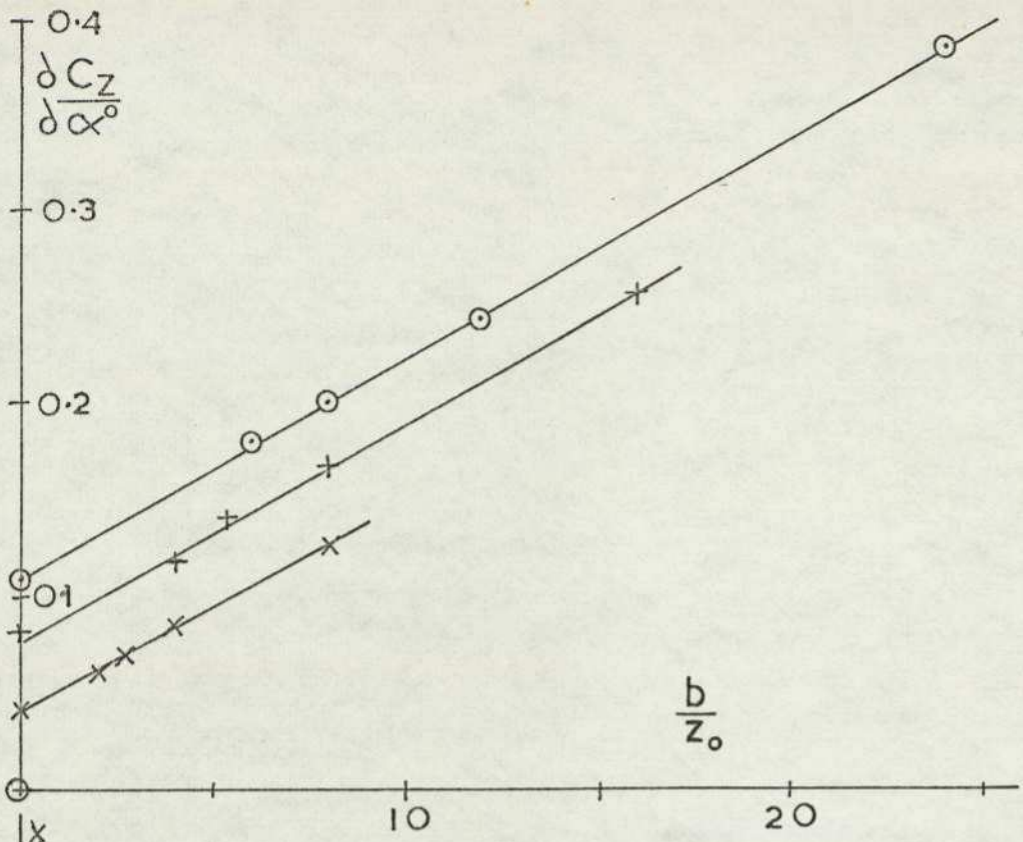

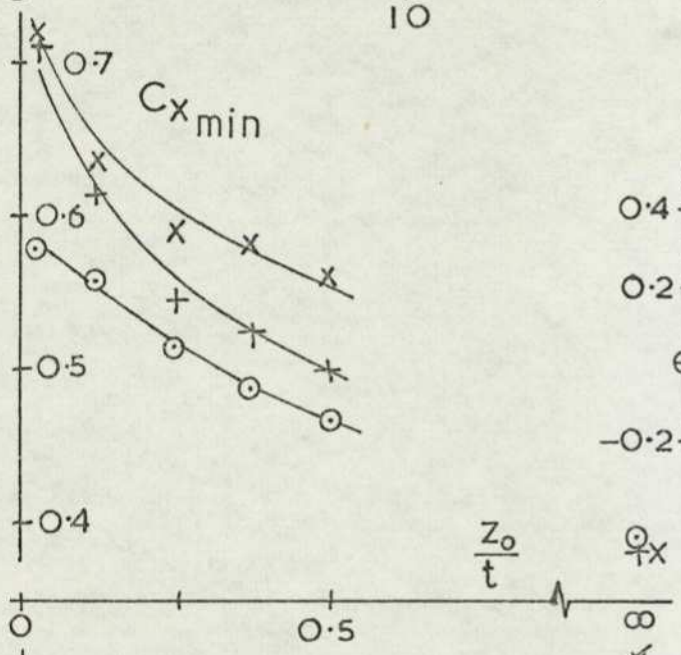

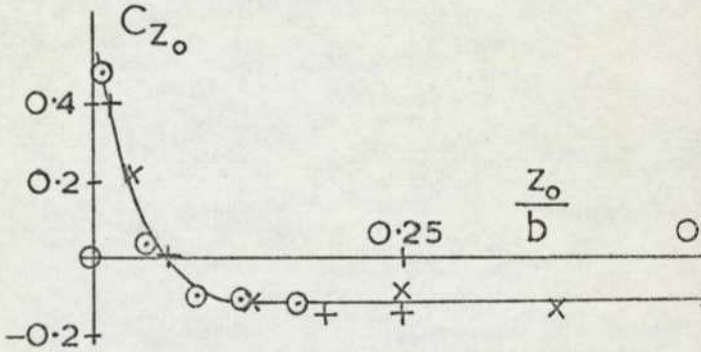

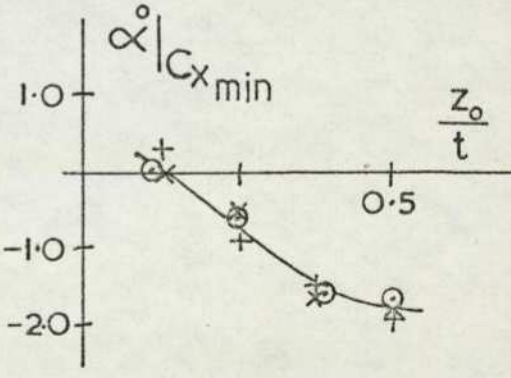

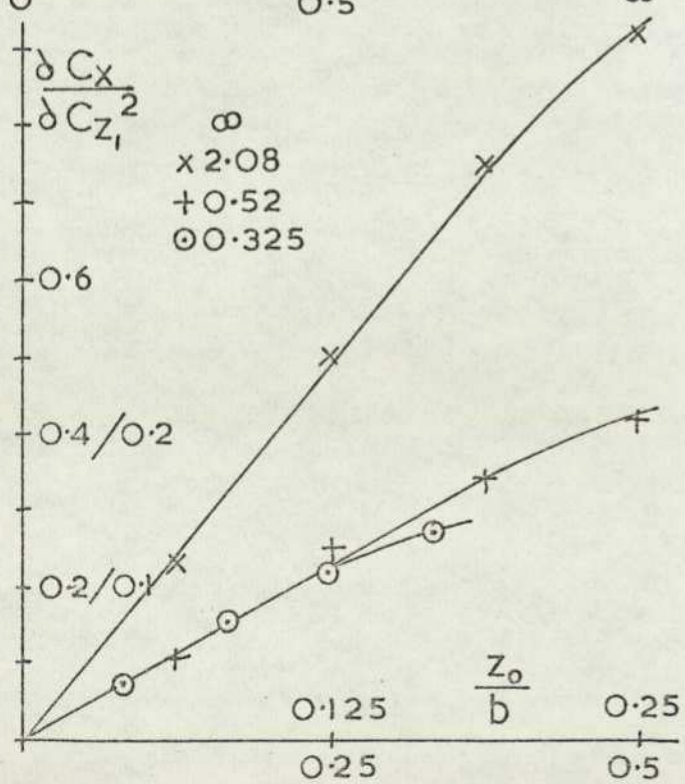

span
block 1N × 0·1
2N + 0·2
3N ⊙ 0·3

FIG. 22(b)

EFFECT OF SPAN

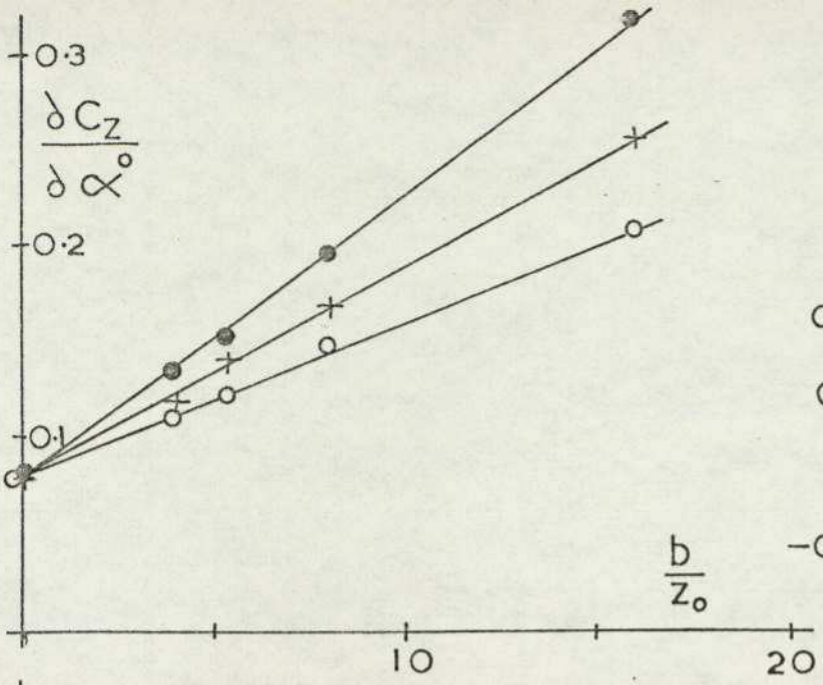

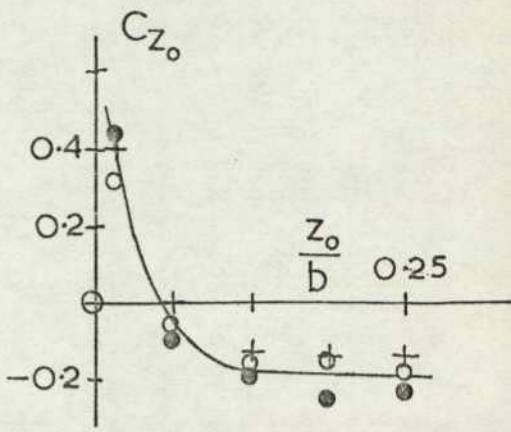

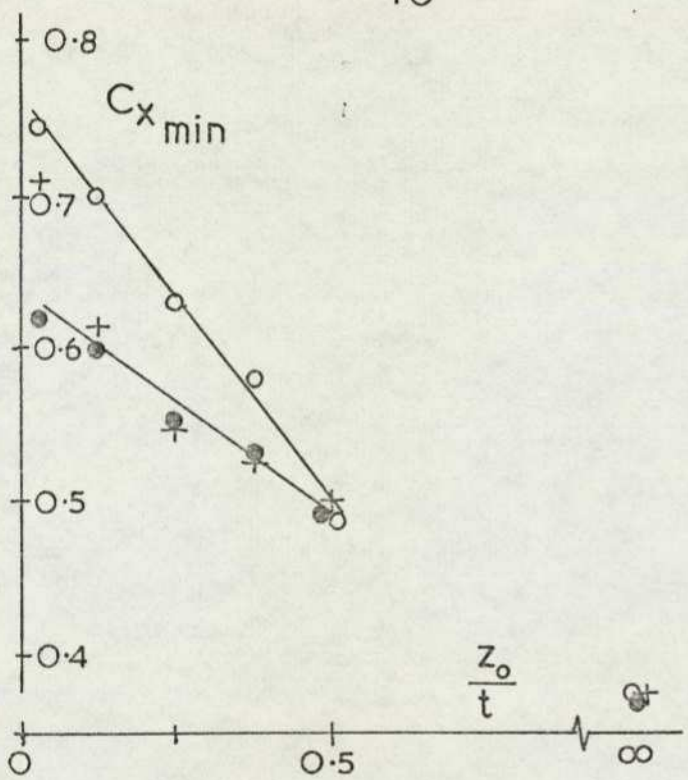

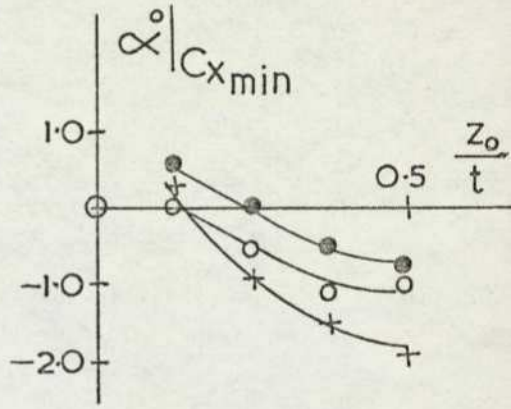

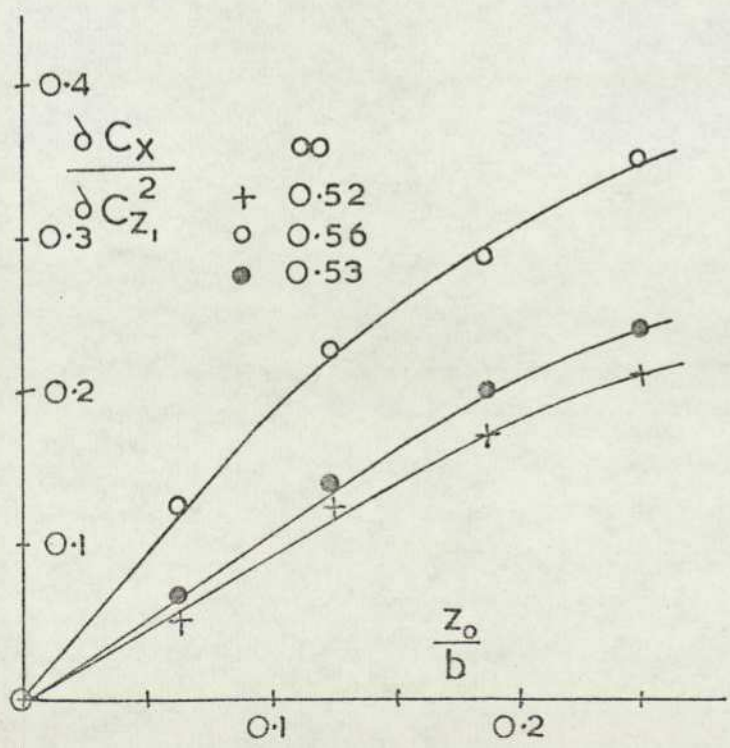

length

block 2N + 0·3
6N o 0·2
7N ● 0·4

FIG. 22(c)

EFFECT OF LENGTH

give similar results for all three blocks when in free stream while near to ground the short block has considerably higher values than the two longer blocks which show very similar results.

Reducing the thickness of the block while keeping the same planform aspect ratio has the effect of increasing the free stream lift slope directly proportional to the base aspect ratio. The increase in lift slope when in ground proximity is similarly increased as is the zero incidence lift coefficient. The minimum drag coefficient is only slightly changed in free stream but is strongly influenced by thickness when near to ground. Only two data points were taken for each block in ground proximity so interpretation of these results is difficult. All the minimum drag incidence values were very close to zero. The increase of $\delta C_x/\delta C_z^2$ with ground clearance reduces approximately proportional to the thickness to length ratio, although at free stream conditions the variation is stronger, **Figure 22(d).**

When the effects of ground proximity on the principal characteristics of the cambered blocks are compared with those for block 7N, the longer version of block 2N, which has a length equal to block 9C and approximately equal to block 12, the lift curve slopes increase less rapidly for both cambered models on approaching the ground. The zero incidence lift for blocks 7N and 9C are similar once corrected for the effects of free stream lift. For blocks 12 the trend is similar but the magnitudes are completely different. For the remaining characteristics only block 9C shows any consistency with previous results. The minimum drag coefficient is reduced on adding the camber and the related incidence is more negative. The curve of $\delta C_x/\delta C_z^2$ for block 9C shows a greater spread of results than for previous blocks although the initial trend and the free stream value are similar to those for block 7N. Free stream results show that lift increased as the maximum thickness position moves aft while the pitching moment becomes increasingly negative.

2.3 Discussion

2.3.1 Free stream data

The minimum drag coefficient is plotted against base aspect ratio for all blocks in Figure 23. For a given nose configuration the

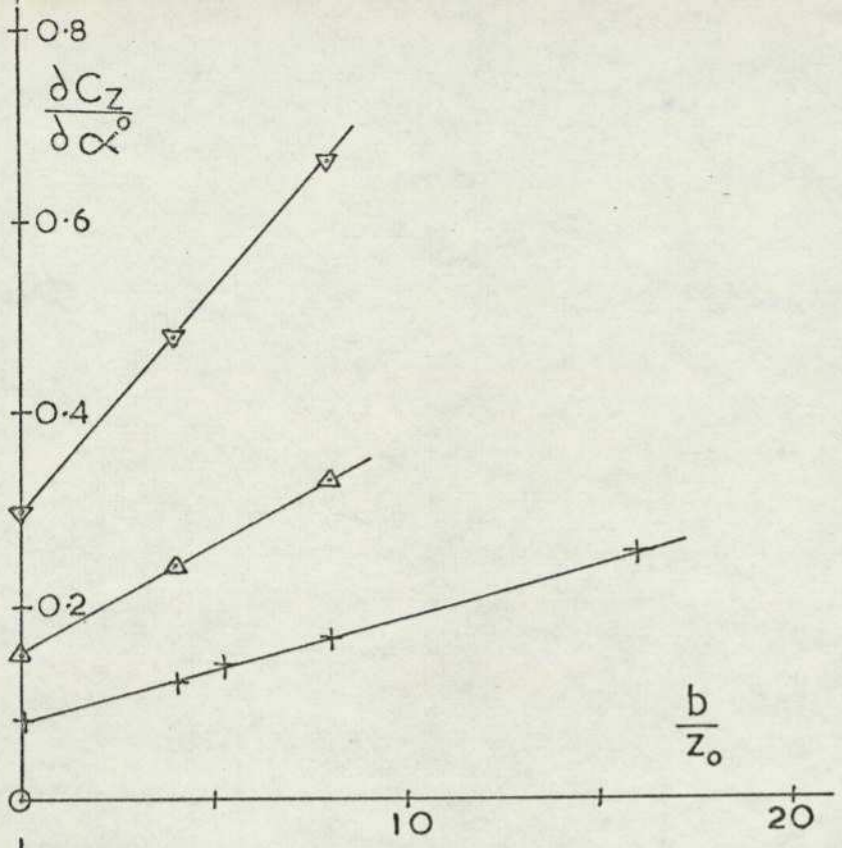

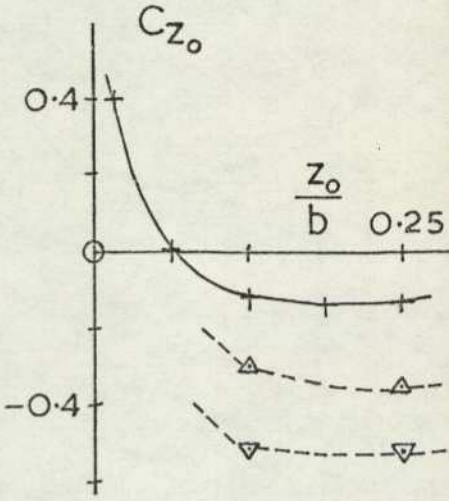

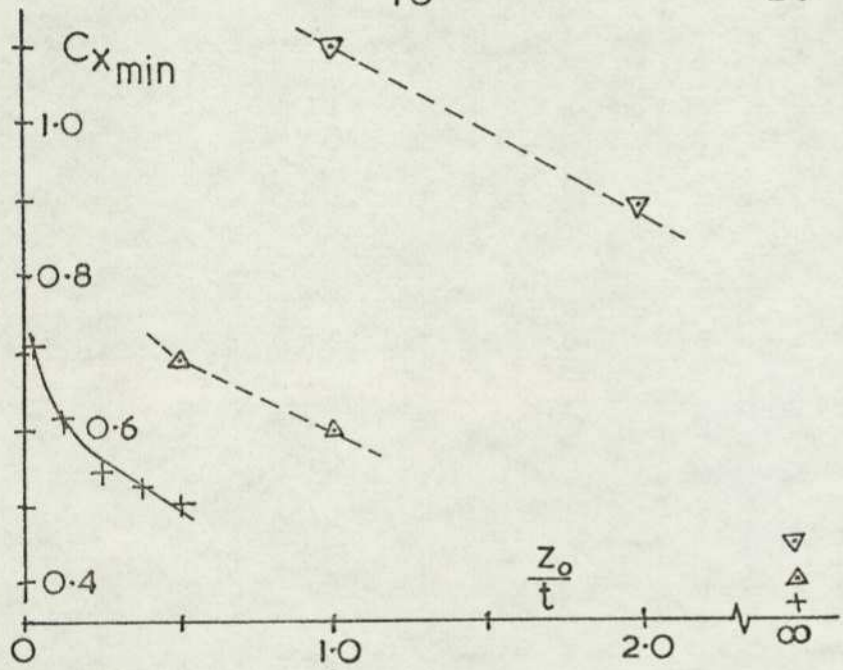

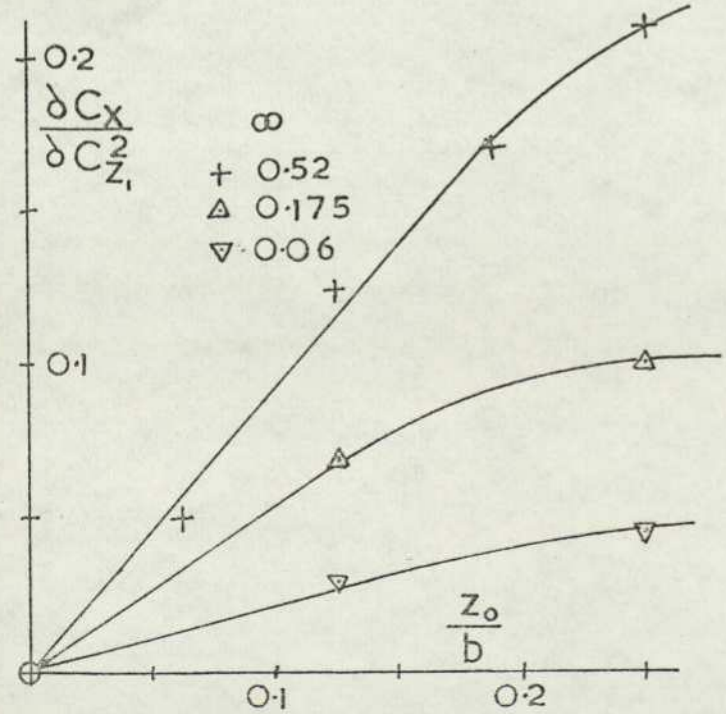

thickne

block 2N + 0·1 m
4N △ 0·05
5N ▽ 0·02

FIG. 22(d)

EFFECT OF THICKNESS

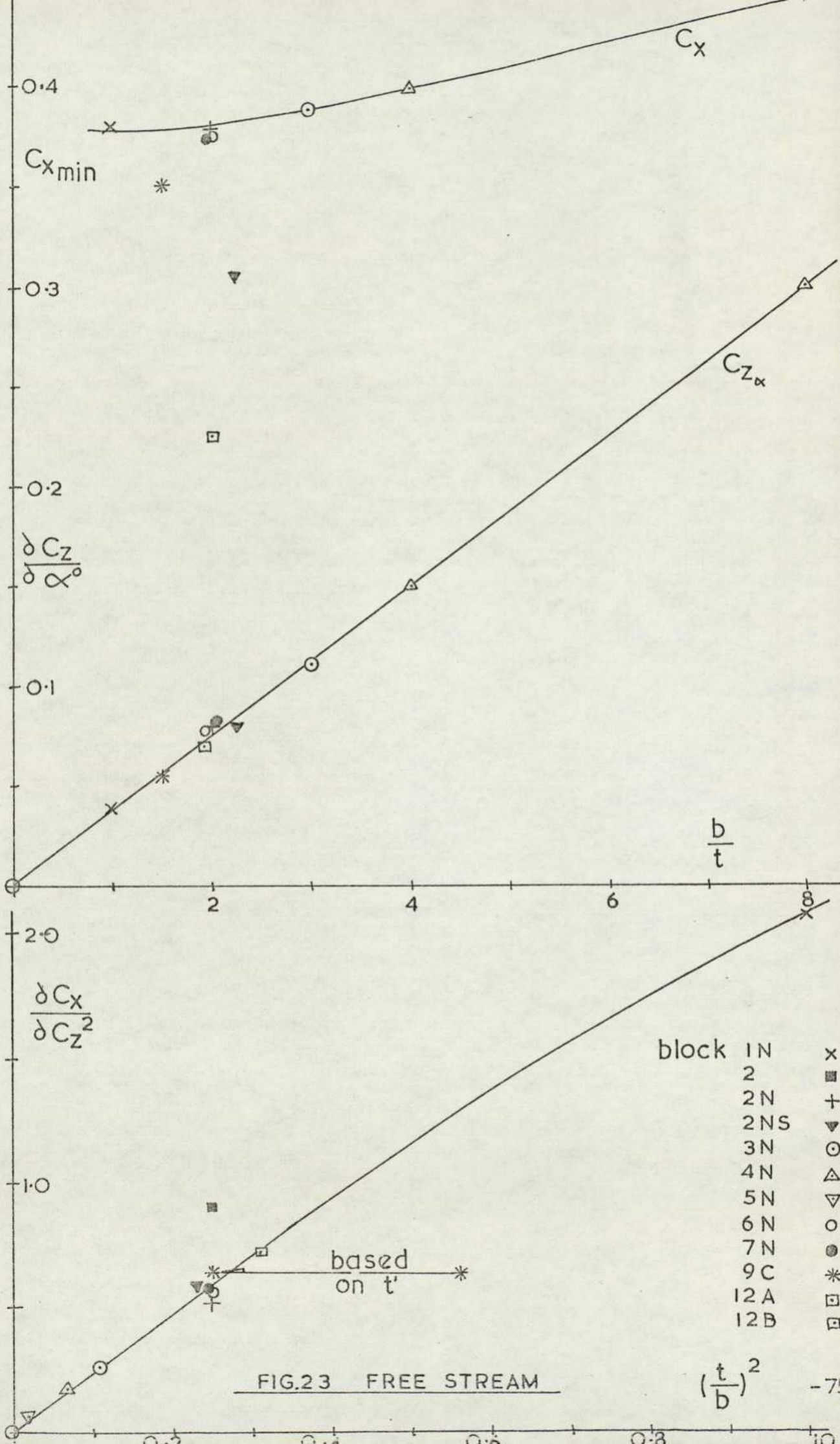

FIG.23 FREE STREAM

drag coefficient is a minimum for an aspect ratio of unity. The trend agrees with drag measurements obtained from flat plates mounted normal to the airstream by Fail, Owen and Eyre (21). The introduction of camber reduces the drag by modifying the slope of the upper separating shear layer, while changes to the body length seem to have a negligible effect. The free stream lift curve slope is plotted on the same graph. All blocks tested fall onto a single straight line through the origin. This implies that lift is independent of both thickness and length depending geometrically only on the span. Slender wing theory for a rectangular planform does suggest that all the lift is carried at the leading edge, and from all the curves of pitching moment against lift the lift acts at 14% of block length aft of the nose. The curve of $\delta C_x / \delta C_z^2$ for all blocks when plotted against $(t/b)^2$ again gives a straight line through the origin for all blocks in the 'N' configuration. There is a greater spread of results for the other shapes but in the case of the cambered body this is improved by taking the base measurements rather than the maximum thickness.

2.3.2 Ground proximity - collected data

A considerable degree of uniformity is obtained for the lift curve slope data when plotted in the form shown in Figure 24. The only significant deviation from the one straight line that all the results tend to collapse onto is given by the basic block data. The independence of the lift force due to incidence from the effects of thickness is apparent. The increase in lift of a body in ground proximity clearly arises predominantly from the flow changes in the gap between body and ground. The zero incidence lift is similarly plotted in Figure 25. There is again a remarkably good collapse of the data to a single curve. Although there appears to be a considerable spread of results, these give a lift coefficient to $\pm$ 2.5% of the length to thickness ratio which represents a small change of lift force in practice. For a typical vehicle having a frontal area of 2 m^2 travelling at 30 m/s this gives a lift force variation of 160N or possibly 1.5% of the weight. A body approaching the ground in an inviscid stream should experience an increasingly negative lift at zero incidence due to the acceleration of the flow in the gap between body and ground. The sudden departure of the

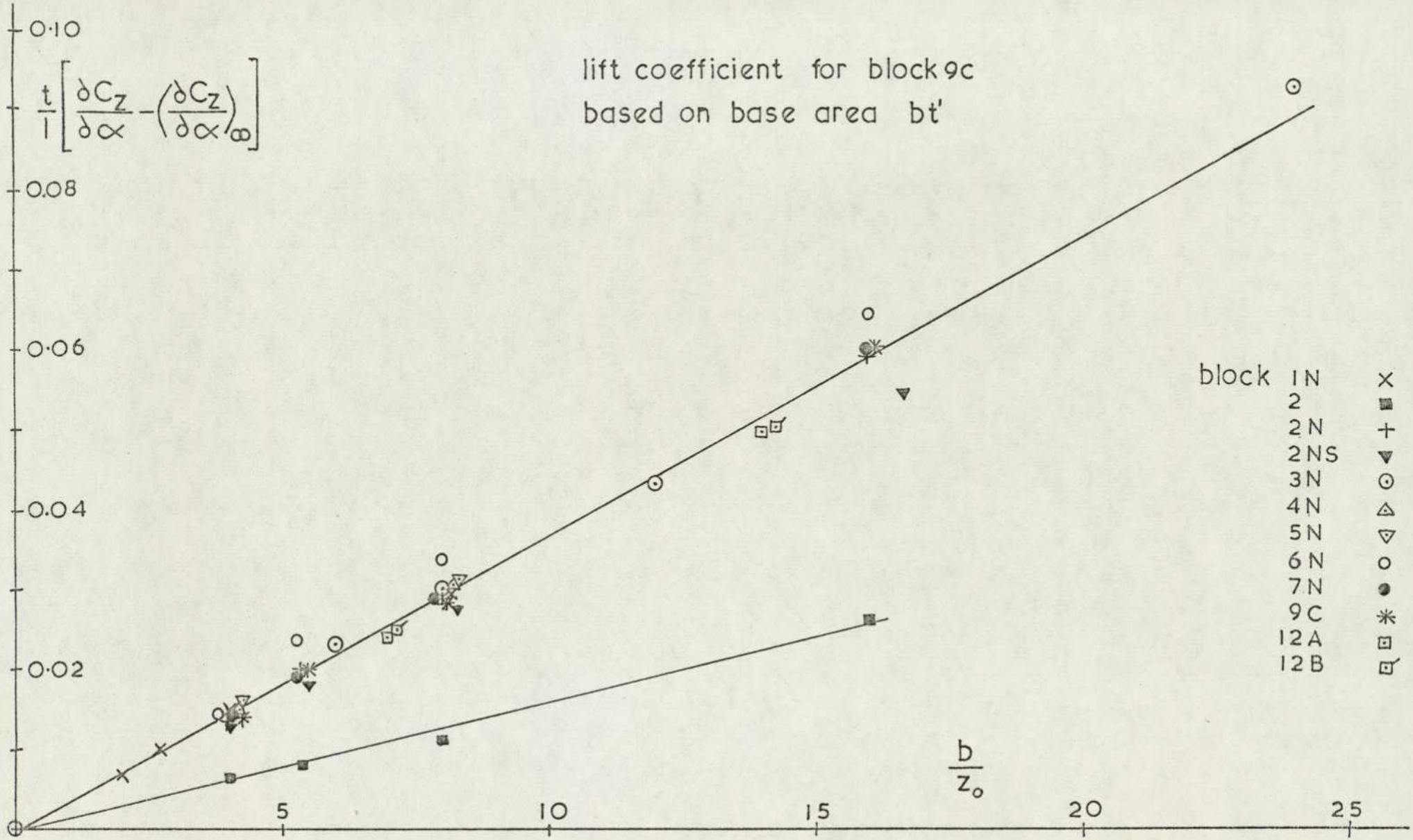

FIG. 24 INFLUENCE OF GROUND PROXIMITY ON LIFT CURVE SLOPE

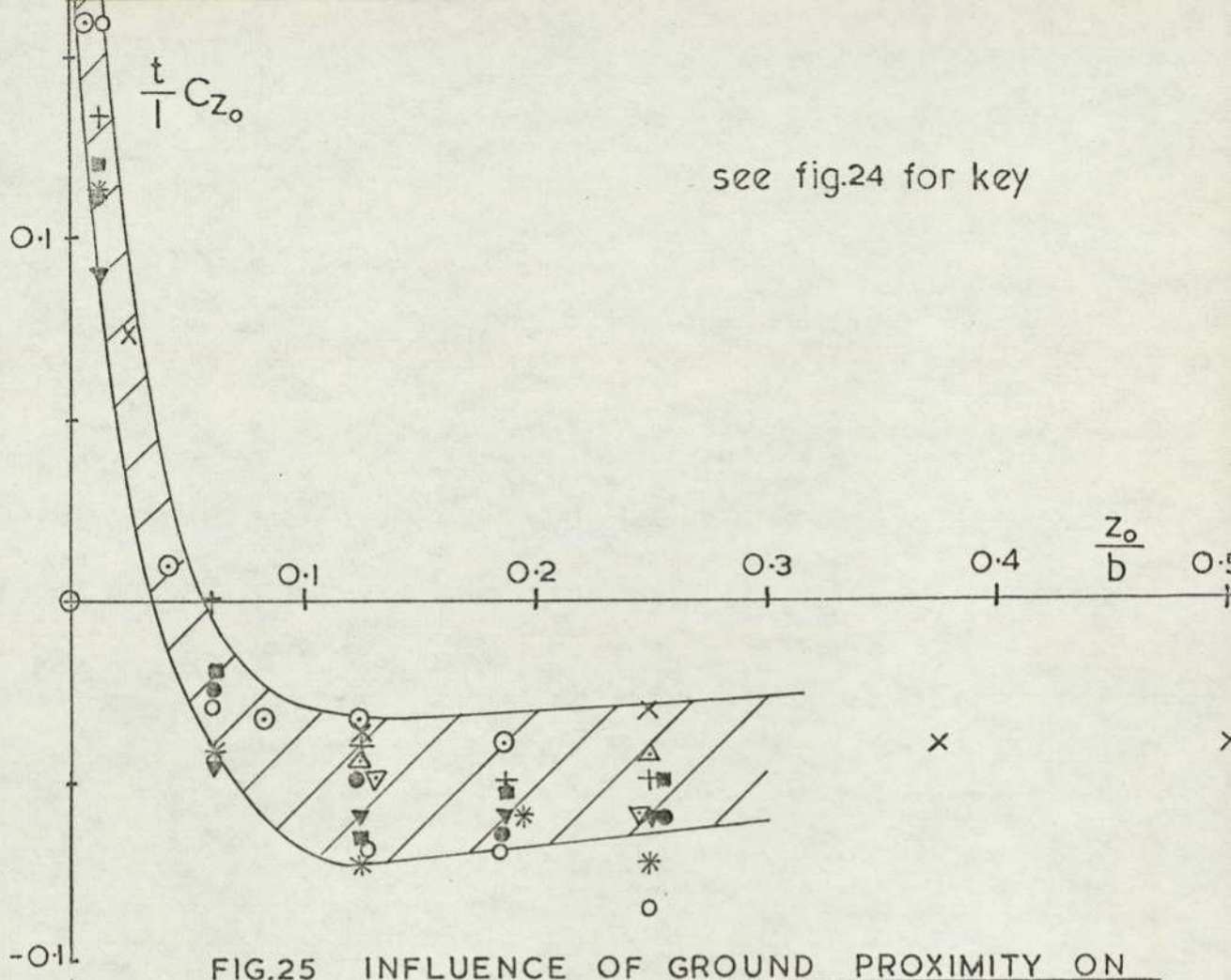

FIG.25 INFLUENCE OF GROUND PROXIMITY ON ZERO INCIDENCE LIFT

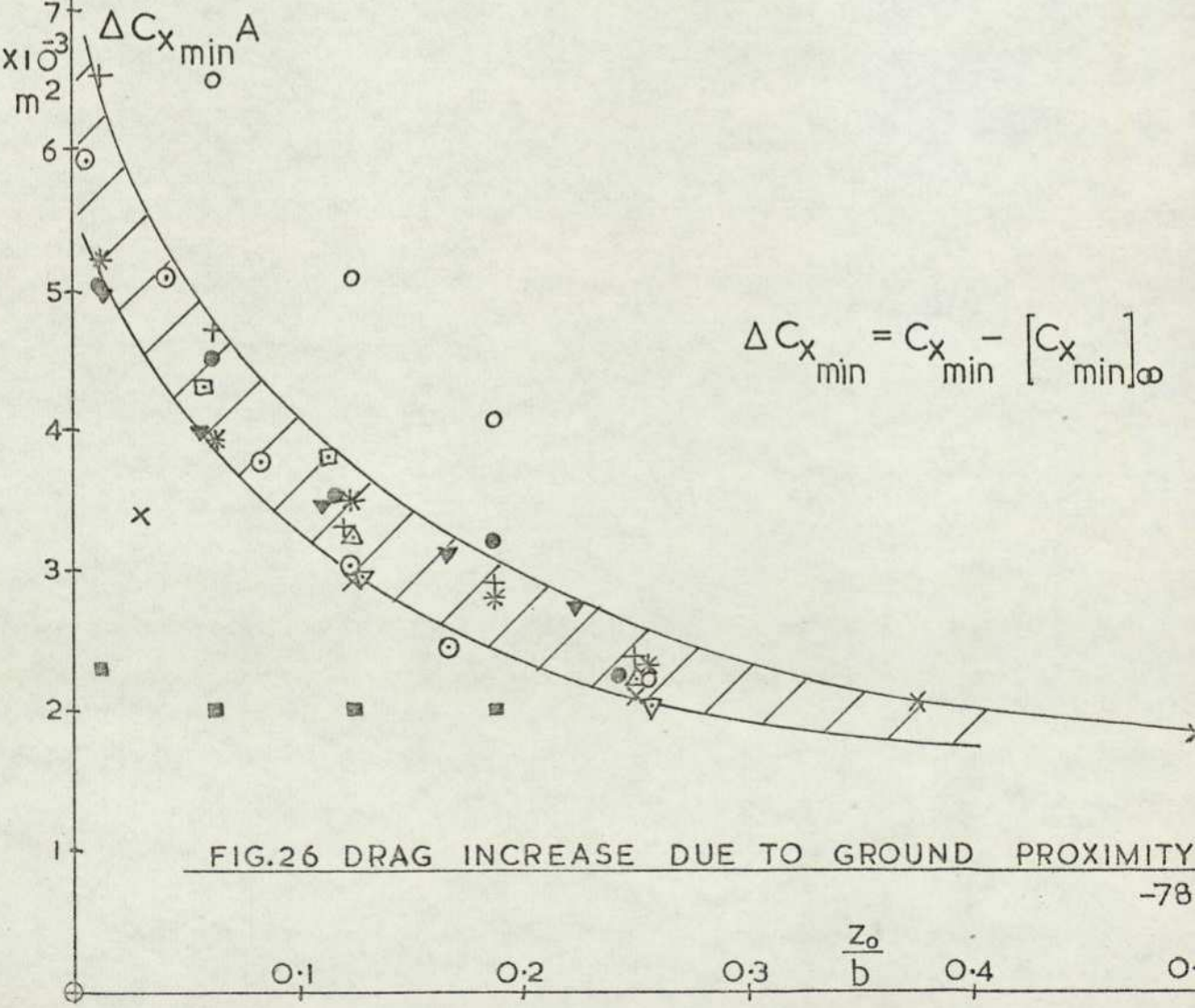

FIG.26 DRAG INCREASE DUE TO GROUND PROXIMITY

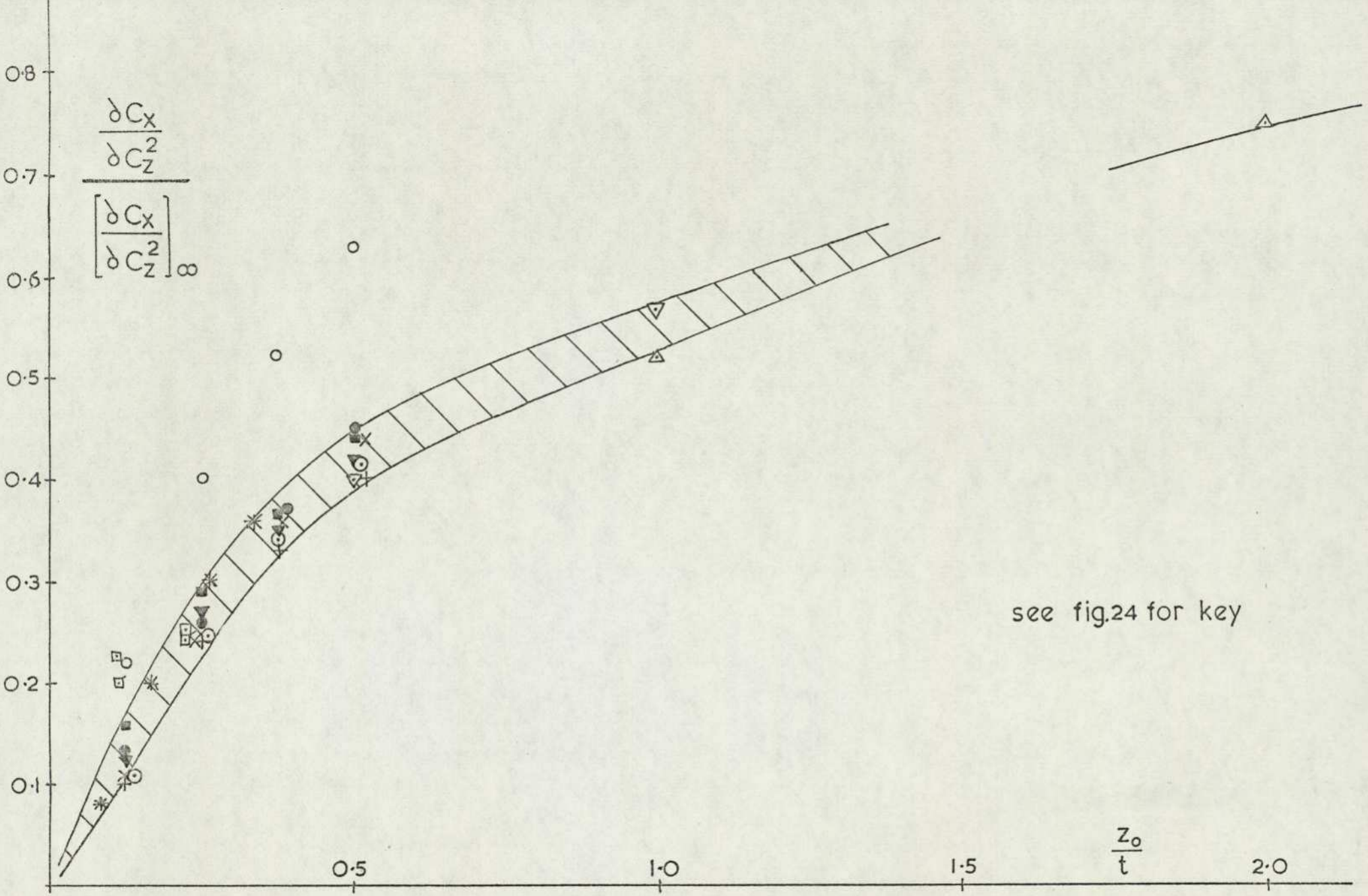

FIG. 27 INFLUENCE OF GROUND PROXIMITY ON INDUCED DRAG

curve from the inviscid case occurs when the ground clearance approaches the local boundary layer [illegible].

The increase in drag at a given airspeed experienced on approaching the ground is shown in Figure 26 to be a function of ground clearance and span only. The exceptions are given by the shortest, narrowest, and bluffest blocks, all other bodies fitting closely to a single curve with the exception of the short block when plotted as in Figure 27. For ground clearances up to one third of body thickness the expression ($\delta C_x / \delta C_z^2$) increases directly proportional to ground clearance. The collapse of the data is remarkable and generates extremely useful design information.

2.4 Forces on car bodies at incidence

2.4.1 Reynolds Number Effects

Drag and lift forces and pitching moment were measured at various tunnel speeds representing Reynolds numbers, based on overall car length, ranging from 0.6×10^6 to 1.05×10^6, for the saloon 1 car model only in various preliminary stages of representation. See Figure 28. The basic model drag coefficient reduces by 22% as the Reynolds number increases by 75%. In common with most other works on road vehicle aerodynamics the moment data is presented in terms of lift at the front and rear wheels. The MIRA blockage correction, Equation (1.20), has been applied to all coefficients. Addition of the transition strip is seen to give an almost constant, but small, reduction in drag throughout the speed range. It also reduces front wheel lift while increasing the lift force at the rear wheels. Fitting the underbody roughness elements increases the drag by almost 10% throughout the Reynolds number range, restores front wheel lift to its non-transition value and substantially increases rear wheel lift. The effects of incidence on this configuration are noticeable only on lift at the front wheels, while the change of Reynolds number has a negligible effect on forces at incidence. Adding the wheels surprisingly produces no change in drag, reduces rear wheel lift slightly but dramatically increases front wheel lift. The clearance between the wheels and the ground board in this test was 5mm. It is clear that substantial modifications to the front wheel lift coefficient arise from the addition of wheels to the basic shape and from changes in vehicle attitude. Less dramatic changes arise from the addition of underbody

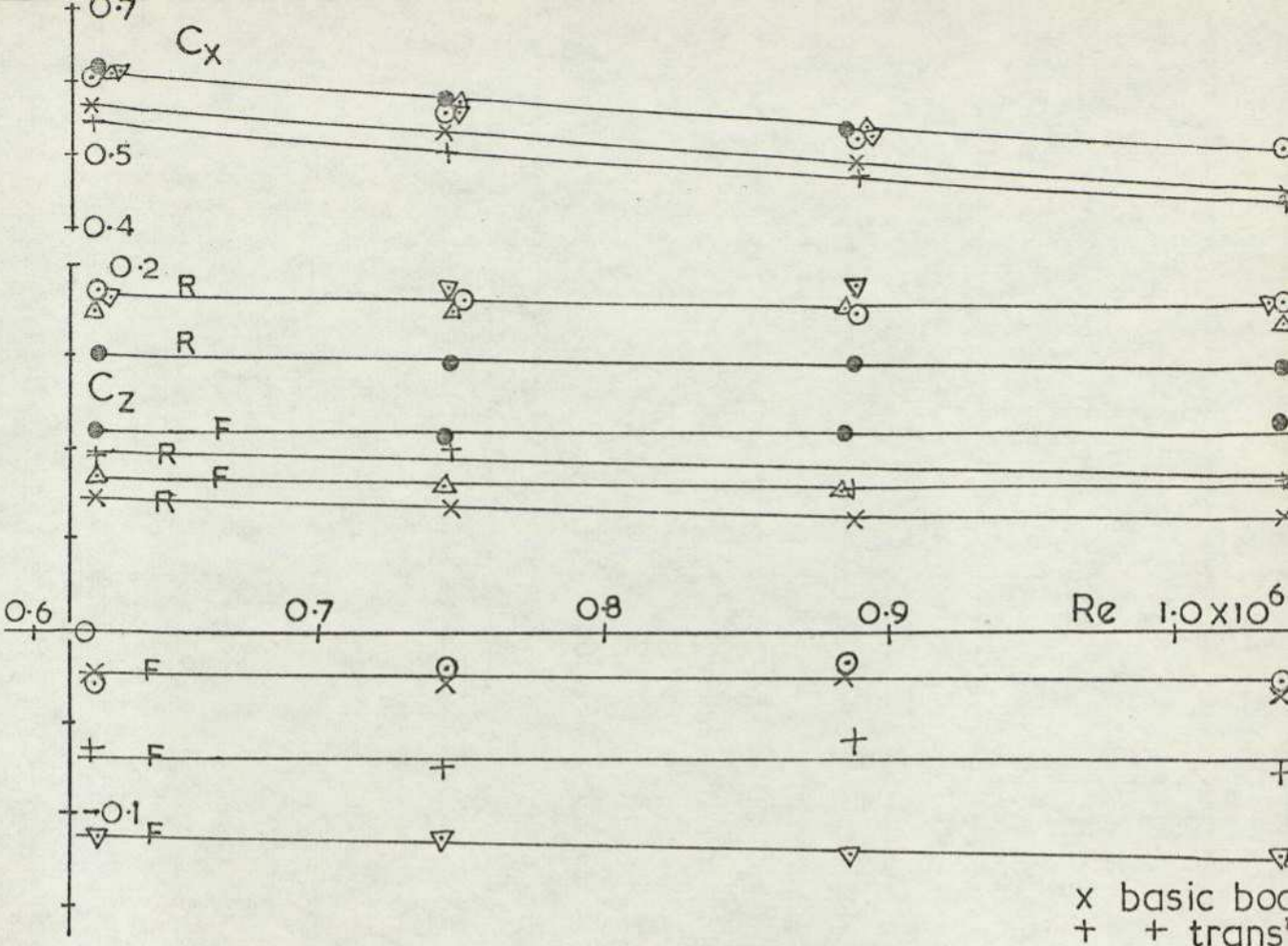

FIG. 28 REYNOLDS NUMBER EFFECTS ON DRAG, FRONT & REAR WHEEL LIFT — SALOON 1

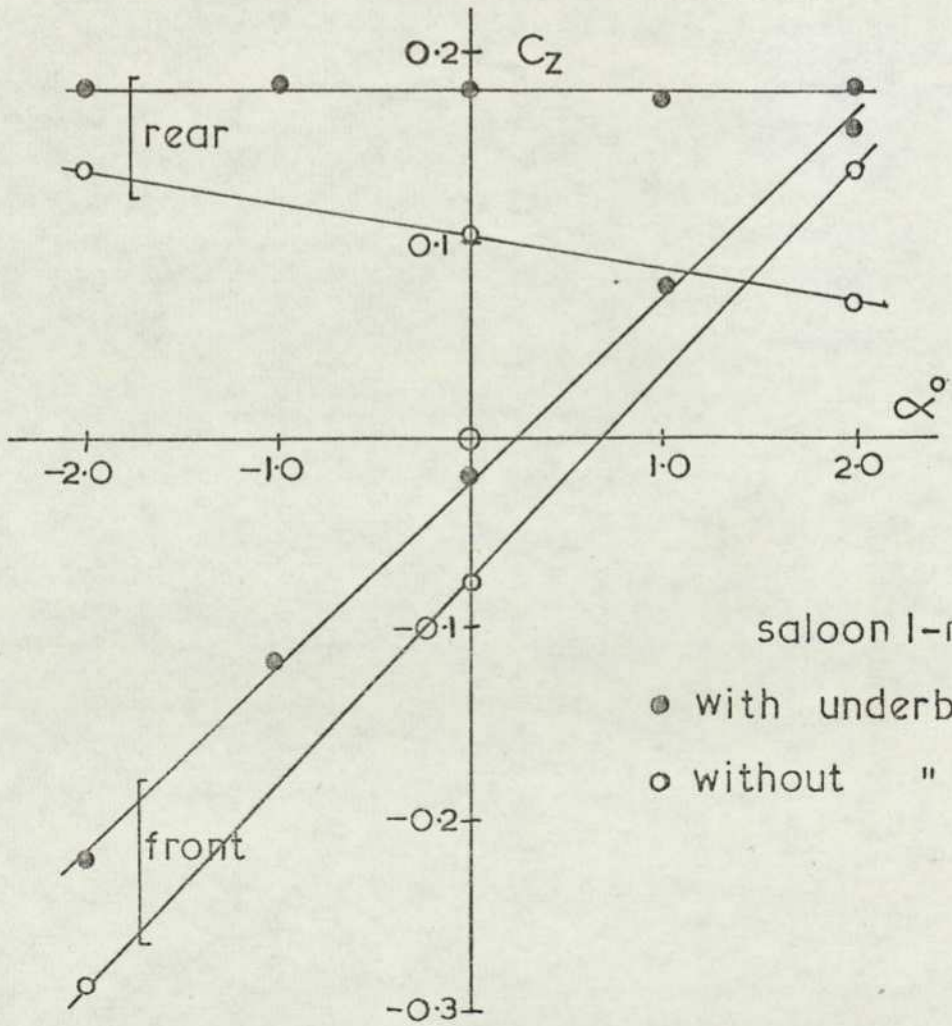

FIG. 29 EFFECT OF ADDING ROUGHNESS TO UNDERSIDE

roughness and transition strips. The rear wheel lift and the overall drag are sensitive to the state of the underbody. All subsequent tests were performed at a nominal 30 m/s tunnel speed, giving a Reynolds number of 0.75×10^6.

The effect that addition of underbody detailing has on the lift curve slope is shown in Figure 29. Without roughness elements on the underside both front and rear wheel lift are incidence dependent with rear wheel lift decreasing with increasing angle. On adding the underbody strips the zero incidence lift at both axles increases, front wheel lift slope reduces by 10% and the rear wheel lift becomes independent of pitch angle. The overall lift variation with incidence remains virtually identical. For all subsequent runs the underbody detailing was fitted as were the nose transition strips.

2.4.2 The influence of ground clearance.

The overhead mechanical balance necessitated a small clearance between wheels and ground to prevent spurious loadings arising from contact. Prior to obtaining lift data for wheeled bodies at incidence, the possible errors, arising from incorrect setting of the gap between wheels and ground, had to be established. Six car models were tested at three heights, the car being raised with the wheels. The different body shapes were modelled by fitting various upper body blocks to modify the side profile. The rear wheel lift and drag are seen in Figure 30 to vary only very slightly with change of wheel to ground clearance. The lift at the front wheels, however, show in all cases, a very dramatic rise when the clearance is less than 2mm. This figure corresponds roughly with the local displacement thickness of the ground board boundary layer, as measured with the model absent. The increase in lift is independent of body shape as shown in Figure 31.

To differentiate between lift effects arising from the wheel to ground gap and those arising from changes to the vehicle body clearance, the latter effect was determined by removing the wheels and varying the height above the ground plane. The result is shown in Figure 31 for three typical shapes as an incremental lift over the value obtained at a clearance of 20mm, which corresponds to the wheel to ground gap of 1mm. Measurements were taken over a considerably greater range of heights than in the previous test. Both front and rear wheel lift increase approximately linearly with reducing ground clearance, with the front wheel lift increasing at a faster rate. Comparison with a similar

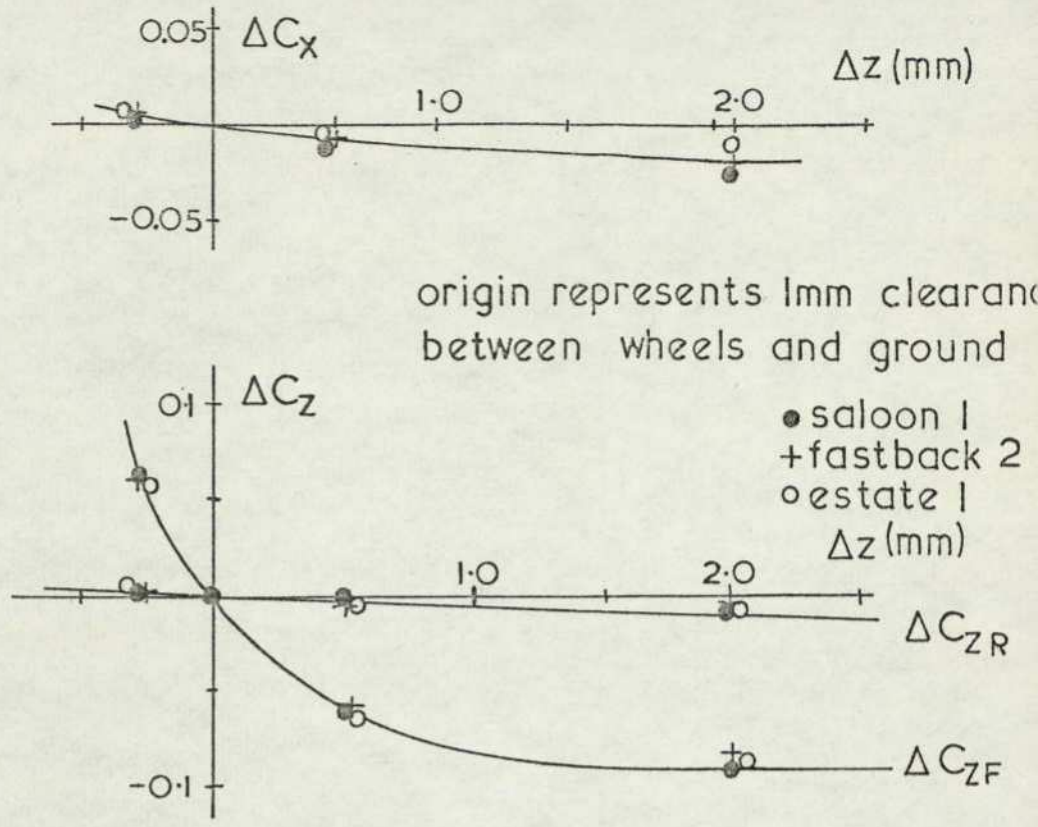

FIG.30 INFLUENCE OF WHEEL TO GROUND CLEARANCE ON LIFT AND DRAG

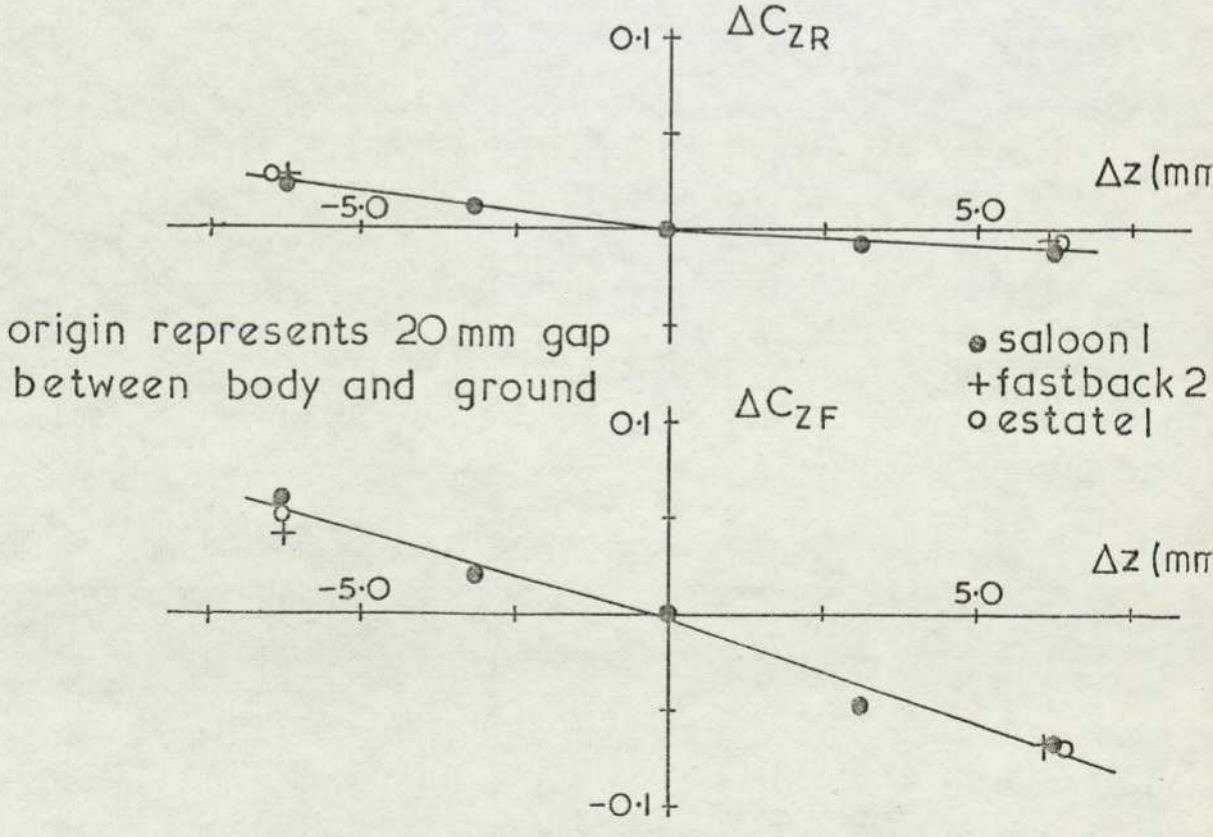

FIG.31 INFLUENCE OF BODY CLEARANCE ON LIFT NO WHEELS

curve for the wheel clearance shows that all the additional rear wheel lift arises from the change of body clearance while the lift at the front wheels is still dominated by the effect of the gap between the wheel and the ground plane. Note the different displacement scales.

These results suggest that the only satisfactory way to obtain lift data on vehicles at incidence is for individual adjustment of each wheel so that the clearance between wheel and ground remains constant, irrespective of the attitude of the body. As this approach would be time consuming; the model could not be easily modified to give this adjustment, and, furthermore, the main object of the experiment was only to establish lift data at zero incidence for direct comparison with the wake studies, a simpler alternative was adopted. In this approach the forces were measured at zero incidence with wheels fitted. The wheels were then removed flush with the underside of the body and the force data obtained over the incidence range of interest. It was assumed that the lift due to the presence of the wheels would be independent of vehicle attitude over the small range of incidence considered. The corrected lift coefficient, C_z, for the car at incidence is then given by

$$C_z = C_{z\alpha} + (C_{zo} - C_{z\alpha})_{\alpha=0} \qquad (2.1)$$

where $C_{z\alpha}$ is the lift coefficient at incidence, α, measured without wheels, and C_{zo} is the lift coefficient at zero incidence obtained with the wheels fitted.

2.4.3 The effect of incidence

The variation of front and rear wheel lift and drag forces with incidence is presented for all car model shapes in Figure 32. The coefficients have been corrected to give the lift on a body with wheels and having a clearance of 0.75mm between the wheels and the ground plane. The drag forces are seen to change only slightly with attitude. The three saloon car models give the highest drag with the estate vehicles experiencing slightly less. The difference reduces as the incidence decreases. There is little difference between the drag coefficients for the three fastback models; they are approximately 20% lower than those for the other two body styles.

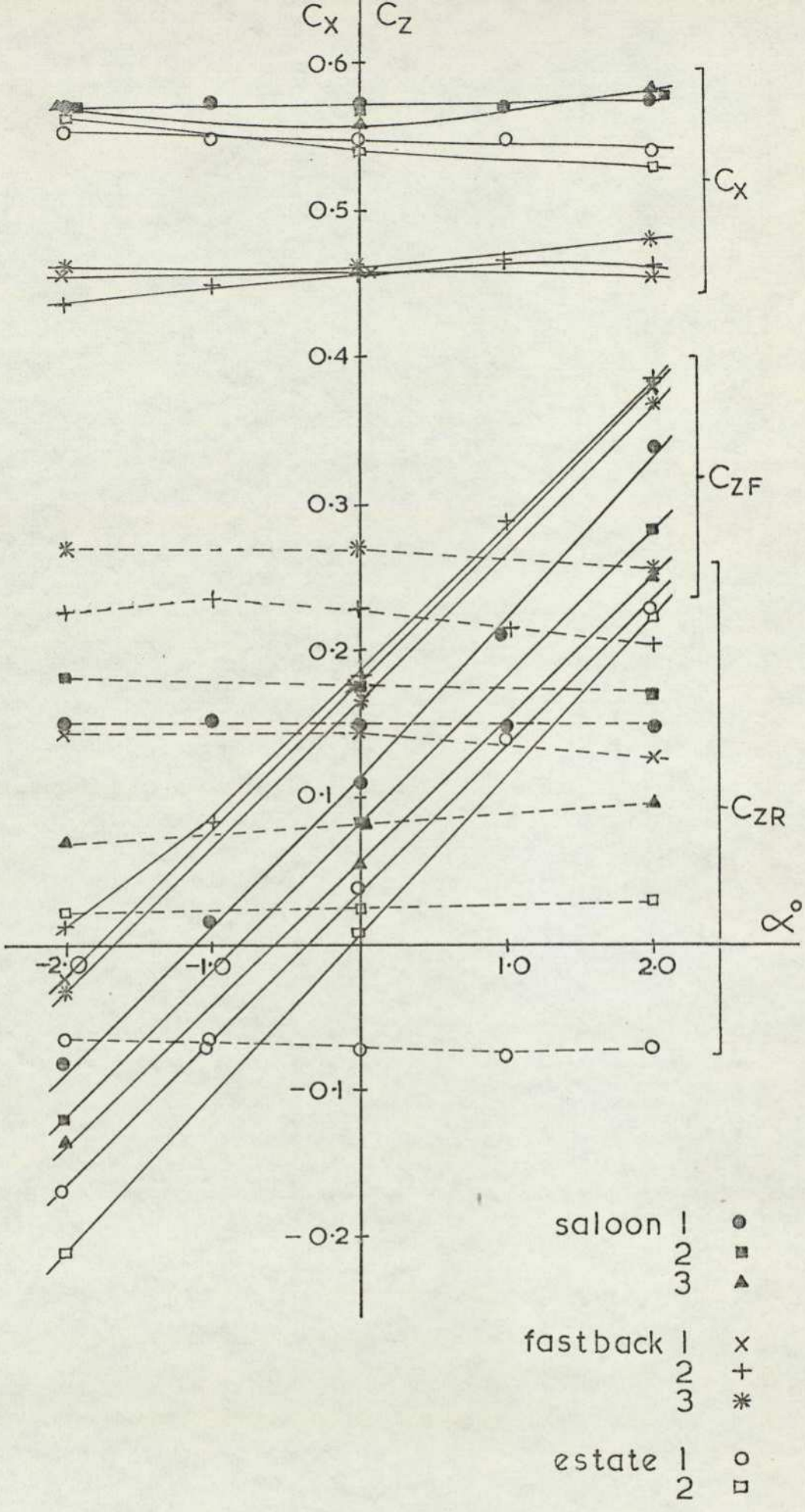

FIG.32 LIFT AND DRAG ON PASSENGER CAR SHAPES AT INCIDENCE

TABLE II: Lift curve slopes - car models

Model		$\delta C_z/\delta\alpha$ deg^{-1}
Saloon	1	0.092
	2	0.098
	3	0.103
Estate	1	0.110
	2	0.121
Fastback	1	0.094
	2	0.090
	3	0.094
Can Am		0.48

Rear wheel lift varies almost negligibly with incidence for all models. The fastback shapes have the greatest lift forces and the intermediate camber model experiences the maximum force. The saloon car models with the longest boot sections, S1 and S2, show almost as much lift on the rear axle, but reducing this length further reduces lift considerably. The Estate 1 model has the lowest value of rear wheel lift. The variations of front wheel lift with incidence is also seen to be very similar for all models; the only difference being recorded for the Estate 2 model which has the most aft windscreen position. The fastback models experience the greatest lift forces, the value increasing with the aft movement of the maximum thickness position. This agrees with the measurements on the cambered rectangular blocks. The saloon 1 model has almost identical lift at the front wheel to the Fastback 3 model, which has the steepest backlight rake. On reducing the boot length of the saloon models the front wheel lift reduces. This is the opposite effect to that found on the fastback models and is presumably related to the rearwards movement of the windscreen. The estate cars experience the lowest lift values at the front wheels with the minimum being found on the Estate 2 model. The overall lift curve slopes for all these models are summarised in Table II, above. The slope tends to increase for all models with the aft movement of the maximum thickness position.

In the last few years racing saloon cars have appeared with front spoilers fitted below the front bumper position: see for instance

Marcell and Romberg (5). It is claimed that these spoilers reduce drag and increase downthrust at the nose, thereby increasing road holding, especially under cross wind conditions. Many road cars now seem to have adopted the device, although this may be purely for 'cosmetic' reasons. To investigate the effect on the vehicle characteristics when pitching, two modifications were made to the front lower leading edge of the saloon 1 model. The first modification was simply to square off the originally well radiused front sill while the second modification extended the vertical front face of the nose downwards to halve the gap between the underside and the ground. The lift and drag characteristics for the Saloon 1 model with and without these modifications is shown in Figure 33. Addition of the squared nose is seen to slightly increase drag while the model with the spoiler suffers a considerably increased drag, especially at negative incidence. This contradicts some experiments with spoilers although Janssen and Hucho (14) have shown that the design and location are critical. The rear wheel lift shows a small degree of dependence on attitude for both nose shapes, albeit of different sign, and the lift increases with the extent of modification. Zero incidence lift at the front wheels reduces noticeably as the leading edge sharpness increases, but whereas the lift slope of the squared leading edge model is very similar to that for the unmodified saloon, the addition of a spoiler makes the front wheel lift essentially independent of incidence. This implies that the handling qualities of a vehicle fitted with such a spoiler are much more consistent than those for a vehicle without as the loads on the steered wheels remain constant irrespective of vehicle attitude or external flow conditions.

In section 2.4.2. the variation of zero incidence lift with ground clearance was examined. Figure 34 shows the effect of incidence at those ground clearances, for the three basic types of passenger car; the Saloon 1, Fastback 2, and Estate 1 models. All three vehicles display similar trends. The rear wheel lift slope is always close to zero and the lift slope at the front wheels increases on approaching the ground. The overall lift derivative $\delta C_z/\delta\alpha$ is plotted against the reciprocal of the ground clearance, for all three models, in Figure 35. The saloon and fastback models display almost identical results while the estate car experiences a considerably greater lift slope at a given clearance. The outer shape of the body therefore has some importance.

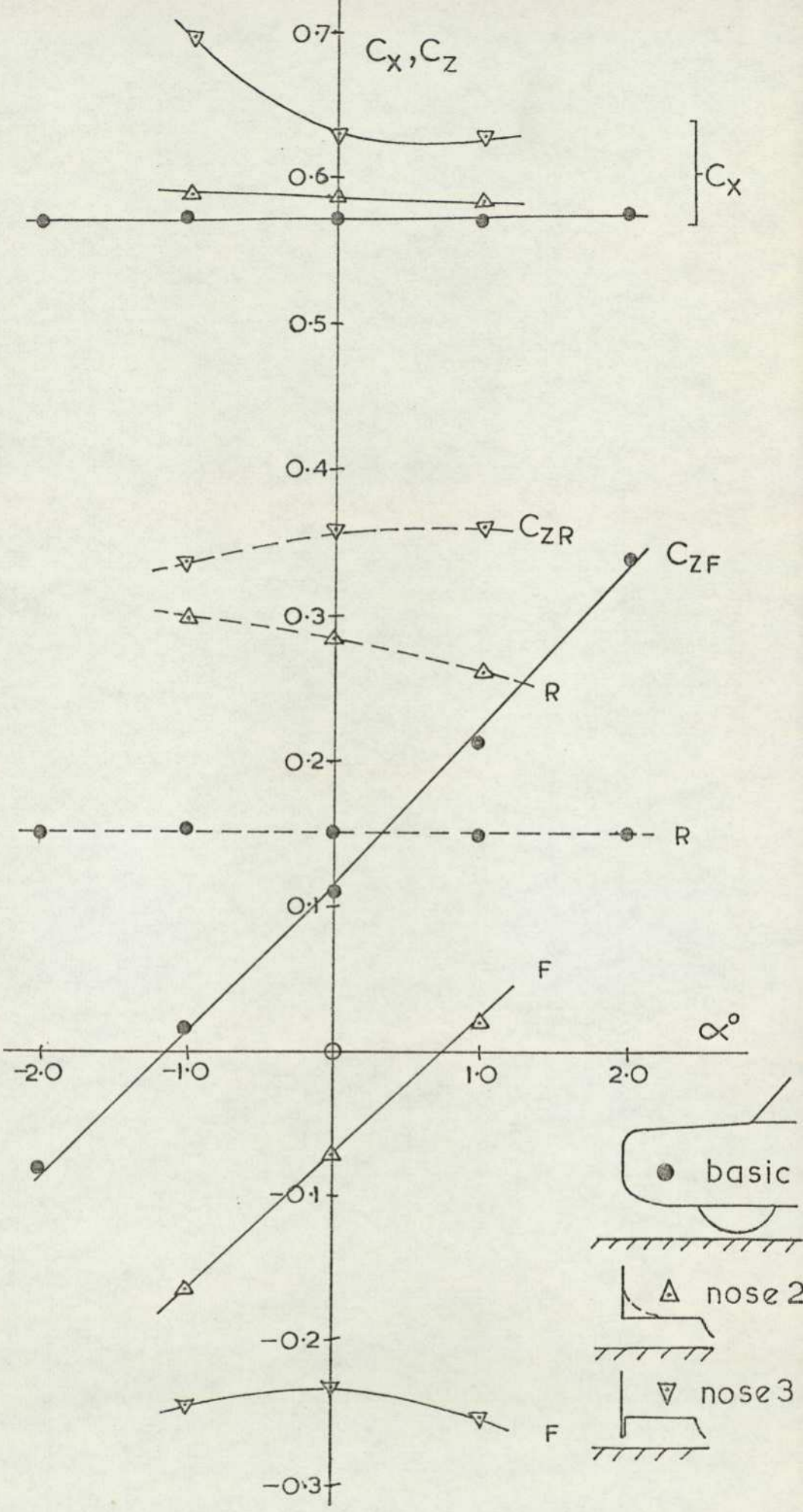

FIG.33 INFLUENCE OF NOSE SHAPE — SALOON

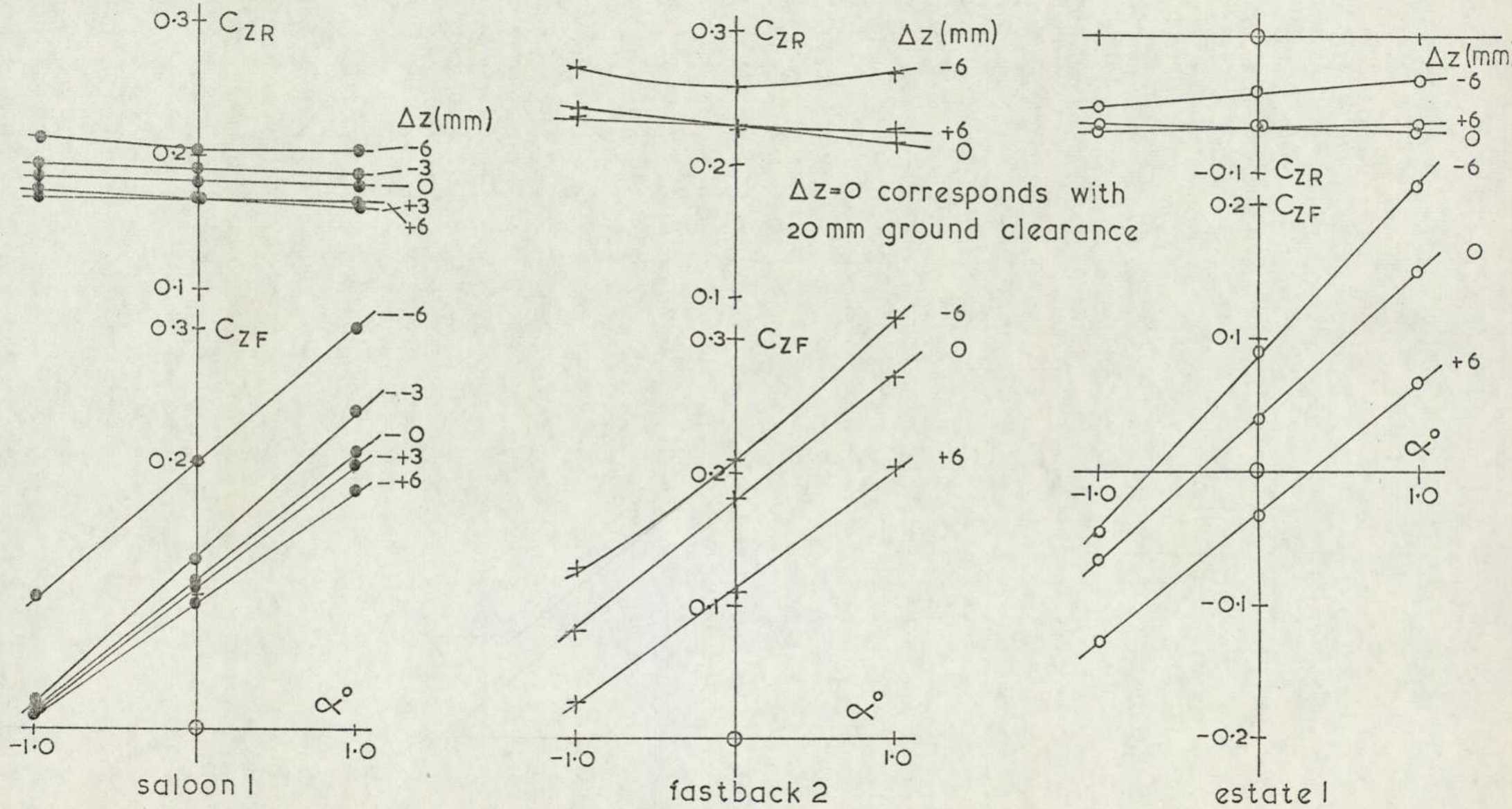

FIG.34 VARIATION OF LIFT SENSITIVITY WITH GROUND CLEARANCE

2.4.4 Incidence at yaw

It is rare for a road vehicle to experience zero yaw conditions for any substantial period of time. The effects of combined pitch and yaw attitudes were studied using the Saloon 1, Fastback 2, and Estate 1 models. The results are shown in Figure 36. Considering the saloon car only, an increase of yaw angle raises both the zero incidence lift, and the lift slope. As before the lift variation is predominantly at the front wheels although at a greater yaw angle there is some dependence of rear wheel lift on incidence. At a yaw angle of 15° the lift slope for the front wheels is 50% greater than at zero yaw. The fastback model experiences greater variation at the rear wheels, although the overall response is similar to that for the saloon. The estate car shows a greater variation of zero incidence lift with yaw but the lift slope with incidence is similar to the other models.

2.4.5 Can Am Racing Car

Figure 37 gives the front and rear wheel lift coefficients for the model Can Am Racing car at incidence. This model was only tested without wheels so the absolute lift values are in error. The presence of wheels would have the effect of increasing the lift. At zero incidence both the front and rear wheels experience considerable downforce and the pitching moment is positive slightly, which is typical of these vehicles. The lift variation with incidence is very high especially at the front wheels although the rear wheels contribute one quarter of the total. It will later be shown that on this model there appears to be considerable separation from the ground plane immediately aft of the model. This is due to a combination of low ground clearance and strong upwash. It is not clear how unrepresentative this might be, but it is possible that it contributes towards the high lift changes by creating higher underbody pressures due to flow stagnation than would exist on an actual vehicle. The behaviour of real vehicles of this type does suggest, however, that extreme changes do take place, see Hulme (13).

2.4 Discussion

2.5.1 Forces on actual vehicles

Some previous measurements of lift due to incidence have been

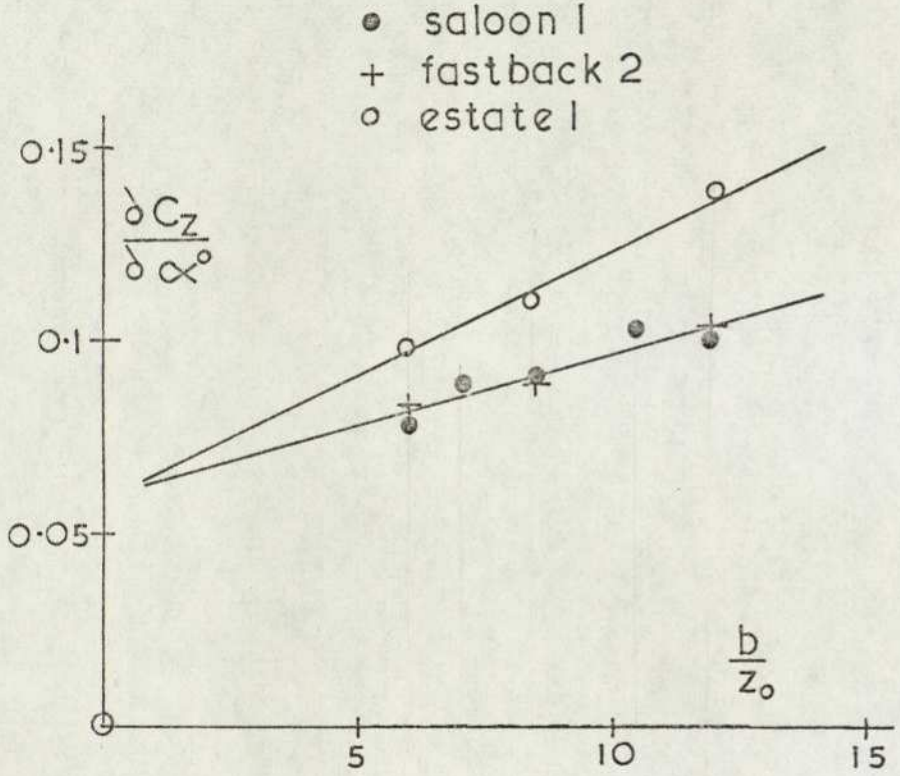

FIG. 35 LIFT SLOPE AS A FUNCTION OF GROUND CLEARANCE

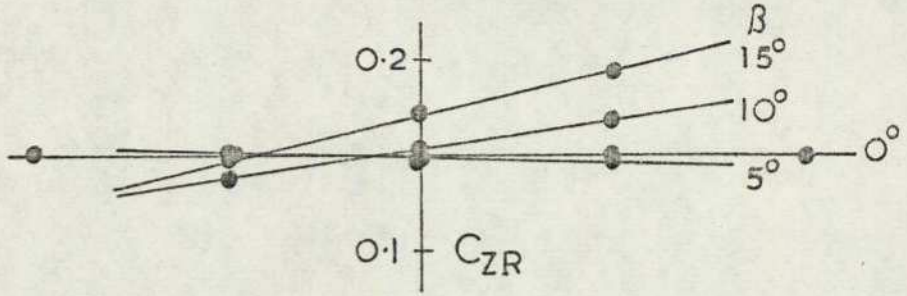

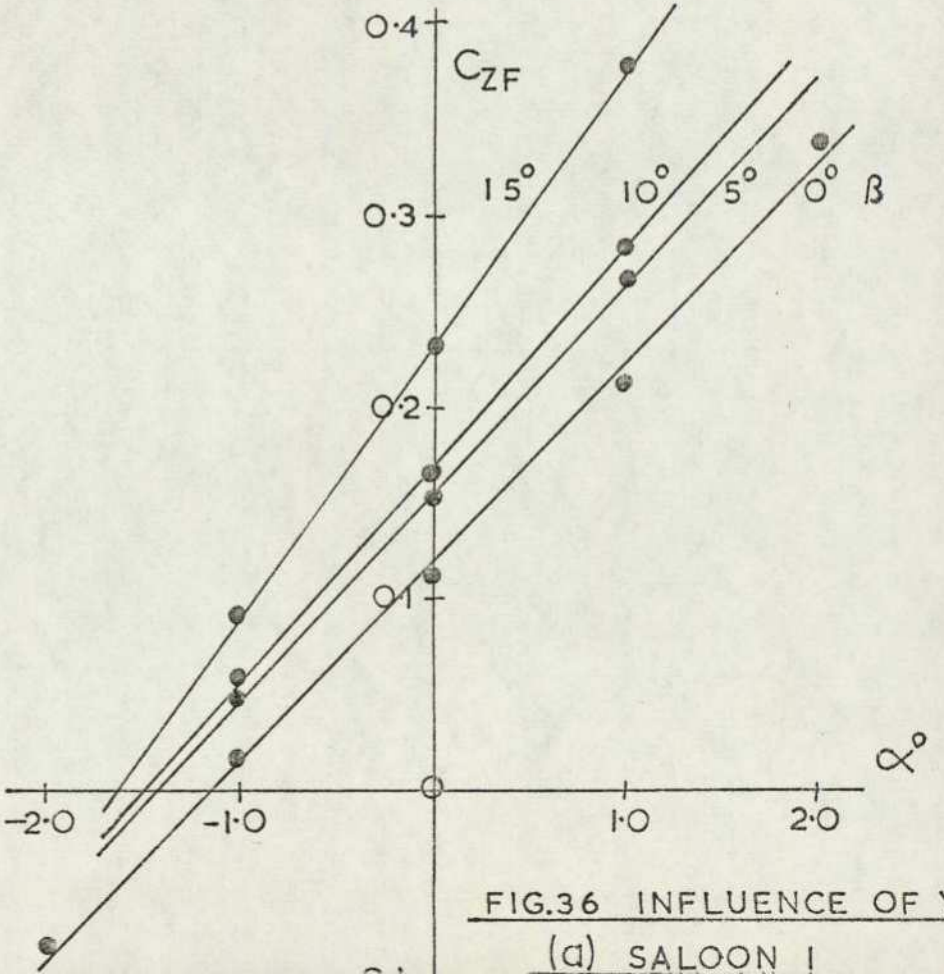

FIG. 36 INFLUENCE OF YA

(a) SALOON 1

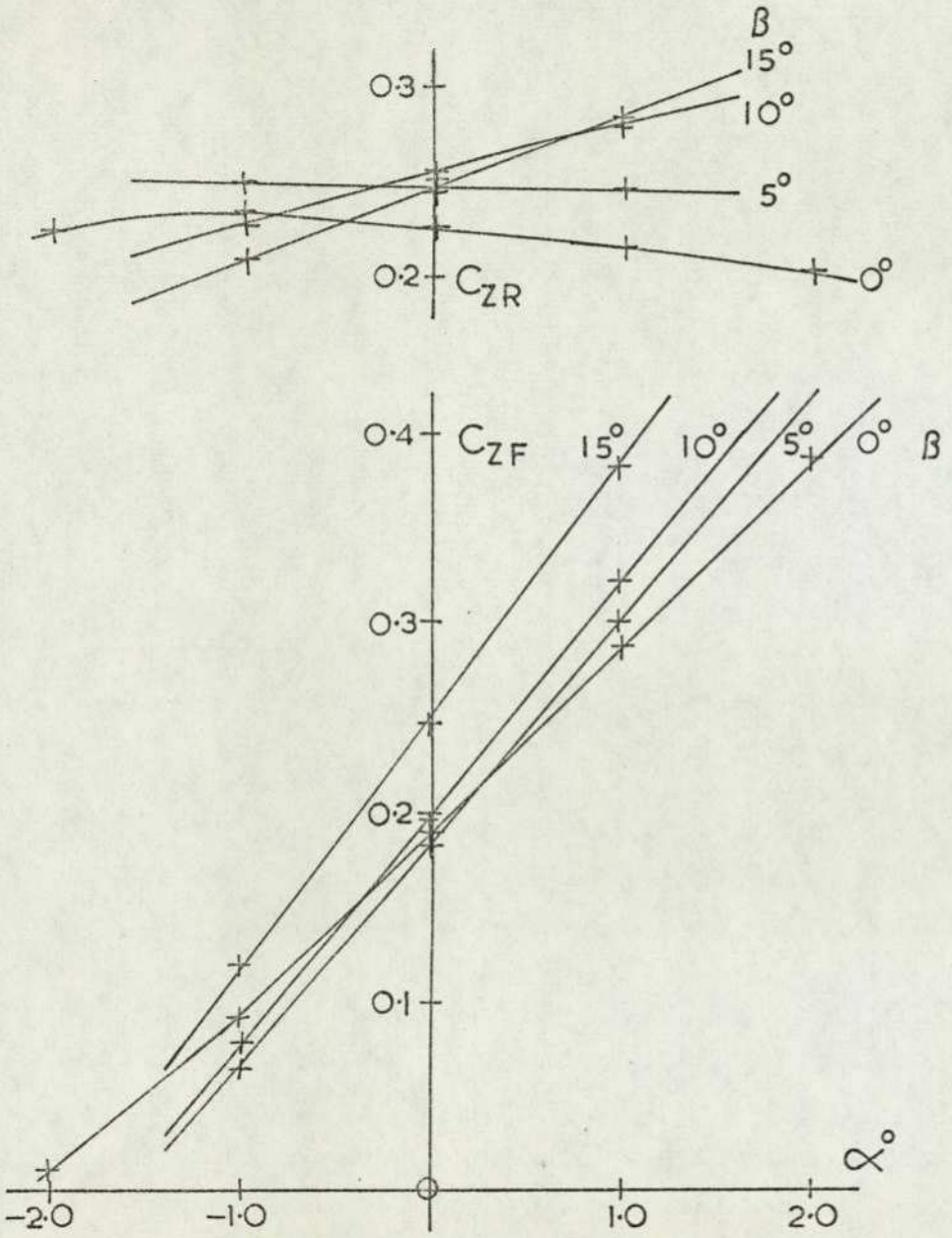

FIG.36(b) FASTBACK 2

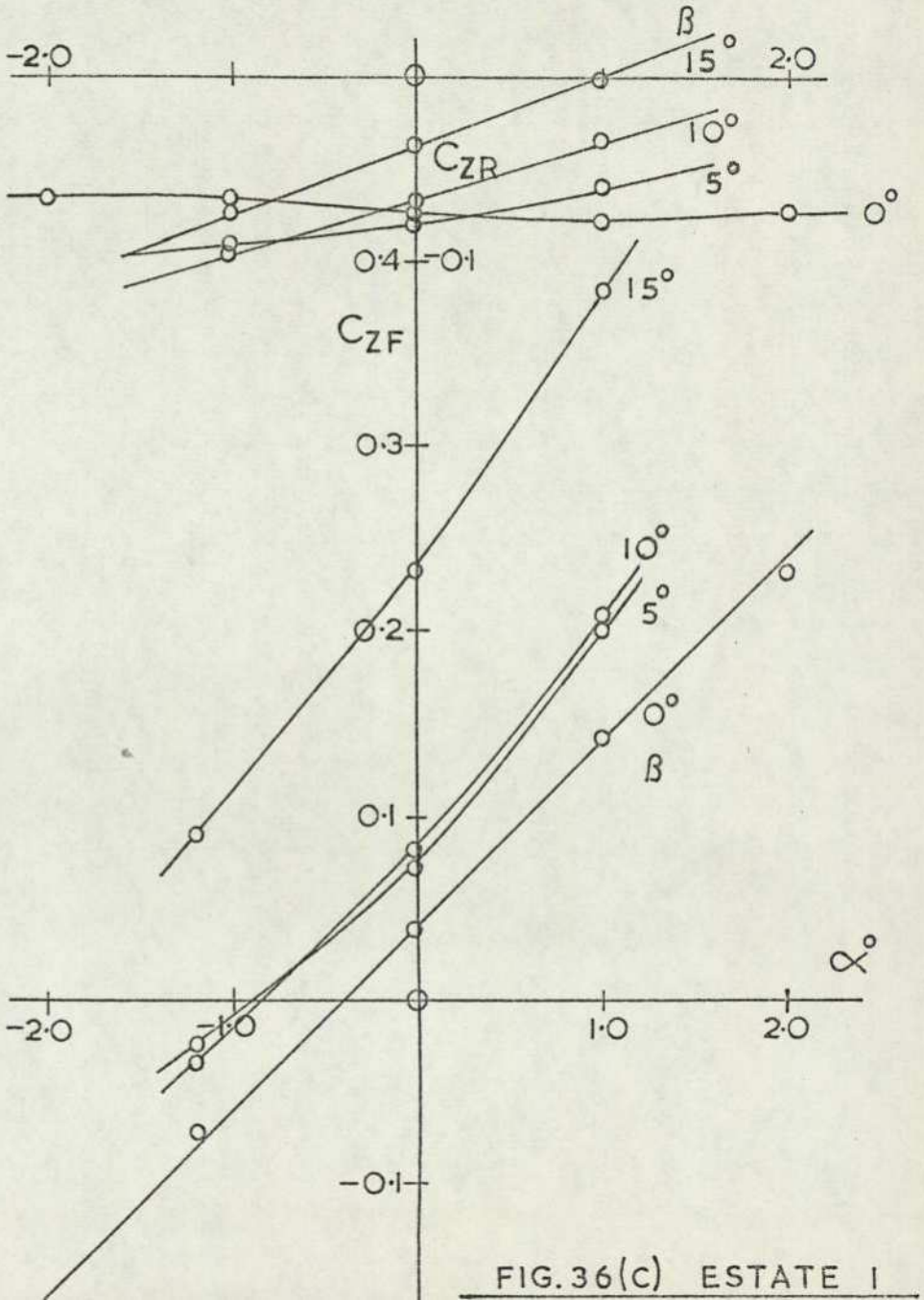

FIG.36(c) ESTATE 1

made with wheels fitted to models and it has been unclear as to the precautions taken to avoid large lift changes arising from variation in wheel clearance. The absolute value of lift is strongly dependent on the state of representation, whether it is wheel clearance, transition, or underbody detailing. Lift variation with incidence is notably more dependent on larger scale geometrical changes. Over the Reynolds number range studied there is a negligible change in lift characteristics although the drag coefficient reduces considerably.

The aerodynamic centre, for all vehicles tested, is situated, longitudinally, very close to the front axle and, vertically, just below the upper surface of the bonnet. All shapes experience a lift coefficient slope close to 0.1 deg^{-1}. This corresponds to a change of lift force at the front wheels when the speed of the vehicle is 30m/s (68 m.p.h.) of 115N (25 lbf) per degree; at 42 m/s (100 m.p.h) this force increases to 242N (55 lbf) per degree. It is possible that the measured values of lift slope differ from those obtained on a real vehicle as the position of maximum variation in lift is also where the greatest inaccuracies in modelling are found. With wheels in place the confining of the flow should increase the lift slope in the same way that lift is improved by the addition of endplates to a ground effect wing. At the same time the local body surface is not usually flat or continuous, as this region is the engine compartment in most vehicles, and is therefore open on the underside. These changes would have opposite effects, although comparison with the data of Janssen and Hucho (14), who show lower lift slopes, suggests that the latter effect may dominate. The results of these authors also differed, however, in showing a drag variation with incidence.

The action of a cross wind, represented in the tunnel by a yawed model, increases both the lift force at zero incidence and the lift slope. The increase in overall lift curve slope is plotted in Figure 38 as a function of the slope at zero yaw for the three vehicle types considered. There is a slight spread of results but the trend is similar for all vehicles. A doubling of lift curve slope occurs at a yaw angle of less than 20°. The saloon car data is extrapolated to give the total lift coefficient at a pitch angle of 2° positive and is plotted against yaw angle in Figure 39. This shows that the lift coefficient approaches unity for a yaw angle of 20°. This incidence angle is possible with many passenger cars and does not necessarily imply an overloaded case.

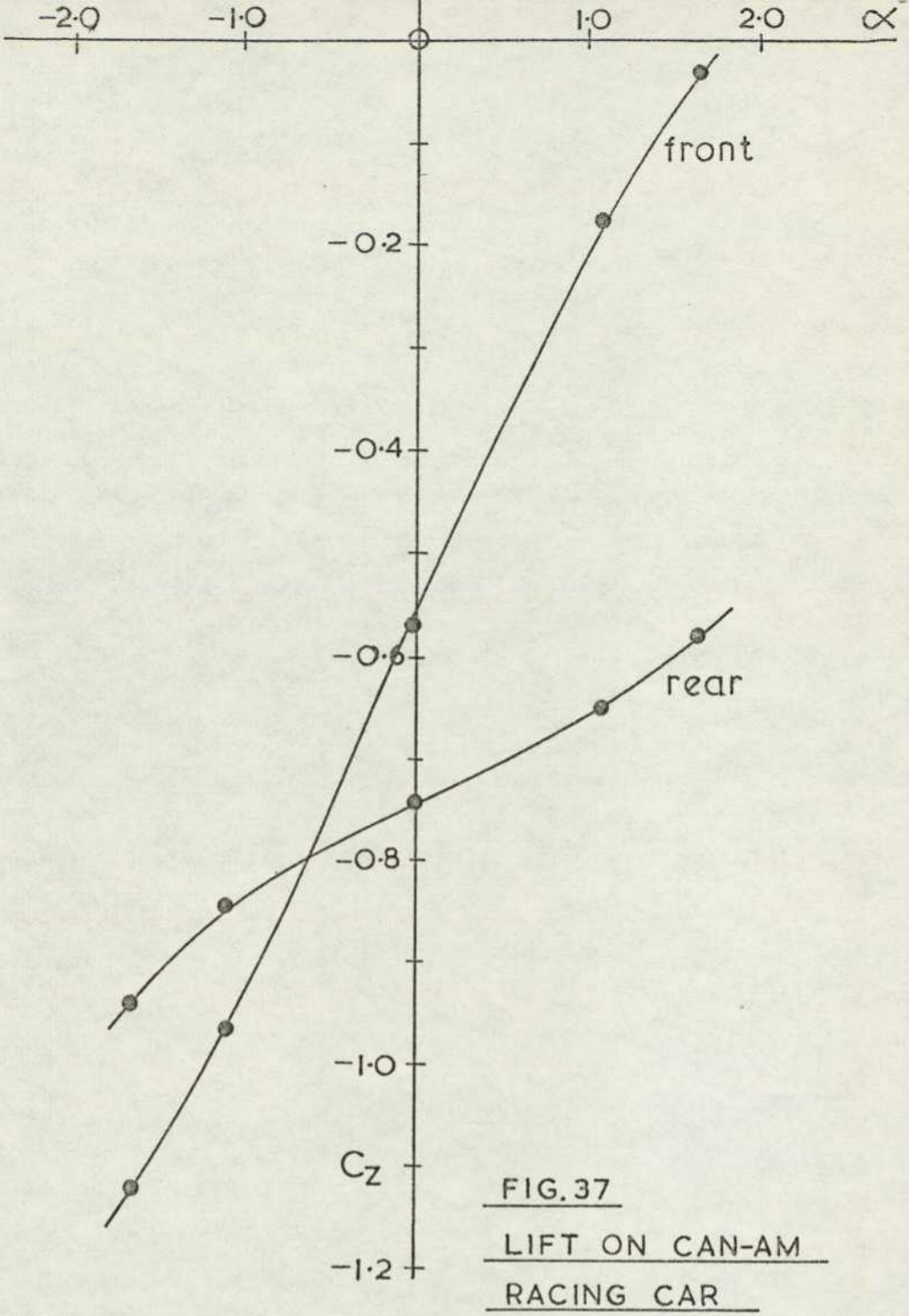

FIG. 37

LIFT ON CAN-AM RACING CAR

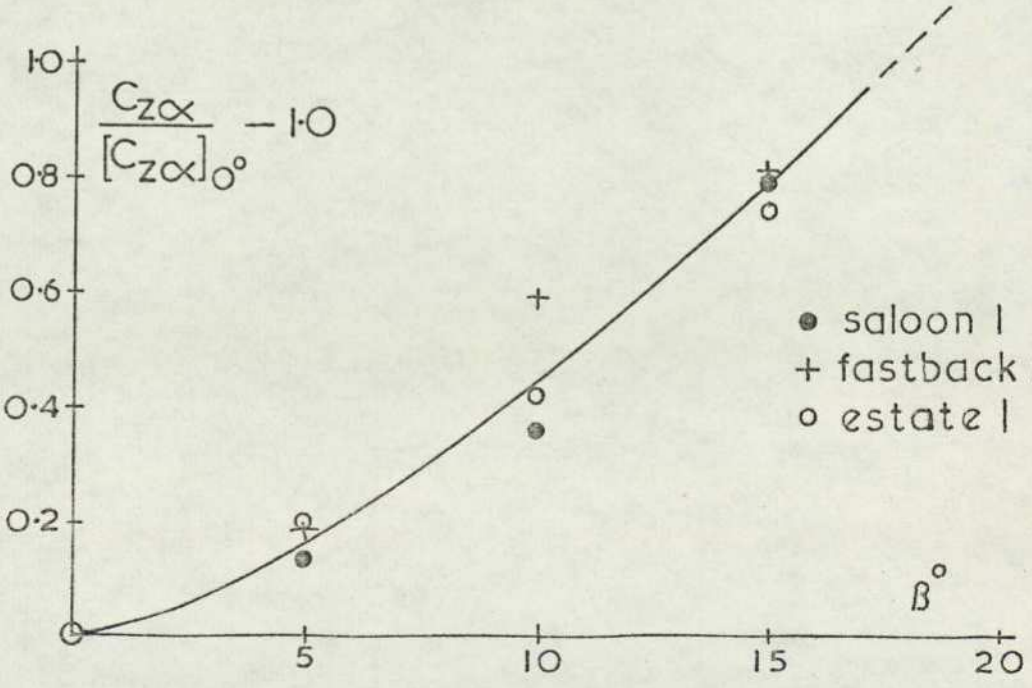

FIG. 38 EFFECT OF YAW ON LIFT CURVE SLOPE

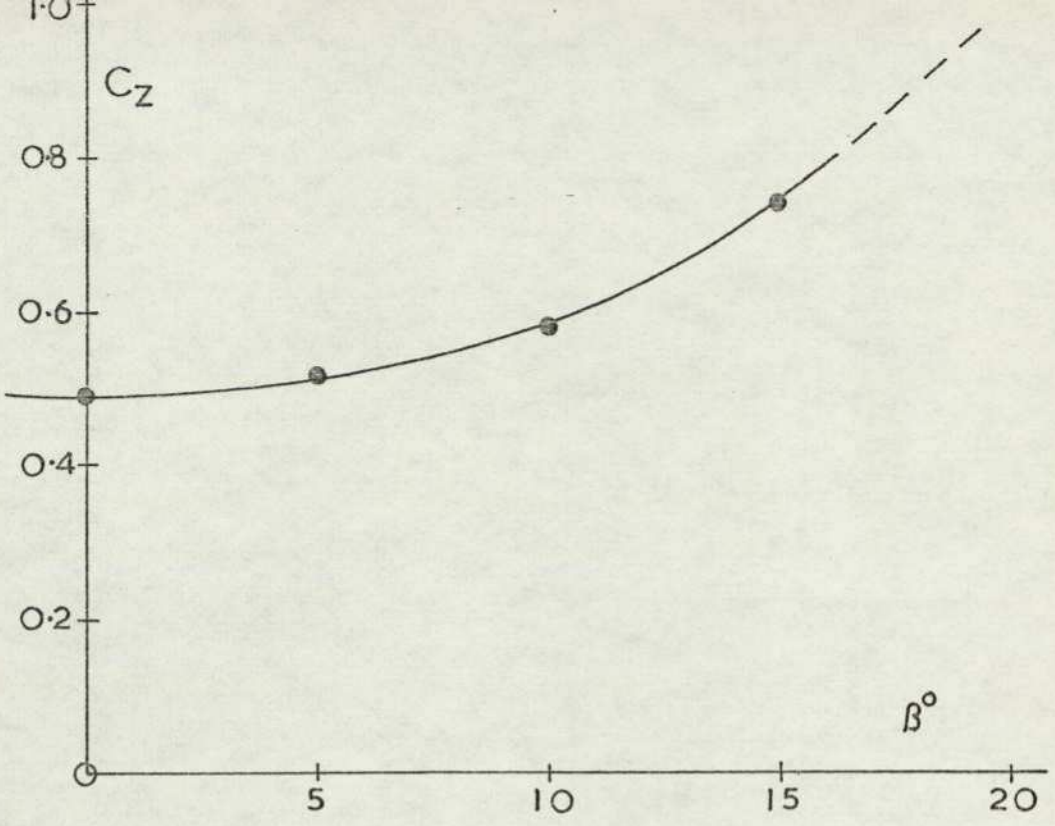

FIG.39 TOTAL LIFT ON SALOON I MODEL AT 2° INCIDENCE

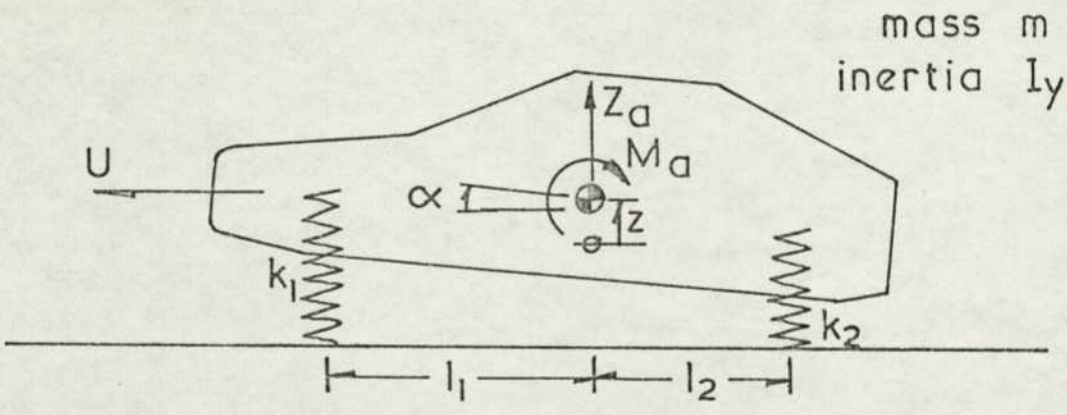

FIG.40 SIMPLE VEHICLE DYNAMICS MODEL

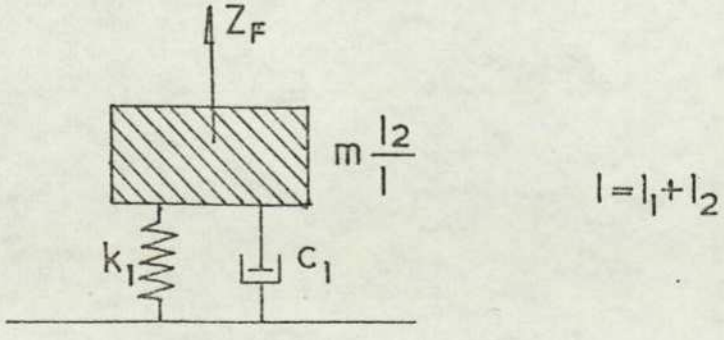

FIG. 41 FRONT SUSPENSION MODEL

To generate an effective yaw angle of 20° would require a cross wind velocity of 10 m/s when the vehicle speed is 30 m/s (68 m.p.h.) and for a vehicle travelling at 42 m/s (100 m.p.h.) a wind speed of 14 m/s would be necessary. The latter velocity can not be considered extreme. Tracked Hovercraft Ltd. (22) took as their design case a value of almost twice this. At the lower speed the saloon car would experience a lift force of 1.1 kN (240 lbf) and this increases to 4.0 kN (900 lbf) at the higher speed. The front wheels under these conditions must be almost completely unloaded. Combined with the rearward shift of the centre of gravity, producing the initial incidence, this change in loading must produce a serious deterioration to the handling. On all the passenger vehicles considered, increasing incidence shifts the centre of action of the lift force forwards while the opposite is true at negative incidence.

The Can Am racing car at incidence develops 1.73 kN (390 lbf) of lift per degree at 63 m/s. At 84 m/s, approximately maximum speed, this figure is increased to 3.0 kN. Eighty per cent of the lift change is carried at the front wheels. These cars have a total weight of less than 1.0 tonne but the high downforce on the bodies at zero incidence means that the front wheels do not suffer positive lift until the vehicle is almost at 2° of incidence, which would represent the total suspension travel. The very high lift forces necessary at the front wheels to overturn one of these racing cars could only be generated by an external disturbance. This could take the form of upwash from another car's wake flow or may be inertial as would occur when the road gradient reduces. It is perhaps disturbing to note that the trend in single seat racing cars, and Formula 1 types in particular, is towards the building of the maximum width bodies available under present restrictions. These machines travel at similar speeds but are of considerably lighter weight and therefore more susceptible to disturbance by the similar aerodynamic loads being generated.

Variation of the ground clearance of the passenger cars produces characteristics similar to those obtained for the rectangular blocks. The intercept on the vertical axis representing the free stream case, agrees closely for all models and with the value for a rectangular block having identical thickness to width ratio. On approaching the ground, however, the estate car lift slope diverges significantly from those for the saloon and fastback models.

It is difficult to explain why the rear end geometry should have an influence when in ground proximity and no effect in free stream. The earlier experiments using rectangular blocks seemed to show that the changes to lift slope arising from ground proximity arose purely from the modified flow conditions in the gap between vehicle and ground. These results, however, show that the flow around the outer body parts, that is well away from ground, appears to be of similar importance. The cambered rectangular block, 9C, in comparison with the basic uncambered block, 7N, revealed a similar trend. The point is emphasised by comparing the lift curve slopes of the rectangular blocks near to ground with those of the estate car, which of the car shapes most resembles a block. The data for the basic blocks tends to collapse to a single line but the estate car results, as a function of ground clearance, have only half the equivalent slope. The saloon and fastback models experience a lift curve slope that is further reduced by 40%. The discrepancy between estate car and rectangular blocks data can be explained by considering the underbody flow. The trailing edge conditions are not sufficiently different between the two cases or over the incidence range of interest to have a large influence on lift. The changes due to incidence must therefore arise from the leading edge flow. The stagnation streamline is probably not influenced strongly by the aft body geometry and so the flow under the leading edge is fairly dependent on the ratio of the nose thickness to the ground clearance. The road vehicles are therefore comparable with rectangular blocks at relatively greater ground clearance.

The differences between the various car designs arises from the influence of the body circulation on the leading edge flow. The greater the vehicle lift the lower the front stagnation point and so the flow under the vehicle 'sees' an effectively thinner body, that is one at relatively greater clearance again.

At the same time these effects would not be noticeable in free stream conditions and the lift is dependent only on the body planform. The action of a spoiler can also be accounted for. The salient lower edge dramatically lowers the front stagnation point, so reducing the sensitivity of lift to incidence.

2.5.2 Vehicle stability under aerodynamic loads.

To examine any aerodynamic influence on vehicle behaviour the longitudinal equations of motion are modified by including aerodynamic terms. These equations, set out below, are simplified by ignoring all damping terms and the primary stiffness and mass of the tyres. The zero change of drag with incidence enables the coupling with velocity error to be ignored. With reference to Figure 40 the equations describing the pitch and heave motion for a body axis system are:

$$\Delta Z = m(\ddot{z}+\dot{\alpha}U) = -(k_2 z_2 + k_1 z_1) + \Delta Z_a \qquad (2.2)$$

$$\Delta M = I_y \ddot{\alpha} \quad = k_2 l_2 z_2 - k_1 l_1 z_1 + \Delta M_a \qquad (2.3)$$

where ΔZ, ΔM are total changes from equilibrium in lift force and pitching moment respectively, on a body of mass m, and pitch inertia I_y, travelling with forward velocity U, and pitch angle α, The vertical displacement z, and stiffness k, are referred to front and rear suspension by the suffices 1 and 2 respectively. The suffix, a, refers to aerodynamic terms, and the suspension is distance, l, from the centre of gravity. The terms z_1 and z_2 can be expanded as

$$z_1 = z + l_1\alpha \qquad (2.4)$$

$$z_2 = z - l_2\alpha$$

where z is the heave displacement of the centre of gravity, and the aerodynamic terms, making the assumption that all the lift variation takes place at the front wheels, can be written

$$\Delta Z_a = \frac{\delta C_z}{\delta \alpha}\alpha \frac{1}{2}\rho U^2 A \qquad (2.5)$$

$$\Delta M_a = \frac{\delta C_z}{\delta \alpha}\alpha \frac{1}{2}\rho U^2 A l_1$$

The characteristic equation, writing s for differentiation with respect to time, is then

$$\begin{vmatrix} ms^2+(k_1+k_2) & ms U+k_1l_1-k_2l_2-\frac{\delta Z_\alpha}{\delta \alpha} \\ k_1l_1-k_2l_2 & I_y s^2+k_1 l_1^2+k_2 l_2^2-\frac{\delta Z_\alpha}{\delta \alpha} l_1 \end{vmatrix} = 0 \qquad (2.6)$$

Many vehicles have almost uncoupled heave and pitch motions arising from

$$k_1l_1 = k_2l_2 \qquad (2.7)$$

and making this simplification it is immediately obvious that the heave root is independent of any aerodynamic terms, being given by

$$s_1 = i((k_1+k_2)/m)^{1/2} \qquad (2.8)$$

The other root, however, still contains an aerodynamic term and is given by

$$s_2^2 I_y = \frac{\delta C_z}{\delta \alpha} l_1 \frac{1}{2}\rho U^2 A - (k_1 l_1^2+k_2 l_2^2) \qquad (2.9)$$

When s is real this equation represents an unstable situation and a critical velocity, U_c, can be defined, after substitution from (2.7) as

$$U_c = \left[\frac{2 k_1 (l_1+l_2)}{\frac{\delta C_z}{\delta \alpha} A \rho} \right]^{1/2} \qquad (2.10)$$

and the mode is a coupled pitch and heave of the c.g. with the centre of rotation at the rear axle. As this is a linearised analysis the same result could have been achieved by consideration of the static stability. Inclusion of damping terms does, therefore, not modify the result. Tyre stiffness, being an order of magnitude greater than suspension stiffness, can be ignored. For $U<U_c$ the natural frequency, ω, of the pitching motion is given by

/ (2.11)

$$\omega_z^2 = \frac{k_1 l_1 (l_1+l_2) - \frac{\delta Z_a}{\delta \alpha} \cdot l_1}{I_y} = \omega_o^2 \left(1 - \frac{\delta Z_a / \delta \alpha}{k_1 (l_1+l_2)}\right) \qquad (2.11)$$

where ω_o is the natural frequency at zero speed. The variation of the frequency with speed can be expressed as

$$\left(\frac{\omega}{\omega_o}\right)^2 = 1 - \left(\frac{U}{U_c}\right)^2 \qquad (2.12)$$

A medium sized saloon car typically has suspension stiffness giving pitch and heave frequencies of about 1.25 Hz, the weight is 0.8 tonne with a wheelbase of 2.5 m and a 50/50 weight distribution. The frontal area is $2m^2$ and substitution of the wind tunnel results for $\delta C_z / \delta \alpha$ gives a critical velocity of 100 m/s (2 25 m.p.h). This is of academic interest to normal road going vehicles, which at typical maximum speeds will not notice any reduction in natural frequency either. There was, however, an instance some years ago, when a gas-turbine propelled Volkswagen 'Beetle', known as the 'Black Widow' became airborne at a speed of 84 m/s .. while performing on a drag-racing strip. For larger passenger cars the frequency of the suspension and the ratio of wheelbase to cross sectional area remain approximately constant and so the critical velocity will increase proportionally with the square root of the mass. The Can Am car, in common with most racing cars, has suspension stiffness which are typicially twice those of a conventional car. The frontal area is reduced by 30% while the lift slope is increased fourfold at the front wheels. These factors combine to give a critical velocity close to 84m/s (200m.p.h.) which is the order of their limiting speed and well above the speed of 63 m/s at which the three overturning incidents have occurred while racing(13).

Besides modifying the natural frequency of a system introduction of aerodynamic effects can alter the damping terms. Consider the flow along the underside of the body. An effective local angle of incidence, α_e, can be created by a geometrical incidence, α , or by a local heaving velocity arising from both a heave velocity, z, and a pitch rate, q. This can be written

/ (2.13)

$$\alpha_e = \alpha - \frac{\dot{z}}{U} - \frac{qx}{U} \qquad (2.13)$$

where x is the distance forward of the centre of gravity, of the station considered. Under a pure heave motion each station of the body experiences the same effective incidence and so the lift force due to a heaving motion can be assumed to act at the front wheels. Lift and pitching moment derivations due to heave velocity can therefore be defined

$$C_{Z\dot{z}} = \frac{1}{U} C_{Z\alpha} \qquad (2.14)$$

$$C_{M\dot{z}} = \frac{l_1}{lU} C_{Z\alpha}$$

where l is the wheelbase. The derivatives due to pitch rate are impossible to define without knowing the distribution of lift force due to incidence. Assuming, however, that the force changes are confined to a region close to the front suspension and therefore well forward of the centre of gravity, a first approximation to the lift and pitching moment derivatives due to pitch rate would be

$$C_{Zq} = \frac{l_1}{U} C_{Z\alpha} \qquad (2.15)$$

$$C_{Mq} = \frac{l_1^2}{lU} C_{Z\alpha}$$

Typically a mechanical damper provides 20% of critical damping. For a single degree of freedom system, Figure 41) representing the front suspension, the damping constant, c_1, is given by

$$c_1 = 0.4\, m_1 \omega_1 \qquad (2.16)$$

where $m_1 = m \frac{l_2}{l}$

Using the values quoted earlier for a typical passenger car the ratio of aerodynamic heave damping to total mechanical front suspension damping is given by

$$\frac{c_a}{c_1} = \frac{C_{z_\alpha} \frac{1}{2} \rho U A}{0.4\, m_1 \omega_1} \qquad (2.17)$$

$$= 0.046\, U\,(m/s)$$

The two expressions become equal at 22 m/s (50 m.p.h.) and the combined damping goes critical at four times this speed. As the natural frequency is reduced, as given by equation (2.12), the critical damping speed is reached earlier at about 62.5 m/s (140 m.p.h.). This is still stable but no oscillatory term appears in the root. The effect on the handling at this speed must be noticeable although between the normal driving speeds of 13 m/s and 30 m/s there is less than a 50% increase in total damping. The Can Am car is found to be twice as sensitive to speed. For any high speed road or race vehicle any device which can reduce lift sensitivity must be of considerably value.

2.6 Conclusions

For the rectangular blocks the lift slope is inversely proportional to ground clearance. The data can be collapsed onto a single curve. Introduction of camber noticeably reduces the lift curve slope at a given ground clearance. In addition for all the rectangular blocks reduction of the data to single curves is possible for the induced drag, the minimum drag, and the zero incidence lift.

The data for the road vehicles shows that for all passenger cars the aerodynamic centre is close to the front axle. Slight variations in lift curve slope are apparent for different designs arising from the influence of nose design and vehicle lift on the flow under the nose. Drag dependence on incidence is negligible. A cross wind increases the sensitivity to pitch.

Aerodynamic forces are shown to have considerable influence on the handling of passenger cars at high speed.

3. GROUND BOARD BOUNDARY LAYER

3.1. Introduction

In Chapter 1 the problem of ground simulation was introduced and discussed. It was decided that a static ground board would provide adequate representation. The flow conditions in the wake of a moving vehicle will differ from those measured in a wind tunnel as the boundary conditions are not satisfied at ground surface. This discrepancy will arise for two reasons. Firstly the force characteristics of the body itself will be modified and will become manifest in the wake. Secondly the wake boundary conditions must be false at the ground surface. From measurements of the static pressure distribution along the ground plane and of total head using a pitot rake the velocity profiles at the surface can be derived and an understanding of the boundary layer growth obtained. Assumptions can be made concerning the development of the ground boundary layer near a moving vehicle and from the differences the possible errors arising from false representation of the ground can be determined.

3.2. Ground board pressure distribution

3.2.1 Rectangular blocks

The pressure distribution along the centre line of the ground board was recorded for every block and car model for which wake studies were to be made. Pressure corrections as given by equation (1.20) have been applied throughout the length of the ground board, although they are probably invalid far from the model. The models were mounted in one of two positions on the ground board depending on whether force or wake data was being obtained. For wake studies the models were mounted close to the leading edge, enabling the traverses to be performed at the sufficient downstream position, while the force measurements were obtained with the model mounted at the mid length of the ground board. To ensure similarity of flow between the two cases the pressure distributions for both situations are compared in Figure 42 for block 2N. The longer ground board length forward of the model gives rise to a slower change in pressure immediately downstream of the ground board leading edge, but this is the only noticeable difference.

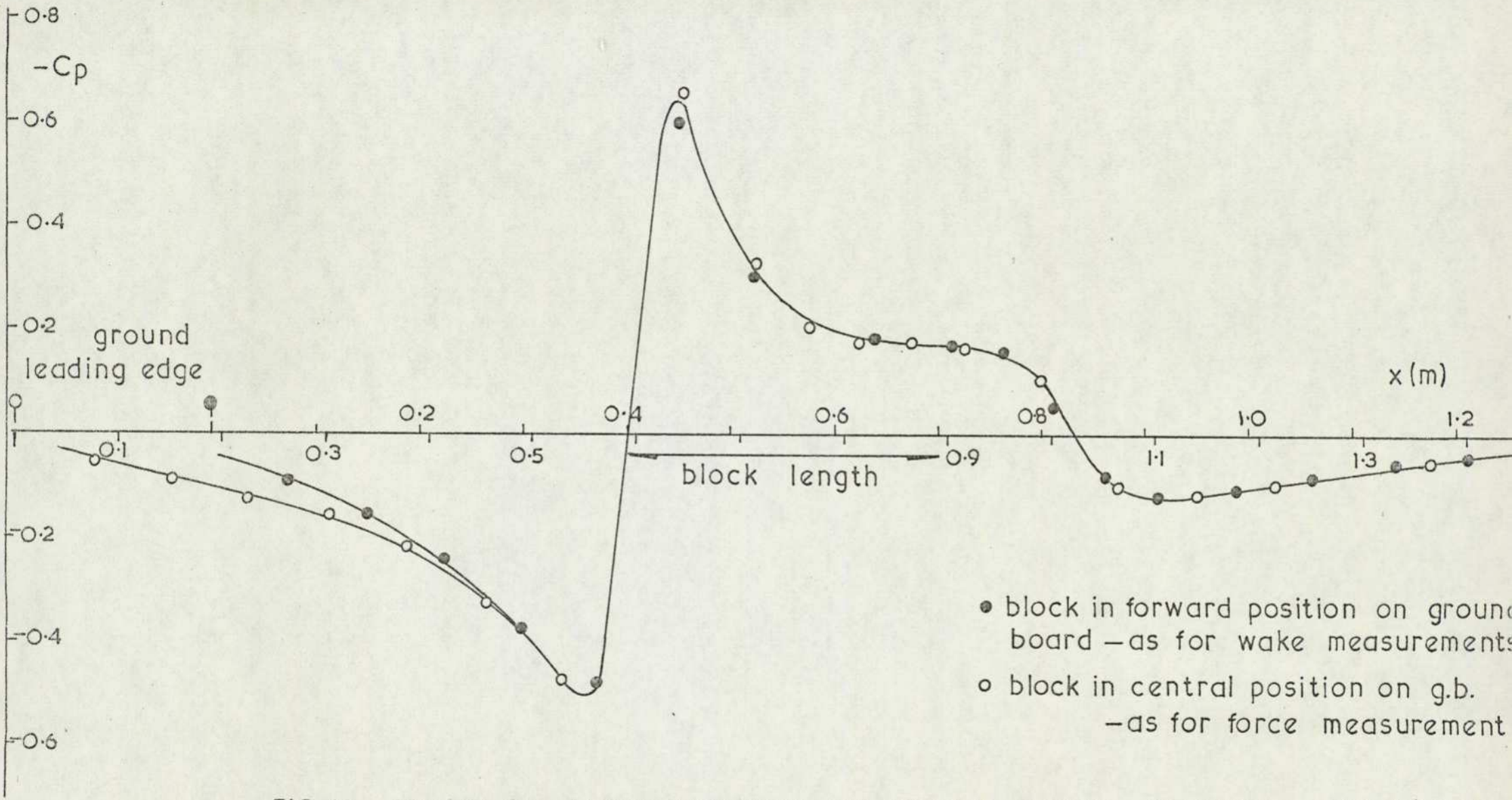

FIG.42 EFFECT OF BLOCK POSITION ON GROUND BOARD PRESSURE DISTRIBUTION

BLOCK 2N

This distribution is typical for all bodies near to ground. Upstream of the model the flow decelerates to a minimum velocity just forward of the model leading edge. A rapid acceleration then takes place under the nose; the maximum velocity being attained just behind the model leading edge. The flow then decelerates to the trailing edge where a base separation, approximately parallel to the ground, occurs. This is inferred from the negligible pressure difference immediately upstream and downstream of the trailing edge. In the near wake the deceleration continues but a pressure recovery occurs as the wake flow develops. Figure 43 (a)-(c) plots the ground board pressure distribution with the block 2N at incidence for various mean ground clearances. At a given ground clearance the upstream pressure distribution shows a slowly increasing deceleration as incidence decreases. Reducing ground clearance similarly increases the rate of deceleration in the upstream region. Beneath the model, however, the pressure distribution is strongly influenced by incidence and ground clearance. For negative incidences the changes in distribution are confined to the region of the model leading edge, with very high suction arising as the nose approaches the ground. At positive incidence the increase in pressure on the underside is almost constant along the entire length, the increase being proportional to incidence. The conditions at the trailing edge tend to be similar in all instances. The lack of acceleration in this region indicates, as before, that the separating shear layer is parallel to the ground in most cases.

For the remaining blocks the pressure distribution is plotted for the zero incidence case, only, and at a constant ground clearance of 25mm; see Figure 44. Block 2NS gives identical results to block 2N while the basic block 2 shows a similar initial flow retardation but a lengthened nose suction area due to the flow separation at the leading edge. Trailing edge pressures are considerably lower for block 2.

On increasing the span, the local pressure, throughout the length of the ground board, similarly increases in magnitude. In Figure 45, the pressure distribution for blocks 2N, 6N, 7N, having constant cross section but of varying length, are compared. The zero displacement represents the nose of each vehicle. Upstream of the block trailing edge the results are almost identical, although the longer model reveals a slightly higher pressure coefficient at mid length and a lower

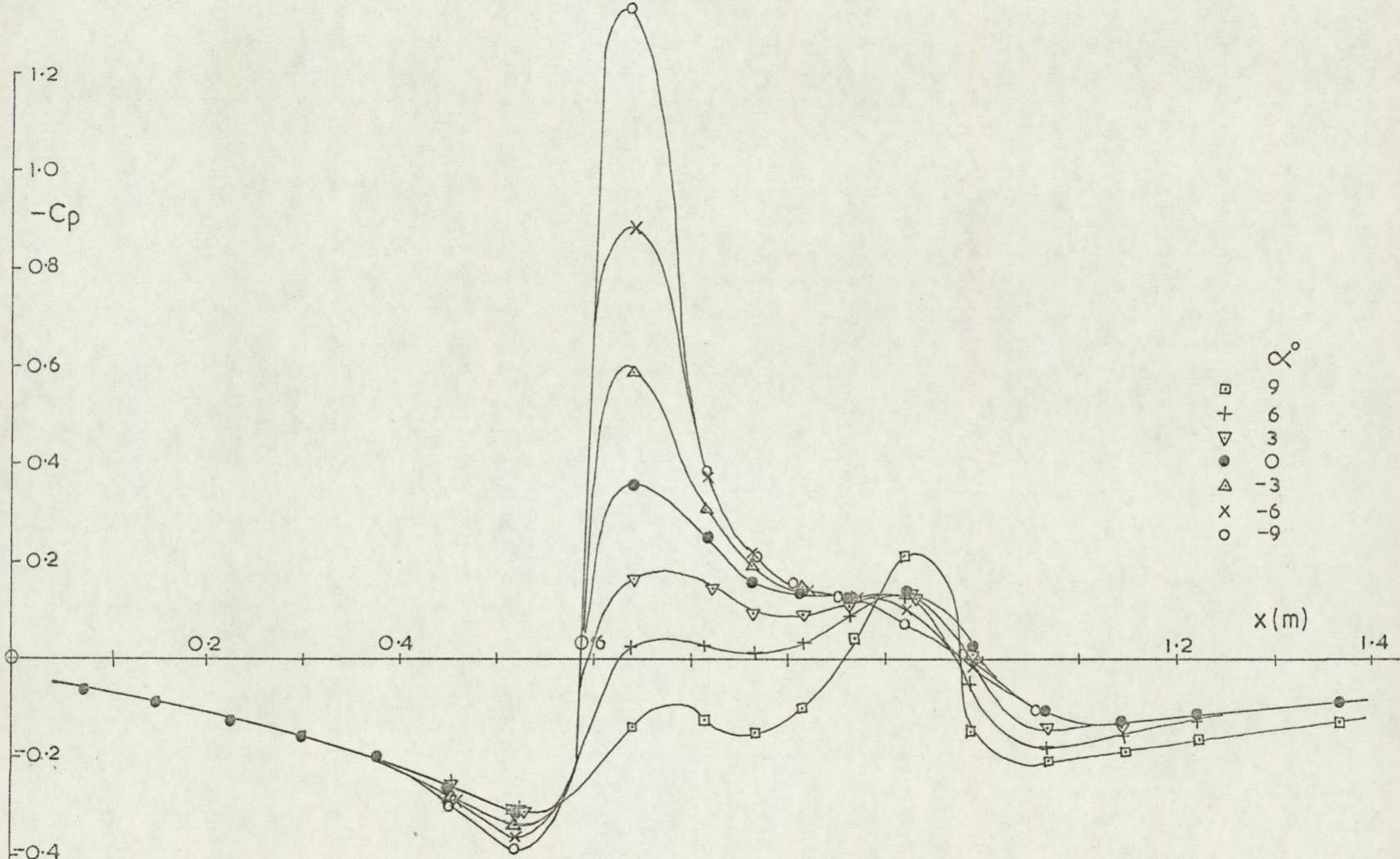

FIG. 43 PRESSURE DISTRIBUTION ON GROUND UNDER BLOCK 2N AT INCIDENCE (a) Z/t=0·5

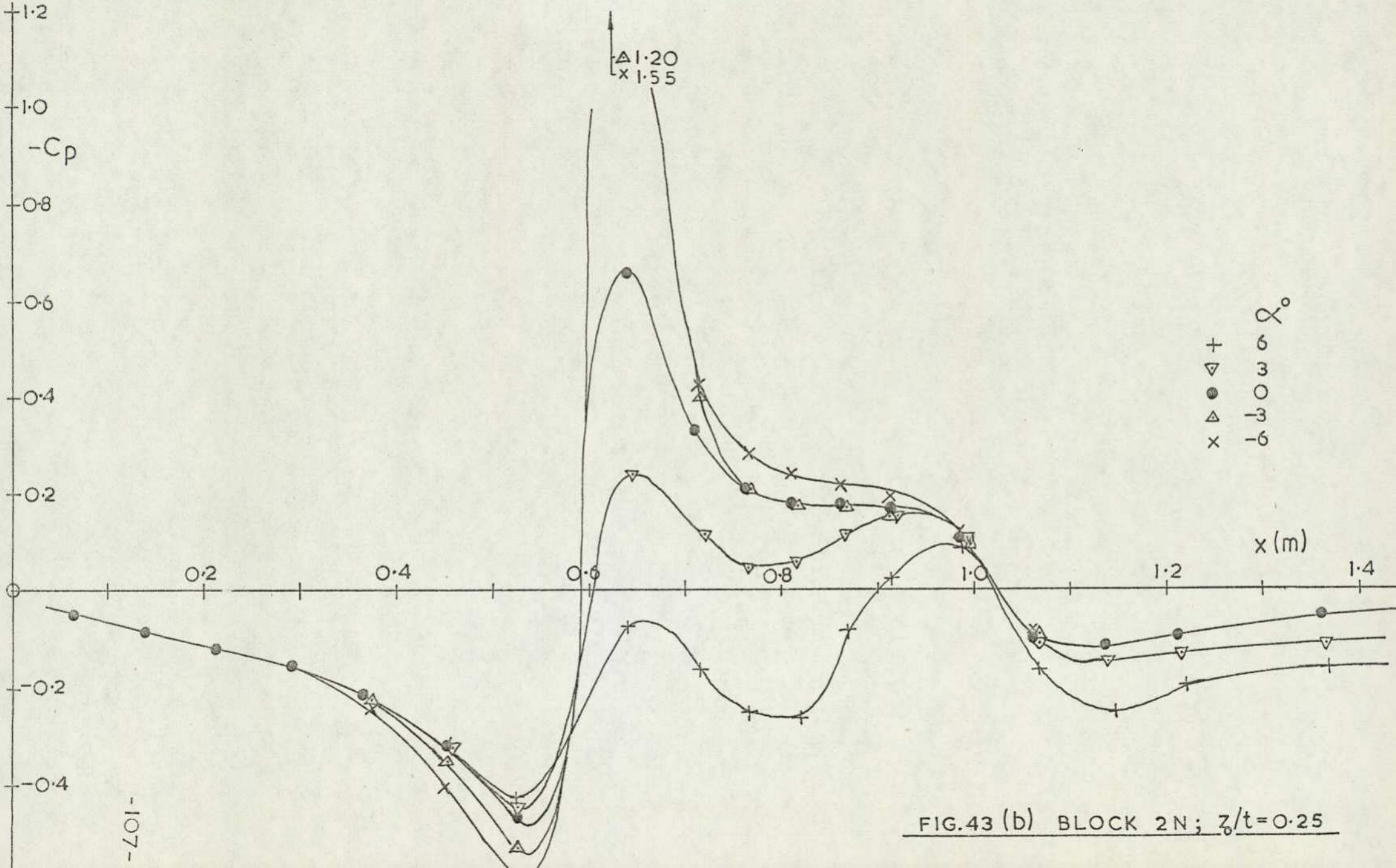

FIG.43 (b) BLOCK 2N; $z_0/t = 0.25$

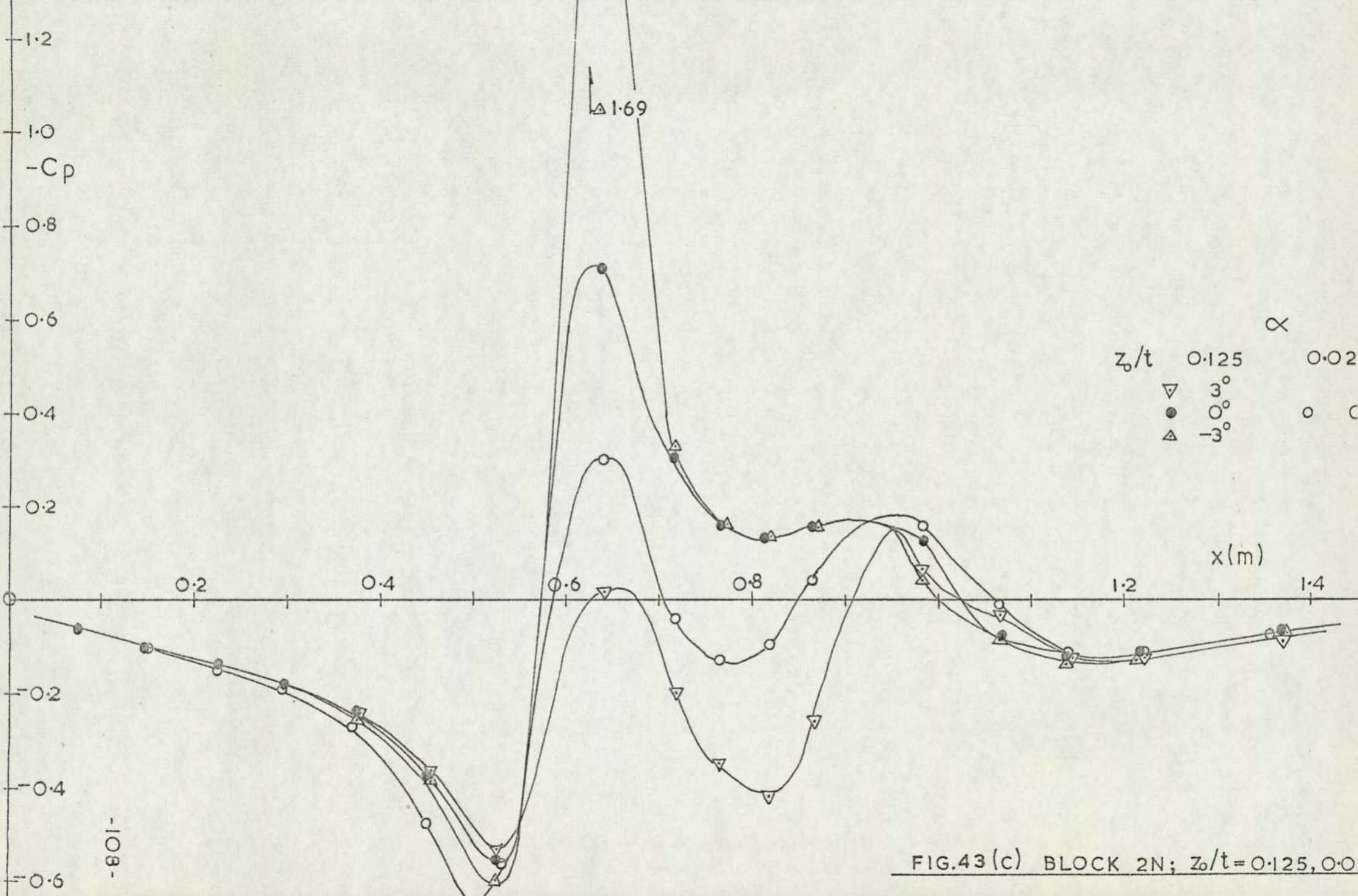

FIG.43(c) BLOCK 2N; $z_o/t = 0{\cdot}125, 0{\cdot}0$

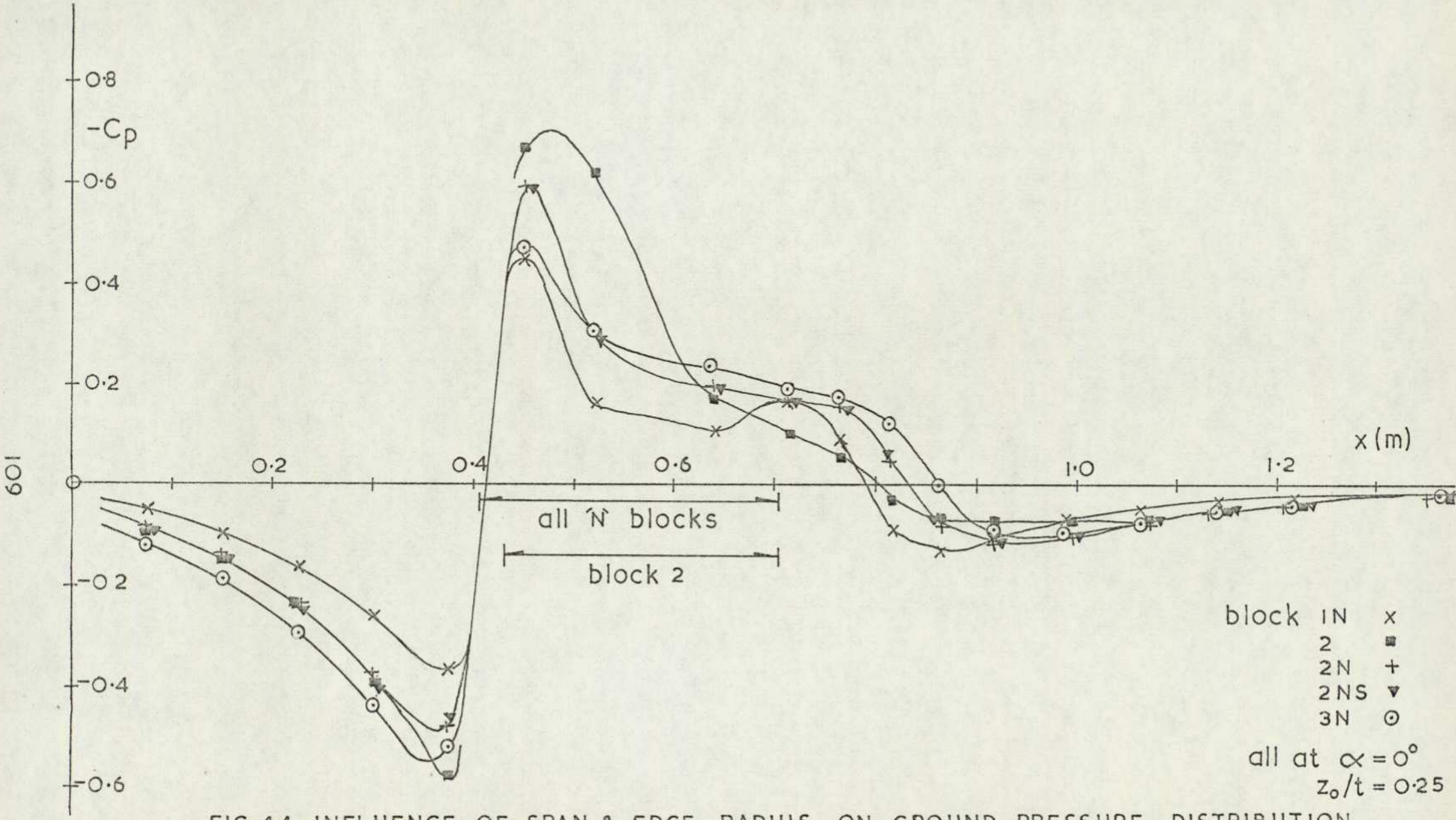

601

FIG. 44 INFLUENCE OF SPAN & EDGE RADIUS ON GROUND PRESSURE DISTRIBUTION

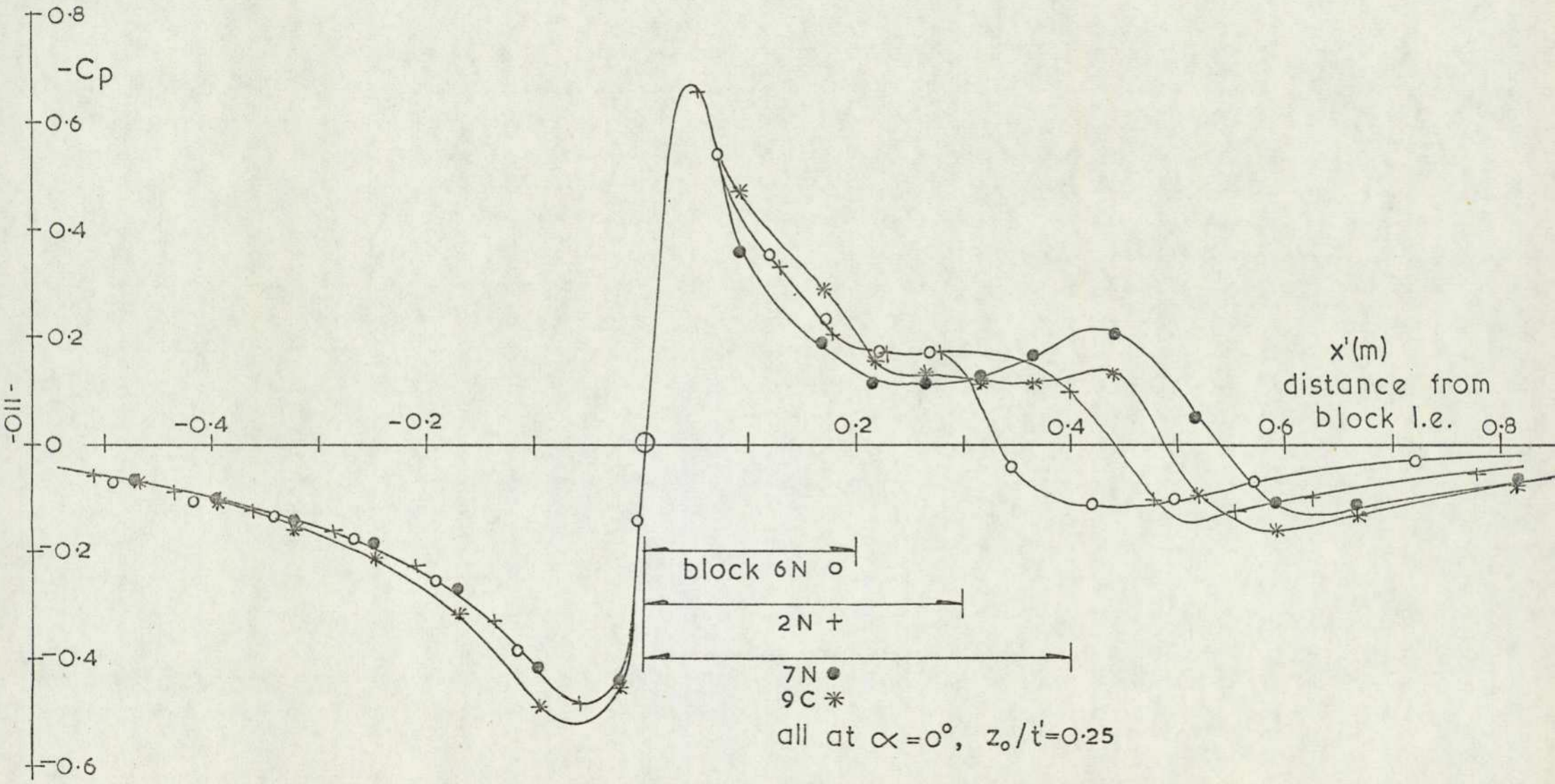

FIG.45 GROUND BOARD PRESSURE DISTRIBUTION— EFFECT OF LENGTH & CAMBER

coefficient near the trailing edge. The same figure shows the pressure distribution beneath the cambered block, 9C. The initial flow deceleration is slightly faster while higher pressure is evident directly under the block, when compared with the uncambered case. At the trailing edge the pressure is higher, while the base flow is modified, suggesting a shorter reverse flow region.

3.2.2 Car models.

The pressure distribution along the ground plane was also measured for the car models. The effect of three model stations are shown in Figure 46 for the saloon car model at zero incidence. It can be seen that the points tend to fall onto a single curve except in the vicinity of the ground board leading edge. In one case the model was without wheels but this appears to have no significance. The pattern upstream and downstream of the model is similar to that for the blocks as would be expected for a region outside of the immediate influence of the model itself. Directly underneath the model the pressure distribution differs in having two peaks, both occurring at the wheel positions, although as noted earlier these have little effect themselves. This characteristic was noticeable for the lifting rectangular blocks. On the same curve the effects of rear end geometry are shown to be of importance only in the region of the trailing edge. The estate car has noticeably lower pressures in this region, the pressure increasing as the geometry becomes less blunt.

Further studies using the saloon car are shown in Figure 47. The influence of Reynolds Number on the pressure distribution is seen to be negligible as would be expected from the force data. Attitude changes are investigated in the same figure, on a displaced curve. A small change of incidence is seen to have no effect upstream of the model but does modify the distribution underneath and aft of the car. No pressure tappings coincided with the peak pressure position, however, so the effect immediately under the nose is uncertain. With the model at yaw differences are confined to the area between the wheels, where increasing yaw produces greater suction. The two additional nose configurations are compared to the normal saloon car in Figure 48. As the sharpness of the nose increases the upstream deceleration increases while the velocity peak under the nose moves forward and increases in magnitude. The pressure variation downstream of the

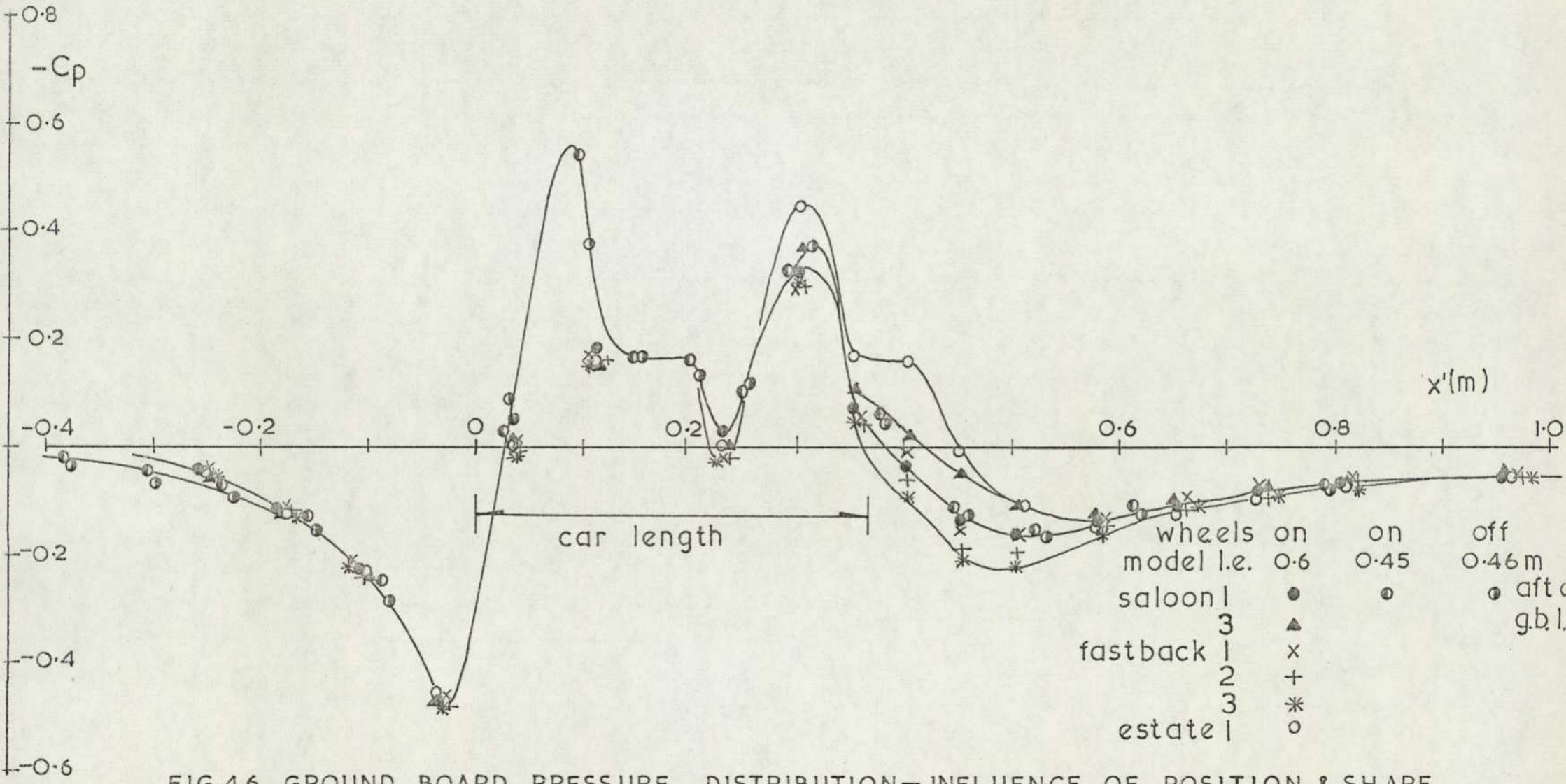

FIG.46 GROUND BOARD PRESSURE DISTRIBUTION— INFLUENCE OF POSITION & SHAPE

PASSENGER CARS

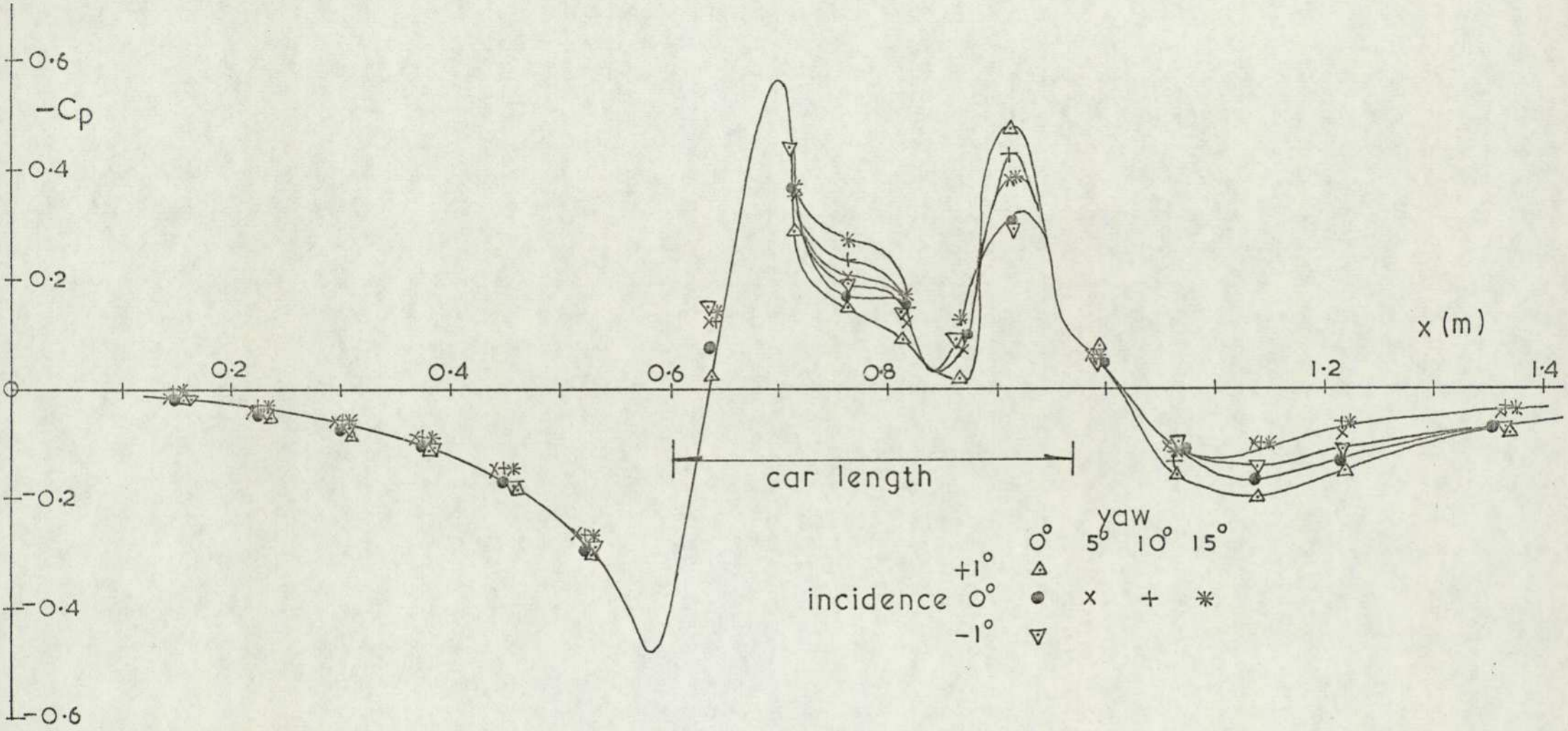

FIG. 47 SALOON I — EFFECT OF INCIDENCE & YAW ON THE GROUND BOARD PRESSURE

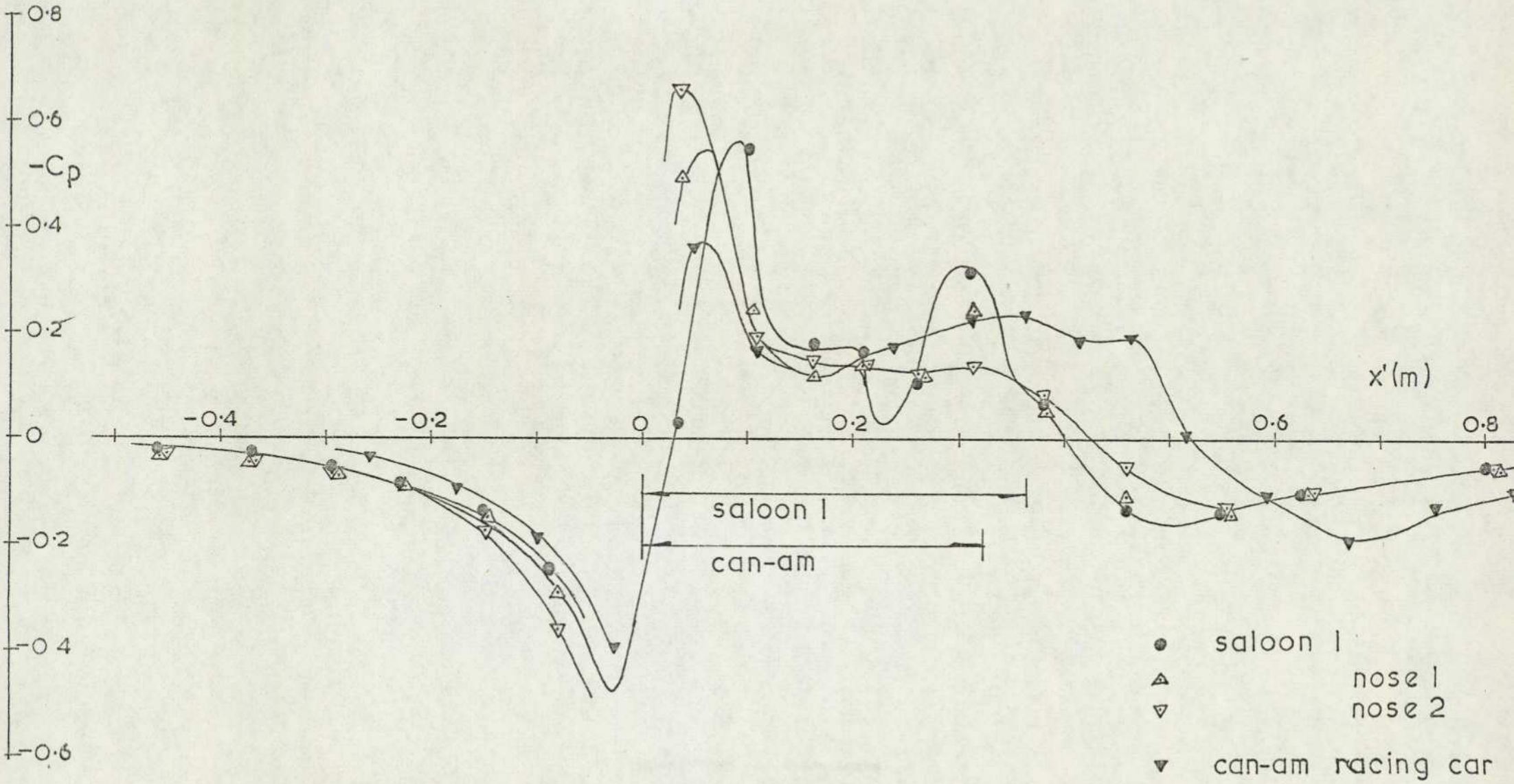

FIG. 48 GROUND BOARD PRESSURE DISTRIBUTIONS FOR SALOON I WITH ALTERNATIVE NOSE SHAPES AND FOR THE CAN-AM RACING CAR

leading peak also becomes considerably more even with the spoiler fitted.

Also shown in Figure 48 is the pressure distribution beneath the Can Am racing car model. This differs in having substantially less change in pressure at the leading edge, while a uniform pressure exists over the entire underside. The uniform pressure extends some way downstream of the model trailing edge and tends to indicate a separated flow reattaching to the ground. The pressure recovery in the wake is then displaced downstream.

3.3 Boundary layer measurements

3.3.1 Velocity distribution

The velocity distribution in the boundary layer upstream of the model and in the flow between model lower surface and ground was determined for a few models, at zero incidence, using a small pitot rake. This simple pitot rake was constructed by glueing lengths of hypodermic tubing of 0.8 mm outside diameter to a thin brass strip. The static pressure was assumed to be constant across the boundary layer, or right across the gap between model and ground, and was derived from the previous measurements of the ground board pressure distribution, obtained without the rake. Measurements were only taken along the centre line of the ground plane. The results for block 2N at 25 mm ground clearance are shown in Figure 49. The approaching boundary layer is seen to slowly thicken. Directly under the model nose the ground board boundary layer is considerably reduced in thickness, while the model boundary layer is just developing. Moving towards the trailing edge the gap flow becomes symmetrical, with the boundary layers on both ground plane and model growing at the same rate. Without the nose, block 2, the build up of the ground board boundary layer, upstream of the model, is more pronounced; Figure 50. Under the nose a region of separated flow is apparent. The flow reattached before 30% of model length aft of the leading edge, although the model boundary layer thickness is considerably thickened. The flow tends to symmetry at the trailing edge but the maximum velocity is 40% lower than for the block 2N case. The flow under the cambered model , block 9C at 37.5mm ground clearance is seen in Figure 51 to be similar to that for block 2N with a high level of symmetry.

With block 2N mounted at different ground clearances , still at zero incidence , the velocity distributions shown in Figure52 were

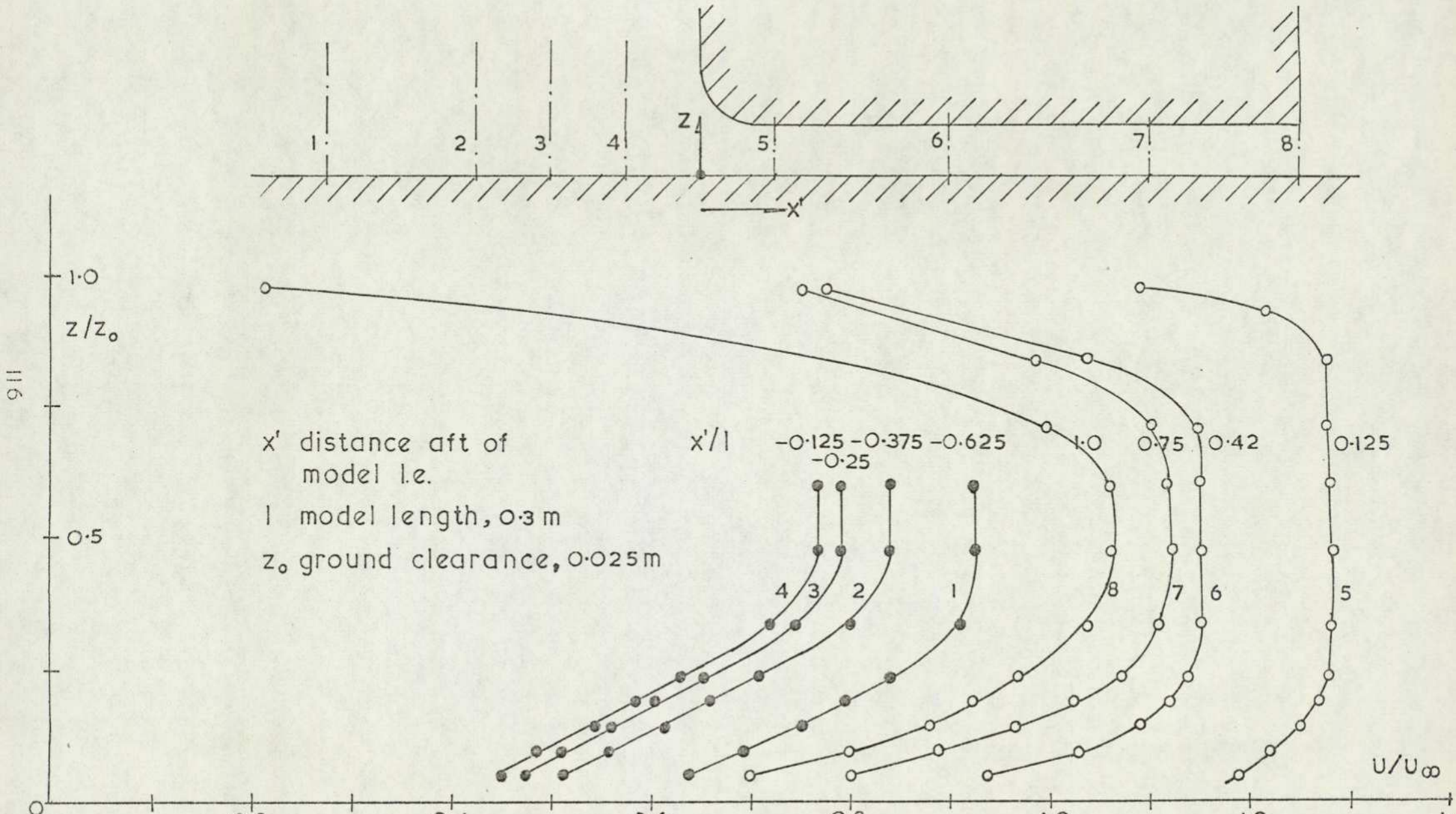

FIG.49 VELOCITY PROFILES IN APPROACHING BOUNDARY LAYER & UNDERBODY GAP — BLOCK 2N

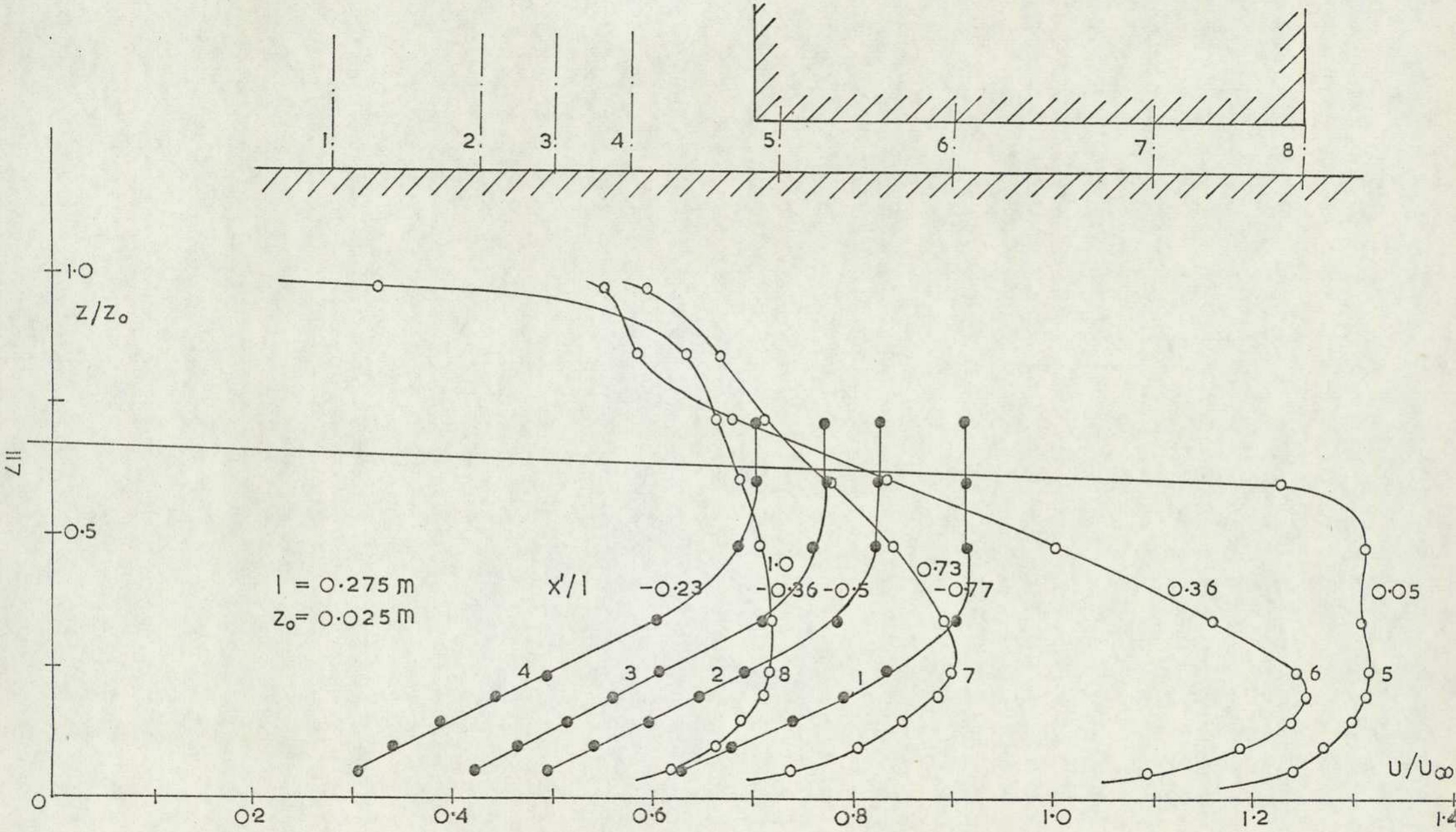

FIG. 50 BOUNDARY LAYER VELOCITY PROFILES — BLOCK 2

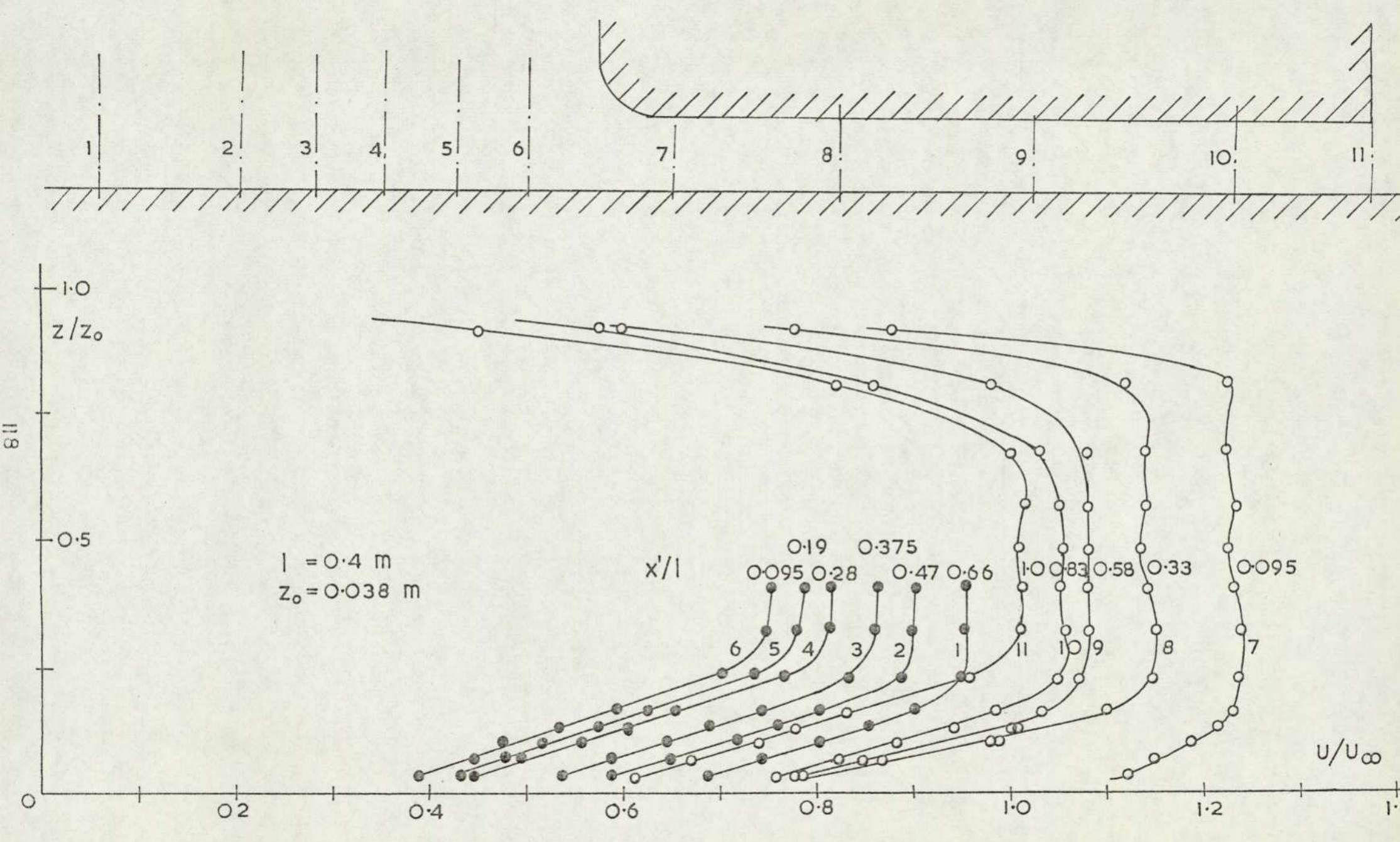

FIG. 51 BOUNDARY LAYER VELOCITY PROFILES — BLOCK 9C

obtained at the trailing edge. When the model clearance is 25 mm, and greater, the ground board boundary layer is identical. At lower ground clearances a flow blockage, caused by the merging boundary layers, is apparent. The peak velocity just exceeds half the free stream value at the minimum ground clearance. In figure 53 the effect of planform modification on the velocity distribution at a given height is seen to be negligible.

The saloon car model, fitted with wheels and having a rough underside, produces an asymmetric flow between model and ground, Figure 54. As in this case the roughness is distributed along the underside the symmetrical flow condition is not restored. The measurement of total head was taken to the model floor by cutting away a narrow centre section from all the roughness strips. At the trailing edge the velocity distribution increases linearly across the gap, and is similar to a fully developed, zero pressure gradient, Couette flow profile.

3.3.2 Boundary layer thickness.

The displacement thickness, δ^*, was determined from the area under the velocity profile curve. For certain configurations, blocks 2N and 9C, this could be defined back to the trailing edge of the block, but in the other cases the displacement thickness could only be derived forward of the model nose. The variations of displacement thickness with position relative to the model leading edge are plotted in Figure 55. In all cases the trend is for the boundary layer displacement thickness to increase on approaching the model nose. At the nose the accelerating flow reduces the thickness considerably and it then continues to grow again at an approximately uniform rate. The only significant deviation between the four results occurs at the maximum pressure point, immediately upstream of the models.

In the case of block 2N, the ground board boundary layer momentum thickness, Θ, has also been computed, and the ratio, δ^*/Θ, known as the form factor, H, was found to be close to 1.5. At a typical test Reynolds Number of 10^6, the expected value of H is about 1.4, but it is known that this can increase considerably under adverse pressure gradients. In comparison, without the model present, measurements of the ground board boundary layer give H as 1.35 which is sufficiently close to the expected value. The variation of δ^* on the bare ground board is plotted for comparison. In general the displacement thickness

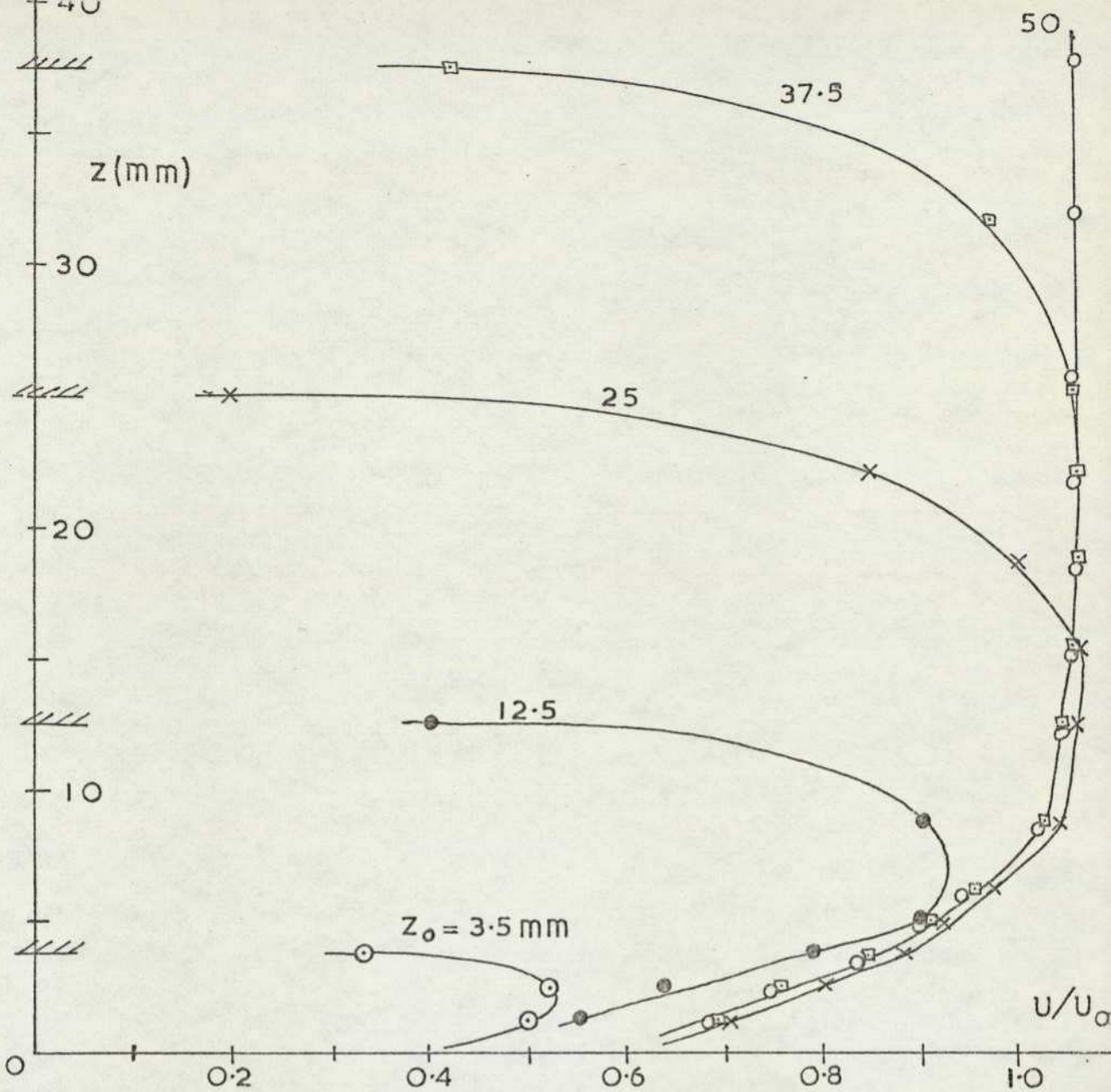

FIG. 52 TRAILING EDGE VELOCITY PROFILES — BLOCK 2N

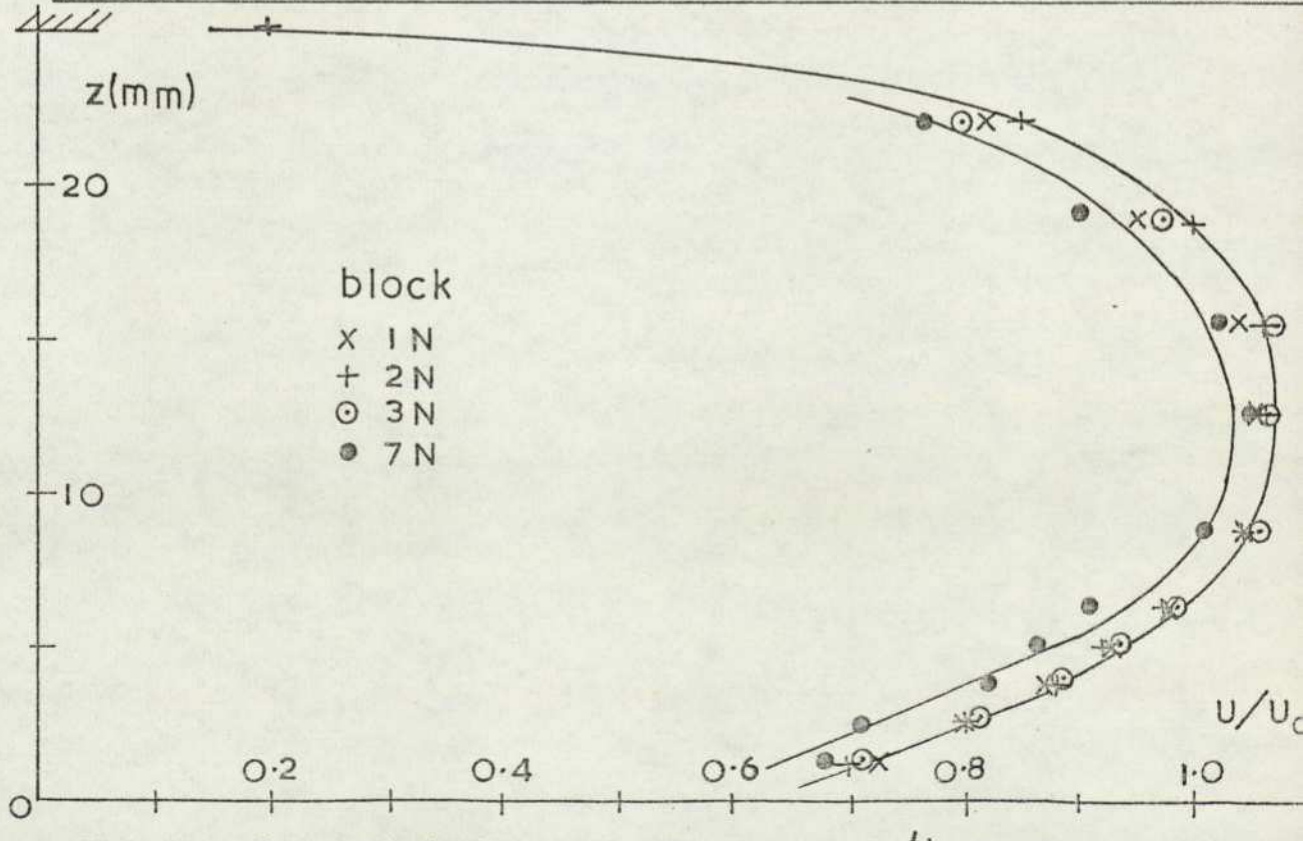

FIG. 53 T.E. VELOCITY PROFILES Z_o/t=0·25

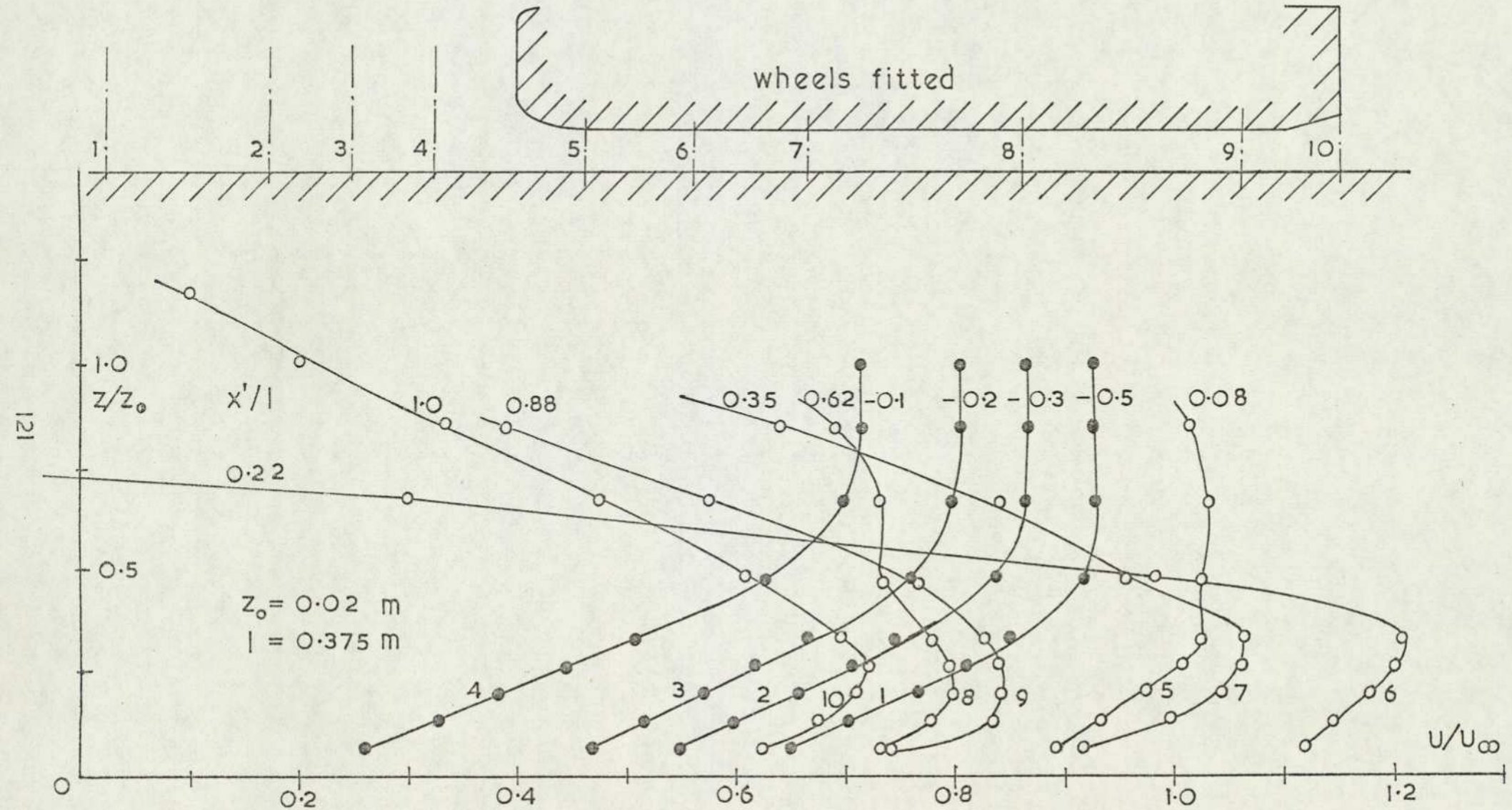

FIG. 54 BOUNDARY LAYER VELOCITY PROFILES — SALOON 1

is greater, with the model present, in the regions of retarded flow, and less where the pressure gradient is favourable.

3.3.3 Theoretical boundary layer growth.

Consider the case of a two dimensional turbulent boundary layer in a pressure gradient. The momentum integral equation is usually written

$$\frac{d\Theta}{dx} + \frac{\Theta}{U_1}\frac{dU_1}{dx}(H + 2) = \frac{c_f}{2} \qquad (3.1)$$

Where Θ is the momentum thickness, H is the form factor, U_1 is the local velocity, and c_f is the local skin friction coefficient. The skin friction term, can, in general, be replaced by

$$c_f = aR_\theta^{-b} \qquad (3.2)$$

Where a, b are constants, and R_θ is the Reynolds number based on momentum thickness. Substitution of (3.2) in (3.1) results in a differential equation of the Bernoulli type. After substituting representative values for the constants and replacing Θ by δ^*/H (assuming H is constant) the solution is

$$\left[\frac{\delta^*}{l}^{1.25}\right]\left[\frac{U_1}{U}\right]^{4.25} - \left[\frac{\delta^*}{l}^{1.25}\right]_o\left[\frac{U_1}{U}\right]_o^{4.25} = 0.02\,R^{-0.25}\int_{x_o/L}^{x/L}\left[\frac{U_1}{U}\right]^{4.0} d\left[\frac{x}{l}\right] \qquad (3.3)$$

where normalisation with respect of vehicle length, l, has been introduced and the Reynolds number R, is also based on this length, and the free stream velocity, U . The suffix, 0, usually refers to the transition point but it is convenient in this instance to take the position immediately upstream of the model influence; that is, where the local velocity can still be considered as equal to the free stream velocity. Under the latter conditions the displacement thickness is approximately given by the value obtained on a flat plate, namely

$$\delta^* = 0.046\,R_x^{-0.2}\,x \qquad (3.4)$$

which on substituting into equation (3.3) gives

$$\left[\frac{\delta^*}{l}\right]^{1.25}\left[\frac{U_1}{U}\right]^{4.25} = 0.02\,R^{-\frac{1}{4}}\left[\frac{x_0}{l} + \int_{x_0/l}^{x/l}\left|\frac{U_1}{U}\right|^{4.0} d\left|\frac{x}{l}\right|\right] \qquad (3.5)$$

In the situation where the model is several model lengths aft of the ground board leading edge, or where the initial boundary layer is very thick, the term under the integral becomes negligible for normal vehicles, as given by the pressure measurements of section 3.1. The displacement thickness equation reduces to the simple expression

$$\delta^* U_1^{3.40} = \text{constant} \qquad (3.6)$$

East (24) intuitively concluded this in arguing that the local ground board boundary layer displacement thickness under a particular wing near to ground was dependent only on the distance separating the model from the ground board leading edge, and therefore on the displacement thickness in the absence of the model. This may well be valid in the case of a wing which is never very close to the ground, but in the wind tunnel testing of typical road vehicle models the same conditions do not apply, and the integral term becomes comparable with the others. As an example the theoretical displacement thickness immediately upstream of the saloon 1 model in the forward location as given by equation (3.5), is 3.7 mm, which compares favourably with the measured value of 3.9 mm, whereas expression (3.6) gives 2.7 mm. Full scale wind tunnel testing of automobiles, thereby increasing Reynolds number by an order of magnitude, would not improve the relative results unless the ratio of displacement thickness to vehicle length was substantially greater than for the model test. In fact for the ground board used in these one tenth scale model tests the displacement thickness at the centre of the bare board is 2.3 mm whereas in the MIRA full scale tunnel it is approximately 41.0 mm (inferred from (23)) which is, relatively, considerably greater, so there is a tendency for equation (3.6) to apply.

3.3.4 Comparison with the moving vehicle case.

The boundary conditions at the ground plane in a typical wind

tunnel test using a static ground board are unrepresentative of the real conditions where a vehicle moves over a stationary surface. To obtain an estimate of the errors arising from this misrepresentation the size of the true ground boundary layer produced by a body travelling near the surface must be established. Initially it must be assumed that the instantaneous pressure distribution on the ground beneath a moving vehicle is identical to that measured on a static ground board in a wind tunnel.

It has already been seen that on the surface of the wind tunnel ground plane the flow which is initially at free stream tunnel velocity decelerates on approaching the model nose. This process is reversed under the nose as the flow accelerates through the gap between vehicle and ground. Along the underside of the car where the ground clearance is essentially constant the velocity is restored to near free stream conditions, decelerating once more on expanding downstream of the vehicle base. Consider, on the other hand, a point on the surface of a road as a vehicle is about to pass. The adjacent fluid is initially a rest. As the vehicle approaches, the point experiences a flow velocity, away from the vehicle, which although increasing in magnitude is always less than the car speed. When the nose is overhead the flow direction suddenly reverses, opposing the vehicle motion, although the velocity magnitude is similar. The point under consideration then experiences a deceleration to a constant, but small velocity as the base passes above. The flow then decelerates through zero so that the velocity vector changes sign, and the direction is once more the same as the vehicle motion as the wake passes. This flow description is also valid for a point fixed on the surface of a moving belt revolving in a wind tunnel environment. Note that the pressure gradients are similar to those on a static ground board only underneath the model; both upstream and downstream of the vehicle the gradients are of opposite sign.

A fluid particle near to the ground under a moving vehicle typically attains 20% of the vehicle velocity whilst traversing a distance approximately equivalent to 10% of vehicle length. The Reynolds number of such a flow near a full size vehicle of 4.5m length, travelling at 30 m/s, is then 2×10^5 which is just subcritical. The boundary layer on the ground under a moving vehicle must therefore be considered to be laminar.

The accelerating flow as the vehicle approaches has a velocity which increases approximately linearly with time , or distance, for a substantial period. From the textbooks , the growth of a boundary layer under such conditions is zero and the momentum thickness, Θ, is given by

$$\Theta^2 = \frac{2\,\nu\,l(m)}{C\,(1+(2H+3))} \qquad (3.7)$$

where $l(m)$ is Thwaites function, which can be given the value 0.22 , H is the form factor, ν is the kinematic viscosity, and C is the constant in the velocity expression

$$\Delta U = Cx \qquad (3.8)$$

where ΔU is the velocity induced by the vehicle. From the saloon car data , after normalising with respect of vehicle length, l , and velocity, U , the value of C is approximately

$$C \simeq 0.15\frac{1}{U}$$

Substituting for the momentum thickness, the displacement thickness, δ^*, can be approximated by

$$\frac{\delta^*}{l} \simeq R^{-\frac{1}{2}} \qquad (3.9)$$

As the vehicle nose passes overhead the velocity changes rapidly in a sinusoidal manner. The problem to be solved is then simply Stokes' second problem; namely the boundary layer growth on an oscillating plate, although the transients and the initial conditions are ignored. From the solution giving the velocity distribution a varying displacement thickness can be derived, but typically the normalised thickness is again of order $R^{-\frac{1}{2}}$.
For the same vehicle considered earlier the Reynolds number is 10^7 and so the displacement thickness is at least an order of magnitude less than that for the turbulent boundary layer on a static ground board upstream of either a model or a full scale vehicle in a wind tunnel. For small scale models mounted over a moving ground of limited speed capability the differences are just as great.

A laminar boundary layer is likely to separate immediately the flow begins to decelerate. At this station, just upstream of the vehicle nose, the Reynolds number based on displacement thickness, R_{δ^*}, and local velocity is given by

$$R_{\delta^*} \triangleq 1250 \text{ for the real vehicle case}$$

$$R_{\delta^*} \triangleq 360 \text{ for the moving ground simulation}$$

Both values are subcritical, confirming the initial assumption, while the latter is below the critical value necessary to produce short separation bubbles.

While both flows are liable to separate the real ground flow immediately becomes turbulent and will reattach in that state under the favourable pressure gradient which occurs as the vehicle nose passes overhead. The following adverse pressure gradient can then be accommodated without separation. The insensitivity of boundary layer growth to considerable changes of Reynolds number (see equation (3.4)) implies that the normalised displacement thickness growth on the road directly under a real vehicle and on a static ground board beneath a model are very similar. This only applies to the region immediately under the vehicle. On the moving belt, however, the upstream adverse pressure gradient will initiate separation followed by laminar reattachment. The flow will not then have sufficient energy to overcome the adverse pressure gradient along the vehicle underside and is likely to separate. This would equally apply to small scale moving model rigs as used by Brown and Seeman (25).

This argument may explain why Beauvais, Tignor and Turner (26), when comparing wind tunnel tests with road test data found general agreement when using a fixed ground but large errors with the moving belt simulation. The suggested differences are shown schematically in Figure 56.

3.3.5 Correction to measured wake velocity profiles.

Downstream of the model base the pressure gradients are small and it can be assumed that the ground board boundary layer continues to grow in an almost identical manner to the boundary layer on the ground plane in the absence of the model. Outside of the displacement

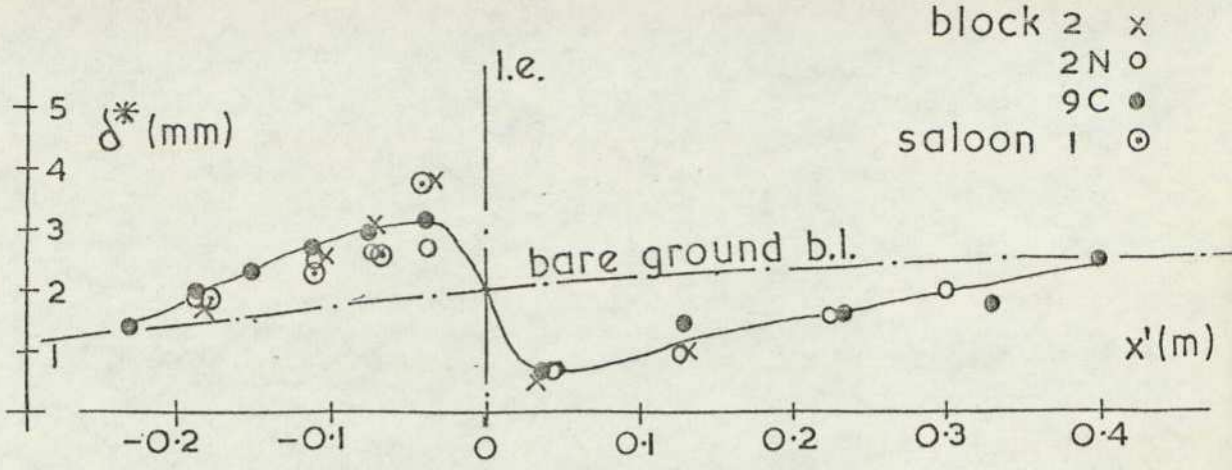

FIG.55 DEVELOPMENT OF GROUND BOARD BOUNDARY LAYER DISPLACEMENT THICKNESS

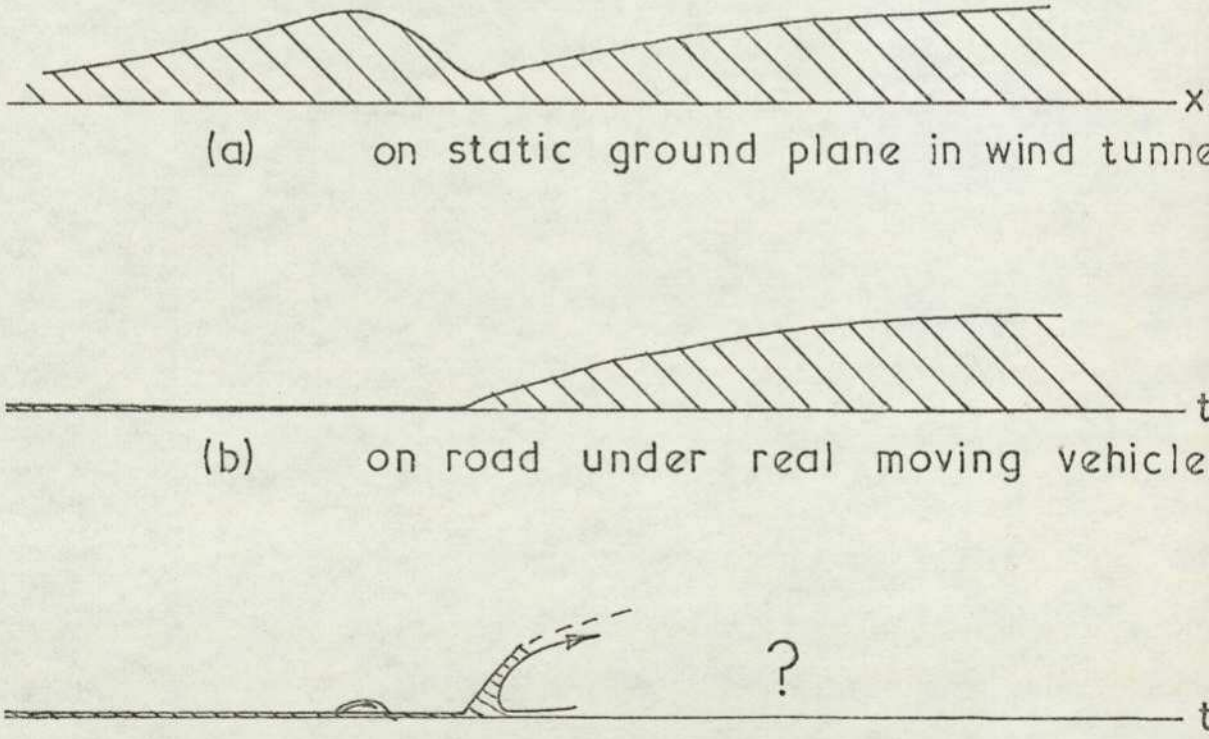

(a) on static ground plane in wind tunne

(b) on road under real moving vehicle

(c) on moving ground in wind tunnel or on static ground under moving model at small scale.

FIG.56 BOUNDARY LAYER GROWTH WITH VARIOUS SIMULATIONS OF GROUND

thickness the effect on the velocity distributions is likely to be minimal. At the extreme downstream position the total boundary layer thickness is nearly 30 mm, so there is a small intrusion into the wake. The modifications necessary to the measured velocity profiles are sketched in Figure 57. Consider initially the velocity profile for a pair of wakes generated by two bodies in mirror image, thus removing any ground effects. The profiles of each wake are obviously identical and following the usual wake flow simplifications the flow velocities can be superimposed. A typical wake profile is then as shown in Figure 57(a). On the static ground plane a boundary layer will develop having an outer velocity, U_1, say, given by the velocity at the height equal to the local boundary layer thickness, δ, and the additional velocity profile will be given by

$$\frac{\Delta U_1}{U_1} = \left(\frac{z}{\delta}\right)^m \qquad (3.10)$$

assuming a typical power law relationship. The resulting velocity profile as measured in the tunnel using a static ground board is shown in Figure 57(b). In the real ground situation, however, the velocity at the ground must be equal to the free stream velocity. A boundary layer therefore develops on the road surface which has an outer velocity given by U_2, say, which is essentially $U-U_1$, because the two boundary layers being considered will develop at a similar rate due, once again, to the insensitivity to Reynolds number. The velocity profile of this boundary layer is

$$\frac{\Delta U_2}{U_2} = \left(\frac{z}{\delta}\right)^m \qquad (3.11)$$

where the exponent can be taken as a first approximation to be equal to that in (3.10). The resulting profile, representing that expected over a road surface is sketched in Figure 57(c). The combined velocity deficit to restore the measured data to a real road case is then quite simply

$$U-(\Delta U_1+\Delta U_2) = U-(U_1+U_2)\left(\frac{z}{\delta}\right)^m = U\left(1-\left(\frac{z}{\delta}\right)^m\right) \qquad (3.12)$$

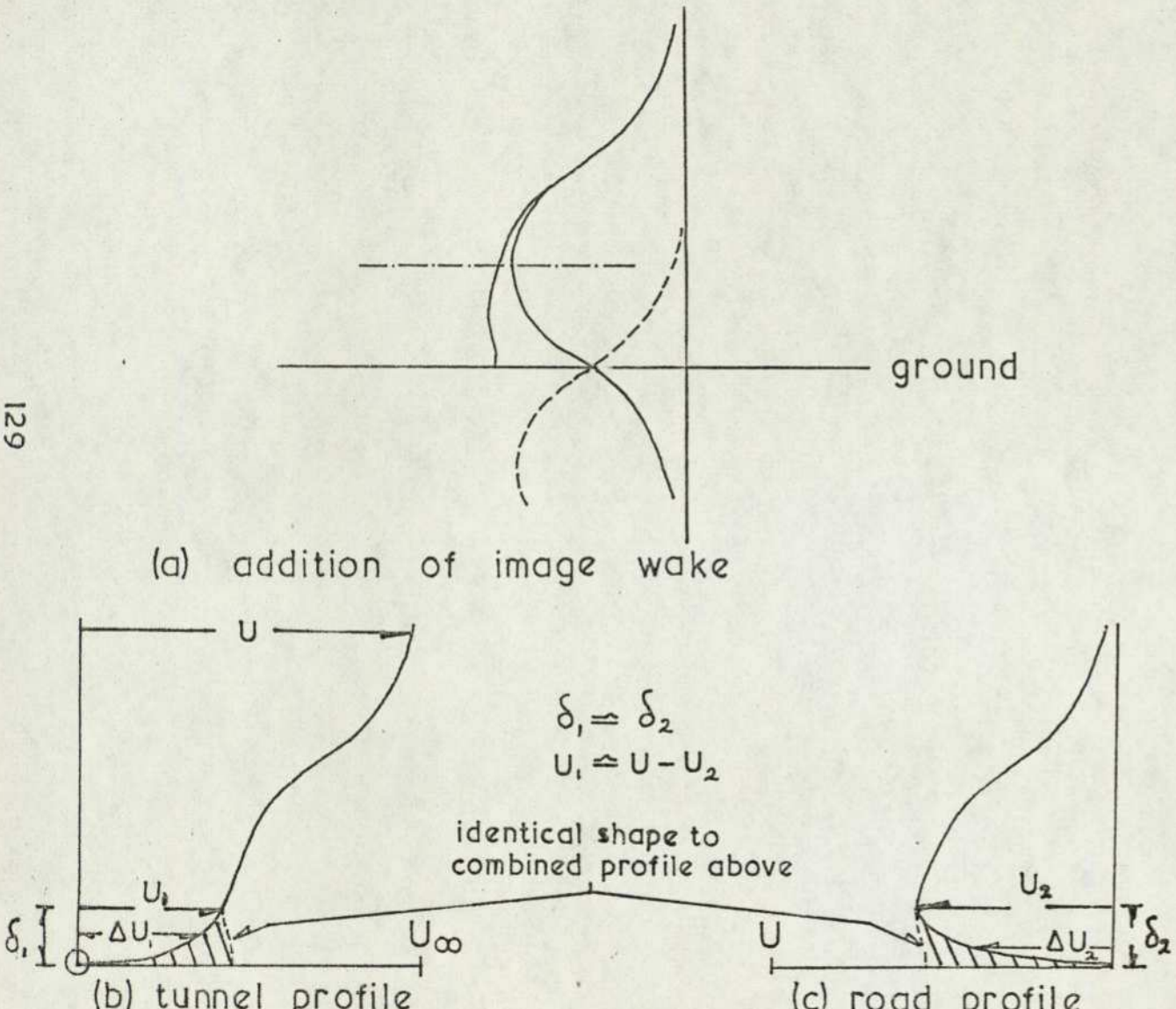

FIG. 57 WAKE PROFILES

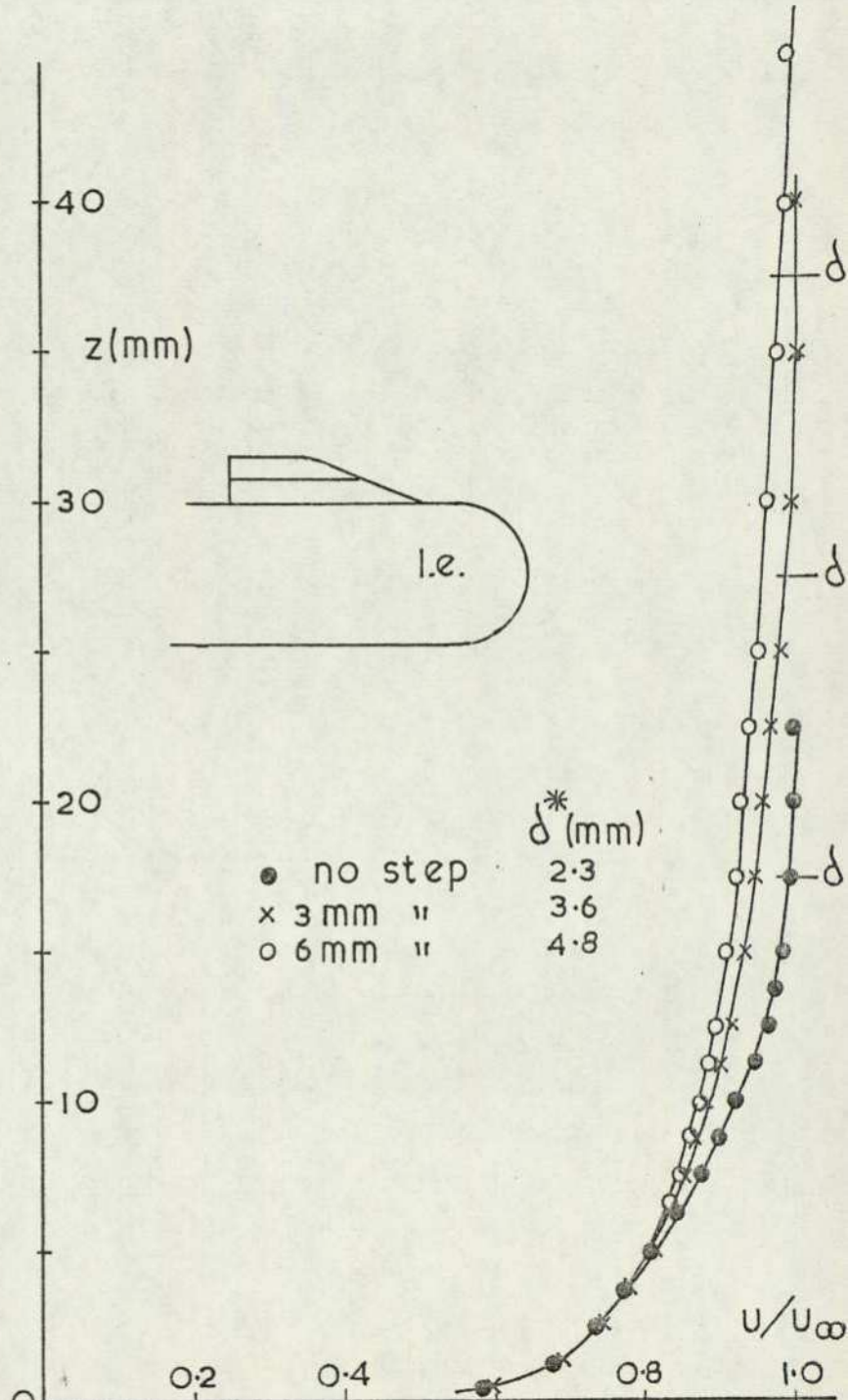

FIG. 58 BOUNDARY LAYER AT G.B. CENTR

With the same assumptions and simplifications as earlier this is the profile as measured in the absence of a model. It is therefore only necessary to know the value of δ, the bare ground boundary layer thickness, when correcting static board data.

3.4 Corrections to force data

The static ground board boundary layer is negligibly different from the boundary layer that develops on the road near a moving vehicle, except upstream of the body. The modification to the approach flow will most likely raise the stagnation point on the static vehicle a distance approximately equal to the maximum displacement thickness of the boundary layer. The local flow changes both under and over the nose of the car may generate spurious forces. The influence of these flow changes cannot be determined directly from wind tunnel tests using a static ground board without applying suction over the entire region forward of the model. The only way to decrease the boundary layer thickness is to move the model nearer to the leading edge and that introduces problems of flow balancing around the ground board. However, the boundary layer thickness can be increased and an extrapolation made to give effect of an initially zero thickness boundary layer. An experiment was therefore performed in which lift forces were measured on three car shapes, saloon 1, fastback 2, and estate 1 models, without wheels and the boundary layer thickness was varied by placing two different boundary layer trips at the ground board leading edge. Each trip was in the form of a backward facing step with a shaped leading edge as shown in Figure 58. The steps were 3 mm and 6mm deep, while each was 12mm long and mounted 40mm back from the ground board leading edge. The velocity distributions across the boundary layer as measured half way along the ground board are compared in Figure 58. The tabulated displacement thicknesses appear to increase uniformly with step size. The pressure distribution was measured on the upper surface of the ground board with the saloon car in place and this showed that, downstream of 0.15 m aft of the leading edge, the presence or otherwise of a strip did not alter the external flow conditions. The front and rear wheel lift coefficients are shown in Figure 59. The results are corrected according to equation (2.1) except that the C_{zo} term is always the lift coefficient as measured with wheels and without any thickening of the boundary layer. All three car shapes experience similar trends, and the effects are approximately independent of incidence.

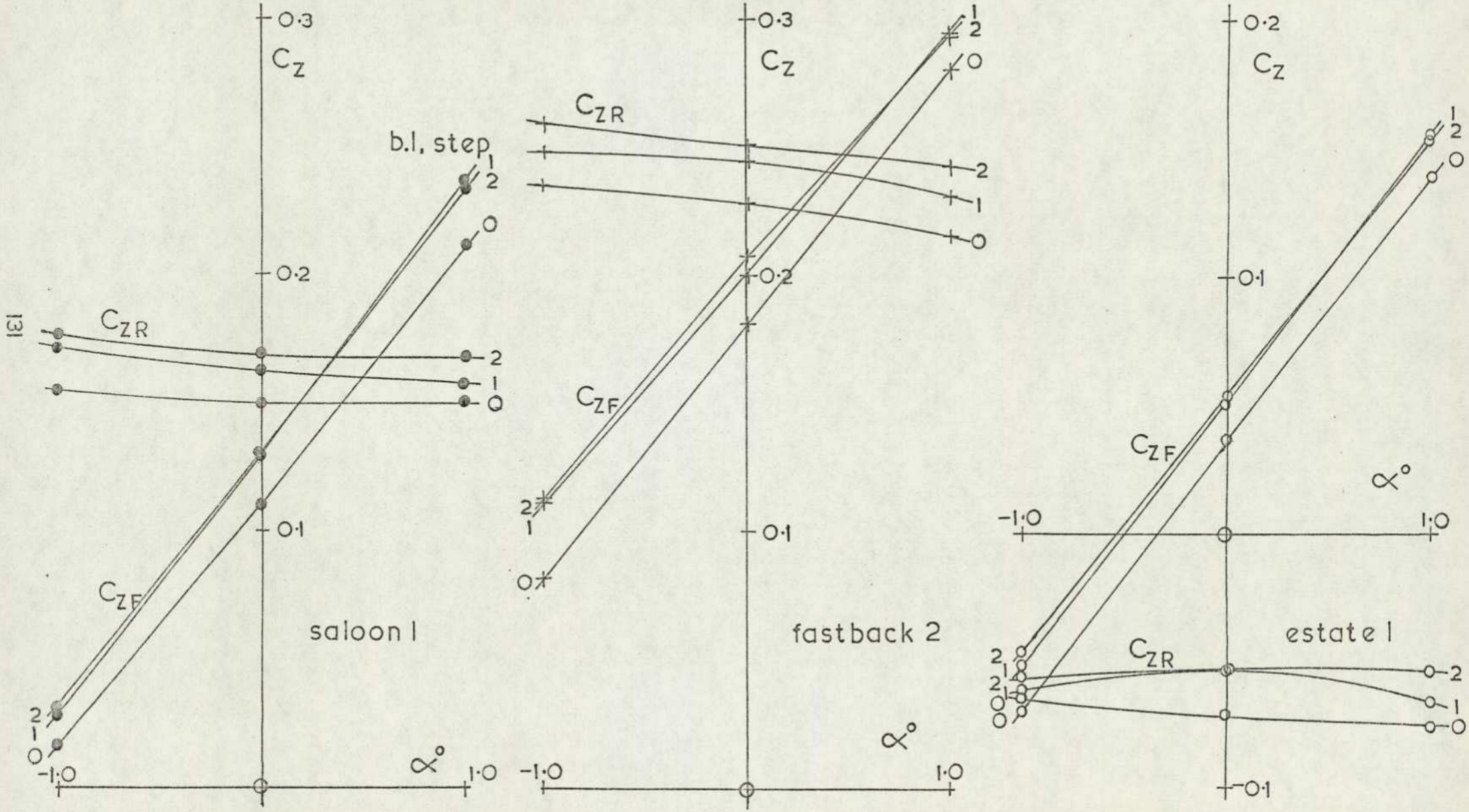

FIG.59 EFFECT OF A THICKENED BOUNDARY LAYER ON CAR LIFT

The front axle lift initially increases on thickening the boundary layer but then appears to level off. At the rear axle the lift coefficient increases throughout the variation in trip size but the incidence effects seem slightly chaotic in the case of the estate car. In Figure 60 the increase in lift coefficient at the front axle is plotted as a function of the boundary layer thickness, normalised to the vehicle ground clearance, z_o, as measured at the centre of the ground plane, in the absence of the model. Although there is a spread of results the trend is definite. Extrapolating to the condition of zero displacement thickness shows a noticeable lift increment at the front wheels, given approximately by $\Delta C_z = -0.3\ \delta^*/z_o$ for all vehicles. It should be remembered, however, that this corresponds to a boundary layer which has zero thickness only in the absence of a pressure gradient but is still subject to the growth according to the expression under the integral sign of equation (3.3) and is therefore still not truly representative of a moving vehicle. No attempt has been made to extrapolate the rear wheel lift data as following the previous discussion on boundary layer growth both the static ground and moving vehicle situations are thought to generate similar boundary layers local to the rear axle. Mason and Sovran (27) in a similar experiment varied the normalised boundary layer thickness on a ground plane and found similar trends in overall lift coefficient but the increase in lift with thickening boundary layer was predominantly at the rear wheels. However, as their models were fitted with wheels the flow in the gap between wheels and ground could have had a dominating influence on the front axle lift and comparison between the results is therefore difficult.

Ignoring the remaining discrepancy in simulation these results suggest that the typical wind tunnel test of a road vehicle, using a static ground board, overestimates the lift coefficient by approximately 0.03 and the measured pitching moment is too positive by an amount given by this increase in lift acting at the front axle. Assuming no change in drag force the incremental moment coefficient about a mid-wheelbase reference point would be 0.015. This value would increase for a thicker boundary layer on the bare ground plane. Tests comparing the lift developed by a moving vehicle with those derived in a wind tunnel have been performed by Beauvais, Tignor and Turner (26) who found that static wind tunnel tests on a Ford Galaxie car model gave lift coefficients

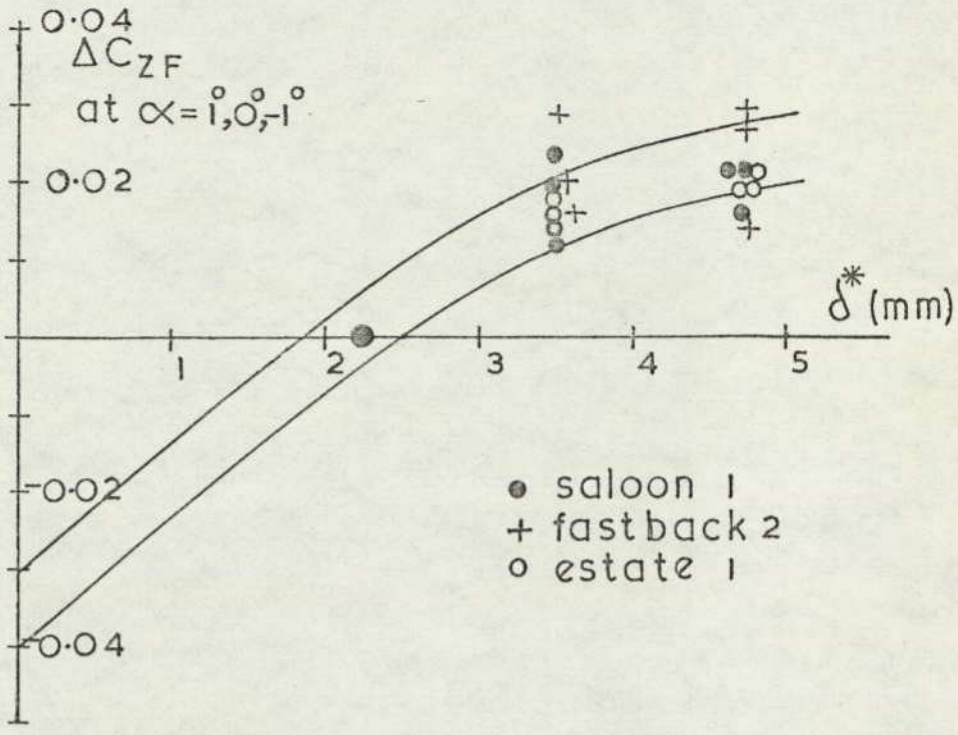

FIG. 60 EXTRAPOLATION TO ZERO B.L. THICKNESS AT FRONT WHEELS

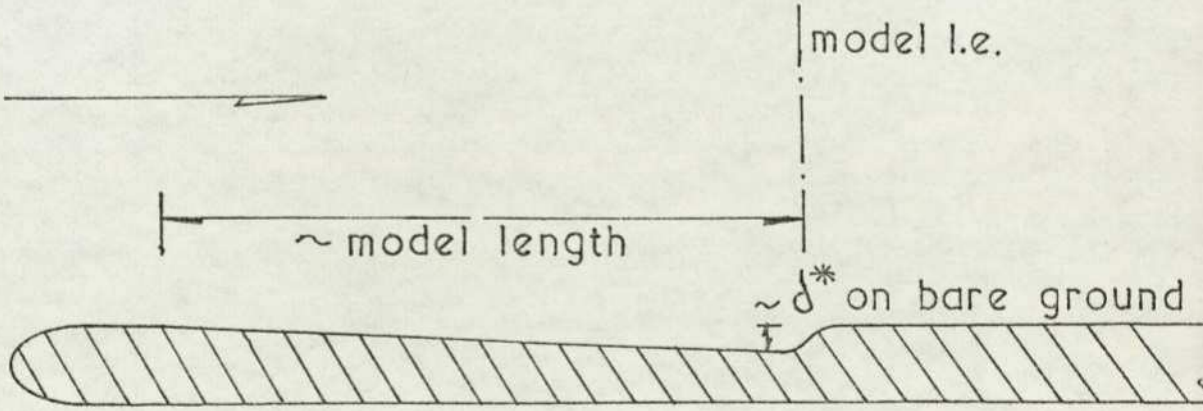

FIG. 61 SUGGESTION FOR DESIGN OF STATIC GROUN BOARD UPSTREAM OF MODEL

varying between 0.570 and 0.596, depending on model clearance, while the full scale vehicle on the road recorded 0.552. At the same time the pitching moment was found to increase from approximately 0.17 on the road to 0.19 in the tunnel. Further confirmation of this trend was earlier given by White and Paish (28), who measured rotational speeds in the trailing vortices of two cars mounted in a wind tunnel and driven along the road. Balance measurements in the tunnel gave lift coefficients of 0.45 and 0.33 respectively, while the maximum rotational speed in the vortex was 25% lower on the road than in the tunnel for both vehicles. Incremental lift coefficients of 0.11 and 0.08 would be expected. As the MIRA tunnel boundary layer is relatively considerably thicker (by 75% in the bare tunnel taking account of scale), the technique just discussed would predict an incremental lift of 0.06. This is considerably less than for one of the vehicles tested but it is at least in the right direction.

These measurements and those of the previous section suggest a form of ground board which may improve measurements on road vehicles. The boundary layer growth upstream of the model must be reduced to nearly zero. As this region is subject to an adverse pressure gradient this cannot occur naturally. The suction required to remove the entire boundary layer is excessive and would have to be distributed. An alternative would be to reprofile the ground board surface forward of the model. This, if done correctly, would maintain an essentially flat displacement surface. A simple ramp would probably be sufficient as shown in Figure 61. The dimensions would not be critical but it would extend approximately a model length forward of the model and the maximum depth immediately upstream of the model nose would be equal to the local displacement thickness on a flat ground plane in the presence of the model. Care would have to be taken to avoid separations but this could be monitored.

3.5 Conclusions

The boundary layer developing on a road as a moving vehicle passes, differs negligibly in thickness from that on a static ground board in a wind tunnel except in the region upstream of the nose. This modifies the lift force acting at the front wheels, the tunnel results overestimating the lift coefficient by approximately $0.3\,\delta^*/z_o$ where δ^* is the boundary layer displacement thickness measured locally in the absence of the model, and z_o is the vehicle ground clearance.

Certain road test data confirms this result. A suggestion is made for modifying a conventional ground board so that the correction is automatic.

The wake profiles as measured above a static ground board will be virtually unaffected above a height equal to the local displacement thickness as measured on the bare ground plane. Where this is significant the velocity profile is modified by subtracting the known profile of the ground boundary layer without the model present, giving the profile to be found on the road.

4. WAKES OF BLUFF BODIES AND ROAD VEHICLES

4.1 Introduction

Although the study of two dimensional bluff body wake flows has been extensive over the years the same is not true of either three dimensional or axisymmetric bodies and plates. A review of previous research on three dimensional plates is given in Appendix C. Earlier studies of the wakes of three dimensional bodies are examined in this introduction.

The wake measurements performed for this thesis fall into three distinct categories. Firstly the wakes of the simple rectangular blocks were investigated under zero lift conditions using a hot-wire anemometer, and mean velocity, turbulence intensity, and periodic effects were studied. These bodies were then set at incidence, to generate lift, and the wake structure determined by use of pressure probes. This was also done for one cambered model. Finally the wakes of typical road vehicles were studied using a combination of both techniques.

4.1.1 Wakes of three dimensional bluff bodies.

The near wake properties of a series of axisymmetric shapes, ranging from a parachute form ($C_x = 1.40$) to an elongated body ($C_x = 0.195$), were investigated by Heinrich and Fekstrom (29). The mean velocity distribution was determined from pressure measurements and the results were compared with an analysis based on the theoretical work of Swain (30). The exponents for the wake width and velocity defect laws were substituted empirically. Although considerable scatter existed both exponents were noticeably higher than predicted, showing a higher growth rate and velocity recovery in the near wake. A good engineering approximation to the decay of the wake was achieved dependent only on the drag of the body generating the wake.

Calvert (31),(32), has measured the near wake properties for a series of axisymmetric bluff bodies. The work on cones of varying apex angle, in which the disc and semi-infinite cylinder form special cases, showed that a universal Strouhal number could be defined for all models. The value obtained was 0.19 and was based on the spacing

Sforza and Mons (40) measured the mean velocity profiles in the wake of a series of plates of varying span mounted at the leading edge of a streamwise flat plate. A reasonable fit to the data for the long span obstacles was provided by an error function expression. Large differences in the decay of the centre line velocity defect were apparent between the large and small objects. No turbulence measurements were obtained.

There have been few measurements of the wakes of tall building type structures. Wootton (41) found that spectral measurements taken at the edge of the wake behind a circular cylinder of finite height yielded two distinct peaks when the probe was mounted near the tip, the lower frequency, associated with the flow over the top, dying away as the probe moved downstream. Mair and Maull (42) reported some unpublished work by Jackson and Samworth on the wake boundaries of a triangular flat plate of small apex angle mounted on a wind tunnel floor, normal to the airstream. These showed a marked downflow behind the upper apex of the triangle.

Measurements of power spectra in the wake of a body of finite height mounted to a tunnel floor in both a uniform and a shear flow have been reported by Maull and Young (43). In a uniform stream the shedding frequency remained constant over the height of the body although the peak became less pronounced near the top. With a shear flow superimposed , two distinct shedding frequencies became apparent. The lower half of the body exhibited one frequency which disappeared as the probe was raised, while the upper half produced a considerably higher frequency. Base pressures along the centre line showed a marked three dimensional effect.

The flow behind model building structures, of varying height to span ratios, and immersed in a two dimensional boundary layer type flow, simulating the earths natural shear layer has been investigated by Hunt and Smith (44) and Hunt (45). In both cases transverse components were always less than, but usually of the same order as, the longitudinal component. Comparisons were made with a theoretical solution for the longitudinal mean velocity deficit, based on the usual simplifying assumptions. Reasonable agreement was found.

between the separated shear layers rather than on the body diameter. The reverse flow 'bubble' boundary where the local velocity becomes zero , was found to coincide with a turbulence intensity minimum. Similarity profiles for all bodies could be plotted for mean velocity, turbulence intensity, and axial static pressure variation. In the second study a disc was set at incidence to the flow and similar measurements performed. A Strouhal number was defined for the periodic base flow in a similar manner as before but its value was increased by 10%. The flow immediately to the rear of the disc was dominated by an almost steady recirculation while the periodic effects seemed to arise from a vortex separating at the trailing edge.

Near wake data for two elliptic bodies; one effectively semi-infinite the other a flat plate, was presented by Trentacoste and Sforza (33). The axial velocity defect law exponent of 0.67 was seen to apply to the semi-infinite body downstream of two base heights. A distinct realignment of the wake axes was clearly shown. Verna (34) had earlier shown with wake velocity contours for a number of bodies that this effect occurs with most non axisymmetric cross section shapes. It was thought to be due to secondary flows.

A prolate spheroid with length to diameter ratio of six and having the lowest drag coefficient yet discussed, $C_x = 0.06$, was tested by Chevray (35). The near wake axial velocity and turbulence intensity profiles showed good similarity throughout the wake . Reynolds stresses were lower than for the disc measurements and tended to confirm that a low rate of production of turbulence within the separation zone gives rise to quick establishment of self preservation.

The near wake of a semi-infinite streamwise cylinder has been investigated by McErlean (36), using pressure probes. Good agreement between the similarity profile of mean velocity and the theory of Hall (166) was obtained. Similarity was achieved beyond three base diameters into the wake. This development distance would appear typical for bodies of this sort.

Calvert (37) studied the near wake of a sphere and found that the Strouhal number for the wake periodicity was identical to the other axisymmetric bodies which had earlier been investigated. At 0.19 this compared favourably with the results of Commetta (38), 0.18 and Kendall (39), 0.20. Addition of a trip wire for transition was found to modify the base flow considerably and to supress the regular shedding of vortices.

4.2 Wake flow measurements
Rectangular blocks, zero lift

4.2.1 Technique

Initially the rectangular blocks were set up in the wind tunnel rigidly mounted to the ground board, or in the free stream case attached to the tunnel floor, at the zero lift incidence as derived in Chapter 2. The model location on the ground plane was nearer to the leading edge than for the force measurements. This was to give the maximum downstream length. Pressure measurements on the ground surface, compared in chapter 3 showed that the differences in pressure coefficient along the ground centre line were negligible. As a further test the ground plane was shifted aft relative to the model and the lift force remeasured. This showed that the difference in zero incidence lift was within the possible setting up error, which was $\pm$0.1 degrees. No account was taken of the difference in mounting between the two cases. A short single strut supported the model off the ground plane. This was located at mid model length and at 25mm off the centre line.

A traverse gear was mounted in the tunnel with the vertical mechanism carrying the hot wire anemometer probe so that the probe body was parallel to the X-axis. The wire was always aligned parallel to the ground surface. The cooling effect on the wire is obtained from the flow components normal to the wire and so the output voltages from the linearisер, (DISA Model 55 D10), denoted by E for the d.c. voltage and e the r.m.s. voltage, represent flow velocities given by

$$E = k_1 \ (U^2+W^2)^{\frac{1}{2}} \qquad (4.1)$$

$$e = k_1 \ (u^2+k_2v^2+w^2)^{\frac{1}{2}}$$

where U.V.W are the mean flow velocity compenents in the x,y,z directions and u,v,w are the corresponding turbulence velocity components. Hoole and Calvert (46) found k_2 to be about 0.2. To avoid confusion the results are always plotted in terms of the output voltages rather than as approximated velocities. The value E represents the longitudinal mean velocity, with only small error under most conditions. When the cross flow velocity, W is

equal to 0.2U the error is only 2% of U . It is expected that the lateral components of turbulence intensity will be of the same order as the longitudinal components for most of the wake so no such simplification is permissible.

4.2.2 Free stream wakes

Horizontal and vertical wake centre line traverses were carried out for blocks 1N, 2N and 3N at four downstream stations. In all cases the traverse nearest the body was within the reverse flow region and the voltage signal has been given a negative sign as if it has direction. Downstream distances have been normalised by the thickness of the body at the trailing edge, Figure 62.

The vortex sheet separating from the base of the body is defined by the turbulence intensity peak while it can be seen that the local turbulence intensity minimum just inside the sheet denotes the edge of the reverse flow 'bubble', as found by Calvert (31). Increasing the width of the body has little influence on the velocity distribution from the vertical traverse, but for the horizontal traverse the distribution changes to one containing a distinct step in the profile. Near to the body the step seems to originate approximately at the position of peak turbulence intensity, which moves rapidly inwards. This might suggest that the step is associated with the thick separating boundary layer on the side walls but it would then still be apparent in the case of block 1N. A similarity profile for the vertical traverse is shown in Figure 62. The wake half width denoted by the suffix $\frac{1}{2}$ is the distance from the centre line to the point where the local velocity deficit is half the maximum. The collapse is fairly good over most of the wake but not very good in the outer region. It is not possible to produce such a profile for the lateral direction. The decay of the centre line velocity deficit as shown in Figure 63 is similar for blocks 2N and 3N with the deficit always greater for the larger span model, and while the square body generates an initially faster decay rate all three exponents are close to - 2/3. Another feature of the rectangular section bodies is the switching of the wake axes, as noted previously by Kuo and Baldwin (47) and Verna (34) for other non axisymmetric shapes. Figure 64 shows plots of the wake half widths. A distinct changeover point can be seen within a few base heights of the base.

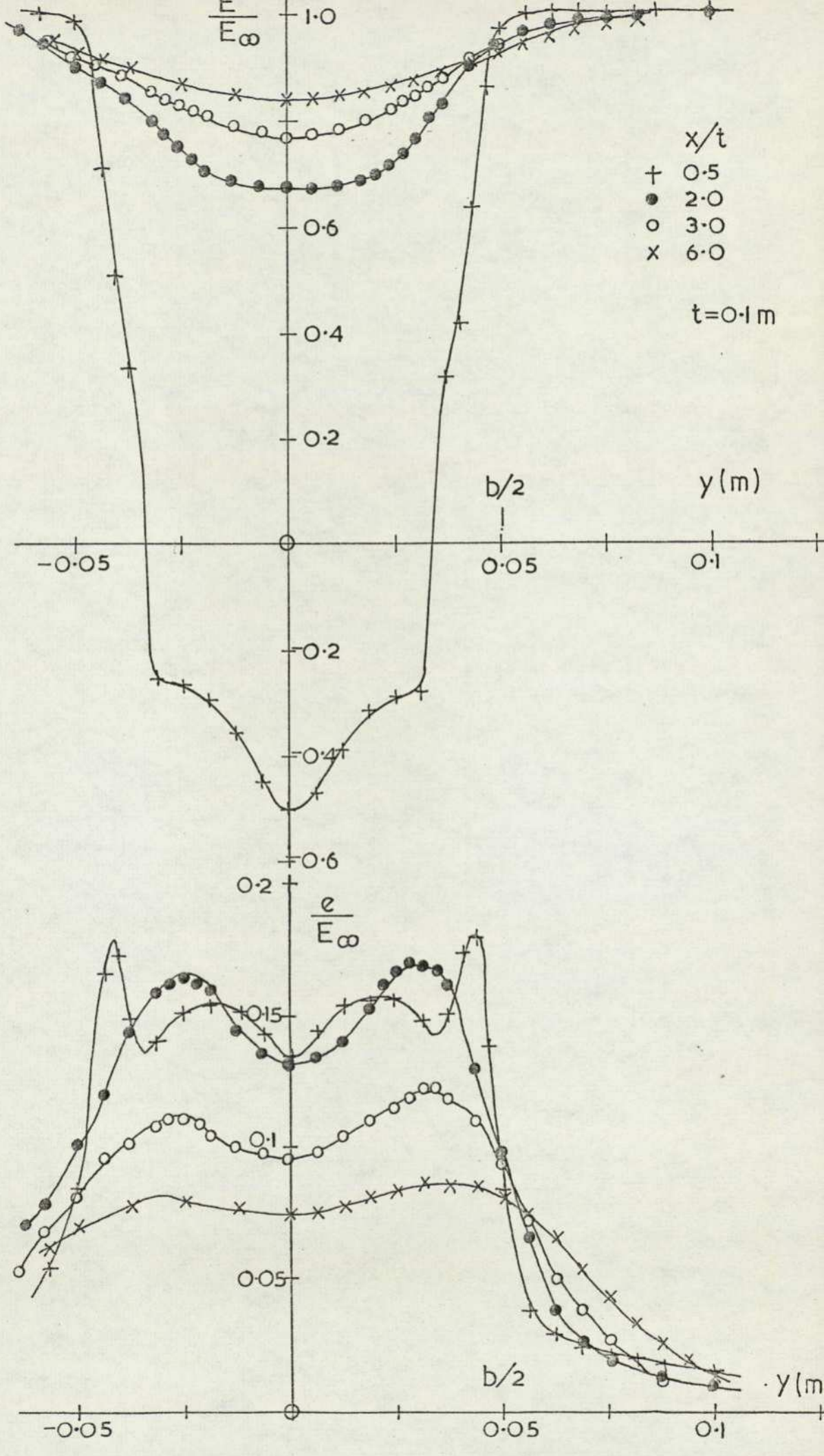

FIG. 62 WAKE TRAVERSES FREE STREAM (a) BLOCKI

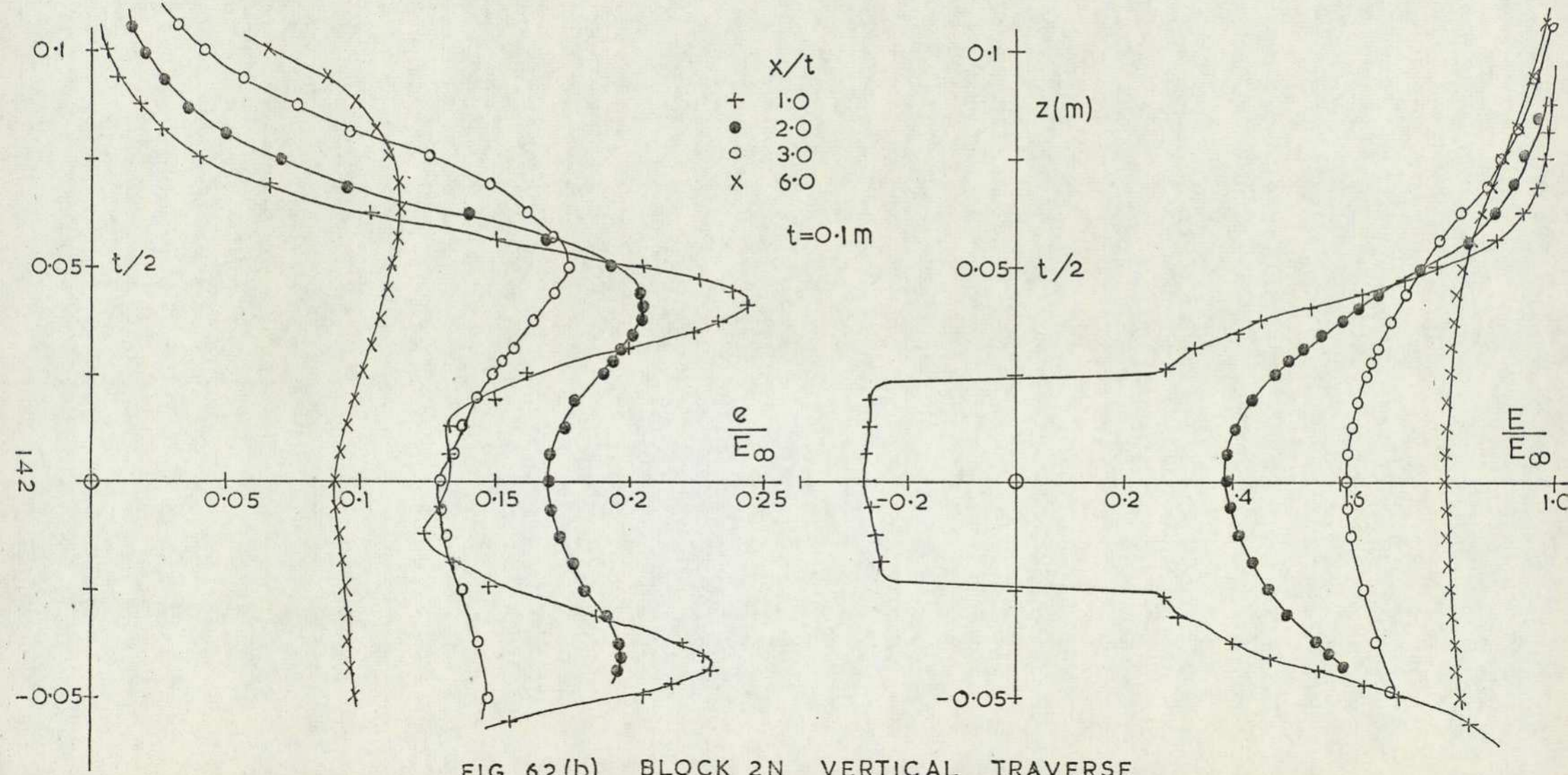

FIG 62(b) BLOCK 2N VERTICAL TRAVERSE

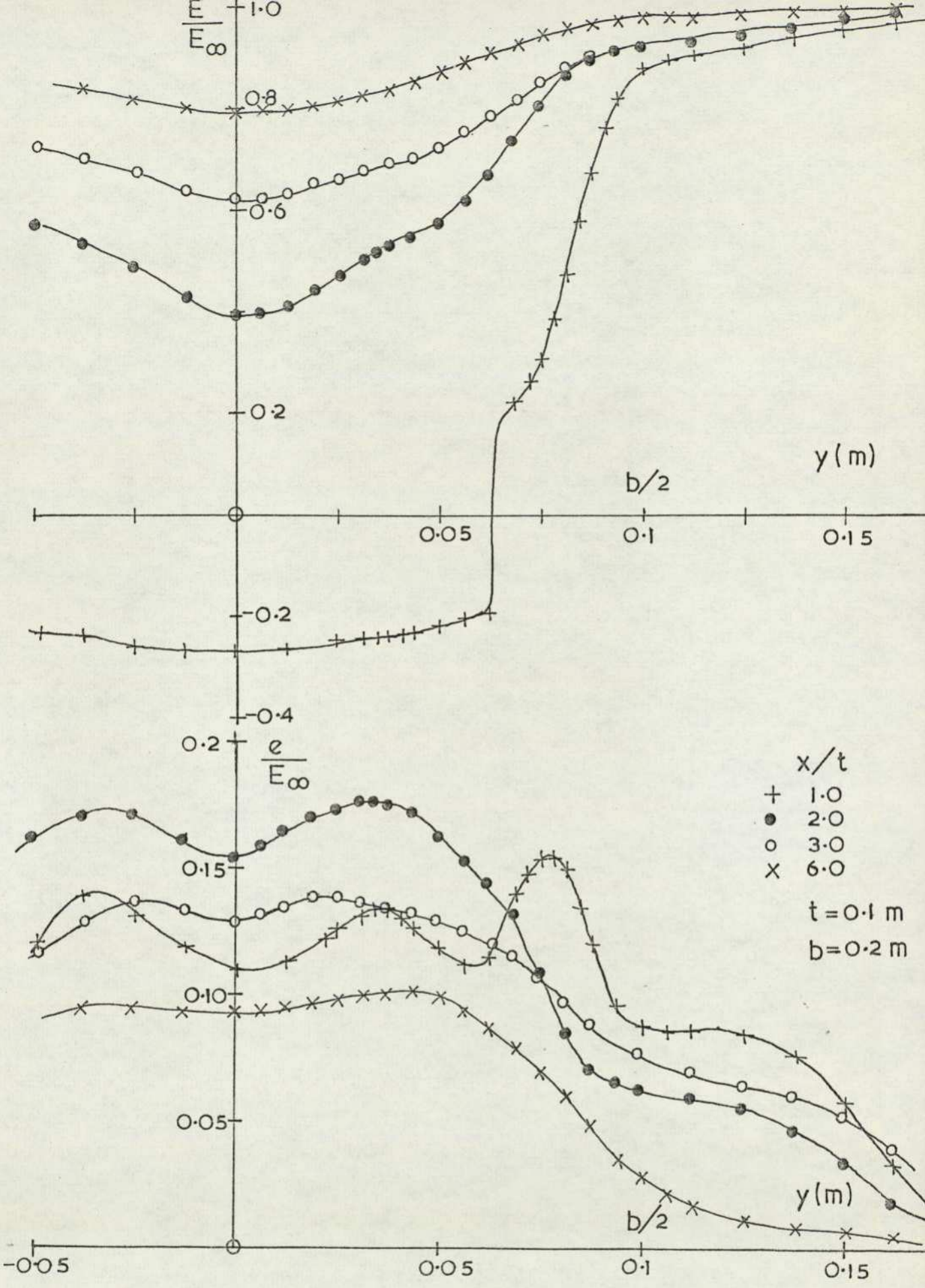

FIG. 62 (c) BLOCK 2N HORIZONTAL TRAVERSE

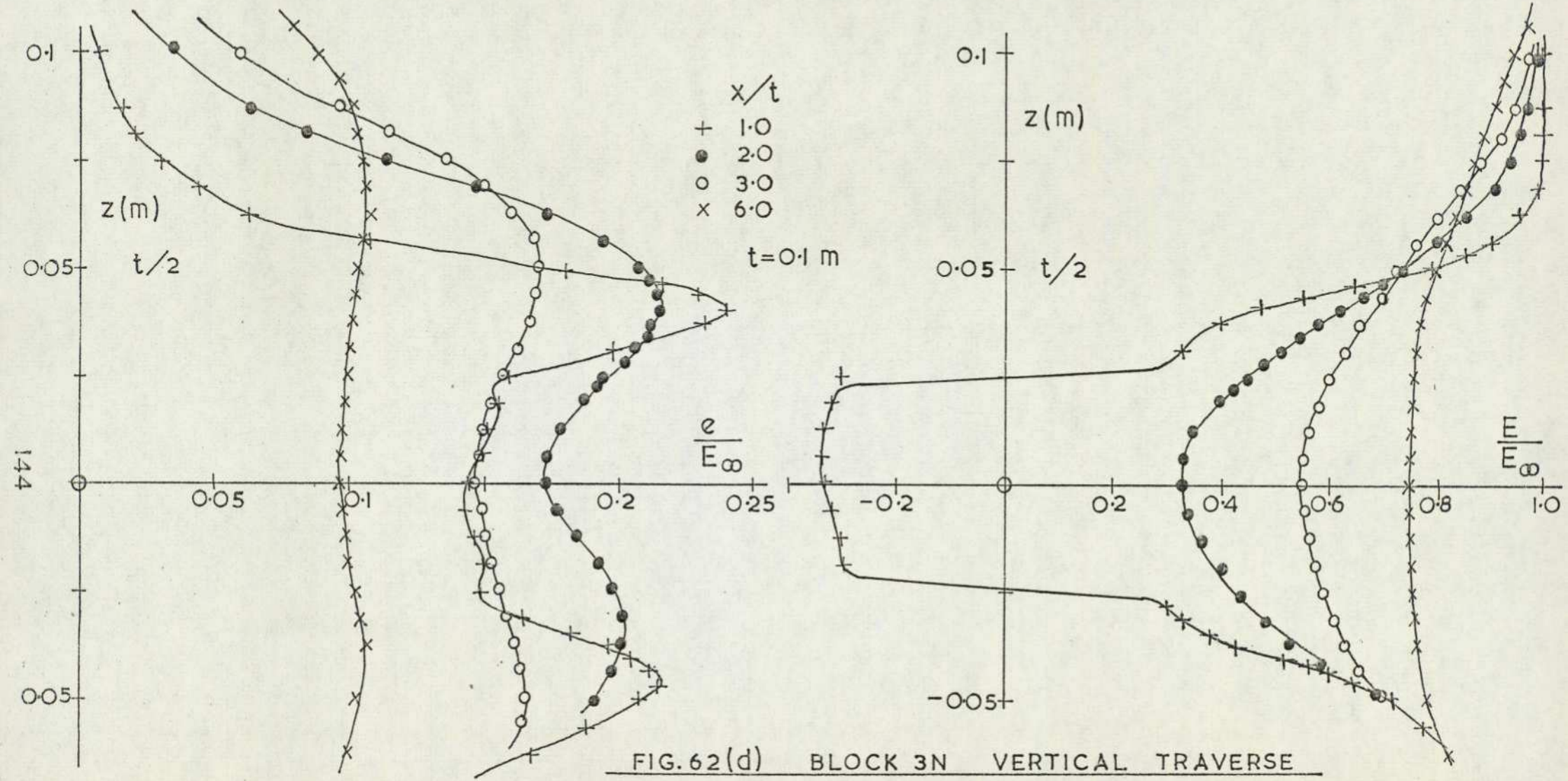

FIG. 62(d) BLOCK 3N VERTICAL TRAVERSE

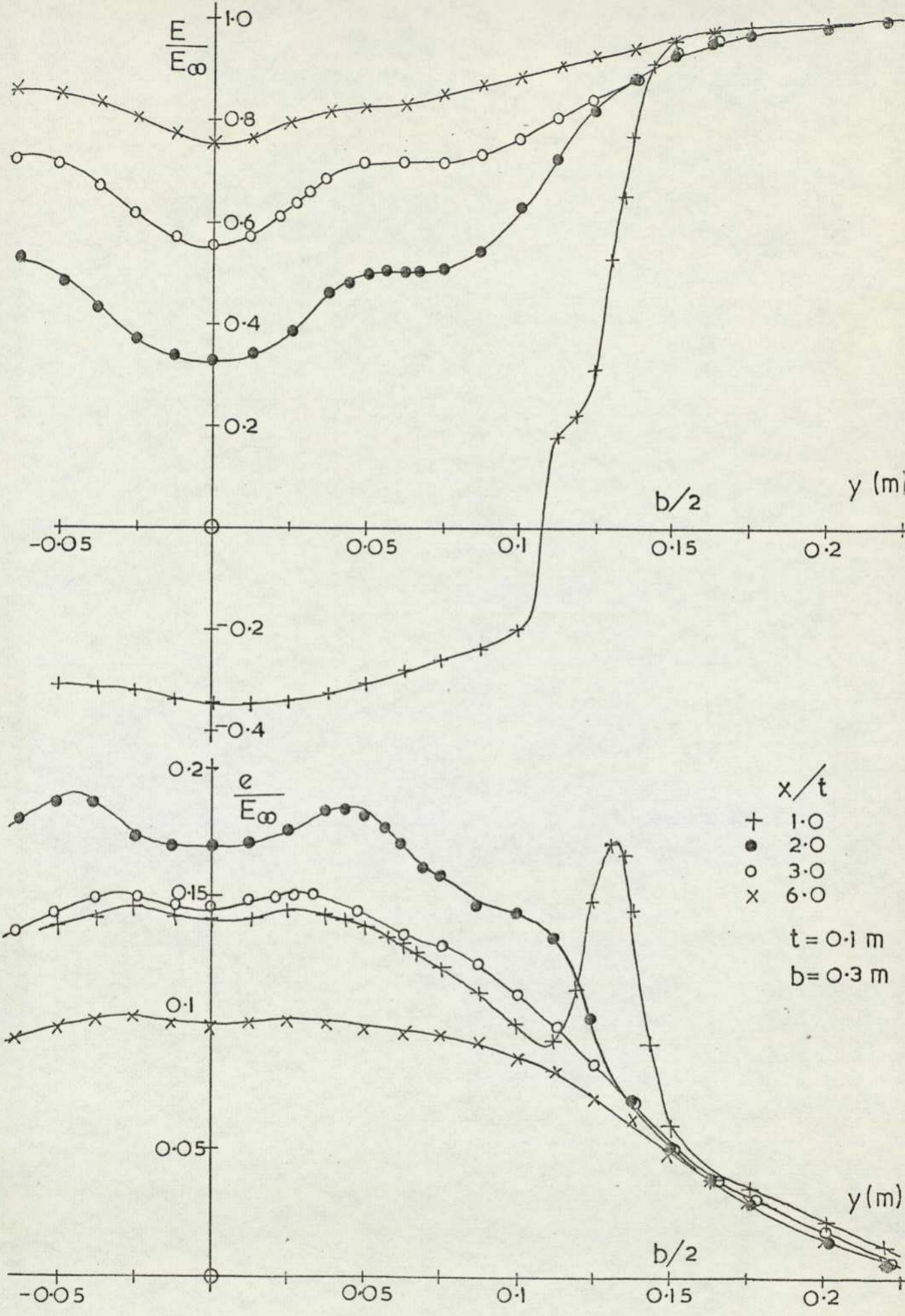

FIG. 62 (e) BLOCK 3N LATERAL TRAVERSE

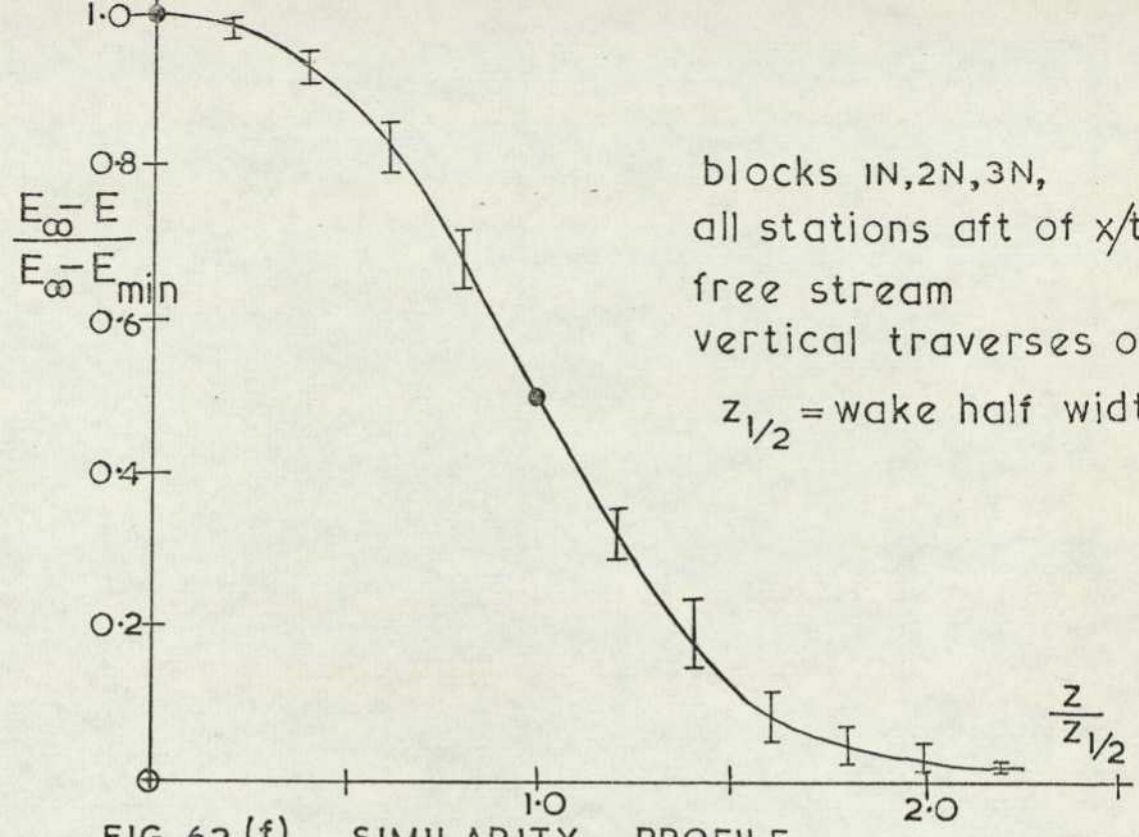

FIG. 62 (f) SIMILARITY PROFILE

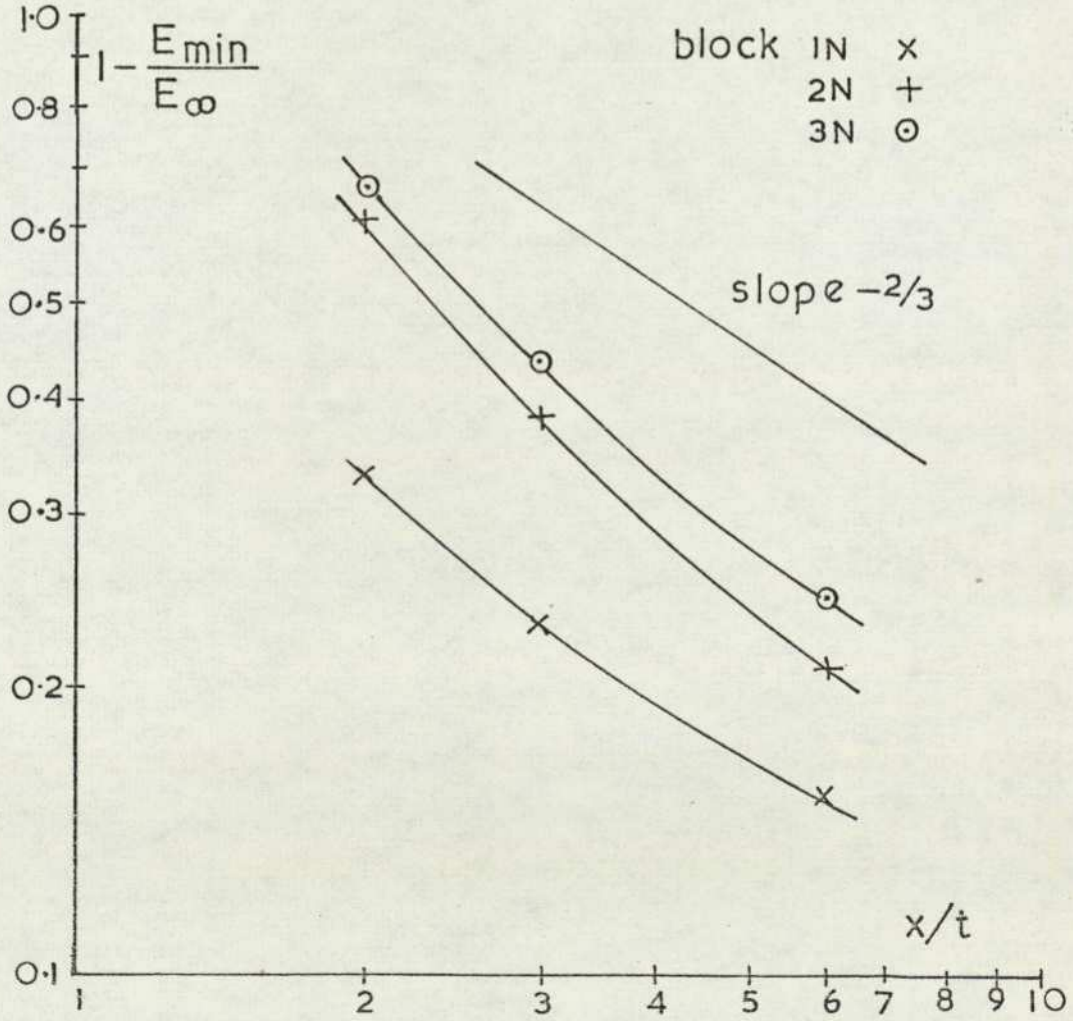

FIG. 63 DECAY OF MAXIMUM VELOCITY DEFICIT

FREE STREAM

Boundary layer measurements immediately upstream of the base were performed for all the blocks. The horizontal surfaces generated thinner layers than the sides, the difference being about 20%. Typically the upper surface boundary layer had a total thickness of 40mm with a momentum thickness of about 5 mm. Nash (48) has shown that provided the momentum thickness is less than 6% of the base height at separation then there is a negligible influence on the base pressure.

Base pressure measurements for the three blocks, Figure 65, show that the square section base has an almost uniform pressure distribution while increasing the span alters the lateral distribution only. The rectangular bodies have a peak suction at about one third span out from the centre line and its magnitude increases with span.

Following Calvert (31) the length of the recirculation region is defined by the peak in the local e/E distribution as measured along the centre line of the wake. These traverses are shown in Figure 66 for the three blocks. Increasing the span increases the 'bubble' length over the range investigated. This follows a similar trend to the flat plates studied by Fail, Lawford and Eyre (49).

To test for periodic effects in the wake the signal from the hot wire anemometer was passed through a frequency analyser. This instrument has a one third octave bandwidth and a narrow band facility. The procedure adopted was to investigate the spectrum using the one third octave bandwidths, any regions of interest being further scanned using the narrow band. The results given are the averaged data from at least two runs. As plotted the vertical axis represents the energy contained within a given frequency band. Thus where a marked peak occurs the energy is predominantly contained within eddies shed at the peak frequency.

The position of the probe was varied around the perimeter of the vortex sheet immediately downstream of the reverse flow region, unless otherwise stated. The results for block 2N are shown in Figure 67. The tunnel speed was set at 30 m/s in all cases. Along the horizontal vortex sheet there is a pronounced peak at 65 Hz, while the vertical sheet exhibits 55 Hz and 125 Hz peaks. Outboard of the vertical sheet a 125 Hz peak is apparent. Six base heights downstream the peak in the spectrum measured on the vertical axis of the wake remains at 65 Hz; Figure 67. The effects of a streamwise displacement on the spectrum measured on the horizontal axis of the wake is also shown in Figure 67. Initially the spectrum has a predominantly 125 Hz frequency

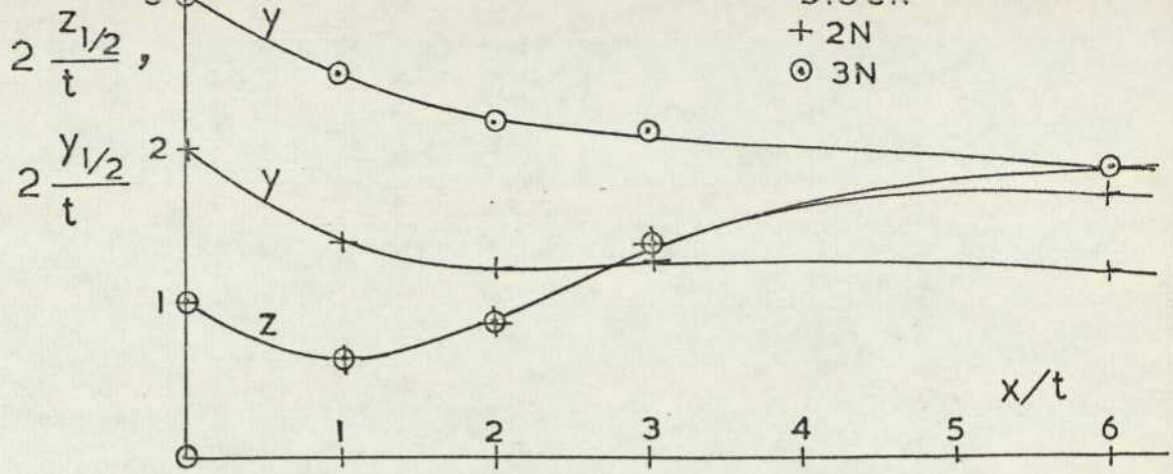

FIG. 64 WAKE HALF WIDTHS — FREE STREAM

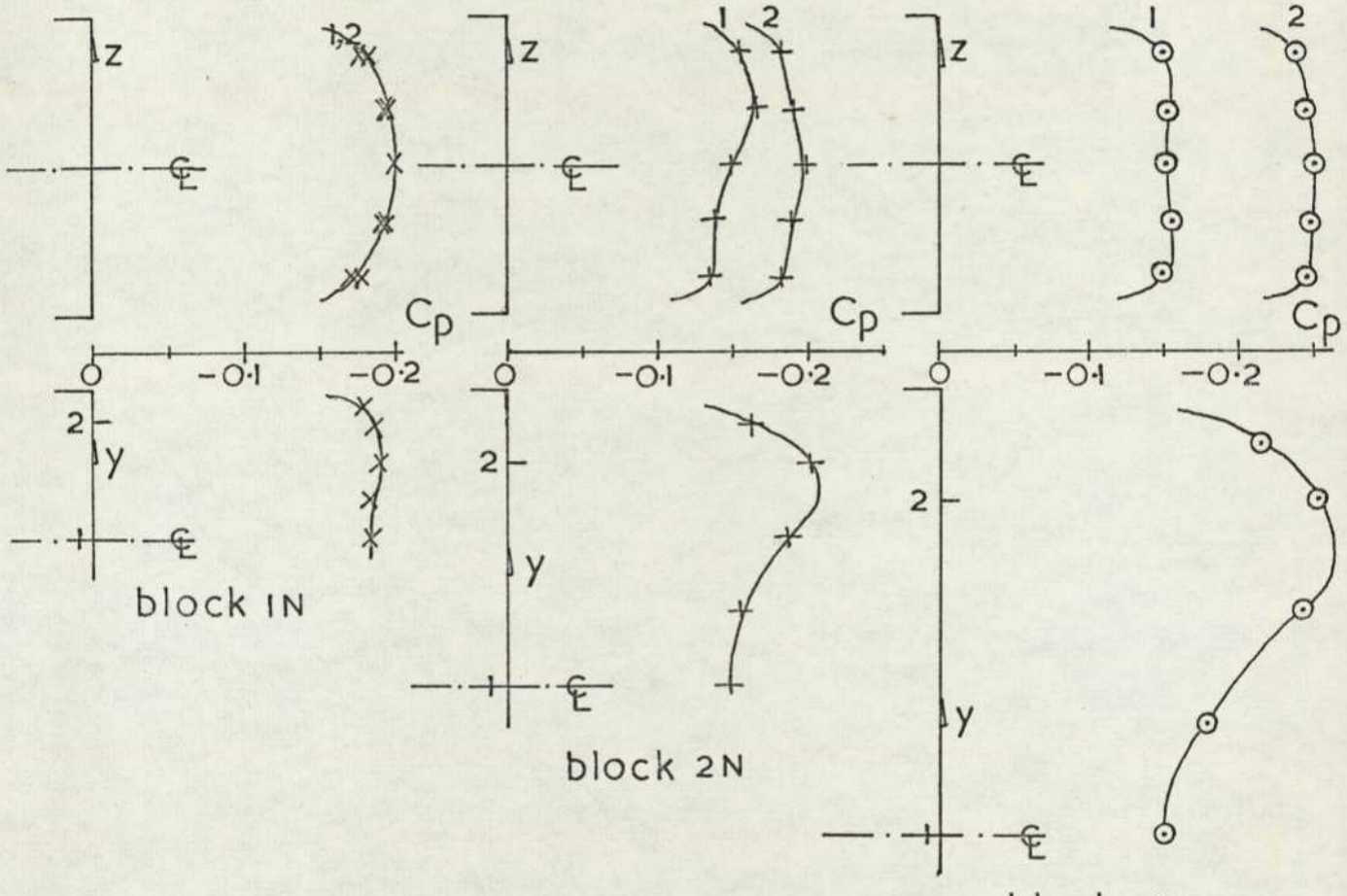

FIG. 65 BASE PRESSURE — FREE STREAM

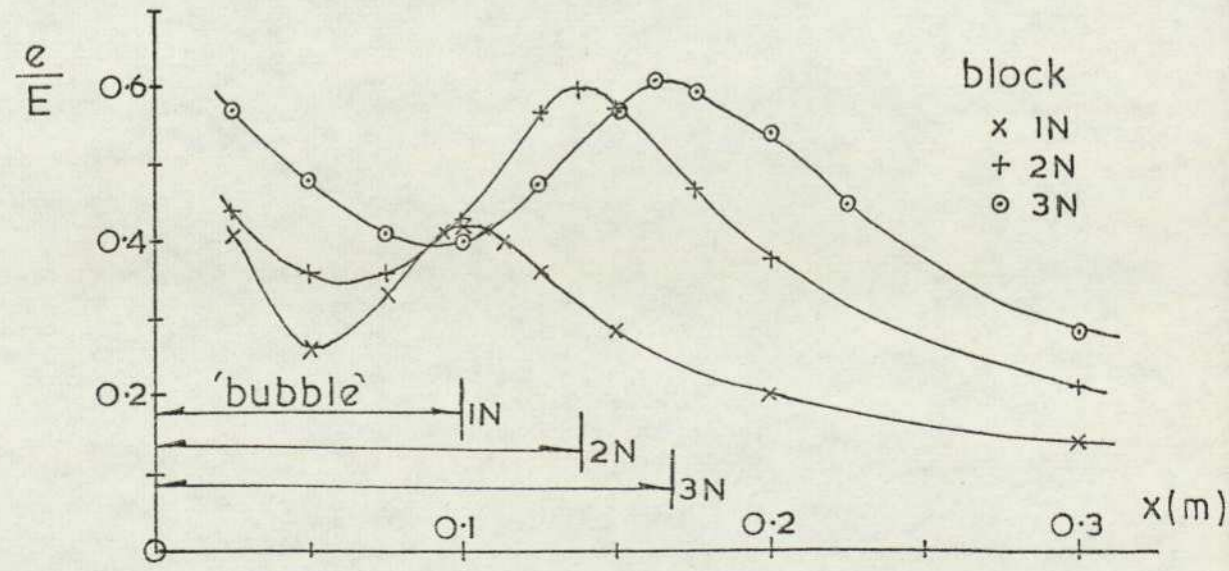

FIG. 66 DETERMINATION OF 'BUBBLE' LENGTH — F.S.

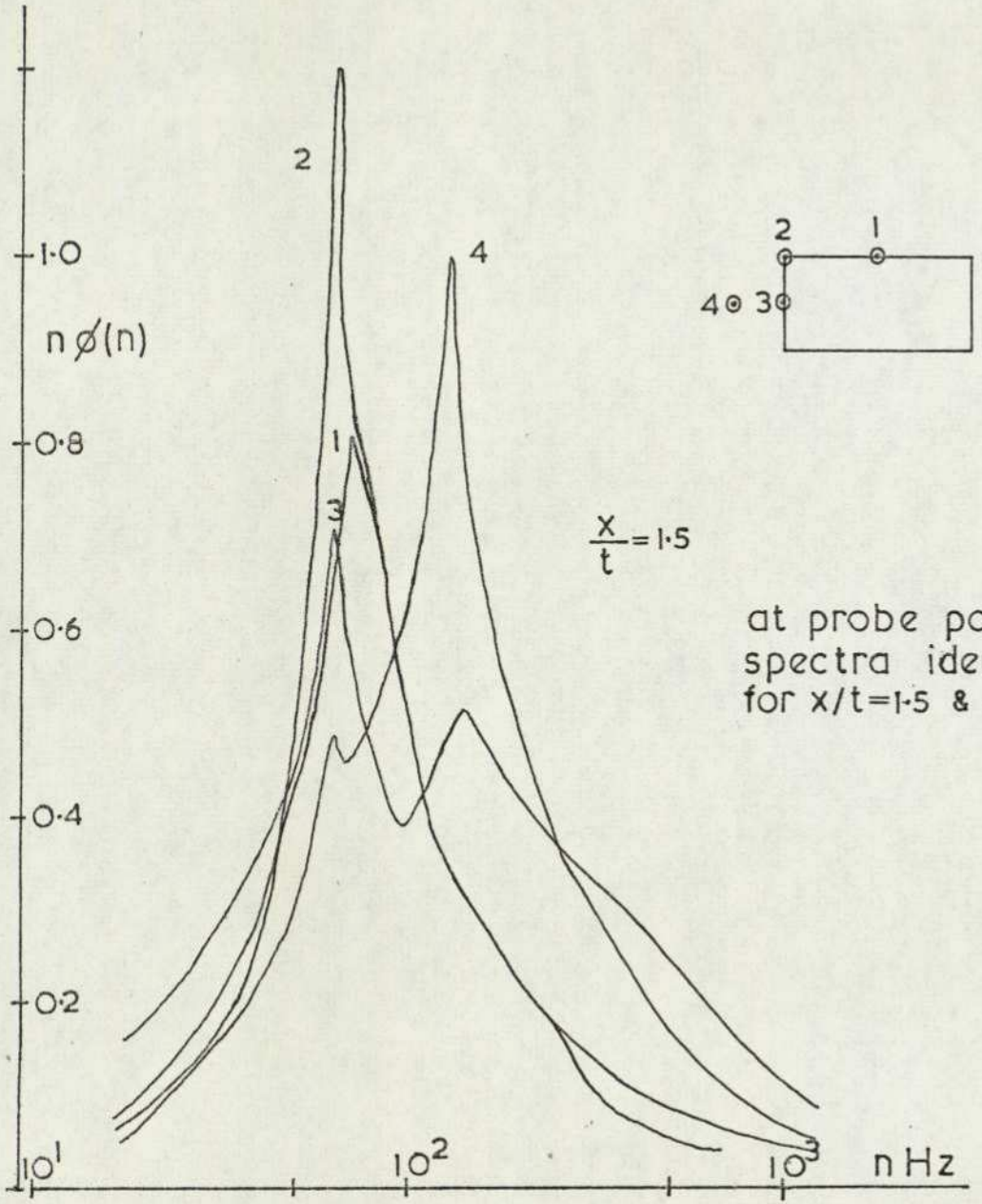

at probe position 1
spectra identical
for x/t=1·5 & 6·0

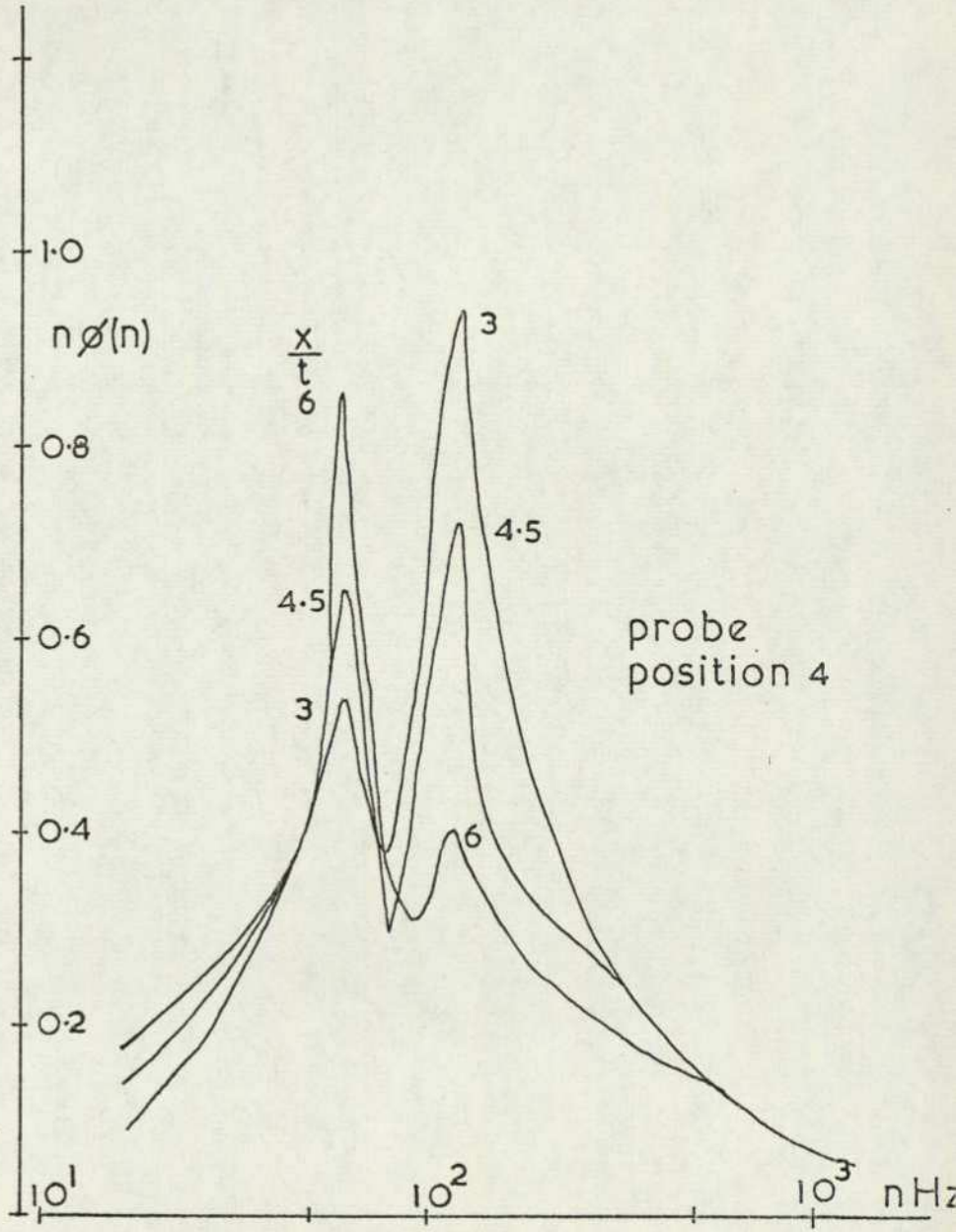

FIG. 67 FREQUENCY SPECTRA — BLOCK 2N, FREE STREAM — INFLUENCE OF PROBE POSITION

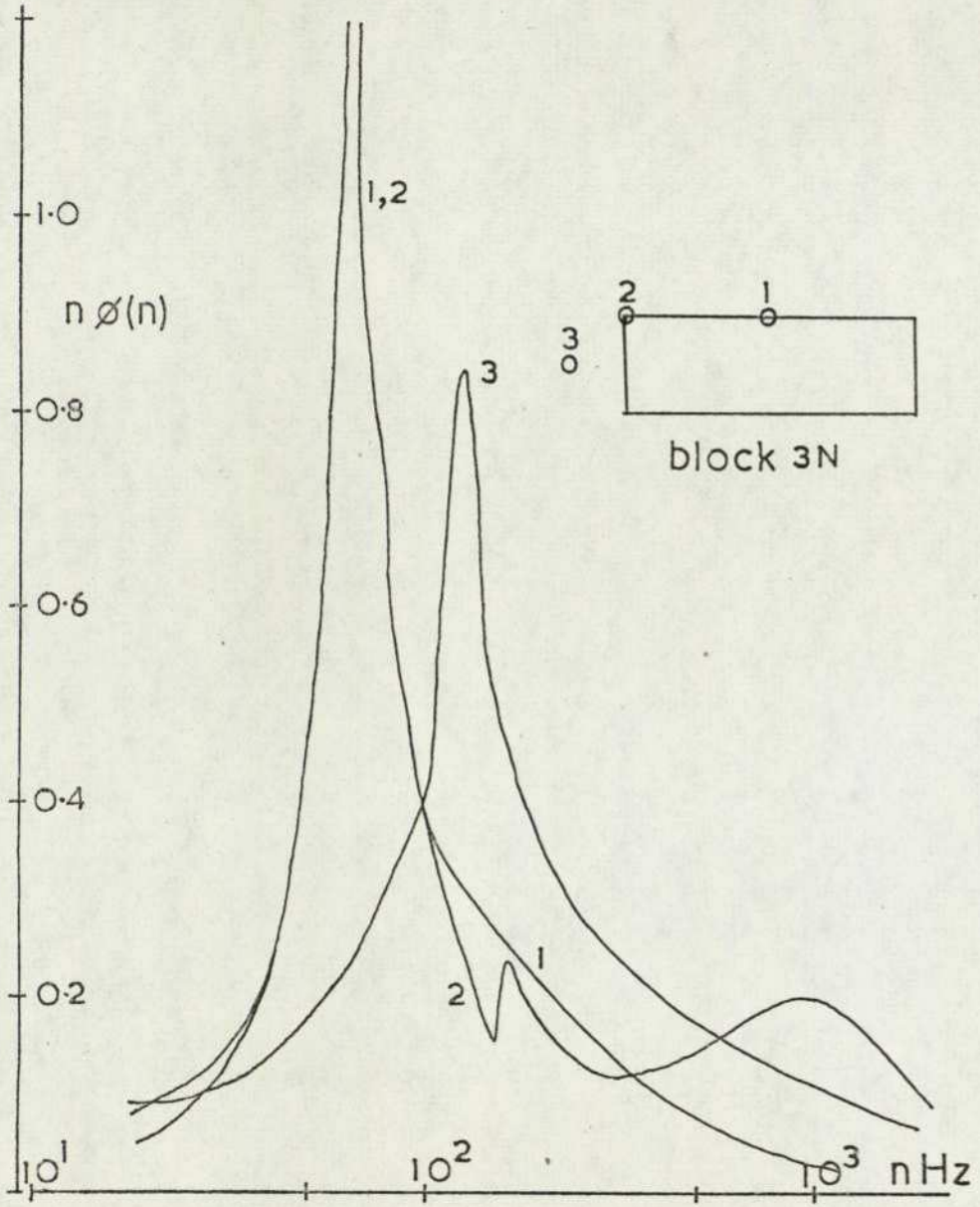

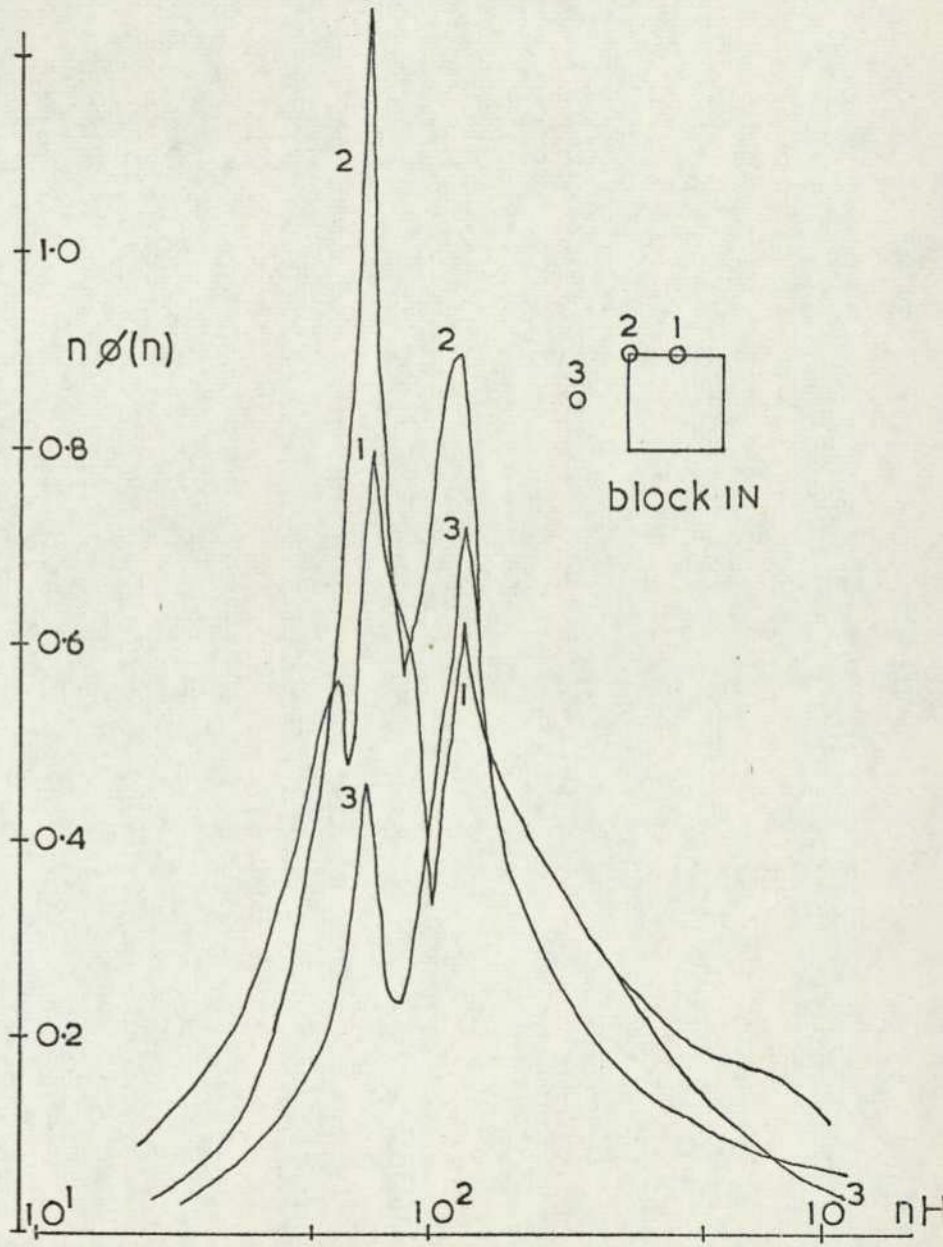

FIG. 68 FREQUENCY SPECTRA — BLOCKS 1N, 3N FREE STREAM, X/t=1·5

but on moving downstream a 60-65 Hz peak emerges. This grows as the higher frequency peak diminishes, the latter becoming practically non-existent by six base heights downstream. The wake is tending towards axi-symmetry beyond this point. The peaks in the frequency spectrum measured in the near wake of block 3N are more pronounced as would be expected for a more two dimensional case, Figure 68. Measurements in the extreme lateral positions show very similar results to the block 2N case. This suggests that the outboard wake regions can be considered as a tip effect superimposed on an essentially two dimensional structure. The square cross section model, block IN, differs in that two distinct peaks are apparent at all positions around the perimeter of the vortex sheet. These occur at 75 Hz and 125 Hz, as also shown in Figure 68. Comparison with the basic block 2 showed that the bluffer model gave reduced peak frequencies of around 55 Hz on the horizontal sheet but 125 Hz remained the peak on the vertical vortex sheet. The thicker boundary layer has presumably an influence here.

4.2.3 Influence of ground proximity.

The wake properties for block 2N have been obtained at various ground clearances. The results of the vertical and horizontal traverse through the wake centre line with the hot wire anemometer are shown in Figure 69. for ground clearances ranging from 3mm to 50 mm. The horizontal traverses show distributions of mean velocity and turbulence intensity which are very similar to the free stream results. The results from the vertical traverse show a considerable influence of the ground. At the largest ground clearance, equal to half the body thickness the wake is initially very similar to the free stream form, except that the turbulence intensity peak for the vortex sheet springing from the edge nearest to the ground is greater. As the wake moves downstream the position of maximum velocity deficit approaches the ground. At the most extreme downstream station ($x/t = 6.0$) the wake profile has completely changed with the maximum velocity deficit occurring at the ground. The lower peak in the turbulence intensity profile has also disappeared. As the ground clearance is reduced the wake deformation to this far downstream state occurs nearer to the model, until for the ground clearance condition, $z_o/t = 0.125$, the vertical wake profiles at all stations downstream of the reverse flow region are of this form.

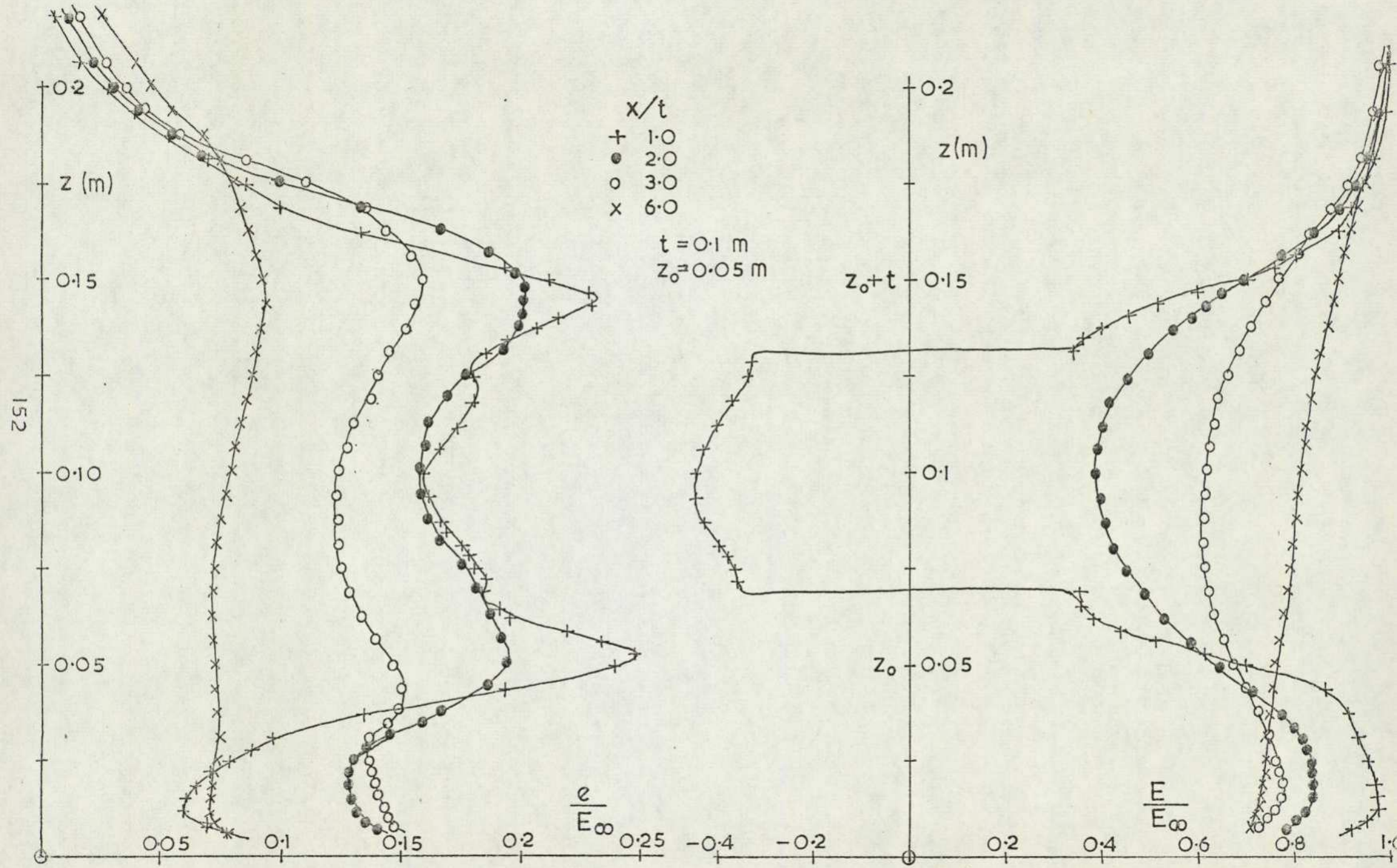

FIG.69 WAKE TRAVERSES – BLOCK 2N NEAR TO GROUND (a) $z_0/t = 0.5$ VERTICAL TRAVERSE

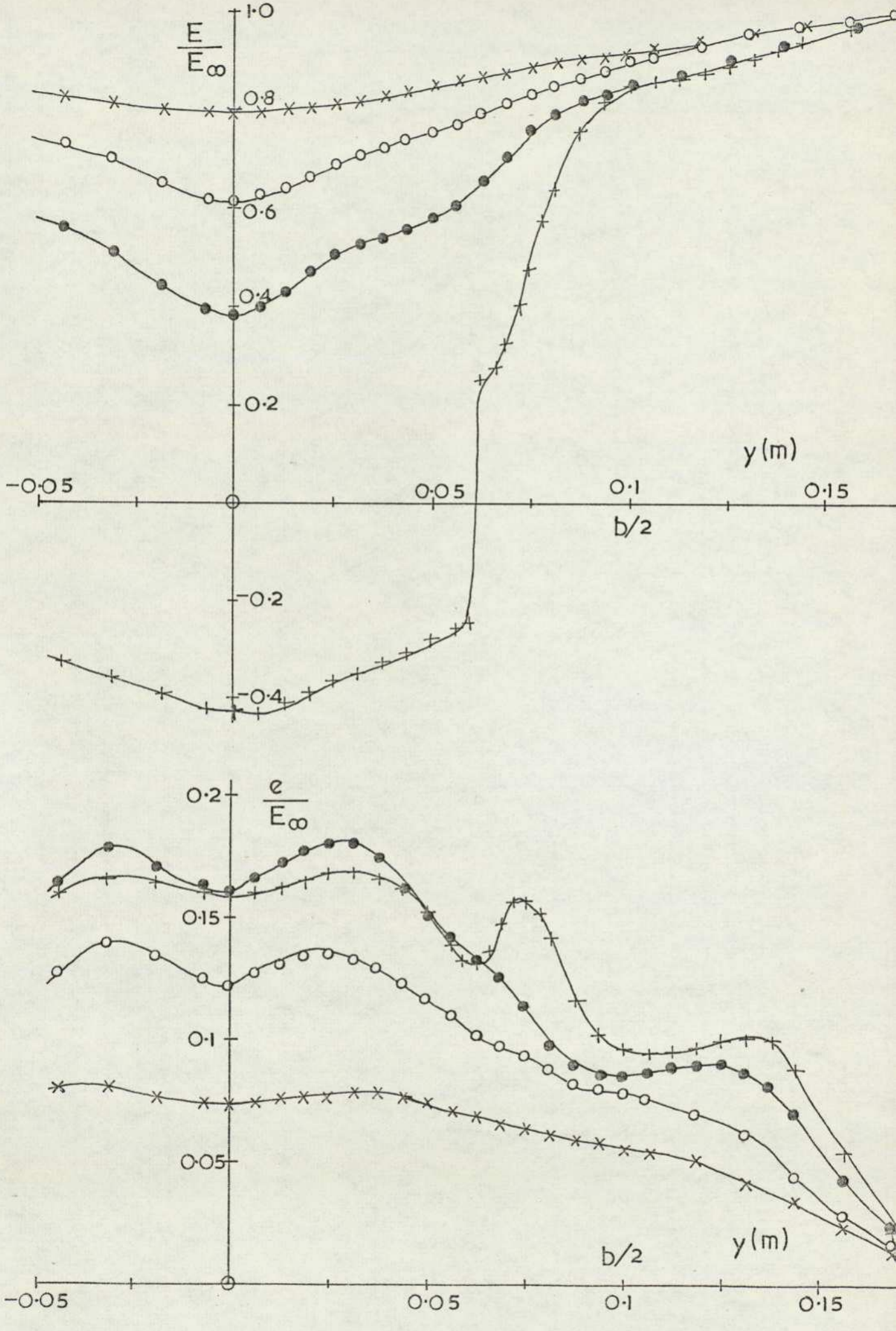

FIG. 69 (b) BLOCK 2N, $Z_o/t = 0{\cdot}5$, LATERAL TRAVERSE

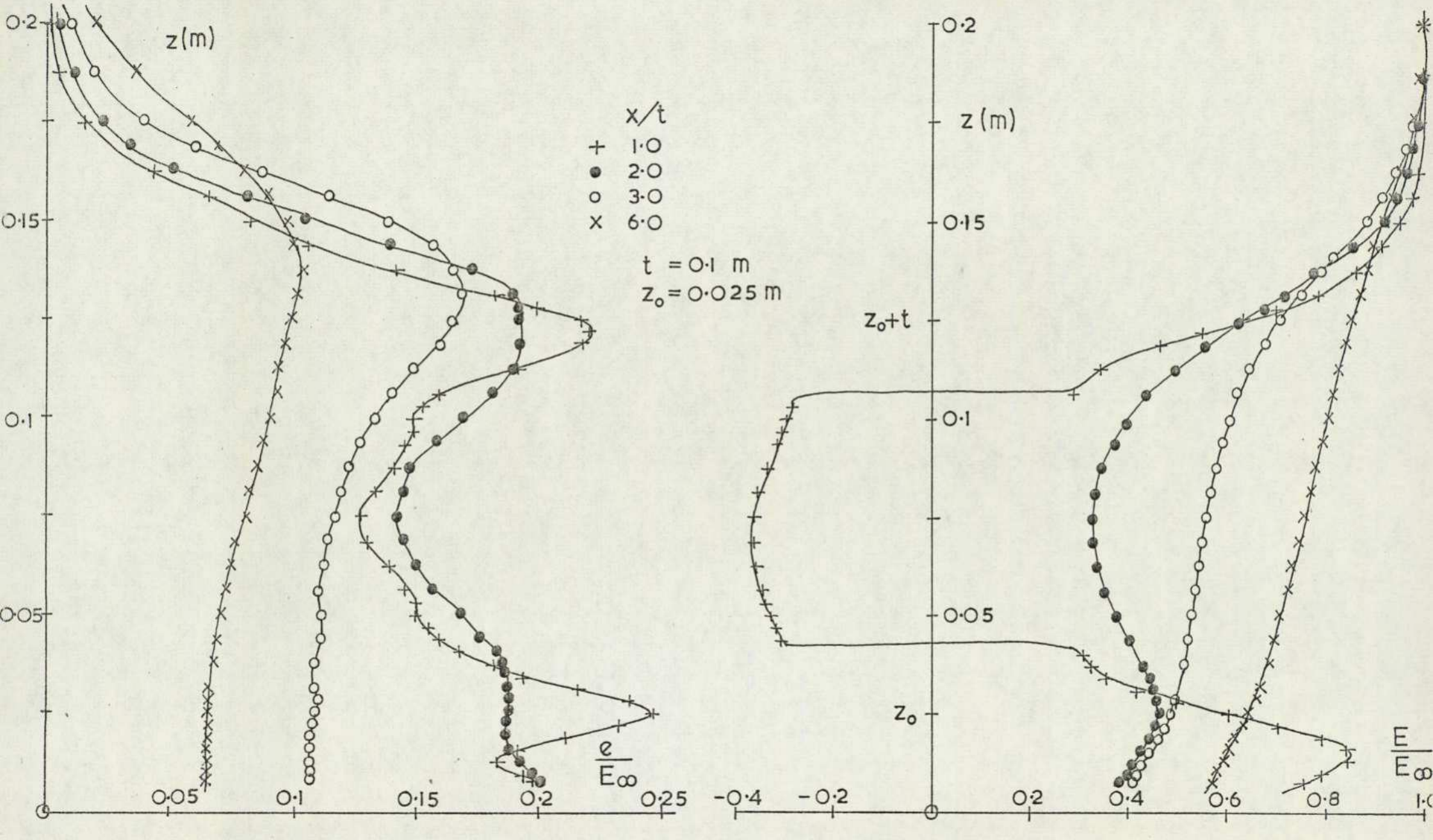

FIG. 69 (C) BLOCK 2N, $Z_o/t = 0·25$, VERTICAL TRAVERSE

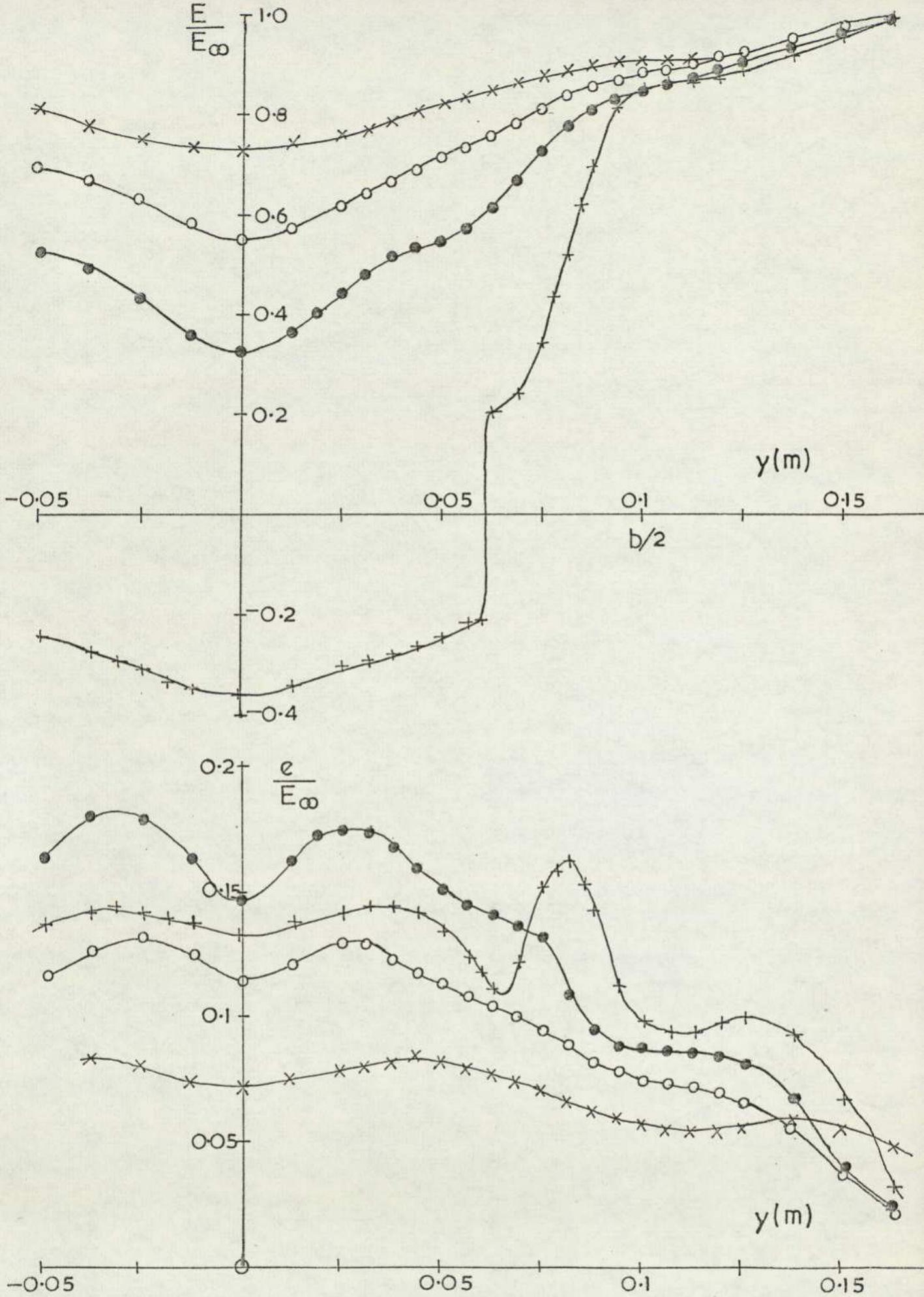

FIG. 69 (d) BLOCK 2N, $Z_o/t = 0{\cdot}25$, LATERAL TRAVERSE

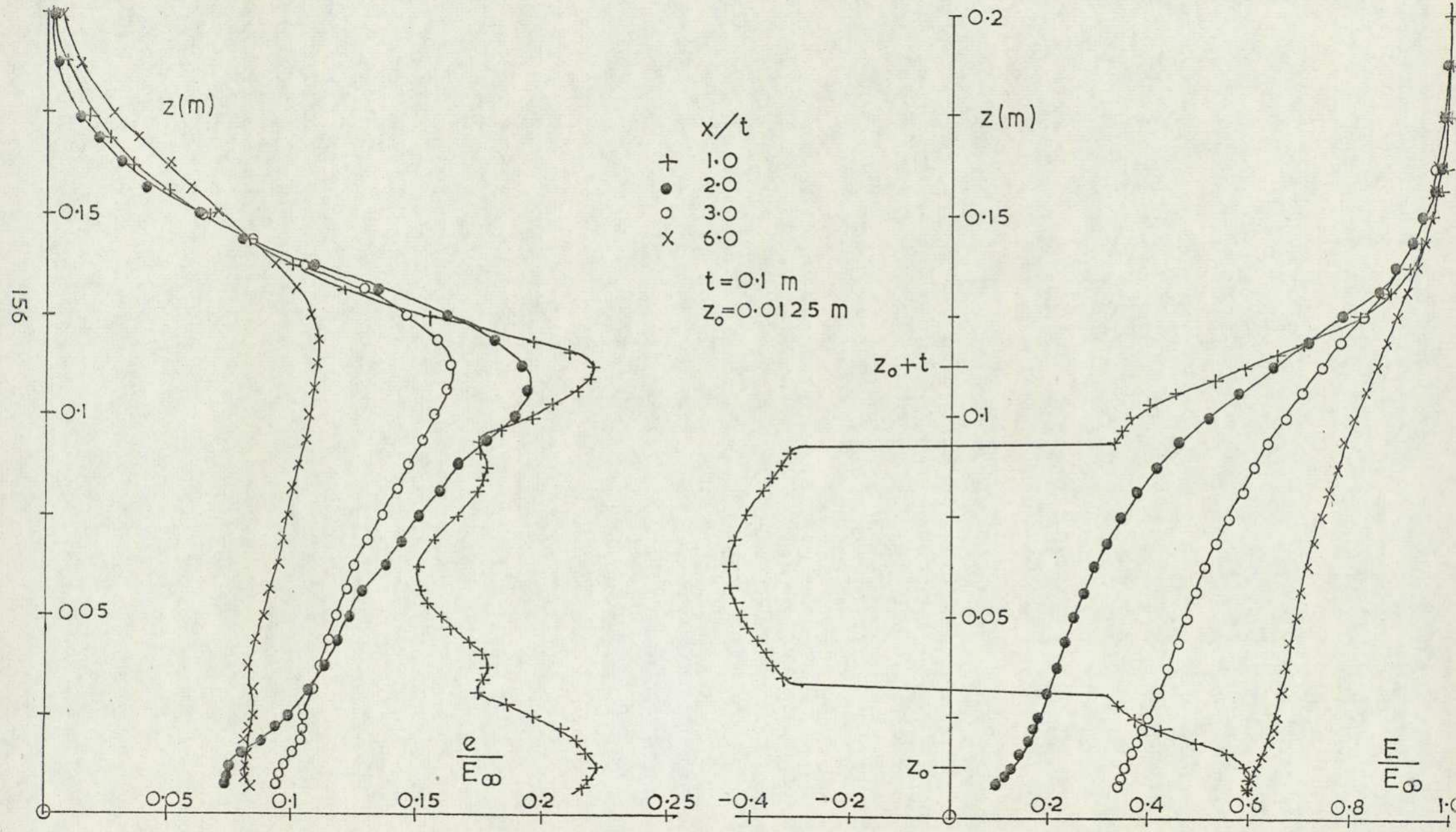

FIG. 69(e) BLOCK 2N, z_0/t=0·125, VERTICAL TRAVERSE

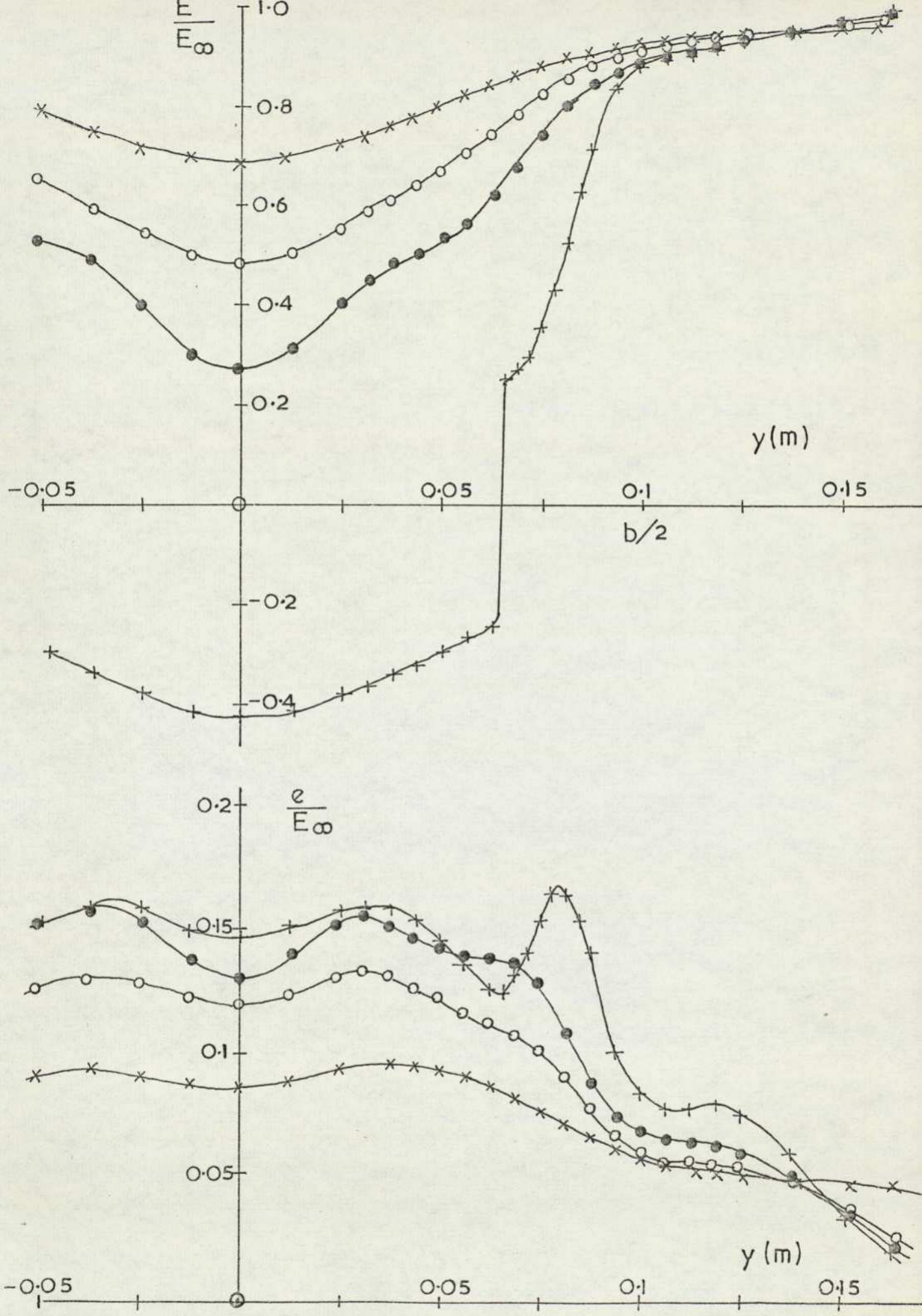

FIG. 69 (f) BLOCK 2N, $Z_o/t = 0.125$, LATERAL TRAVERSE

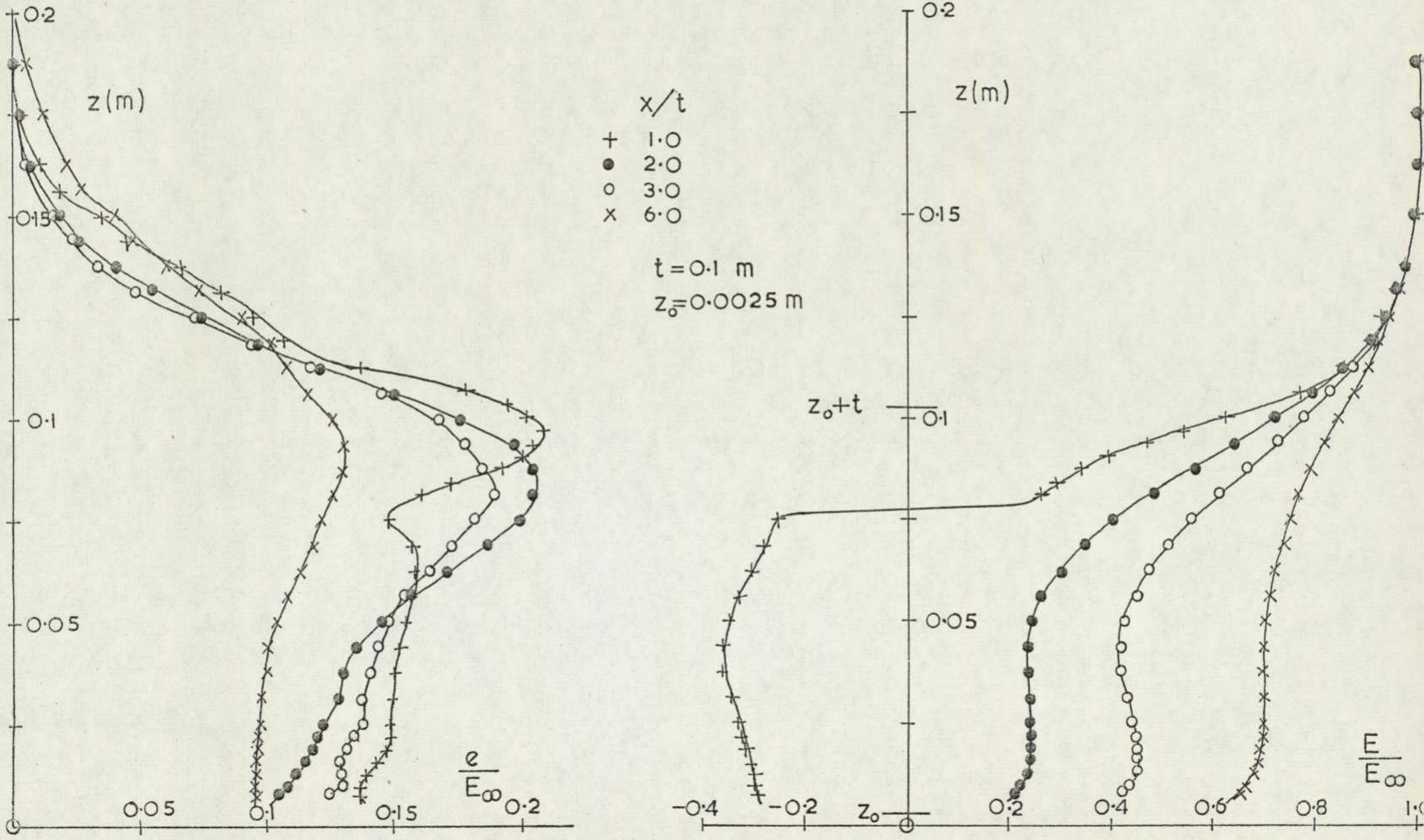

FIG. 69(g) BLOCK 2N, z_o/t=0·025, VERTICAL TRAVERSE

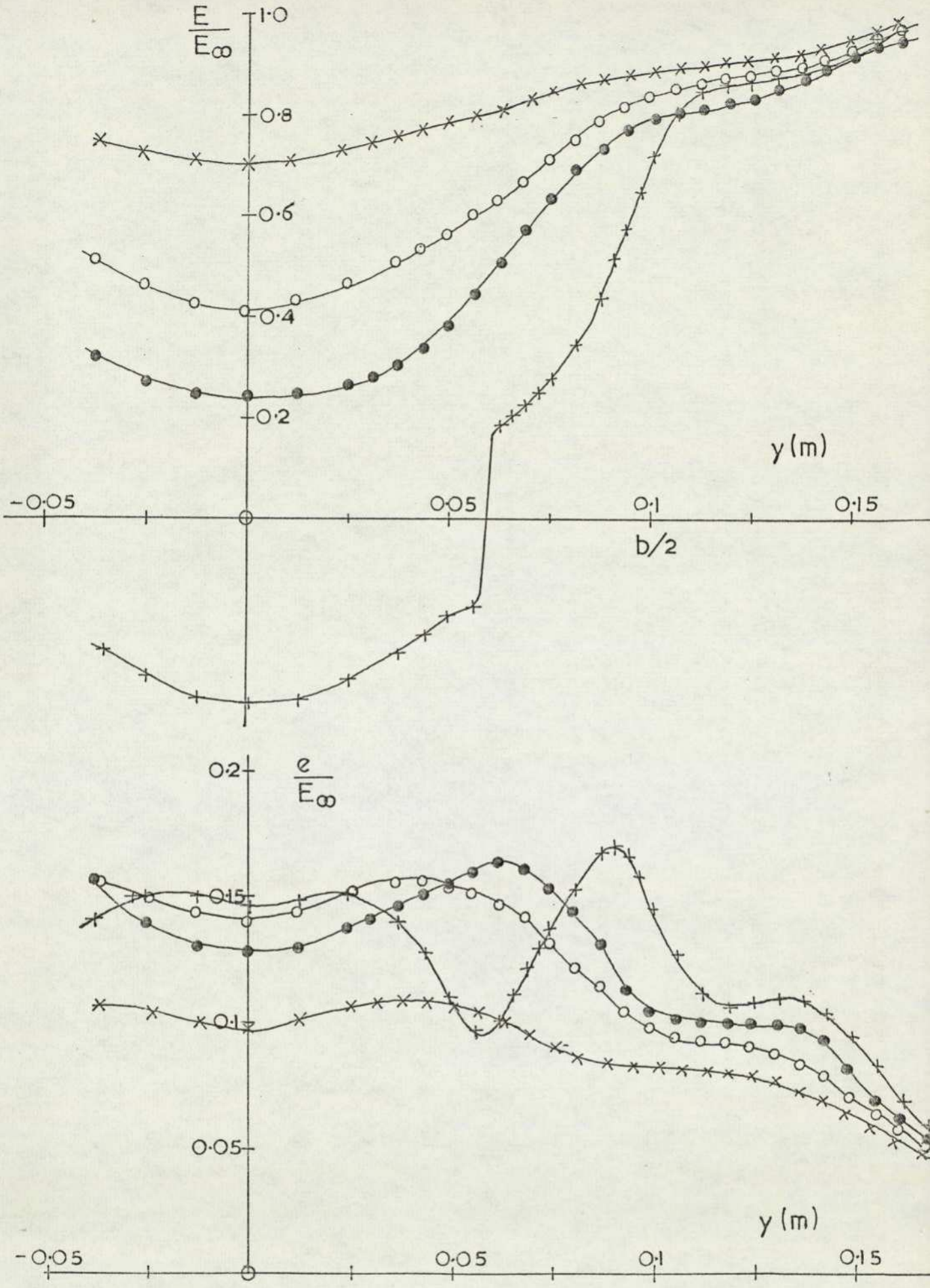

FIG. 69 (h) BLOCK 2N, $Z_o/t = 0{\cdot}025$, LATERAL TRAVERSE

At the minimum ground clearance, $z_o/t = 0.03$, there is no vortex sheet at the lower edge and the flow at the trailing edge forms a closed bubble with the separating shear layers reattaching to the ground plane. The ground board pressure distribution confirms this as did smoke tunnel tests, although the latter were performed at a considerably lower Reynolds number and might therefore be expected to behave slightly differently.

Distributions of E/E_∞ and e/E_∞ have been obtained for blocks 1N and 3N at one ground clearance only, $z_o/t = 0.25$, and these are shown in Figure 70. In figure 71 the decay of the maximum velocity deficit is plotted for all cases in ground proximity. For the far wakes where the maximum deficit is very close to the ground the deficit is taken at the height of the local boundary layer thickness as measured in the absence of the model. This was discussed in Chapter 3. When the rectangular models have ground clearances of 25mm and less, $z_o/t < 0.25$, the decay rate follows a constant power law throughout the region of measurement. The exponent is close to - 2/3. The square model attains this value aft of three base heights downstream. In all cases the maximum velocity deficit at any particular downstream location is greater than the free stream condition but the difference reduces as ground clearance increases. Increasing the span also delays the velocity recovery.

'Bubble' measurements, Figure 72, show that the length of the reverse flow region increases with reducing ground clearance and with increasing span, as was noted for the freestream case. Squaring the leading edges, block 2, reduces bubble length.

A more thorough investigation of the near wake was performed on block 2NS, with nose and side plates, at a ground clearance ratio, z_o/t, of 0.25. The vertical traverses show that the 'bubble' contour remains highly symmetrical, although the ground is close, while the horizontal traverses display the loss of energy in the outer shear layers and the emergence of turbulent energy peaks at a more inboard position, Figure 73. The maximum velocity deficit, Figure 71, is always slightly greater than for block 2N as would be expected from the greater span, but the exponent of the power law is again very close to - 2/3. The 'bubble' length is similarly longer, Figure 72. Contours of mean velocity and

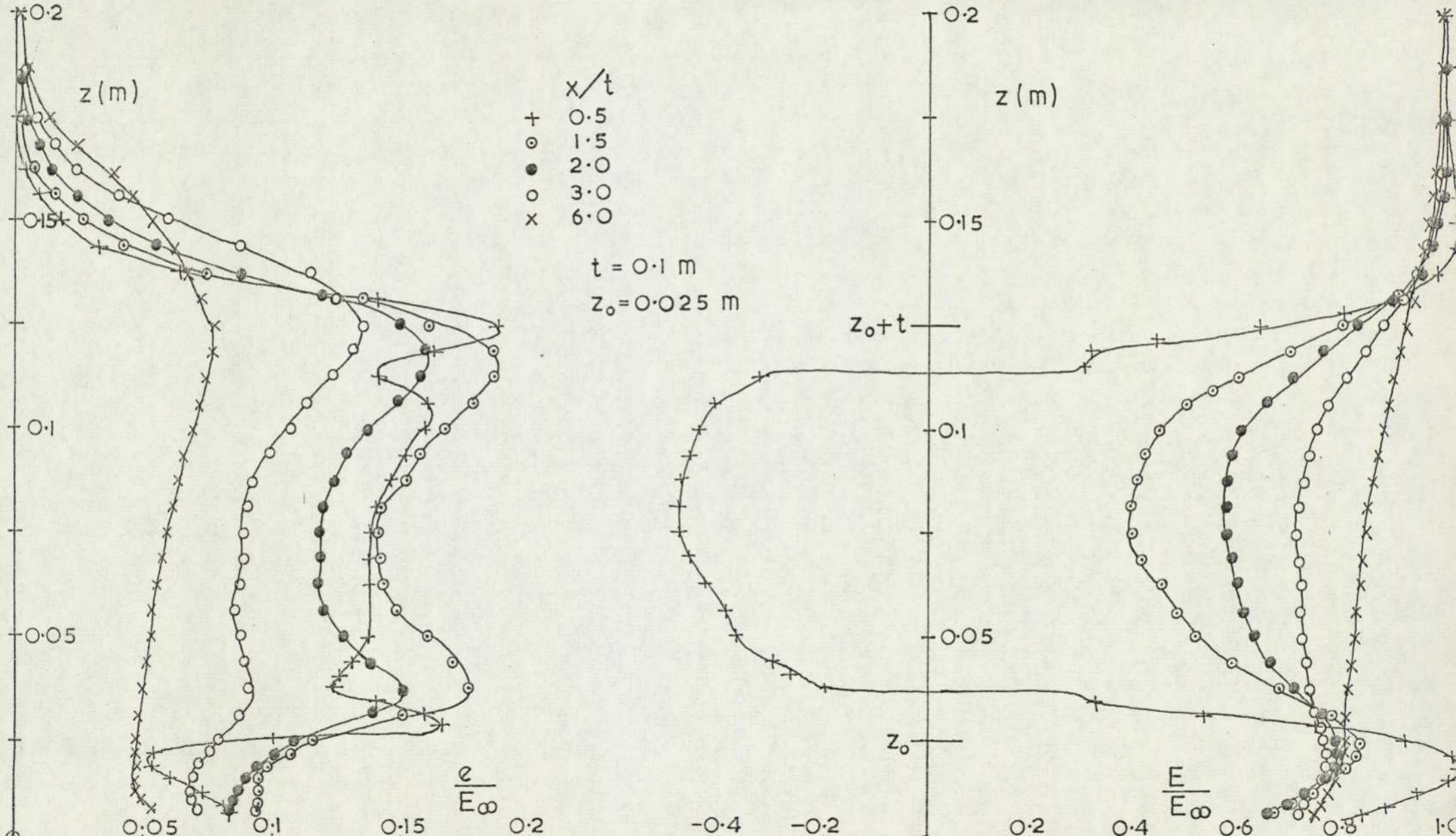

FIG.70 WAKE TRAVERSES (a) BLOCK IN, z_0/t=0·25, VERTICAL TRAVERSE

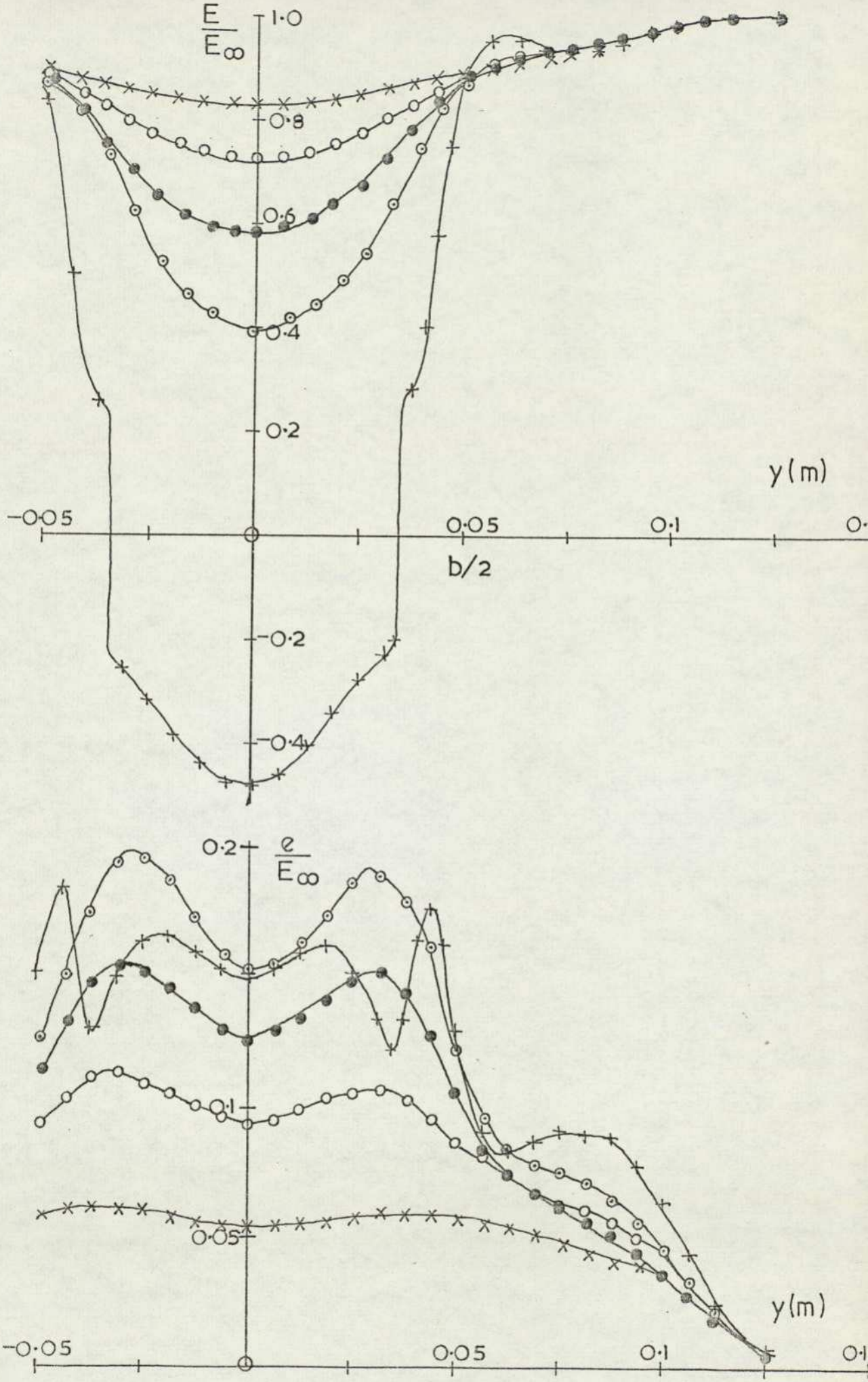

FIG. 70 (b) BLOCK IN, Z_o/t 0·25, LATERAL TRAVERSE

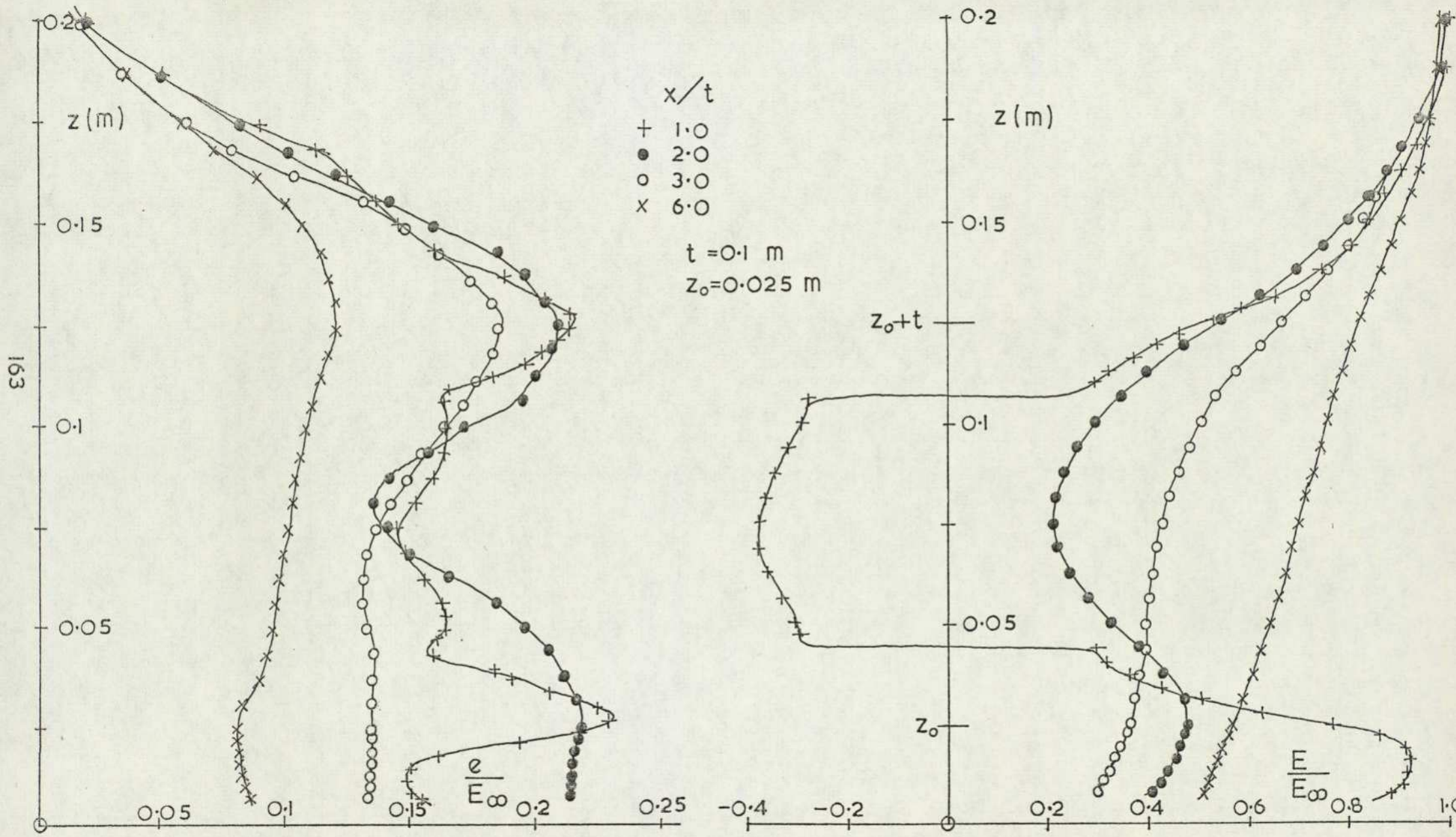

FIG. 70 (c) BLOCK 3N, z_o/t=0·25, VERTICAL TRAVERSE

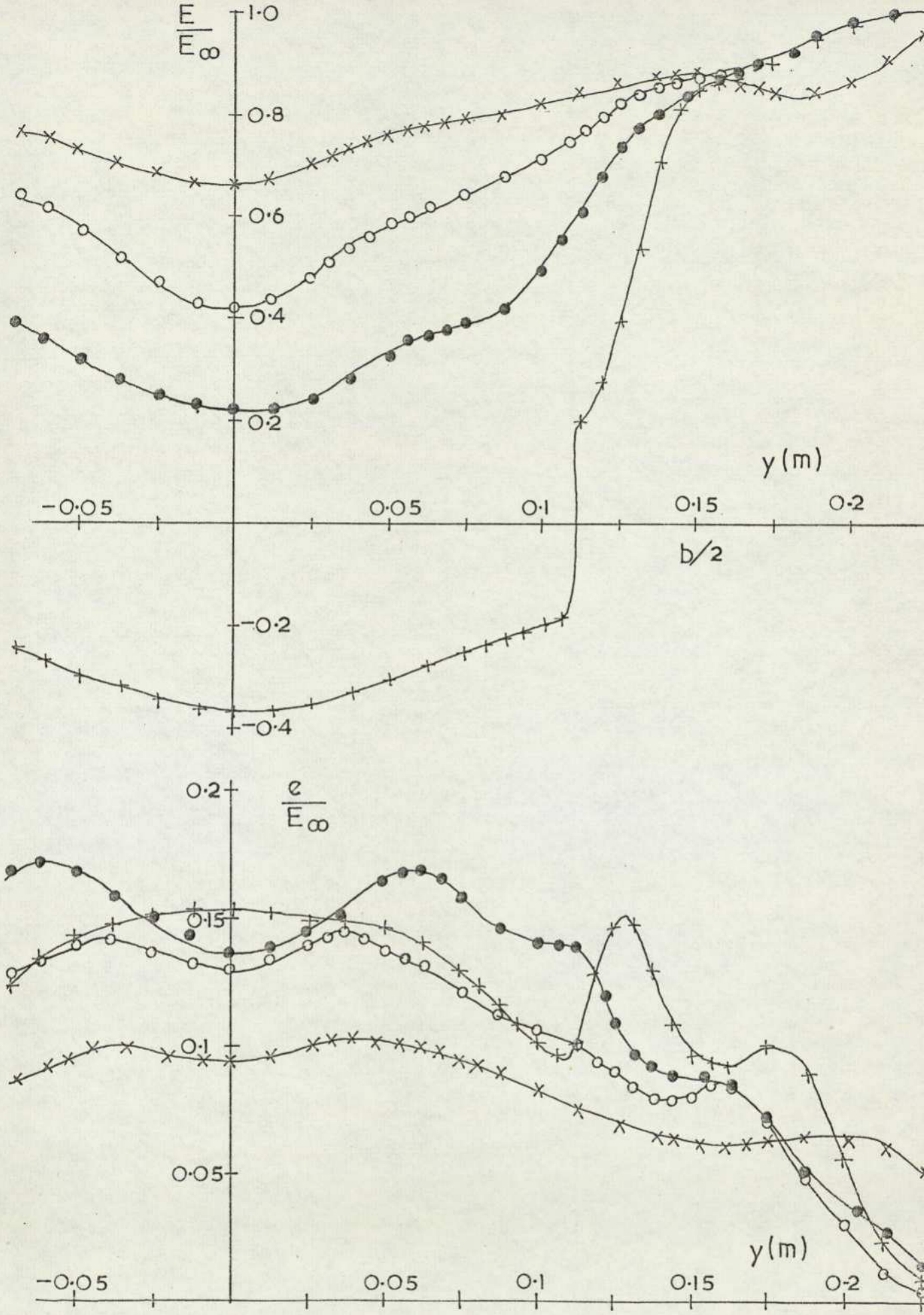

FIG.70(d) BLOCK 3N, Z_o/t 0·25, LATERAL TRAVERSE

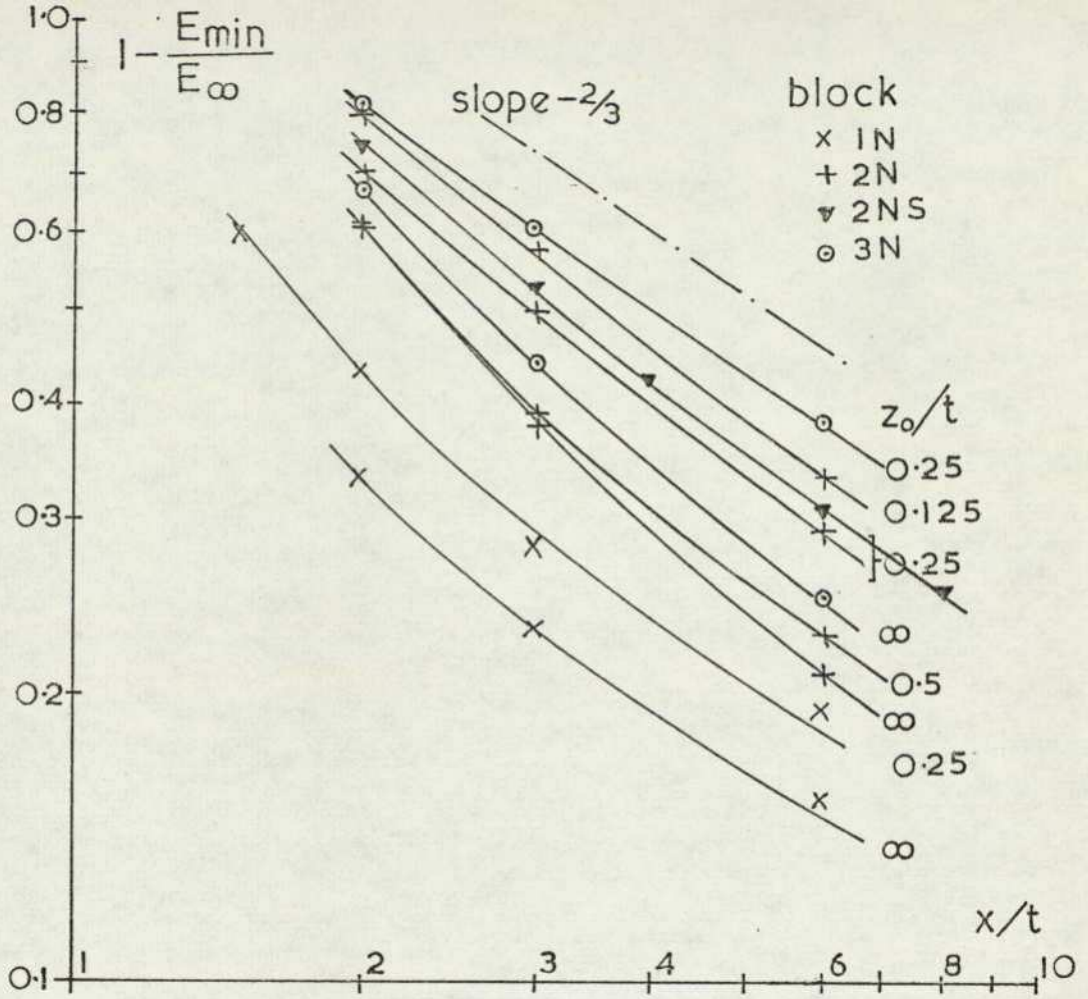

FIG.71 EFFECT OF GROUND PROXIMITY ON WAKE DECAY

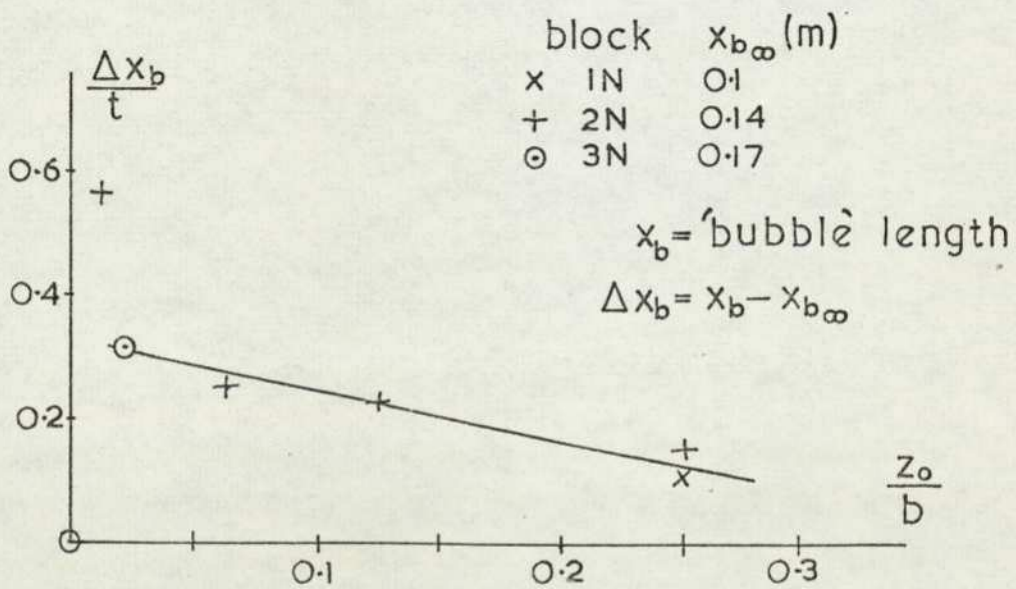

FIG.72 INCREASE IN 'BUBBLE' LENGTH ARISING FROM GROUND PROXIMITY

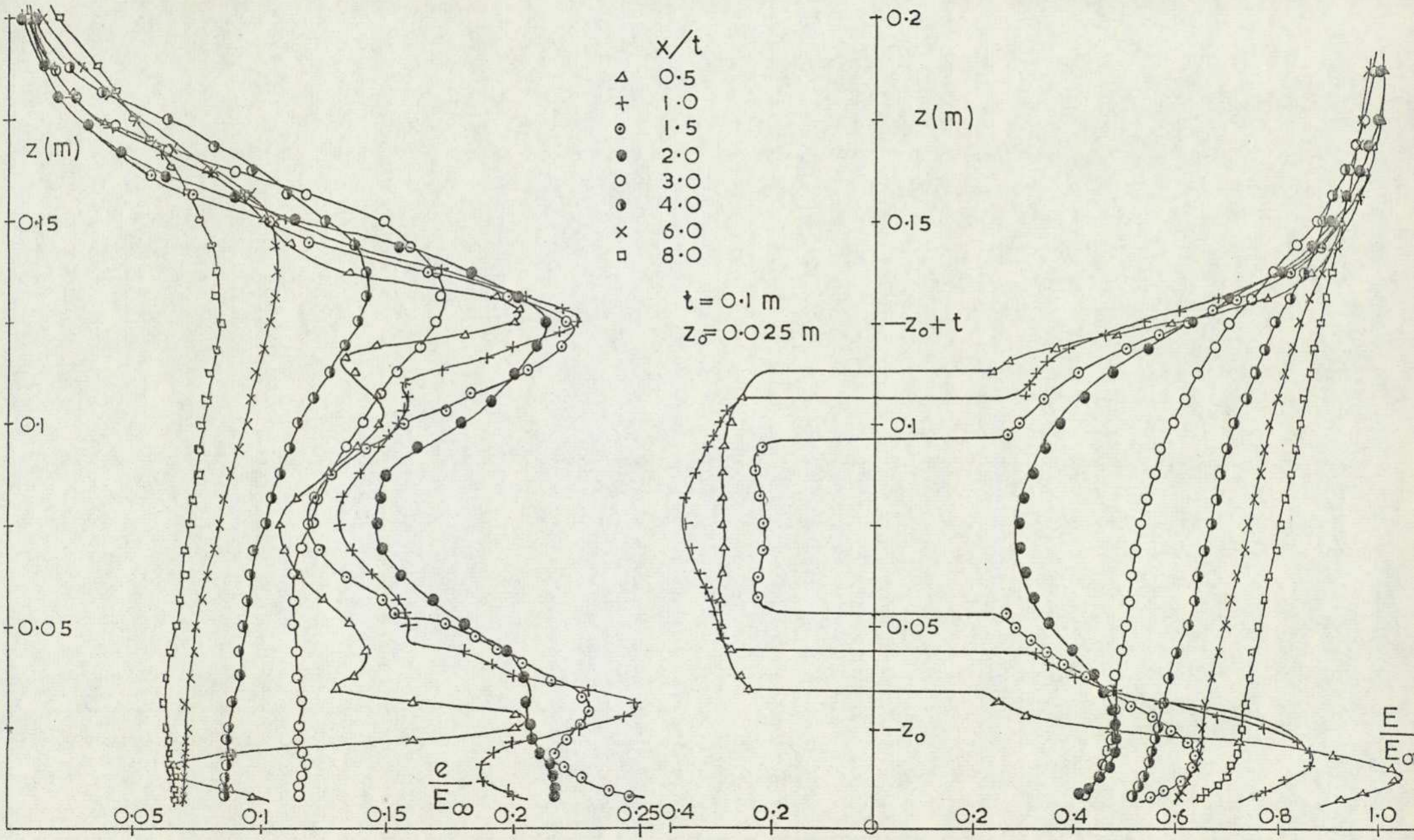

FIG. 73 WAKE TRAVERSES (a) BLOCK 2NS, $z_o/t = 0.25$, VERTICAL TRAVERSE

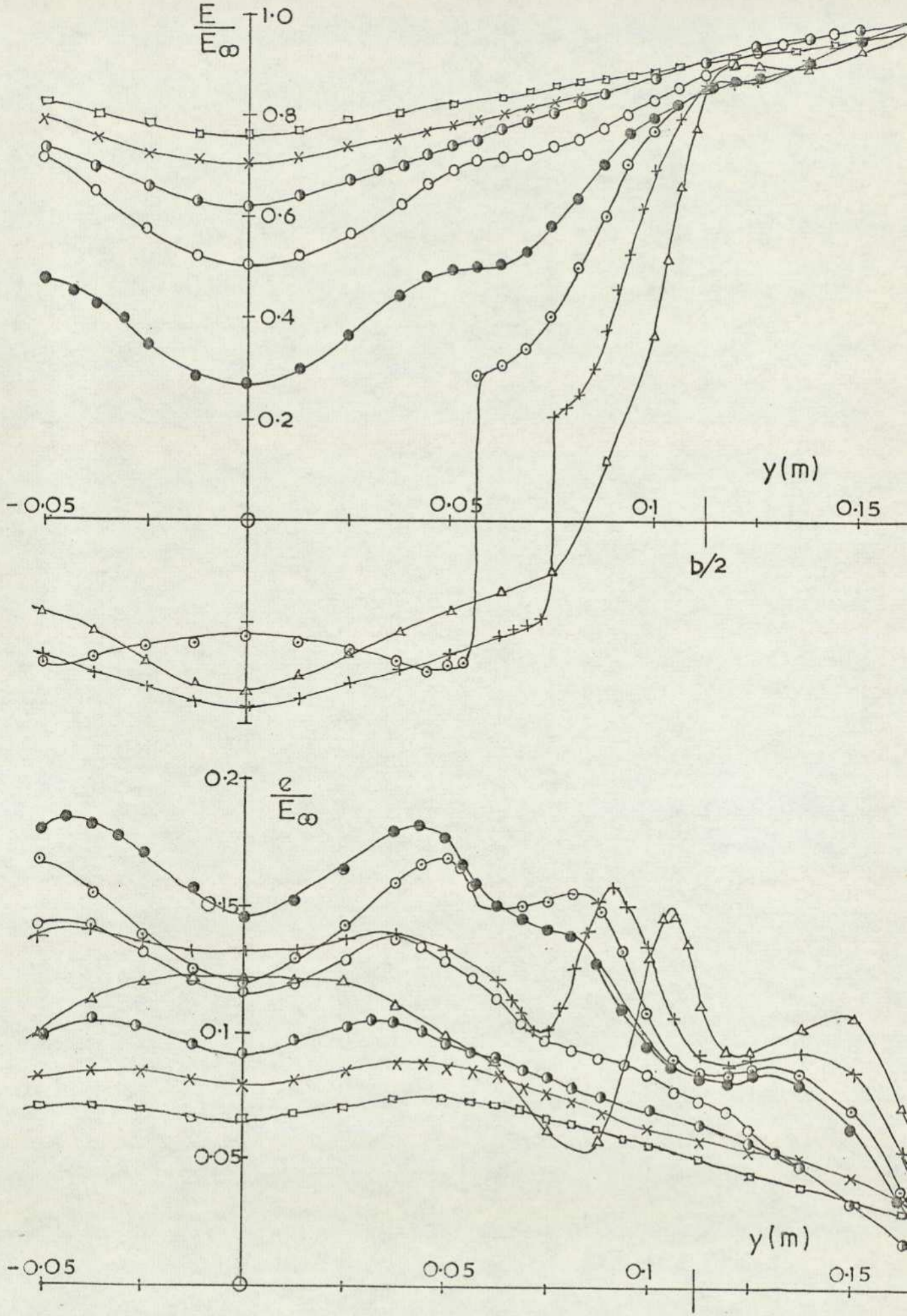

FIG. 73 (b) BLOCK 2NS, $Z_o/t = 0.25$, LATERAL TRAVERSE

turbulence intensity were plotted at two downstream stations; one immediately aft of the reverse flow region, at $x/t = 2.0$, and the other near the trailing edge of the ground board at $x/_t = 6.0$, see Figure 74. The contours of mean velocity at the upstream station show a distortion of the wake in the region of the body corners. A high degree of symmetry is again apparent. Contours of e/E_∞ at the same location show peaks at the centres of the horizontal shear layers, but these extend out a small way spanwise and then turn inwards slightly, to enclose an approximately square region. At the downstream station the outer velocity contours are approximately semi-elliptical with the minor axis aligned with the vertical axis through the body centre line and the major axis on the ground plane. The deformation noted upstream persists for the upper corners of the mean velocity contours, while only the upper turbulence intensity peak remains.

The total head pressure distribution gives a good approximation to the velocity for flows which have small transverse velocities and are not highly periodic. It is assumed that the static pressure measured outside the wake is equal to the static pressure within the wake. Using a pitot rake mounted at $x/t = 3.0$ the contours of velocity shown in Figure 75 were obtained for blocks 1N, 2N and 3N at $z_o/t = 0.25$. All show the retarding influence of the ground and the distortion around the corners of the body.

Base pressure measurements were obtained for block 2N at zero incidence while mounted at different ground clearances. These are shown in Figure 76. Except for the lowest clearance the distributions have similar forms. There is negligible variation in base pressure at a given spanwise position but the horizontal distribution shows a distinct off centre peak. The situation is reversed when the body is practically touching the ground.

Frequency spectra for blocks 2N, 2NS and 2 at $z_o/t = 0.25$ are shown in Figure 77. For block 2N the upper shear layer exhibits a slightly reduced predominant frequency from the free stream case, as does the side vortex sheet. A Reynolds number check on the frequency measured in the latter position showed that a 46% reduction in velocity reduced the shedding frequency by 49%. The lower shear layer gives rise to a 90 Hz shedding frequency however, which is confirmed by an 85 Hz measurement for the block 2NS in this position. The gap flow must

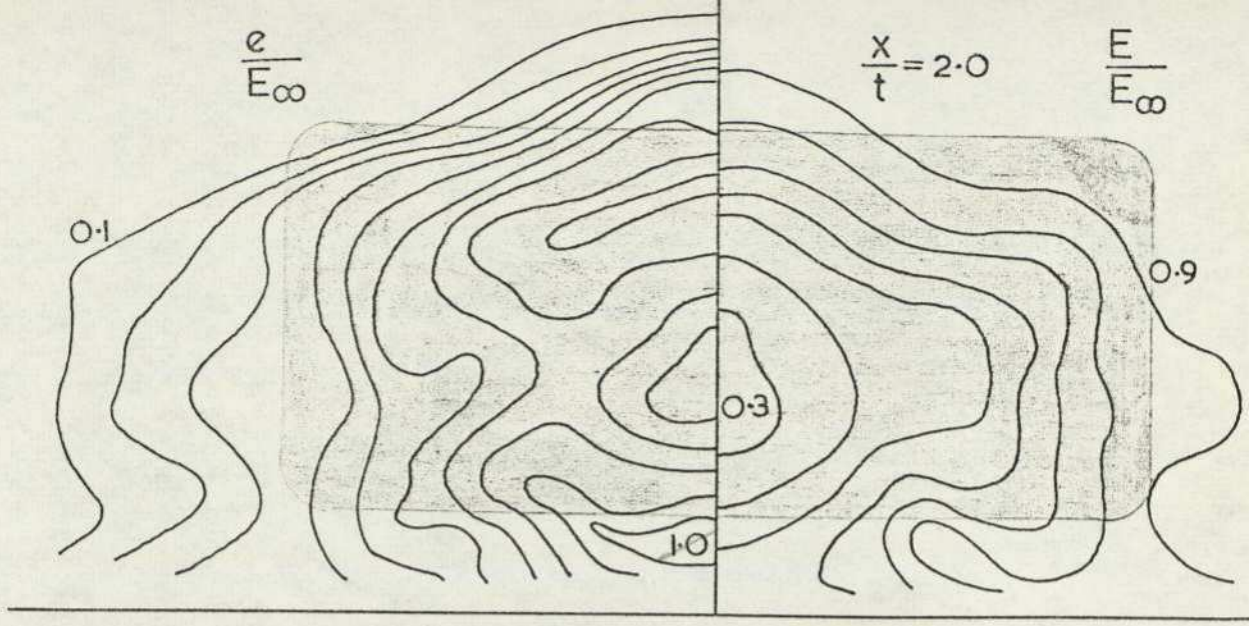

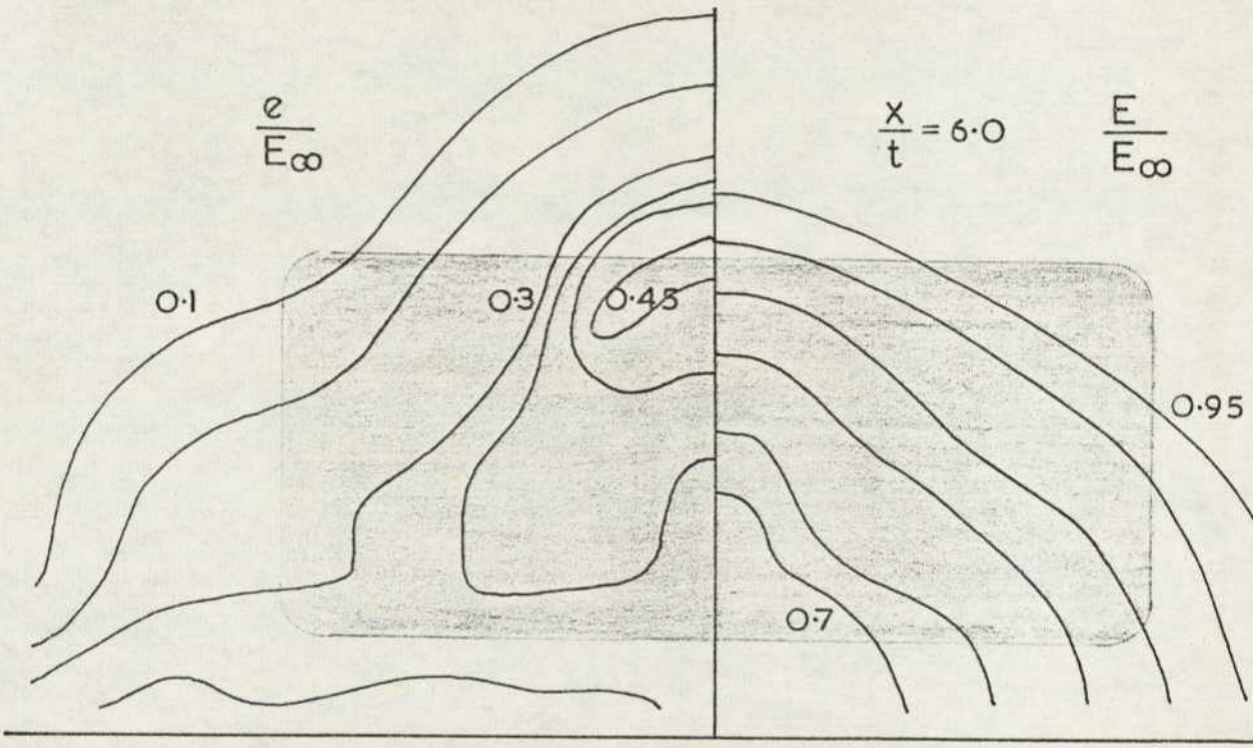

FIG. 74 BLOCK 2NS – CONTOURS e/E_∞, E/E_∞

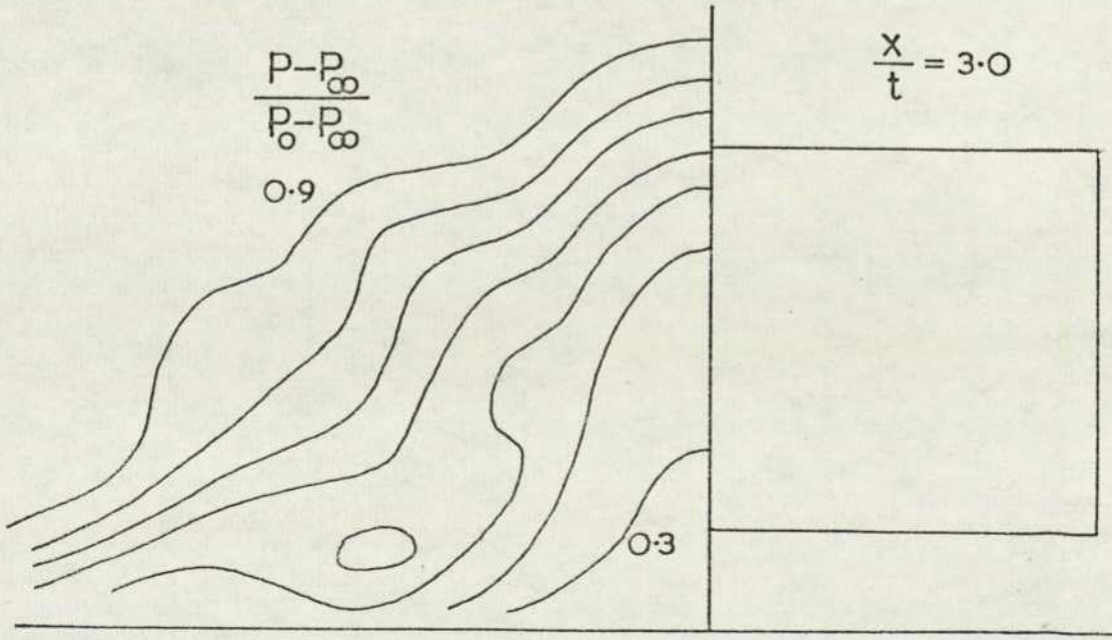

FIG. 75 BLOCK 2N – PITOT CONTOURS, $Z_0/t = 0.25$

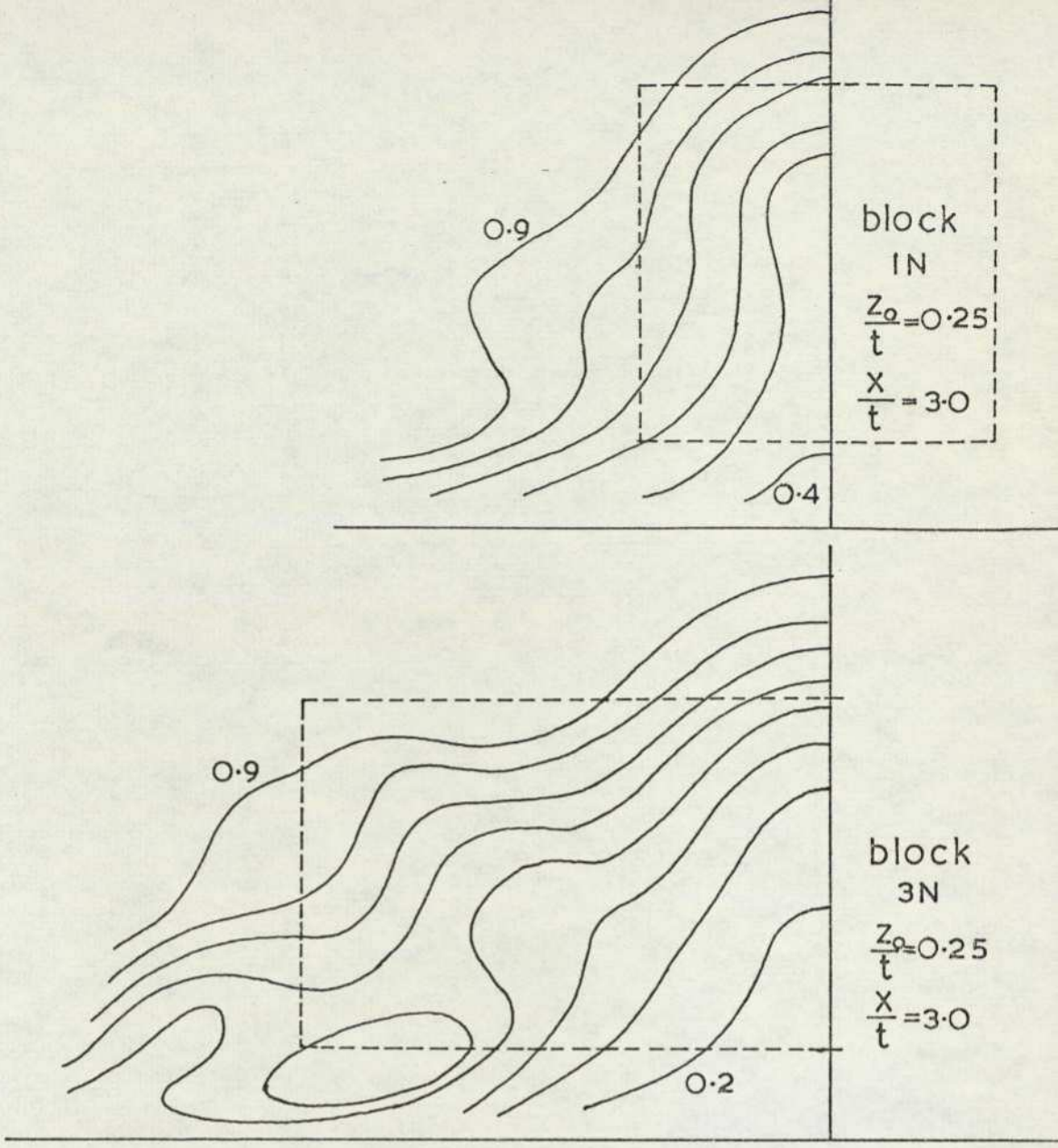

FIG. 75 PITOT CONTOURS – BLOCKS 1N, 3N

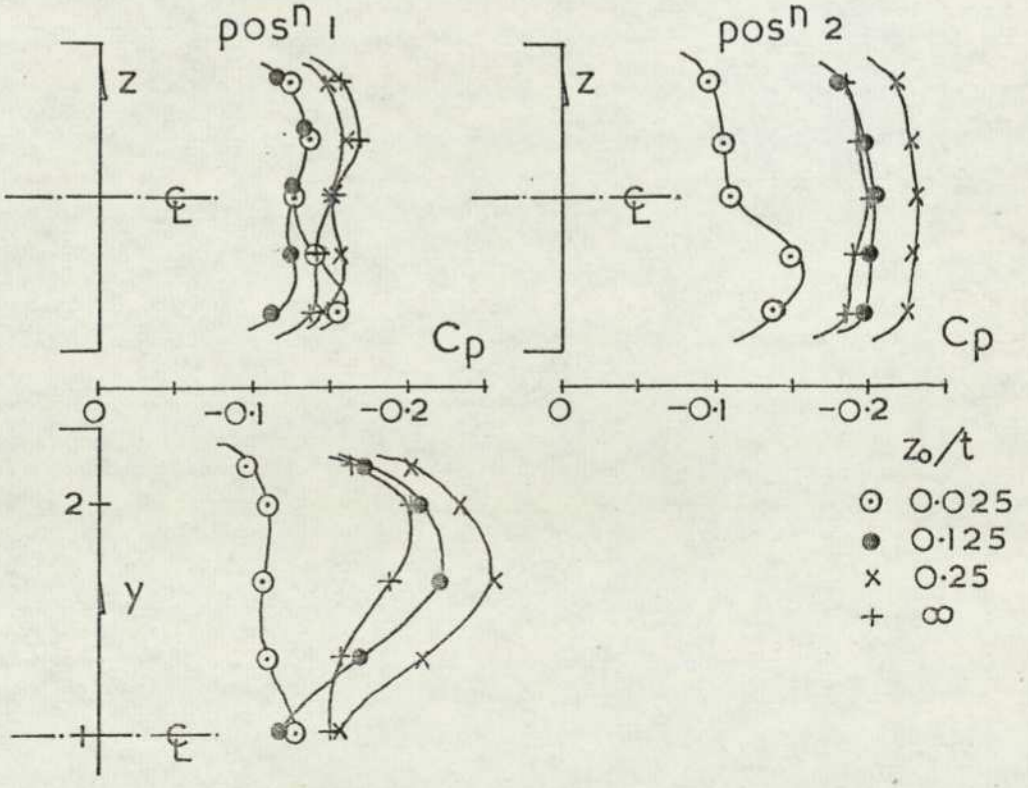

FIG. 76 BASE PRESSURES – BLOCK 2N, ZERO INCIDENCE

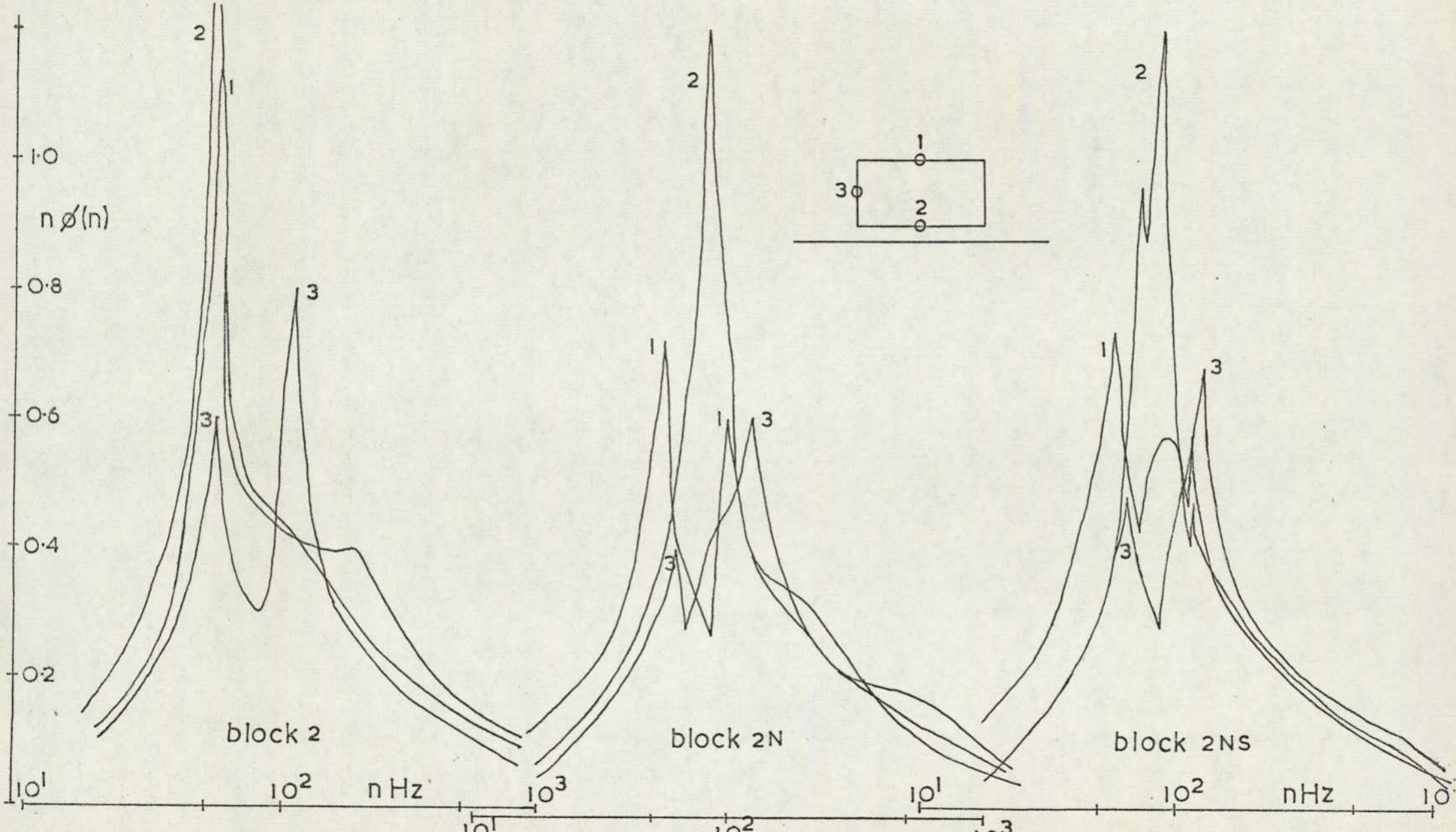

FIG.77 FREQUENCY SPECTRA (a) BLOCKS 2, 2N, 2NS, $z_o/t=0{\cdot}25$, $x/t=1{\cdot}5$

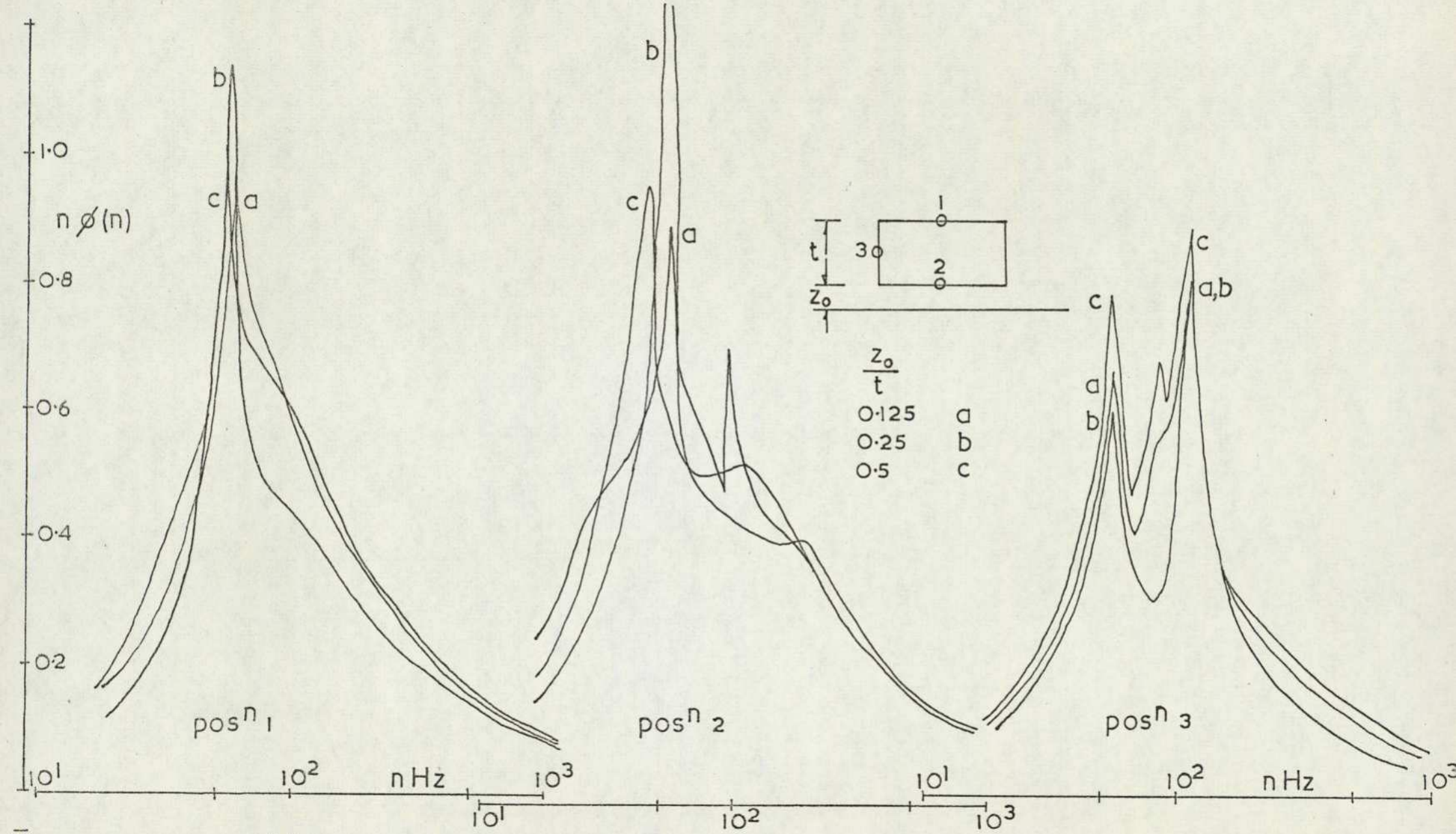

FIG.77 (b) EFFECT OF GROUND CLEARANCE ON BLOCK 2 SPECTRA; $X/t = 1{\cdot}5$

therefore influence the shedding frequency, although the local velocity is not significantly different to the free stream condition. All subsequent measurements of spectra were performed on the basic blocks. For block 2 the frequency spectra are compared, for a given probe position relative to the block as the ground clearance is reduced, in Figure 77. This shows a negligible difference due to the ground proximity, but the very bluff leading edges do not allow any inference to be drawn regarding the effect of ground on other blocks. Measurements were similarly performed on the other basic blocks in ground proximity but they are not reproduced here because they show no significant difference from the free stream case.

4.2.4 Discussion

The wake immediately downstream of the rectangular blocks at zero lift conditions is characterised by the distortion at the corners of the wake of the velocity contours. If the vortex sheet separating at the base is considered at its inception then a simple explanation is possible. To simplify matters, no boundary layer is allowed to develop on the body. The vorticity generated at separation is then simply $U^2/2$ per unit length. This sheet has the same cross section as the body, see Figure 78, and it moves downstream, initially, with velocity $U/2$. Allowing the vortex sheet to grow for a small distance it is obvious that being free it will become distorted by itself. In fact at the corners it cannot develop at all because if it were to do so an infinite upstream velocity would be implied on the adjacent vortex sheet. The initial wake must consist of four bounded vortex sheets with strong longitudinal (streamwise) components of vorticity near the corners. These will combine to give an inward flow at the corners, which would distort the wake in the manner found in the experiments. At the same time, for the rectangular bodies, the smaller vortex sheets arising from the side edges, will progress downstream at a lower rate than the wider horizontal sheets. This tends to reduce the longitudinal vorticity components in the side sheets so that the later distortion in the horizontal sheets could allow the wake to distort sufficient to show a switch of the major and minor axes.

It is interesting to note that, taking the formulation of Calvert (31) for the Strouhal number, S, given by

$$S = \frac{nd'}{U_m} \qquad (4.2)$$

where d' is the spacing between the shear layers, as given by the peaks in the turbulence intensity, n is the frequency, and U_m is the velocity just outside the wake and is given by

$$U_m = U_\infty(1 - C_{pb})^{\frac{1}{2}} \qquad (4.3)$$

where C_{pb} is the uncorrected base pressure coefficient and U_∞ is the free stream velocity, then the Strouhal number for blocks 2N and 3N with a shedding frequency of 65 Hz, taking the mean base pressure, is 0.20. Calvert found that a universal Strouhal number existed for axisymmetric bluff bodies which was approximately 0.19.

When the ground is approached the wake takes on a noticeably different velocity profile, changing from a typical Gaussian shape to one which is almost a boundary layer type profile. To a certain extend this is illusory. Consider a two dimensional wake flow near to ground, subject to the usual wake flow simplifications, namely; all velocity components differ only slightly from free stream values, and are in the free stream direction only. It is then permissible to remove the ground and replace it by an image wake. Taking the shape of each wake velocity profile, as given by the measured similarity profile for the free stream case, the resulting velocity component is simply the sum of the velocity components due to the model and its image. The profiles are shown in Figure 79 for various ratios of wake half width, as measured in the free stream, to the distance of the body centre line above the ground. As this ratio increases, implying a growing wake, the transformation in the velocity profile is clearly seen. Restriction to two dimensional wakes is not necessary as the simplifications are equally applicable to three dimensional non-lifting wakes.

On the road these wake profiles would be modified according to the scheme set out in Chapter 3. The resulting far wake profiles then become reminiscent of wall jet flow, Glauert (50), as also shown in Figure 79, except that there is a momentum loss rather than a gain.

No evidence was found throughout these measurements of any flow separation at the ground apart from the lowest ground clearance

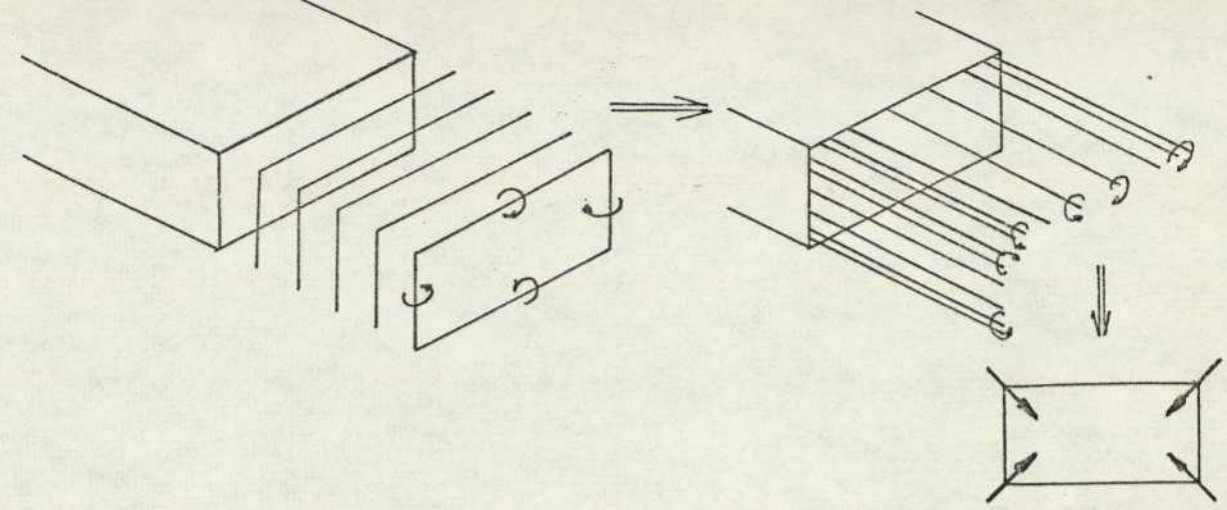

FIG. 78 DEVELOPMENT OF TRAILING VORTEX SHEET

two bodies moving in space

one body moving close to fixed ground

$t+2z_o$

$z_{1/2}$

free stream similarity profile

0·5

0·7

0·9

1·0

1·1

1·2

mirror wake

$\frac{t+2z_o}{2z_{1/2}}$

FIG. 79 MODIFICATIONS TO PROFILE AND VELOCITY DEFICIT

tested, $z_o/t = 0.03$. This confirms the ground board pressure distribution data of Chapter 3, Figure 43. This setting is the only one for which the total boundary layer displacement thickness of body and bare ground exceeds the ground clearance, which could represent a crude limiting condition.

4.3 Wake flow measurements

Lifting bodies

4.3.1 Introduction

The highly three dimensional nature of a lifting body wake requires a different measuring technique to that employed for non lifting body wakes. This arises because of the directional sensitivity of the hot wire anemometer, as discussed in 4.2.1. This property of the probe may be used to advantage, in measuring all flow velocity and turbulence components, by rotating the probe through a number of positions. At least six positions are required in the method due to Davies (51). The technique is very time consuming and is only applicable in situations where the flow is not time dependent. The author built such a probe system with the anemometer mounted beneath a twelve position stepping switch. The set up was rather bulky and the mechanical development alone took considerably longer than planned so no reliable measurements were taken. As the interest of this research was more general, with a number of body configurations being investigated over a range of incidence and ground clearance, the initial requirement was for a simple but effective way of determining the overall nature of the flow. This calls for a less sophisticated device than that described, in both instrumentation and operation, and was eventually done by measuring the total head distribution through the wake. A loss of total head occurs in regions of vorticity whether it is a non lifting wake or a vortex flow. For the first few measurements a Kiel probe, as described by Kiel (52), was used. This was made by the author and had an outer diameter of 2.5 mm. It was found to be insensitive to yaw beyond forty degrees. It was realised, however, that as most of the flows being investigated did not include very high transverse velocities and in general the flow angle is less than twenty degrees a plain square ended pitot tube should have been adequate. According to a study reported in Bryer and Pankhurst (53) a tube with an inner to outer diameter ratio of 0.663 will show a reduction from the true total head of approximately three per cent of the dynamic head at twenty degrees of yaw. This improves as the wall thickness is reduced. A pitot rake was therefore constructed with square ended large bore tubes and in a comparison with the total head contours derived from measurements using the Keil probe in the wake of Block 2N at 6^{o}

incidence and at a mean ground clearance of 25mm gave essentially identical results. All subsequent pressure measurements were therefore obtained using the rake. The pressure rake consisted of twenty eight pitot tubes spanning spanning 0.21 m with half the tubes spaced at 5mm. In the middle of the rake pitot tubes were placed 5mm above and below the central tube. Static pressure probes were mounted at the extremities of the rake. The pressure data is presented as contours of total head pressure coefficient given by $P-P_\infty/Po-P_\infty$ where Po, P_∞ are the local total head and static pressure recorded at the same downstream location but outside the wake, and P is the measured total head in the wake. In a turbulent flow the pitot reading, P is given by

$$P = P_\infty + \tfrac{1}{2}\rho\,(U^2+V^2+W^2+u^2+v^2+w^2)$$

where P_∞ is the local static. Assuming there is small static pressure variation across the wake the contours give a reasonable value for $(U/U_\infty)^2$. They do provide a quick and effective overall picture of the flow and thus define regions requiring further measurements. The hot wire anemometer was used in this way to provide information on turbulence intensities and periodic effects.

To generate the wakes two types of lifting configuration were investigated. Firstly the rectangular blocks were set at incidence while later a cambered model was used.

4.3.2 Rectangular blocks at incidence.

Contours of total head, for all blocks, were obtained at three downstream stations, x/t = 3.0, 4.5, 6.0. The rake was always aligned parallel to the ground and with the pitot tubes in the free stream direction. The rake was traversed across the wake to find the position of maximum total head deficit, which was aligned approximately with the central tube of the rake using manometer readings from the main rake to give horizontal location and the three tubes on the rake centre line to give vertical position. A complete vertical traverse was made across the wake at this lateral position with measurements being taken at intervals of 12.5mm. Any single contour plot is then made up of at least 400 pressure points. If the rake did not

extend to the wake centre line then a further vertical traverse was made along this axis. To ensure symmetry a single horizontal traverse was always made, at the same height as the total head minimum, completely across the wake.

The contours, for blocks IN, 2N, and 3N mounted in free stream at six degrees incidence, are shown in Figure 80. From earlier force measurements it is obvious that little lift is being generated and this is apparent from the little distortion in the contours. The centre of the wake is displaced noticeably downwards by a similar amount for all blocks. Throughout the following diagrams only the maximum and minimum contour values will be given unless a step change is introduced.

Total head contours are similarly plotted in Figure 81, showing the effect of the approaching ground on Block 2N at incidence angles of four, six and eight degrees. In each case the ground clearance quoted is that measured at mid-length. Even for the lowest lift case, a distinct off-centre maximum in the total head deficit is shown. This can be compared with Figure 75 which represents the zero lift case. It can be assumed, then, that the flow modifications are related to the generation of lift and so the deficit in total head can reasonably be expected to represent a developing vortex. For a given incidence and ground clearance the trailing vortex moves outwards noticeably as it moves downstream but there appears to be negligible vertical motion. As the ground clearance is reduced the spacing between the vortices increases and a similar effect occurs on increasing incidence. At the largest lift conditions the vortex becomes isolated from the main part of the wake. The upper central part of the wake does not significantly differ over a wide range of conditions which suggests that the vortex is springing from the lower surface of the body. Also shown in Figure 82 are the contours for blocks IN and 3N respectively, mounted at six degrees incidence and at two intermediate ground clearances. In the case of block IN a high degree of symmetry is achieved while with the higher span model an inner less pronounced total head minimum is apparent. The latter was visible in the wakes of certain block 2N configurations but it cannot be readily explained.

The path of the vortex can be plotted as it moves downstream and Figure 83 shows plan and rear views for all the blocks.

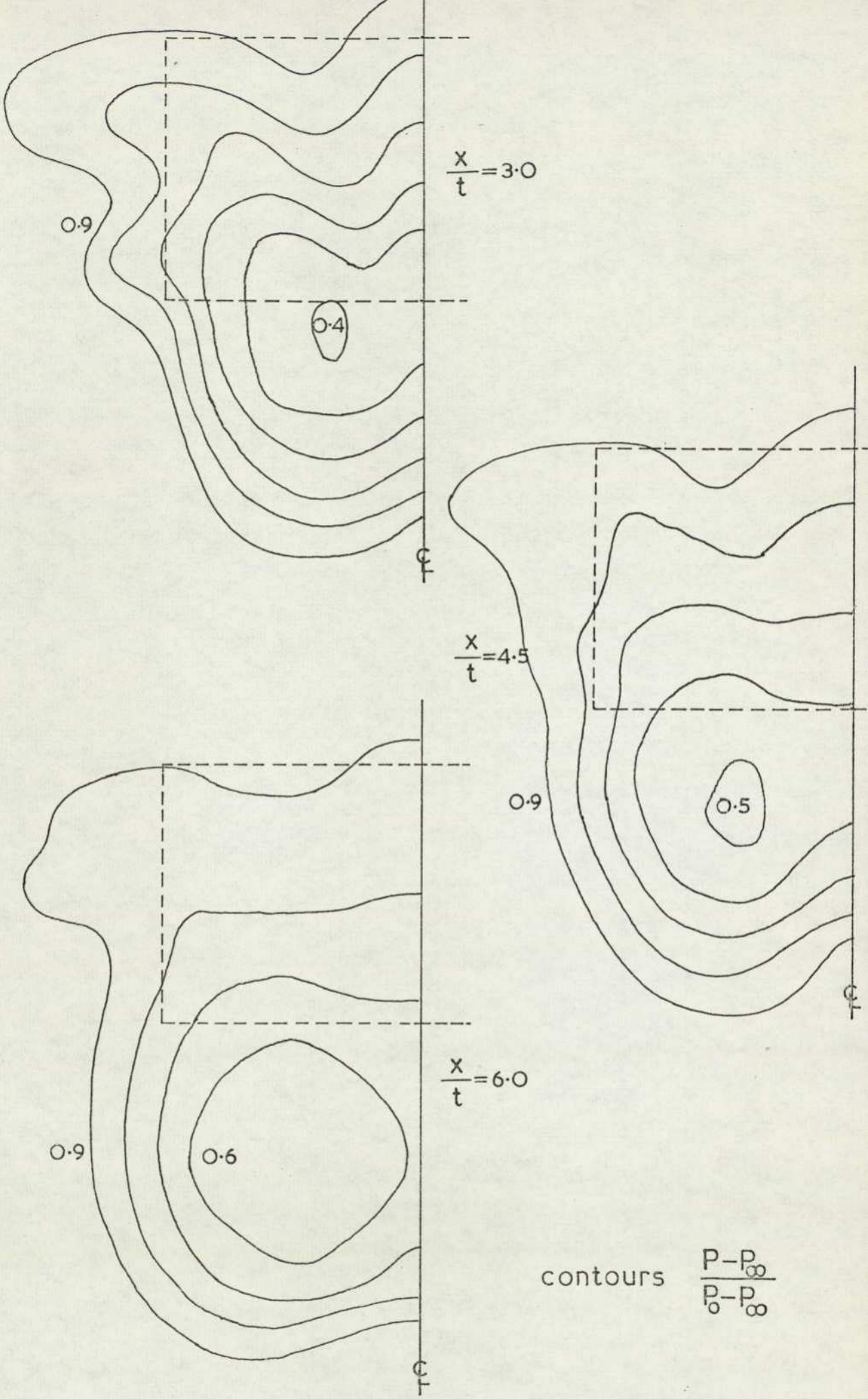

FIG. 80 PITOT CONTOURS — FREE STREAM (a) BLOCK 2

$\alpha = 6°$

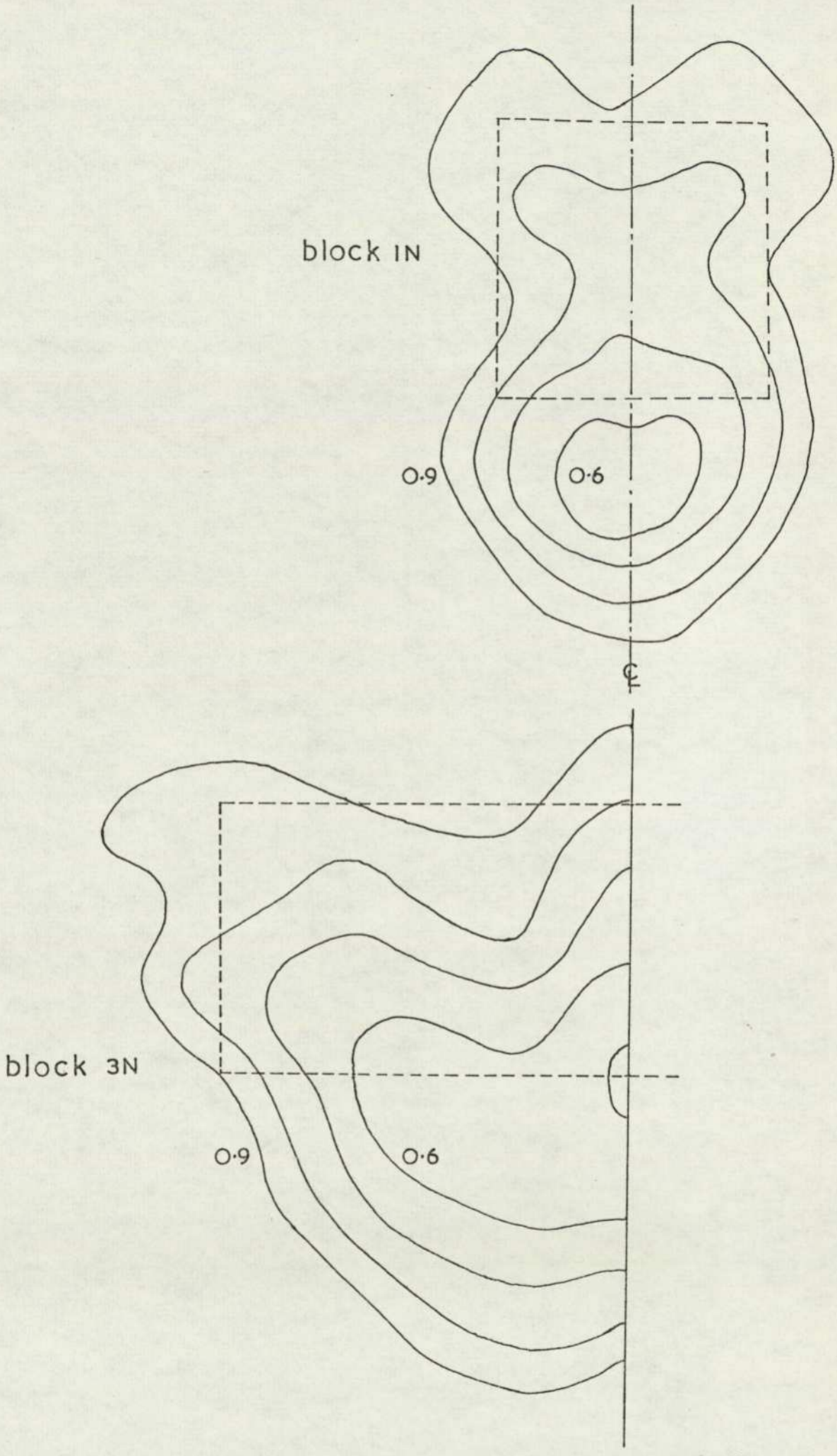

FIG. 80(b) BLOCKS IN, 3N – FREE STREAM, $\alpha = 6^\circ$, $x/t = 4{\cdot}5$

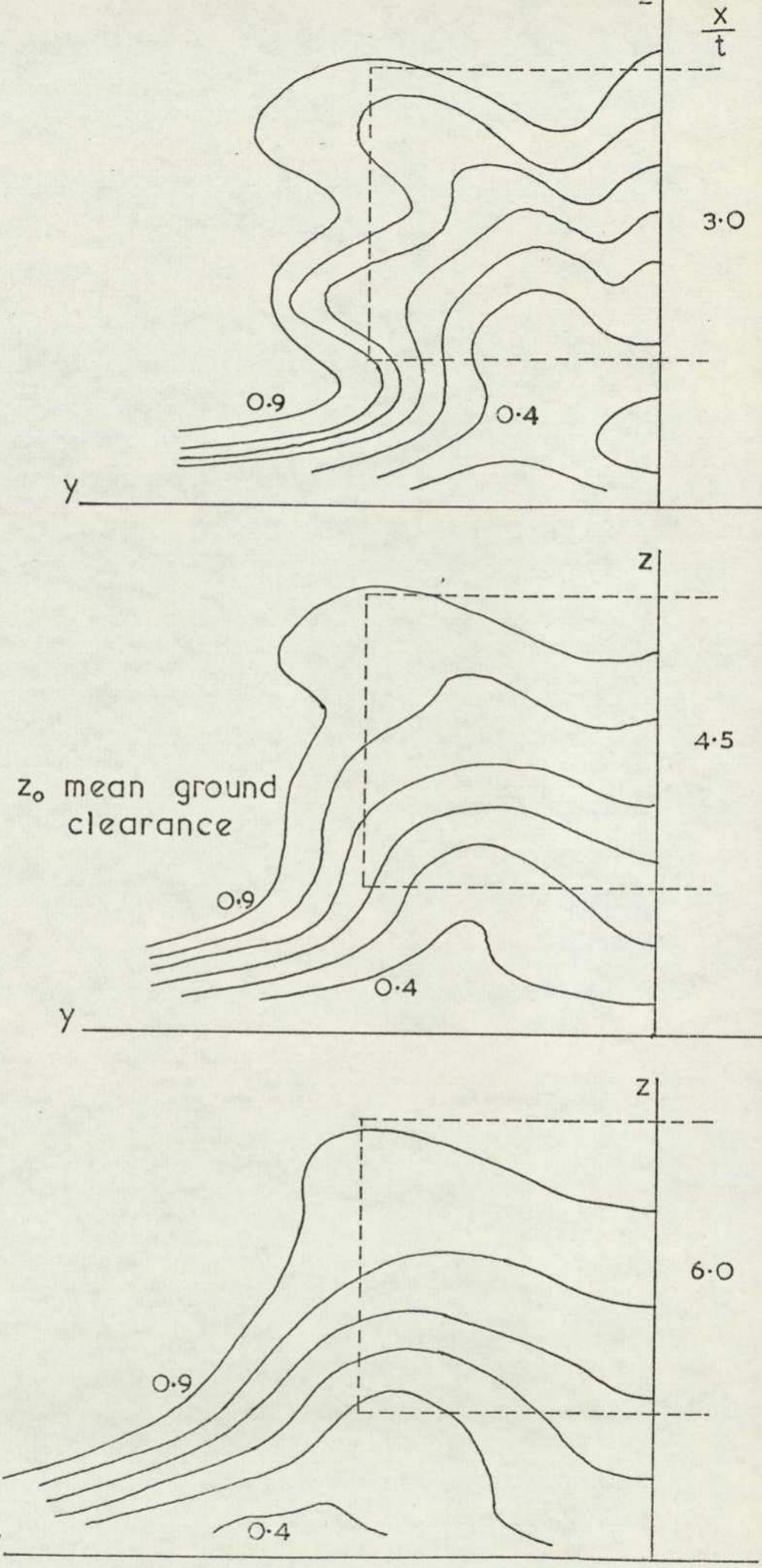

FIG. 81 PITOT CONTOURS—BLOCK 2N IN GROUND PROXIMITY

(a) $\alpha = 4°$, $z_o/t = 0.5$

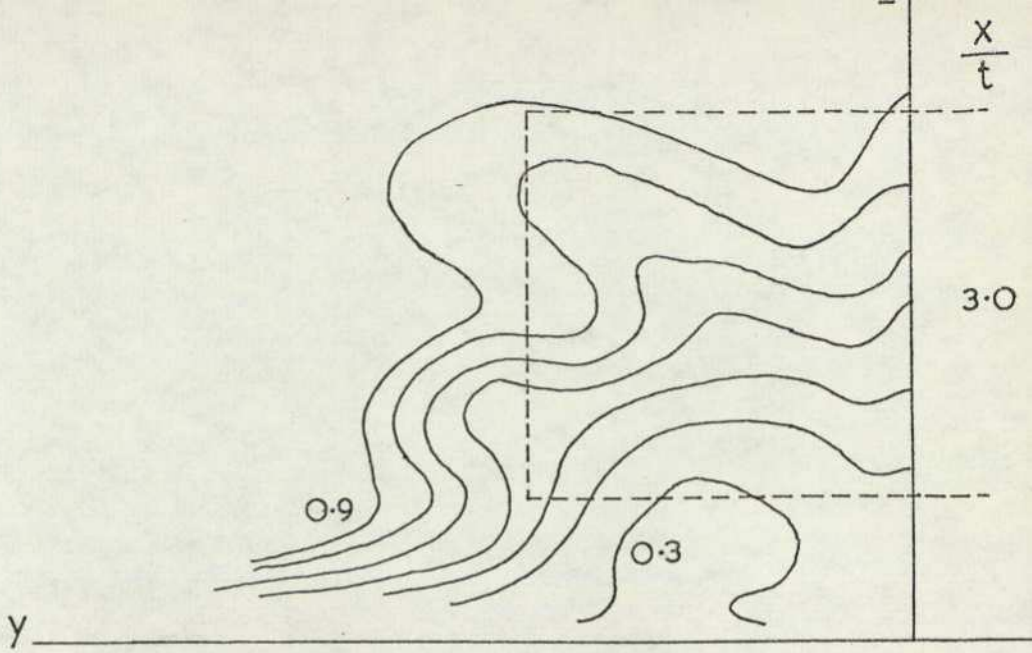

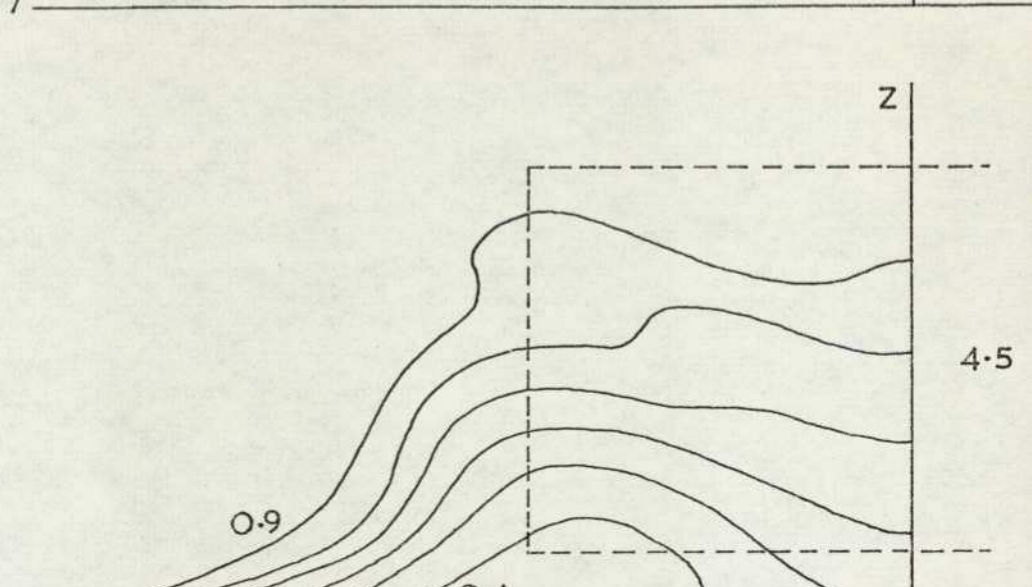

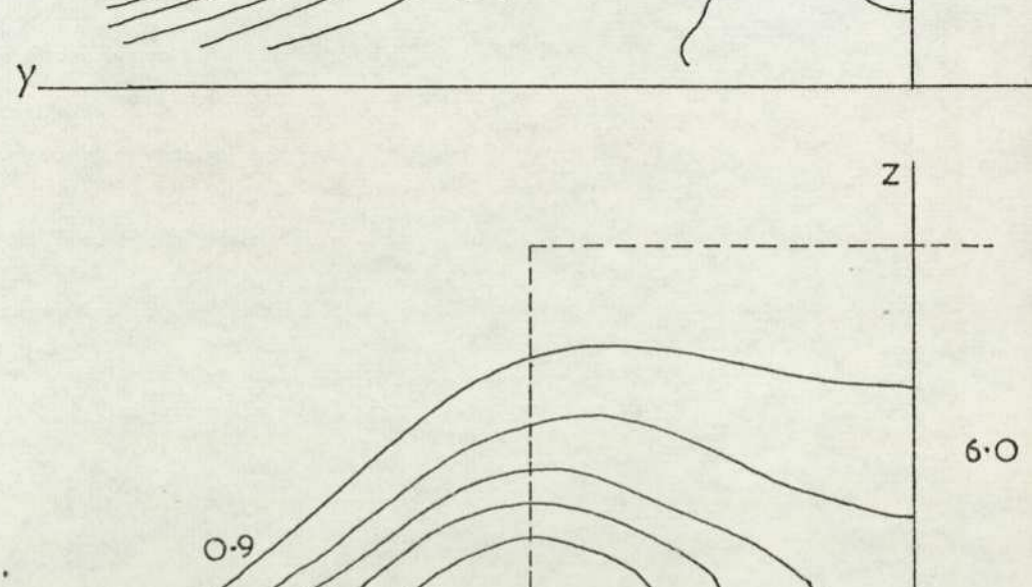

FIG. 81 (b) BLOCK 2N $\alpha=4^{\circ}$, $Z_0/t=0.375$

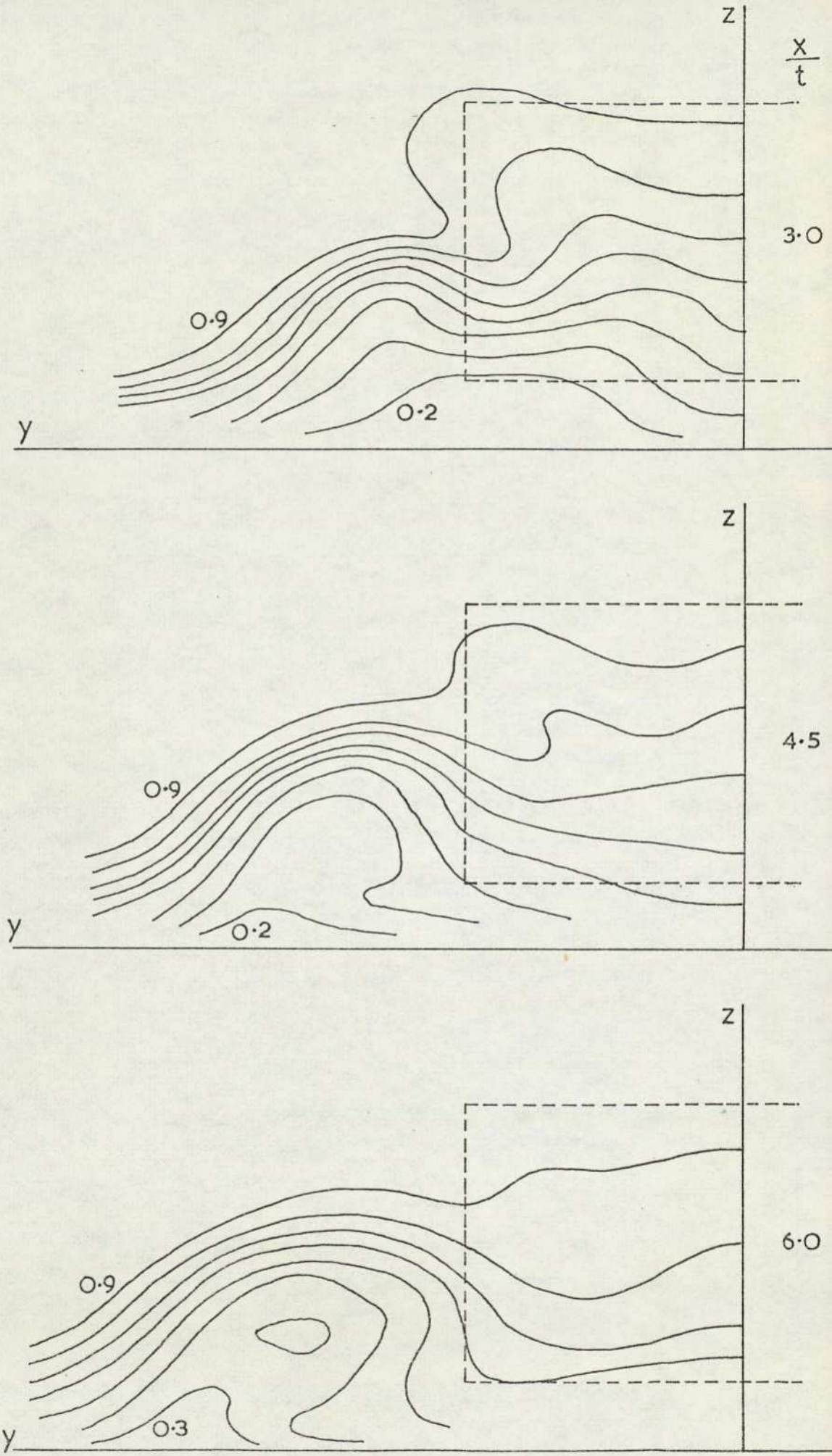

FIG. 81 (c) BLOCK 2N $\alpha = 4°$, $z_o/t = 0.25$

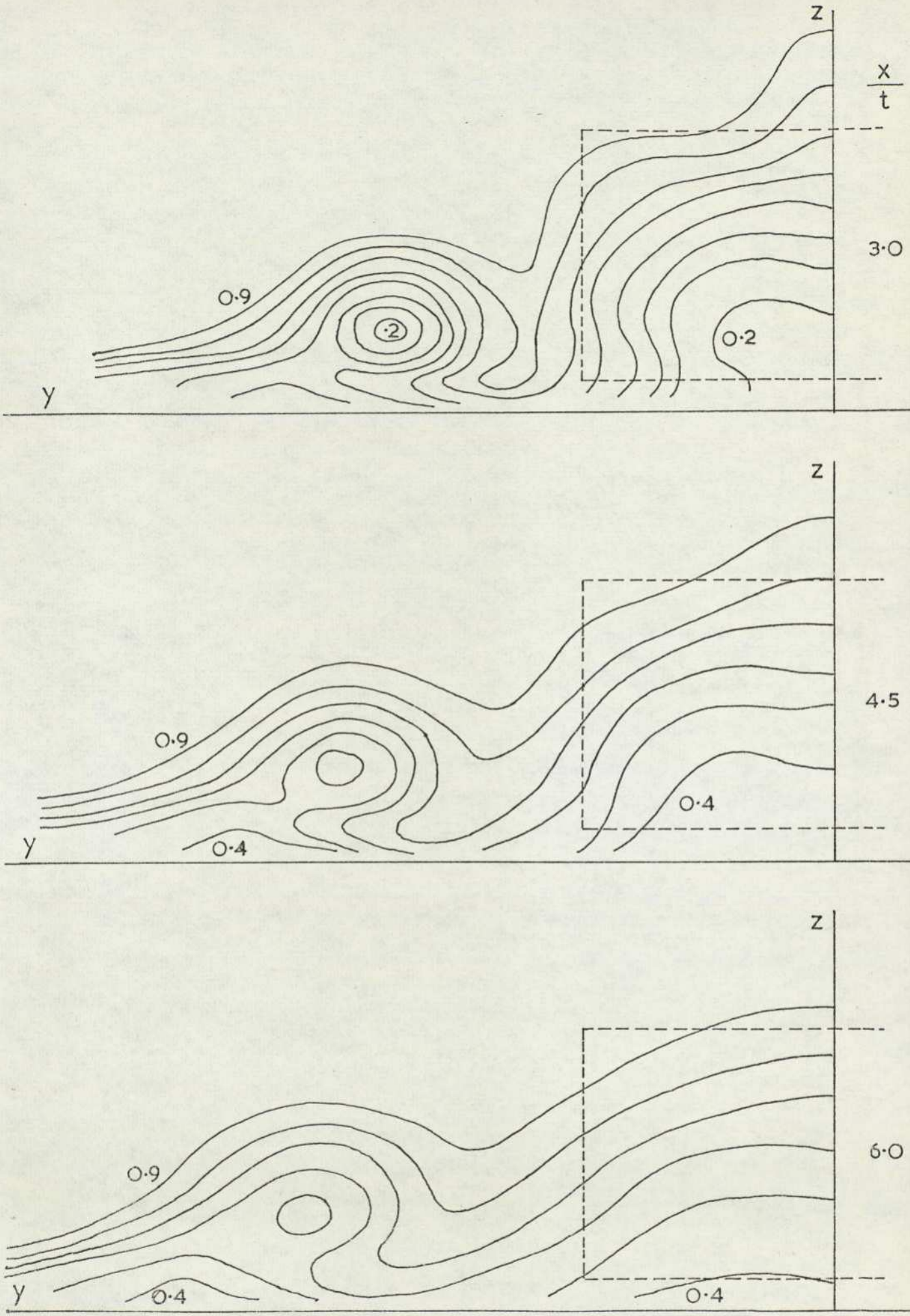

FIG. 81(d) BLOCK 2N $\alpha = 4^\circ$, $Z_0/t = 0.125$

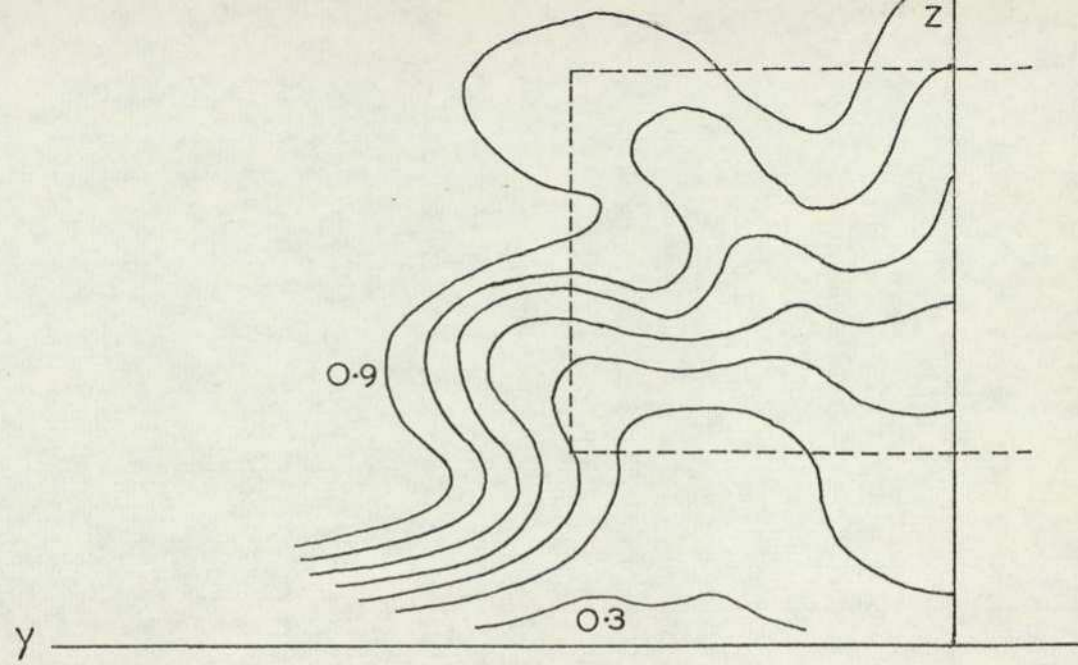

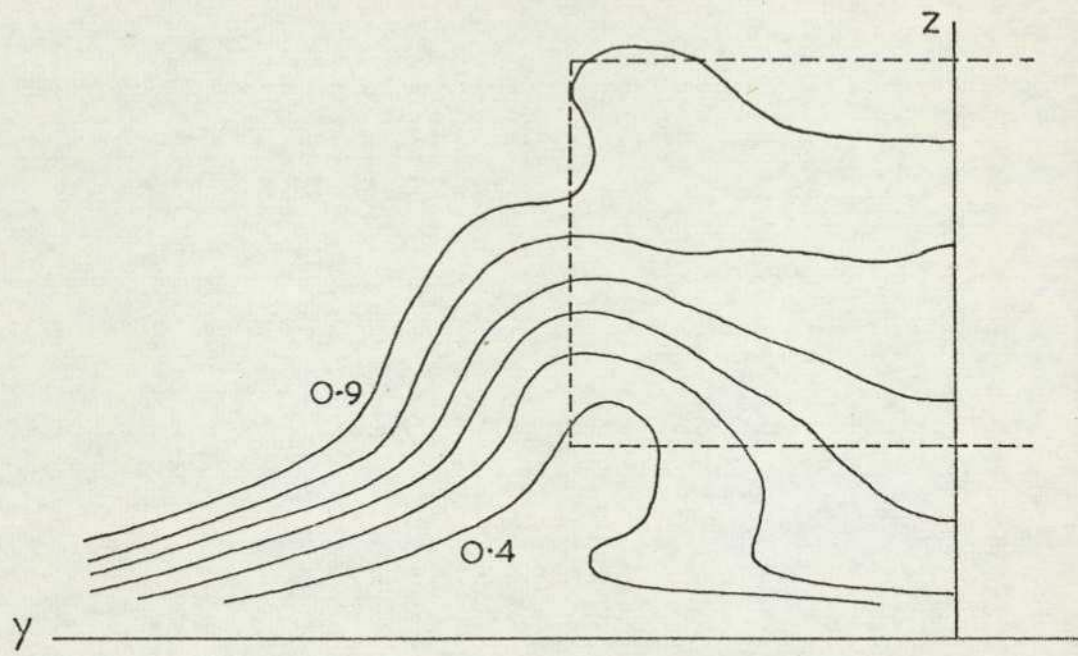

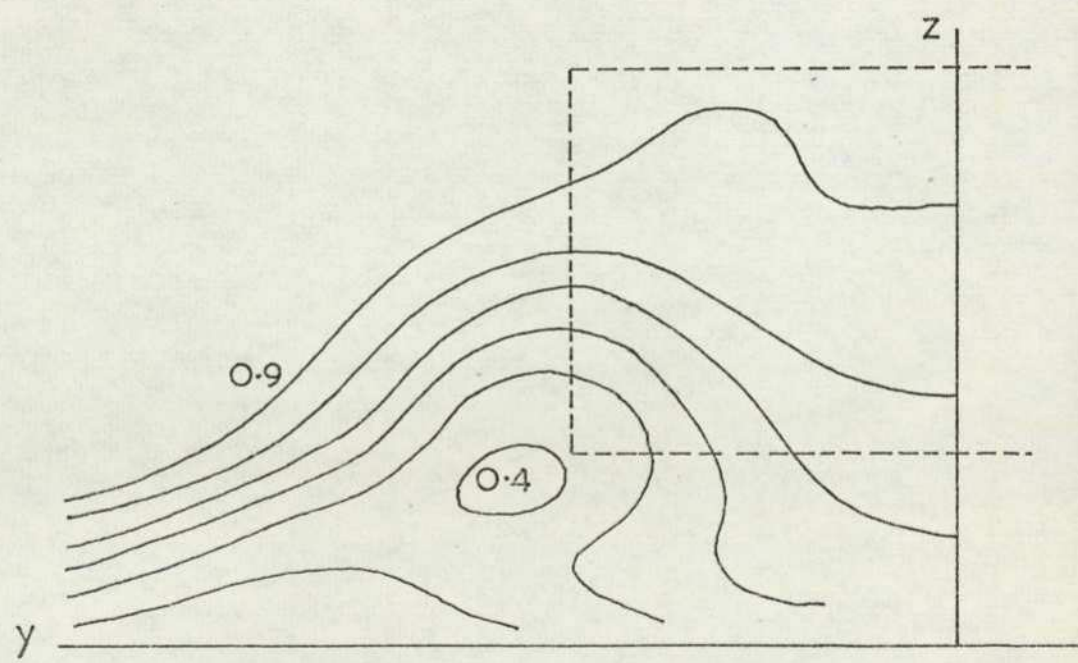

FIG. 81 (e) BLOCK 2N $\alpha=6^{\circ}$, $Z_0/t=0.5$

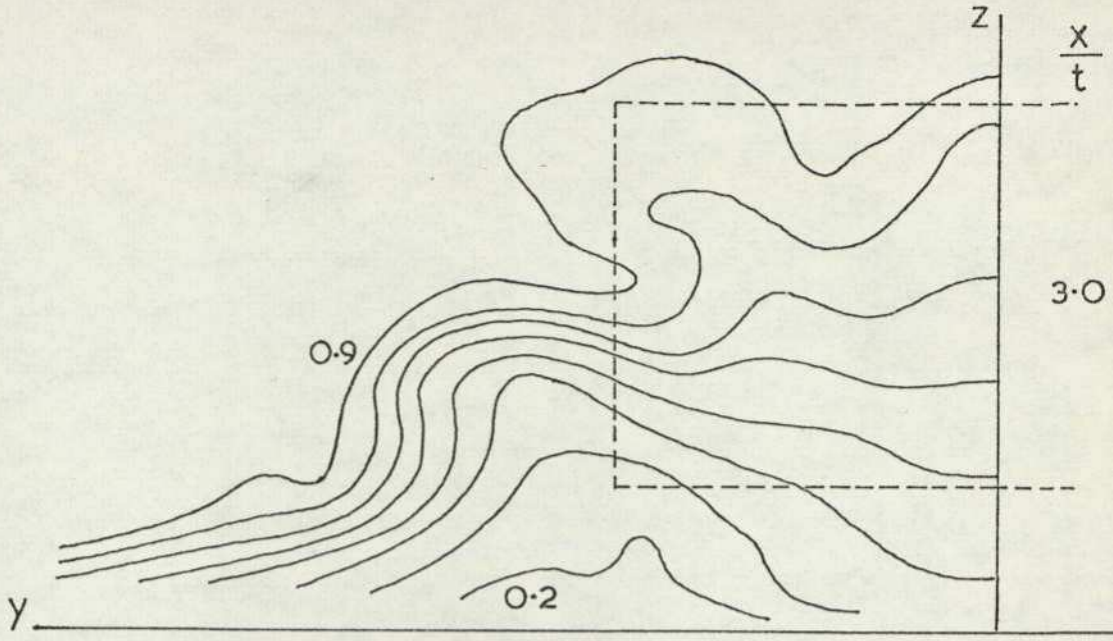

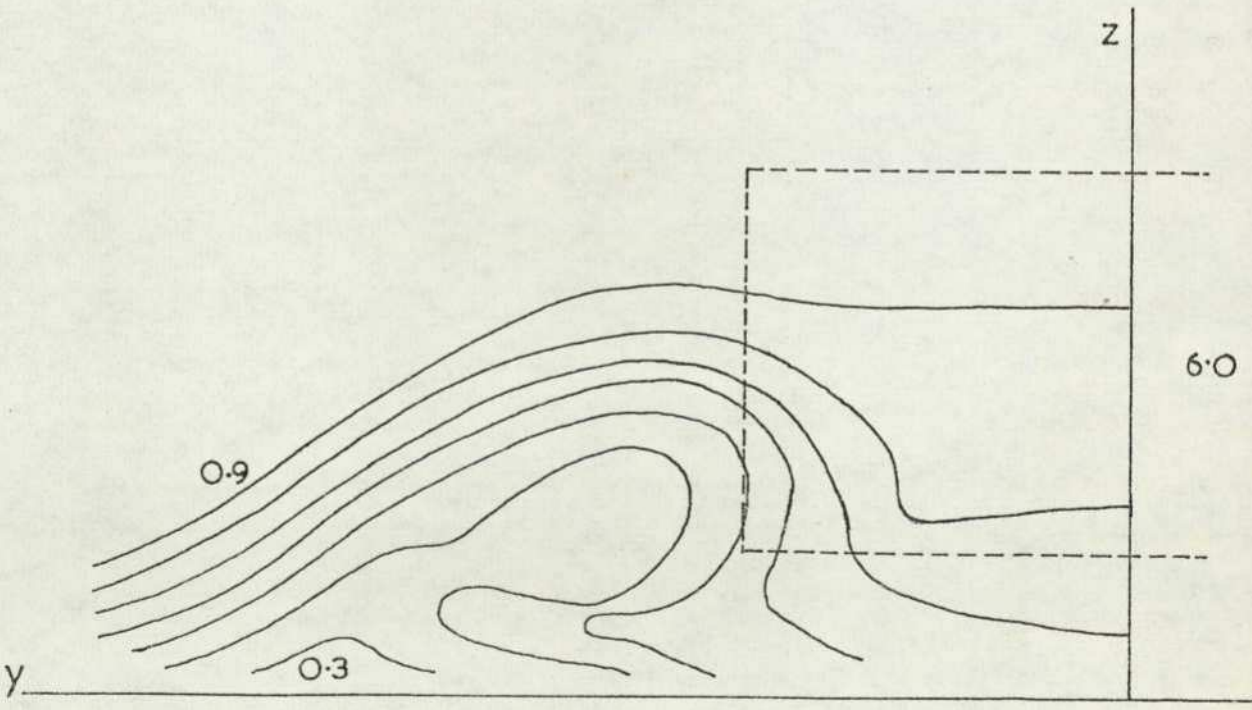

FIG. 81 (f) BLOCK 2N $\alpha = 6^{\circ}$, $Z_o/t = 0.375$

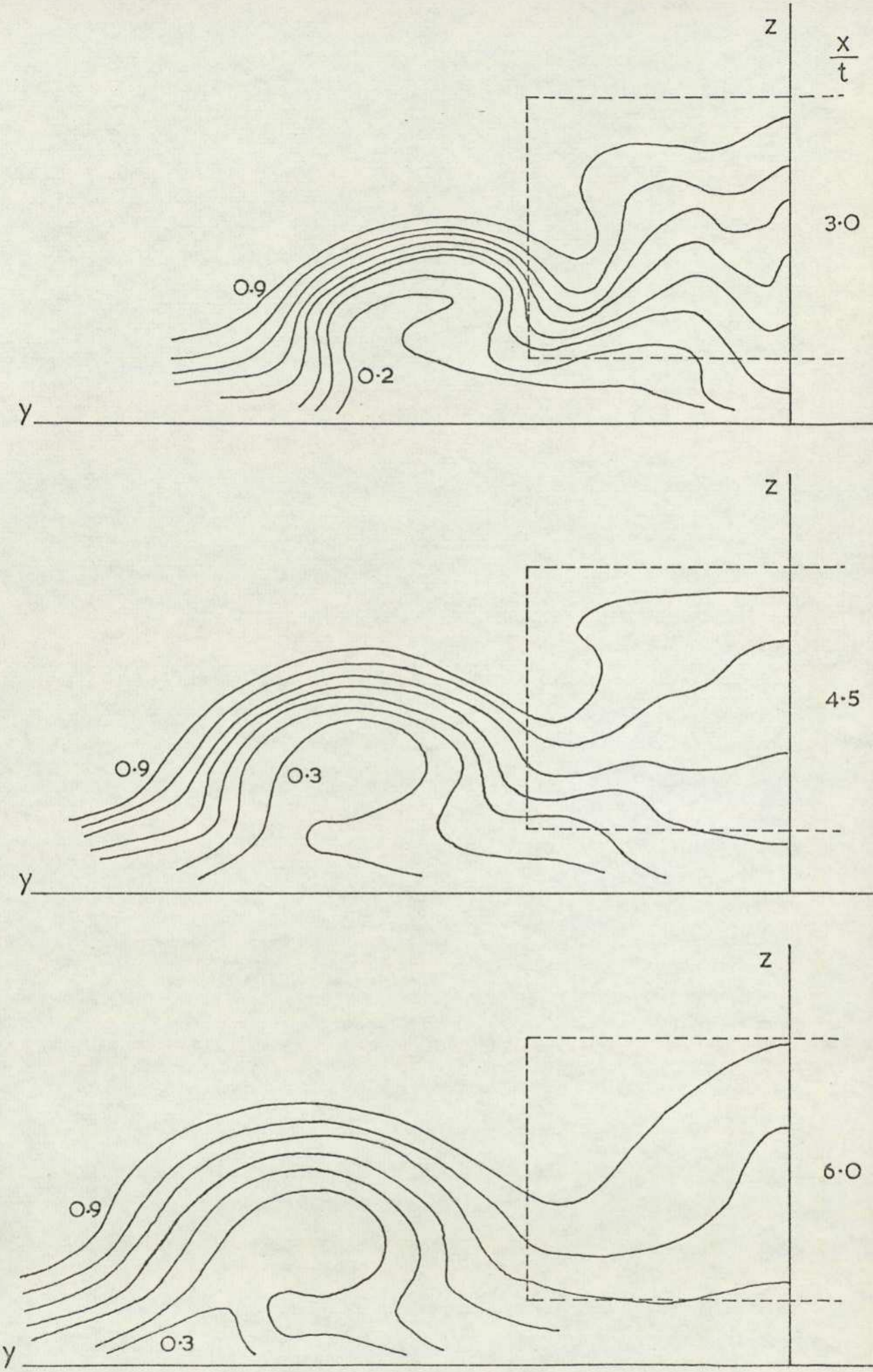

FIG. 81 (g) BLOCK 2N $\alpha=6^{\circ}$, $z_o/t=0{\cdot}25$

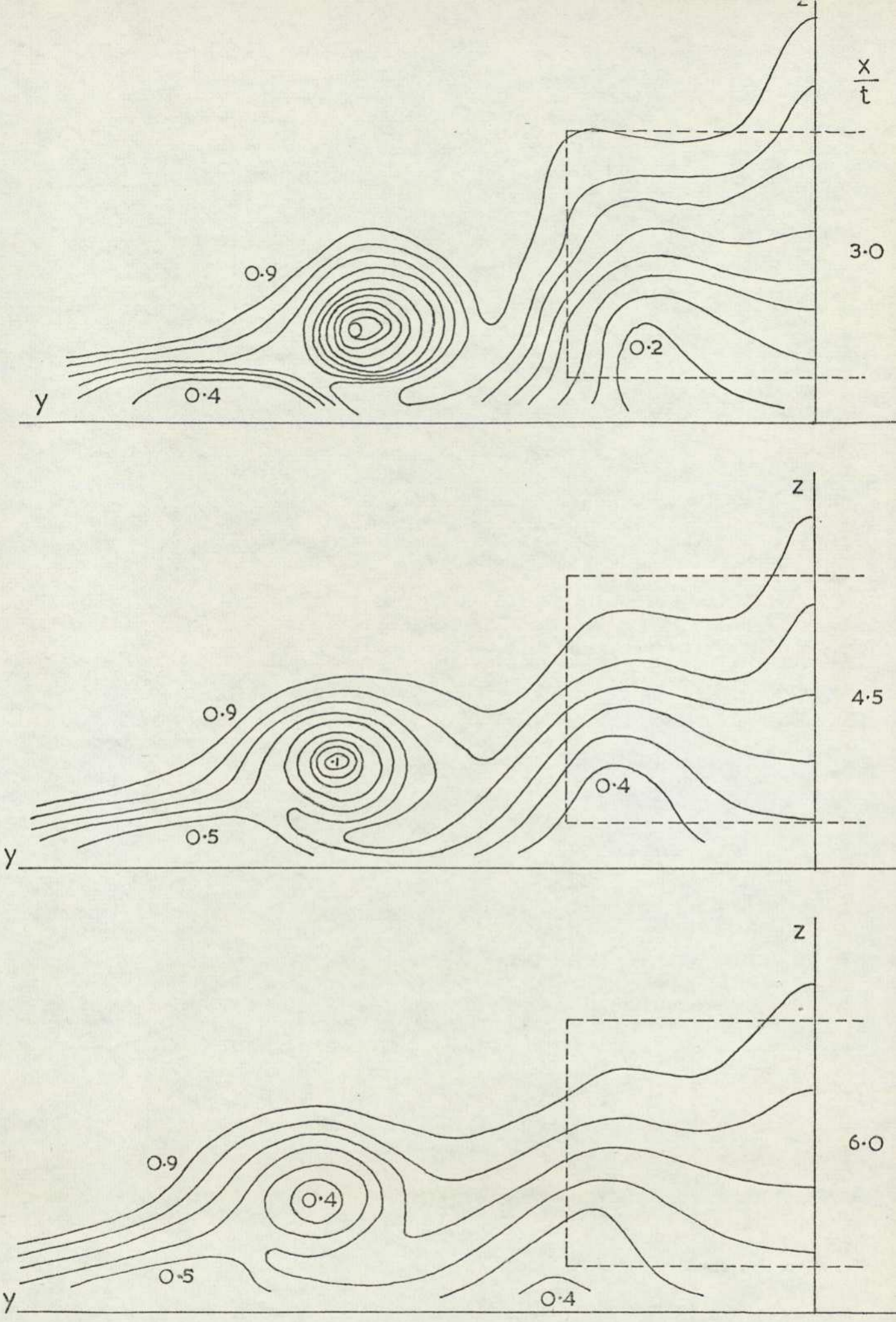

FIG. 81 (h) BLOCK 2N $\alpha = 6^\circ$, $Z_0/t = 0{\cdot}2$

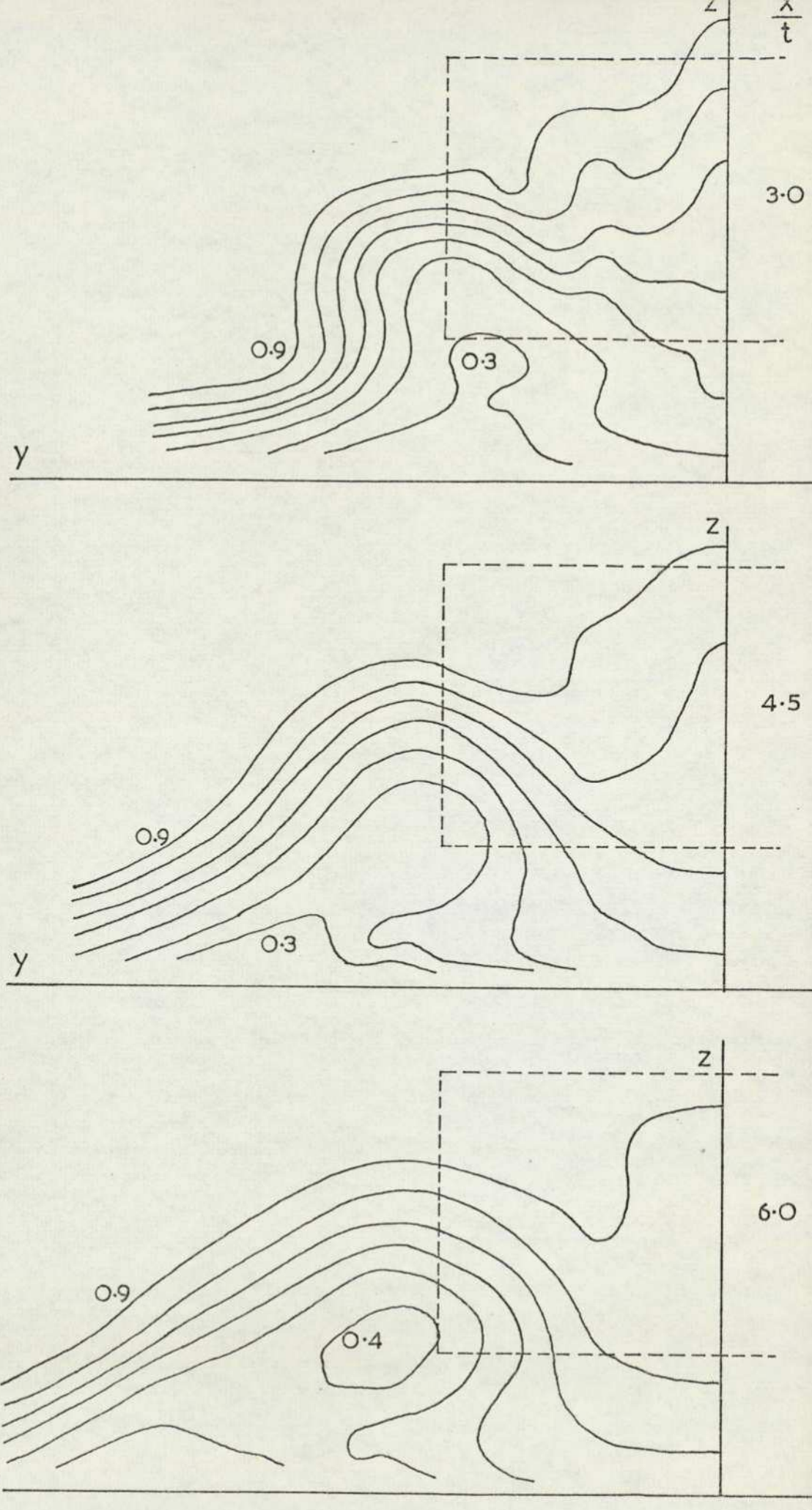

FIG.81 (i) BLOCK 2N $\alpha=8^{\circ}$, $z_o/t=0.5$

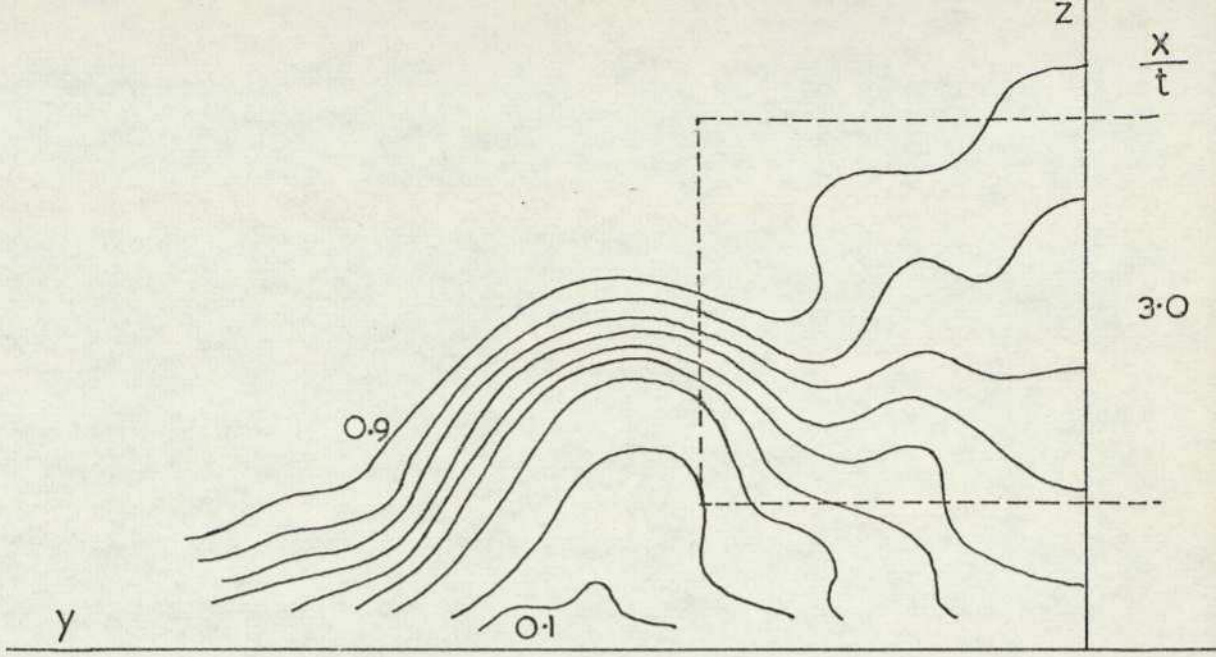

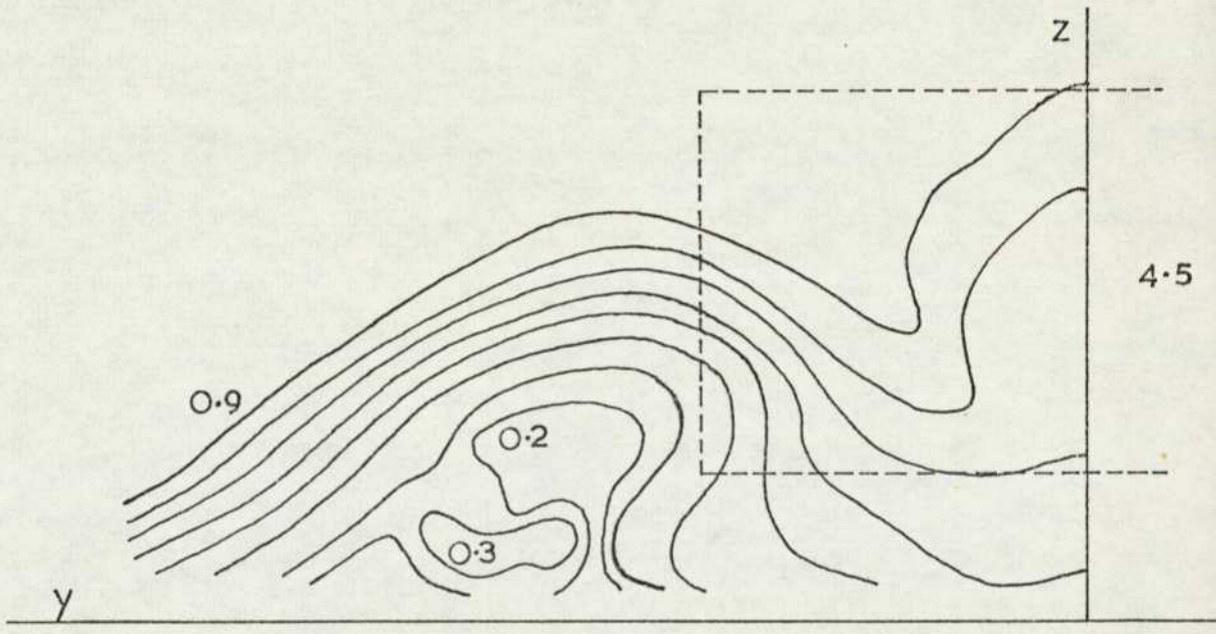

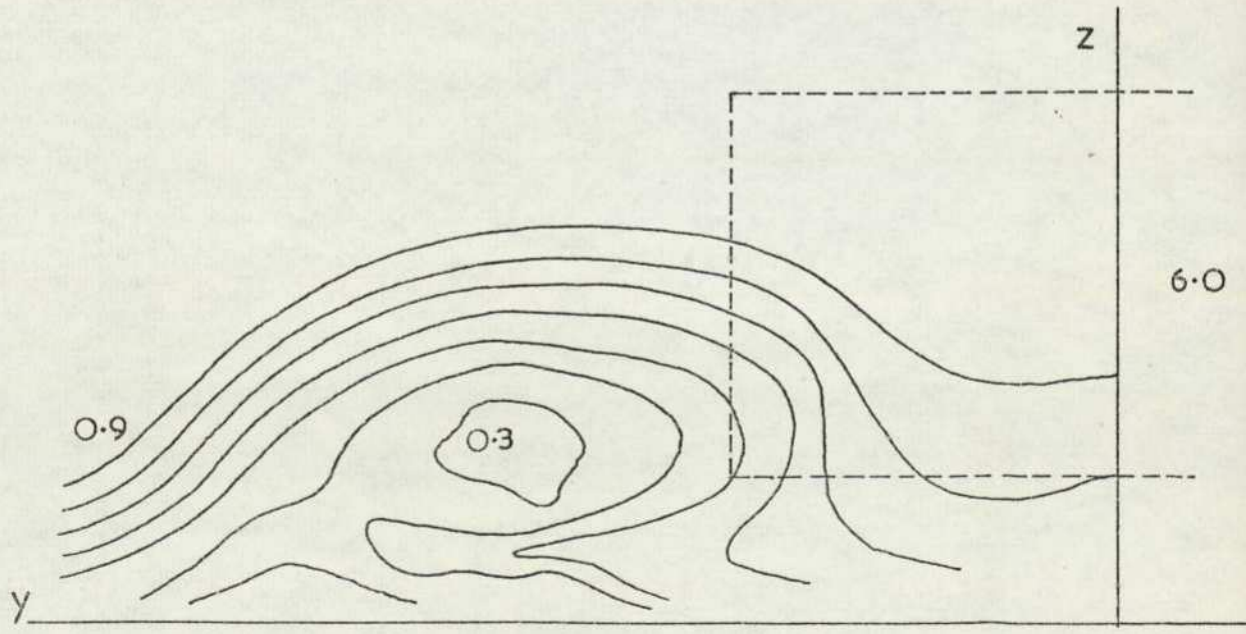

FIG. 81 (j) BLOCK 2N $\alpha=8^{\circ}$, $Z_o/t=0.375$

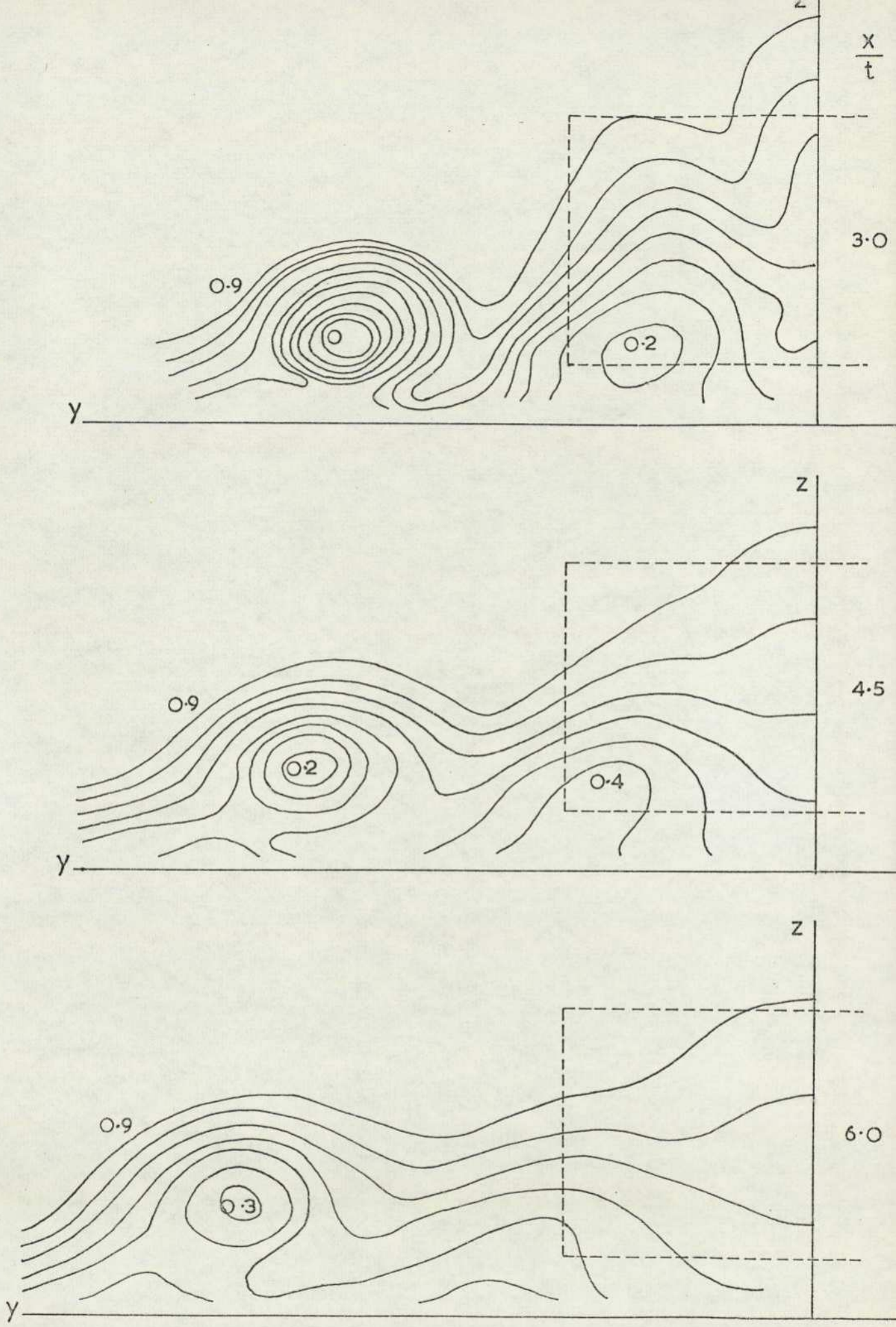

FIG. 81 (k) BLOCK 2N $\alpha = 8^\circ$, $Z_0/t = 0.25$

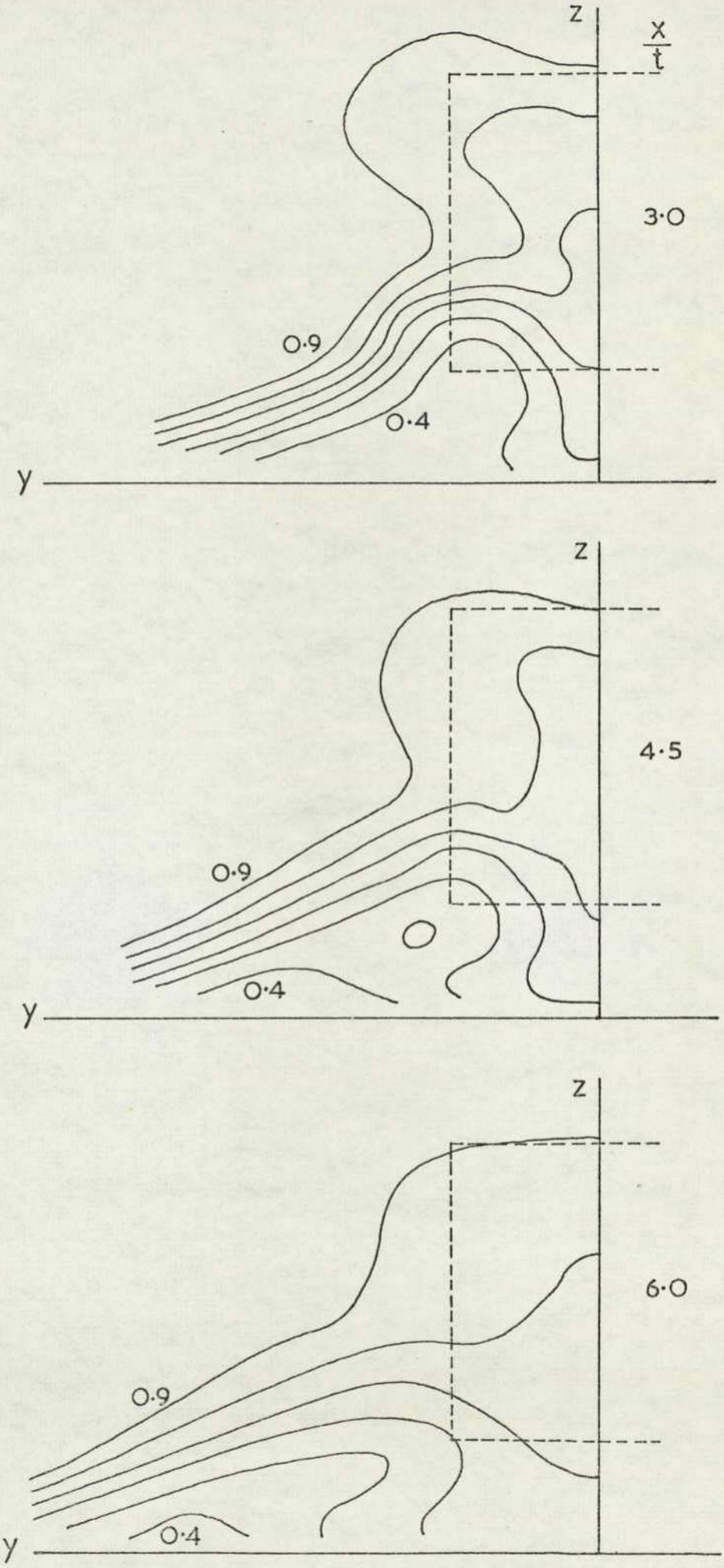

FIG. 82 PITOT CONTOURS — BLOCK IN

(a) $\alpha = 6°$, $z_0/t = 0{\cdot}375$

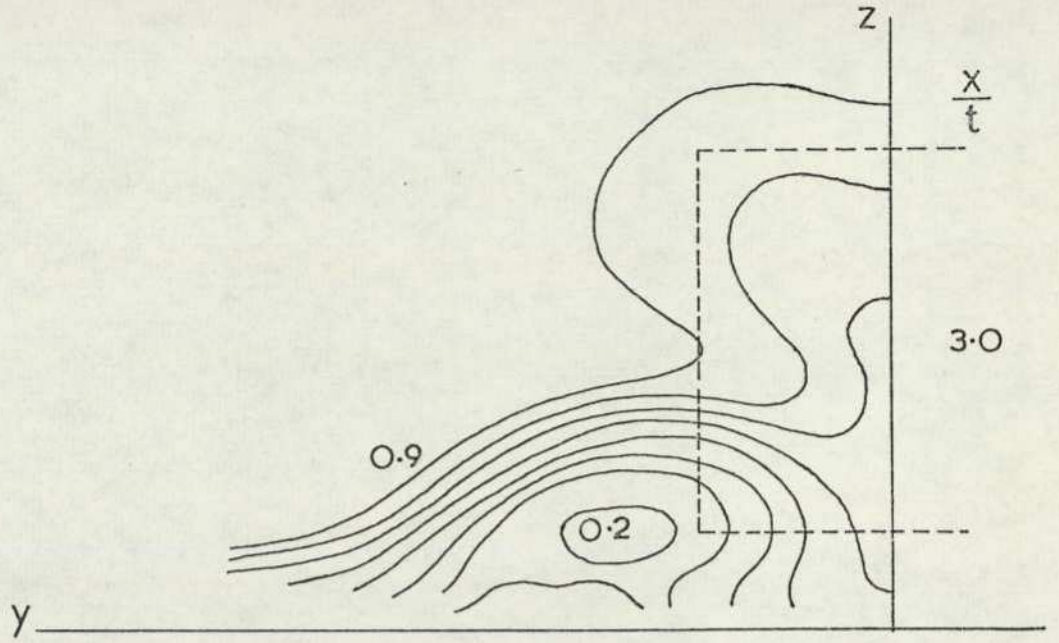

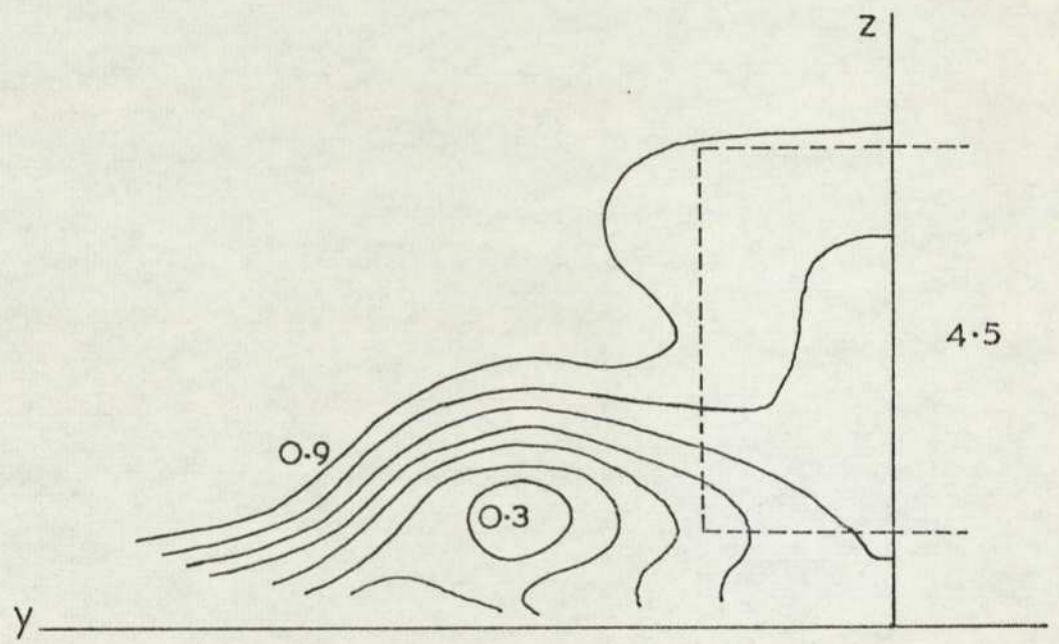

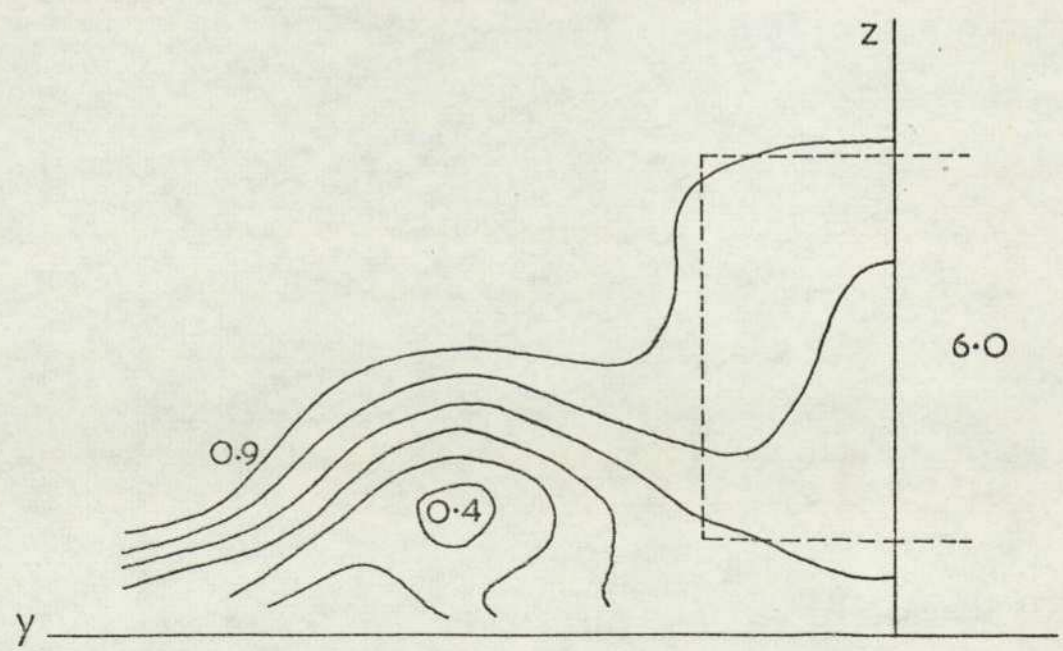

FIG. 82 (b) BLOCK IN $\alpha = 6^{\circ}$, $z_0/t = 0{\cdot}2$

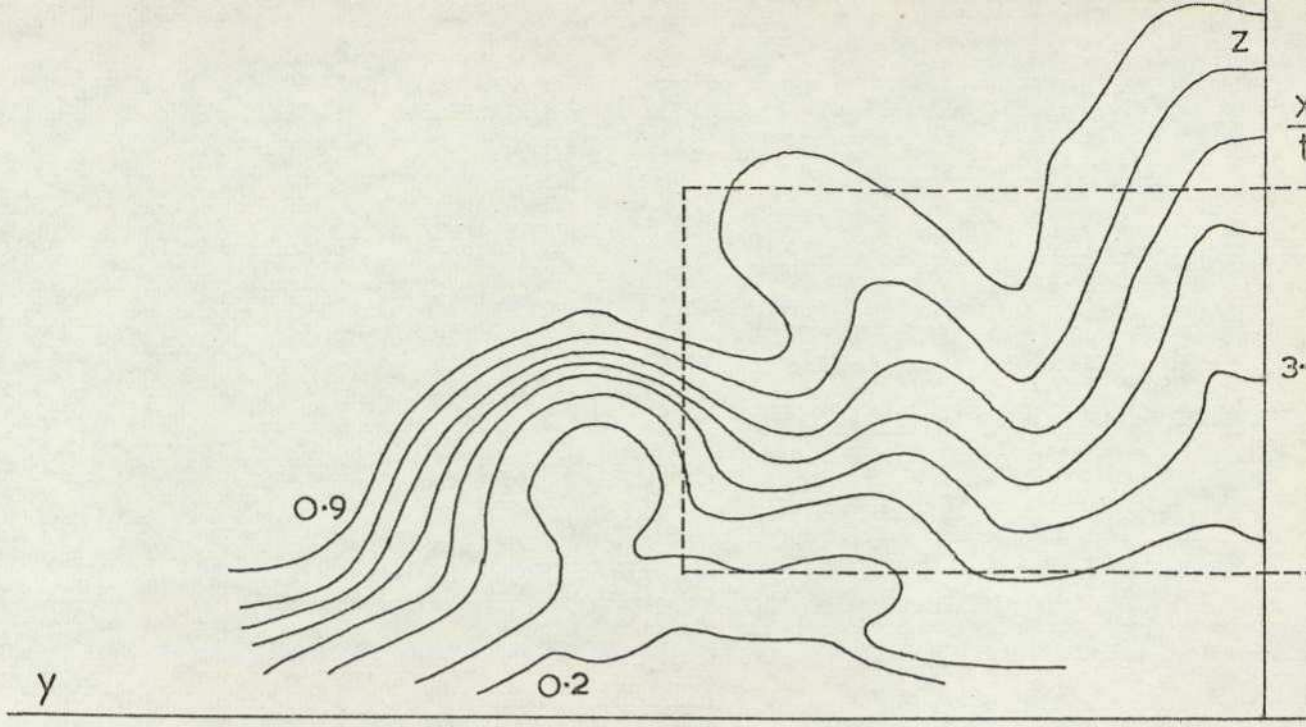

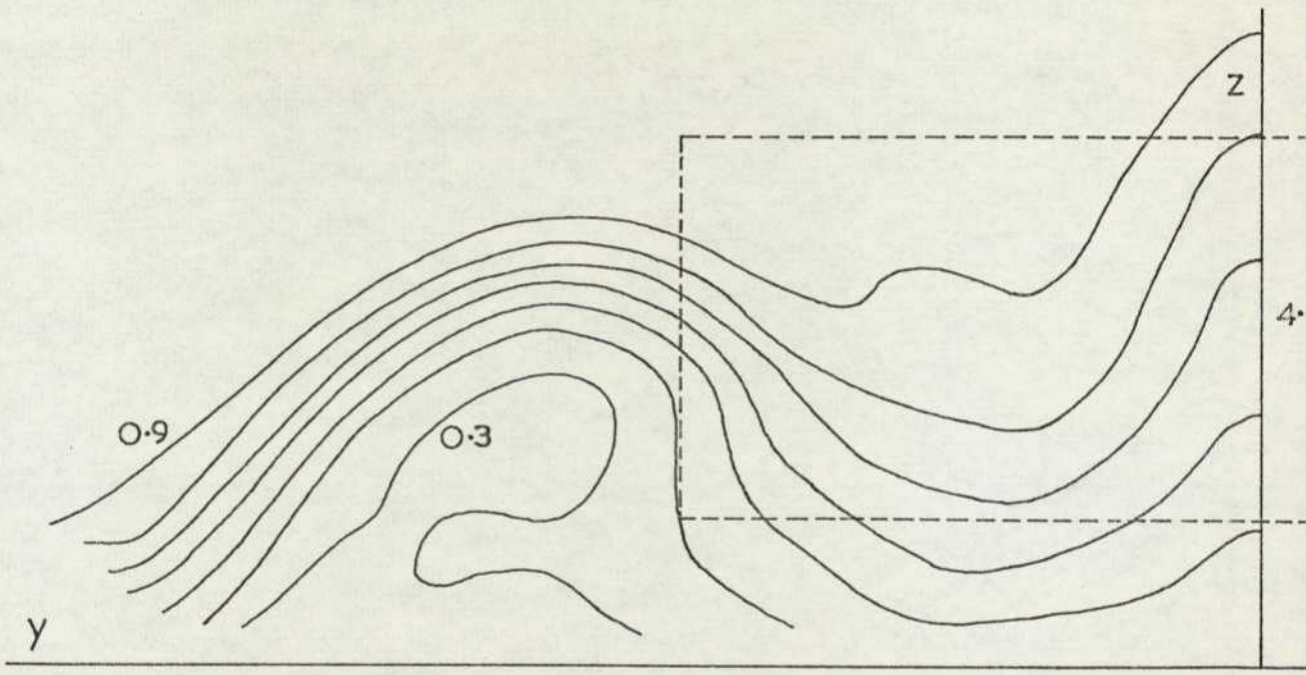

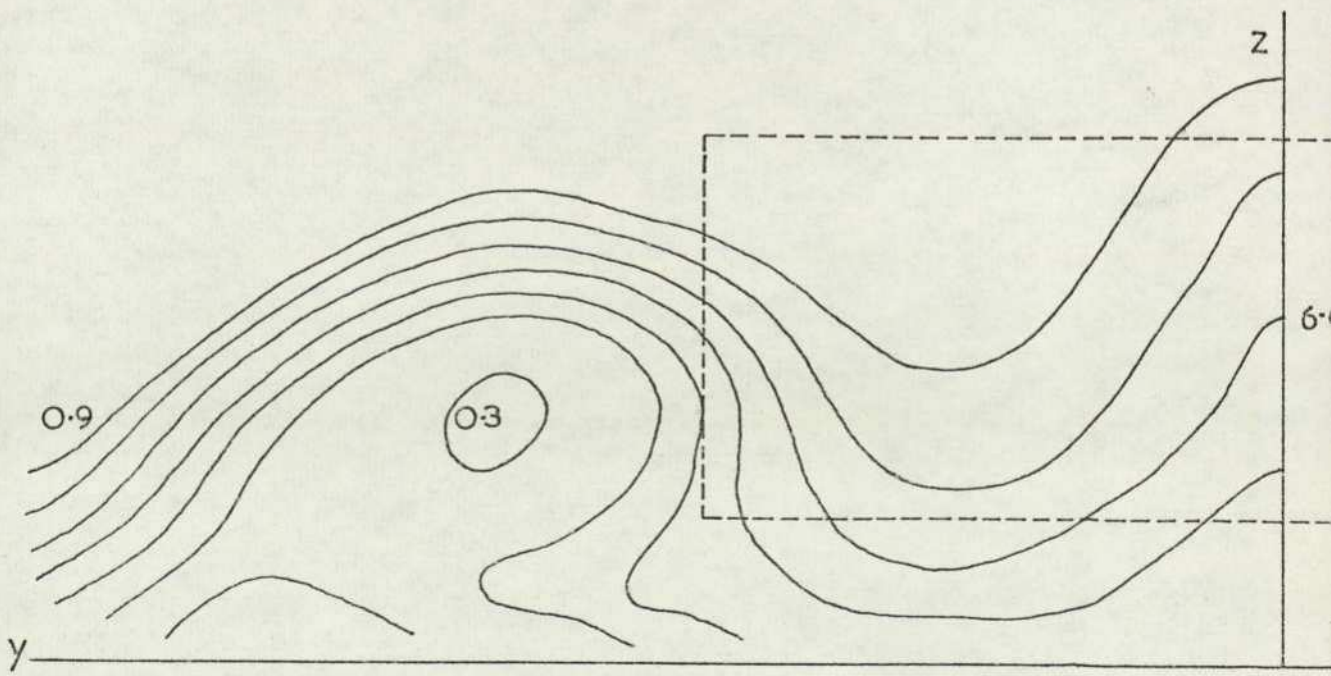

FIG 82 (C) BLOCK 3N $\alpha = 6^{\circ}$, $Z_o/t = 0.375$

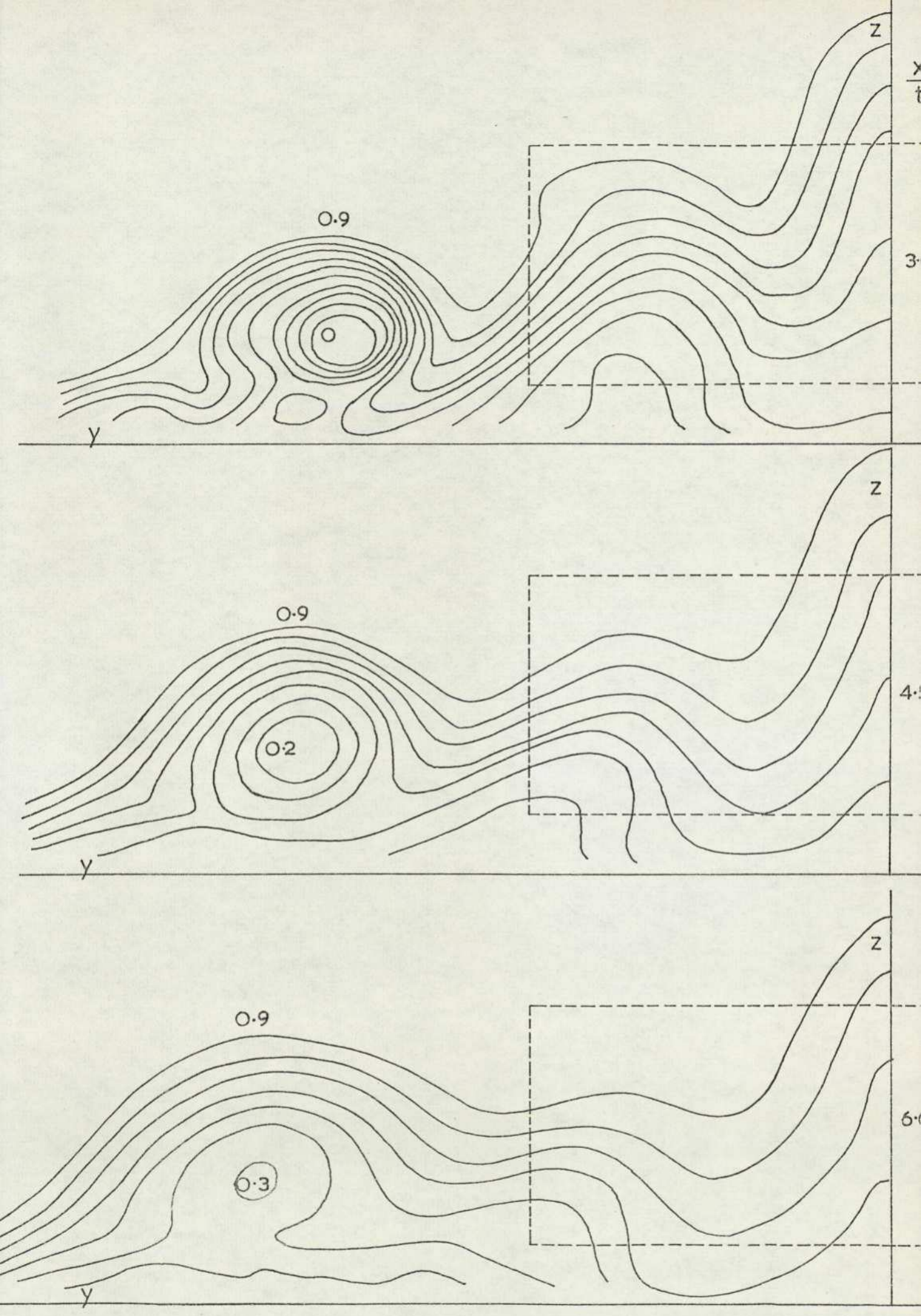

FIG. 82 (d) BLOCK 3N $\alpha = 6°$, $z_0/t = 0{\cdot}25$

Note that the length scale in the x - direction is half that in the y - direction. It has sometimes been possible to define a lateral position of the vortex core but not its vertical location. In all cases the trailing vortex spacing increases as it moves downstream, as would be expected for a lifting body. The displacement increases almost linearly over the range investigated while at the same time the vortex moves slightly upwards. For all ground clearances and incidences the height of the vortex core lies within a very narrow range for a given body; this height increasing slightly with span.

Base pressure measurements were performed on block 2N at $z_o/t = 0.25$ for various angles of incidence. These are shown in Figure 84. As before negligible variations in base pressure occur for a particular spanwise position. All incidence angles give a similar marked spanwise variation except for the extreme negative incidence block which gives a constant base pressure over the entire base.

A few traverses were performed, using the hot wire anenometer, vertically and horizontally through the maximum total head deficit point, as defined by the pitot rake measurements. The probe was always aligned as in the previous section and measurements were only taken for block 2N set at six degrees of incidence. Assuming cylindrical flow in the vortex core; that is no radial component exists, then for the horizontal traverse the probe output E/E_∞ represents $(U^2+W^2)^{1/2}/U_\infty$, where W here is the circumferential flow velocity component, while in the vertical traverse it measures U/U_∞. Initial measurements, Figure 85, show the traverses at various downstream stations, which inexplicably differ from those of the pressure measurements, with the model set at a ground clearance of 25mm. Lateral traverses show a distinct velocity deficit in the vortex core the amount of the wake contained in this region increasing with downstream displacement. The turbulence intensity distribution shows that initially the vortex is masked by the bluff body but on moving downstream the vortex appears to carry an increasing proportion of the turbulent energy. Across the core itself the distribution is almost constant. The vertical traverses show the presence of turbulence intensity peaks either side of the minimum velocity. These are probably the rolling up vortex sheet. To investigate briefly the effect of reducing ground clearance a single vertical and horizontal

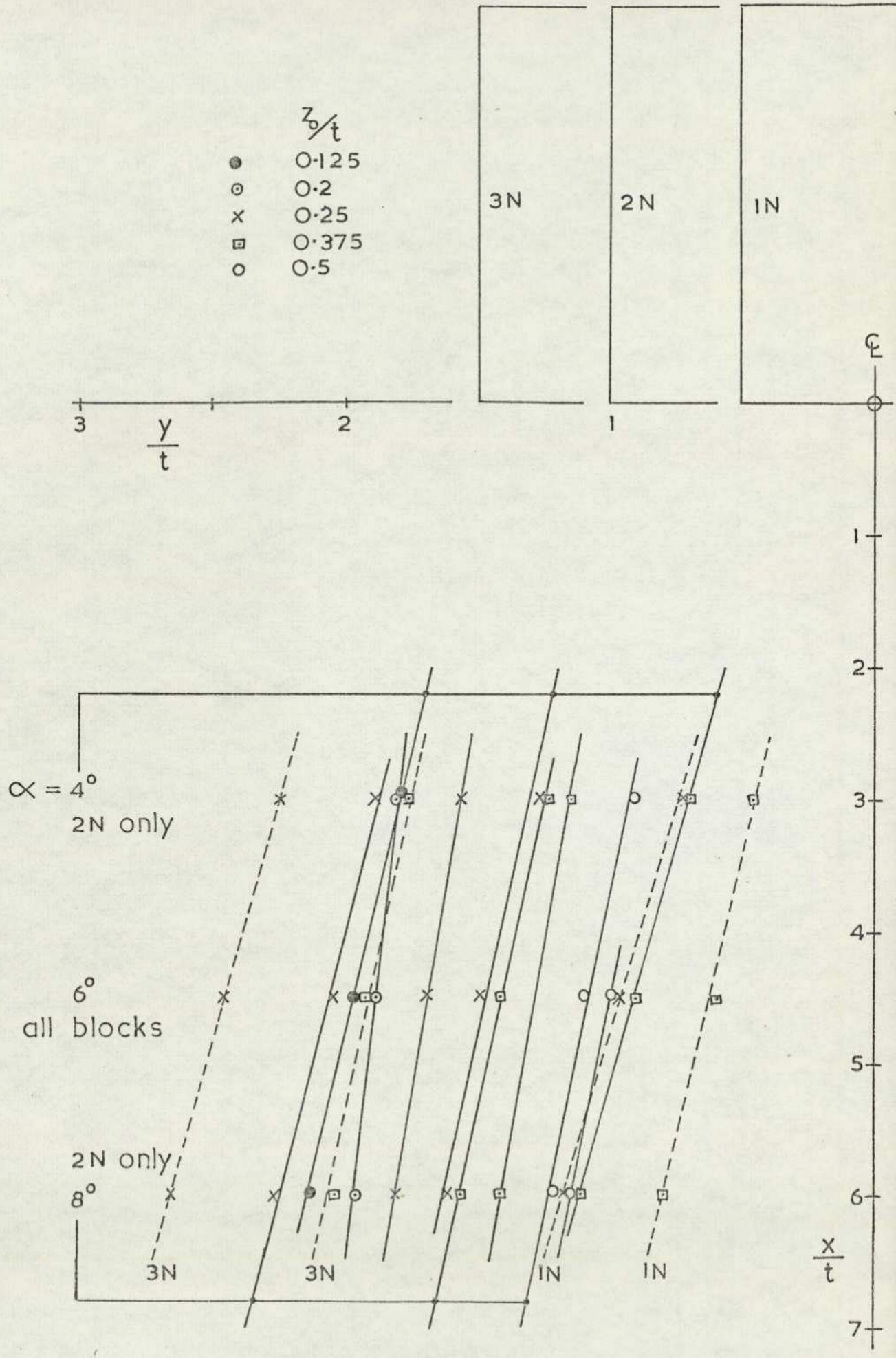

FIG. 83 PATH OF MINIMUM TOTAL HEAD (a) PLAN

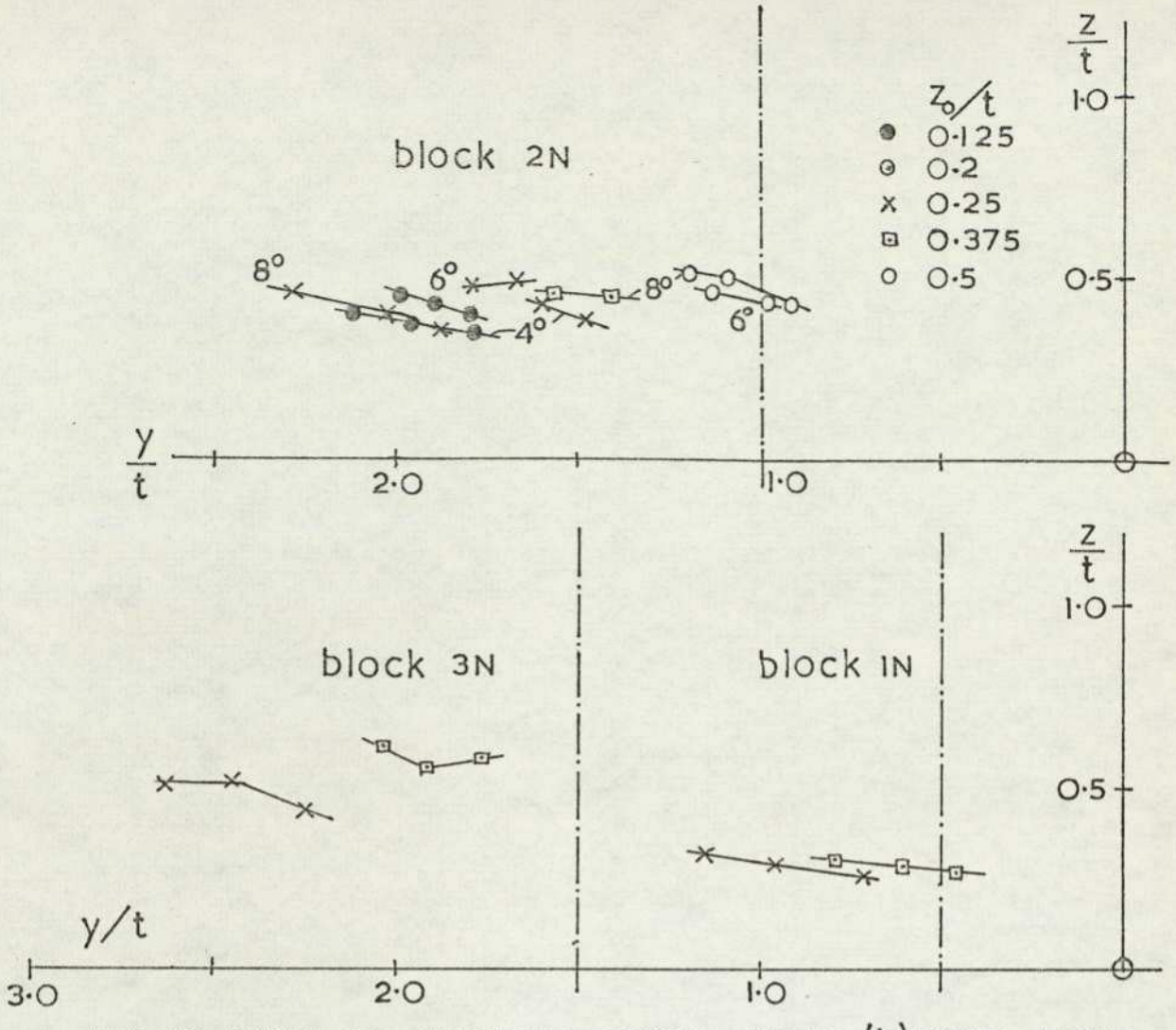

FIG. 83 PATH OF MINIMUM TOTAL HEAD (b) REAR VIEW

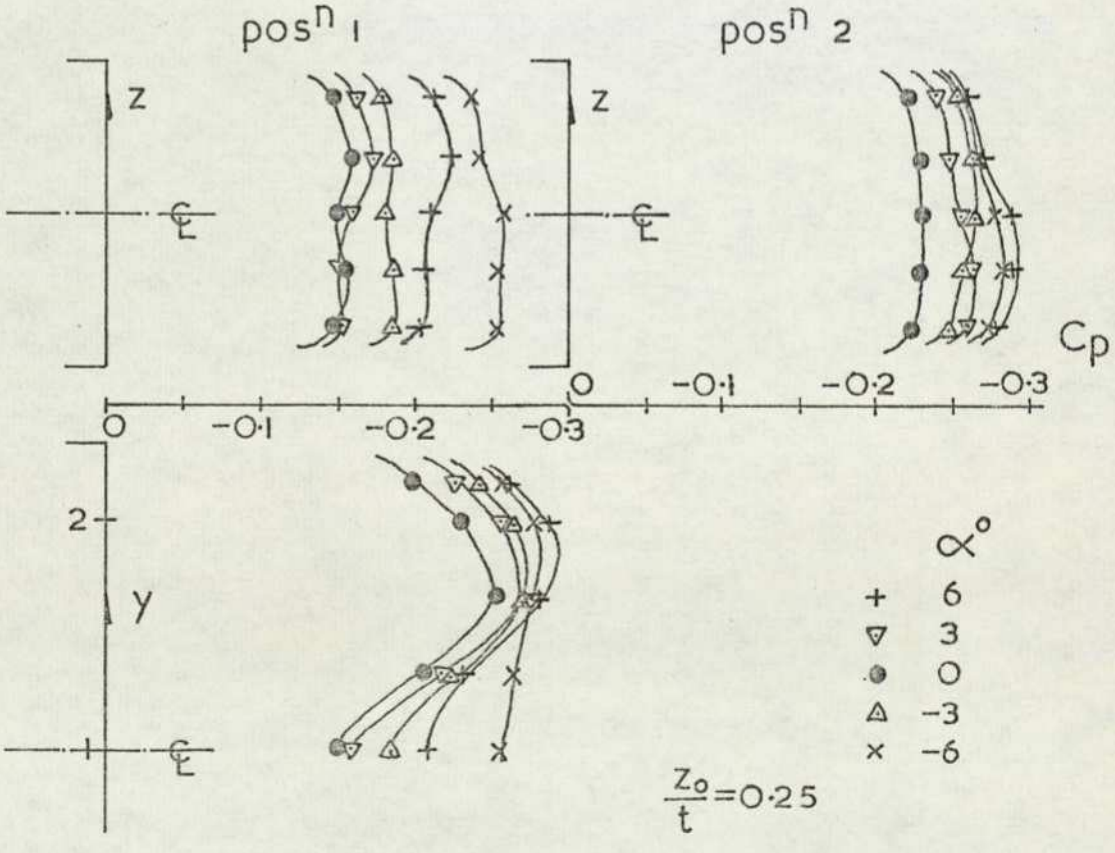

FIG. 84 BASE PRESSURES — BLOCK 2N AT INCIDENCE

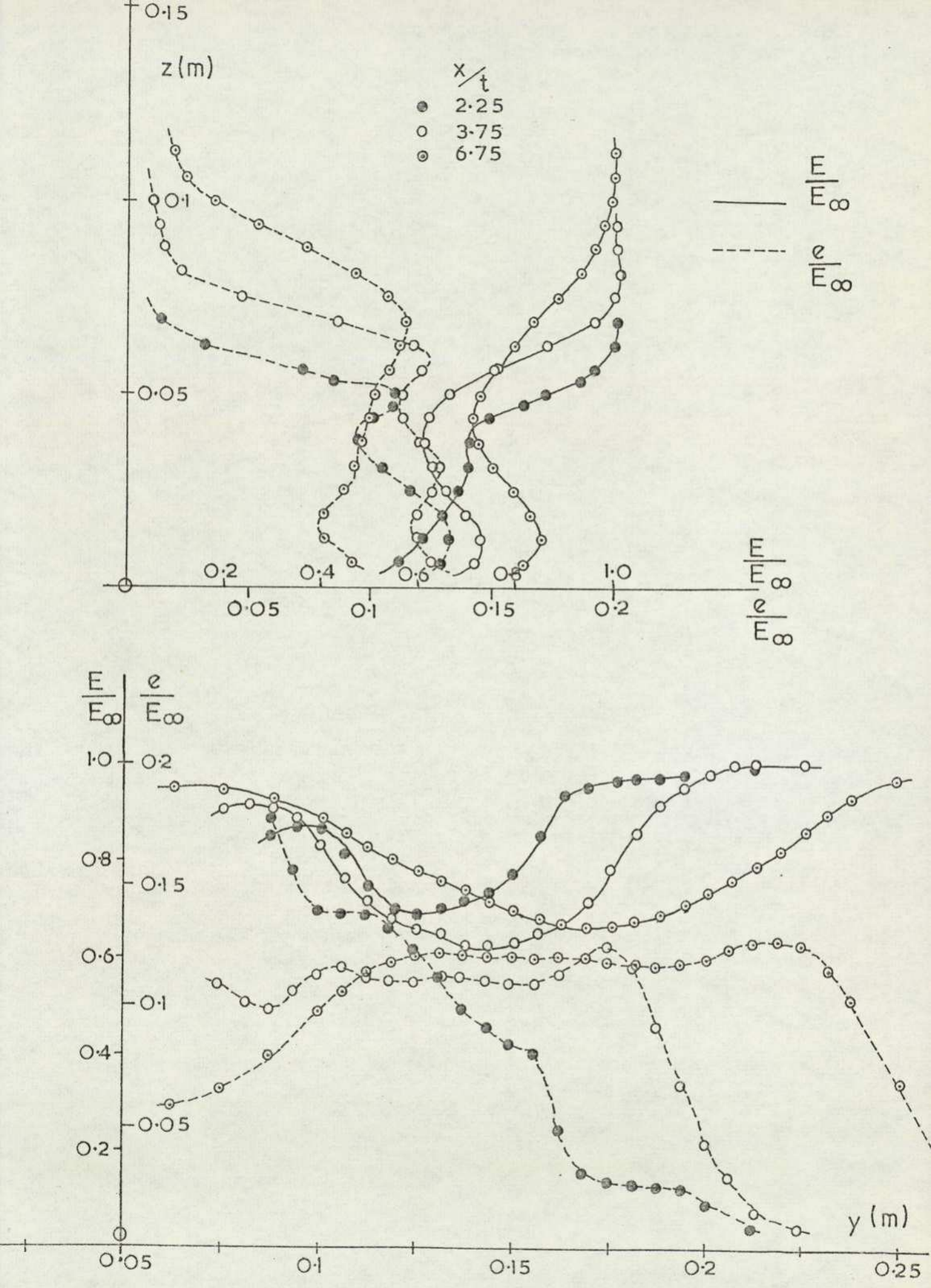

FIG. 85 TRAVERSES THROUGH POSITION OF MINIMUM TOTAL HEAD — BLOCK 2N $\alpha = 6^\circ$, $z_o/t = 0{\cdot}25$

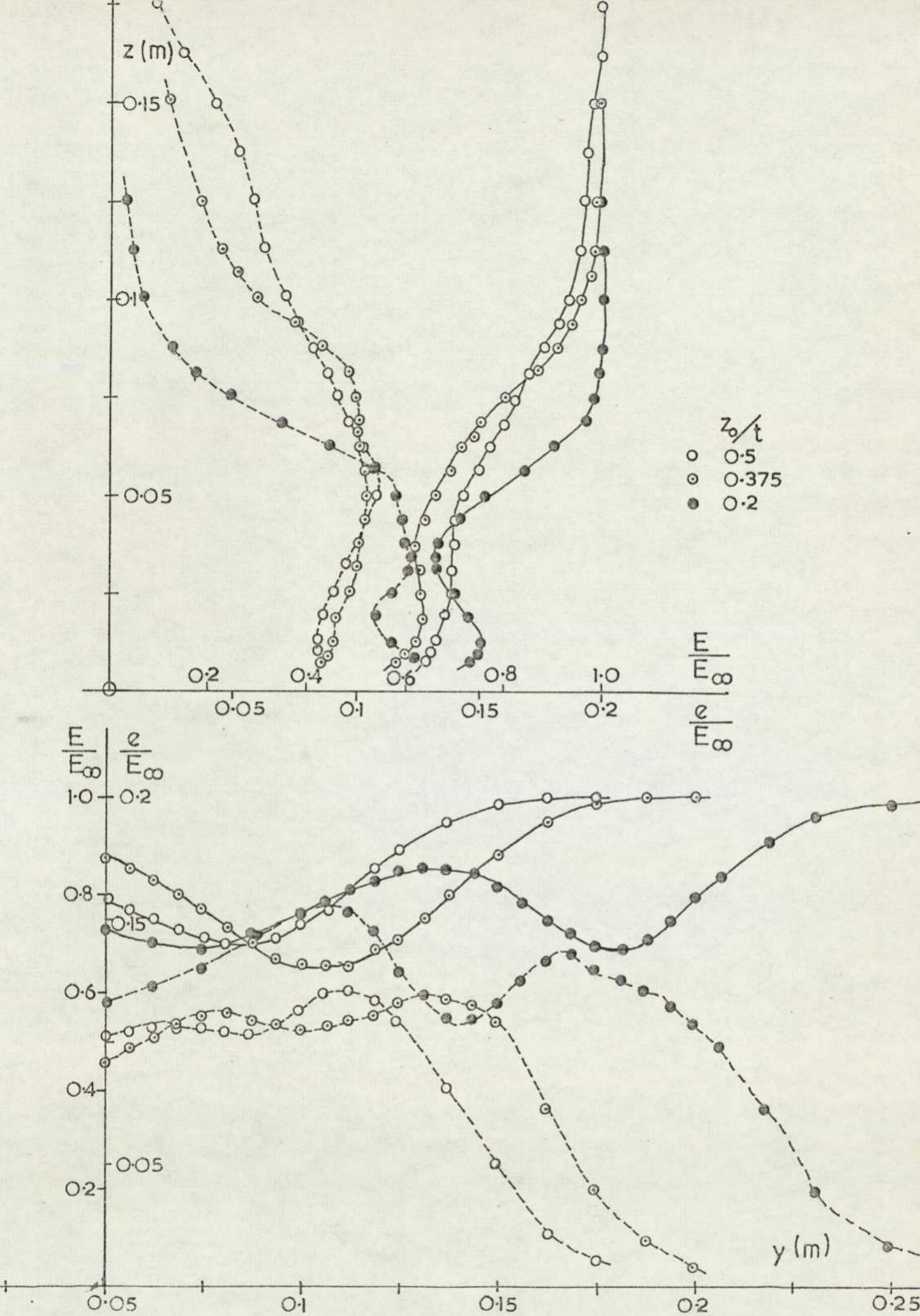

FIG. 86 TRAVERSES THROUGH POSITION OF MINIMUM TOTAL HEAD — BLOCK 2N $\alpha = 6^\circ$, $X/t = 4{\cdot}5$

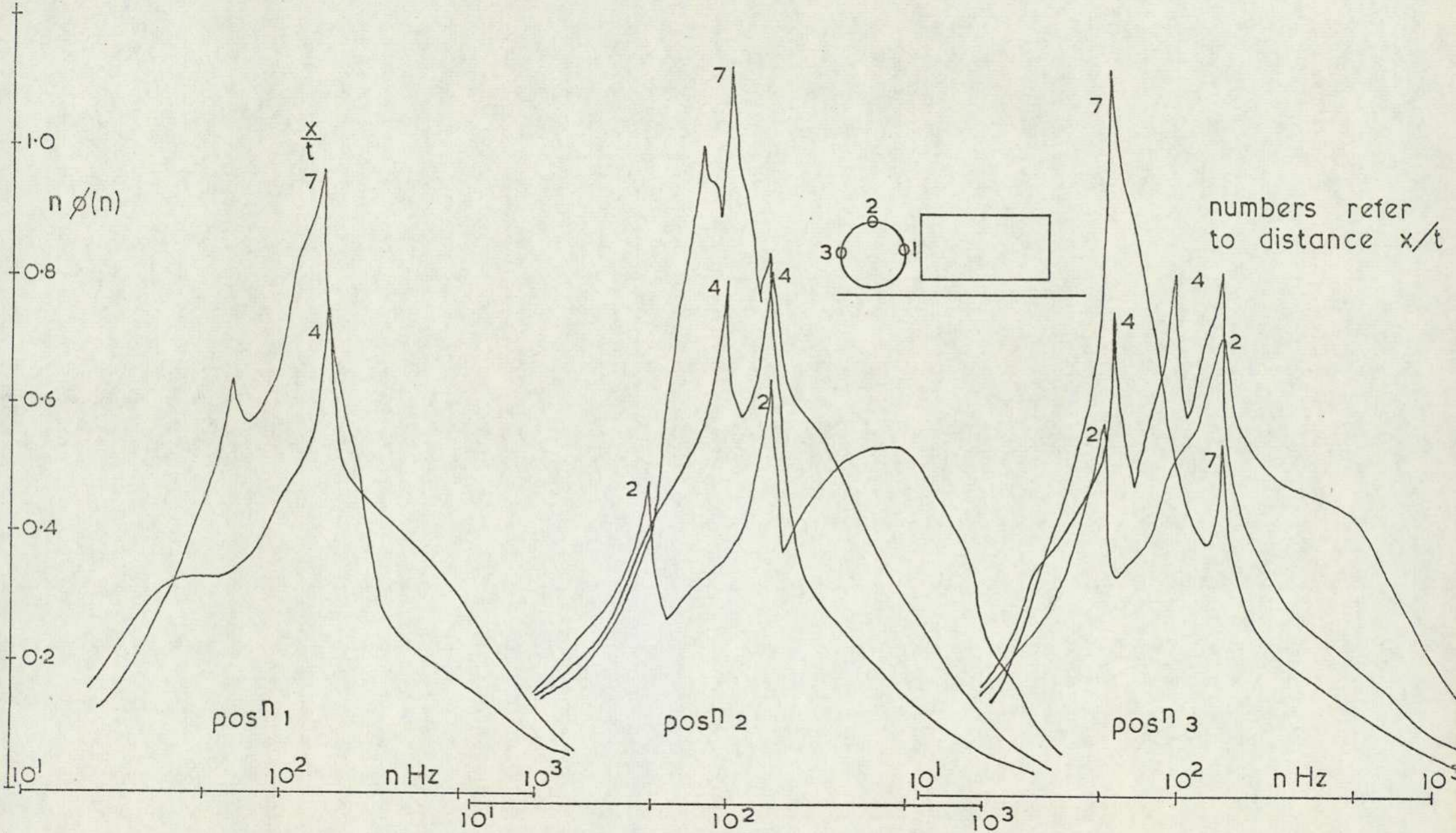

FIG. 87 FREQUENCY SPECTRA — BLOCK 2N, $\alpha = 6^\circ$, $z_o/t = 0{\cdot}25$ — EFFECT OF TIME

traverse was performed as before but at one station, x/t = 4.5, Figure 86. At the higher ground clearance the wake is contained in two outer regions and the turbulence intensity is almost constant across the entire wake. By the lowest ground clearance the wake has divided into three regions with the central part exhibiting an off centre turbulence intensity peak as for the non-lifting wakes. Outside of this is a clearly defined region of velocity deficit which can be associated with the vortex from the pressure measurements. This region has again a fairly constant turbulence intensity distribution which is superimposed on that from the central wake. The vertical traverses through the vortex cores again shows up the constant turbulence intensity that occurs across the vortex.

A frequency analysis was performed on the signal from the hot wire probe when the anemometer was placed near the outer edges of the vortex, as defined by the turbulence intensity region. Measurements are shown in Figure 87 for block 2N only, mounted at 25mm ground clearance and six degrees incidence. Three downstream positions were investigated and at each three spectra are obtained corresponding to upper, inner and outer edges of the vortex. At all positions peaks occur at frequencies of 50-60 Hz and 140-160 Hz. As the wake moves downstream it becomes more ordered, the turbulence energy being contained within a narrower frequency band. A particular frequency becomes associated with each position of the probe. The outer location gives a distinct 55 Hz peak, while the inner produces 150 Hz, and a frequency of 105 Hz is dominant at the upper probe psoition.

4.3.3. Cambered block, zero incidence.

The cambered block, 9C, was set with the flat underside parallel to the ground plane and at various ground clearances. Pitot rake measurements were taken at three downstream stations; x/t = 2.0, 3.0 and 4.0. The total head contours are shown in Figure 88 and it can be seen that a distinct change, from the results typical for a body at incidence, has taken place. The wakes for the cambered block all have similar form with the central part of the wake deflected noticeably downwards and with the maximum total head deficit occurring just inboard of the block sides as projected downstream. The spacing between the vortices remains essentially constant, for a particular configuration, with distance from the model and moves very slightly outwards as the ground is approached.

This is shown in the plan view of the vortex core location, Figure 89 Also shown is a side view of the vortex centre position. This shows a drop in height on moving downstream, while a reduction of model ground clearance has a similar effect. At the lowest clearance the minimum total head does not define the vortex as interference with the ground has occurred.

Traverses with the hot wire probe, were performed vertically and horizontally through the minimum total head position, for the four ground clearances at $x/t = 2.0$. These are shown in Figure 90. Additional measurements were made at $x/t = 4.0$ for the model at 25mm ground clearance while in all cases vertical traverses through the wake centre line were made. Along the wake centre line the velocity profiles are very similar to boundary layer profiles; only at the highest ground clearance is a typical wake profile observed. At the station nearest the model the turbulent intensity distribution always shows a distinct peak, the height of which increases with model ground clearance. By the downstream station this peak has disappeared. A distinct velocity deficit is measured across the vortex, and, as with the block at incidence, the turbulence intensity across this region is almost constant.

Frequency spectra were obtained for the cambered model mounted at $z_o/t = 0.25$ with the probe at $x/t = 2.0$, Figure 91. The most distinct periodic effects were measured on the centre line of the wake and show a strong 65 Hz peak and a lesser one at 125 Hz. All the other spectra show two peaks; one at 120-125 Hz, the other between 70-80 Hz.

4.3.4 Discussion

The striking feature of these lifting body wakes is the difference that exists between the effects of incidence and camber. While the trailing vortex of the former experiences an essentially horizontal motion the other moves almost vertically downwards. Consider the flow mechanisms in each case. Under the blocks at incidence a large pressure gradient exists between the centre line of the body and the side edges which are approximately at free stream pressure. This ensures that a cross flow arises, which, if strong enough will separate from the salient body edges, producing a vortex that will continue to be fed from the cross flow under the body. The evidence of the vortex paths downstream of the blocks at incidence supports this idea. Even if no separation

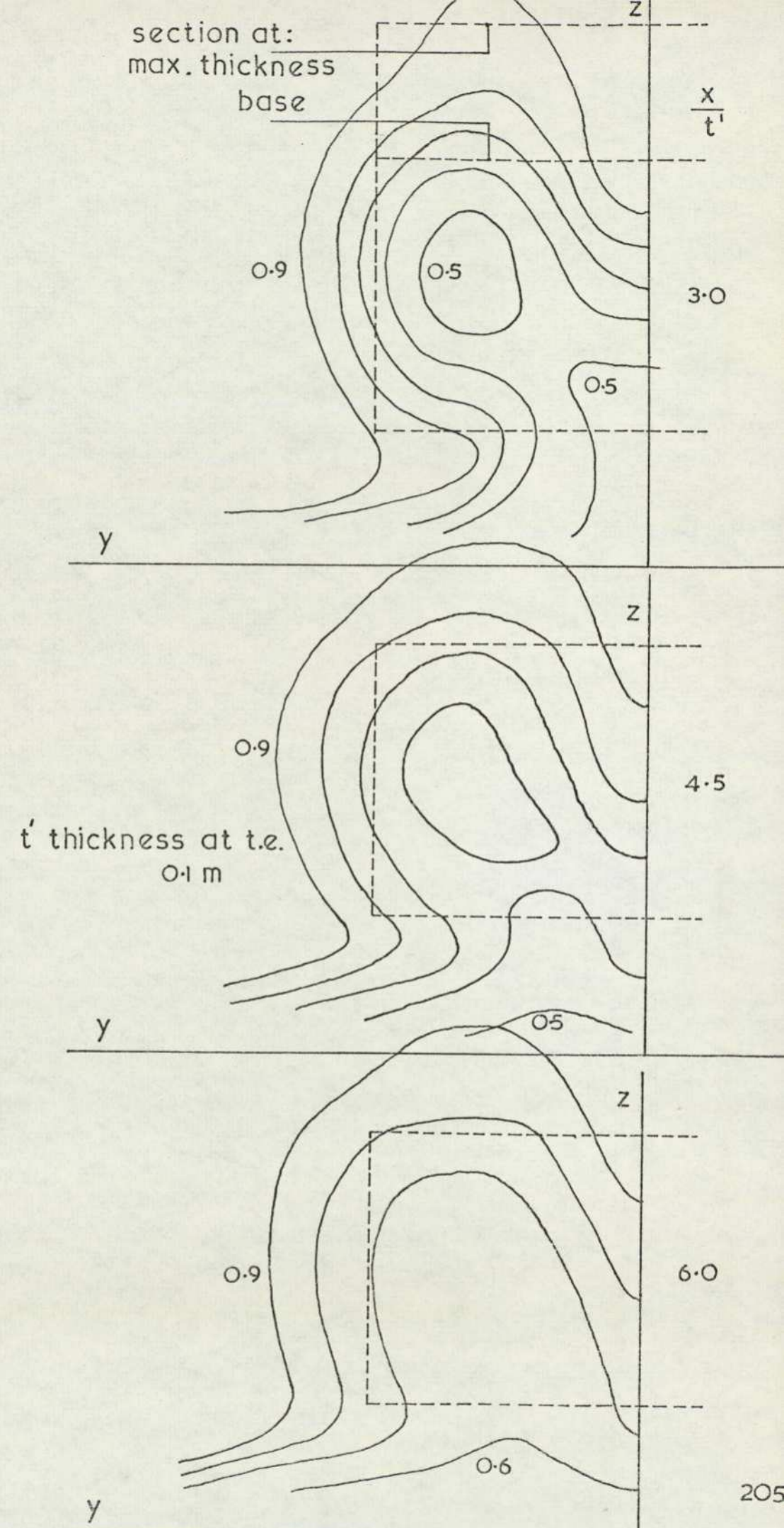

FIG. 88 PITOT CONTOURS — BLOCK 9C $\alpha = 0°$, $Z_0/t' = 0.5$ (a)

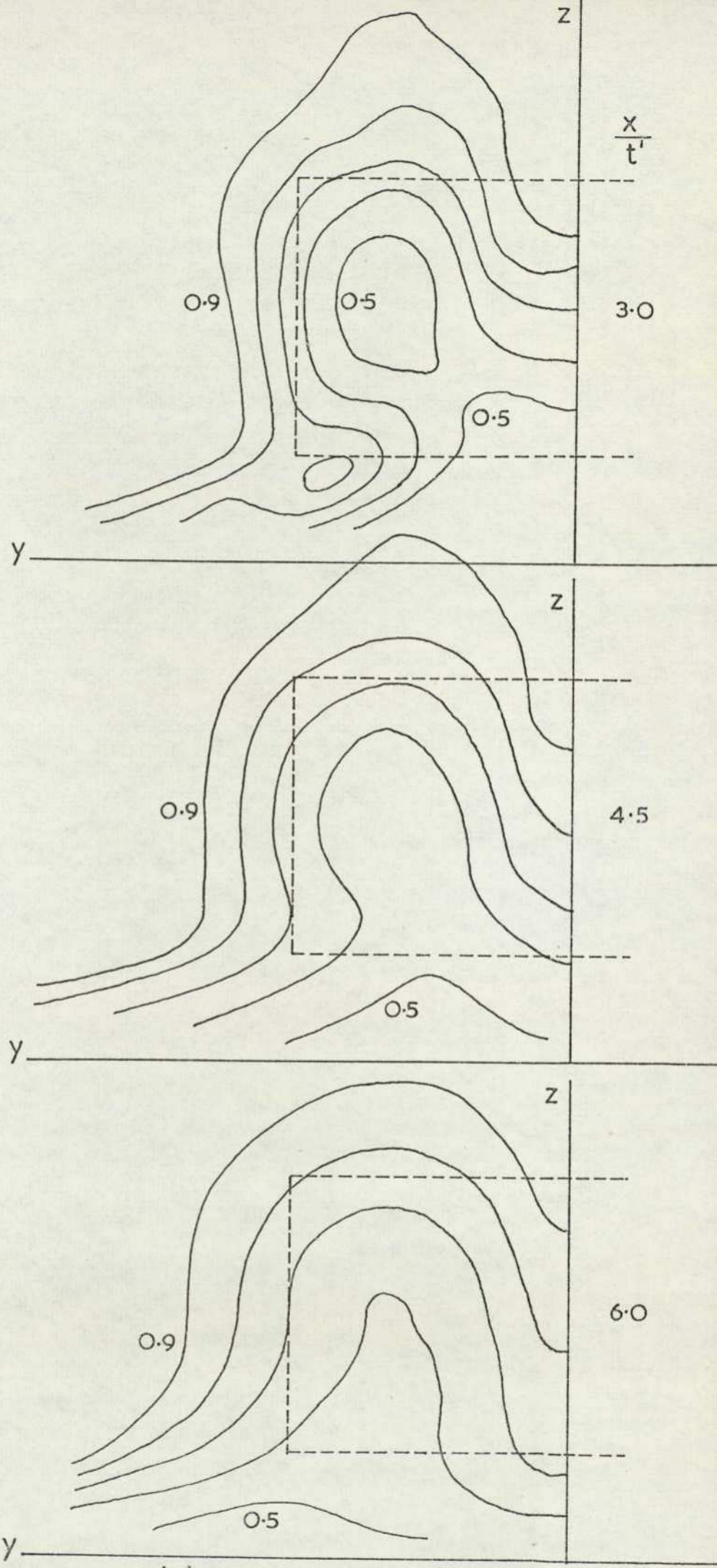

FIG. 88 (b) BLOCK 9C $z_o/t' = 0.375$

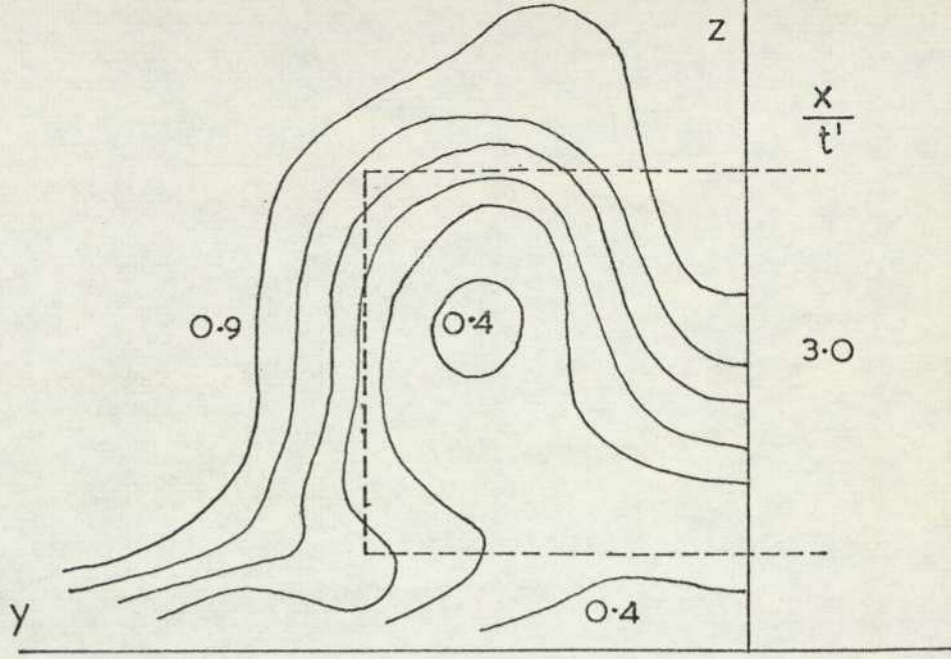

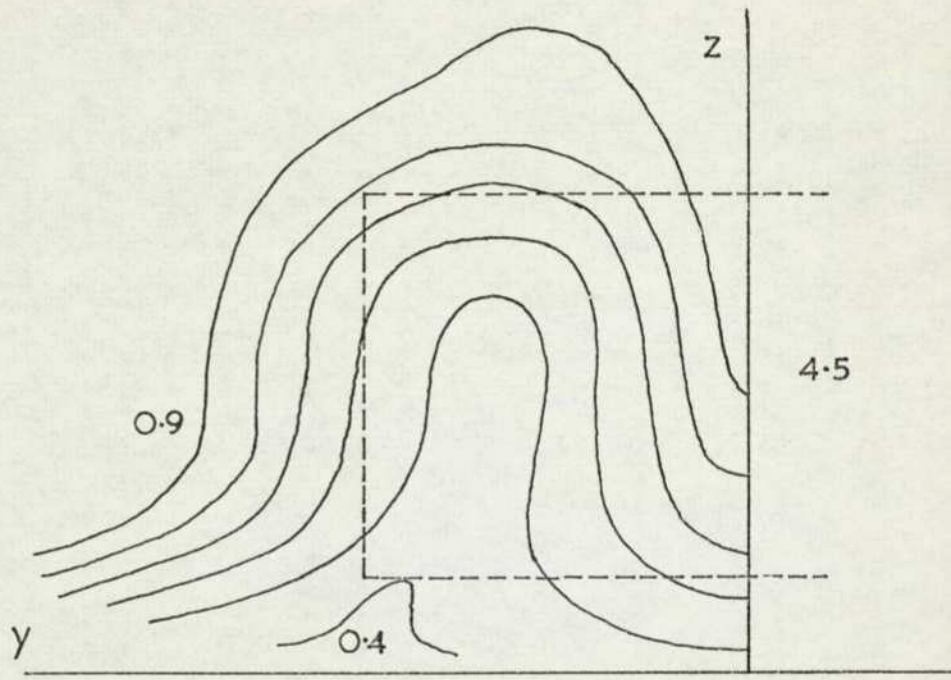

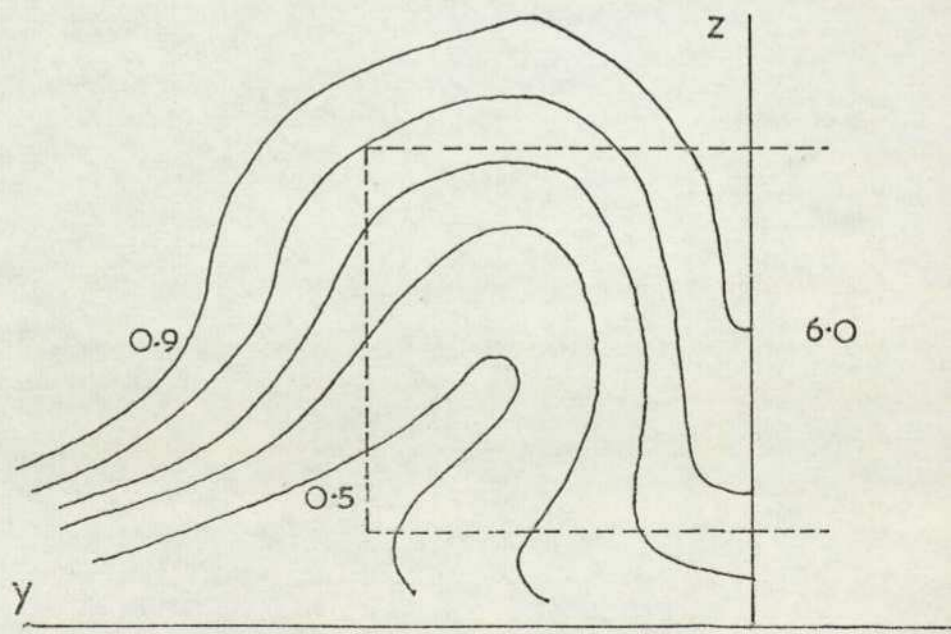

FIG 88 (c) BLOCK 9C $z_o/t' = 0{\cdot}25$

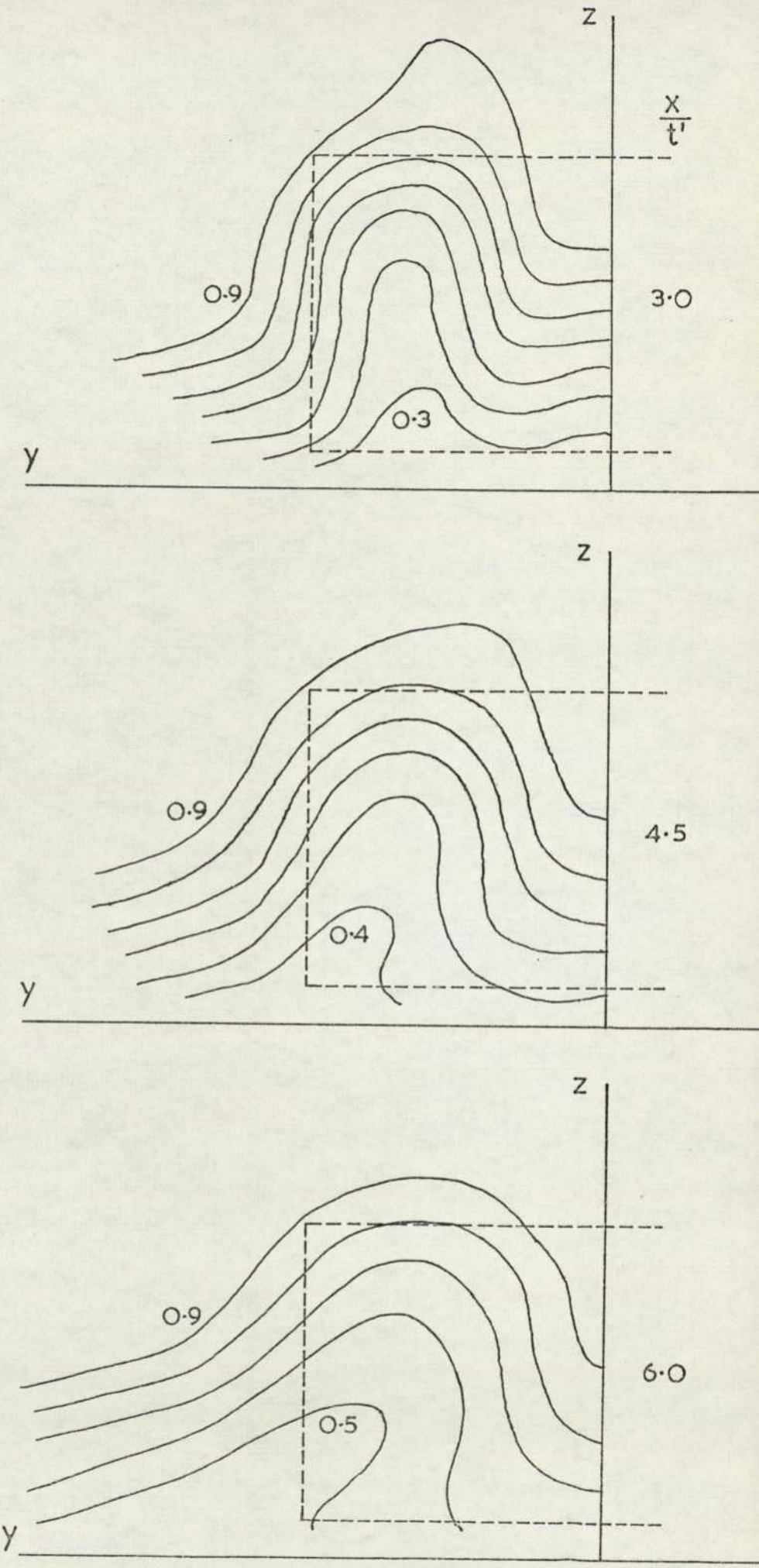

FIG. 88 (d) BLOCK 9C $z_o/t = 0.125$

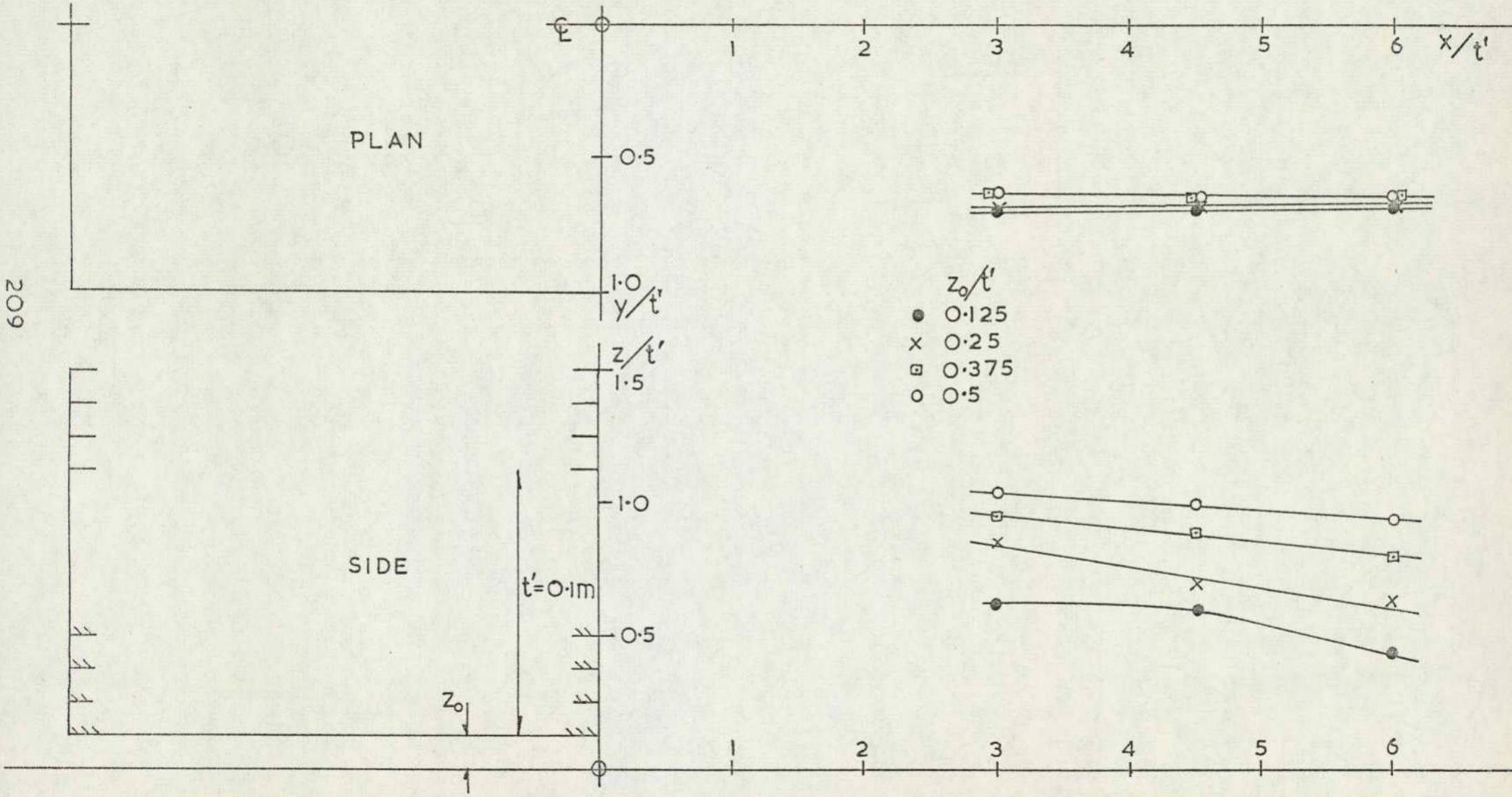

FIG. 89 PATH OF MINIMUM TOTAL HEAD FOR CAMBERED BLOCK 9C

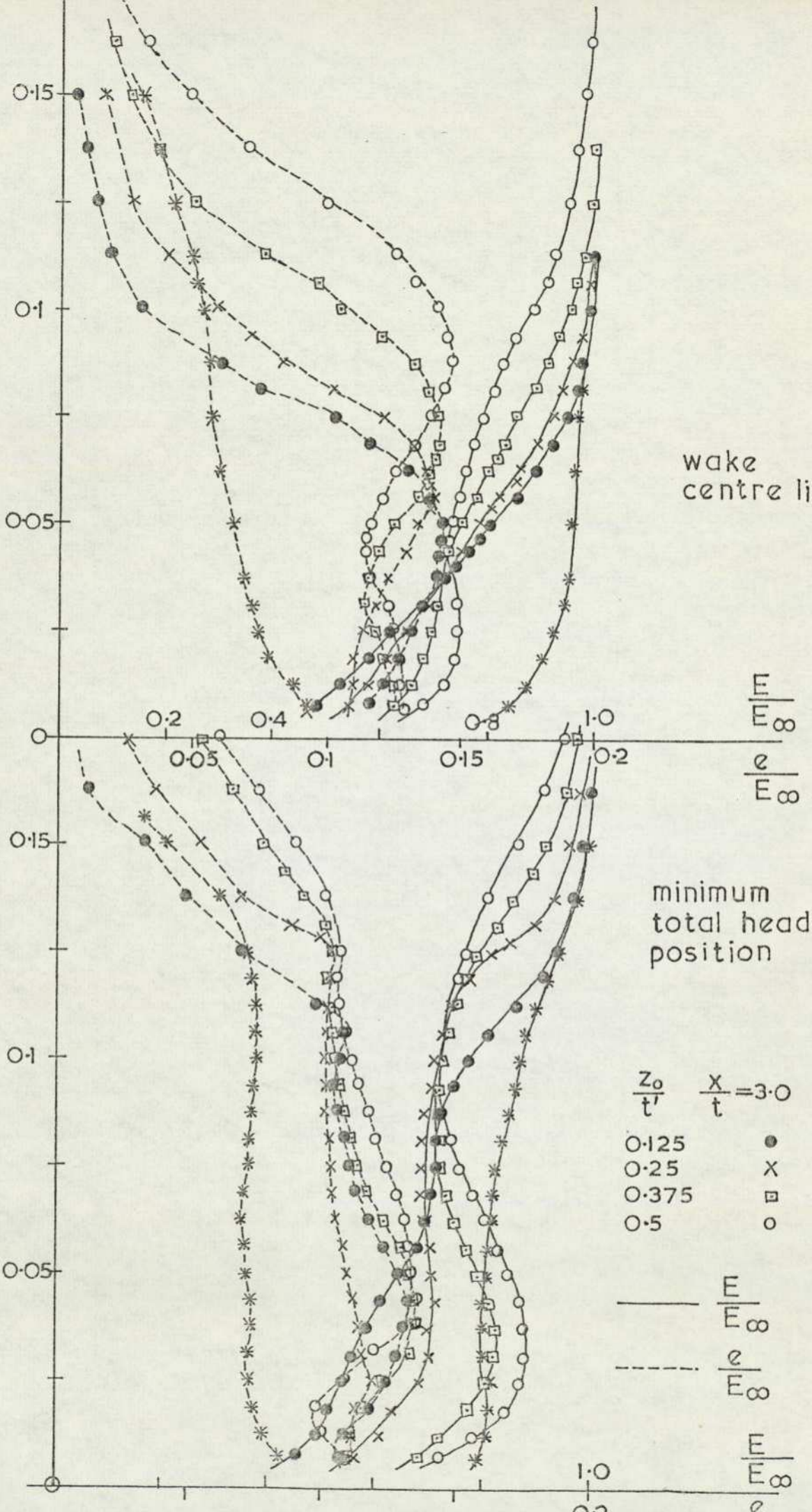

FIG. 90 WAKE TRAVERSES—BLOCK 9C (a) VERTICAL

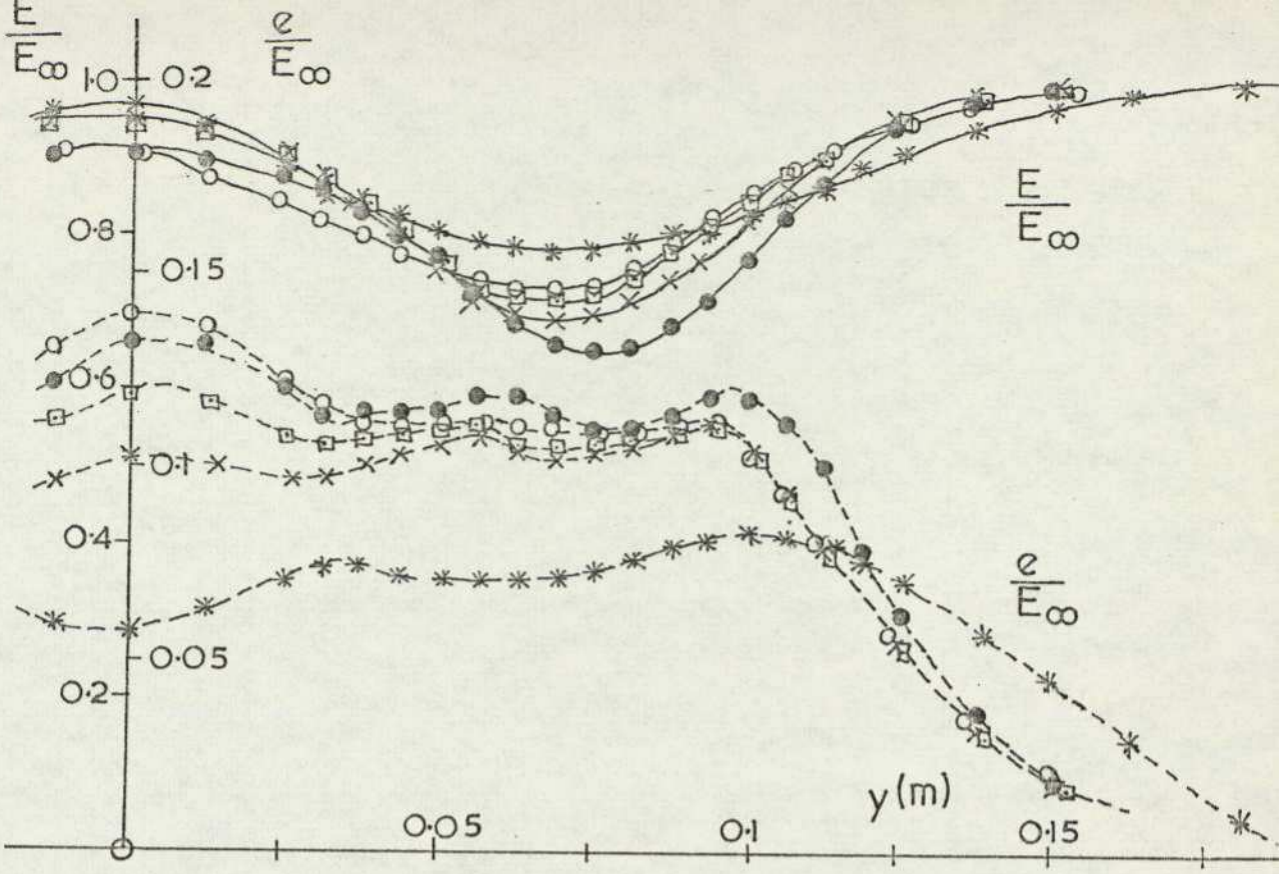

FIG. 90 (b) BLOCK 9C LATERAL TRAVERSE

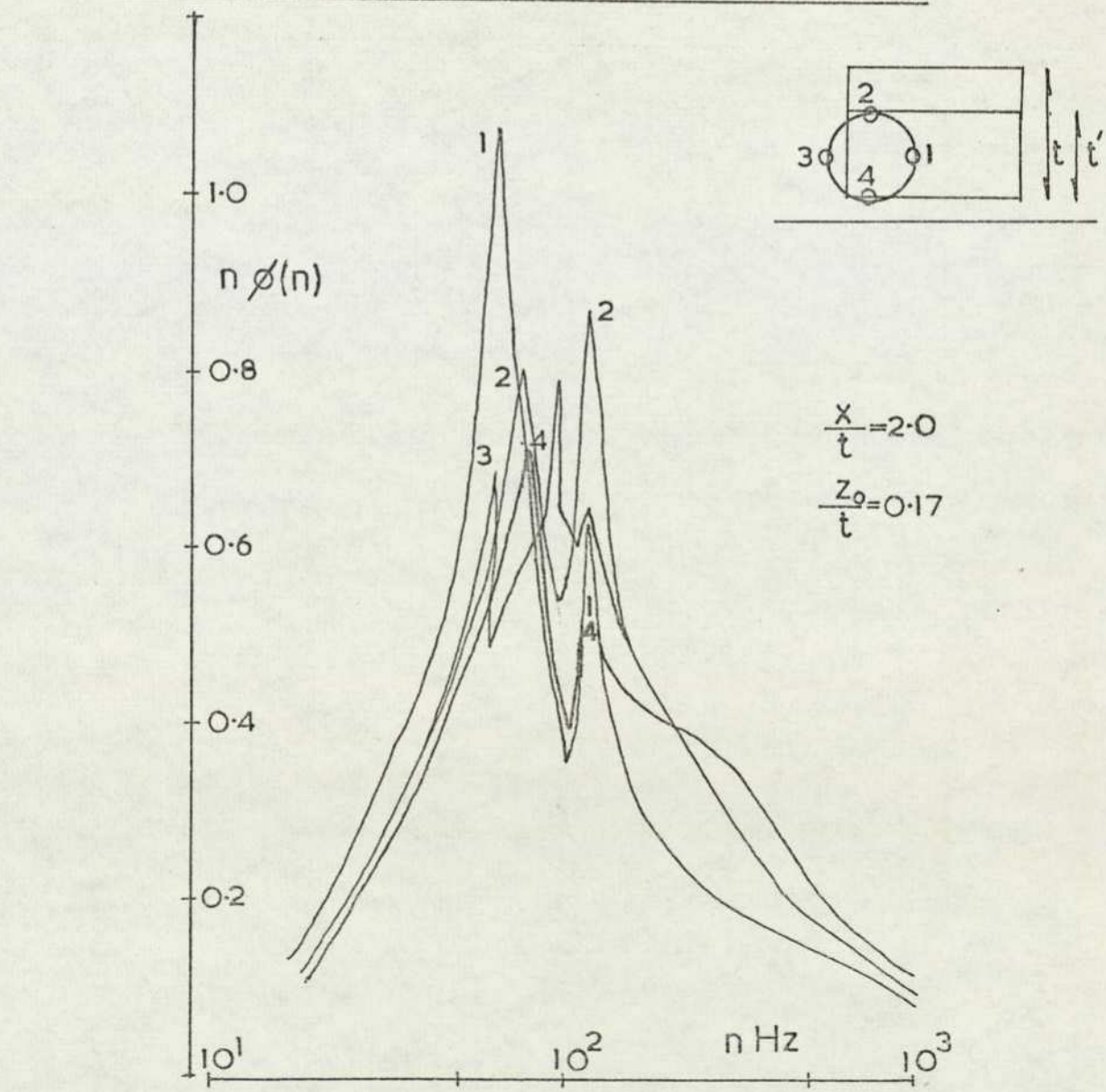

FIG. 91 FREQUENCY SPECTRA — BLOCK 9C

along the side edges exists, as in the case of low incidence or high ground clearance, the trailing vortex structure arising from the small crossflow under the body may still dominate that from the upper body surfaces. This would not be true if there were camber on the upper surface and for the cambered case investigated here, which has the lower surface at zero incidence the opposite is true. In this situation a trailing vortex structure, arising from lift effects, will only develop downstream of the upper surface trailing edge; the contribution of the side edges will be negligible, and so the conditions in the near wake will be little different from those in free stream. Thus in the former case the vortex is generated close to the ground so that it becomes dominated by its own mirror image rather than its pair generated on the opposite side of the vehicle. In the cambered model case the vortices are formed far enough from the ground that their own influence is greater than that of the ground images and they tend to behave as in free stream.

This can be substantiated by analysing the motion of a pair of line vortices above a ground plane. The situation is identical to a line vortex approaching a right angle corner. The path, given in most fluids' text books, (Lamb (54)) is simply

$$r \sin 2\Theta = a \qquad (4.4)$$

where r, Θ are the polar coordinates of the vortex, and a is a constant, which is also the assymptotic vortex spacing. The curve is plotted in Figure 92, and it can be seen that over most of its path it is almost parallel to either the y-or the z-axis. Only in the vicinity of the origin does the path deviate significantly. The velocity, V , parallel to the y-axis is given by

$$V = \frac{\Gamma}{2\pi a} \left(\frac{2z}{a} \right)^{-3} \qquad (4.5)$$

where Γ is the vortex strength, and this velocity is plotted on the same graph. The vertical velocity W, is obtained by substituting y for z in equation (4.5). These velocities do not reach their

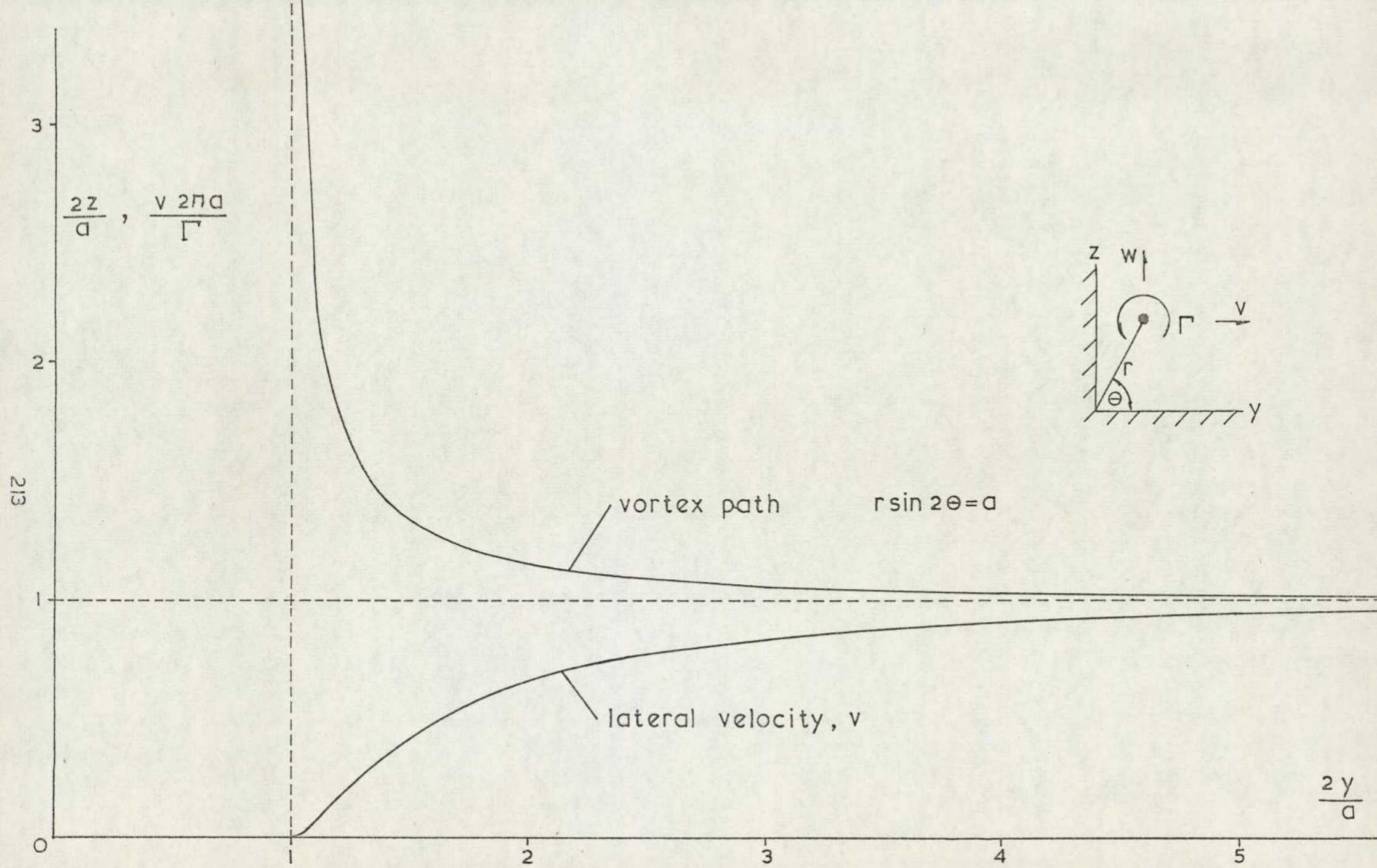

FIG. 92 PATH AND VELOCITY OF VORTEX IN A CORNER

assymptotic free stream value quite so readily.

Substituting typical initial vortex positions it can be seen that from the blocks at incidence a flow parallel to the ground results while the cambered blocks produce an almost vertical motion. It does not explain why in the case of the blocks at incidence an increase of span raises the vortex location when the opposite would be expected. Similarly the slight increase in core position as the vortex moves downstream is not predicted. This characteristic has been noted for aircraft vortices near to the ground by Dee and Nicholas (55), and Harvey and Perry (56) subsequently showed that the vortex rise could be due to a secondary separation on the ground. There is little evidence of separation in these wake flows, but a distinct thickening of the boundary layer on the ground is apparent. To examine this further, a series of measurements were taken with the Kiel probe close to the ground and aft of block 2N set at six degrees incidence and 2.5 mm ground clearance. Total head contours are shown in Figure 93 for downstream stations $x/t = 1.5$, 2.25 and 3.75. At the station nearest to the block base a separation region is apparent, extending over most of the model span. It does not include the central part of the wake which explains why it was not noticeable on the pressure measurements. The separation is most likely to arise from the expansion of the flow aft of the recirculation region although it is possible that it is the last stage of the reverse flow bubble. It is unlikely to be a spurious pitot measurement due to an acute local flow angle because these are not expected at such a location. By the next station the separation has spread outwards under the growing vortex and while more pronounced is of generally less extent. It disappears by the final station which is, in any case, between the stations used for the pitot rake measurements. Having established that a limited separation takes place there is no reason to suspect that it is either a product of the vortex or that it produces a rise in the vortex position.

With regard to the flow periodicity, it is unclear whether this arises from the shedding of a vortex ring along a vortex tube structure formed by the trailing vortex elements or whether the trailing vortex sheets roll into a pair of trailing vortices which then process downstream in a helical fashion. Levy and Fosdyke (57) have shown that the latter is stable while an earlier paper showed the former mode to be unstable. The increasing order shown by the flow as it progresses downstream might

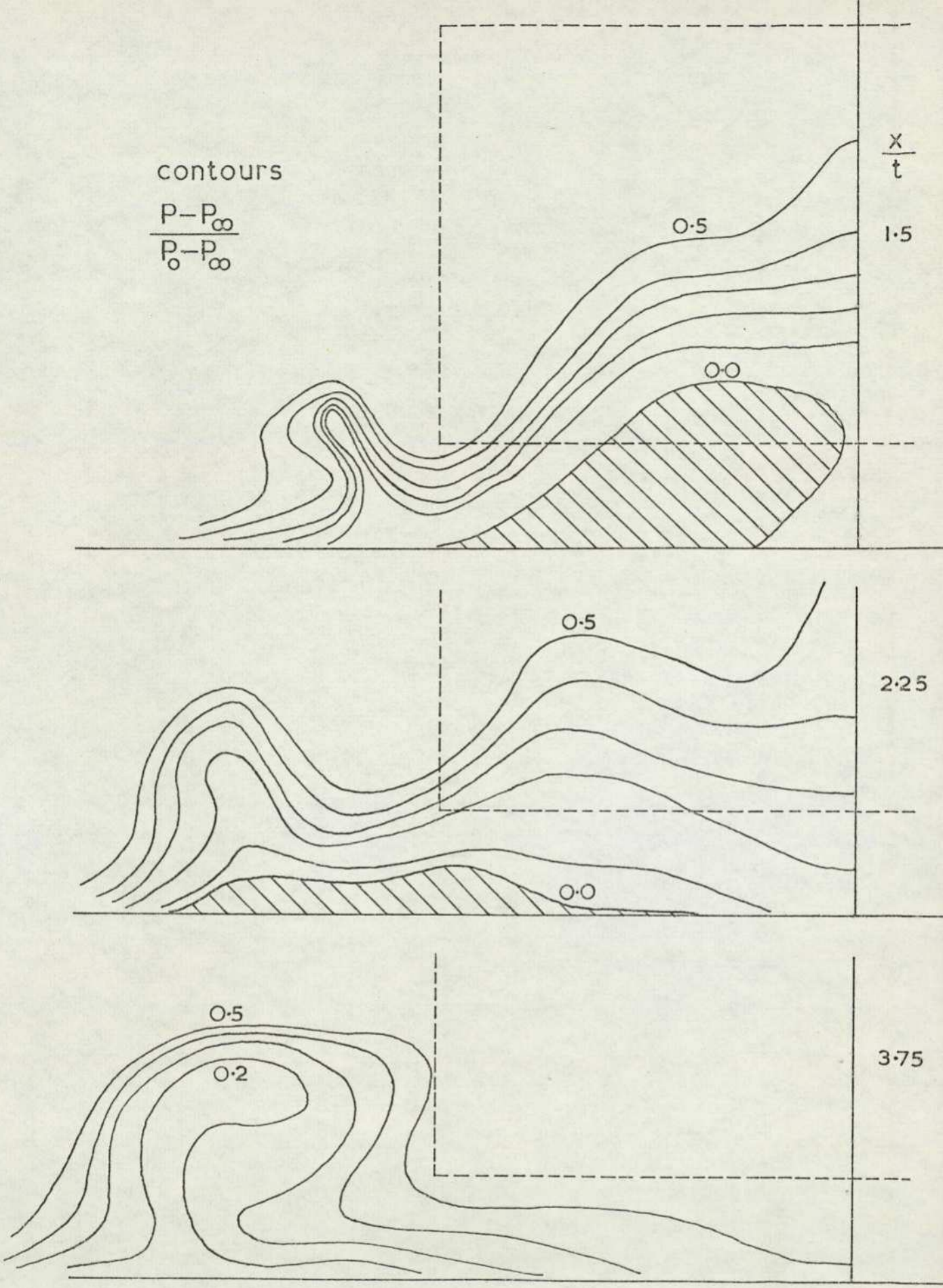

FIG. 93 PITOT CONTOURS OBTAINED FROM KIEL PROBE MEASUREMENTS, SHOWING SEPARATION REGIONS. BLOCK 2N, $\alpha = 6^\circ$ $Z_o/t = 0{\cdot}25$

then indicate that the helical structure is formed, but detailed correlation measurements would be required to verify it.

4.4 Road Vehicle Wakes

4.4.1 Introduction

A few very brief studies of road vehicle wakes have been reported. Lind Walker (59) inserted a paddle wheel arrangement in the trailing vortex of a saloon car and obtained a figure for the trailing vortex strength. An induced drag term was then deduced. A similar device was later used by White and Paish (28) in a study of the lift forces on cars. The lift obtained from the wake measurements was often quite different from that recorded on the force balance under identical tunnel conditions. It was also found that differences in the rotational speed of the paddle wheel existed between tunnel and road tests, but these were consistent. An interesting finding was the narrow spacing between the trailing vortices. In all cases this was found to be less than half the car width and it reduced with vehicle lift. Pothoff (19) in a determination of the induced drag of model vehicles near to ground also used a rotating vane device. In addition a tuft grid was placed downstream of the model to locate the vortex cores. The spacing between the vortex cores was found to increase sharply as the ground was approached, the shape of the body having little significance. Away from the ground, however, the car shapes produced vortex spacings considerably lower than those found for a streamlined shape; the latter being approximately that predicted for an elliptical load distribution. For one of the road vehicle models, considerable differences were found between the two methods used for finding vortex position. Finally P ringham and Bowman (60) have recently reported some exhaust flow studies using both model and full scale vehicles. The influence of exhaust pipe geometry on the entrainment of exhaust gases into the near wake was established.

The techniques employed for this study of road vehicle wakes were a combination of those previously described in sections 4.2 and 4.3 and in addition a small rotating vane and a yaw probe were used. The procedure adopted was also similar to that used previously.

Pitot contours were used to define the vortex core and traverses were then made horizontally and vertically through this point with the hot wire anemometer, the yaw probe and the rotating vane. Additional traverses were made vertically along the wake centre line.

Whereas the rotating vanes used in earlier investigations were of the paddle wheel type the vane used here was a simple cylinder. The cylinder was 2mm diameter brass tubing, 25mm long, and the axis of rotation was normal to the cylinder at its mid length. For a bearing a 1mm diameter tube was inserted along the axis of rotation and the vane rotated about a short length of piano wire which was mounted to the traversing gear. To measure rotational speeds a stroboscope was used, while the vane had one arm painted black and the other silver to avoid elementary counting errors. The surface condition of the vane had a pronounced effect on speed of rotation. A couple of small burrs on the end of the vane were found to induce a rotational speed of 1500 revolutions per minute, when the vane was mounted in the free stream. After removal of the burrs the speed dropped to 60 r.p.m, but difficulty was experienced in reducing this figure. Only very few measurements were obtained with this device.

The yaw probe was of the two hole type, ensuring that the distance between the orifices was kept to a minimum. The probe was made from two 2 mm diameter tubes with the ends chamfered at 45°. The difference in the two pressures, p_1 and p_2, is a measure of the flow angularity. Provided that the flow angles in both pitch and yaw are less than about 15° then the flow angle, ψ, in the plane of the probe holes is given by

$$\psi = k \frac{p_1 - p_2}{P - P_\infty} \qquad (4.6)$$

where k is found from the probe calibration in a uniform stream. The value of P is the local total head as measured separately using the pitot rake while the assumption of uniform static pressure, P_∞, continues. According to Bryer and Pankhurst (53) the effect of stream turbulence on the determination of flow direction is small for this type of probe. The influence of shear cannot, however, be so readily ignored, although no attempt is made to correct for it. This is justified where the total velocity gradient in the plane containing the probe orifices is small, which is true in all cases to be studied, except possibly where radial flow components are considered.

Unless otherwise stated all the following measurements were taken at a nominal tunnel speed of 30 m/s.

4.4.2 Wake measurements

In this section the wake data obtained for the passenger cars, the lorry, and the Can-Am racing car, is presented. As with all previous wake measurements these vehicles were mounted at the forward ground board location. The distance from the leading edge of the ground board to the vehicle nose was in all cases close to 0.40 m. It has been shown in section 3.2.2 that this change of location has a negligible influence on the conditions prevailing upstream of the model. The distance between the trailing edges of the model and the ground plane is then approximately 0.75 m although in only one case, the large lorry model, was a measuring station taken beyond 0.45 m aft of the model. The influence of the ground t.e. can be ignored. The model mounting strut was 10mm diameter and as with the rectangular blocks was offset 25mm from the model centre line. The height of the model was adjusted so that the clearance between the wheels and ground was always 1mm. As before the origin of the wake axes is taken as the point on the ground board that is directly beneath the centre of the model trailing edge.

The pitot pressure contours are shown for six passenger car shapes in Figures 94-99. Measurements were made at six downstream stations in each case extending four and a half model heights into the wake. The wakes are presented in order of increasing lift. The estate car with nearly zero lift shows a disturbance arising from the upper longitudinal roof edges, which could arise from the slight negative flow angle in the stream. As the lift increases the downwash at the centre of the wake increases and the saloon car shows a distinct vortex pair structure. The fastback models display an increasingly pronounced vortex pair dominating the wake. The roof generated vortices appear well inboard for these shapes; the displacement increasing with decreasing rear roof slope. The distance between the main vortices increases at the same time. In all cases the wake form is similar to that of the cambered rectangular models, the vortices move downwards on travelling downstream but exhibit negligible lateral motion.

To represent the effect of a cross wind, three vehicle models were set at yaw. The saloon 1 model was yawed 5,10 and 15 degrees and pitot contours obtained at three downstream stations in each case,

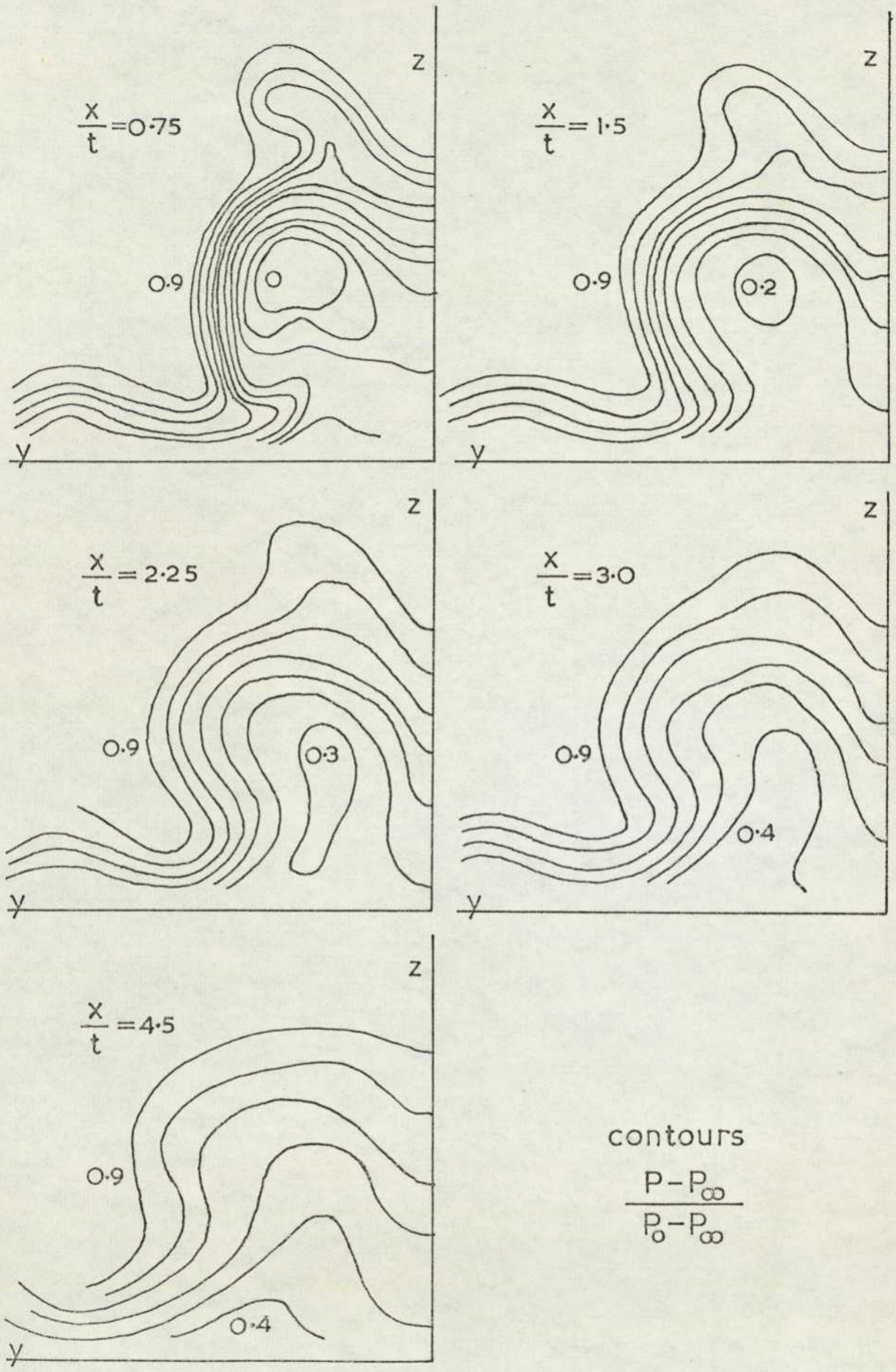

FIG. 94 PITOT CONTOURS — SALOON 1

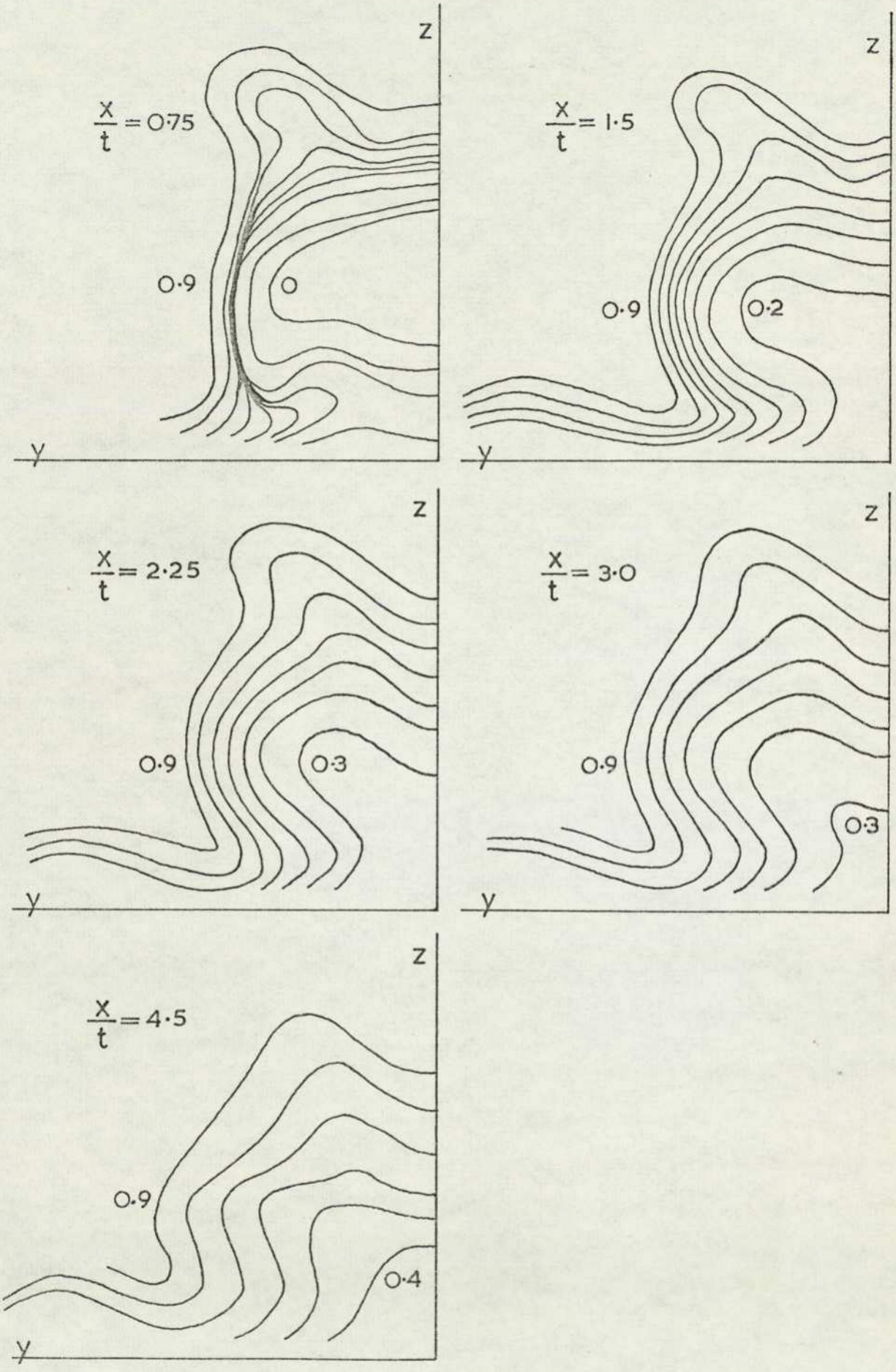

FIG. 95 PITOT CONTOURS — SALOON 3

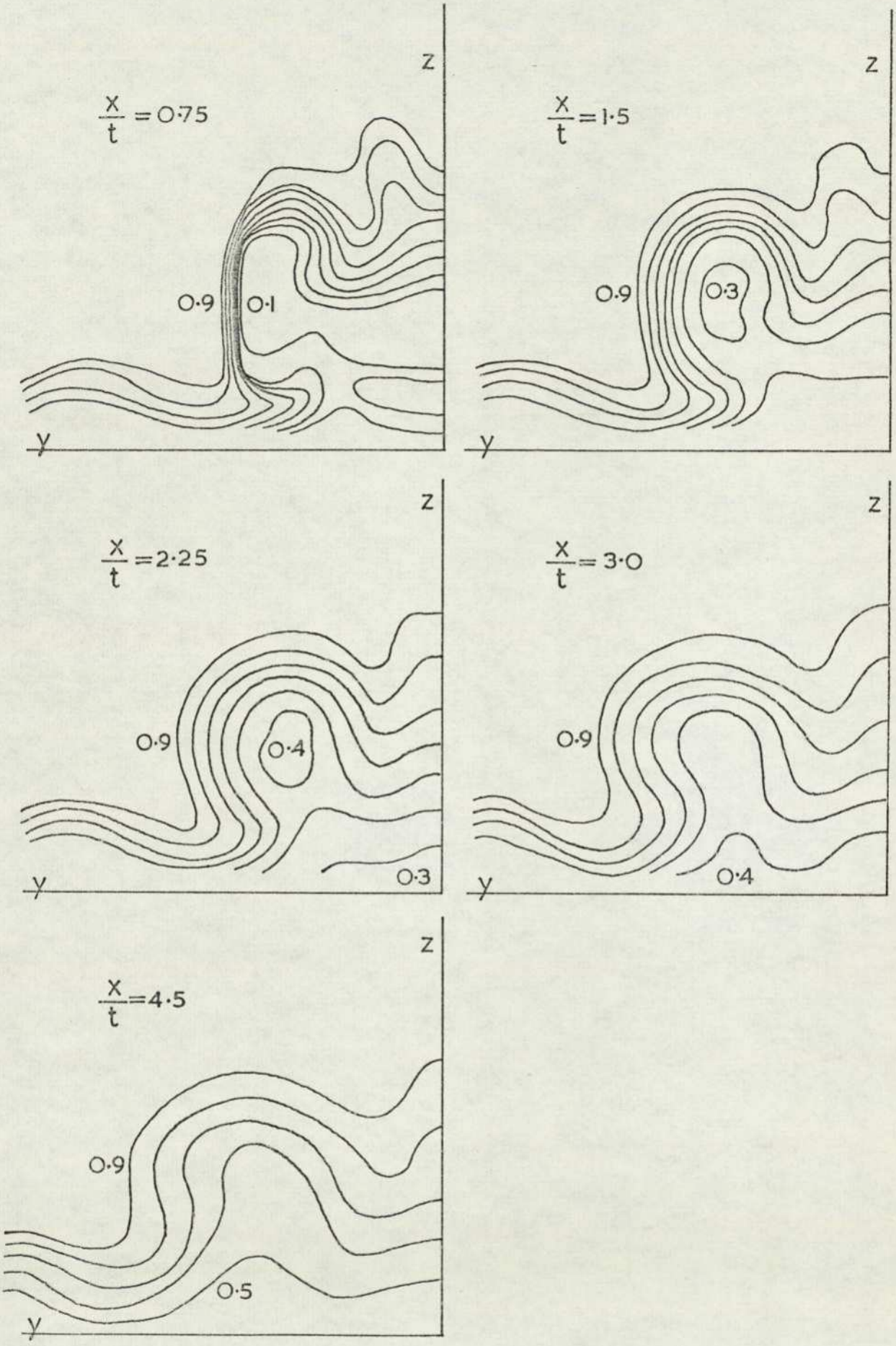

FIG. 96 PITOT CONTOURS — FASTBACK 1

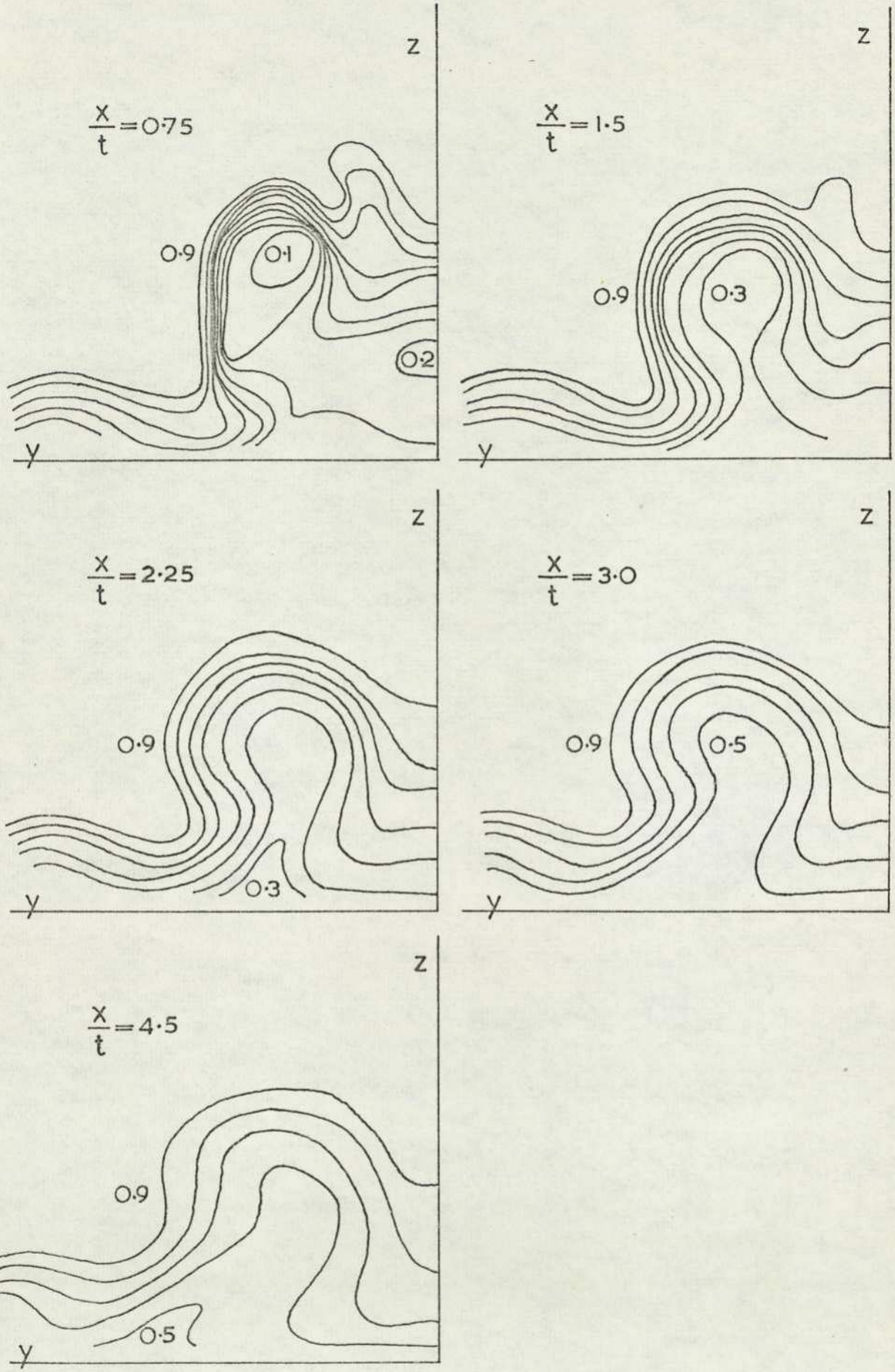

FIG. 97 PITOT CONTOURS — FASTBACK 2

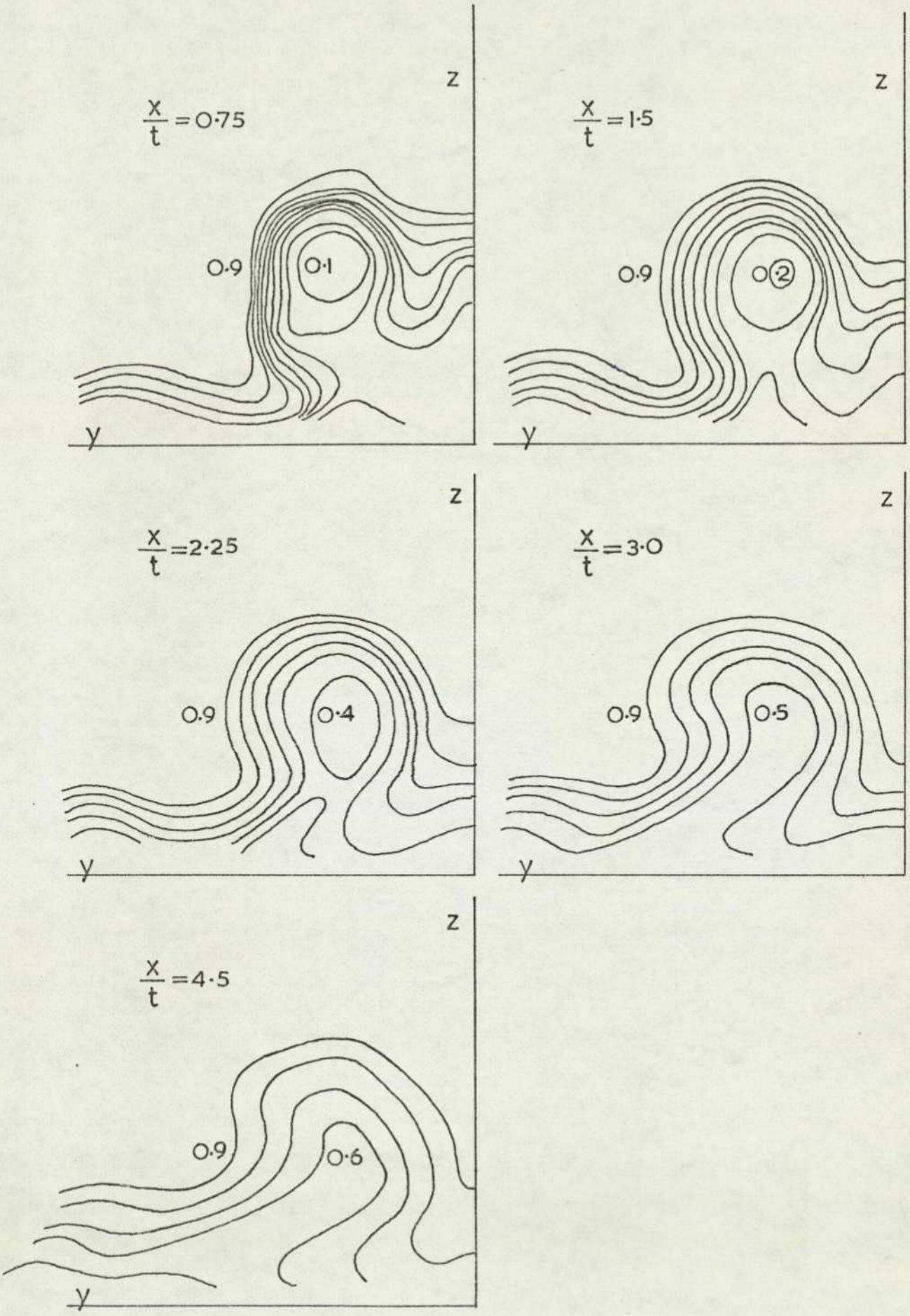

FIG. 98 PITOT CONTOURS — FASTBACK 3

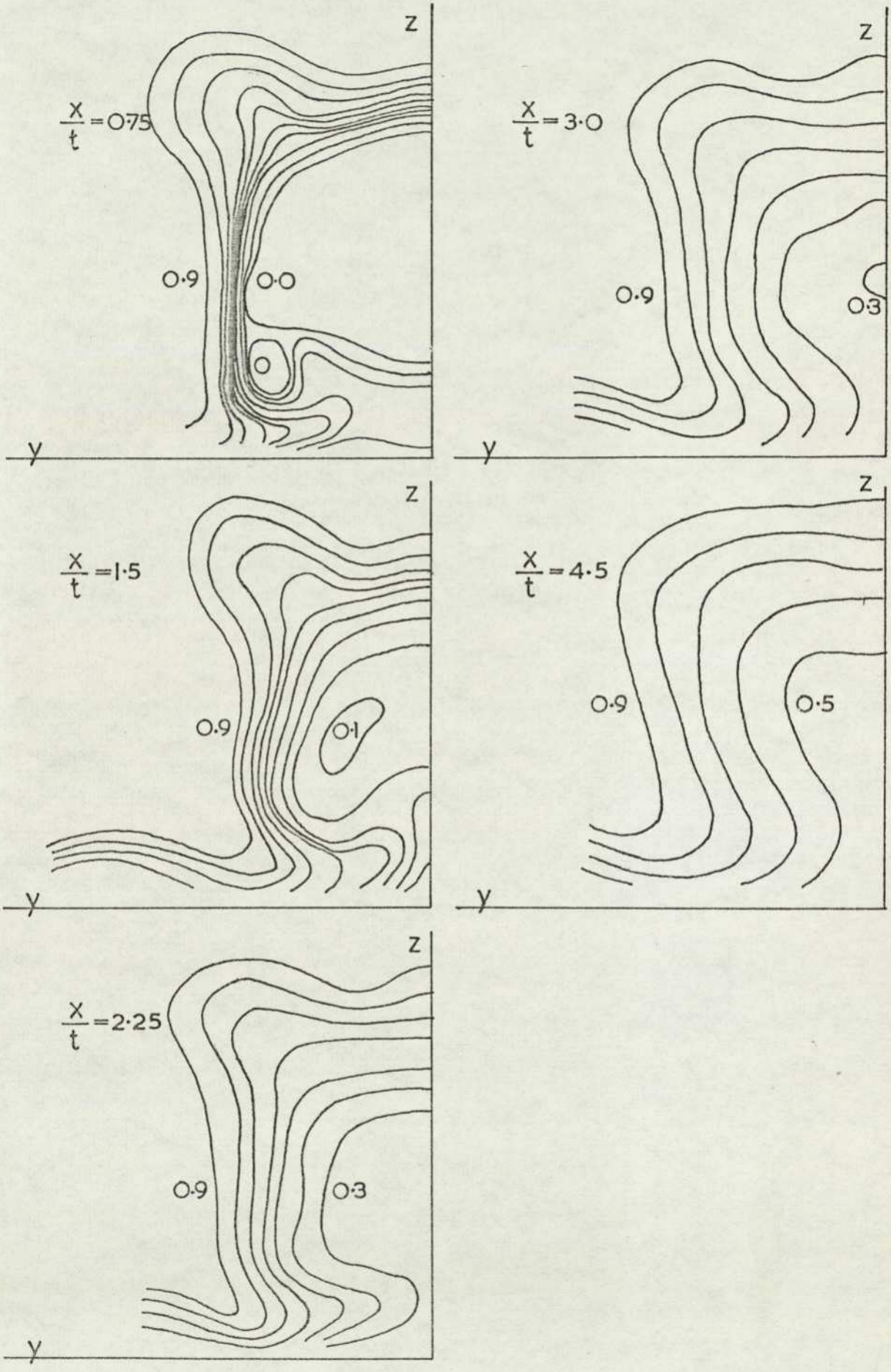

FIG. 99 PITOT CONTOURS — ESTATE 1

Figure 100. The origin of the wake represents the point directly behind the centre line of the base on the ground board and in the direction of the free stream. The wake is dominated by two vortices. The vortex on the windward side, left looking towards the model, is essentially the same as that arising on the unyawed model. The lee-side vortex arises from the cross flow over the roof and by inference rotates in a similar direction to the first vortex. The right-hand vortex of the unyawed model has almost disappeared at five degrees of yaw. The lee-side vortex moves rapidly downwards on travelling downstream and the displacement increases with increasing yaw. Both vortices show a movement to the left, that is reducing the angle between the stream direction and the car axis. Similar measurements were performed on the fastback 2 and estate 1 models set at ten degrees of yaw; Figure 101. The estate car wake exhibits a very pronounced vertical motion of the lee-side vortex as it moves downstream, while this vortex for the fastback model becomes almost separated from the rest of the wake.

To represent a lorry shape the basic block 1 was given a different nose section to represent a lorry cab, and four crude wheels were added. The pitot pressure wake contours are shown in Figure 102 for three downstream stations. The intermediate station differs insignificantly from the wake contours measured on the rectangular block. The distortions in the sides of the wake could arise from flow separations but are more likely the result of longitudinal vortices forming downstream of the body corners. At the most upstream station a jet of air with velocity approaching that of the free stream emerges from underneath the vehicle but its energy is soon dissipated. As a comparison traverses were performed in the wake of the large lorry model which was later to be used for wake interference studies. This lorry was relatively higher and had better underbody and wheel simulation and the results are shown in Figure 139.

The racing car (Can-Am type) shape was tested without wheels as it was felt that these would not contribute significantly to the wake flow. The downstream position of the contours was measured from the trailing edge of the wing and the body height for normalisation was taken to be the maximum thickness of the body ignoring the wing. Figure 103 shows the pitot pressure contour. These differ noticeably from the saloon car wakes because the vehicle is generating considerably downforce. At the upstream station the separated reverse flow region extends to the

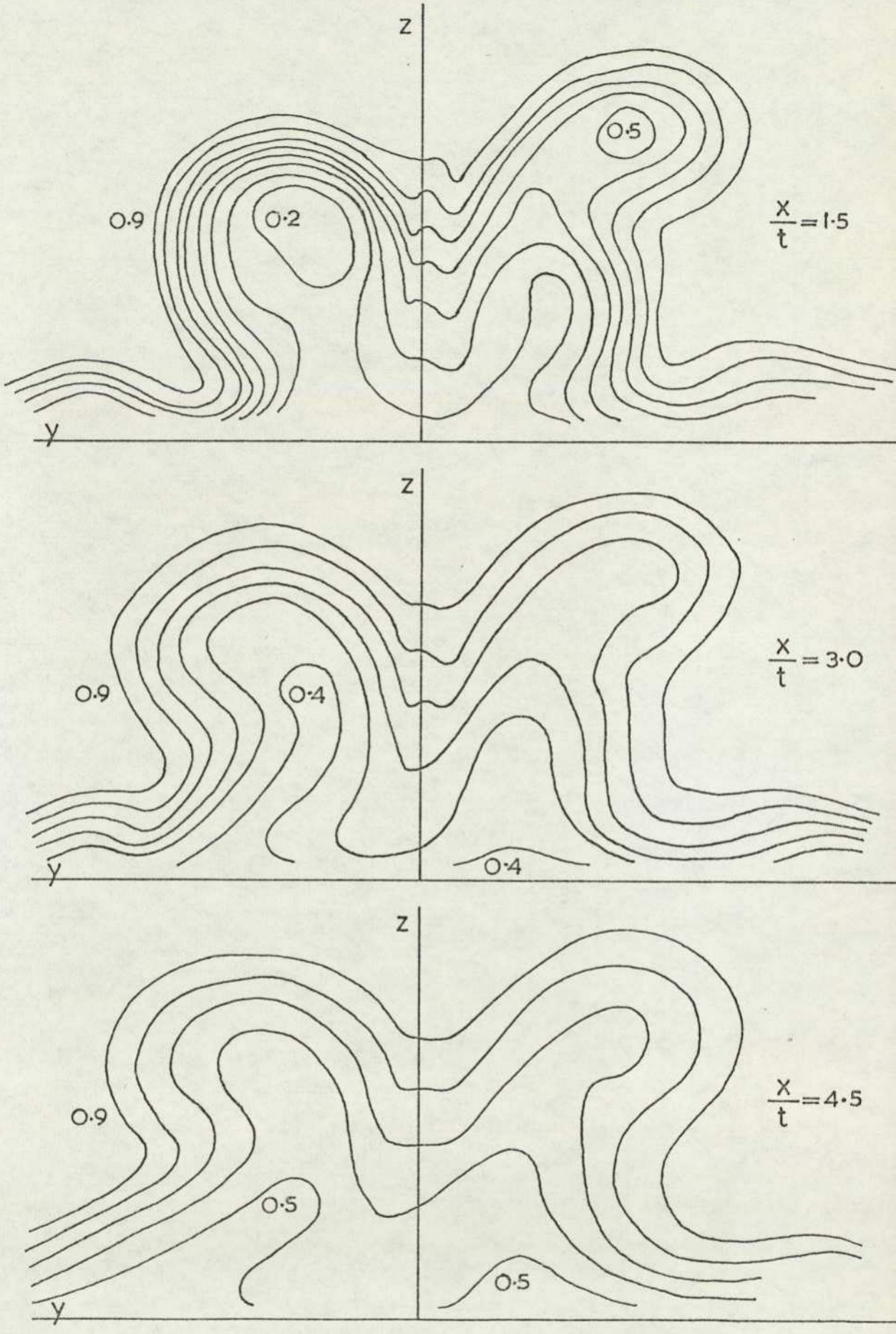

FIG.100 PITOT CONTOURS — SALOON 1 (a) 5° YAW

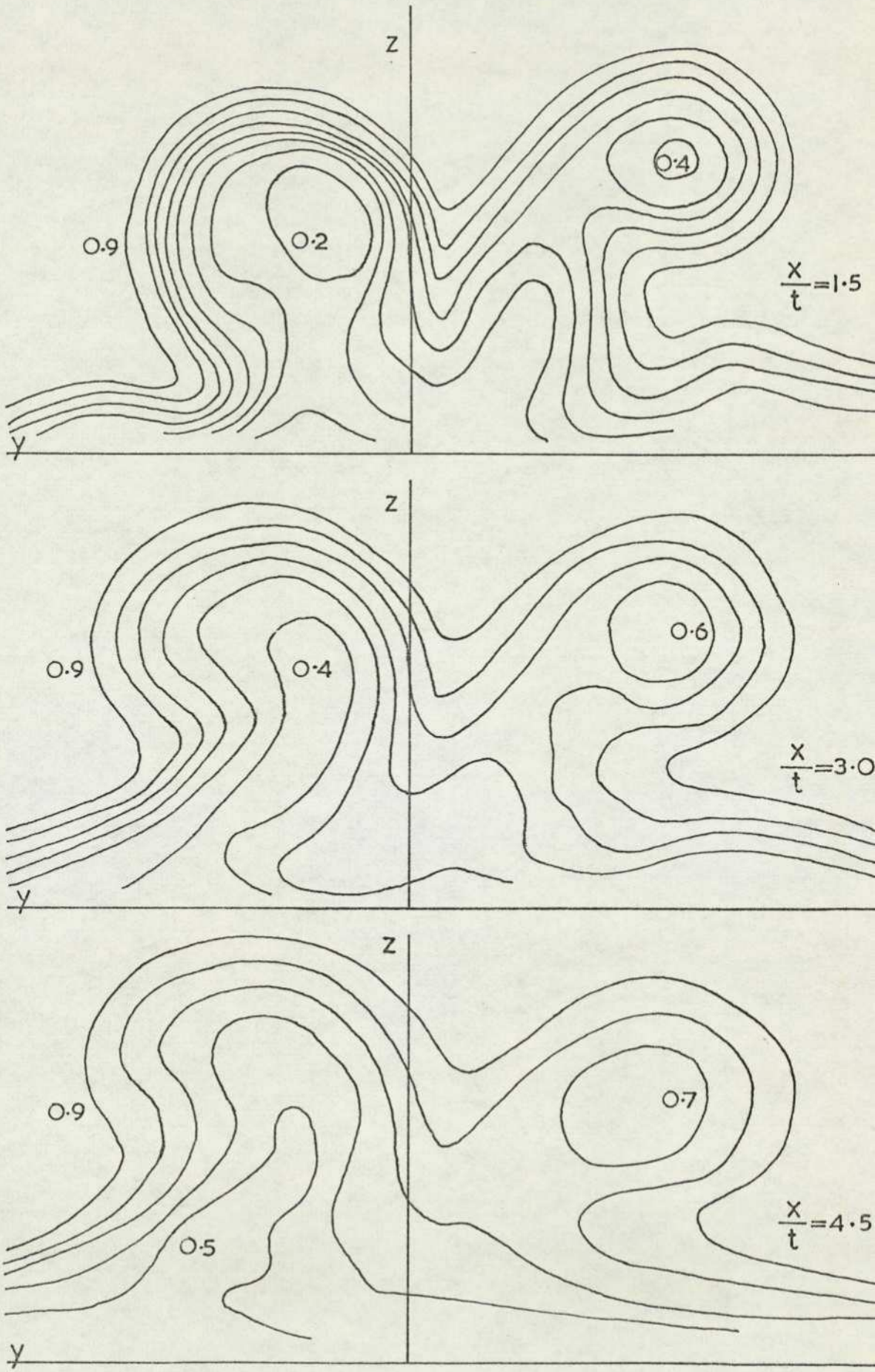

FIG 100 (b) SALOON 1, 10° YAW

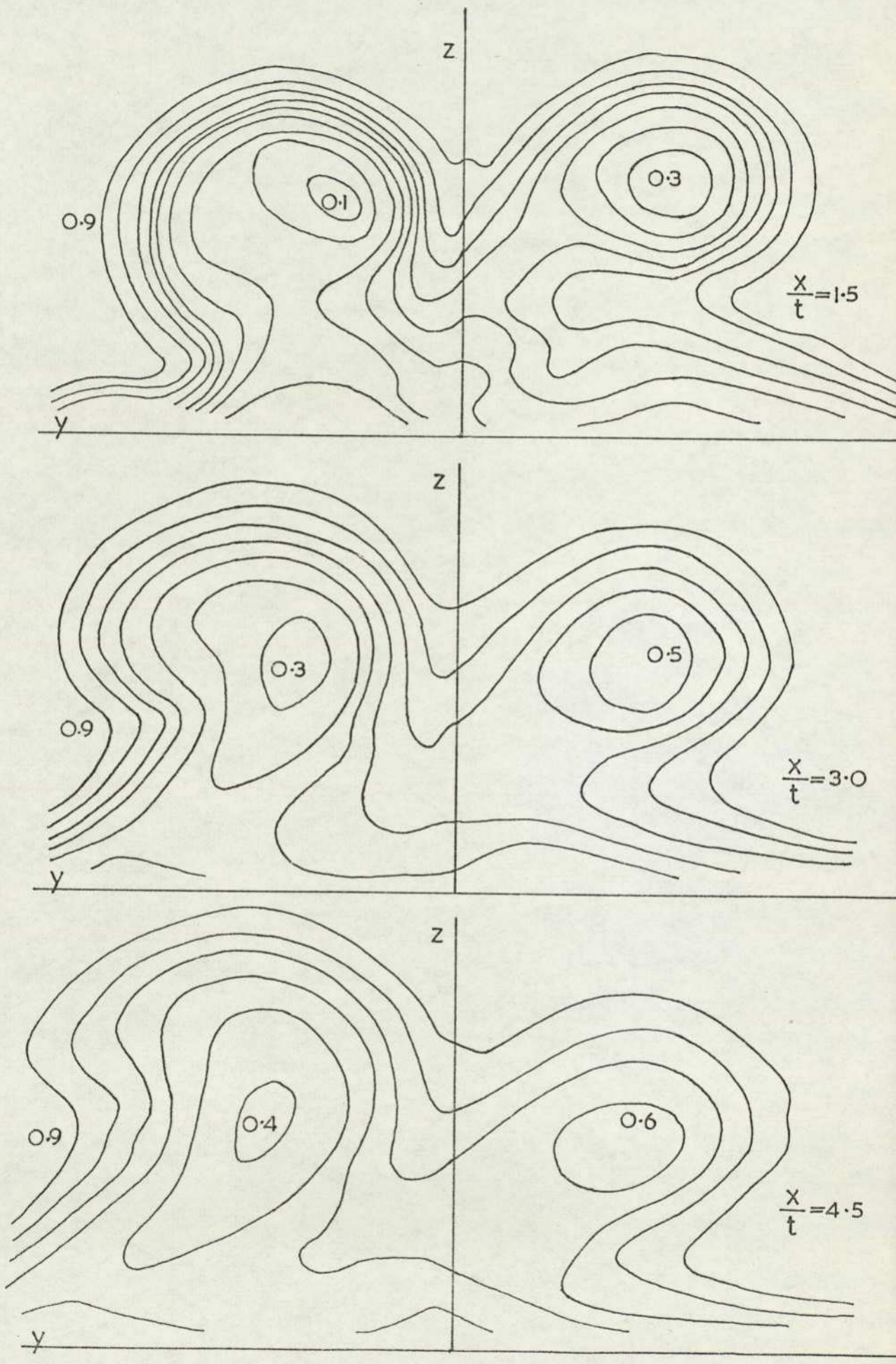

FIG. 100 (c) SALOON 1, 15° YAW

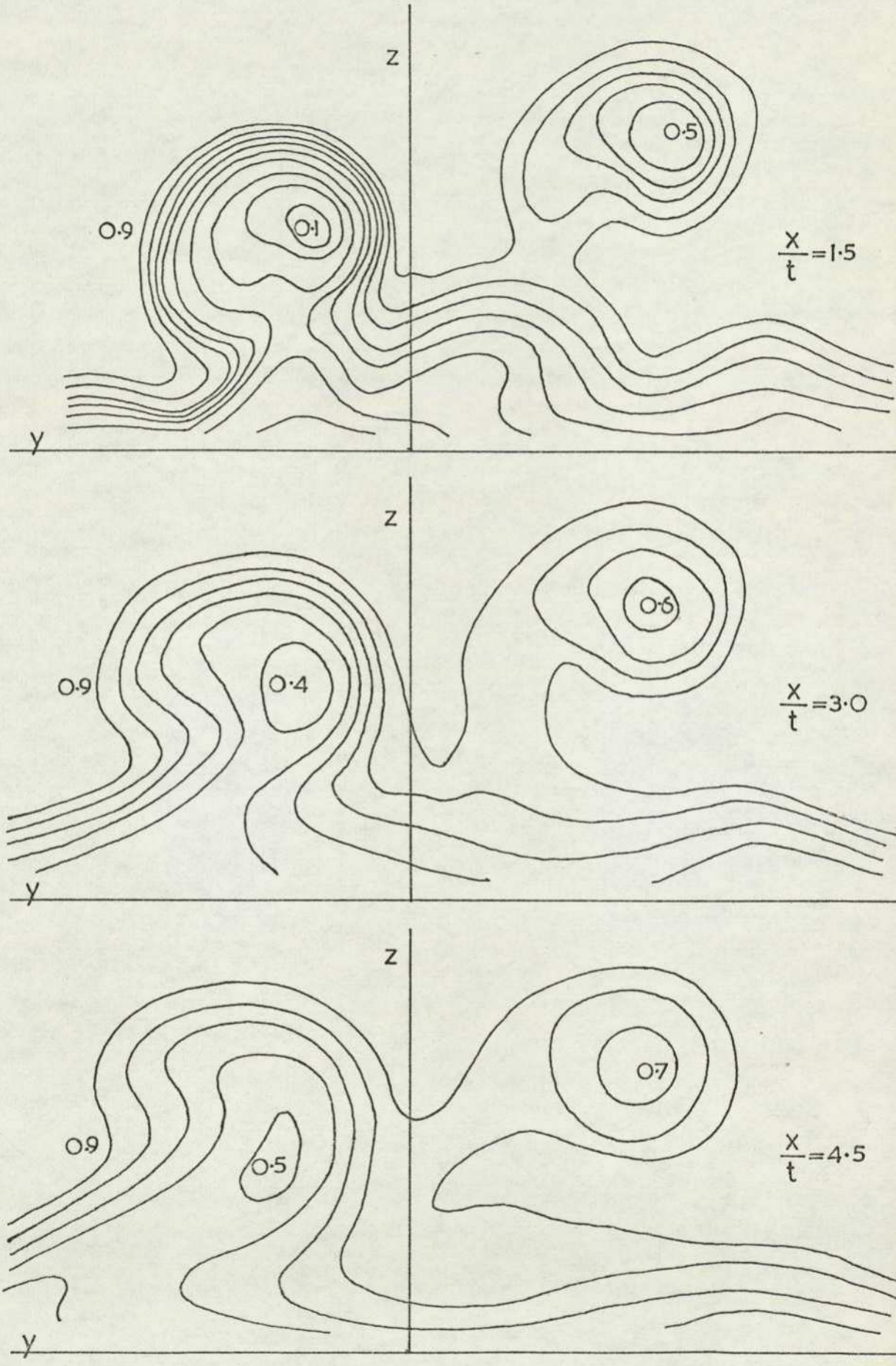

FIG. 101 PITOT CONTOURS (a) FASTBACK 2, 10° YAW

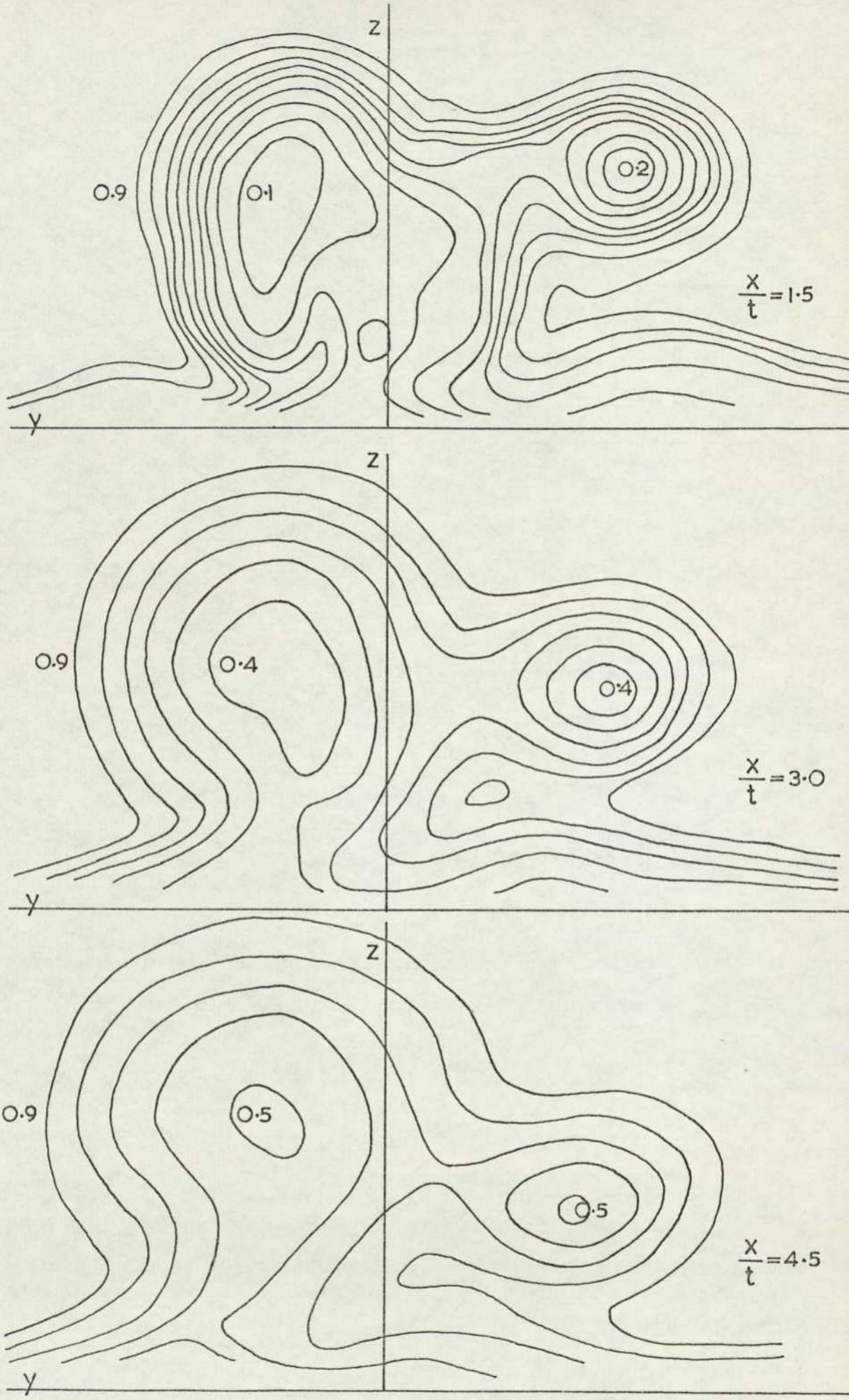

FIG 101 (b) ESTATE 1 , 10° YAW

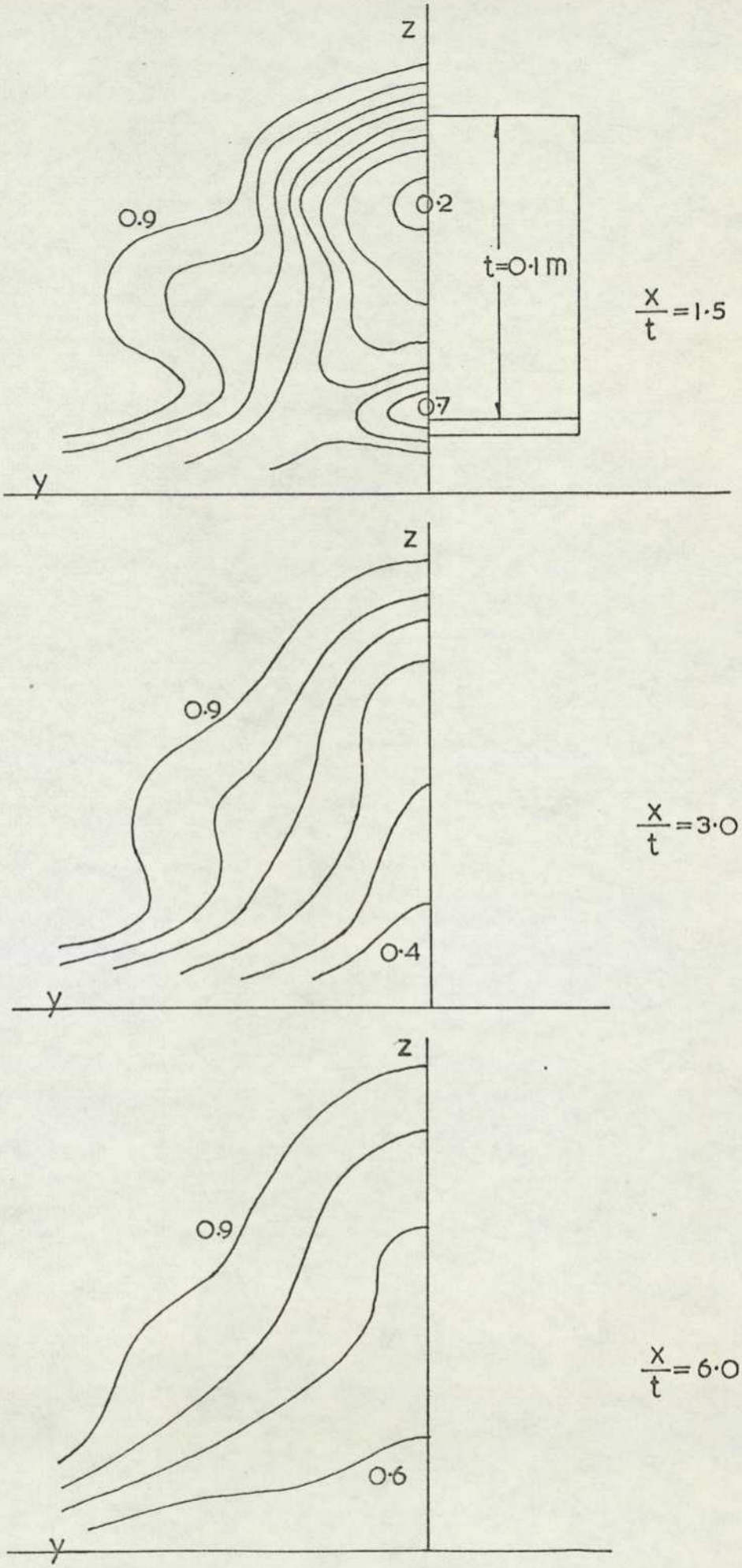

FIG.102 PITOT CONTOURS — SMALL LORRY MODEL

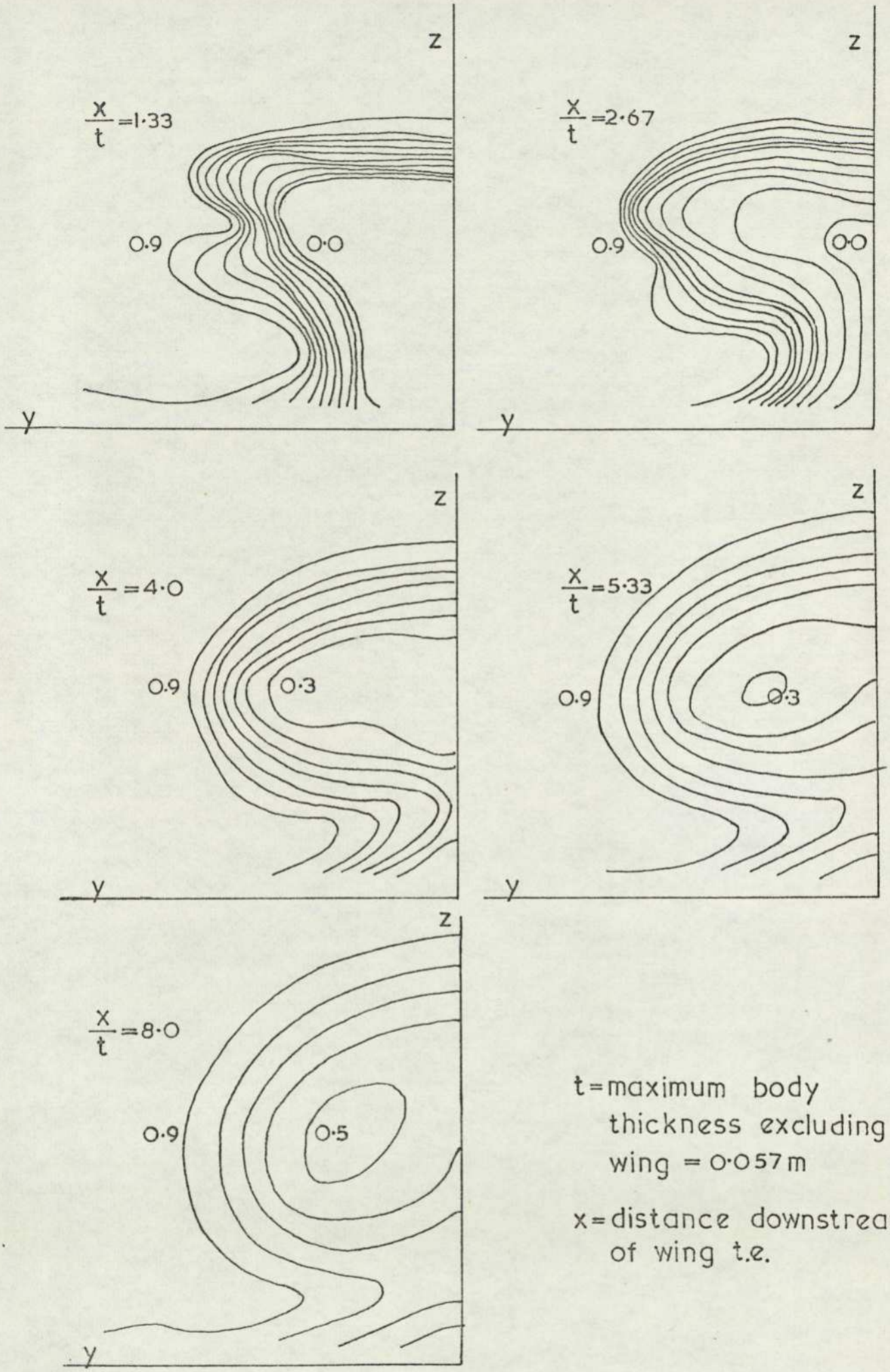

t = maximum body thickness excluding wing = 0·057 m

x = distance downstream of wing t.e.

FIG.103 PITOT CONTOURS — CAN-AM RACING CAR

ground plane and this persists to the following station. On moving downstream the wake centre moves sharply away from the ground although the vortices do not appear to shift noticeably. A slight asymmetry is apparent throughout these contours.

Base pressures were measured at the centre of the base for all passenger vehicles. As no static tapping was provided the pressure was measured by a static pressure probe taped to the model base with the single static hole facing upstream and opening onto a shallow hole drilled into the model base. These pressure coefficients, corrected by the MIRA system, are given in Table 3, below. It can be seen that the pressure is lowered as the roof canopy is moved aft. Note that the estate 2 model uses the same upper body as the saloon models.

Having established the existence of a trailing vortex pair for the saloon 1 and fastback models vertical and horizontal traverses were performed through the position of minimum total head using a temperature compensated constant temperature anemometer. Figures 104 to 107 show the mean velocity and turbulence intensity profiles obtained for the saloon and fastback models. Asymmetry between each trailing vortex is apparent in the horizontal traverses. A distinct minimum in the D.C. signal occurs in the region of the vortex core although this disappears on the vertical traverse at large downstream distance due probably to the effects discussed in 4.2.4. The horizontal distribution of turbulence intensity is dominated near to the base by a distinct pair of peaks either side of the velocity minimum. This feature persists throughout the wake, the spacing between the peaks increasing with distance downstream of the base. For the vertical traverse, only one turbulence intensity peak is apparent at most stations, and this occurs above the velocity minimum. A lower peak is noticeable at the most upstream station of the Fastback 2 and 3 models and there is a suggestion of the peak moving rapidly towards the ground.

In the case of the saloon car model more detailed traverses were performed at the station $^{x}/t = 2.25$ and from these contours of E/E_{∞} and e/E have been constructed, Figure 104. The d.c. output of the probe which is a measure of the longitudinal velocity component shows an almost identical set of contours to the pitot pressure results. Note that the pitot contour values represent velocity ratio squared while the d.c. output approximates the velocity directly. The peak

TABLE III: Base pressures - passenger cars

Model		$-C_{pb}$
Saloon	1	0.19
	2	0.185
	3	0.18
Estate	1	0.16
	2	0.17
Fastback	1	0.23
	2	0.23
	3	0.23

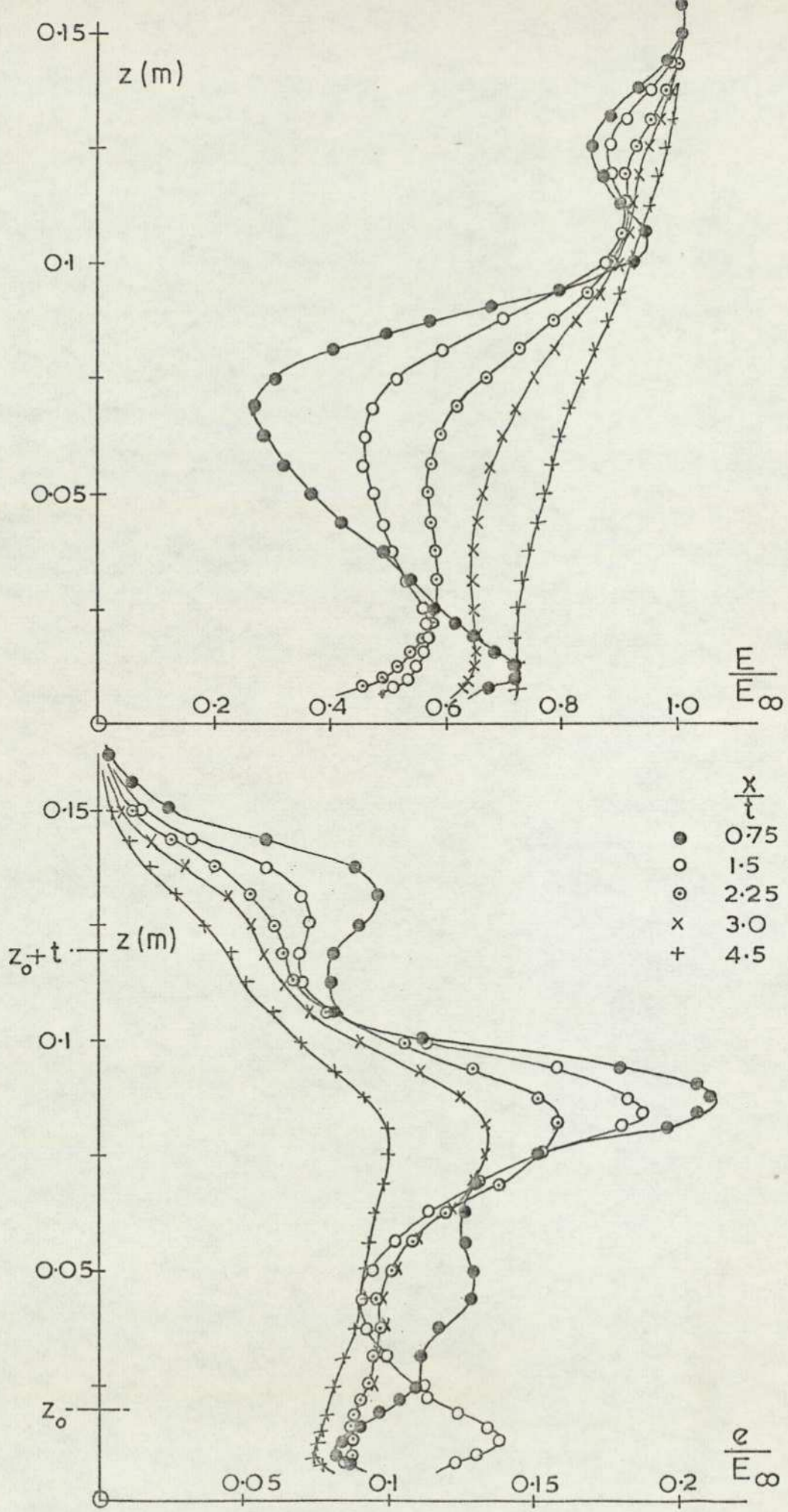

FIG. 104 TRAVERSES THROUGH POSITION OF TOTAL HEAD MINIMUM USING HOT WIRE ANEMOMETER

(a) SALOON 1, VERTICAL

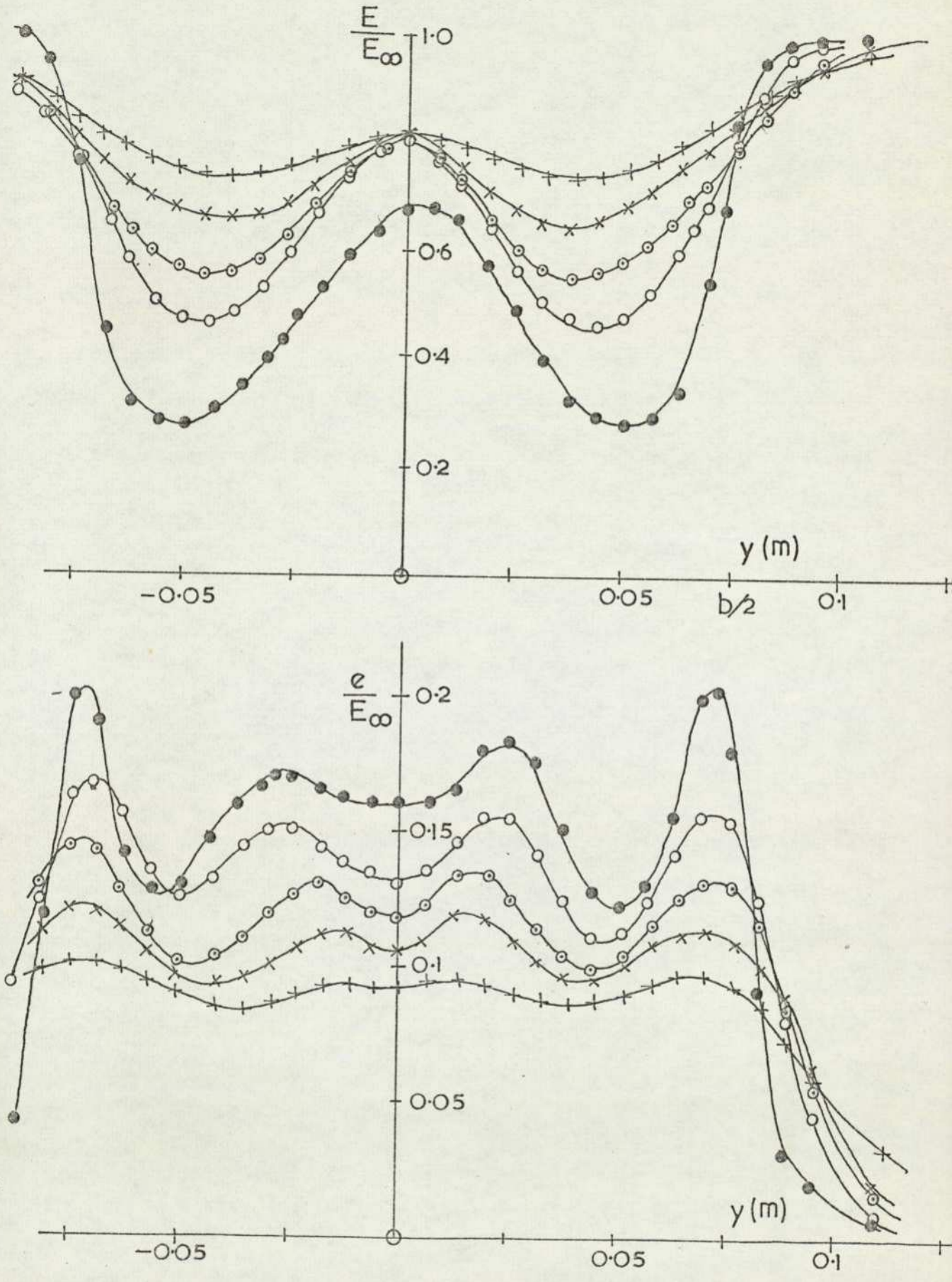

FIG. 104 (b) LATERAL TRAVERSE — SALOON 1

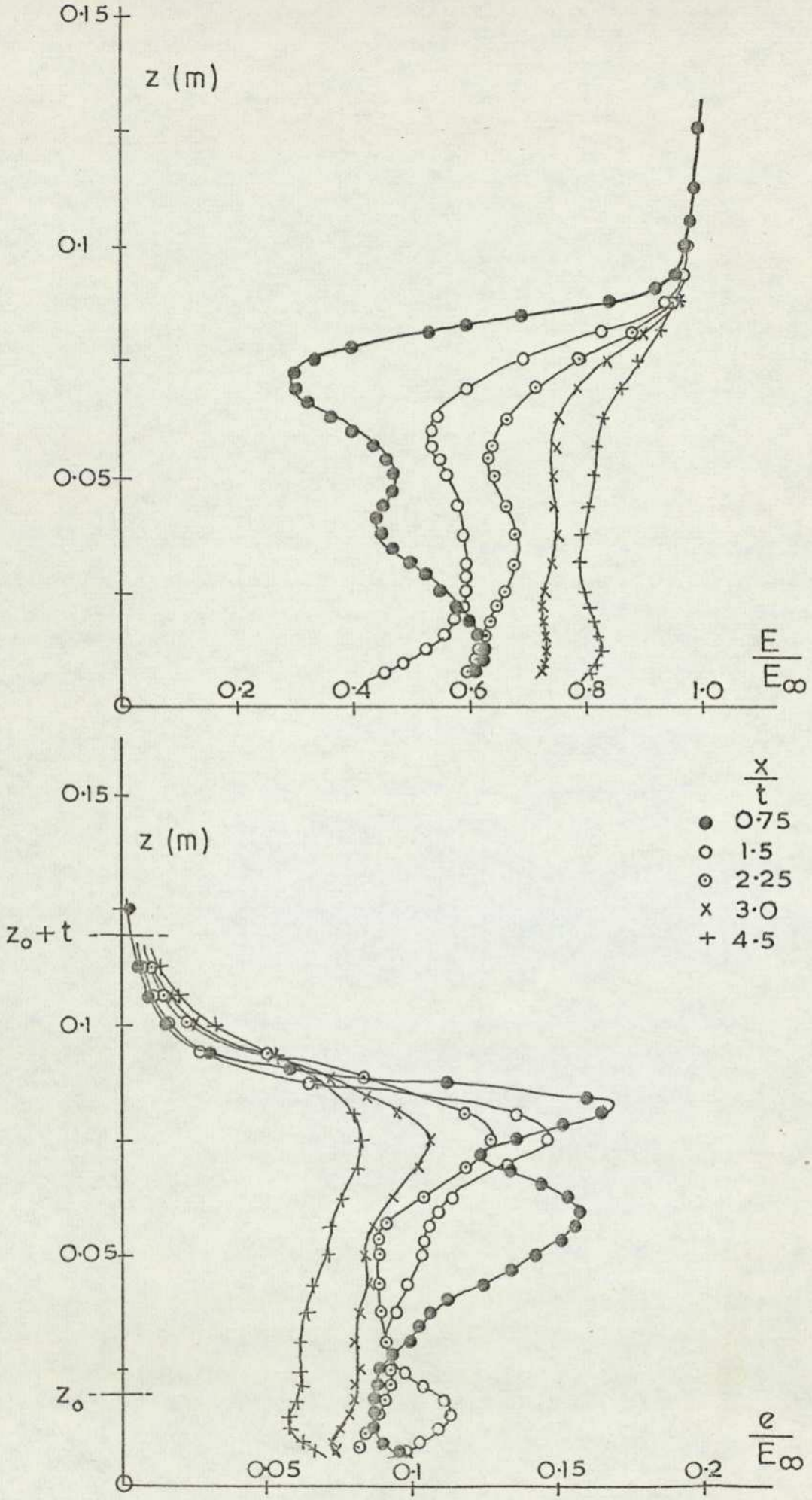

FIG.104 (C) VERTICAL TRAVERSE — FASTBACK 2

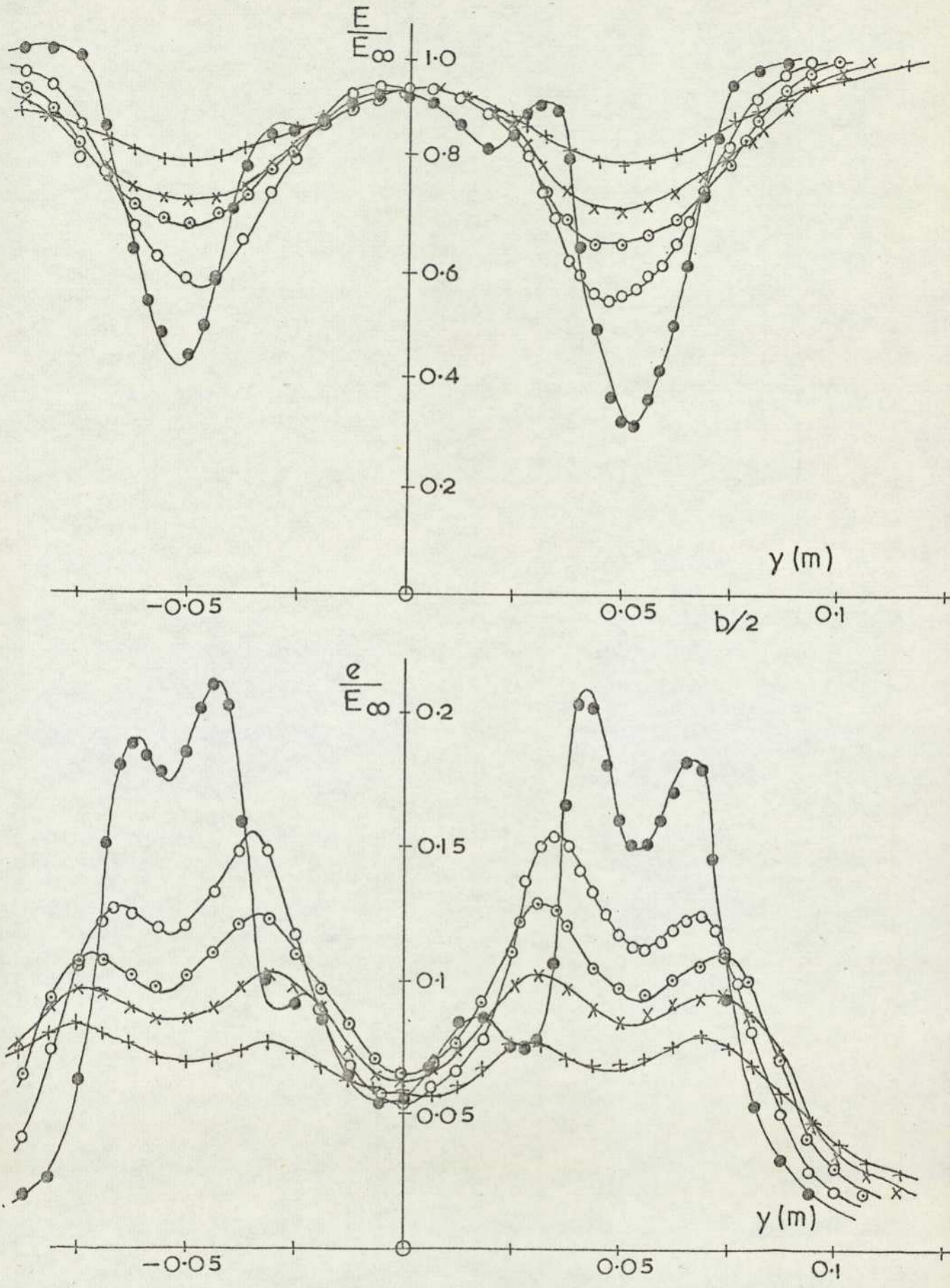

FIG.104 (d) LATERAL TRAVERSE — FASTBACK 2

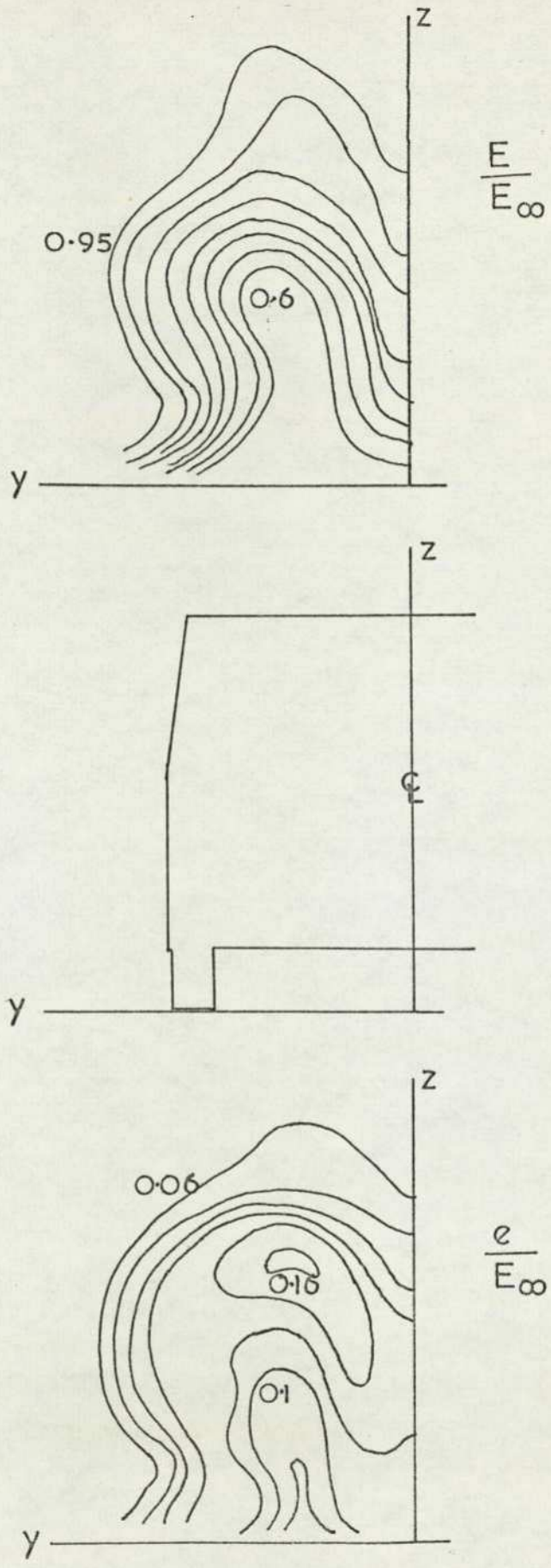

FIG.104 (e) CONTOURS $\frac{E}{E_\infty}$, $\frac{e}{E_\infty}$ — SALOON 1 $\frac{x}{t}=2{\cdot}25$

turbulence intensity occurs at the boot upper surface level, but a degree of symmetry exists about a line drawn from the origin through the vortex centre.

In addition vertical and horizontal traverses, through the minimum total head position, were made using a two hole yaw probe. Downwash and cross flow velocities at various downstream stations are shown in Figure 105 for the saloon 1 and fastback 2 models. Both cross flow curves show similar trends. In the saloon case the missing section of the curve for the station nearest to the base arises because the local flow conditions are outside the calibrated range and so do not give sensible results. At this same station an inward flow is apparent for both models adjacent to the ground surface. At the three stations furthest from the base, the cross flow at the ground is outwardly directed and appears constant for a particular model. In the case of the fastback model this velocity is one quarter of the free stream velocity. The downwash distribution for the saloon car shows a peak downwash at the centre of the two vortices as would be expected for a closely spaced vortex pair. For the fastback model the peak occurs off centre. In both cases the bias in favour of the downward component of flow would suggest that the vortex is moving downwards fairly rapidly.

A complete set of traverses was performed for the saloon car model at station $^{x}/t = 2.25$. From these the local velocity vector was determined and the flow is shown in Figure 106. The length of each arrow in the figure is equal to the local total velocity of cross flow and the direction is indicated correctly. The station is the arrow tail.

A few measurements were made using the rotating vane described in the introduction. The rotational speed of this device was never constant but fluctuated continuously over $\pm$ 5% of the mean reading with a period of approximately three seconds. Vertical traverses were made through the maximum total head deficit point at $^{x}/t = 0.75$ and 1.5, for the saloon car model, and a single horizontal traverse was performed at the latter station, Figure 107. At the upstream station a high level of vorticity is apparent at the roof level and close to the ground; both approximately equal in strength but opposite in sign to that of the main vortex. The former is evident in the pitot contours while the latter has shown up previously in the cross flow profiles. Both disappear at the next measuring station. Short traverses were performed at several

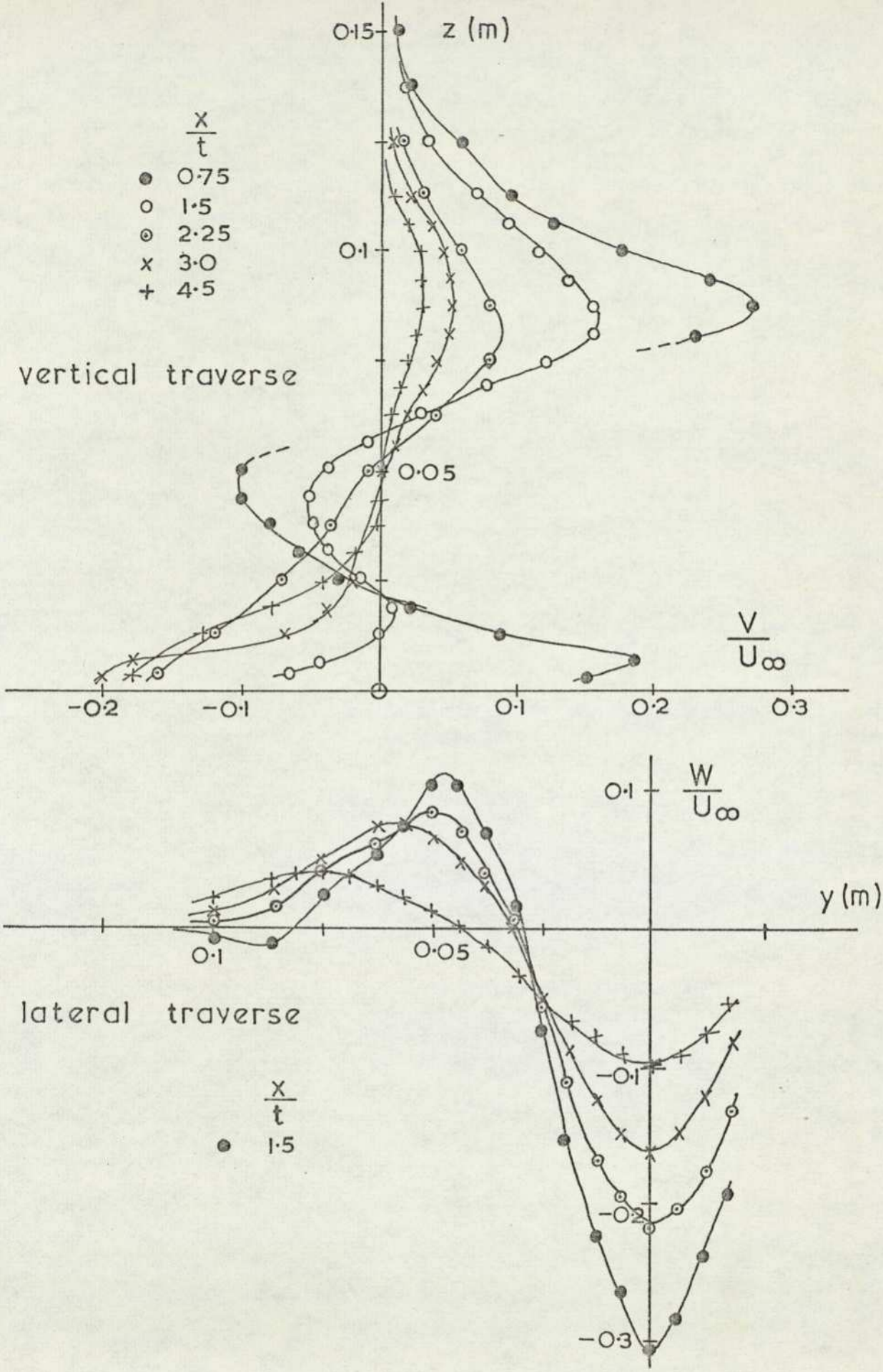

FIG.105 TRAVERSES THROUGH POSITION OF TOTAL HEAD MINIMUM USING YAW PROBE (a) SALOON 1

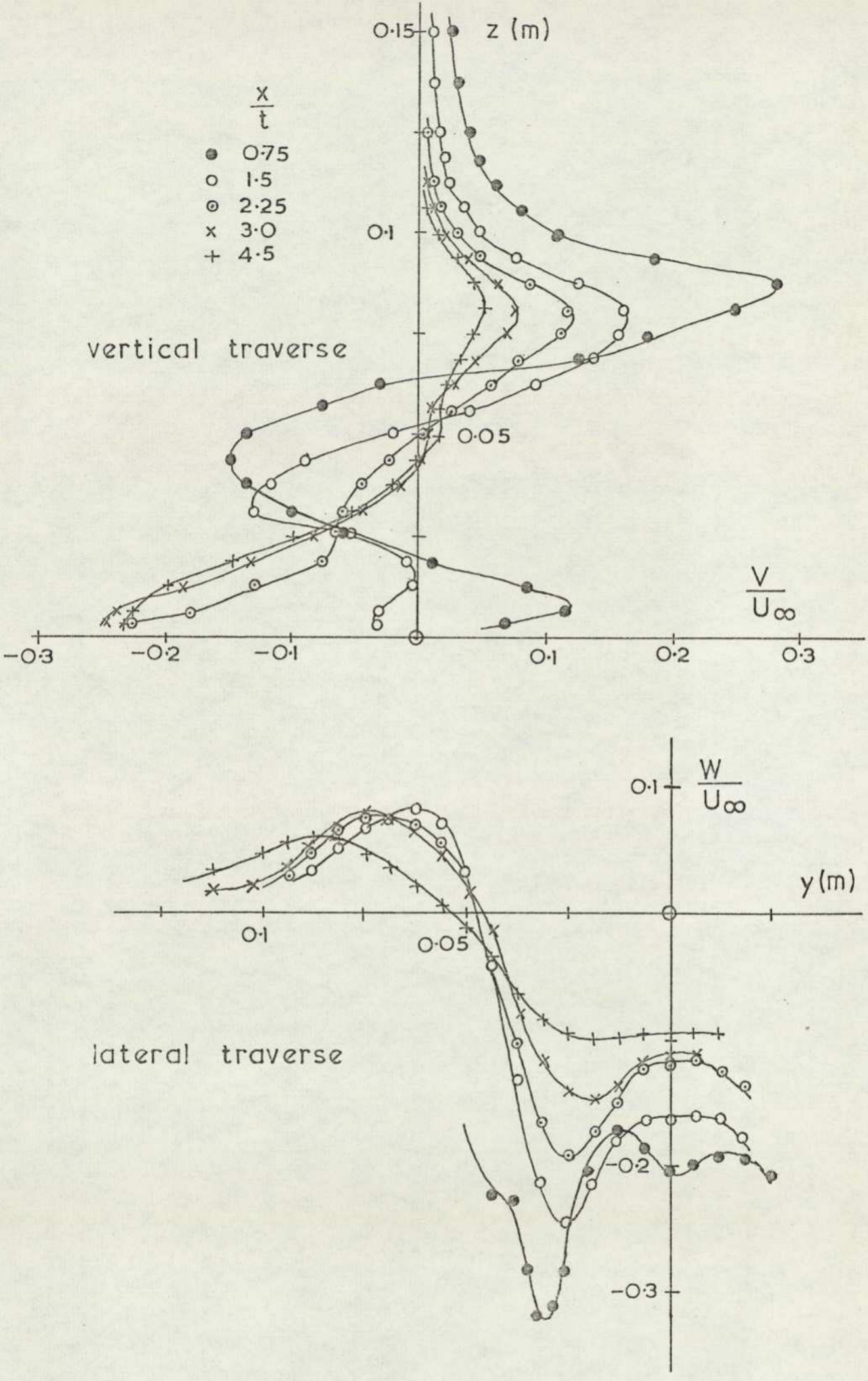

FIG.105 (b) FASTBACK 2

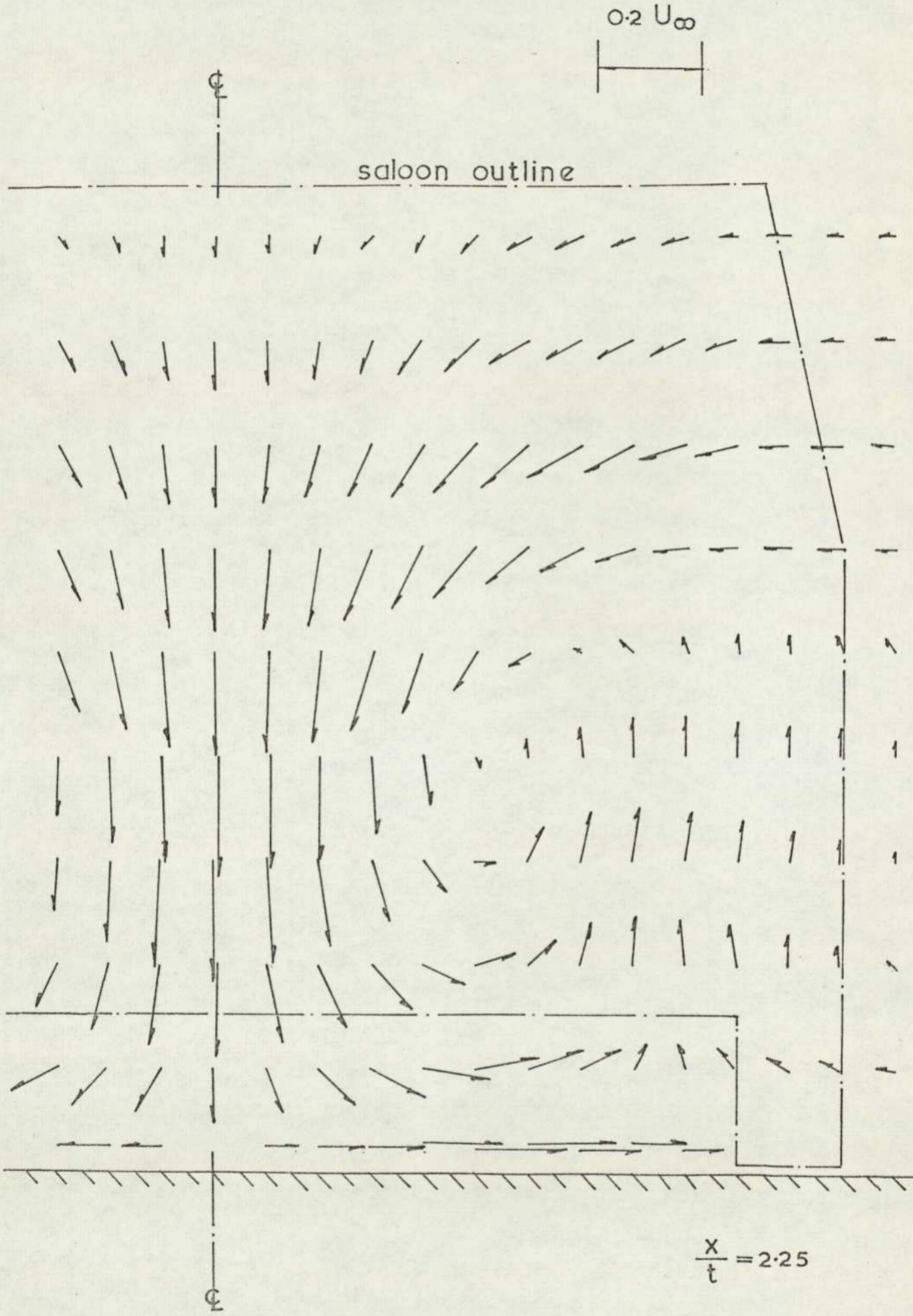

FIG.106 TRANSVERSE VELOCITY VECTORS SALOON 1

stations, for all car shapes that experienced significant lift, in the expected region of the vortex cores, to find the peak rotational speed. These are plotted in Figure 108 and it can be seen that all the results fall into a fairly narrow band while in general the rotational speed increases as the lift force. It was felt that the device was too crude to justify further measurement.

Vertical traverses along the wake centre line were performed for the saloon 1 and fastback 2 models, using the hot wire anemometer and the yaw probe, at the stations previously investigated. The anemometer results are shown in Figures 109 and 110. In both cases the wake adopts a typical boundary layer profile; the saloon profile being fuller than that of the fastback model as less of the wake is entrained by the vortices. The pitch velocities are given in Figure 111. At the upstream station both cars show an upward flow immediately above the ground plane but this feature soon disappears. The saloon car initially shows greater downwash velocities than the fastback model but this situation is soon reversed, and only arises because the peak downwash for the fastback model occurs off-centre.

The estate 1 car model, which experiences very little lift, has the maximum total head deficit occurring on the wake centre line. Vertical and horizontal traverses were performed through this point using both the hot wire anemometer and the yaw probe. The results of the traverses with the hot wire probe at stations corresponding to those used with the other car models are shown in Figure 112. The separated flow is clearly seen at the upstream station, but in comparison with the traverses behind the rectangular blocks, the lower surface vortex sheet, as defined by the turbulence intensity peak, is soon dissipated. Figure 113 shows the results from the yaw probe traverses. The vertical velocities on the centre line show an anti-symmetrical flow at $^{x}/t = 1.5$ with the flow converging on the wake centre. On moving downstream the flow is predominantly upward which is consistent with the slight negative lift force experienced. The vertical velocity distribution as obtained from the horizontal traverse shows a central upward flow changing direction on moving outwards. A single horizontal traverse to measure lateral velocity components was performed at $^{x}/t = 2.25$. This shows a distinct inward flow in the region of the vortex sheet.

A limited number of traverses were performed in the wake of the Can Am racing car; again using both probes. Vertical traverses

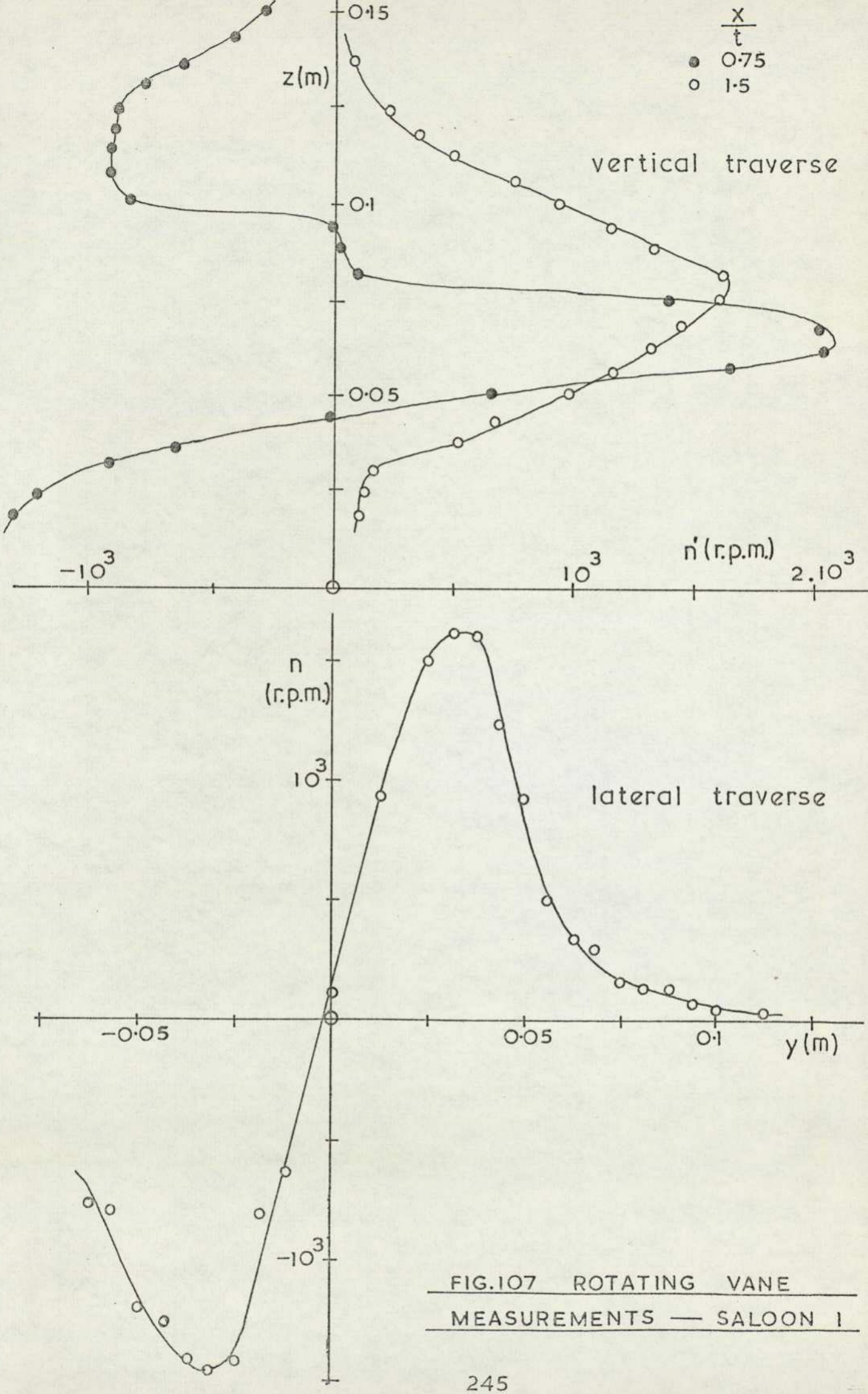

FIG.107 ROTATING VANE MEASUREMENTS — SALOON 1

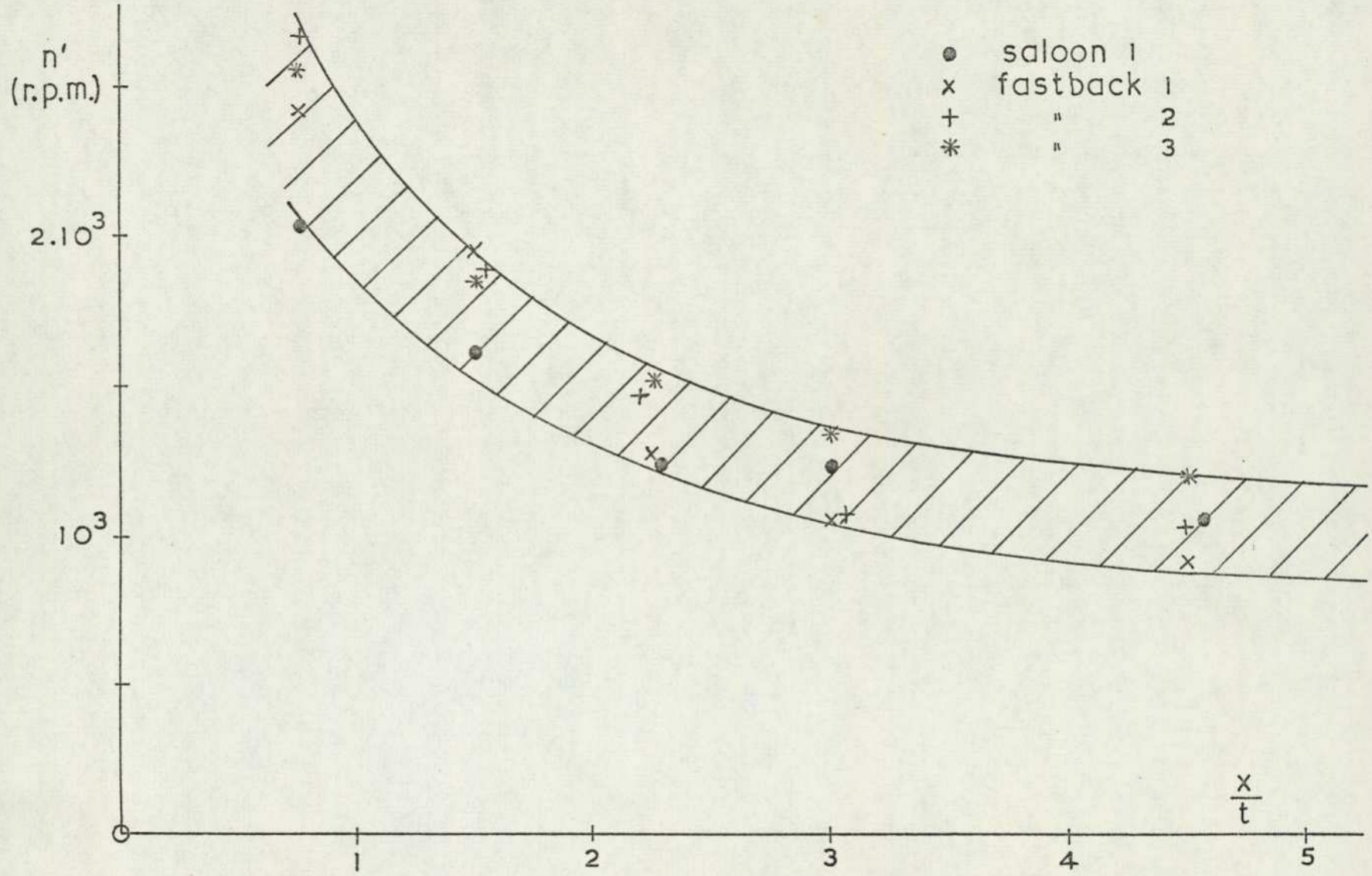

FIG.108 DECAY IN MAXIMUM ROTATING SPEED OF VANE

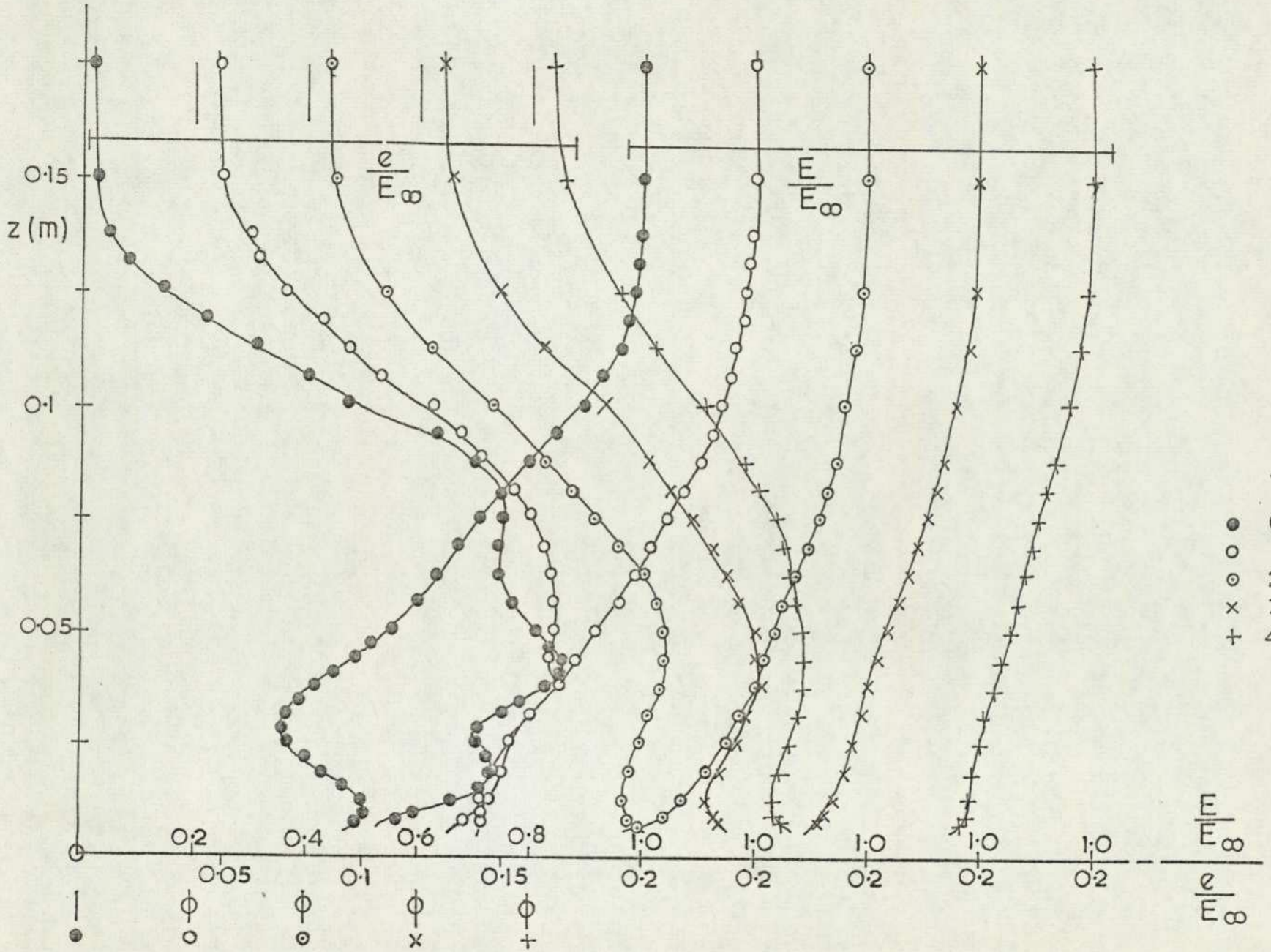

FIG.109 WAKE CENTRE-LINE TRAVERSES — SALOON 1

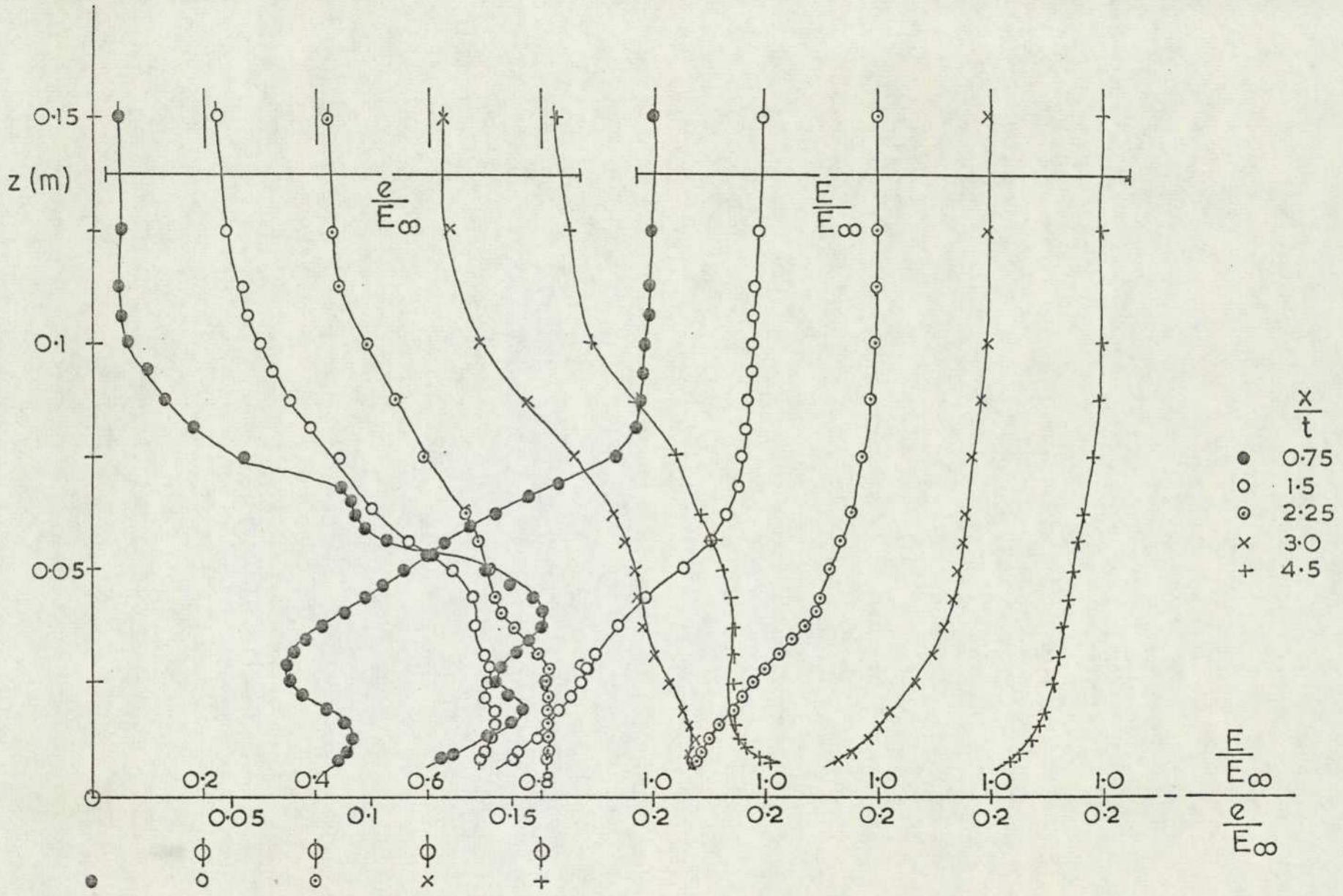

FIG. 110 CENTRE-LINE TRAVERSES — FASTBACK 2

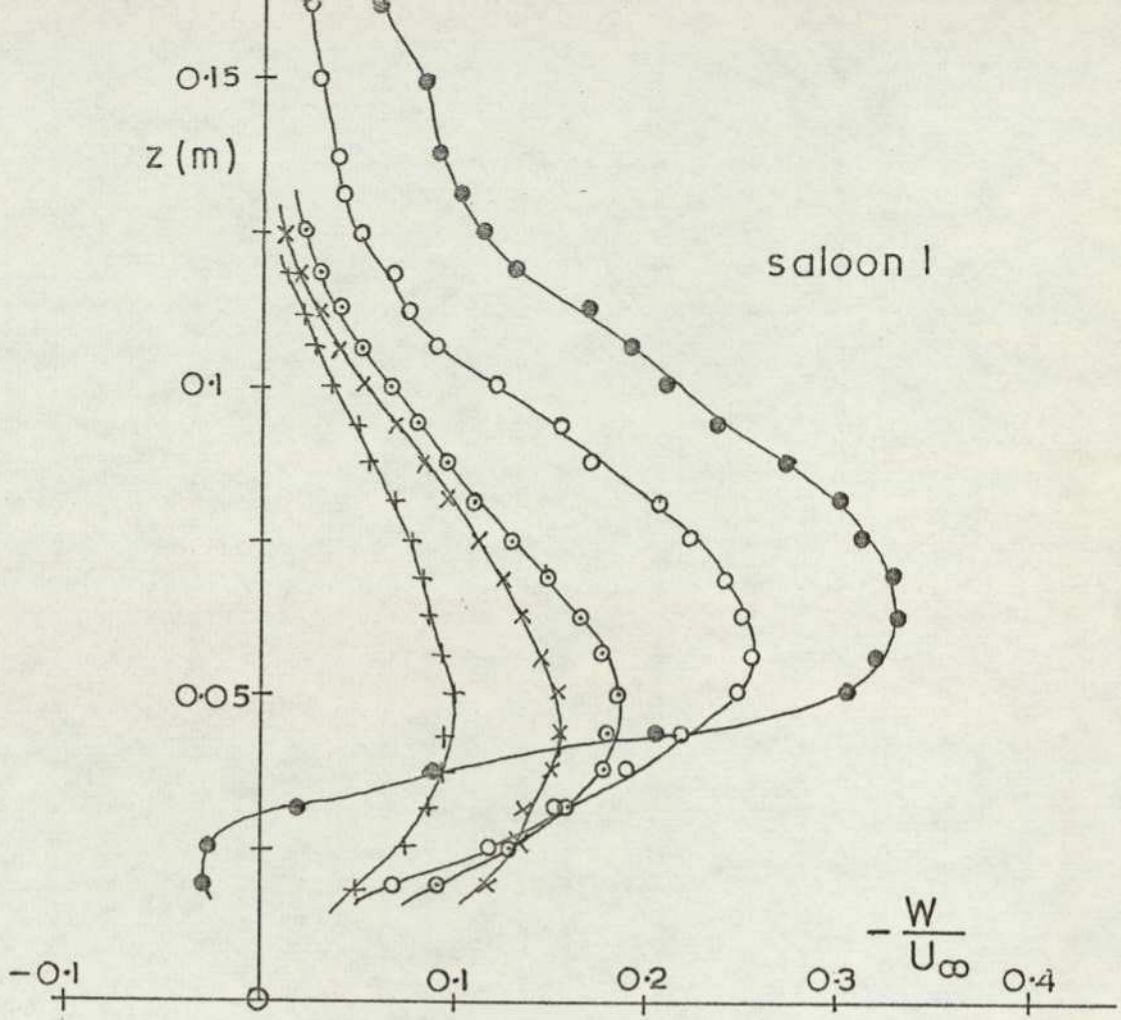

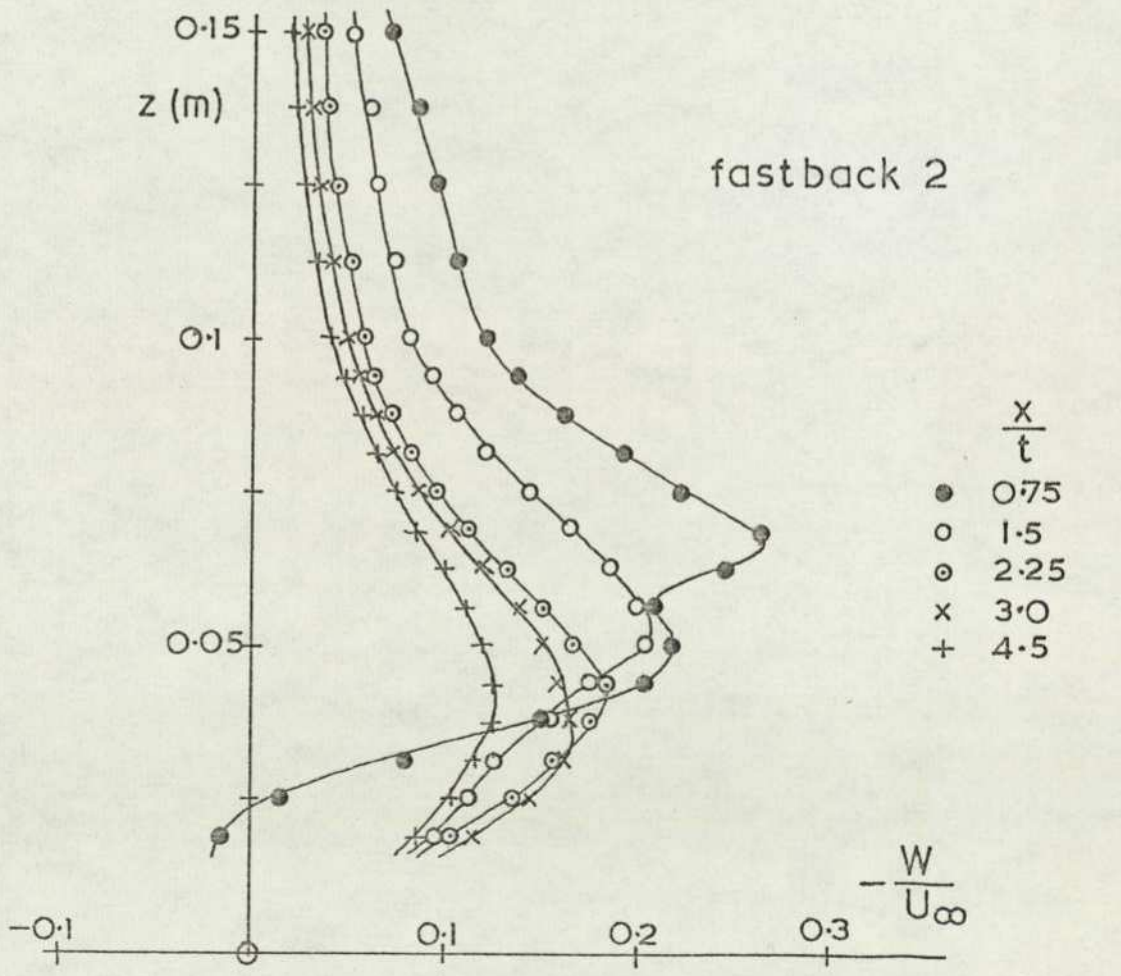

FIG. III DOWNWASH ON WAKE CENTRE-LINE

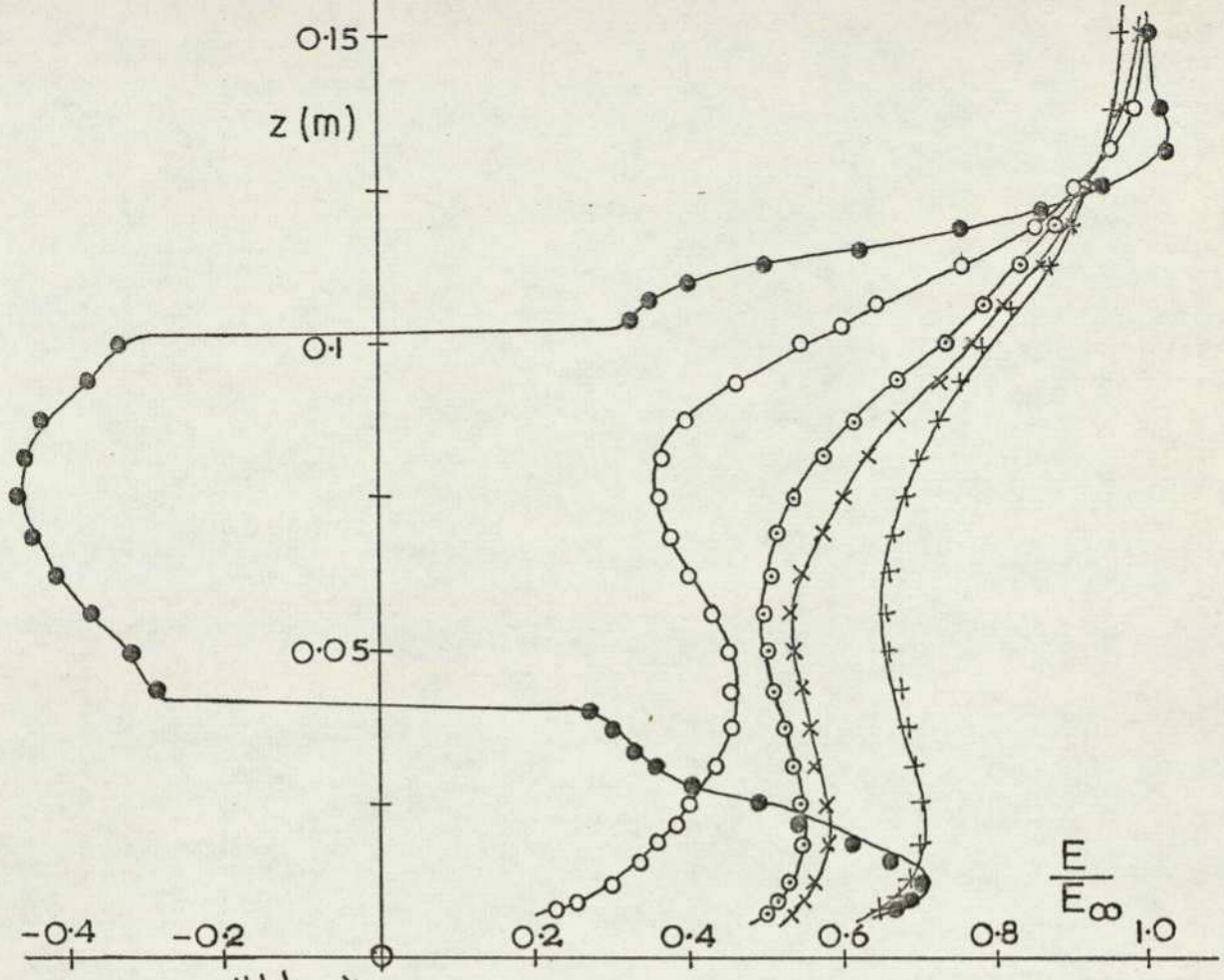

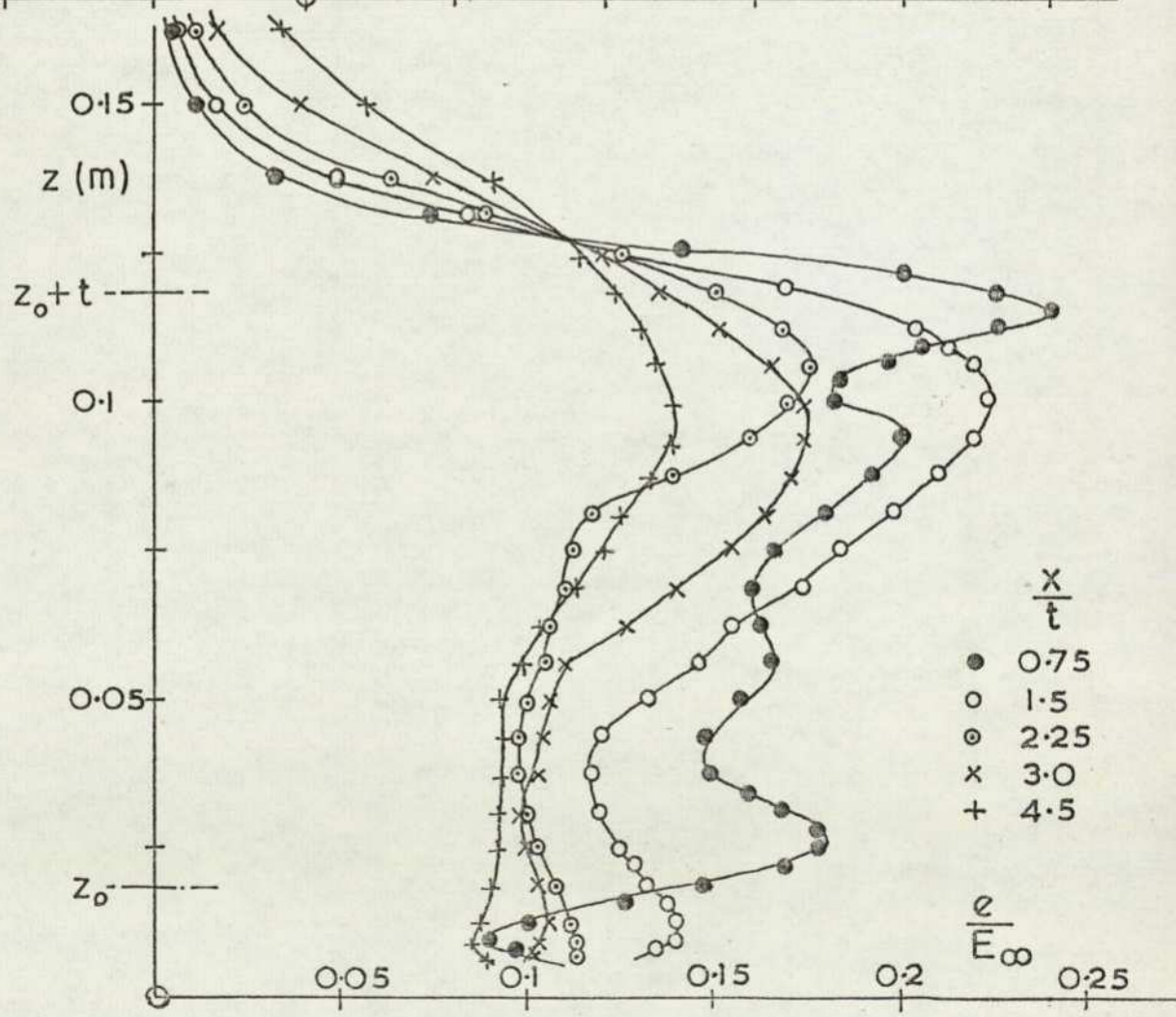

FIG. 112 WAKE CENTRE-LINE TRAVERSES — ESTATE I

(a) VERTICAL

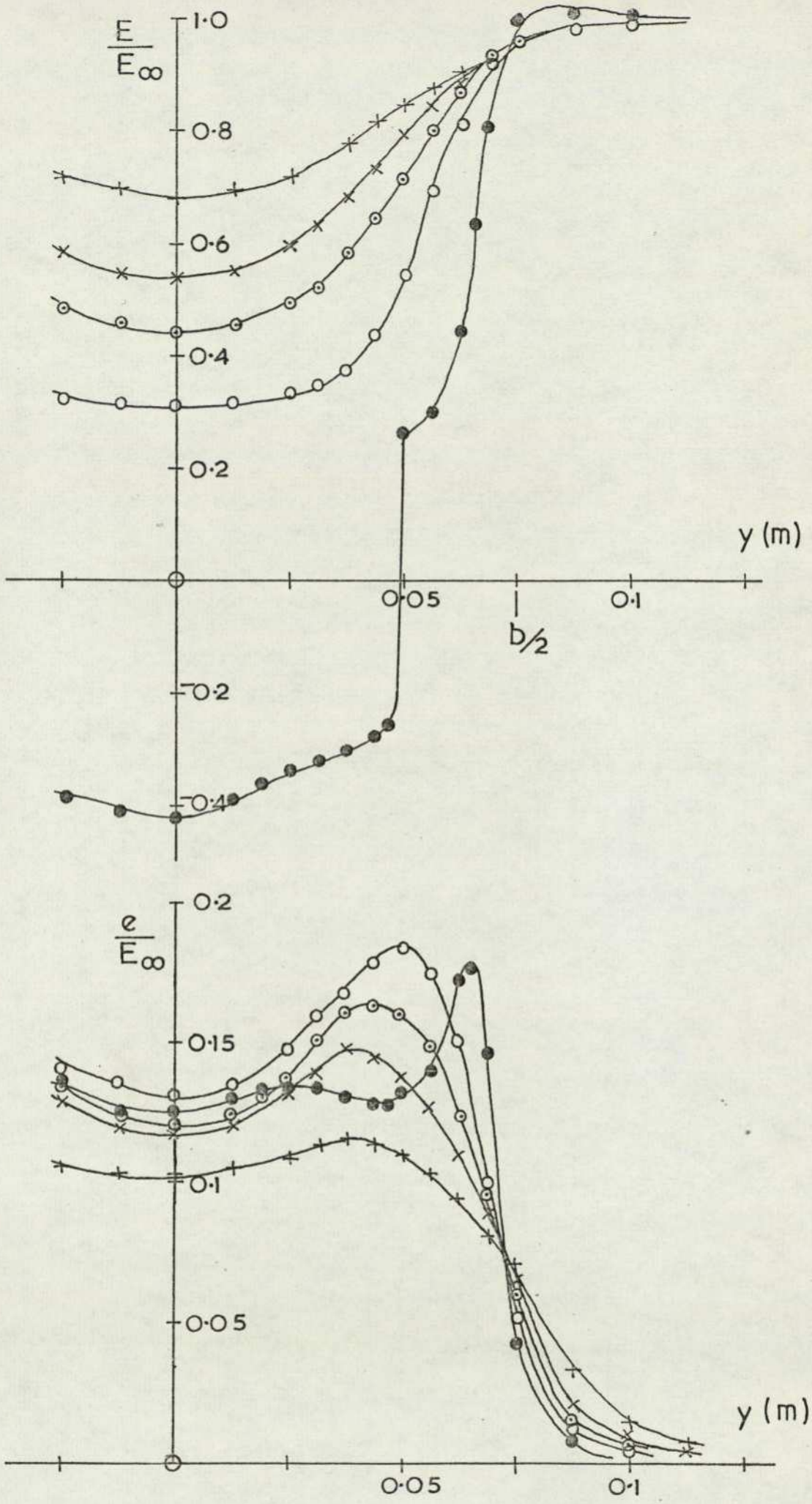

FIG.112(b) LATERAL TRAVERSE — ESTATE 1

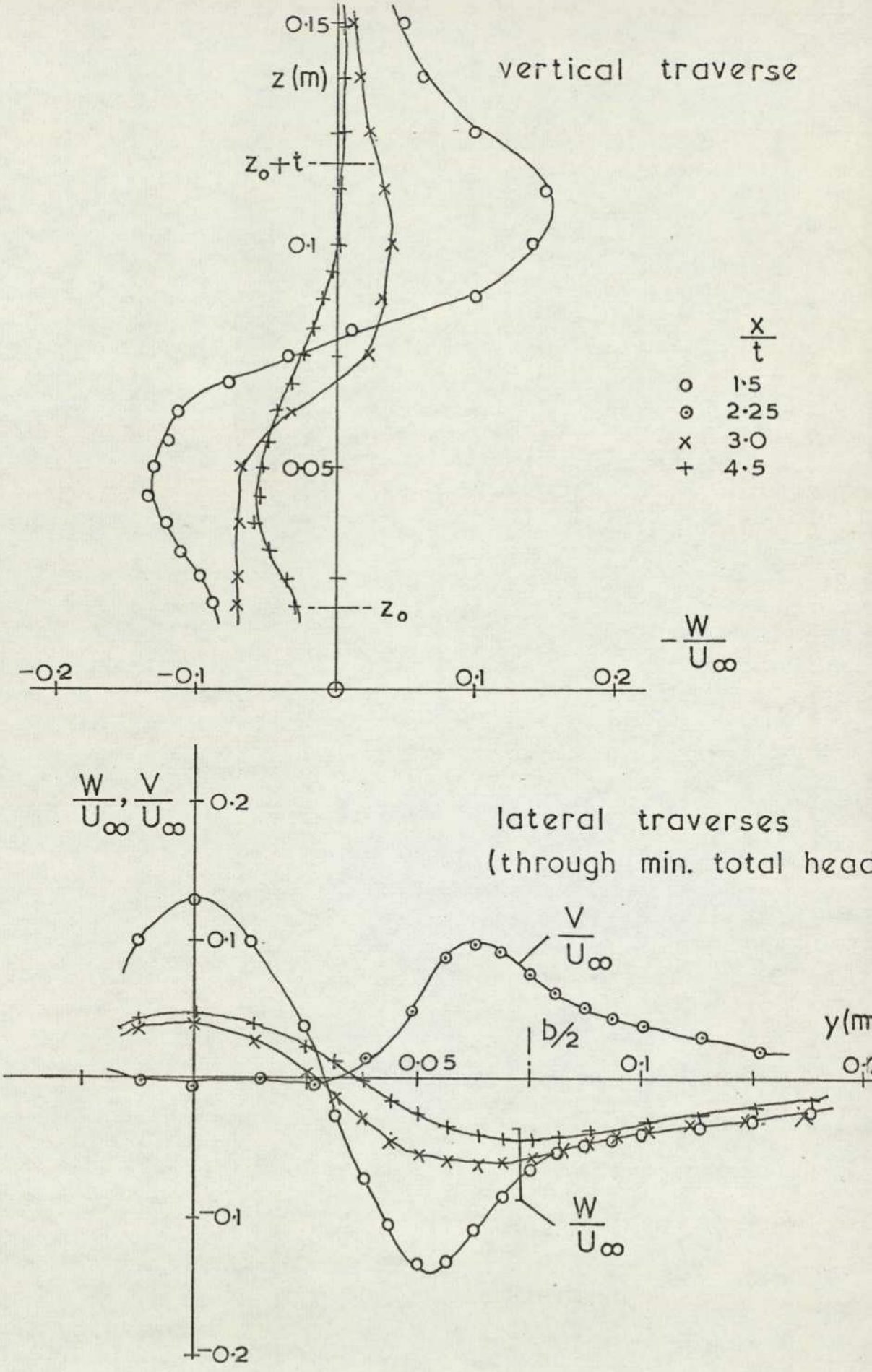

FIG. 113 TRANSVERSE VELOCITIES — ESTATE 1

with the hot wire anemometer at the upstream stations, Figure 114, confirm the earlier pitot measurements which showed the spearated flow region in the base extending to the ground plane. The main wake flow is seen to move upwards considerably, once downstream of this region. The negative lift experienced by this vehicle is apparent from the cross flow velocities shown in Figure 115. Large vertical velocities are apparent on the wake centre line even at the extreme downstream station.

To investigate the extent of the reversed flow region at the vehicle base a further series of vertical traverses were made along the wake centre line using the hot wire anemometer. All the passenger car models seen previously were studied, and the results are shown in Figure 116. The three fastback models show very similar profiles except that the reverse flow region extends further downstream for the fastback 1 model. There exist slight differences in the turbulence intensity levels above the upper vortex sheet. This sheet moves downwards on moving downstream whereas the vortex sheet springing from the underbody moves parallel to the ground. The saloon car model shows similar profiles which again differ significantly only in the unseparated region. Velocity profiles measured above the boot upper surface are shown in Figure 117, , and these show that the flow has reattached well forward of the boot trailing edge. A traverse performed immediately downstream of the boot trailing edge, at x = 2 mm , where the flow can be assumed to be parallel to the boot rear surface, measured a vertical velocity equal to 16% of the free stream velocity. On shortening the boot length the separating flow from the roof eventually encloses the boot trailing edge. The reversing flow is indicated by the pronounced turbulence intensity minimum above the boot surface. This was confirmed by tuft studies on the boot upper surface, which in addition showed that not all the boot was necessarily immersed in a separated flow. For the saloon 2 model only the very centre of the boot trailing edge was affected while the saloon 3 model boot was entirely immersed in the reverse flow bubble. As the model configuration approaches that of the estate car higher turbulence levels occur and the velocity profiles become fuller.

Horizontal traverses in the stream direction were performed to establish the length of the reverse flow bubble, a technique previously

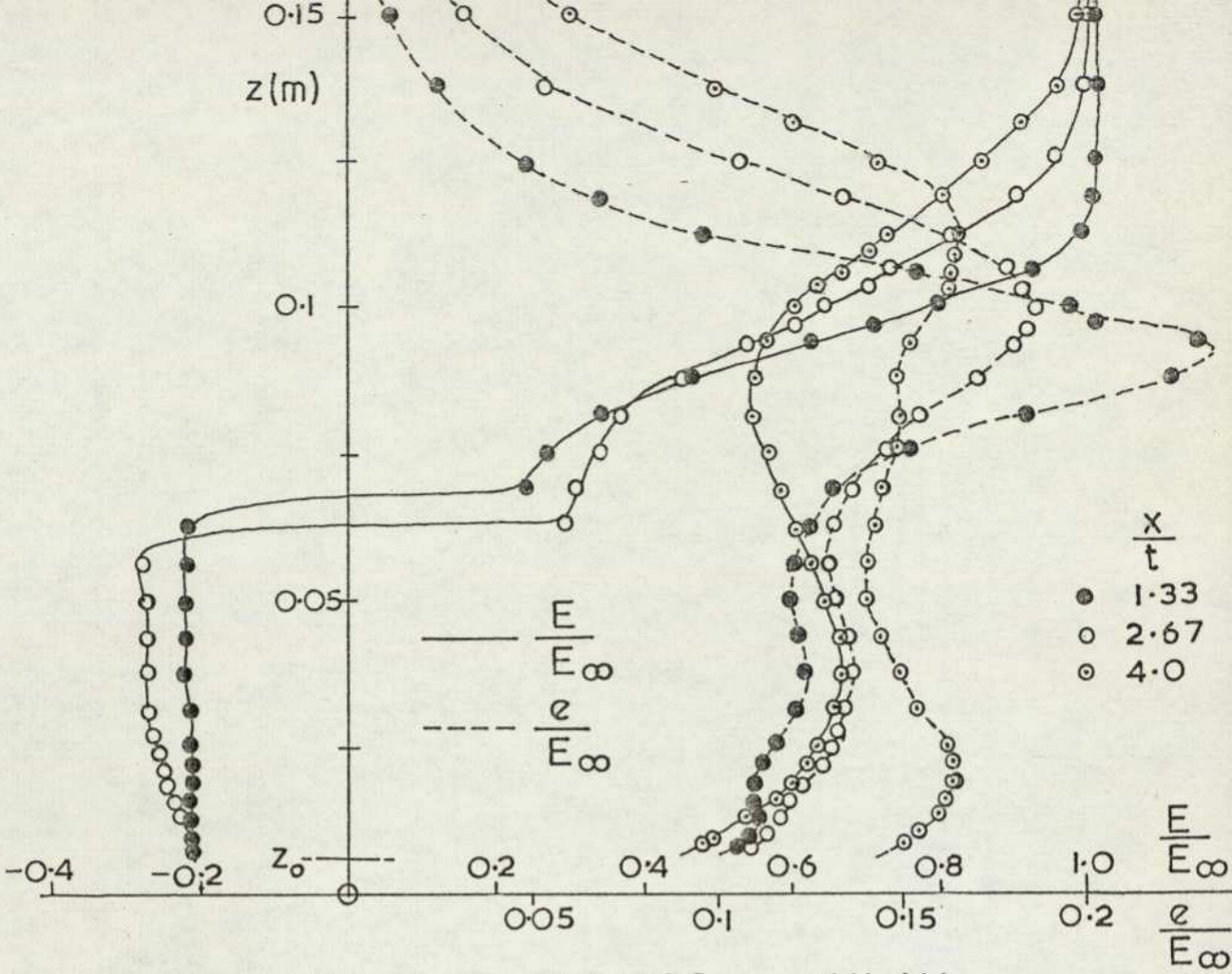

FIG.114 CENTRE-LINE TRAVERSE — CAN-AM

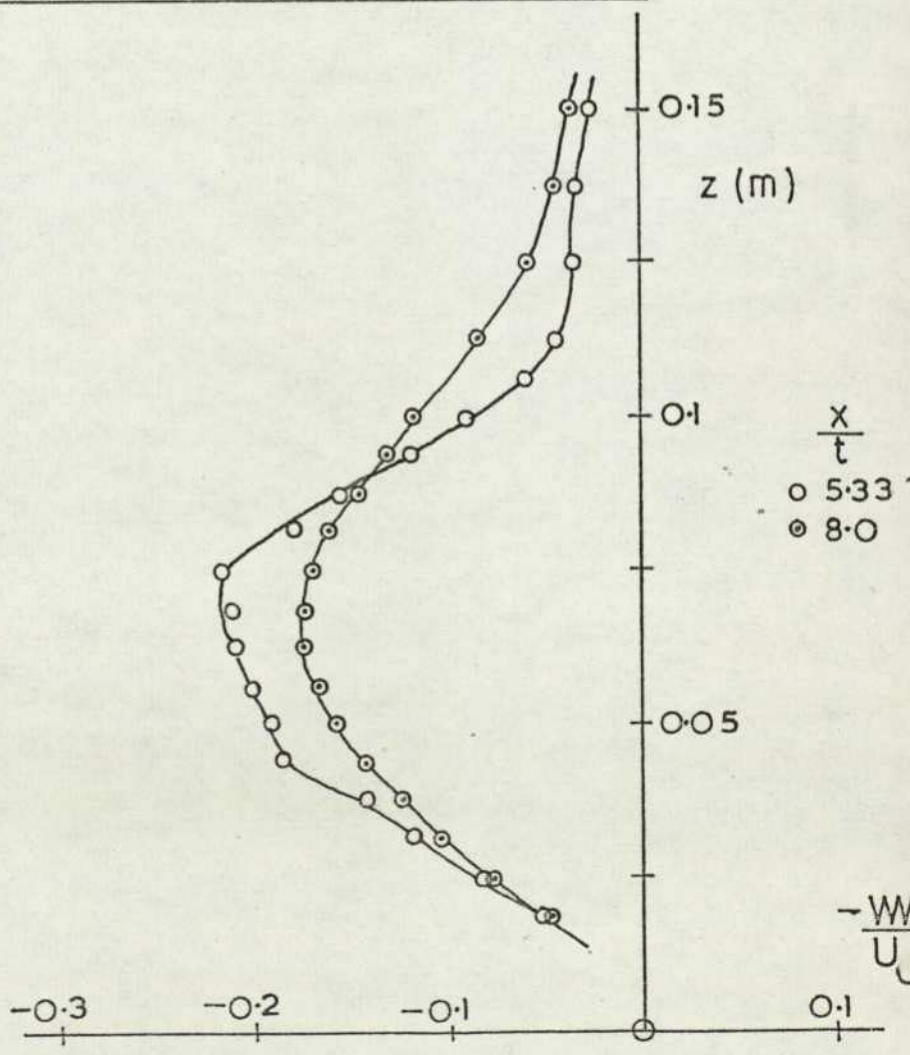

FIG.115(a) DOWNWASH ON WAKE CENTRE-LINE; CAN-

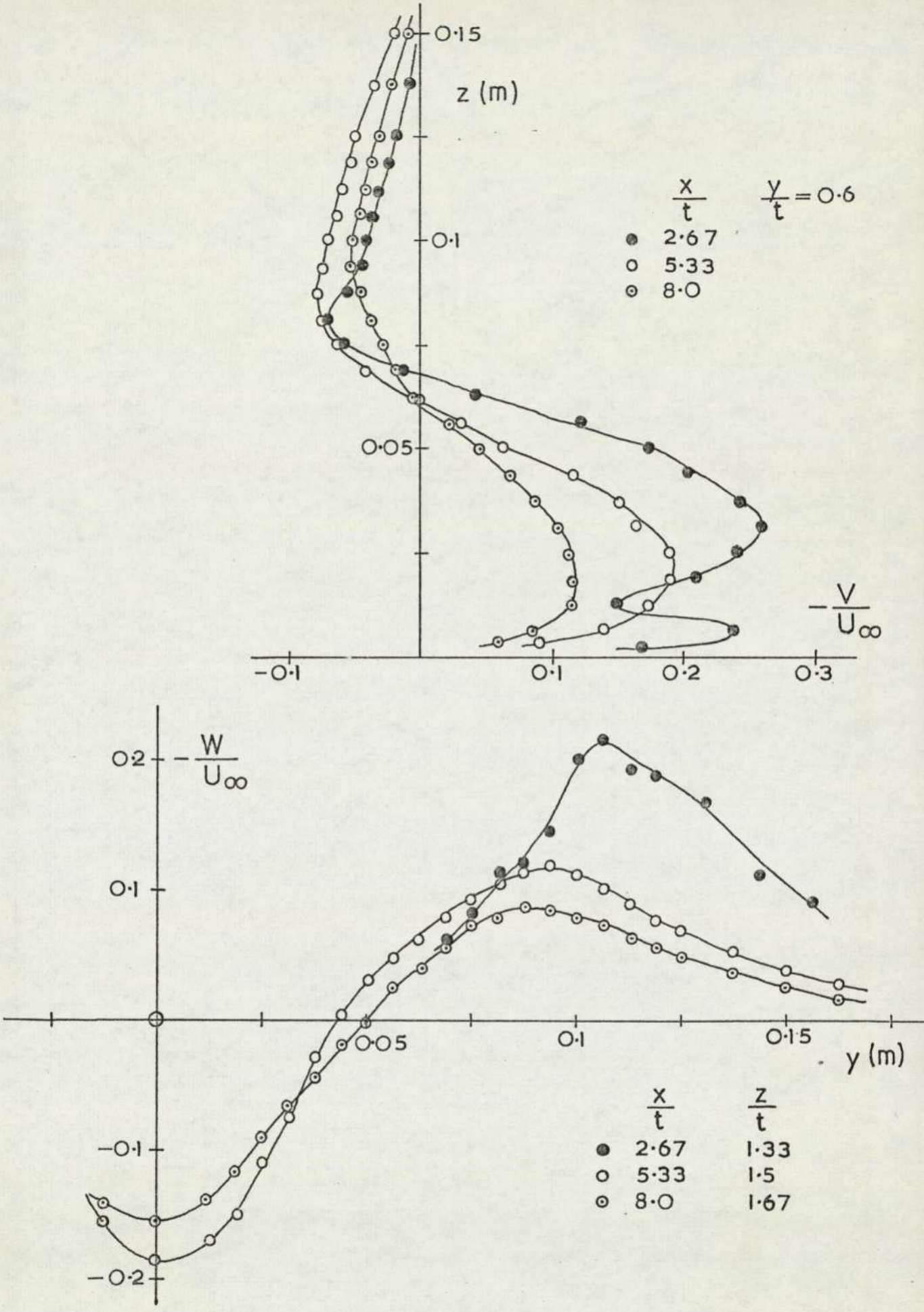

FIG. 115 (b) TRANSVERSE VELOCITIES ; CAN-AM

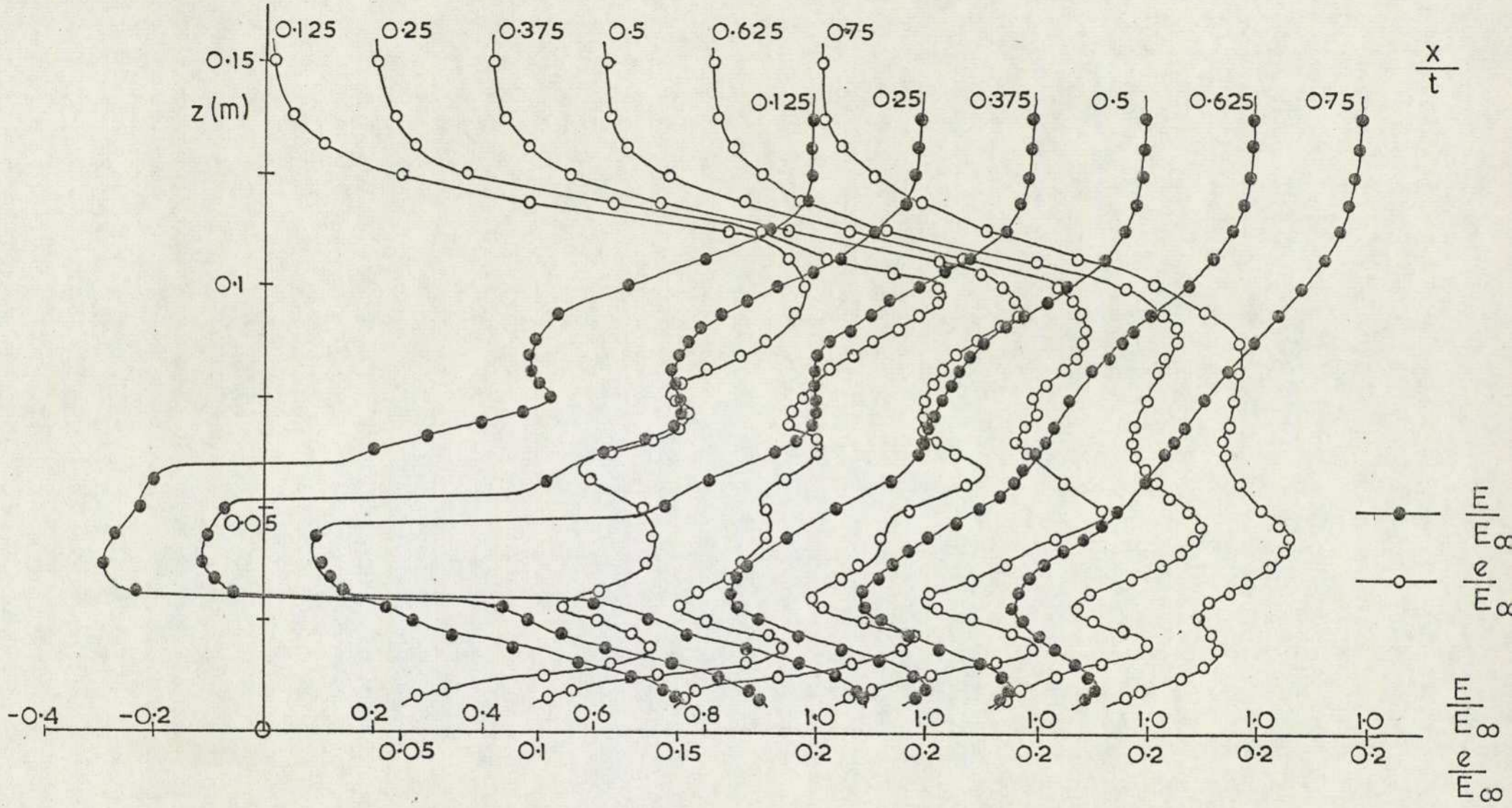

FIG.116 NEAR WAKE CENTRE-LINE TRAVERSES (a) SALOON 1

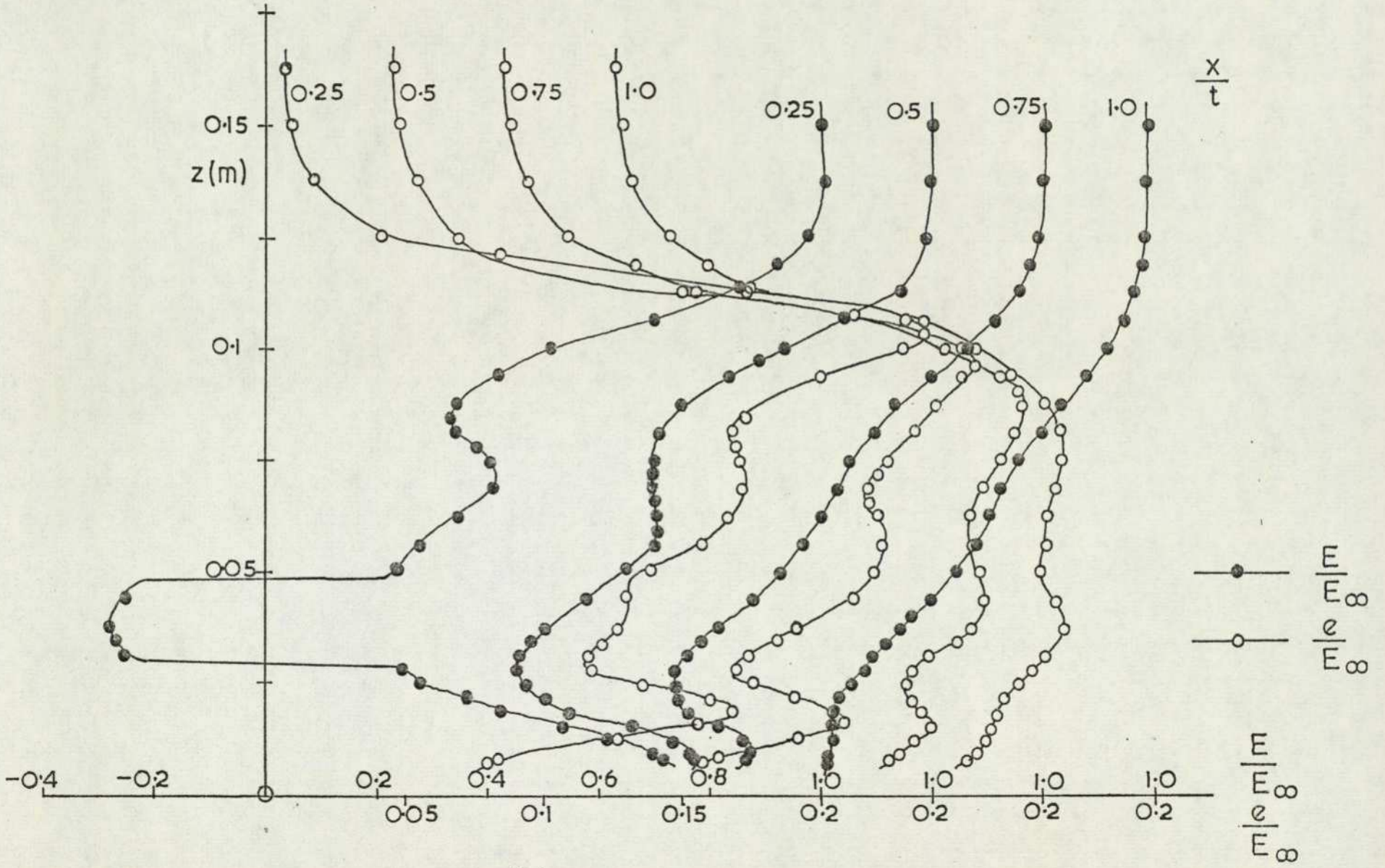

FIG. 116(b) SALOON 2

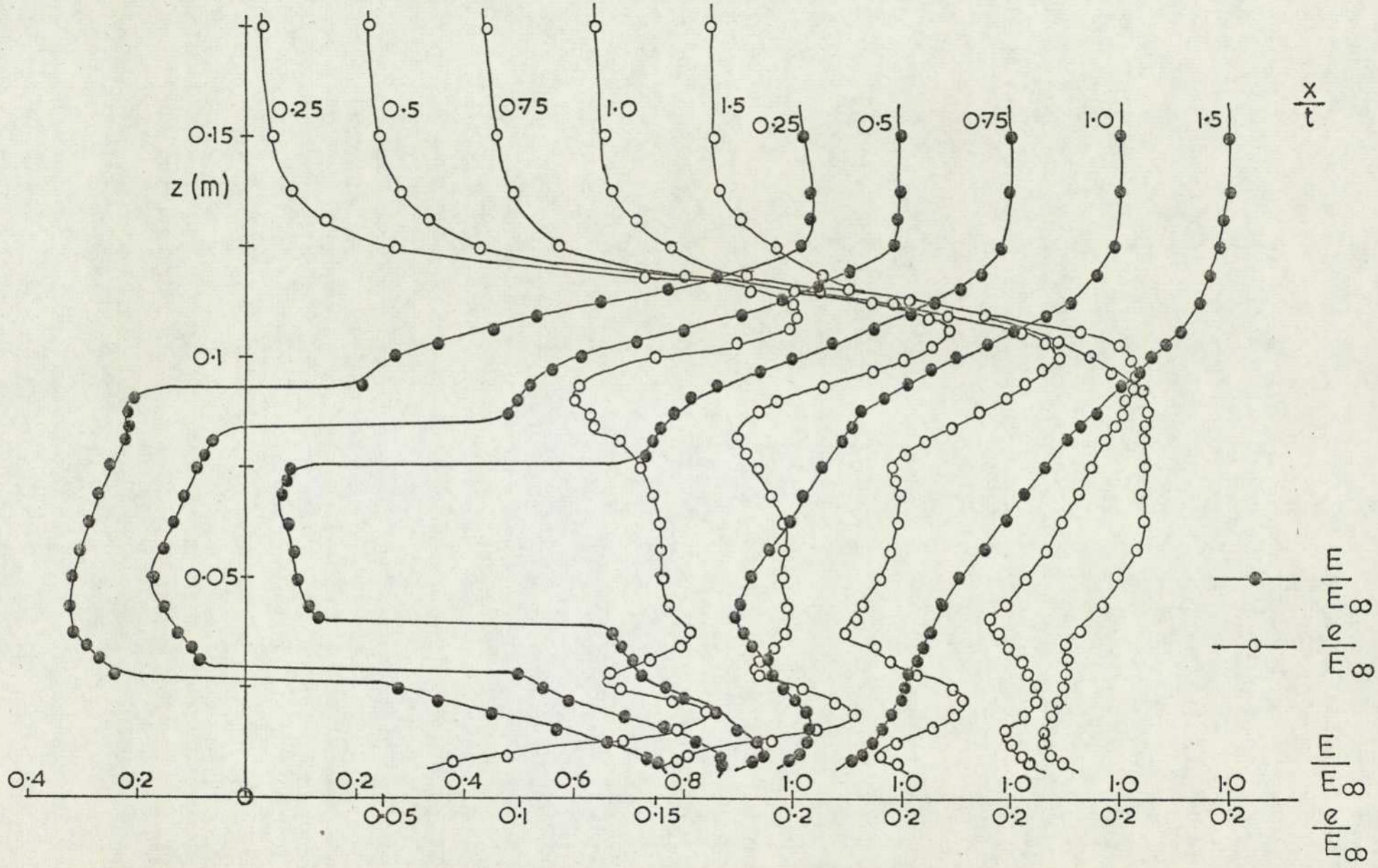

FIG. 116 (C) SALOON 3

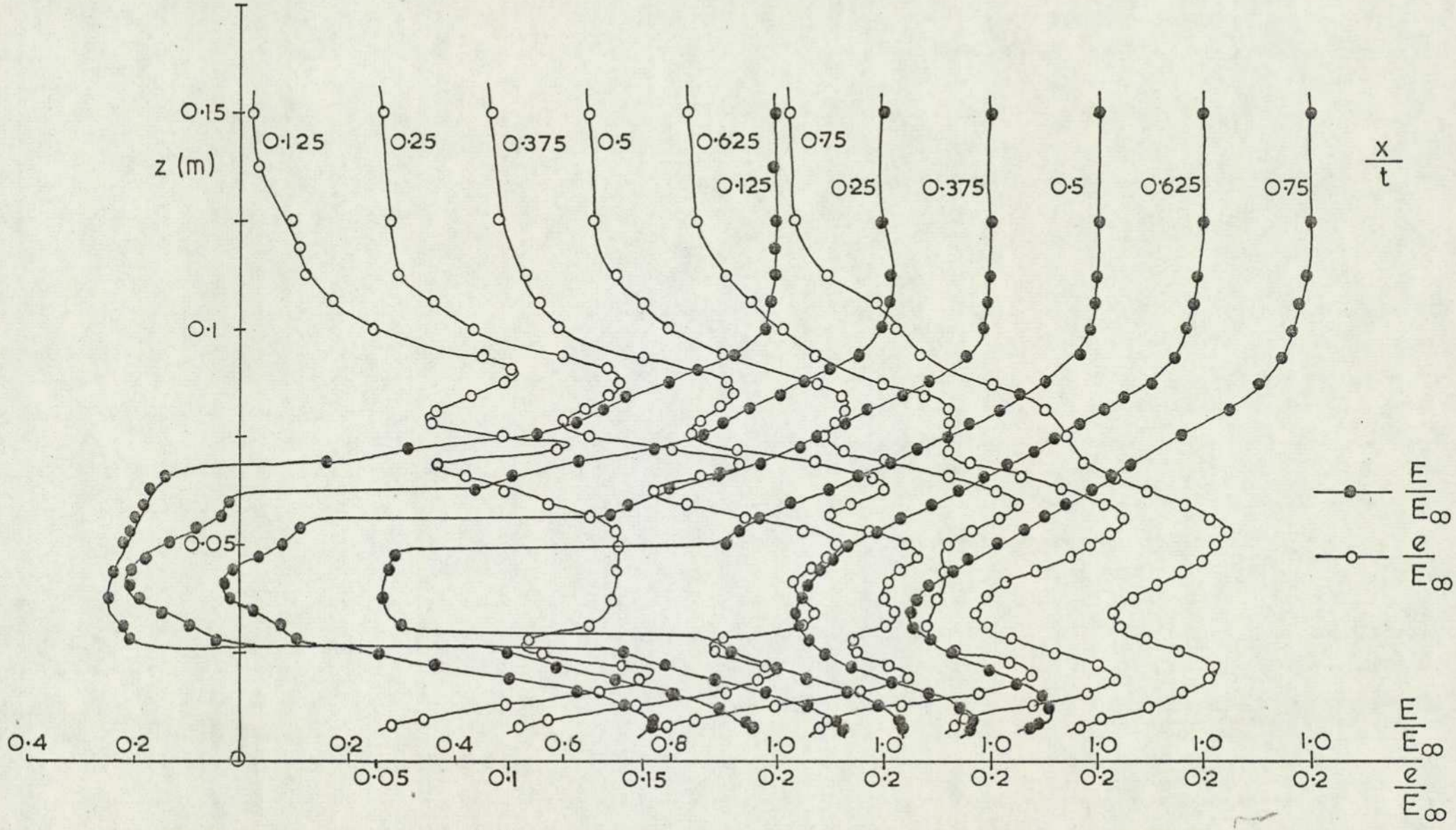

FIG. 116 (d) FASTBACK 1

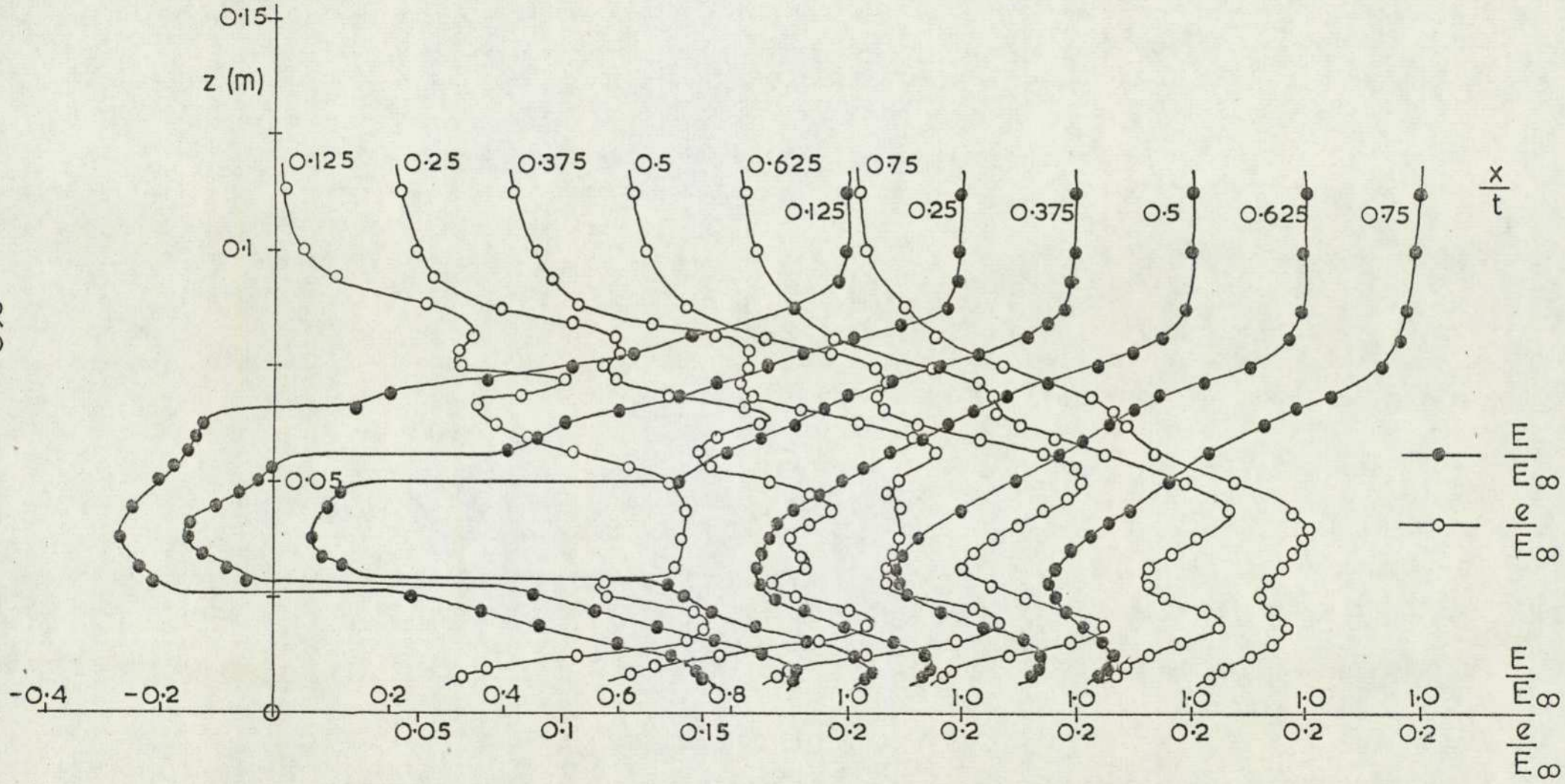

FIG. 116 (e) FASTBACK 2

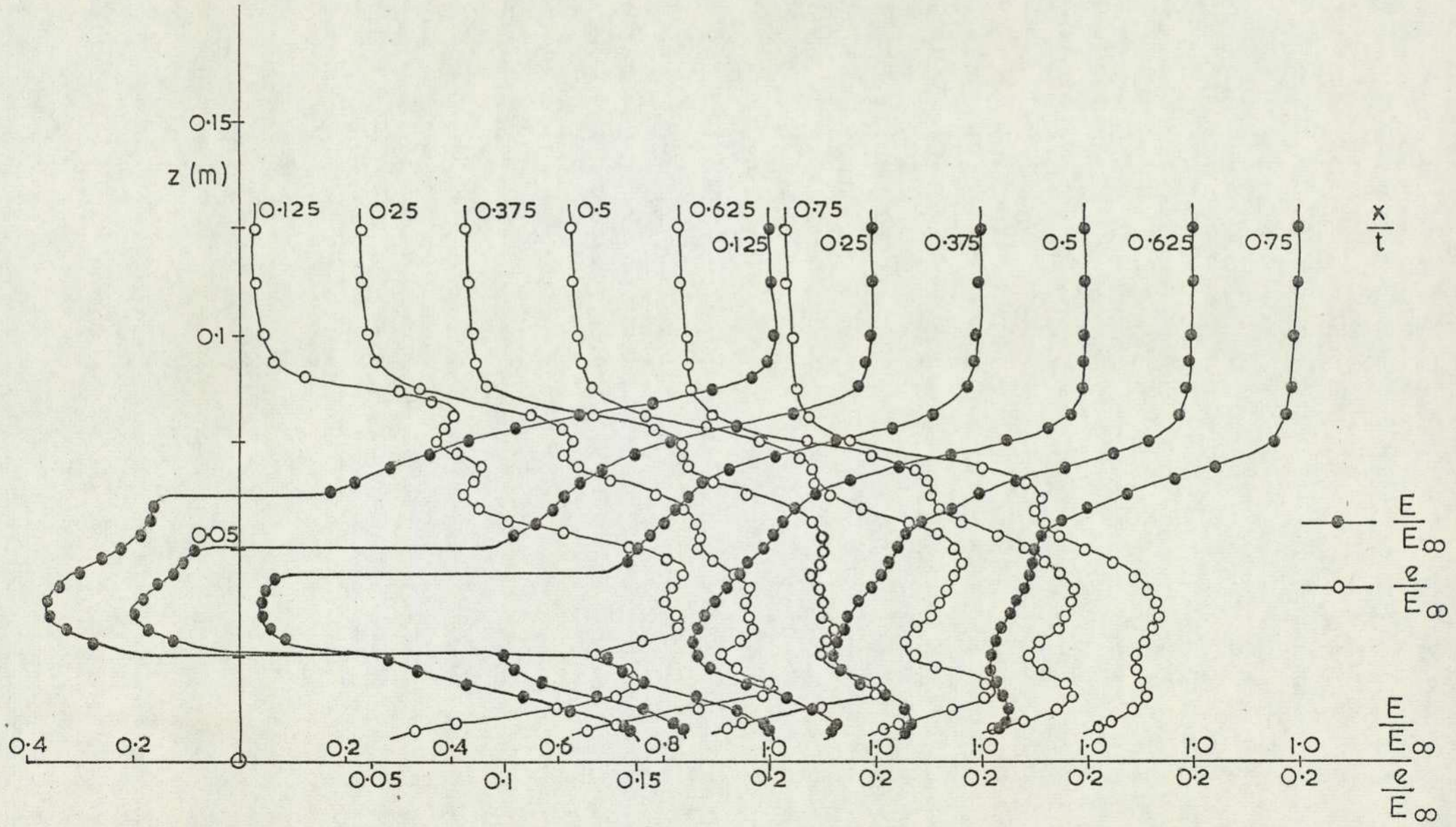

FIG. 116 (f) FASTBACK 3

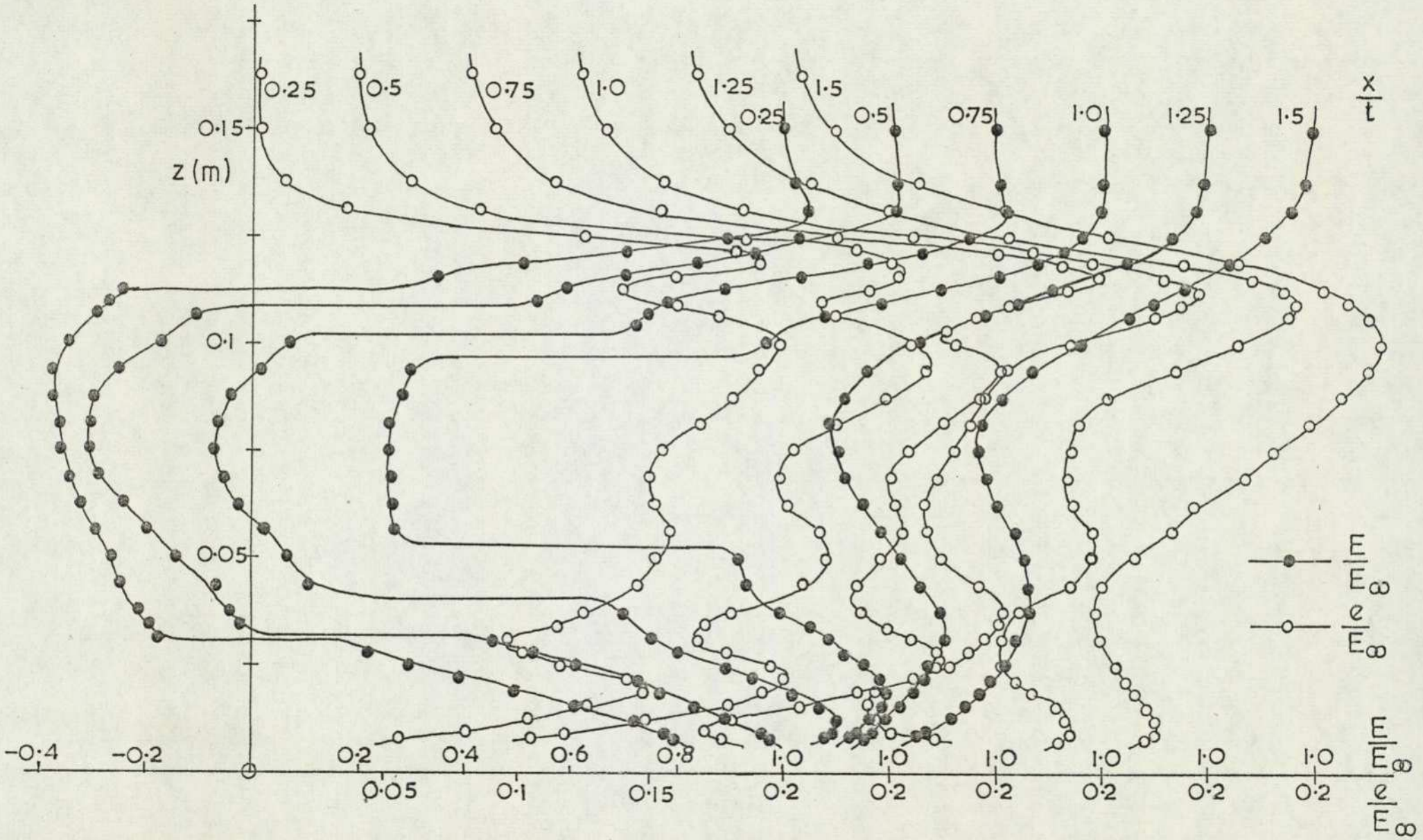

FIG. 116 (g) ESTATE 1

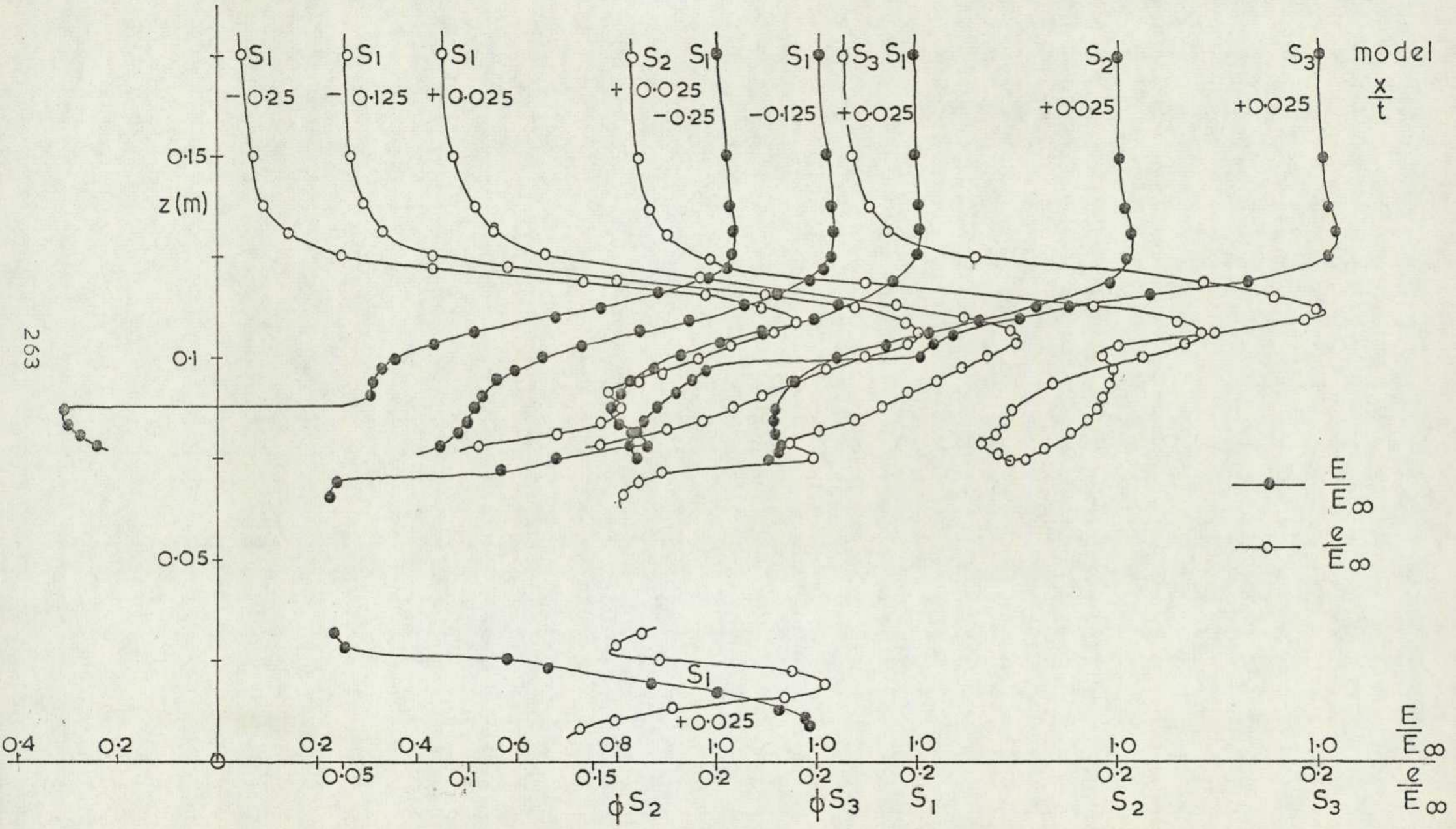

FIG.117 FLOW OVER BOOT & TRAILING EDGE — SALOONS 1,2,3.

employed on the rectangular blocks. These were performed for all models and include the effect of an increase in Reynolds number on the saloon 1 measurement. A 25% increase in Reynolds number was found to have no influence on bubble length; a result typical of separated flows.

Periodic effects were studied using the same techniques as before. The hot wire probe was located for a given downstream station at the position of peak turbulence intensity in four points around the vortex sheet. For the saloon car and the three fastback models the vortex sheet surrounded the vortex core while for the estate car model the readings were taken centrally on the side, top and bottom sheet. All readings were made at $x/t = 2.25$ except for the saloon model for which measurements were performed throughout the wake. Comparison of the estate car spectra, shown in Figure 118, with those obtained behind the non lifting rectangular block 2N reveals similar results, when the probe is positioned near to the upper and side vortex sheets. In the case of the sheet separating from the lower surface this has less pronounced periodicity than the upper sheet although the frequency is still the same.

In contrast the vehicle developing most lift, fastback 3, indicates a similar spectrum, Figure 119, for all points on the vortex sheet with two clearly defined peaks, one at 75 Hz and the other near 250 Hz. The higher frequency peak dominates in all positions except the one nearest to the ground. The fastback 2 model produces very similar spectra, Figure 119, except that more energy is now contained at the lower frequency and the frequency of the other peak in the spectrum is reduced. Figure 120, for the fastback 1 model, reveals less ordered spectra, but the only differences are that a peak of 125 Hz. appears on the inboard part of the sheet and that the lower probe position gives a broader peak at the lower frequency and no peak at the higher frequency. With the probe in the outboard positionthe upper frequency peak occurs at a lower value than for the previous models.

The saloon car model, with the probe positioned at $x/t = 2.25$, produces a series of spectra which continue the trend of the fastback 1 model. The upper frequency peak is again reduced, this time to 180 Hz, but no other spectrum gives this frequency peak, Figure 120.

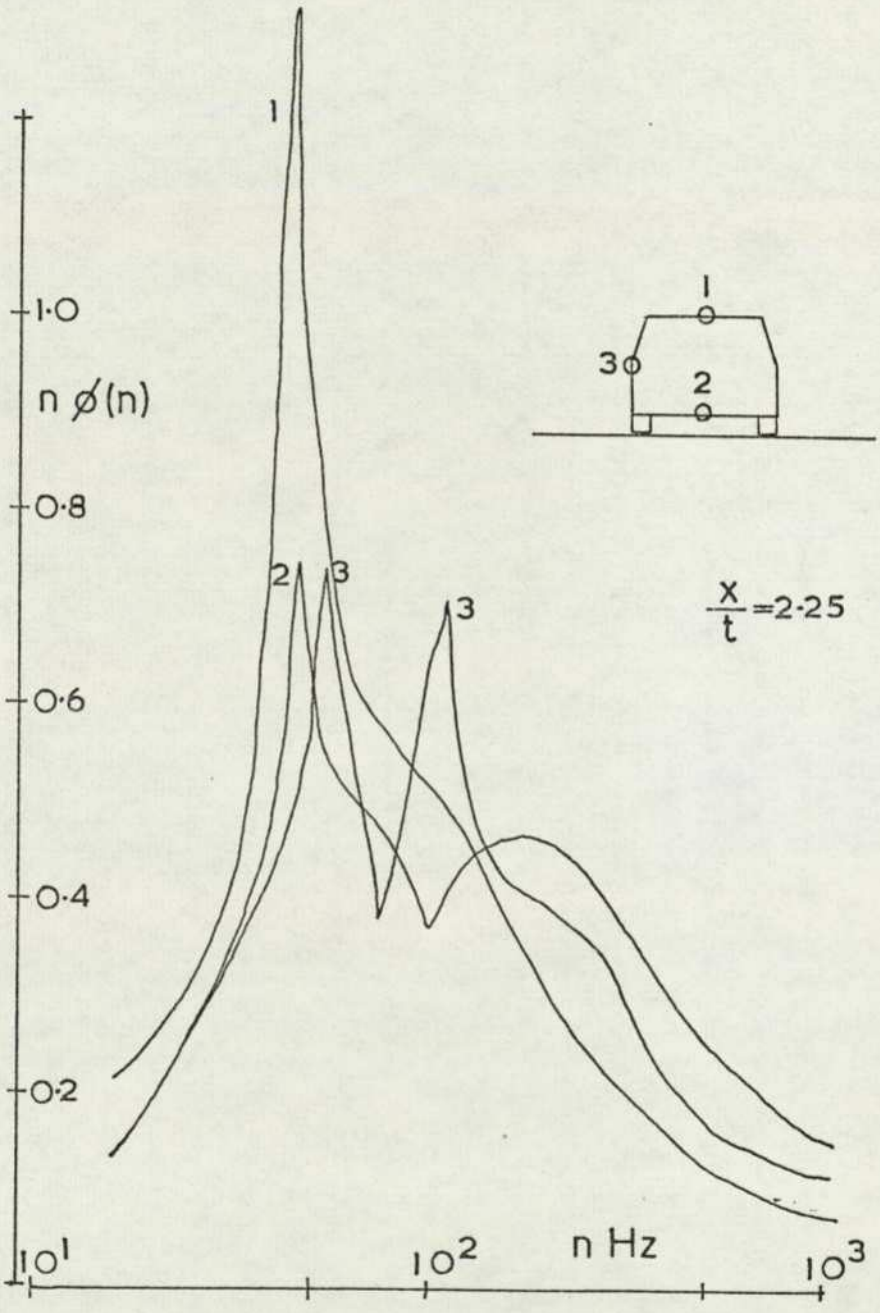

FIG. 118 FREQUENCY SPECTRA — ESTATE 1

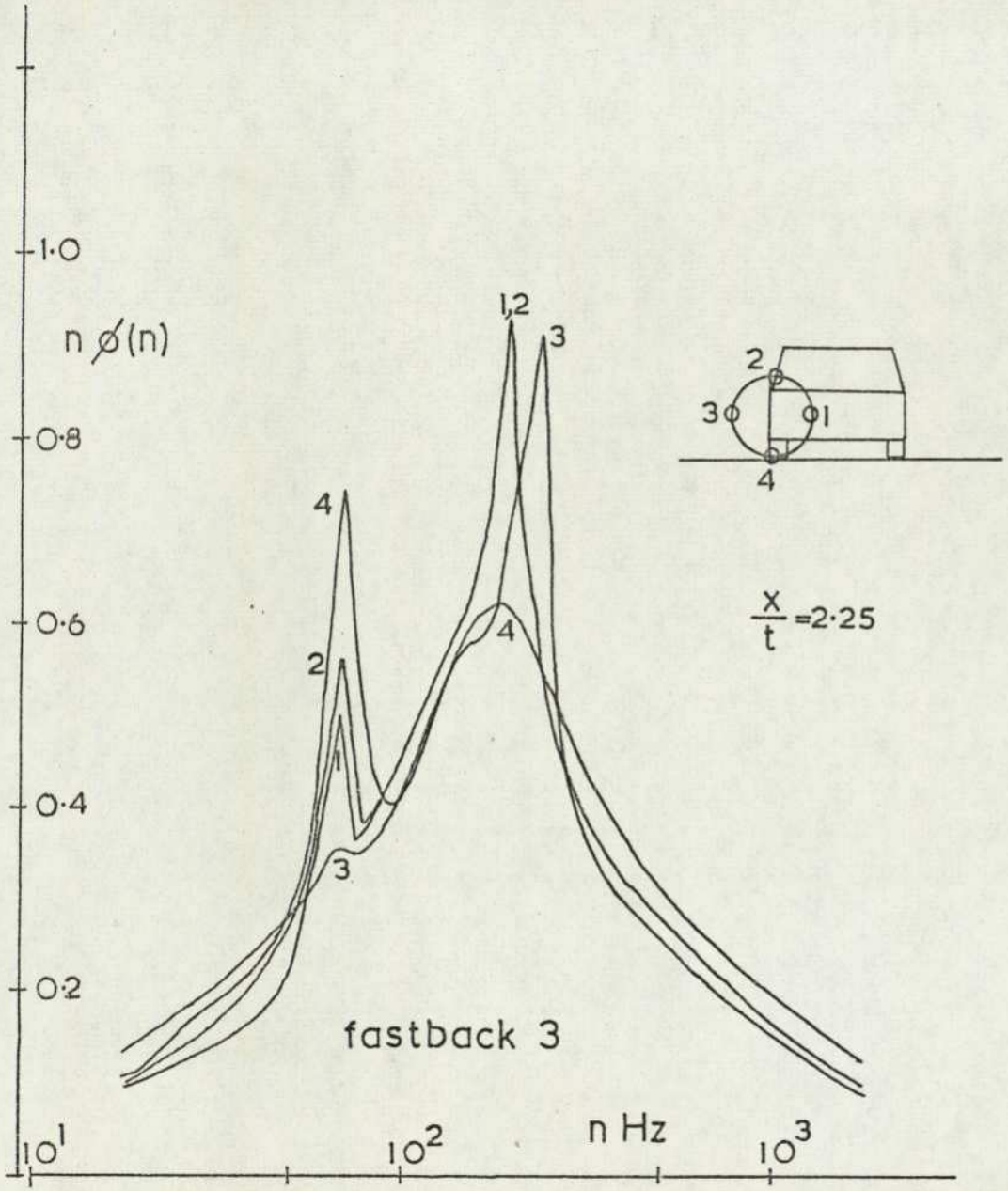

$\frac{x}{t}$ =2·25

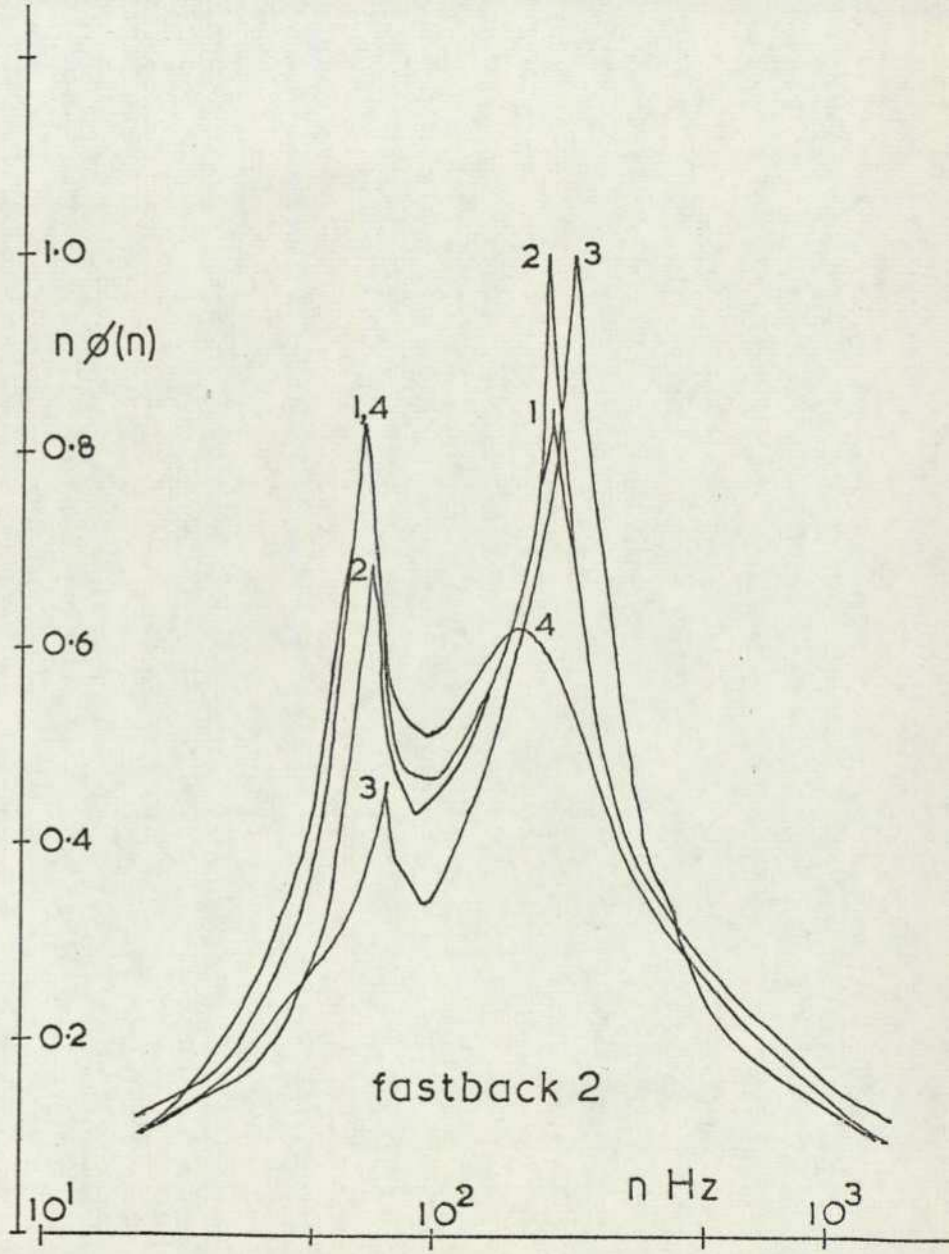

FIG. 119 FREQUENCY SPECTRA

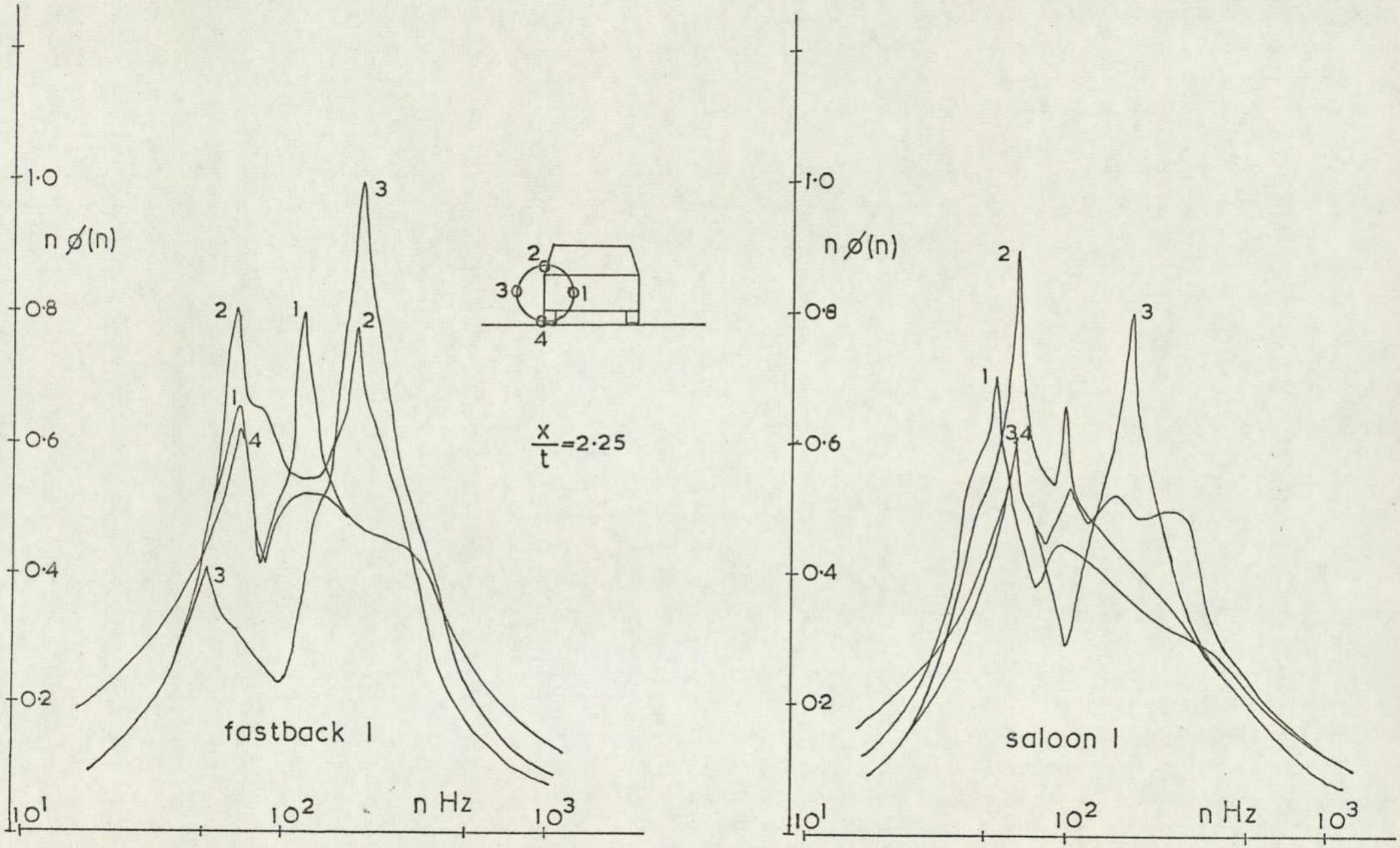

FIG. 120 FREQUENCY SPECTRA

The influence of downstream location on the spectra is shown in Figure 121 for the wake of the saloon 1 model. When mounted nearest to the model base the probe in the outboard position gives a single peak spectrum. On moving downstream this changes to a two peak spectrum similar to the fastback models, and the amounts of energy within each peak change so that the lower frequency finally dominates. With the probe situated on the uppermost part of the vortex sheet the initial spectrum indicates peaks at 175 Hz and 75 Hz. The higher frequency peak rapidly reduces in frequency on moving downstream. A similar result emerges with the probe positioned inboard of the vortex. Mounting the probe nearest to the ground again produces two peaks in the turbulent energy spectrum, one at 65 Hz and the other at 300 Hz. On travelling downstream the lower frequency remains unaltered but the upper frequency peak reduces to 100 Hz. In general the wake which initially contains energy at two distinct frequencies becomes dominated by the lower frequency on moving downstream, although the upper frequency persists in the outboard region of the vortex throughout the wake.

A single additional spectrum was obtained on the wake centre line immediately downstream of the separation bubble. This is shown in Figure 122 and reveals a dominant peak at 95 Hz with additional peaks at 65 Hz and 170 Hz.

4.4.3 Discussion

In this discussion consideration is given to the flow properties only. The consequences of these flows as experienced by a driver of a road vehicle is left to Chapter 5.

The initial stage in the wake formation, the near wake is characterised by the reverse flow region produced by the flow separation at the trailing edge boundaries. The estate car separation bubble is very similar in extent to that for the rectangular block while the flow profiles for all the car shapes that develop significant lift are remarkably similar considering the differences in body geometry immediately upstream of the base. To define the region of reverse flow the contour of zero velocity has been plotted in Figure 123 for all the car shapes. The position of zero velocity is defined similarly to Calvert (31) by a local maximum in the ratio of the r.m.s. to D.C. voltage output

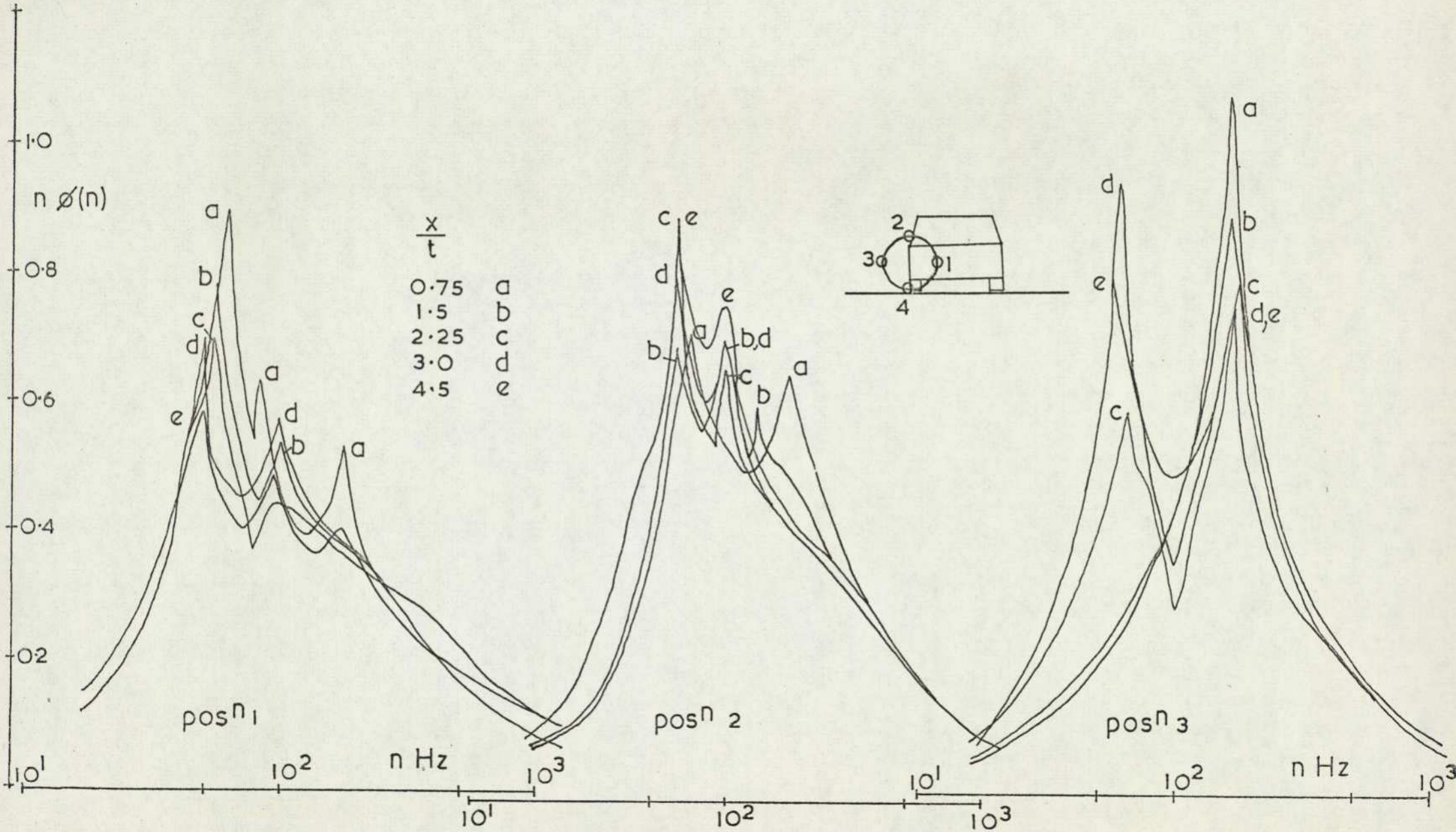

FIG.121 FREQUENCY SPECTRA — SALOON I EFFECT OF TIME

FIG. 121 [CONTINUED]

FIG. 122 SPECTRUM—SALOON 1, WAKE C.L.

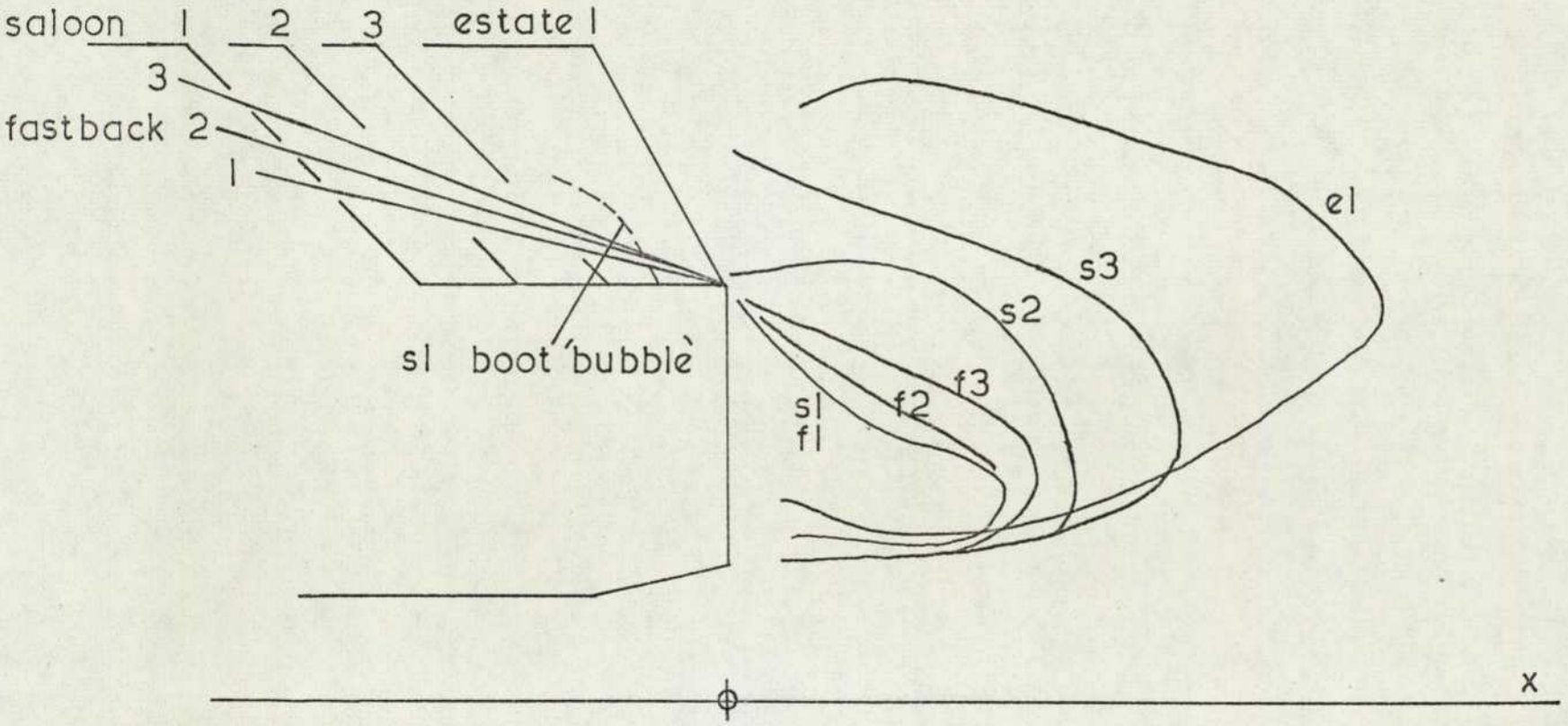

FIG.123 REVERSE FLOW 'BUBBLE' SHAPES

from the hot wire anemometer, e/E. The longitudinal extent of the bubble was defined from a single horizontal traverse in the free stream direction through the position of maximum reverse velocity. The saloon 1 and fastback models show identical contours while reducing the boot length increases the extent of the reverse flow region. While the saloon 2 contour just remains attached at the boot trailing edge the saloon 3 bubble fails to do so and the bubble size rapidly approaches that for the estate car. As with the rectangular blocks significant reverse flow velocities are present for all vehicles. These approach 40% of vehicle speed.

Four of the models develop sufficient lift to produce trailing vortices which have been detected by four different measuring techniques. The vertical position and the lateral spacing of the vortex centres as defined by the maximum total head deficit from the pitot pressure results, the maximum velocity deficit from the hot wire anemometer data, the zero transverse flow velocity from the yaw probe maasurements, and the maximum rotational velocity of the rotating vane, are plotted in Figure 124. All the models have virtually identical vertical paths for the vortex cores irrespective of the measuring technique or the vehicle geometry. The vertical core positions are ill defined at large downstream distances when using the longitudinal velocity methods. The lateral spacings of the vortices of the fastback models shows that the spacing reduces as the vehicle lift increases with all the paths showing initial convergence followed by a divergent motion. In the case of the fastback 2 model these paths are essentially confirmed by both the yaw probe and the rotating vane measurements. The saloon 1 car wake, on the other hand, shows a convergence of the vortices followed by a parallel motion, when using data from the hot wire anemometer and the pitot rake, while the yaw probe and rotating vane results, which in themselves are very similar show a slowly diverging path. The two sets of results, while initially substantially different, are in broad agreement downstream of $x/t = 2.5$. As it is considered preferable that vortex data be obtained from transverse velocity measurements directly rather than be inferred from longitudinal velocities the former results are taken as being correct. It must therefore be assumed that pitot measurements are unsuitable for determination of vortex core locations in the wake downstream of a large separation region. The velocity of the vortex itself is unlikely to introduce noticeable errors in the yaw probe data.

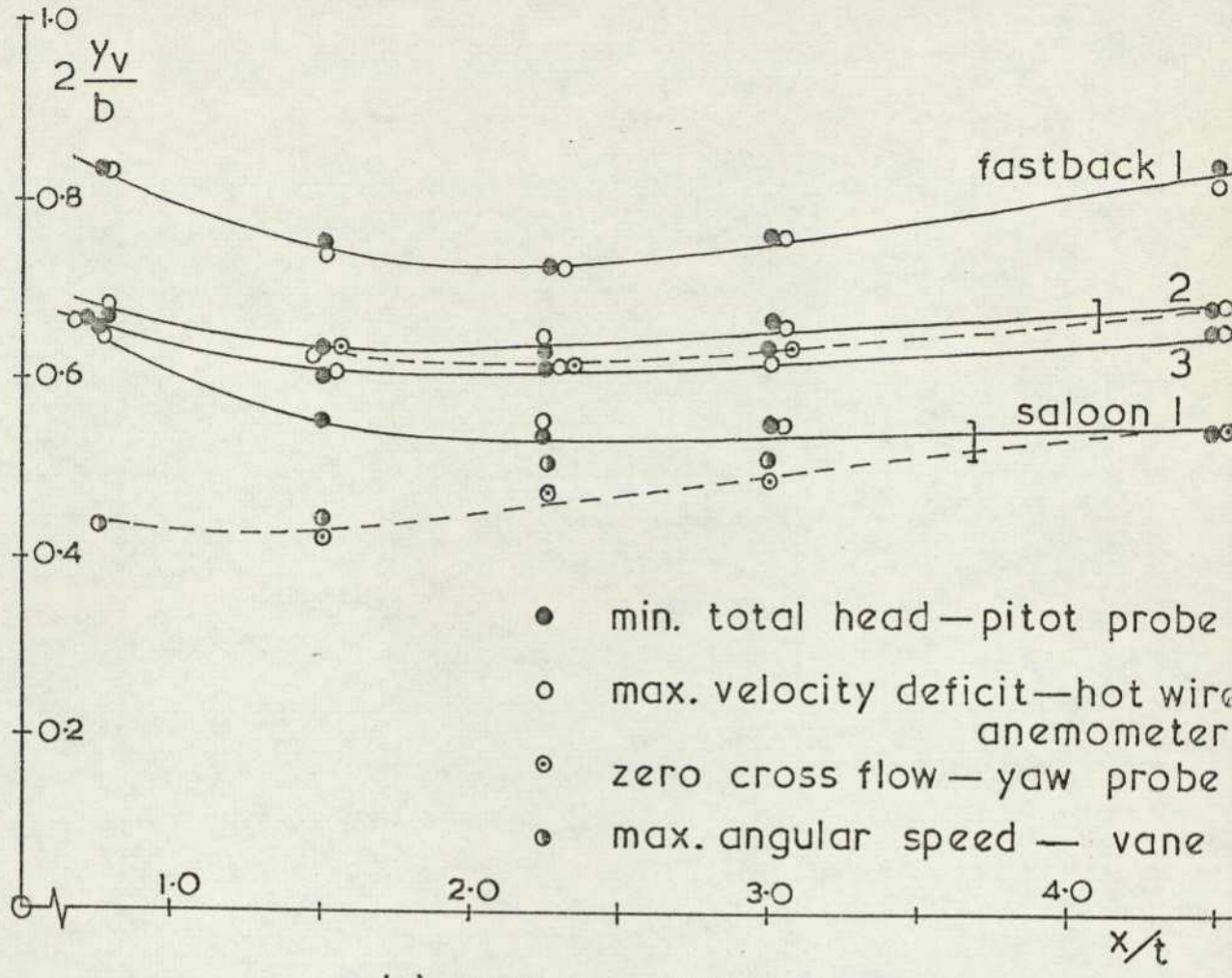

(a) VORTEX SPACING

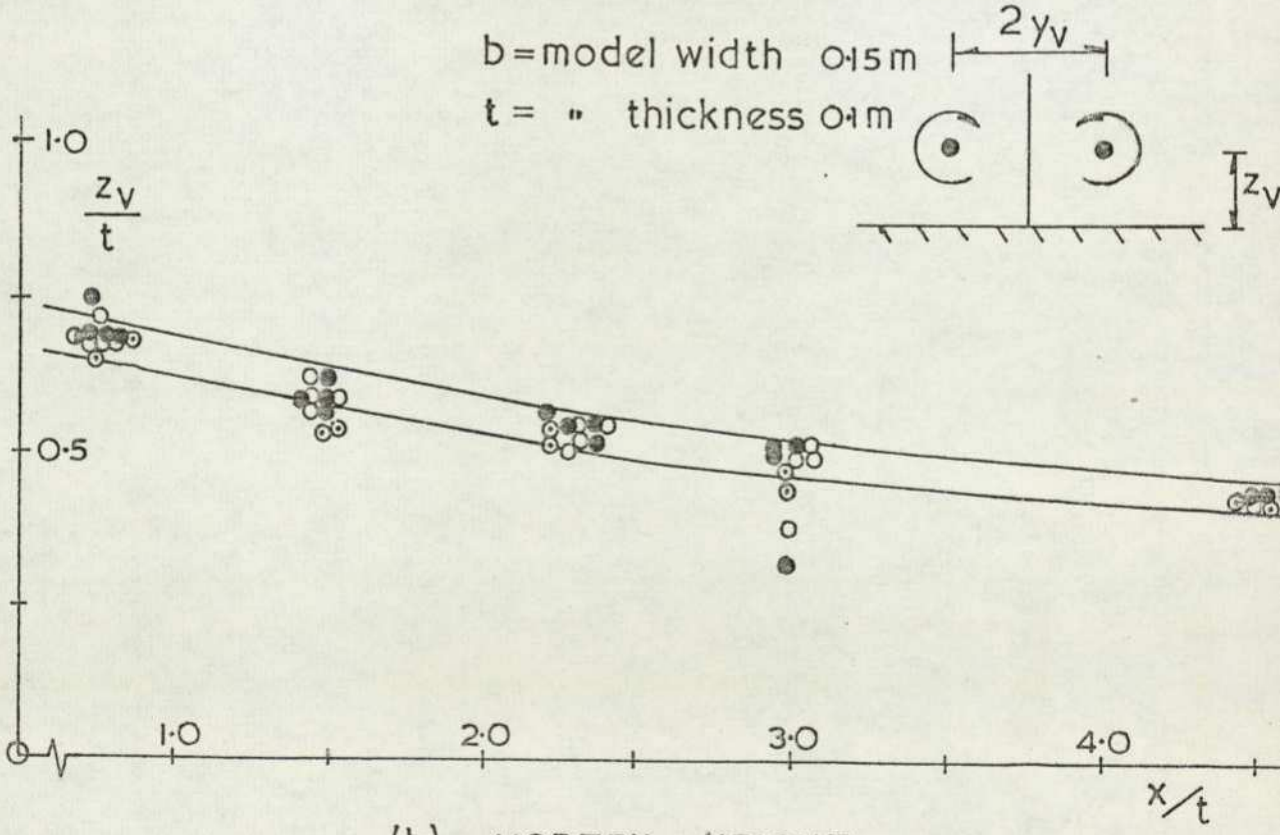

(b) VORTEX HEIGHT

FIG. 124 VORTEX PATHS AS DEFINED BY THE FOUR TECHNIQUES

Although the vortex core position may be in error there is no reason to suspect the pitot data itself which is still representative of flows behind real vehicles. The same may not be true at the ground surface, however. No separations on the ground board were visible when tufts were stuck onto it but the pressure measurements suggest that sudden changes in the flow direction do occur. All the pitot contours show a considerable thickening of the ground board boundary layer outboard of the trailing vortices, as seen previously with the lifting rectangular blocks. The cross flow velocities for the saloon car as measured at $x/t = 2.25$ using the yaw probe show a reversal of flow direction at the ground in a similar position to the thickened boundary layer. The local flow structure is shown in Figure 125 (a). Further upstream both the saloon and fastback models show that immediately behind the trailing edge an inward flow exists directly beneath the vortex and an upward flow occurs on the wake centre-line, just above the ground. Both flow features are associated with the flow expansion downstream of the vehicle base and the result is a vortical motion in the corner of the planes of symmetry which opposes the main vortex, Figure 125(b), although this motion soon disappears.

To ascertain the representative nature of these ground flows, consider Figure 125(c), which shows the flow near to the ground due to combined longitudinal and transverse components in road and tunnel situations. At the ground surface, the velocity components in both situations are zero relative to the ground. Just above the ground the transverse velocities are equal. The longitudinal velocity in the tunnel at the same height is $U-U_1$ where U is the tunnel speed and U_1 is the local velocity in the wake. On the road the longitudinal velocity is U_1 and so, provided the two longitudinal velocities are of the same order and Reynolds number criteria are not violated, then the two flows will behave similarly. These remarks are only valid close to the ground.

However, the flow in the base of the Can Am racing car must be unrepresentative. In the wind tunnel the recirculation region extends to the ground plane whereas on the road flow reversal is not likely to occur below the level of the vehicle underside. As the shear layer separating at the vehicle base extends to the ground, and the mass flow rate through the trailing edge gap will be small, it is reasonable

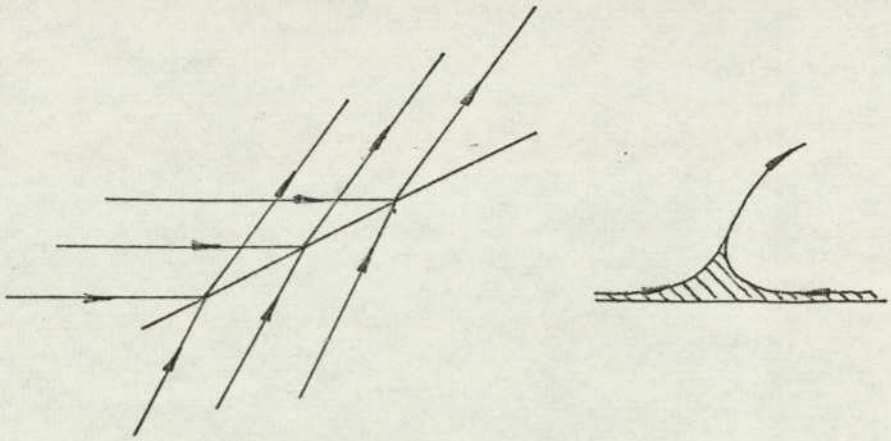

(a) cross flow separation

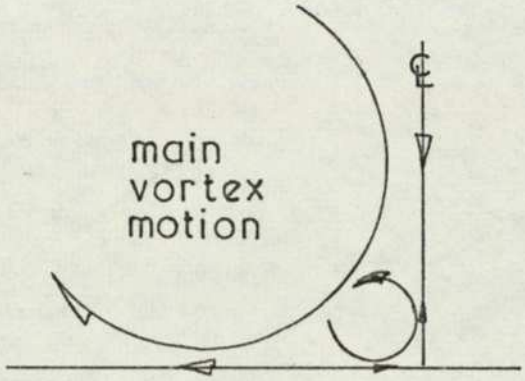

(b) vortex opposing main flow near x-ax

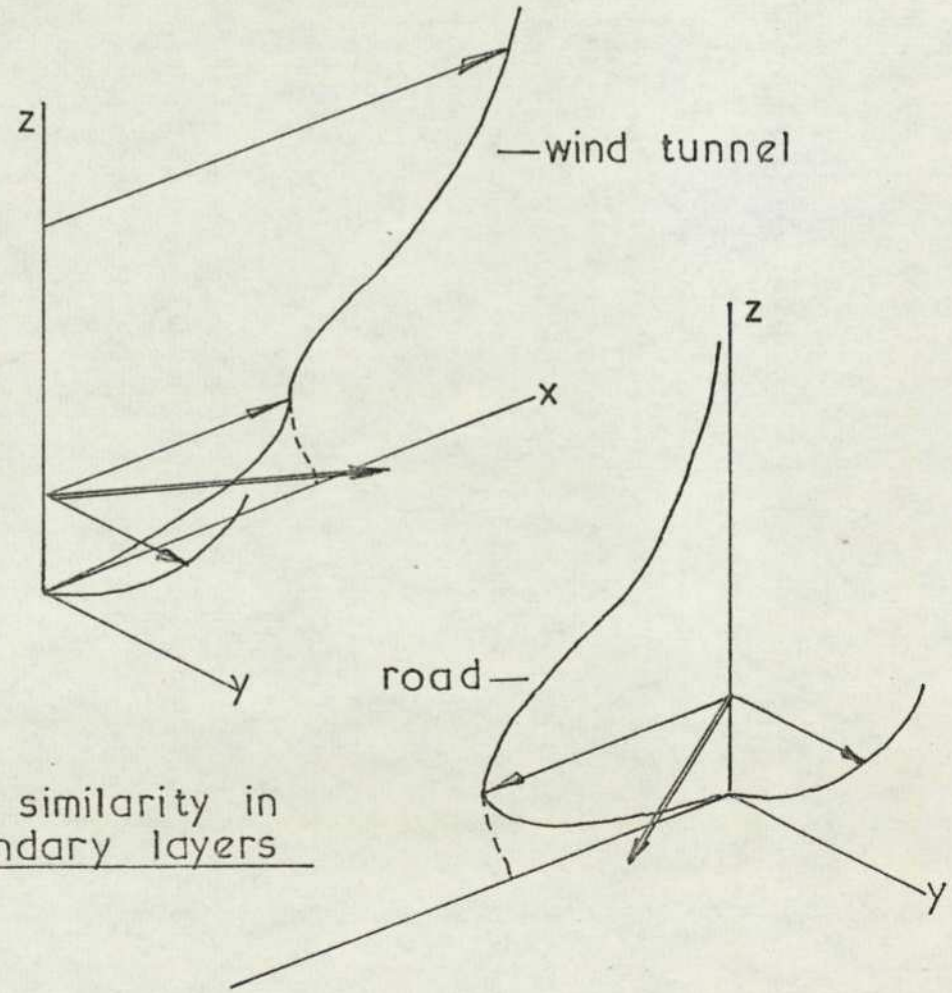

(c) flow similarity in boundary layers

FIG.125 FLOWS ADJACENT TO THE GROUND

to expect that the base recirculation region will not be significantly different in extent to that measured here.

In general the trailing vortices generated by the lifting car shapes experience both lateral and vertical motions, and the wakes are not therefore represented by either the cambered blocks, which generated vertical motion of the vortices only or the blocks at incidence, which produced purely lateral vortex movement.

Theoretical studies of the rolling up of the trailing vortex sheet behind wings in free stream have been made by numerous authors, and the problem has been treated in detail by Cone (61). For comparison the streamlines for a vortex pair near to ground, or, identically, for a vortex in a corner, have been determined. The complex potential, W_1, for a line vortex of strength, Γ, situated at $y = y_v$, $z = z_v$, is given by

$$W_1 = \phi_1 + i\psi_1 = \frac{-i\Gamma}{2\pi} \ln \left[\frac{(\Omega - (y_v + iz_v))(\Omega + y_v + iz_v)}{(\Omega - (y_v - iz_v))(\Omega + y_v - iz_v)} \right] \quad (4.7)$$

where ϕ_1, ψ_1, are the velocity and stream potentials respectively, while Ω is the complex variable of the y-z plane, y + iz. Substituting k for the expression $e^{-4\pi\psi/\Gamma}$ and after some manipulation the result is

$$y^2 + z^2 + y_v^2 + z_v^2 \cdot = \frac{4}{1-k} \left[(yz_v + zy_v) - k(yz_v - zy_v) \right]^{1/2} \quad (4.8)$$

which is really of little use. A graphical solution has been obtained and the corresponding streamlines are plotted in Figure 126 for the vortex symmetrically situated in the corner. A circular form is approached close to the vortex. For the vortex in free stream the corresponding streamlines are always true circles.

The vortex in a corner experiences both a vertical and horizontal velocity. In general it is not possible to superimpose a flow which would satisfy all the boundary conditions but taking the simple corner flow given by

$$W_2 = C\Omega^2 \quad (4.9)$$

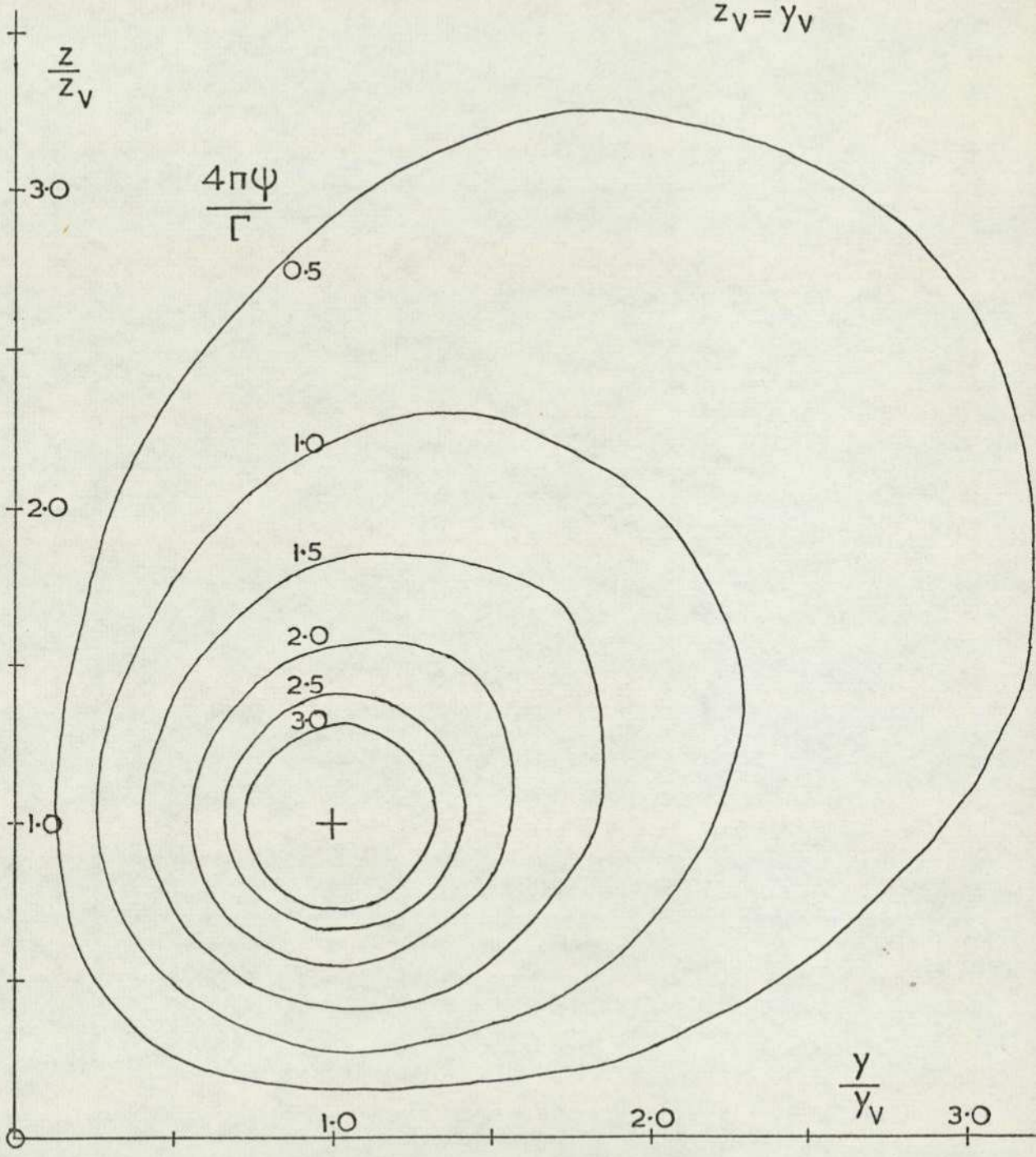

FIG. 126 VORTEX IN A CORNER

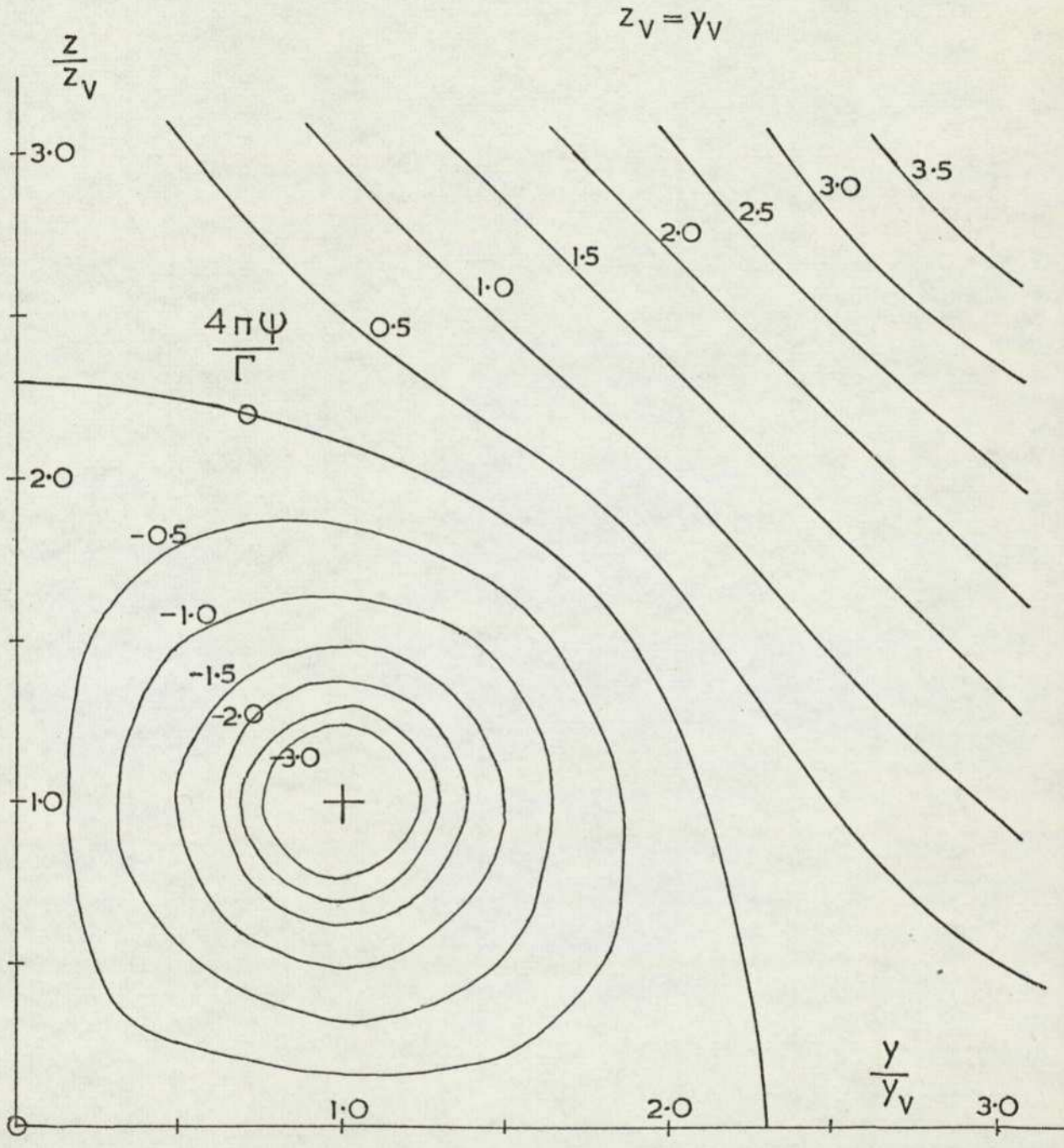

FIG. 127 VORTEX IN A CORNER WITH SUPERIMPOSED CORNER FLOW

where $W_2 = \phi_2 + i\psi_2$ and C is a constant, the flow conditions at the origin and at the vortex can be satisfied, when $y_v = z_v$ only. This corresponds to the vortex symmetrically placed in the corner, again, and the constant, C, is given by

$$C = \frac{\Gamma}{16\pi y_v z_v} \qquad (4.10)$$

The potentials can be superimposed and the solutions for $\psi_1 + \psi_2$ = constant were found graphically as before. The resulting streamlines are plotted in Figure 127. The stagnation streamline is independent of the circulation value, and is almost circular in shape. As the vortex moves towards the ground and away from the z-axis the fluid within the closed boundary must stay with it. At some point the boundaries dividing the two vortices above the ground will no longer include the vertical axis and the streamline pattern of a vortex pair near to ground, after a sufficiently long period, will be the same as the free stream case except that the pairing for a particular vortex becomes its mirror image. Cone (61) has shown that the closed boundary in this case is nearly elliptical in shape with a minor axis at the ground plane of length equal to 1.2 times the vortex spacing and a major axis 77% larger. As the vortex spacing is reduced to $(2)^{-1/2}$ times that investigated here, the area enclosed is considerably reduced.

The decay of the maximum speed of the rotating vane is shown in Figure 128. All models display an approximately similar rate of decay, this being close to the reciprocal of the square root of the distance downstream from the base. As this distance is directly proportional to the life of the vortex this tends to support the theoretical work of Squire (62) and Owen (63) and the experimental studies of Rose and Dee (64), amongst others, which showed that that the maximum circumferential velocity due to the vortex varied with the inverse root of time. The peak downwash is plotted for the saloon 1 and the fastback 2 models on the same curve. This shows a considerably faster rate of decay but then it must be remembered that the vortices are moving apart.

The hot wire anemometer results can be expected to be accurate near to the vortex core where circumferential velocities are small. The decay of the maximum velocity deficit in the vorted is plotted in Figure 129.

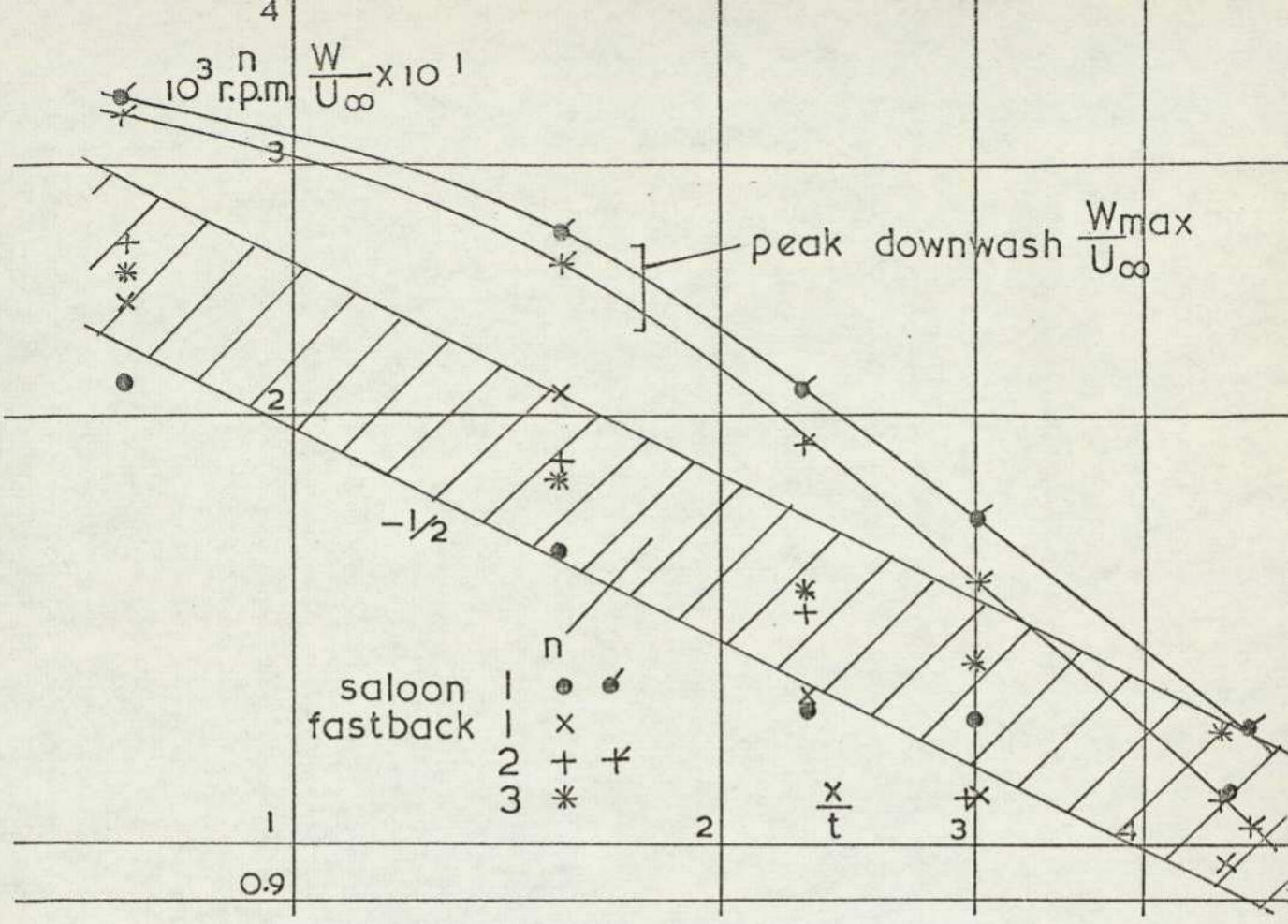

FIG.128 DECAY OF ROTATIONAL VELOCITIES IN A TRAILING VORTEX

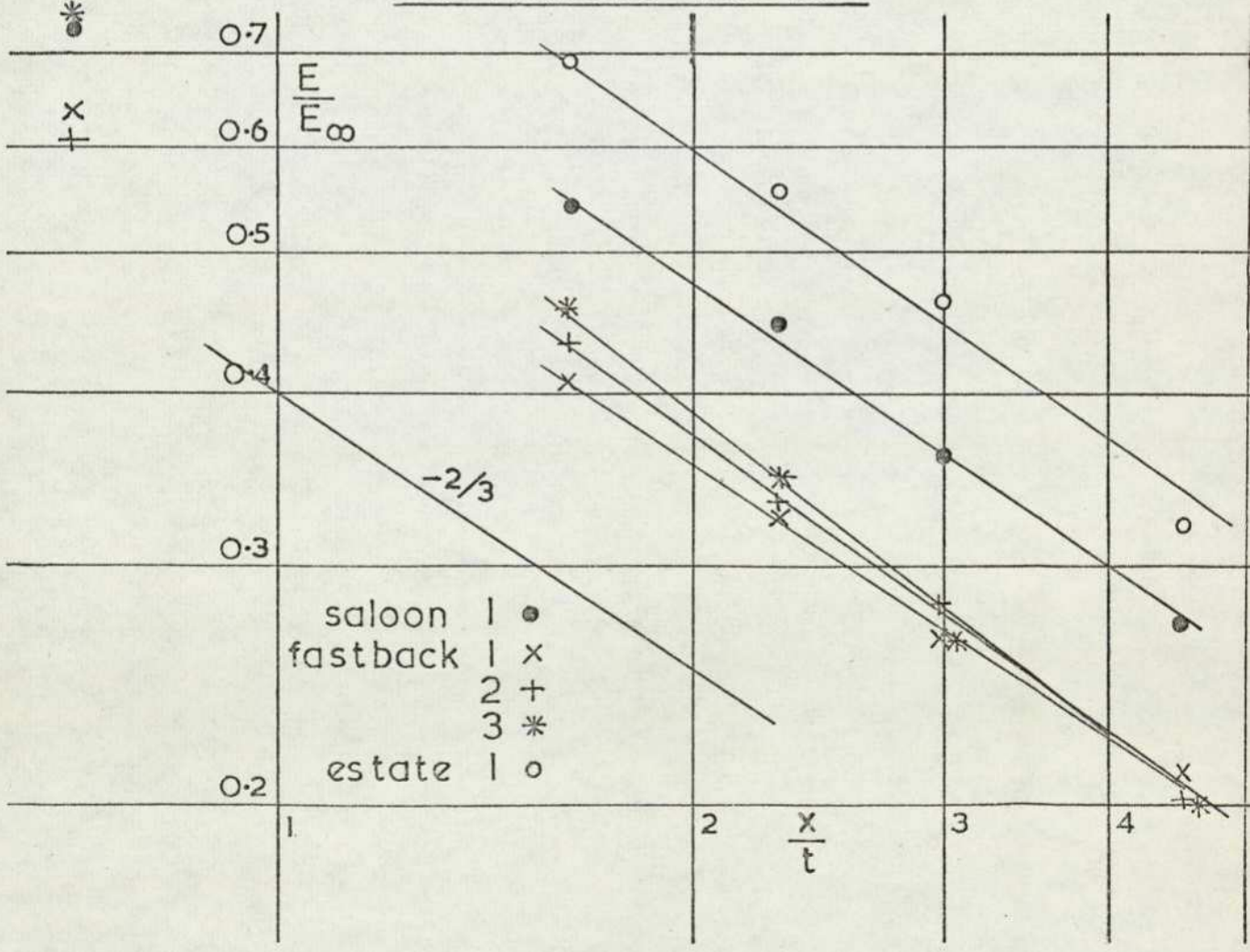

FIG.129 DECAY OF AXIAL FLOW IN VORTICES

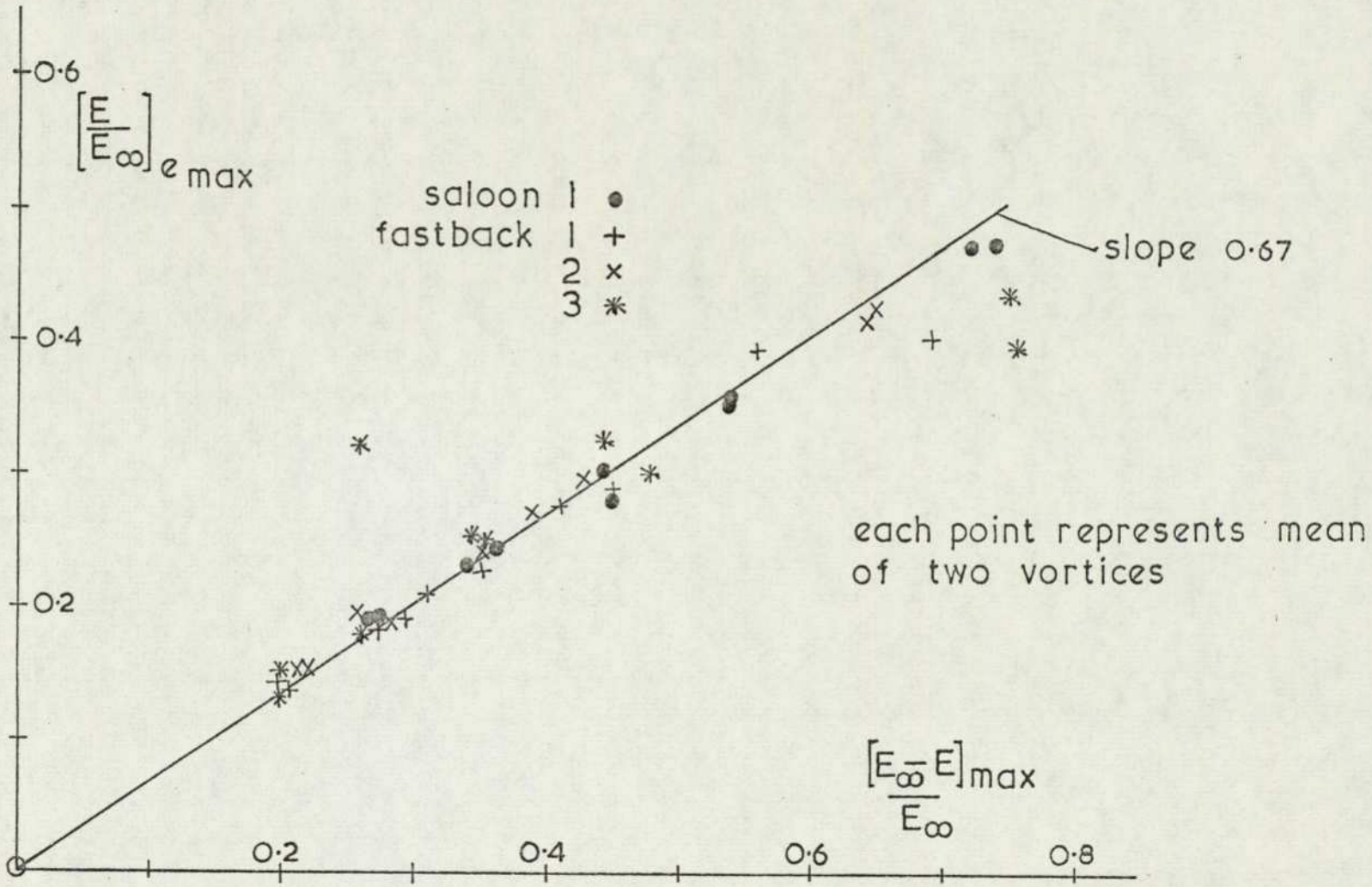

FIG. 130 VELOCITY OF VORTEX SHEET

and this shows that for all lifting models the decay is proportional to the downstream distance raised to the power of $-2/3$, approximately. The estate car wake is seen to behave similarly and indeed this is the same decay rate that has been found for any bluff non-lifting body.

Figure 130 plots the longitudinal velocity at the vortex sheet position, as indicated by the peak turbulence intensity, against the maximum velocity deficit. The data presented is the mean of a particular traverse. It can be seen that throughout the wake, the vortex sheet moves in the vehicle direction with a speed equal to two thirds of the maximum velocity deficit in the vortex.

The vortex sheet that separates at the base distorts strongly downwards at the wake centre line, and gives the impression of forming a pair of vortex tubes. As noted earlier for the cambered model and in the data obtained by Paish and White (28) for full size cars the initial vortex spacing for all these vehicles is small, varying between 40% and 60% of the car width. This implies a strange spanwise lift distribution on the vehicle. From the work of Widnall and Barrows (65) it is known that the lift distribution on a wing approaches a parabolic form as the ground clearance becomes small. However this does still not produce a vortex spacing which is as small as that found in these experiments.

The earlier results for the periodic effects in the wakes of non-lifting bluff bodies showed that a Strouhal number of about 0.2 could be defined for all of the bodies. The estate car, which has an identical distance between the shear layers at separation shows a similar dominant frequency, close to 60 Hz, although, as before, higher frequencies are apparent in the side vortex sheets. All the lifting car shapes show a frequency peak at around 75 Hz which, with a base separation height reduced by 45%, represents a slightly lower Strouhal number. The influence of the rear end geometry is probably important here. In addition the near wake is dominated by a peak at considerably higher frequency and, as stated earlier, this appears to be a function of lift. It can be seen in Figure 131 that the frequency increases approximately proportional to lift. This dependence on the lift suggests that a helical trailing vortex exists as a vortex ring structure should show no dependence on lift, the vortex strength of such a ring being related to vehicle velocity only, while a rotating vortex tube or line

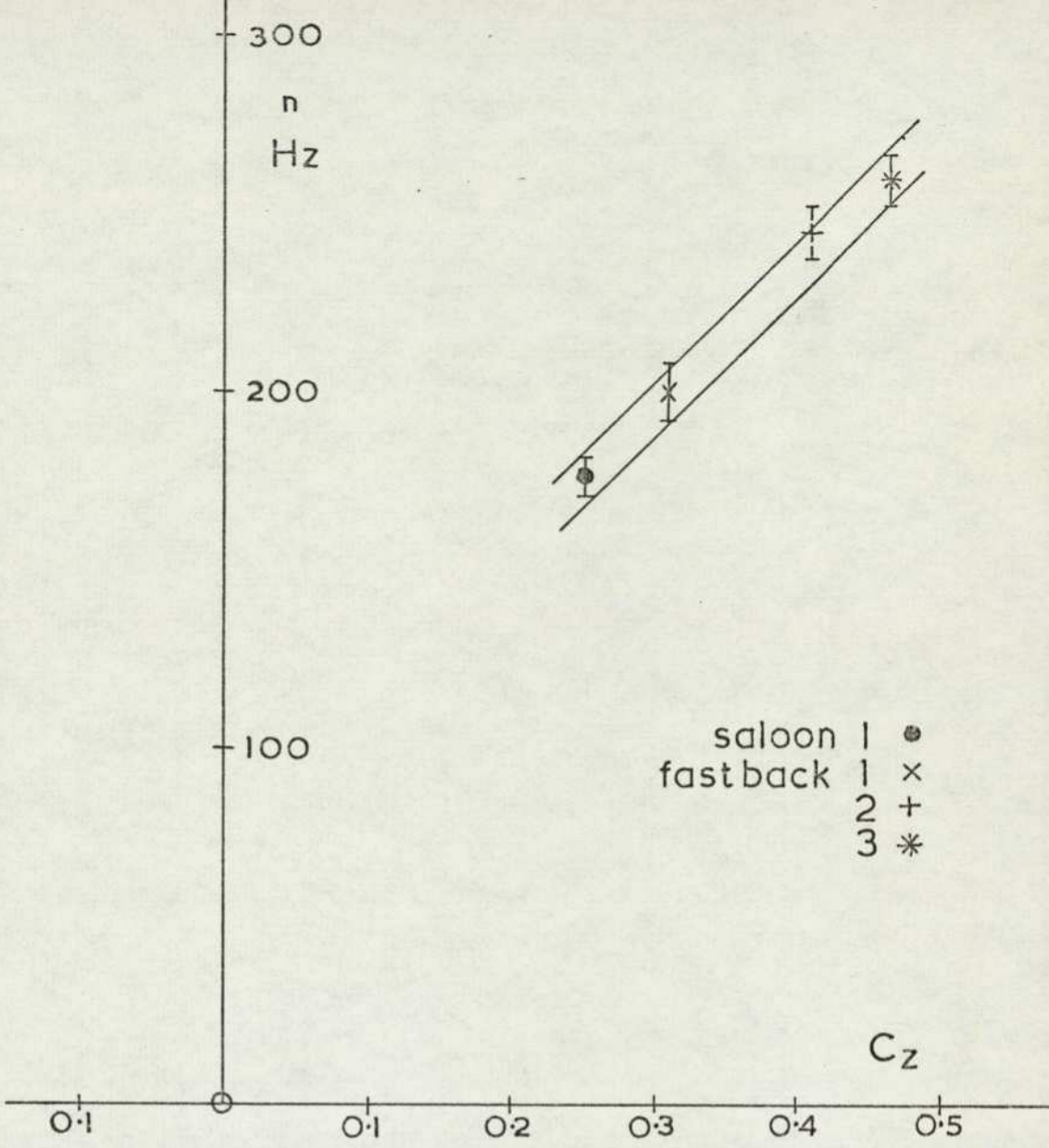

FIG.131 RELATION BETWEEN LIFT AND THE HIGHER FREQUENCY PEAK

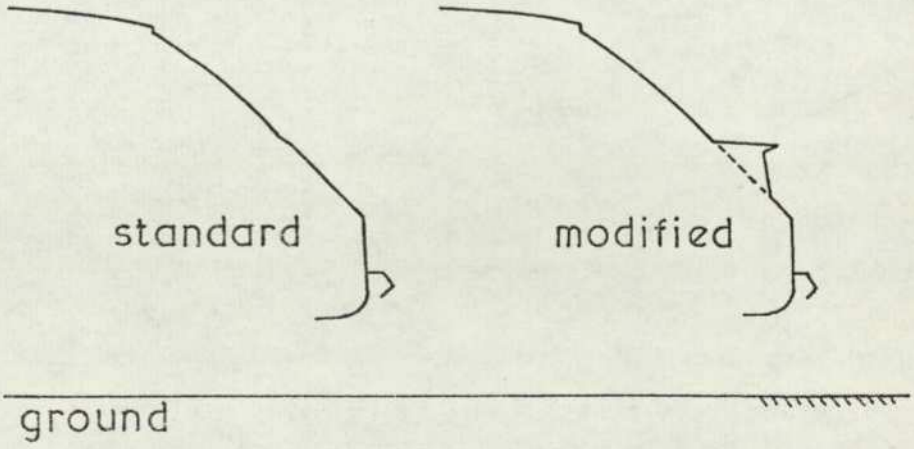

FIG.132 MODIFICATION TO BOOT DESIGN OF A TYPICAL SMALL CAR

vortex would not be time dependent. The theoretical work of Levy and Fosdyke (57) showed that the rotational and translational speed of a helical vortex was dependent on the vortex strength. The coexistence of a ring and helical vortex structure, which is implied by the two frequency peaks is difficult to explain. In relating the periodic measurements to full size road vehicles, the Strouhal number remains invariant, and so at 30 m/s a vehicle ten times larger would have a frequency of one tenth that measured here. A frequency of 7.5 Hz at this speed corresponds to a wavelength of 4.2 m or approximately a car length. The frequency associated with the helical structure of the wake is considerably higher and 20 Hz corresponds to a considerably shorter wavelength 1.55 m.

4.5. Conclusions

No dramatic effects due to ground proximity are evident for the wakes of non-lifting bodies, except that the vertical distribution of longitudinal velocity increasingly adopts a 'wall wake' profile as the ground is approached. Interesting three dimensional effects are explained by the action of secondary flows.

The wakes of lifting bodies near to ground display one of two distinct vortical structures. For bodies at incidence close to ground the crossflow developed in the underbody gap generates a longitudinal vortex as the flow emerges at the body sides. This vortex is produced sufficiently close to the ground that its subsequent motion is purely horizontal. The vortex development is similar to that above low aspect ratio wings.

A cambered body, with a flat lower side, on the other hand generates trailing vorticity which is essentially confined to the upper surface. The initial motion of these vortices is similar to that for a free stream wake, vertically downwards.

The road vehicles that develop lift forces show an intermediate state , where both transverse and vertical velocities of the vortex core are apparent. This vortex is nothing more than a distortion of the vortex sheet that separates at the vehicle trailing edge. Very narrow vortex spacing is apparent.

A road vehicle at yaw produces a noticeably modified trailing vortex structure with the wake characterised by two strong co-rotating vortices.

Axial velocities for both lifting and non lifting wakes tend to decay at a similar rate; proportional to (time)$^{-2/3}$ while for the transverse velocities the exponent is -1/2.

Distinct periodic effects were found for all wakes. The proximity of ground modified the local shedding rate in non-lifting wakes while in general a Strouhal number of approximately 0.2 could be defined for all three dimensional bodies generating zero lift. This value is almost identical to that found for various two dimensional and axi-symmetric bodies. Higher frequencies are apparent near the tip of three dimensional bodies. These disappear on travelling downstream. Cambered lifting bodies produce two distinct shedding frequencies one of which gives a constant Strouhal number and the other is lift dependent.

5. THE INFLUENCE OF WAKE FLOWS ON DRIVING CONDITIONS

5.1 Introduction

The wake flow results from the fact that air is a real fluid. This implies the existence of drag forces which naturally consume power. In addition wake flows of road vehicles manifest themselves to drivers in a number of unpleasant ways. In this chapter the problem of reduced visibility, arising from the introduction of particles into the wake, is discussed along with the forces that a vehicle experiences when immersed in the wake of another. The latter problem is extended to cover the effects of vehicle proximity in general. Finally certain other aerodynamic characteristics of road vehicles directly attributable to the effects of a wake flow are briefly considered.

5.2 Rearward visibility

The shear layers that separate at the vehicle base enclose a region of recirculating flow. In adverse driving conditions, whether dry or wet, droplets of water or particles of dust, thrown up by the tyres, enter the lower shear layer via the boundary layer growing on the vehicle underside. The process of turbulent mixing ensures that many of these droplets cross into the reverse flow area to settle on the body surfaces enclosed by the 'bubble'. If the surface happens to include the backlight then the rearward visibility of the driver will be impaired. From the zero velocity contours, shown in Figure 127, it can be seen that this situation cannot arise with the saloon 1 or any of the fastback models. Although the rear screen of the saloon is enclosed by a reverse flow region this does not extend to the boot trailing edge where the flow is in the stream direction, and so particles entering the wake downstream of the boot cannot communicate with the upstream reverse flow region. As the boot length is shortened the two 'bubbles' can intersect allowing the rear view to become obscured. This will occur when the boot length is just shorter than on the saloon 2 model. It is possible to define whether separation will or will not occur for a particular vehicle rear geometry by a limiting angle between the line joining the boot trailing edge to the roof separation point and the vertical axis. This can be called the effective backlight angle and it is assumed that the body geometry between these two points is not particularly relevant. The limiting

angle is therefore between 56°, representing the saloon 3 model, for which the flow at the boot trailing edge is definitely reversed, and 62°, for the saloon 2 model, which just maintains an attached flow. Janssen and Hucho (14)have shown that a sudden jump in both drag and rear wheel lift occurs on fastback models when the backlight angle is between 55° and 60° and they suggest that flow separation occurs when the angle is 56°.

To prevent the build up of deposits on the backlights of vehicles with steeply angled rear surfaces a number of car manufacturers have tried using small deflectors, similar in concept to the Townend ring found on the noses of early radial engine aircraft, mounted either on the roof trailing edge or to the vertical rear edges. The additional fitting of windscreen wipers for the rear window suggests that the aerodynamic device is ineffective. The reasons for failing to work are probably that the vanes are too small and are normally too deeply immersed in the vehicle boundary layer. Insufficient external flow energy is therefore diverted into the reverse flow region. The problem can possibly be eliminated by using carefully designed turning vanes but the only sure way to avoid poor rearward vision is to increase the effective backlight angle. An article by Clarke (66) has shown that a simple modification to the rear design can produce favourable results. The car modifications are sketched in Figure 132. It is interesting to note that the backlight angle on the original car is approximately 45° which is sub critical, while after modification the effective angle is 60° and just above the limiting angle. This is a useful confirmation of the flow results.

5.3 Forces on a car in proximity to a lorry

5.3.1 Preliminary comments

The aerodynamic characteristics of road vehicles have almost invariably been determined for the vehicle in isolation. The real vehicle however, is very rarely out of the presence of other road users, and a considerable part of driving time is spent in passing, or being overtaken by, other vehicles. When the manoeuvre is carried out at high speed, as would happen, for instance, on a motorway, substantial forces can be generated for which the driver must take corrective action.

A number of wind tunnel investigations of the interference

effects between vehicles have been made, and as part of this research the author undertook a series of static wind tunnel tests to determine the aerodynamic forces on various cars immersed in the wake of a lorry. It became clear that the maximum load changes occurred outside of the wake region so the work was extended to cover the general effects of proximity. The main results of this study have been previously reported and are contained in the Appendix to this thesis. Included in that paper is a summary of the previous research on the interference problem. Subsequently a number of authors have produced similar studies, dealing with the influence a large vehicle exerts on a smaller one. Choulet, Favero and Romani (67) studied all force and moment components on a car carrying out one fixed overtaking path relative to a lorry. In addition the effect of a cross wind was investigated by yawing both models, and was found to be considerable while large changes in pitching moment and lift force were found. Heffley (68) in a similar wind tunnel experiment investigated the interference effect produced by lorry and bus shapes on a variety of passenger cars including a car and caravan combination. Comparisons with full scale measurements of flow angle close to a truck and in front of an overtaking car were made. A pressure tapped model was used by Johnson, Speckhart and Bridwell (69) to investigate interference effects between rectangular blocks simulating large bluff road vehicles. The only data to be derived using moving vehicles was obtained by Brown (70) who used models mounted on a cable drive system. Different passing speeds could be represented and cross winds were simulated by ducting the output from an array of fans across the track.

5.3.2 Additional force measurements

Limited working section length in conventional wind tunnels means that the study of such phenomena as the overtaking manoeuvre is restricted in the size of the models that can be used while ensuring that the ground board length available allows adequate model spacing and that sufficient flow settling occurs upstream of the force model. Manipulation of the force model position, as already described by the author can effectively double the working section length while limiting the boundary layer thickness on the ground plane. In addition, it was felt that as the major disturbances occur only at the extremities of the lorry, an increase in ground board space was obtainable by reducing the lorry length. Two additional rear cargo sections were built, giving an overall lorry model length of 0.255 m and 0.765 m. These models have been described in Section 1.3.3 and are shown in Figure 11, along with

the car models.

The influence of Reynolds number on the drag force experienced by the three car and three lorry models is shown in Figure 133.

Measurements of side and drag force and yawing moment coefficients were made as before but using only the saloon car configuration, as the force model. The results are shown in Figure 134, for the longest lorry, and Figure 135 for the shortest lorry. It is apparent that data obtained in the region of the nose disturbance, and forward of this point is very similar for all three lorry models. The same is true at, and downstream of, the rear disturbance. The region between these two peaks shows that there is an effect of lorry length; the shorter model tending to reduce the suction experienced by a car half way along its length. Using the shorter lorry model to obtain force measurements at greater downstream distances within the wake of the lorry shows that the force changes occur slowly. All drag curves exhibit a small disturbance near to one car length downstream of the lorry base. This is probably the region of closure for the reverse flow bubble at the lorry base. All the car models except the fastback, experience a thrust when very close to the lorry trailing edge. A check on repeatability and the Reynolds number effect is shown in Figure 136.

Measurements of lift force and pitching moment were made using the saloon car model mounted at a limited range of positions in proximity to the shortest lorry model. Considerable variations occur when the car is just in front of the lorry, Figure 137. Small lateral position changes produce quite large lift variations ($\Delta C_z \doteq 0.3$) while in the wake of the lorry the car experiences an increase in both lift and pitch.

The response of the car model to incidence variation when in proximity to the lorry was examined at two positions. The spacing between models was half the car length, with the car mounted on the lorry centre line both upstream and downstream of the lorry. When the car is upstream of the lorry, Figure 138, the lift variation is similar to that in free stream, but the car in the lorry wake has considerably reduced sensitivity to incidence.

5.3.3 Discussion

In order to assess the flow field in which the car is immersed a few measurements of wake properties were made downstream of the short lorry model. Pitot pressure contours are shown for three stations in Figure 139. A small separation is apparent at the upstream station.

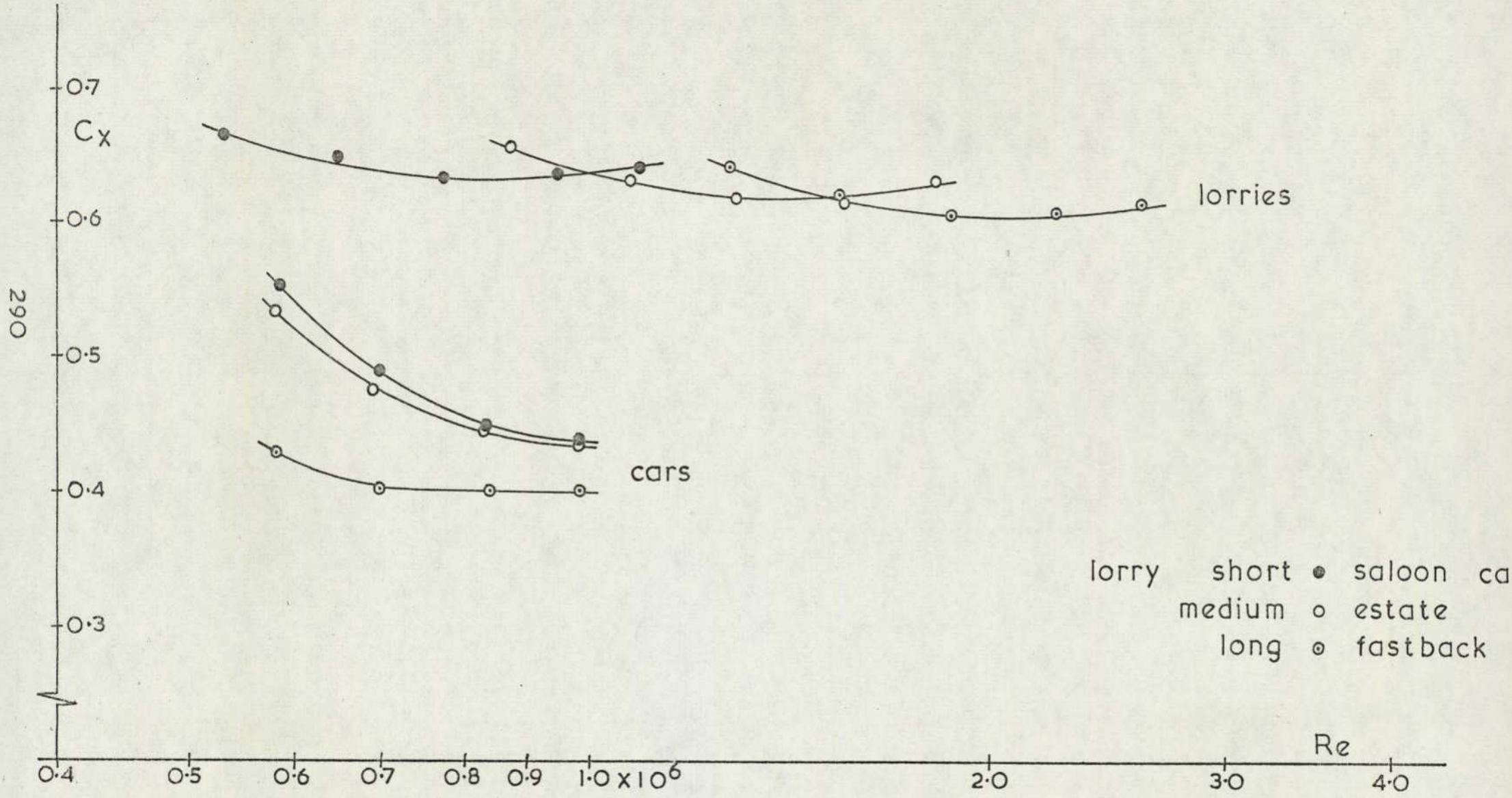

FIG. 133 INFLUENCE OF REYNOLDS NO. FOR VEHICLE SHAPES USED IN OVERTAKING EXPERIMENT

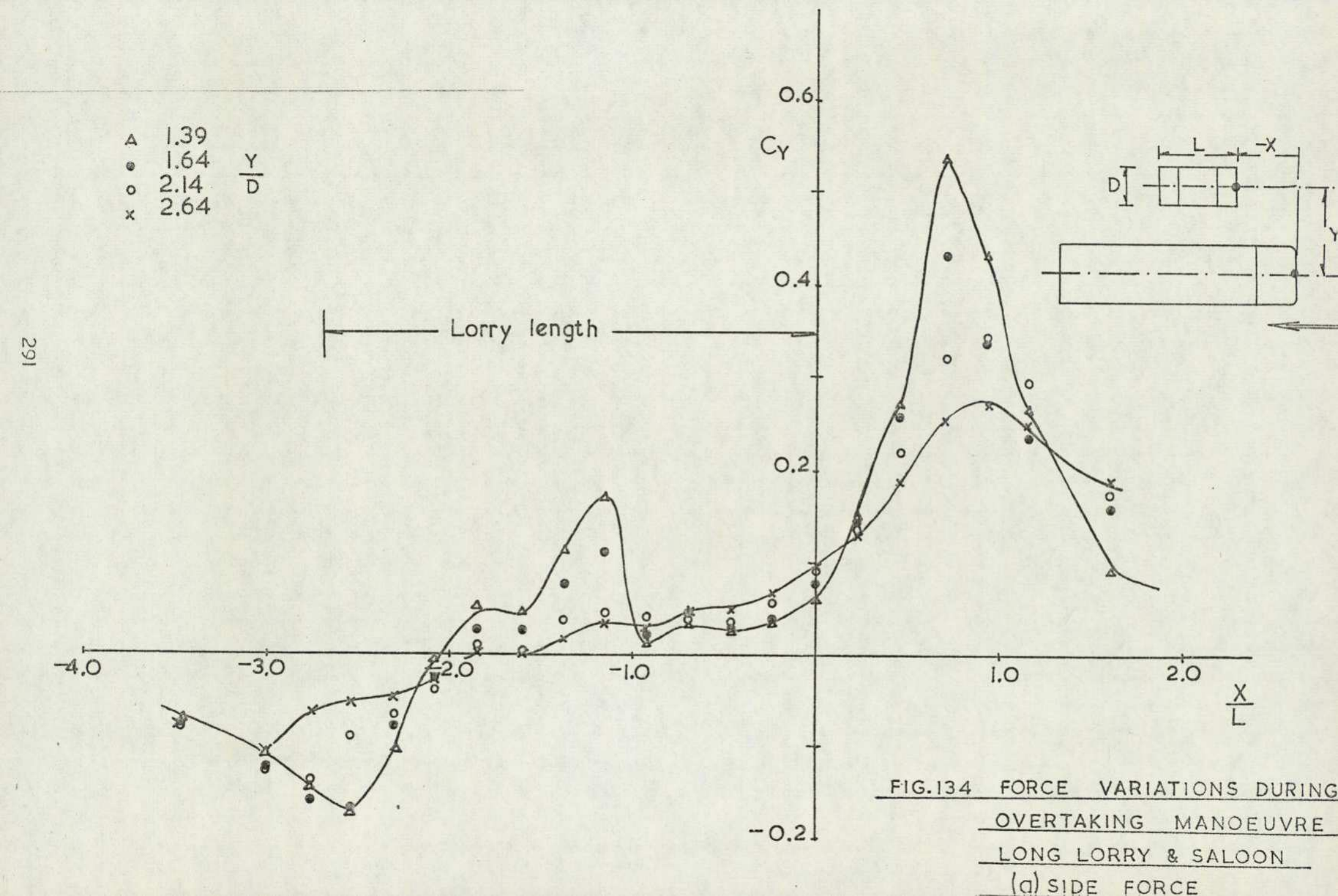

FIG. 134 FORCE VARIATIONS DURING OVERTAKING MANOEUVRE LONG LORRY & SALOON (a) SIDE FORCE

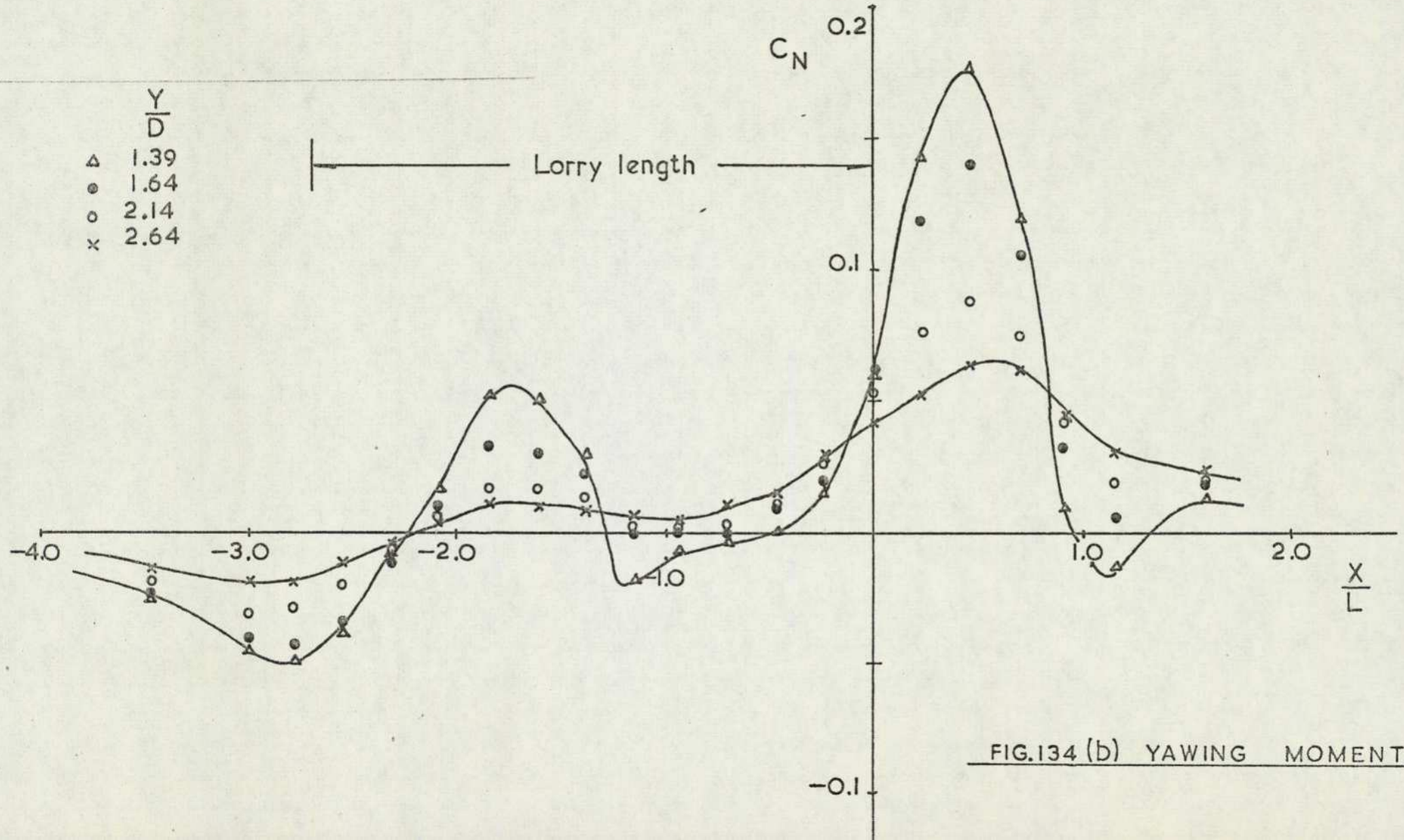

FIG.134 (b) YAWING MOMENT

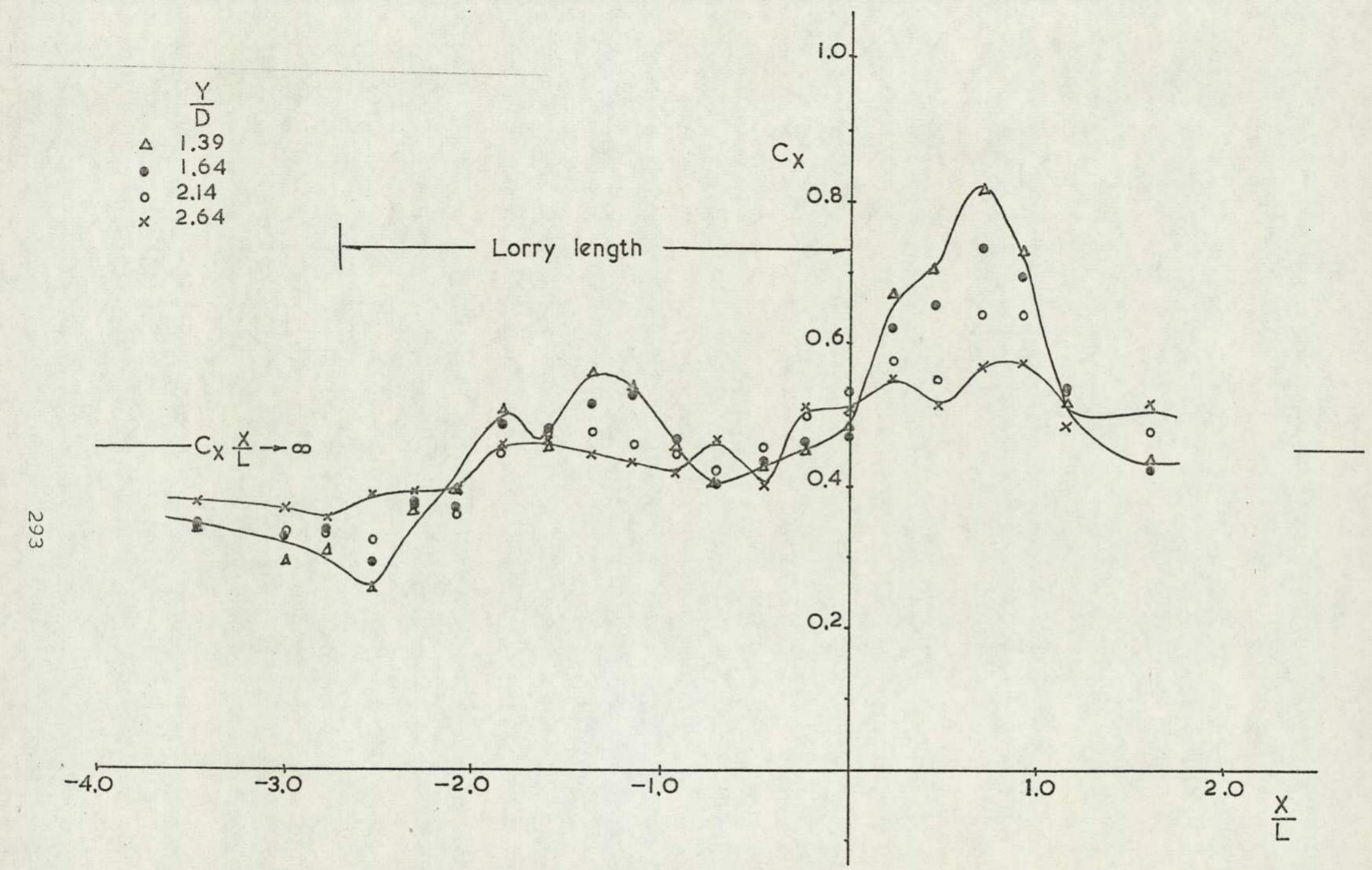

FIG. 134 (C) DRAG FORCE

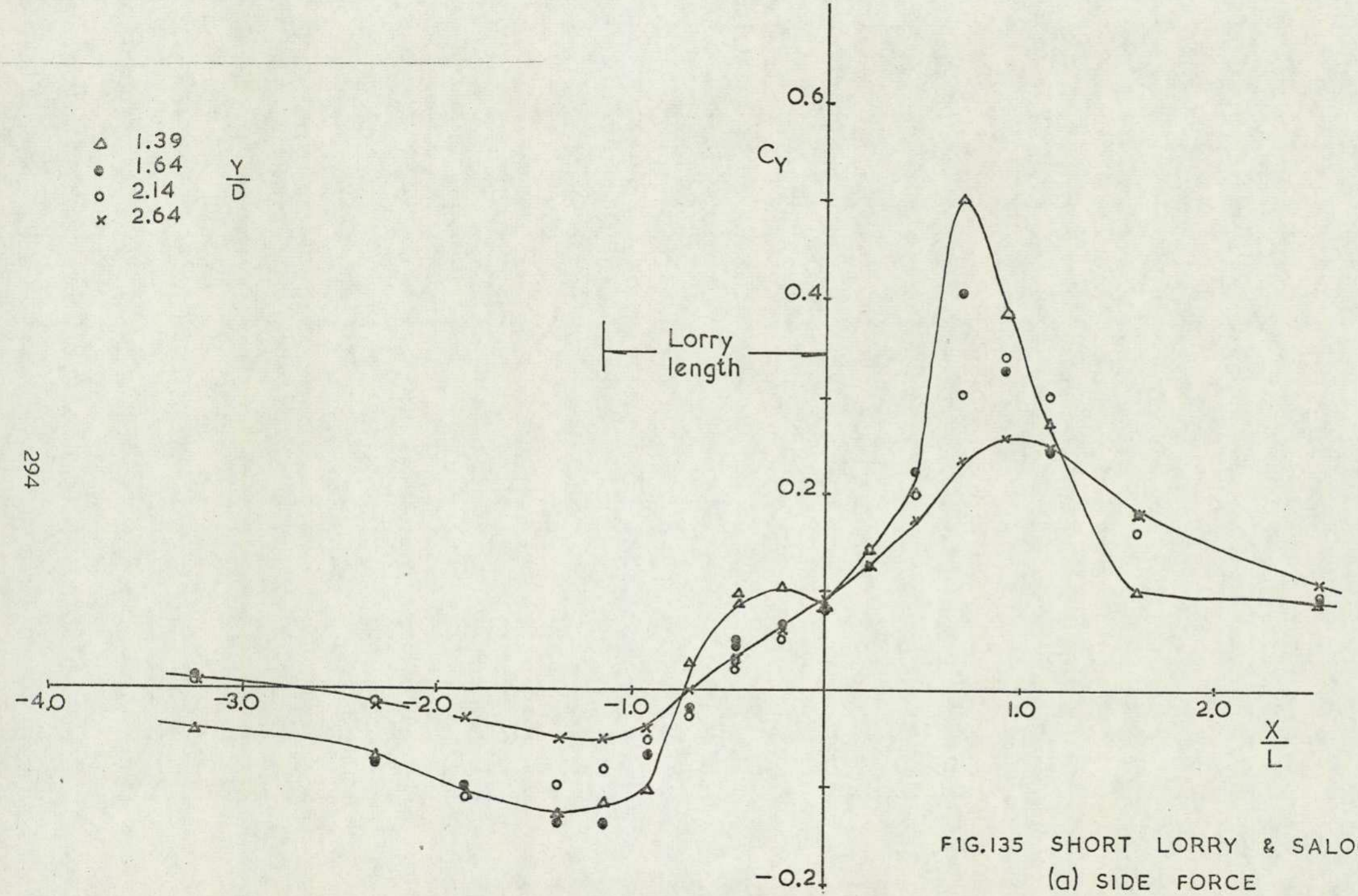

FIG.135 SHORT LORRY & SALOON
(a) SIDE FORCE

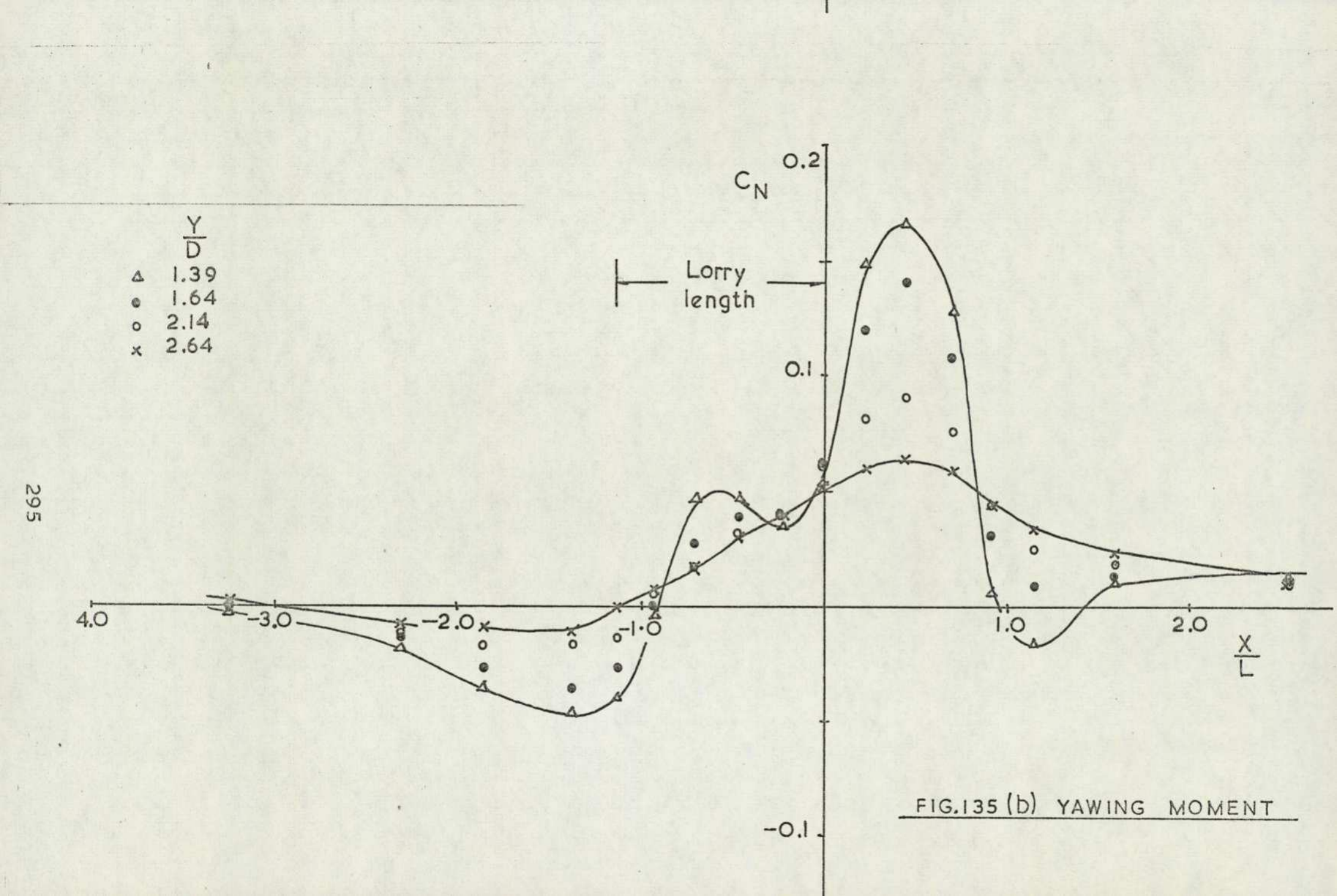

FIG.135 (b) YAWING MOMENT

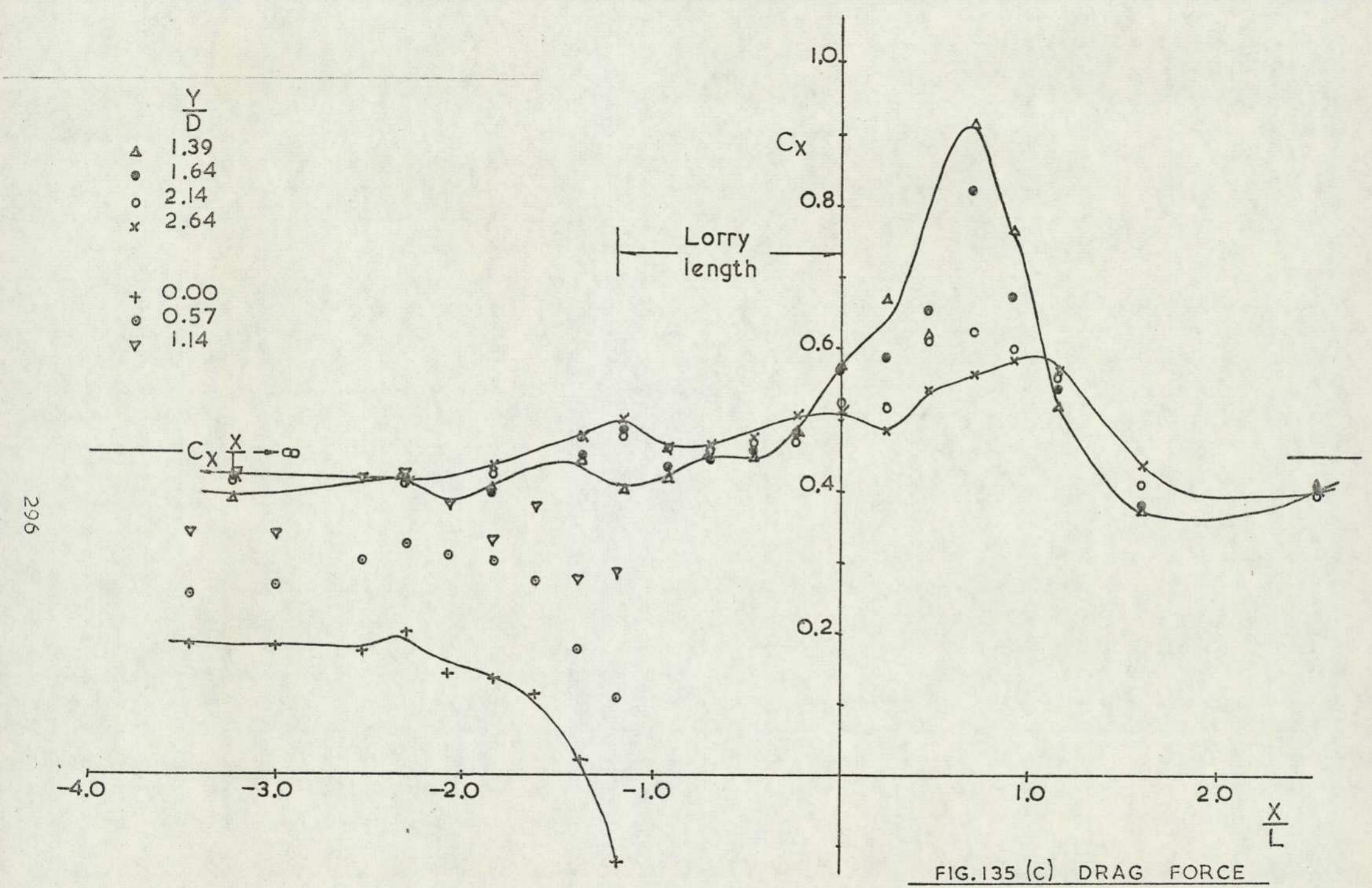

FIG. 135 (C) DRAG FORCE

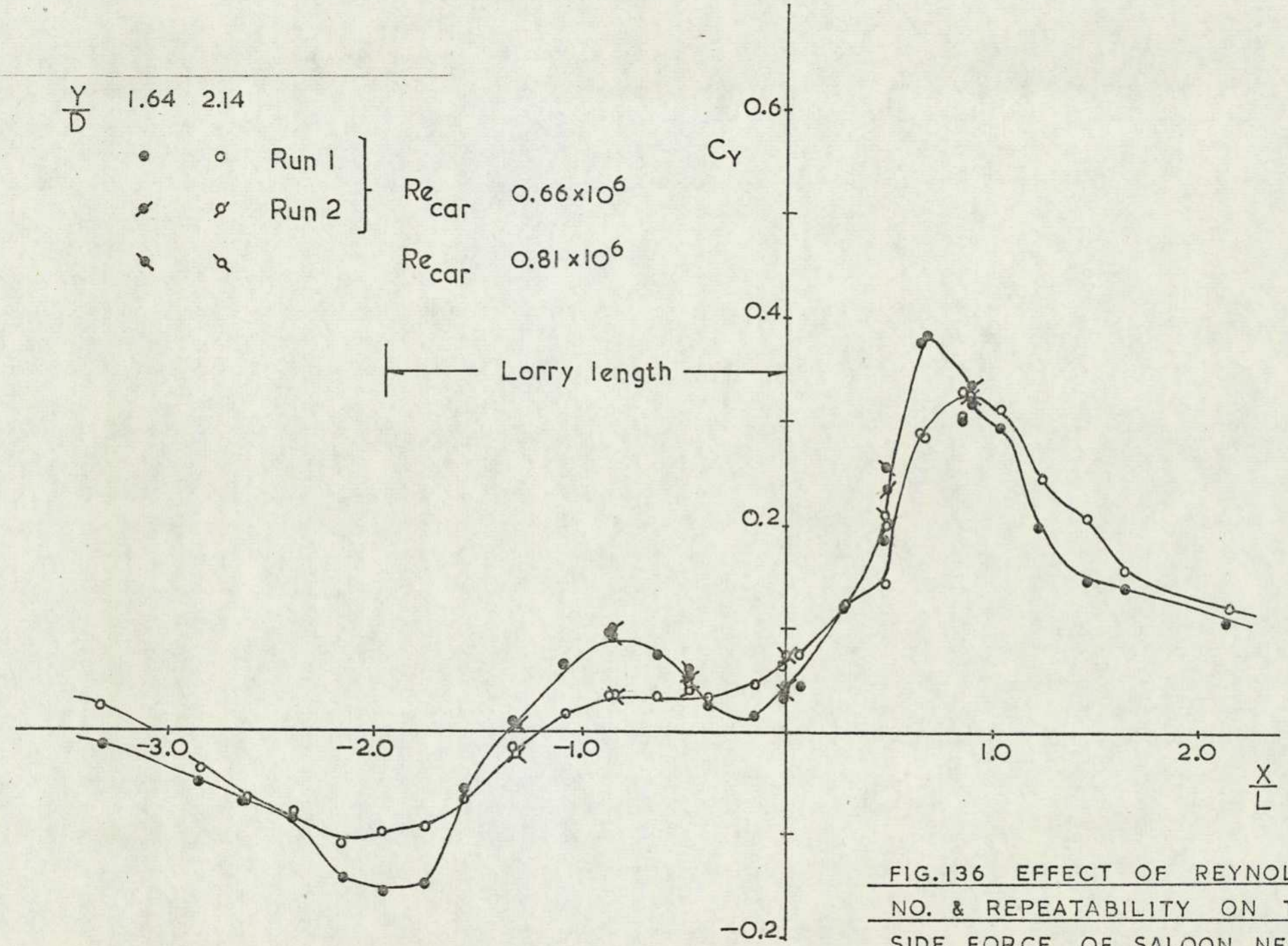

FIG. 136 EFFECT OF REYNOLDS' NO. & REPEATABILITY ON THE SIDE FORCE OF SALOON NEAR MEDIUM LENGTH LORRY

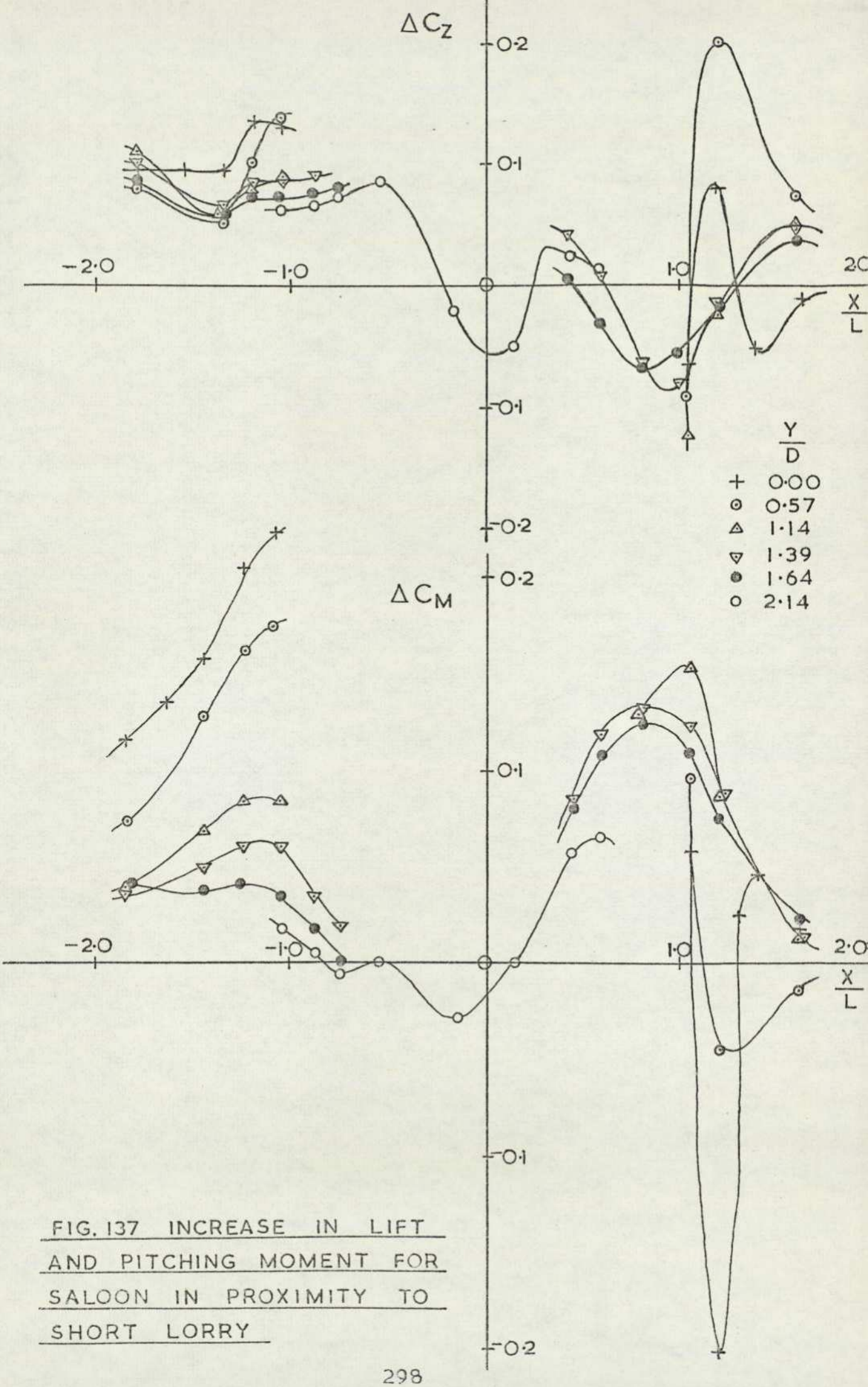

FIG. 137 INCREASE IN LIFT AND PITCHING MOMENT FOR SALOON IN PROXIMITY TO SHORT LORRY

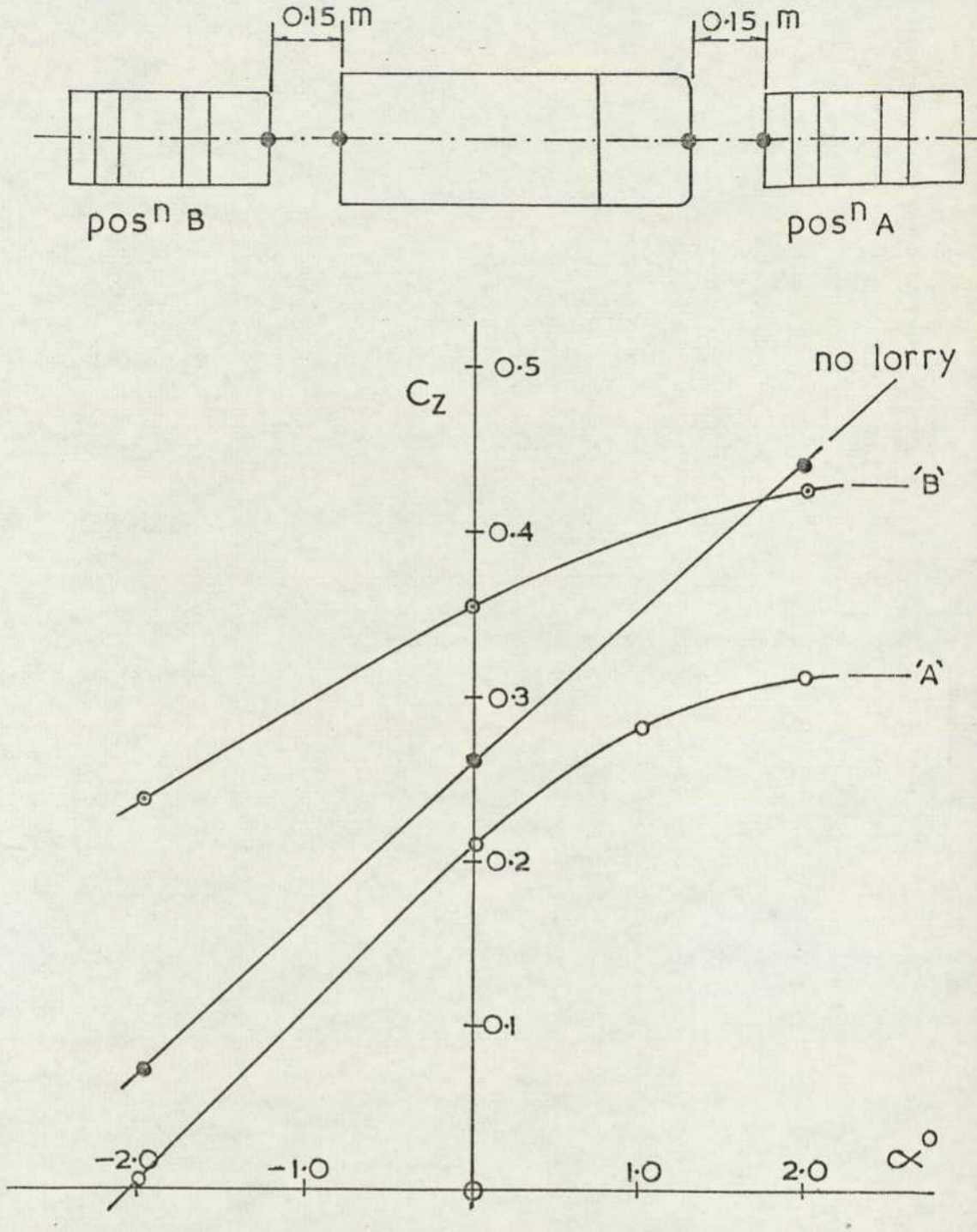

FIG. 138 LIFT SENSITIVITY TO INCIDENCE FOR SALOON 1 IN PROXIMITY TO SHORT LORRY

This occurs on the ground immediately behind the wheels of the lorry. The general contour shape differs slightly from that found for the smaller lorry model, Figure 102. The greater degree of underbody roughness may account for the more pronounced retardation of the flow near to the ground while the fact that the larger model has well radiused longitudinal edges results in less distortion in the corners of the wake. The downstream station of the larger model corresponds approximately with the upstream station of the smaller model. A limited number of traverses were performed with the hot wire anemometer. The results of these are shown in Figure 140. The horizontal traverses were made at a height of 40 mm at three downstream stations. A distinct turbulence intensity peak is apparent throughout the wake at a position just inboard of the vehicle sides. Three vertical traverses were performed at one downstream location and at different spanwise positions. The profiles are of complicated shape at a position corresponding approximately with the turbulence intensity peak of the horizontal traverse while the wake is not noticeable at the outboard station.

The static wind tunnel simulation employed here is obviously only representative of two vehicles travelling at equal speeds. An extrapolation of the data, as indicated in the appendix, can be safely used for the situation where the overtaking speed is small in relation to the vehicle speeds. This assumes that the lateral force changes arise solely from a superimposed cross flow. An interesting point made in that paper was that given this simplification the curves shown represent any combination of vehicle speeds if the velocity term necessary for non dimensionality is the product of the two vehicle speeds.

With regard to dynamic effects there are two limiting conditions. Firstly the response of a vehicle to a 'steady' gust must be considered. The results of a theoretical analysis by Hucho and Emmelman (71) imply that if a typical car encounters a lateral gust of sinusoidal shape and having a rise distance, the distance required for the cross wind to reach its maximum value, of more than five vehicle lengths, then the response is quasi-static; the lateral loads are approximately proportional to the local cross wind angle. For a rise time less than half this an increasing overshoot in the loads is apparent. From the results of this study of overtaking the rise distance is typically greater than half the car length relative to the lorry.

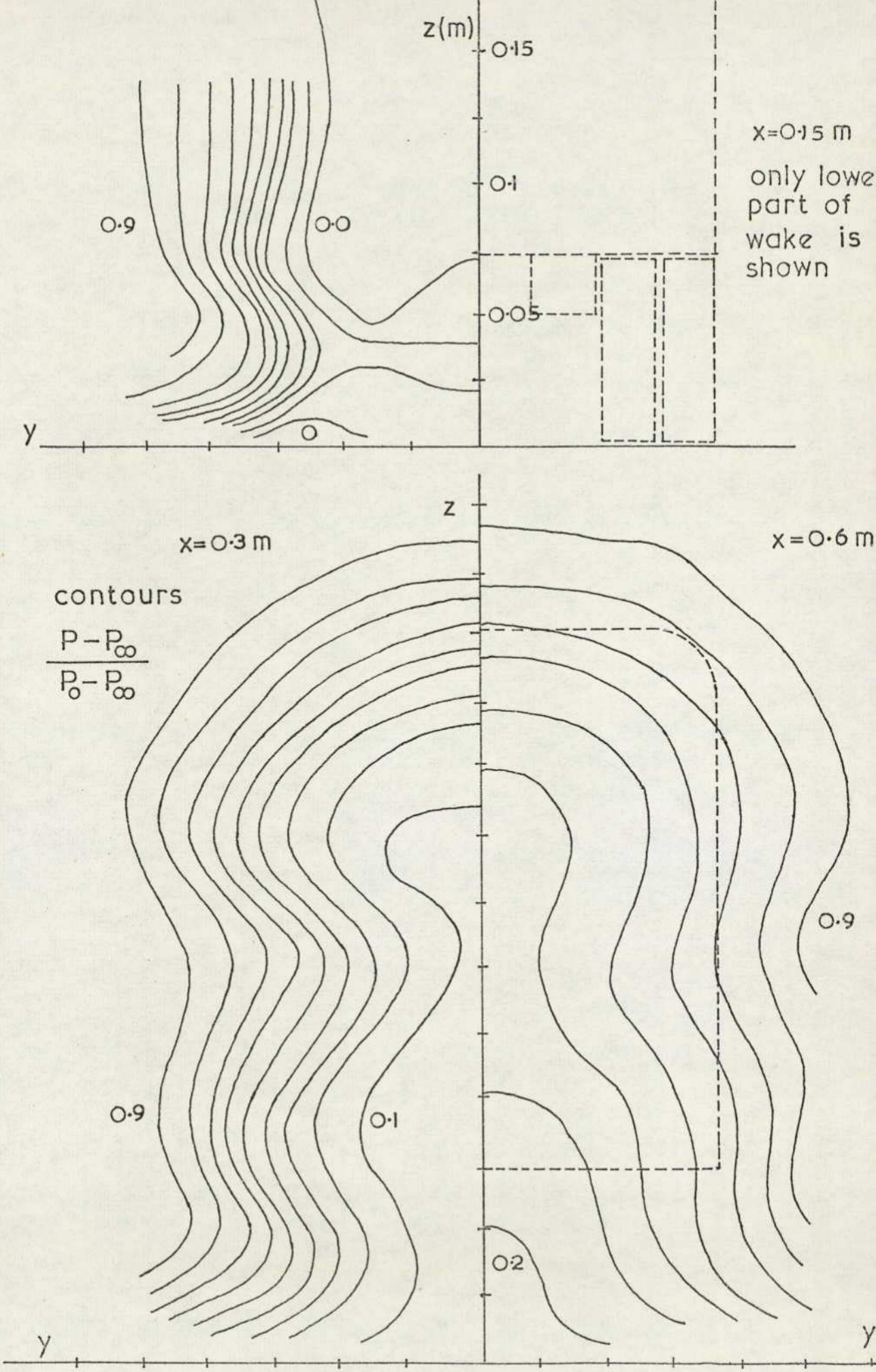

FIG. 139 PITOT CONTOURS — LARGE LORRY (SHORT)

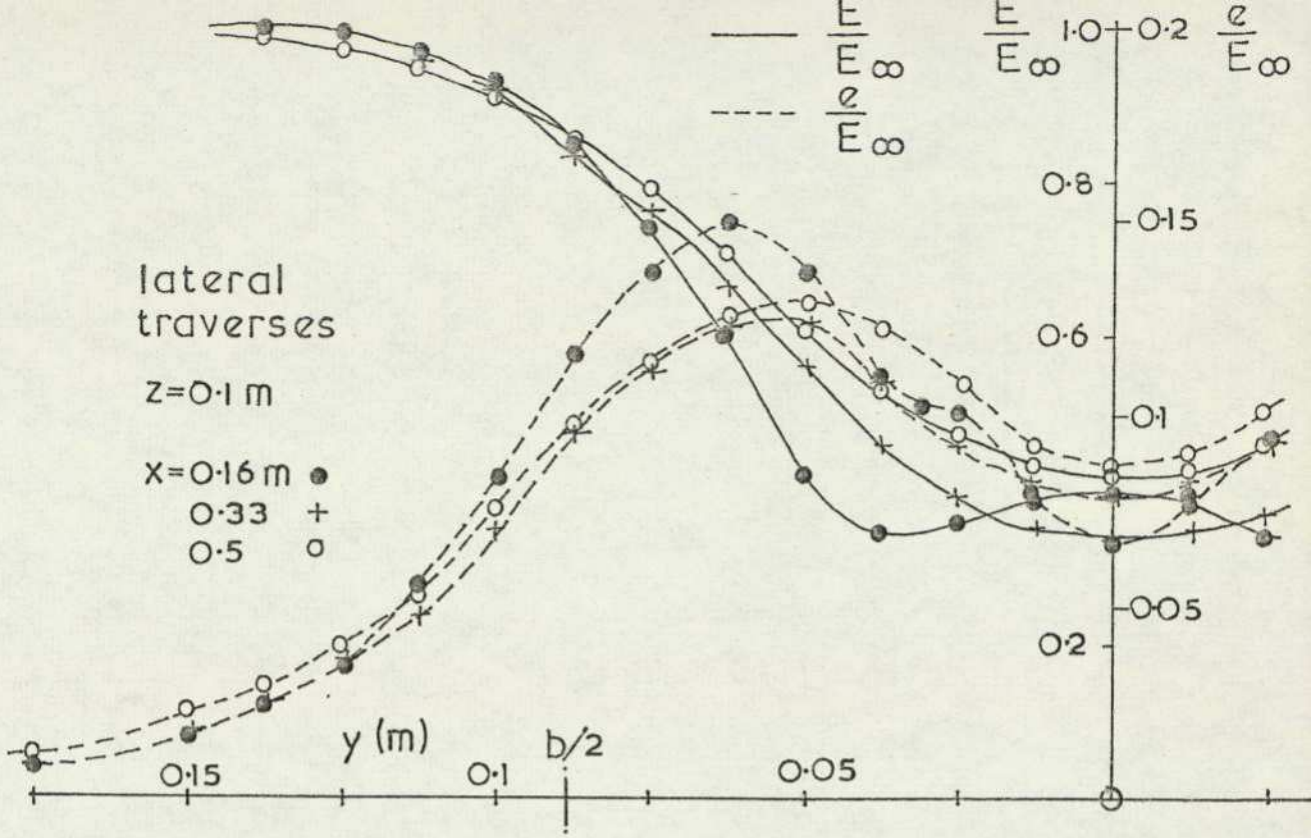

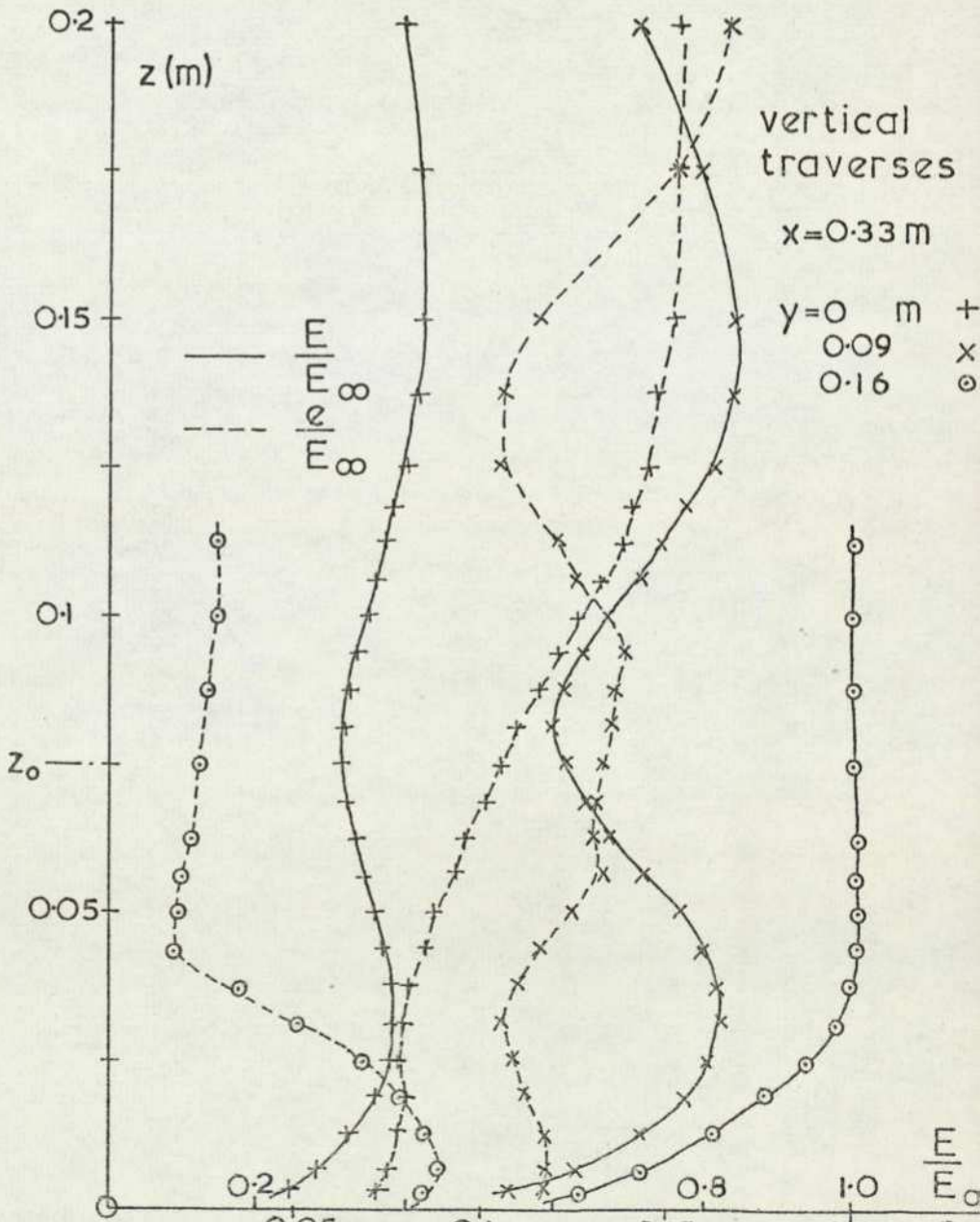

FIG.140 WAKE TRAVERSES — LARGE LORRY

The disturbance rise distance relative to the car is given by

$$\frac{U_c}{2(U_c-U_l)} \quad \text{car lengths}$$

where the suffices c,l, refer to the car and lorry velocities respectively. The overtaking speed is therefore limited to 10% of the car speed. As the lateral spacing between vehicles increases the rise distance of the gust becomes greater and so a greater overtaking speed can be represented.

Secondly, the response of a real vehicle will be different if the frequency of any disturbance approaches the natural frequency of the vehicle suspension system. The vertical forces are not periodic but the lateral loads vary in a highly periodic manner when the vehicles are close together. The wavelength, λ, of this disturbance is approximately twice the car length, so the input frequency, ω, to a passing car will be

$$\omega = \frac{U_c-U_l}{\lambda} \qquad (5.1)$$

where U_c and U_l are the speeds of the two vehicles. Typically the natural frequency, ω_n for the rolling motion of a car is about 1.5 Hz while the lateral frequency is somewhat higher due to the tyre stiffness being fairly high, about 6 Hz. The steady state representation is therefore invalid when

$$U_c-U_l = \lambda \omega_n \qquad (5.2)$$

ie the overtaking speed is 13.5 m/s. This condition is distinctly higher than the previous one. The steady state representation in a wind tunnel of the overtaking situation is therefore valid for moderate overtaking speeds only.

An elementary exercise to predict the peak side loads experienced by a small vehicle in the presence of a larger one was performed. The small vehicle was assumed to have a negligible effect on the flow around the lorry. The length and height of the lorry, being much greater than the car dimensions were considered to be unimportant. Consequently the lorry was replaced by a two dimensional rectangular surface extending downstream and vertically to infinity. The car itself was

removed and the forces upon it determined from the sensitivity to a yaw flow and the local cross flow angle. The problem is therefore reduced to the determination of the flow up a step as shown in Figure 141. The theorem of Schwarz-Christoffel can be used to transform the surface of the step, representing the plane of symmetry and the lorry surface, in the z-plane to the real axis of the ξ-plane. Milne-Thomson (72) has shown that a convenient solution can be obtained using a uniformising variable, t', where

$$\xi = \cosh t' \qquad (5.3)$$

so that for a step height, h, and free stream velocity, U

$$z = \frac{h'}{\pi} (t' + \sinh t') = x+iy \qquad (5.4)$$

$$w = \frac{h'U}{\pi} \cosh t' = u+iv \qquad (5.5)$$

define the flow velocities at a given station.

As it is found that the flow properties change dramatically over the length of the car, replacing the vehicle by a single point representation was employed. A typical car in a cross flow experiences peak loadings at the extremities of the vehicle but for this computation the reference points were taken to be the front and rear axle positions. Denoting the front and rear axle conditions by the suffix F and R respectively the side force coefficient C_Y and the yawing moment coefficient C_N are given by

$$C_Y = \left(\frac{\delta C_Y}{\delta \beta}\right)_F \frac{\tan \beta_F}{\cos^2 \beta_F} + \left(\frac{\delta C_Y}{\delta \beta}\right)_R \frac{\tan \beta_R}{\cos^2 \beta_R} \qquad (5.6)$$

$$2\, C_N = \left(\frac{\delta C_Y}{\delta \beta}\right)_F \frac{\tan \beta_F}{\cos^2 \beta_F} - \left(\frac{\delta C_Y}{\delta \beta}\right)_R \frac{\tan \beta_R}{\cos^2 \beta_R} \qquad (5.7)$$

where β is the flow angle.

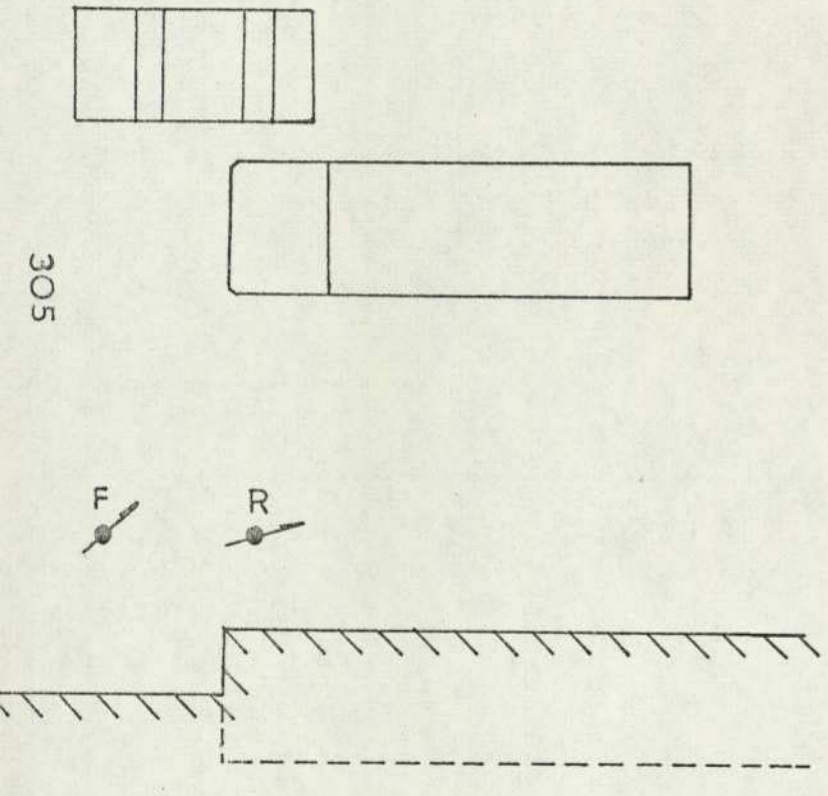

FIG. 141 REPRESENTATION OF LORRY BY 2-D STEP

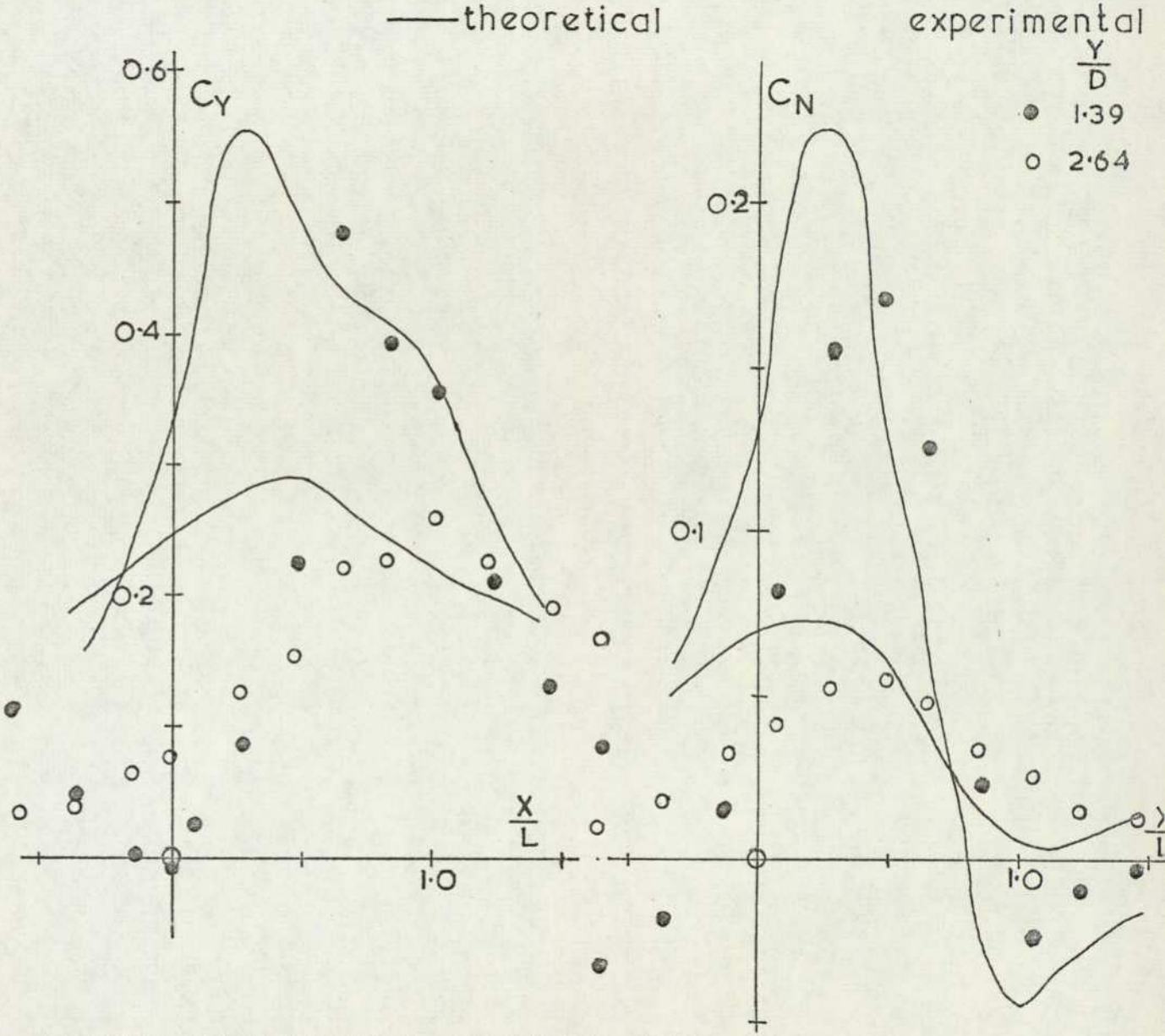

FIG. 142 COMPARISON BETWEEN THEORY & EXPERIMENT

SALOON

The theoretical curves for the inner and outer experimental lateral positions are shown in Figure 142 compared with the collected saloon car experimental data. Although the peak values are comparable in amplitude they are of the order of half a car length out in location.

5.4. Interference effects between racing cars

A class of vehicle, which has shown itself to be highly susceptible to aerodynamic interference effects, is the Can-Am racing car. Three incidents have occurred in which one car travelling very close behind another at high speed has been completely overturned. See for instance the report of the first incident at the Road Atlanta circuit as given by the driver, Hulme (13)

For the measurement of the effects of vehicle proximity a similar model to that constructed for the wake measurements was made. No attempt was made to scale a particular vehicle but the typical characteristics of these vehicles; the sharply angled nose and the large rear wing, were both modeled. As shown in the lift force data, both models experienced a slight nose up pitching moment and substantial downforce

Measurements of lift and drag force, and pitching moment were obtained with the force model in front of and behind the other model, and a few additional lateral positions were investigated. The incremental coefficients are presented in Figure 143. When approached from behind the force model is only subjected to a slight increase in drag and pitch. The vehicle that is moving closer, however, experiences very dramatic changes in both lift force and pitching moment, which are accentuated by a slight lateral offset. The worst effect is felt by a vehicle which changes position, when immediately downstream from just to one side of the leading vehicle to directly behind, Figure 144. The lift coefficient increases by 1.8, which represents a force of 8.0 kN at 62 m/s (150 m.p.h). This force is comparable to the all up weight of a typical Can-Am car. The lift increase is accompanied by a similarly dramatic rise in pitching moment so that all the lift is generated at the front axle. This represents a highly unstable situation. The present generation of wide bodied Formula 1 cars would be subject to load changes of a similar magnitude.

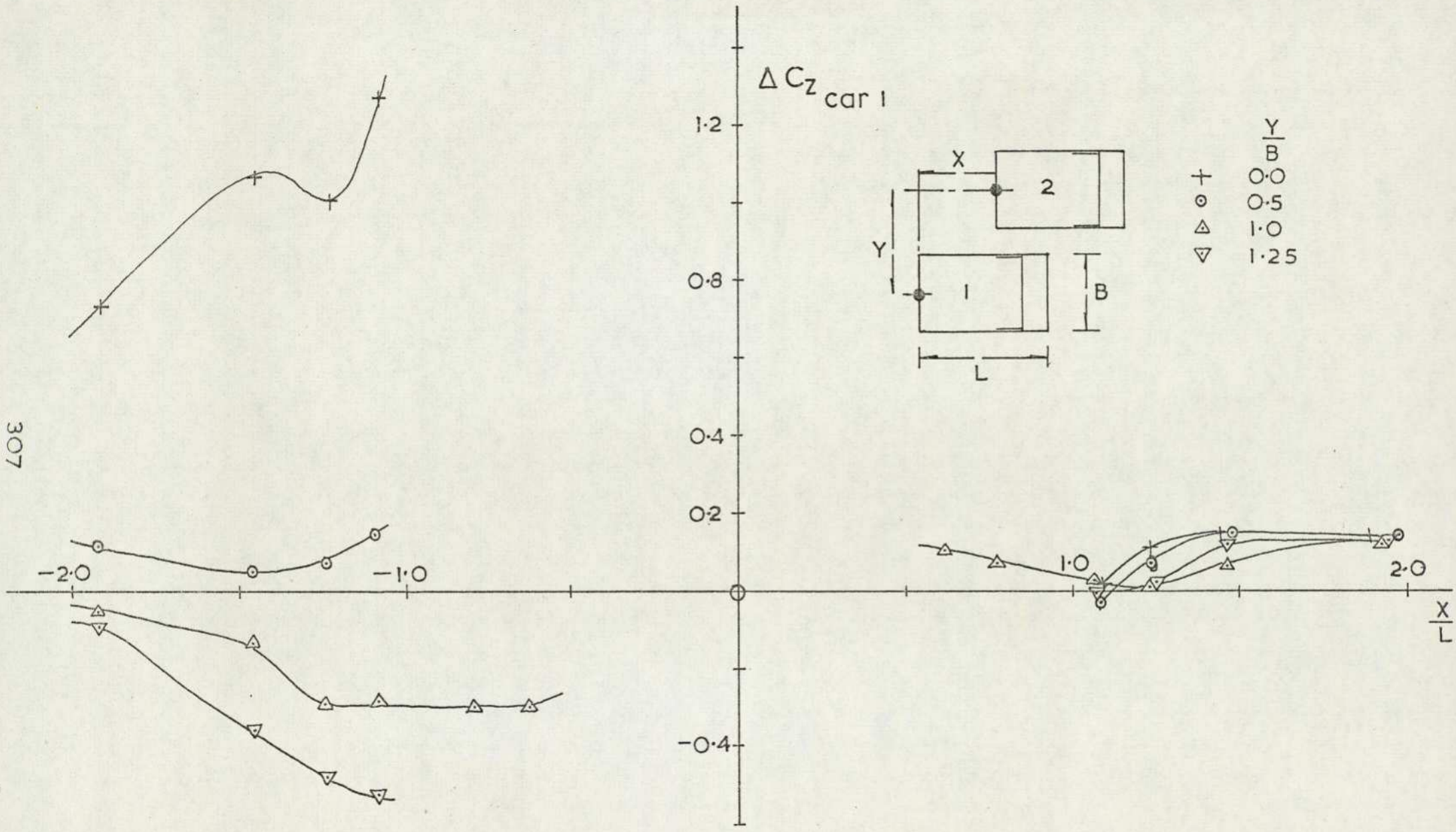

FIG. 143 FORCES ON CAN AM RACING CAR IN PROXIMITY TO ANOTHER (a) LIFT FORCE

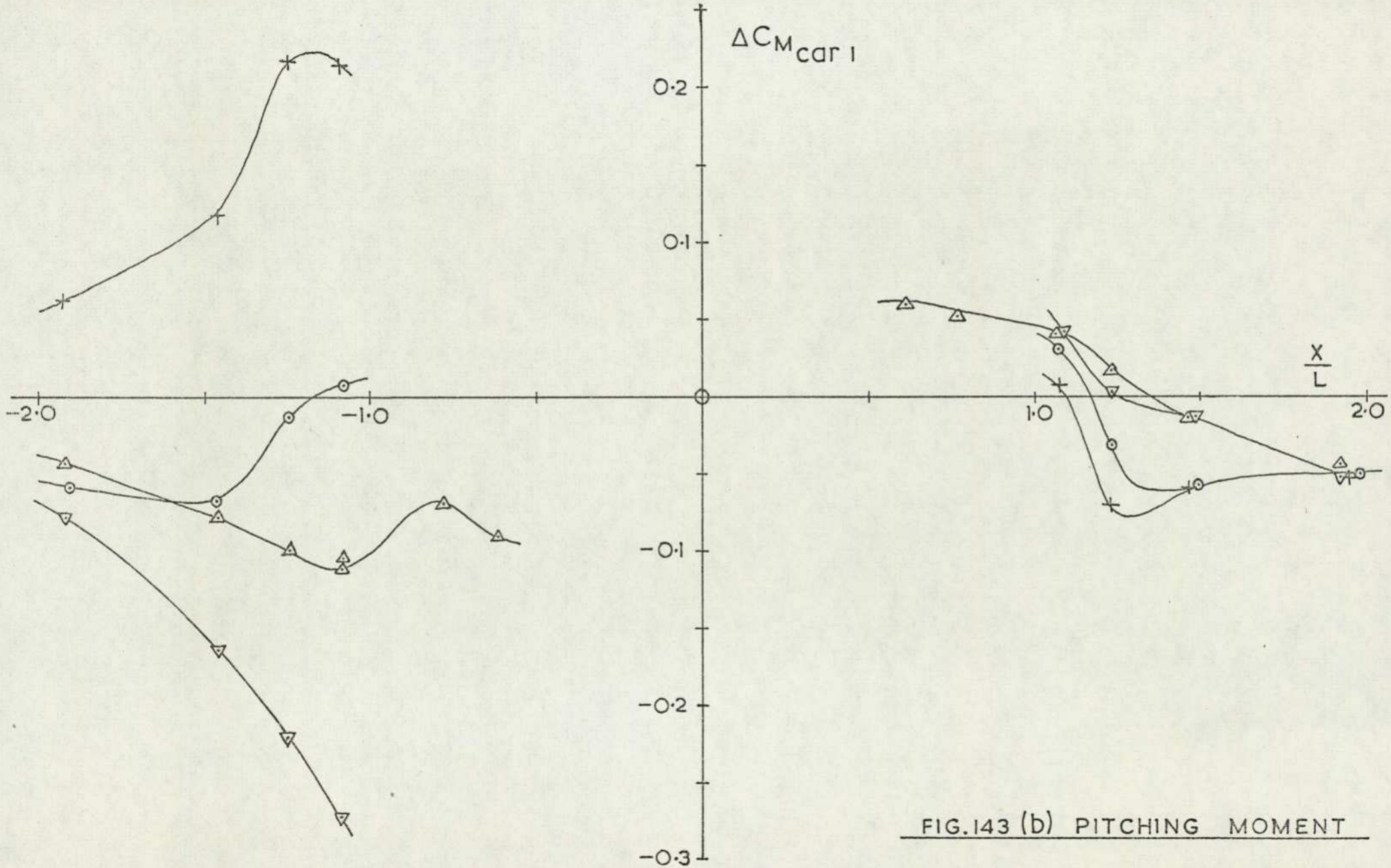

FIG. 143 (b) PITCHING MOMENT

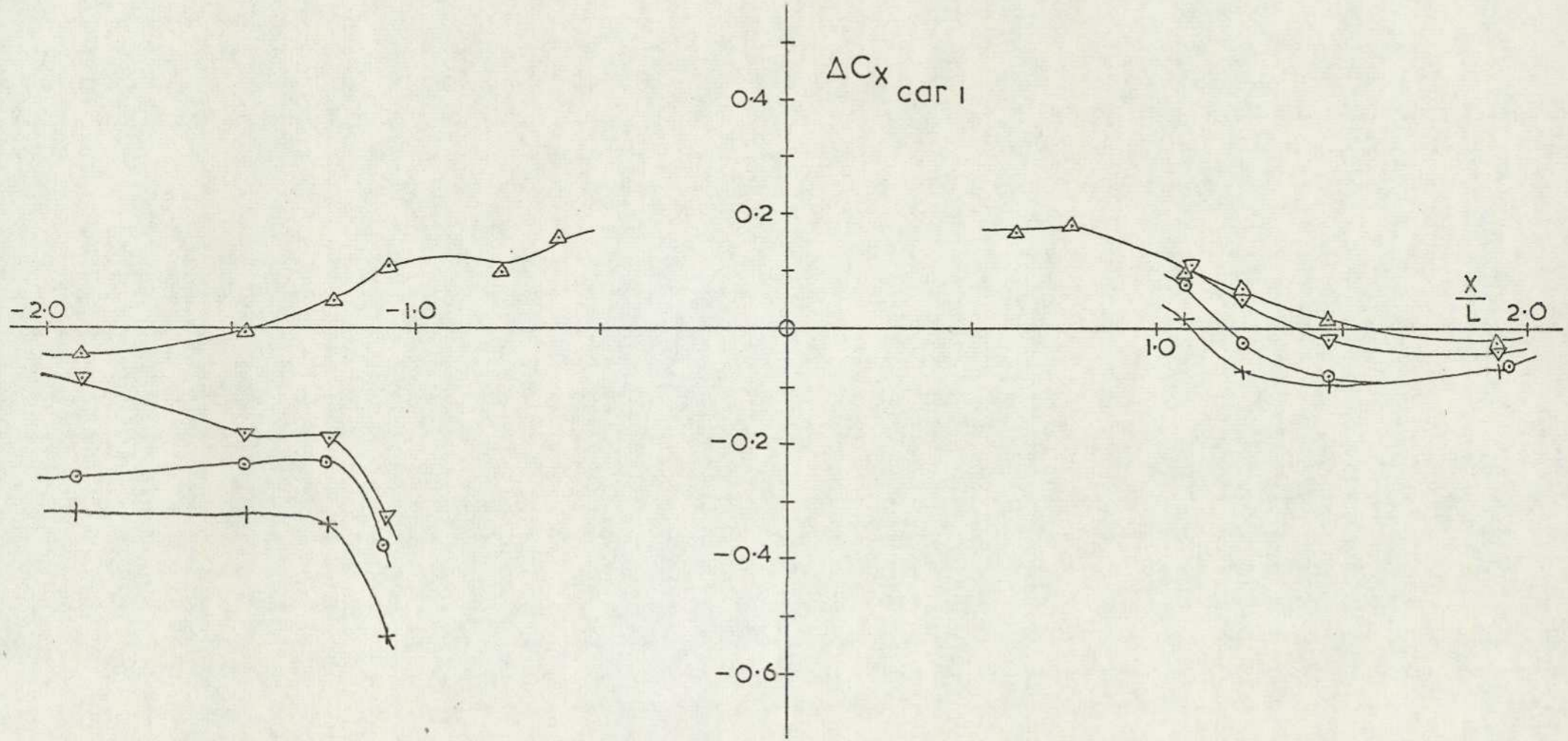

FIG. 143 (c) DRAG FORCE

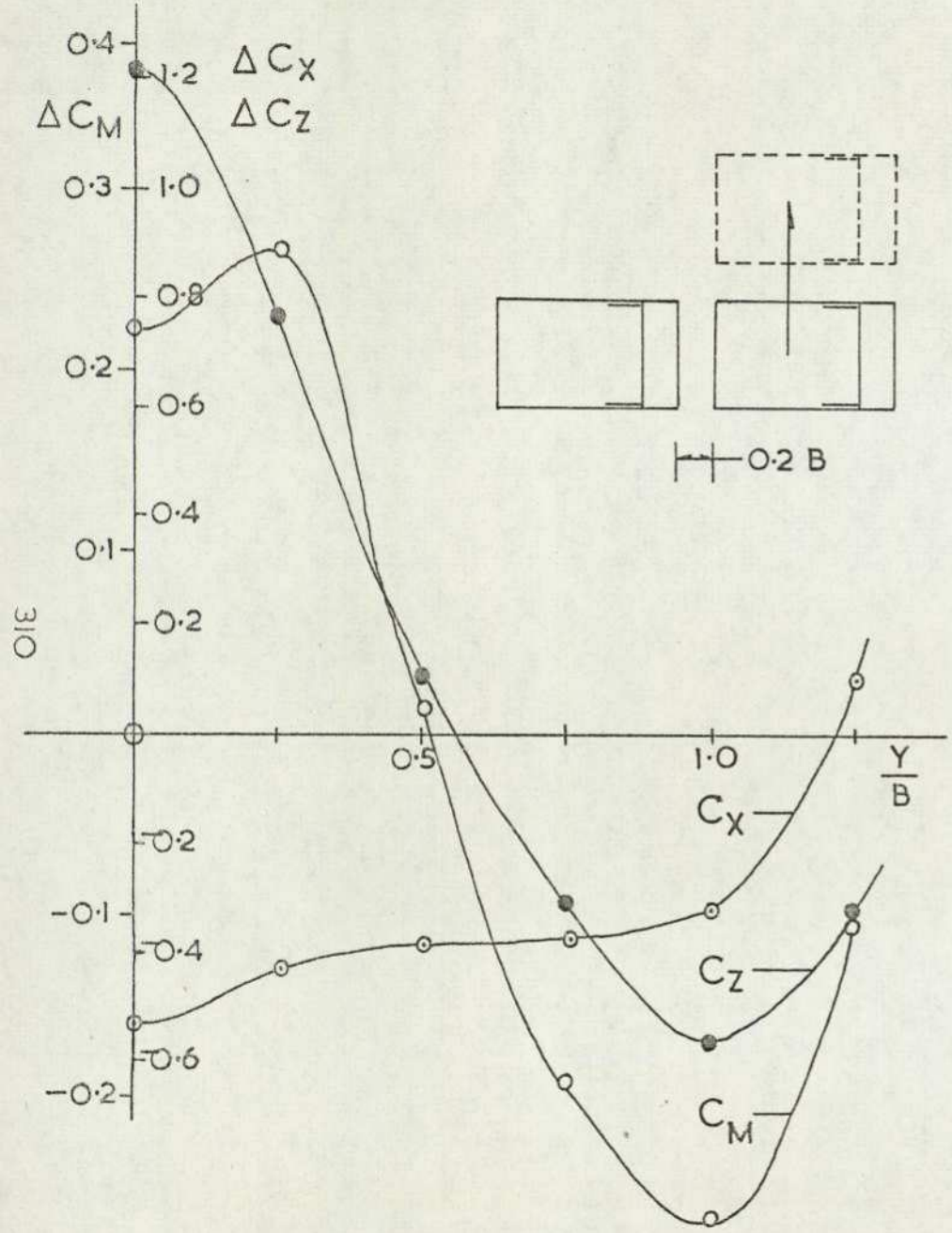

FIG.144 FORCE VARIATION WITH OFFSET

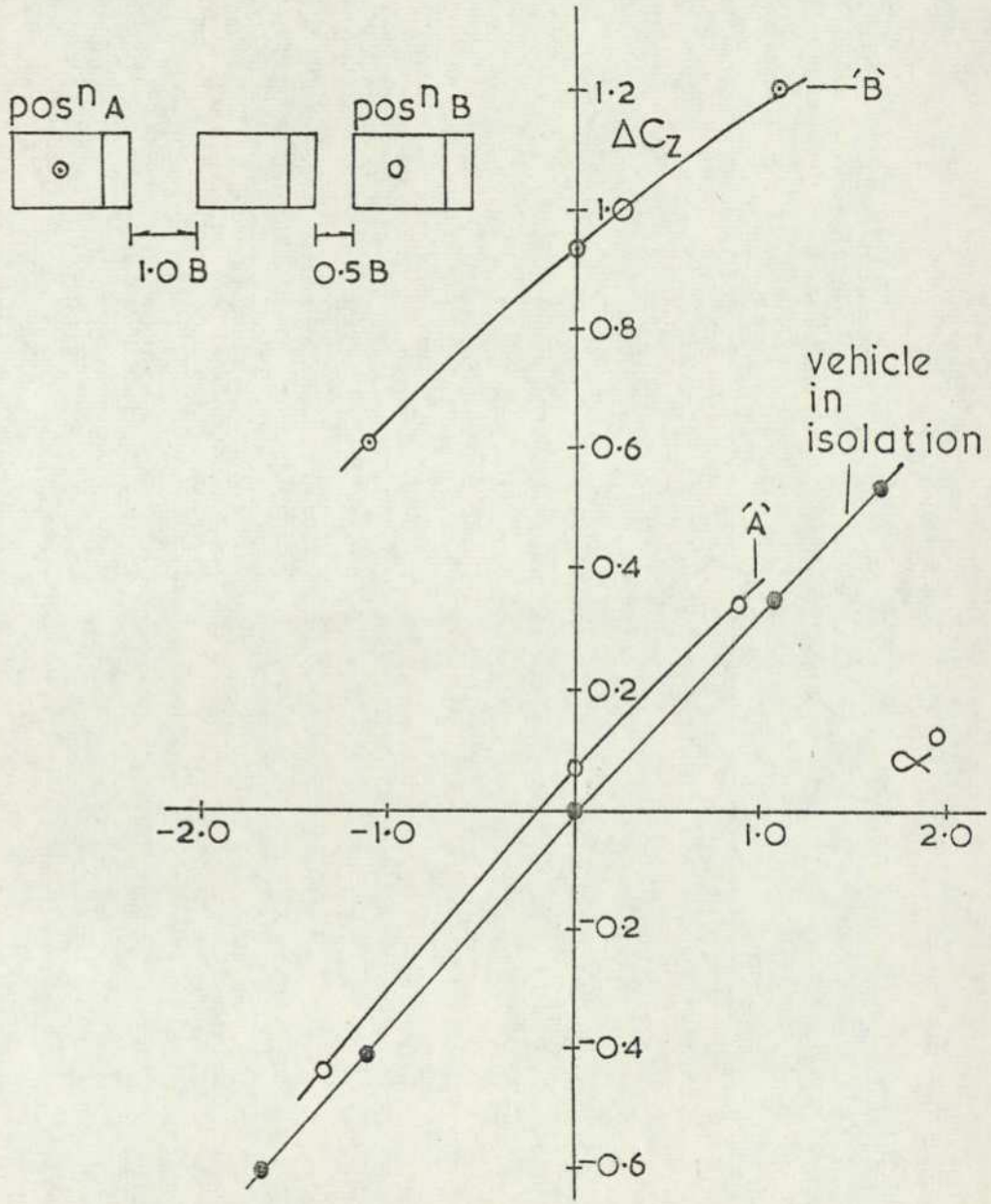

FIG.145 EFFECT OF VEHICLE PROXIMITY ON SENSITIVITY TO INCIDENCE

The lift and pitching moment sensitivities to incidence for a vehicle immediately upstream and downstream of another are compared with the results for an isolated vehicle in Figure 145. It can be seen that the lift curve slopes are identical for the free stream case and the situation where the force model is upstream. When submerged in the wake of the other vehicle the slope is reduced by 20%.

5.5 Additional wake induced problems

A problem often encountered by fastback vehicles is strong sensitivity to cross winds. Pictures of these cars often show that flow separation occurs upstream of the trailing edge but below the roof line, and in many instances it can be seen that the wake extends well forward of the rear of the car. This implies that the separation point will shift considerably under different external flow conditions. The lift force at the rear axle must therefore be similarly susceptible to changing cross winds, in addition to having a basically high lift force when at zero yaw, Carr (73). Janssen and Hucho (14)have shown that by varying the backlight angle between 50° and 60° the flow separation point, at zero yaw, changes from the roof line to the trailing edge, while the rear wheel lift coefficient increases by 0.25. The rear wheel lift coefficient for various car shapes, at yaw, is shown in Figure 146. While most vehicles, including all the fastback models, show only a slow variation with yaw, the saloon 3 model experiences a sudden rise in lift at the rear axle, immediately, on being yawed. For this particular model the separated flow at the roof does not reattach to the boot under zero yaw conditions. On being yawed, however, the flow must generally reattach to give the increase in lift force. The reason for the fastback models not giving similar behaviour is that the rear slope is always too great for separation to occur upstream of the trailing edge. The usual way to cure the problem is to place a spoiler at the trailing edge which encourages the flow to behave predictably while effectively reducing backlight slope and rear wheel lift.

A problem associated with the accumulation of dirt on the backlight, in bad weather, is the obscuring of rear lights, which creates a hazard because the reduction in light intensity is accentuated at the time the lights are most necessary. The problem is particularly acute on lorries. The effect occurs irrespective of the design of the vehicle

because the lights are invariably enclosed in the recirculation bubble. Goetz (74) has shown that an improvement can be gained by ribbing the light cover to promote clean flow locally. An alternative solution might be to mount the lights clear of the reverse flow region. This usually implies being mounted clear of the bodywork; either to the side of, or above, the car. The former could create a pedestrian hazard while the latter infringes height regulations regarding location of lights, and would be impractical in the case of a lorry. The problem can be overcome by adopting a solution similar to that shown in Figure 147. Here the lights are mounted at the vehicles sides but sufficiently forward of the trailing edge that there is no communication between the reverse flow regions arising at the light itself and the vehicle base. A beneficial effect on drag force might also be found.

The driver immersed in a wake in bad weather already has a visibility problem because of spray being thrown up by the vehicle in front. Once again this problem is most acute on lorries and numerous attempts to limit it have achieved little success, Sherard (75). The spray is created from water thrown up by the tyres, hitting the bodywork, and then atomising. The spray then fills the wake, through the process of turbulent mixing, and remains there until gravitational forces overcome the fluid effects. In the case of a lorry, the spray from the front wheels fills the separation region that usually exists at the leading edge of a bluff body. This region can extend laterally a considerable distance, and on motorways the effect is noticeable well into the adjacent lane. In such a situation it would seem desirable to radius the leading edges of both cab and body so that the separation region is eliminated. In addition to creating less of a nuisance to other road users this would also lower drag which should benefit the lorry operators. In the wake itself there appears to be no easy solution for either cars or lorries. Reducing the size of the wake by streamlining the vehicle may not help because this usually implies a greater lift in the case of a passenger car. A more pronounced vortical structure is therefore generated which enables the spray to persist even further downstream. The fitting of mud flaps to cars is no solution as it increases the size of the reverse flow region and being close to the ground probably encourages spray into the main wake.

Periodic effects in the wake may have an influence on the noise experienced inside a downstream vehicle. Tempest and Bryan (76) have

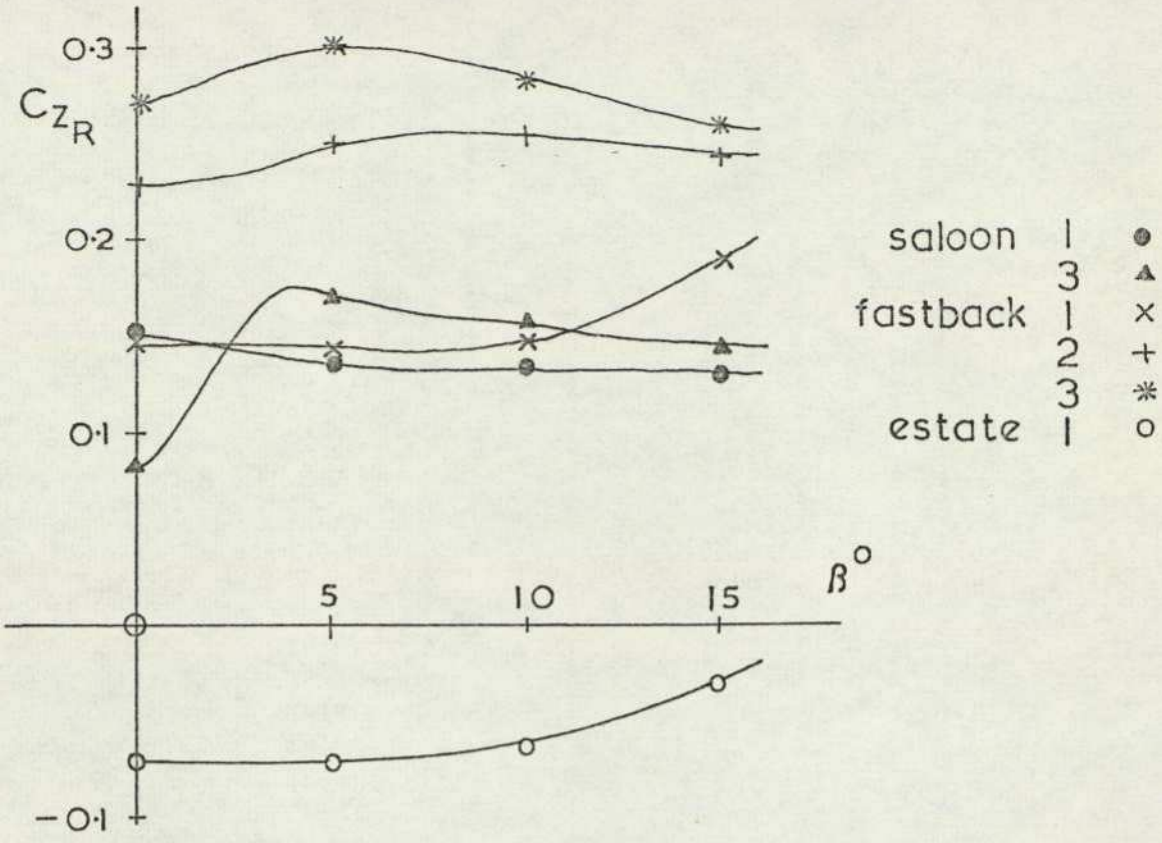

FIG. 146 REAR AXLE LIFT ON CARS AT YAW

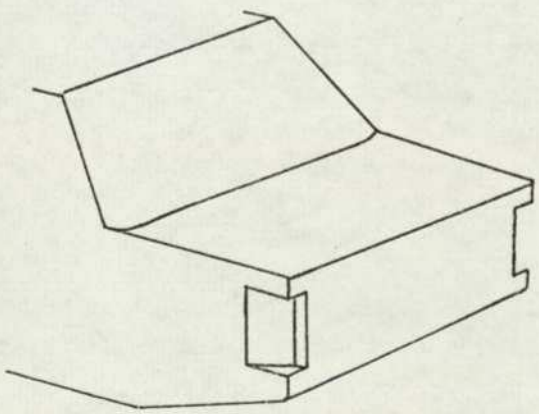

FIG. 147 SUGGESTION FOR REAR LIGHT CLUSTER DESIGN TO REDUCE DIRT ACCUMULATION

shown that very high levels of noise are apparent at frequencies below 5 Hz. This frequency is much lower than that due to sources such as engine or body vibration or aerodynamic inputs arising from flow separation at the windscreen pillars. The small scale lorry model, which is about 1/25th scale produces energy peaks at 75 Hz at 30 m/s as recorded by a probe stationary relative to the lorry. At full scale and similar speed this would correspond to 3 Hz as sensed by an observer in a car travelling a fixed distance downstream of the lorry. The low frequency noise may arise therefore from the passage of a car through a relatively slowly varying flow field.

5.6 Conclusions

The forces on a car submerged in the wake of a lorry only change significantly very close to the lorry. The dominant effects of proximity are experienced when the car overtakes the lorry.

For two Can Am cars racing close together very large changes in lift force and pitching moment can be experienced especially when lateral changes in position occur.

From the design point of view, the obscuring of rearward vision in bad weather can be eliminated if the effective backlight slope is at least 60° from the vertical. This simultaneously reduces the vehicle sensitivity to cross winds. A design for limiting the dirt accumulation on rear lights has been presented.

The spray problem encountered while overtaking heavy lorries can be reduced by radiusing the leading edges of the cab, although suppression of spray in the wake of both cars and lorries is likely to be extremely difficult.

6. CONCLUSIONS

The wake characteristics of road vehicles and of basic rectangular blocks near to ground have been determined from a series of wind tunnel tests. Prior to obtaining this data a study was made of the results of other investigators, using various methods of ground simulation. This established that the most suitable ground representation for wind tunnel testing of road vehicles is the static ground board. Of the usual wind tunnel corrections the only ones found to be significant for bodies near to ground were those due to blockage and a cross flow correction for vehicles at yaw.

It was necessary to ascertain the forces on the bodies generating the subsequently studied wakes. All the shapes showed an increasing sensitivity of lift force to incidence as the ground was approached, but the lift generated by the addition of camber was not found to be dependent on ground clearance. For many parameters all the data could be collapsed to a single curve, generating useful design information.

The car shapes all revealed considerable changes in lift due to incidence, the effect increasing with yaw. An increase in camber was found to reduce the sensitivity through a modification of the flow under the nose. A distinct effect on handling was found from an analysis of the equations of vehicle motion and certain racing car designs were shown to be dangerously sensitive. Lift sensitivity to incidence was dramatically reduced by mounting a spoiler under the nose.

From modifications to the ground board boundary layer a lift force correction for wind tunnel tested road vehicles has been devised. This is applicable at the front wheels only and from previously published data is seen to have some justification.

A simple velocity correction to convert wake profiles obtained in a wind tunnel when using a static ground board to the equivalent for a moving body over a fixed plane was determined. This simply subtracts the local ground board boundary layer velocity profile as measured in the absence of the model. Little evidence of ground board separations were found. For these bodies, developing small lift forces, the limiting ground clearance is given by the ground board boundary layer displacement thickness at the model trailing edge position.

The rectangular blocks set at zero lift incidence show interesting three dimensional effects, which can be explained by

considering the longitudinal vorticity generated downstream of the trailing edge. On approaching the ground the initially Gaussian wake profiles adopt an increasingly 'boundary layer' appearance. This can be related to the interference of the mirror image wake.

The lifting bodies develop totally different wake forms dependent on whether the lift is generated from the influence of camber or incidence. Along the underside of bodies at incidence near to ground, a strong cross flow is produced which can easily separate from the vehicle sides to initiate a vortex in a manner similar to that over a slender wing. The wake downstream of the body remains but the vortices, under the action of the local image move rapidly sideways with negligible vertical motion.

Cambered blocks with flat lower surfaces, on the other hand, produce vortices with very narrow spacing that move vertically downwards as if in free stream. The influence of the image is very small in the rear wake investigated.

The passenger car shapes that develop lift, the saloon and fastback models, form vortex wakes that initially show an intermediate state. The vortices experience both vertical and lateral motion. Four methods were used to define the wake characteristics. The pitot pressure method was found to be inadequate for defining the vortex core location in one instance. The estate car and lorries which generate negligible lift forces produce almost symmetrical wakes similar to those for the non lifting blocks although the underbody roughness of the road vehicles has an influence. The Can-Am racing car model, typical of racing machines that develop extremely high downloads, generates a distinct wake in which the centre moves rapidly away from the ground under the action of the two vortices. High vertical velocities were apparent.

For all the wakes longitudinal velocities were found to have a decay rate exponent of - 2/3 while for rotational velocities in the trailing vortices this was - 1/2

Periodic effects were not dominant in these three dimensional bluff body wakes but a Strouhal number close to 0.2 could be defined for most blocks in both free stream and ground proximity. Higher frequencies were apparent near the tips of the blocks but these decayed on moving downstream. The cars that generate noticeable trailing vortices showed two distinct

frequency peaks one of which was strongly lift dependent while the other was constant. The former was believed to be associated with a helical vortex.

The wake flow manifests itself to a driver in a number of unpleasant ways. A car immersed in the wake of a lorry was found to experience noticeable force variations but these were dominated by the changes that occur when the car is alongside the lorry. One racing car, however, travelling close behind another can experience very serious destabilising forces capable of overturning it.

To limit visibility problems a few suggestions for vehicle design have been made. From measurements of the recirculation bubble it has been found that a minimum 'effective backlight slope' of 60^{o} is required to stop the accumulation of dirt on the screen. This also reduces the sensitivity of rear wheel lift to a cross wind disturbance. An idea for reducing the deposits on rear lights has been presented but there appears little hope of a simple solution for reducing the spray problem except that occurring at the front of lorries.

This problem of spray is one of the most discomforting aspects of modern driving and deserves considerable attention in the near future.

APPENDIX A

A REVIEW OF GROUND VEHICLE AERODYNAMICS.

A.1 Introduction

Over the past eighty years of investigation into the aerodynamics of vehicles that operate close to the ground a considerable amount of data has been accumulated. Although substantially less effort has been devoted to this aspect of aerodynamics than to aircraft related problems, a complete survey of previous work would still be an immense task. In this chapter a very brief review of previous studies is presented although where more appropriate a particular investigation is introduced in the introduction to the relevant chapter.

A.2 Road Vehicle Aerodynamics

Early experiments on road vehicle aerodynamics were primarily aimed at reducing the drag force experienced. Ludvigsen (77) has given a fascinating account of the earliest developments, while Koenig-Fachsenfeld (78) has reported extensively on the thorough German experiments performed prior to and immediately after W.W II. It is interesting to note that since 1950 when separate wings and headlights disappeared no further improvement has been made in the drag coefficient of typical road vehicles; indeed in recent years the trend towards lower drag coefficients has been reversed. Interest in drag reduction is still evident, however, whether by modification to the overall shape of the car, Janssen and Hucho (14), increasing edge radii, Carr (79), or the fitting of spoilers, Marcell and Romberg (80), and the smoothing of the underbody roughness, Carr (82), Turner (81).

Over the past fifteen years the response of a vehicle to a yawed flow, which represents a steady cross-wind, has received considerable attention. The most thorough investigations are due to Bowman (83), Barth (84) and Carr (79) although most of the literature is devoted to this one aspect. The vehicle motion arising from entering a gust has been examined experimentally by Lay

and Lett (85), and Bundorf, Pollock and Hardin (86), using full size vehicles and by Beauvais (87) using models. Theoretical treatment of the same problem has concerned many authors especially Hawks and Larrabee (88), Hales (89) and Russell and Scibor-Rylski (90). A cross wind as represented in the wind tunnel has a uniform velocity. In practice the natural wind is a shear flow. The influence of a velocity gradient on the lateral characteristics of typical road vehicles has been investigated by Maccabee (91).

The aerodynamic characteristics of a car-caravan combination at yaw have been obtained by Beauvais (92) while Griffiths (93) and Waters (94) have considered the influence of caravan shape on the drag force. Hawks (95) has considered the response of such a combination to a wind gust.

Many detail design features on cars can benefit from the attention of an aerodynamicist. Passenger compartment ventilation has been studied by Goetz (74) who also devised a means of keeping rear lights free from road deposits. The effect that cooling flow through the radiator has on the external aerodynamics has been investigated by Turner (81) and Janssen and Hucho (14). Dawley (96) has measured the lift of windscreen wiper blades and the cooling flow of air through wheels to the brake surfaces.

By replacing the car shape by a lamina, simple theoretical estimates have been obtained for lift and pitching moment, Morelli (97), and also the lateral derivatives, Larrabee (16) and Hucho and Emmelmann (71). A more sophisticated method for predicting the loading places a distribution of vortex loops over the entire body surface, Stafford (17). Encouraging results have been obtained.

Apart from a few early wind tunnel experiments on the drag of commercial vehicles, Schlichting (98), Flynn and Kyropoulos (99), this aspect of road vehicle aerodynamics has been largely ignored until recently. A number of devices have appeared which aim to reduce the aerodynamic resistance. These either modify the flow

over the cab roof or deflect the flow around the sharp leading edges of the truck body; Kirsch, Garg and Bettes (100).

The influence of pitch angle on the aerodynamic characteristics of road vehicles has been considered in Chapter 2, while in Chapter 5 the interference effects between road vehicles in close proximity were investigated.

A.3 Racing Cars and Land Speed Record Vehicles

Designers of racing cars have for a long time recognised the need for aerodynamic research. For commercial reasons a great deal is never published, but early experiments concentrated on drag reduction and improving lateral stability, Lind-Walker (59). The outlawing of all enveloping bodywork ensured that the flow field around Formula cars became dominated by the effects of the rotating wheels. The aerodynamic effects created by rotating wheels have been investigated in isolation, Morelli (101), Fackrell and Harvey (102), and combined with typical bodies, Stollery and Burns (9), Stapleford and Carr (103), Scibor-Rylski (104). The improvement in cornering speeds obtained by applying an aerodynamic download at the wheels has encouraged a proliferation of wing-like devices fitted to racing cars. This has tended to concentrate research to lift reduction, Pothoff (19), Scibor-Rylski (105), Jim Clark Foundation (106), although drag is still of concern to less powerful racing cars.

Sports racing cars with enclosed wheels tend to be unstable at high speeds. Improvements to the handling have been made by fitting front and rear spoilers, Bowman (107), Pothoff (19), Scibor-Rylski (104), while redesign of the nose shape has been considered by Sussex and Northcote-Smith (108), Stollery and Burns (9), Boyce and Lobb (109).

It has been suggested by Pershing (110) that an improvement in the performance of dragsters could be realised by reducing the aerodynamic drag.

The importance of drag reduction for land speed

record cars has always been obvious. In 1929 Irving's Sunbeam Golden Arrow was the first such car to be wind tunnel tested (Irving (111)). More recently the drag coefficient has been lowered to 0.12 for both M.G., (Ludvigsen (77)) and Golden rod (Korff (20) record breaking vehicles. Donald Campbell's Bluebird had a drag coefficient of 0.16 (Stollery and Burns (9)) but the need for minimising lift by modification of the camber line was recognised. Transonic tunnel tests were necessary for the model of Blue Flame (Torda and Morel (112)) which subsequently achieved 622 m.p.h. (280 m/s). Speeds in excess of Mach 1.0 are now being contemplated by both American and Russian groups. In a considerably lower speed range the speed and stability of motor cycles have been improved by the application of wind tunnel testing during the design stage (Schlichting (98), Cooper (113)).

A.4 Trains

The first known wind tunnel experiment on the drag of trains was reported by Goss (114), performed three years earlier in 1895. Periodically there have been attempts to streamline trains. Johansen (115) measured lateral forces as well as drag on convential and streamlined train configurations. This remained the standard work on the subject for many years. Recently, however, considerable attention is again being paid to the aerodynamic characteristics of high speed trains. Gawthorpe (116) has given a comprehensive review of the research to date and the problems requiring solution. The need to reduce power consumption, in which aerodynamic drag forms the major component, is still the most important problem (Hara, Kawaguti, Fukuchi and Yamamoto (117)). Of great concern is the drag rise associated with running into and through tunnels, Gaillard (118). The aerodynamic loads arising from two vehicles running on adjacent tracks and the forces on trackside objects immersed in the wake flow have also been considered (Hara et al (117).

Theoretical estimates of the loading on train-like bodies have been made by Morrow and Maccabee (119),

the method requiring a distribution of source-sinks over the entire body surface.

A.5 High Speed Ground Transport and other Ground Effect Machines

A number of groups throughout the world are developing tracked high speed ground vehicles for operating in the speed range 400-500 km/h, and utilising a variety of suspension systems. While the attention has switched from the hover vehicles to magnetically supported ones, the aerodynamic problems remain the same. A number of wind tunnel studies have been made, Grunwald (12) and Tracked Hovercraft Ltd.,(22), in which various body shapes and track geometries have been investigated. Theoretical studies of the aerodynamic characteristics of such bodies have been made by Woolard (120) using the 'slender body' approach. In competition with these systems are the tracked ram wing designs which utilise aerodynamic lift for support and stability, Barrows (121). Theoretical estimates for the lift to drag ratio, based on slender wing theory, have been obtained by Barrows and Widnall (65) while a more sophisticated approach using vortex lattice distribution which can account for tracks that are non-planar has been developed by Davis and Harris (122).

In addition to these tracked vehicles just considered, conventional hovercraft have been studied for a number of years and free flying ram wings have been built. Wind tunnel studies of the external aerodynamic characteristics of hovercraft seem to be rare, the exceptions being Trebble (123), Andrews (124), Zeitfuss and Brooks (125). Ram wing vehicles have been experimentally investigated by Kumar (126), Ando (127), Gallington, Miller and Smith (128) while numerous authors have obtained theoretical characteristics; Ando (129), Ashill (130), Widnall and Barrows (131).

A.6 Wings

An extensive literature is available on the effect of ground on the lift of wings. Betz (132) extended

biplane interference theory to account for the presence of the ground. A summary of the early experiments, for which a variety of ground simulation methods were employed, and theoretical methods, has been given by Pistolesi (133). Tani, Taimi and Simidu (134) investigated in detail the effect of ground on a monoplane wing and compared their results with theory. The pressure distribution around a two dimensional wing in ground proximity was measured by Bagley (135). The effects of finite aspect ratio were studied by Fink and Lastinger (136) using 22% thick wings. Whereas previous investigations had measured ground effect with the wing clearance similar to that for a landing aircraft, this investigation studied very low ground clearances. Little change in zero incidence lift due to height variation was observed but there was considerable effect on the lift curve slope. All the wings exhibited height stability at positive incidence. Carter (137) performed tests on a unity aspect ratio wing having similar section, and found large improvements in lift to drag ratio attributable to the fitting of endplates. Little influence of ground proximity on profile drag was noted. Numerous authors have investigated the influence of ground on low aspect ratio delta wings, among them Kirkpatrick (138) and Fox (139). Berry (140) employed a moving and stationary ground to compare lift and drag measurements for a wing of aspect ratio 6. Differences only became apparent at very low ground clearances or at high incidence. Similar comparisons have been made for VSTOL aircraft models; Turner (141) and later South (142) deriving a limiting value of lift, dependent on geometry, above which a moving ground is essential.

A.7 Rectangular Blocks in Ground Proximity

Basic rectangular blocks have been investigated by Barth (143) under yawed conditions while set at small fixed ground clearance. The effects of variations in length to height ratio, width to height ratio, and edge radiusing, on side force and yawing moment, were studied. With coefficients based on side area the lateral characteristics were found to be identical for a considerable

range of length ratio. The side force derivative with yaw was a maximum with the length to height ratio equal to 2.0 although below this value non-linearities were present. A similar effect was noticable for the yawing moment. At a fixed length ratio the side force coefficient increased with increasing width to height ratio at yaw angles below 0.2 radians but above this yaw value the effect was reversed. The position of the centre of pressure was found to be 40% of the length aft of the nose for all the long bodies. This position moved aft with increasing width ratio, and reducing length ratio while it moved forward on radiusing the transverse edges. Rounding of the longitudinal edges had no influence on the location of the centre of pressure but it did reduce the side force at yaw.

Carr (144) has measured the six force and moment components on a rectangular body of fixed overall dimensions while varying the edge radius, ground clearance and nose shape. Drag forces were dramatically reduced by small edge radiusing; a radius of 10% of the body height was sufficient to give a drag reduction of 75% when compared with a sharp edged body. For the latter model, variation in ground clearance had little effect on drag but increasing the radius produced different effects. Fitting of a well-rounded nose had little influence on drag at small yaw angles but gave a marked reduction above 0.1 radians of yaw. Increasing the ground clearance tended to increase all coefficients, especially at yaw. The lift variation with yaw was most noticably increased on reducing the edge radius. High rolling moment derivatives were found on all bodies, with edge radius having only a small effect. The drag results were a striking confirmation of the conclusion of Lay (145) that the lowest vehicle drag coefficient can be obtained on a simple rectangular shape with radiused edges, and that in addition this geometry gives highly desirable yaw characteristics for all other forces and moments.

APPENDIX B

GROUND SIMULATION - THE ALTERNATIVES.

B.1 Alternative Ground Representations

A variety of techniques have been employed in the past to simulate the ground plane in a wind tunnel. These are shown schematically in Figure 1. The most commonly used method is a simple flat plate representing the ground. This board is usually mounted away from the tunnel floor, often at the centre line of the tunnel. The model is typically mounted just clear of the ground by an amount approximately equal to the boundary layer displacement thickness, at the model position. The presence of the model gives rise to a circulation around the combined ground and model and various devices have been used to control the flow over the leading edge of the ground plane; the most common being a trailing edge flap. The advantage of this system is its simplicity. It is inexpensive, easy to make and instal. It suffers the disadvantage that the flow boundary conditions on the surface of the ground are incorrect. For a real moving vehicle the fluid is stationary relative to the ground at some distance away from the vehicle. In the wind tunnel this relative velocity becomes equal to the free stream velocity (the simulated forward speed of the vehicle). A boundary layer therefore develops on the ground which is unrepresentative of the real situation. If the ground plane length upstream of the model is fairly short and the model ground clearance is considerably greater than the local boundary layer displacement thickness then the influence on the model is likely to be small.

An even simpler alternative is to mount the model directly to the floor of the working section. This arrangement suffers from the relatively thick boundary layer found in such a position. The thickness of this boundary layer can be halved by applying sufficient suction through a slot in the floor just upstream of the model. The boundary layer thickness can also be reduced by use of a 'scraper' (Dumsby, Wardlaw and Marsden (146))

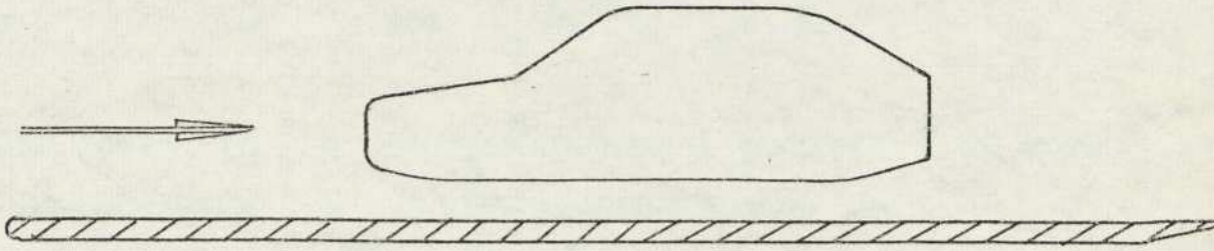

(a) FIXED PLATE

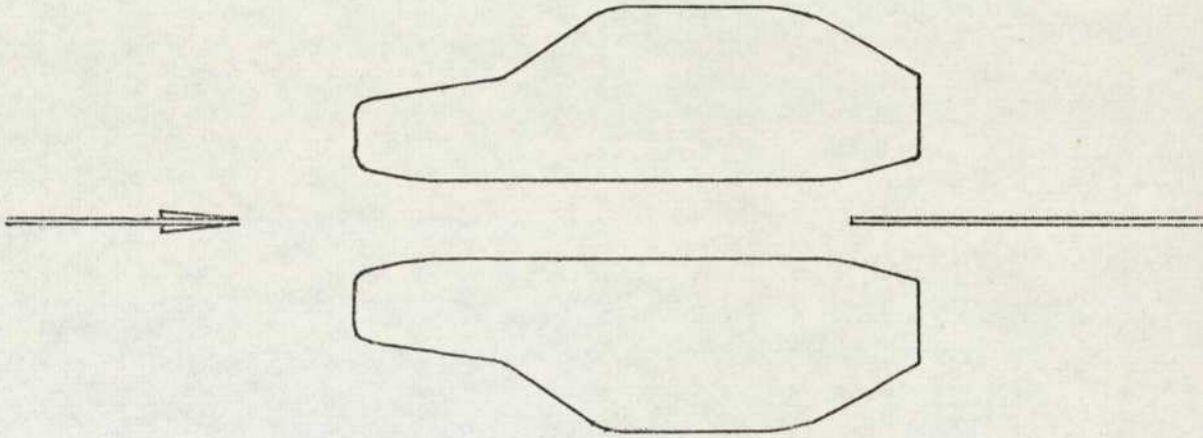

(b) MIRROR IMAGE

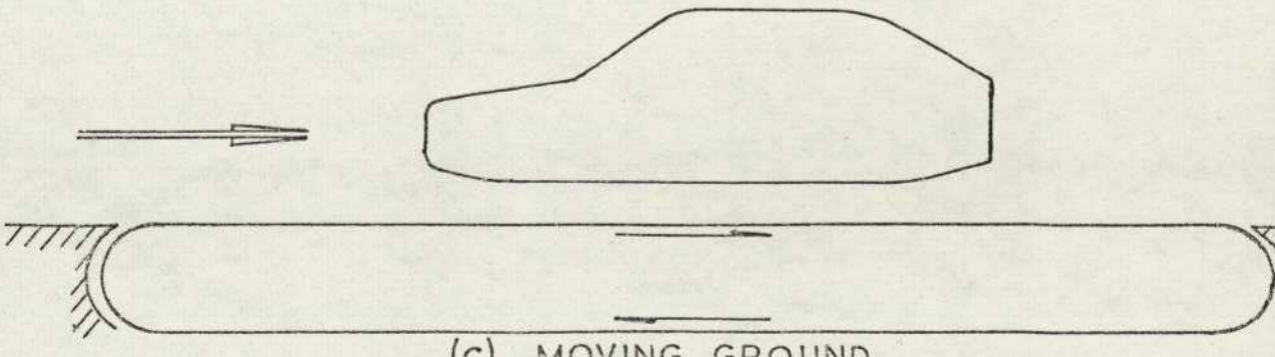

(c) MOVING GROUND

FIG.1 BASIC GROUND SIMULATION TECHNIQUES

consisting of two lengths of thin angle strip mounted to the tunnel floor to form a vee, apex forward, immediately upstream of the test object. The same conditions then exist as over a separate ground plane.

It is sometimes suggested that suction can be distributed over the entire region of the ground plane occupied by the model, thereby removing the boundary layer completely, Bettes (147). There would seem to be few advantages to such a scheme. The flow rates required would be very high and to neutralise vertical flow components at the surface would entail using alternative suction and blowing slots. Local flow rates would have to be matched to individual vehicle configurations and displacements.

The elimination of the ground boundary layer can be accomplished by removing the ground plane completely and substituting an image model to maintain flow symmetry. The flow conditions on the plane of symmetry still do not accurately represent the true conditions in that no boundary layer is developed at all, however, the system should represent an improvement over the fixed ground technique. This does not apply where turbulence exists, as in the wake of the vehicle, because mixing then takes place across the plane of symmetry. This problem can be alleviated by placing a thin plate on this plane downstream from the point where the wake flows or the body-generated boundary layers intersect. The requirement of two absolutely identical models is a disadvantage as is the need for very careful setting up to avoid errors arising from the sensitivity of bodies near to ground to attitude changes.

The only way to obtain correct boundary conditions in a wind tunnel is by use of a moving ground plane where the ground surface becomes the upper part of a continuous belt. This system has been developed by Butler, Moy, Pound (148) but is, however, subject to a number of disadvantages, which tend to preclude its use. They are costly to manufacture and install, and the running procedure is lengthy because of the need to continuously maintain equal belt and tunnel speeds. The frontal area of a ground

plane containing a moving surface is very large because of the need for large diameter rollers. This implies that correction factors are inevitably higher. A fairing has to be placed over the front of the leading roller housing, and this generates a boundary layer which would tend to persist along the ground unless removed by suction. Suction, additionally, has to be applied to the underside of the moving belt to reduce its lift. Balance mechanisms cannot be mounted direct to the ground and so require a sting or over head supports, further increasing interference effects.

An alternative model technique is to have a moving model. This may be mounted on a rotary arm or be part of a linear facility. The former method is subject to errors arising from considerable swirl generated by motion of the model and arm, Kumar (149). The latter may either be connected to another moving vehicle, Smith (150), or run on a long straight track, Curtiss and Putman (151).

B.2 Comparisons Between Methods

A number of authors have performed experiments using identical models but over differing simulations of the ground. Heald (152) measured the drag coefficient of a car model with several static ground representation techniques, while Stalker (153) reports on earlier comparative tests. In both cases considerable variation was found. A year earlier, Lay (145) had performed a number of tests using the image technique, no ground, and flat plates with and without suction and in this case considerable variation was again found in drag coefficient. An investigation of flow patterns around two dimensional car shapes was made by Ono (154) using fixed ground, image and moving model techniques. The difference in flow patterns was more noticable in the comparison between fixed ground and moving model than for the image and moving model case. Schmid (155) carried out drag measurements in a series of wind tunnel experiments using most of the methods discussed in B.1 and including the moving ground approach which had been developed by Klemin (156). The discrepancy between fixed and moving ground methods was

found to vary from 0.8% to 12% depending on model geometry.

Full scale measurements of lift and drag were obtained by Gross and Sekscienski (2) and compared with three forms of fixed ground; a conventional full span board, a partial span board and a small ground board fixed to the model, where the interference between model and ground was determined from force and moment measurements of the ground plane alone but in the presence of the model. In the tunnel the lift, drag and side forces were found to be comparable for all methods up to 20° of yaw, and for all moments using the full and partial span ground boards. The interference method gave totally different moment data. It produced, however, the most favourable comparison with the full scale lift and drag data.

A detailed comparison of model forces using several models and two different moving ground rigs has been made by Carr and Rose (23). The moving ground showed a 5% increase in drag and had a similar effect on the lateral derivatives. Lift forces were reduced by up to 10% depending on the yaw angle while little change was noted for the pitching moment. It should be pointed out that the fixed ground in these tests was simply the stationary belt which allows the development of a considerably larger boundary layer thickness than would occur over a conventional static plate. The advantages to be gained by correctly simulating the boundary conditions at the ground and by the use of rotating wheels were considered to be small in relation to the effort expended. Turner (81) performed a similar comparative test using a single car model. A difference was found in lift force only and even this was considerably less than the lift variation due to yaw. To determine the effect of the enlarged boundary layer over the stationary belt, the moving ground was run at different speeds relative to the airstream and measurements of the boundary layer thickness were taken. With the belt stationary the thickness was twice that for a typical static plate of similar size, and it was found that to generate the comparable boundary layer thickness the belt had to be run at 35% of wind speed. The total lift variation between this speed and full speed was then reduced by 60%. These

results were extended by Beauvais, Tignor and Turner (26) who measured lift and drag forces on a similar full scale vehicle on the road. The suprising result was that the moving ground data seriously underestimated both lift (24.5%) and drag (5.6%) whereas the error from fixed ground plane tests amounted to 3.3% and 2.4% respectively. Ontani, Takei and Sakamoto (157) have similarly compared full scale and tunnel data on lift and drag forces. Complete agreement was found between full scale vehicles on the road and in the tunnel, while quarter scale model measurements underestimated drag by 10%.

Early wind tunnel tests on a locomotive and tender by Klemin (158) using fixed and moving ground, no ground and image methods showed that the first two techniques gave identical results for drag coefficient, while the measurement from the image method was 30% higher, and with no ground at all an increase of 45% was found. Volgepohl (159) compared drag measurements of a single railway coach, obtained from a wind tunnel model, with full scale track measurements. The model results underestimated drag by 5% although the error was found to increase to 15% as surface detail was removed. In wind tunnel tests on a tracked air cushion vehicle, Tracked Hovercraft Ltd. (22) found that both lift and pitching moment were sensitive to the length of track forward of the model leading edge. Grunwald (12) measured the aerodynamic characteristics of several elongated bodies in ground proximity using stationary and moving belt and image methods. The image approach was found to give greater lift and lateral derivatives as well as more negative pitching moment. Stopping the moving ground belt was found to reduce the lift curve slope by almost 50% although as stated earlier this method is representative of no other fixed ground technique.

A few authors have attempted to correct data obtained with static ground for the influence of the boundary layer. In an investigation of the ground effect on the pressure distribution over a two-dimensional wing Bagley (135) measured boundary layer thickness on the ground under the leading and trailing edges of the wing and hence deduced a correction for incidence. Unpublished

work by Smith and others at RAE Farnborough, reported by East (24) demonstrated substantial increases in lift when the extension of the static ground board leading edge forward of a delta wing model was reduced. East found that variation of boundary layer thickness on the ground board strongly influenced the lift force, the effect being most noticable on low aspect ratio wings. A correction factor was devised, dependent only on the boundary layer thickness in the absence of the model. Turner (141) has compared lift measurements for several wings over moving and fixed ground surfaces. From the discrepancies between the two, limiting conditions of lift and ground clearance were obtained for which use of a moving ground becomes necessary. Stricter conditions were deduced by South (142), based on lift coefficient and ground clearance.

These wing tests were predominately at large ground clearances. For ground effect wings which operate at very low clearance the most common test technique utilises image models. Ashill (160) compared image and fixed ground methods, finding little difference, while Kumar (161) has compared image tests with results from a rotating arm facility.

The evidence suggests that for most test purposes, where lift is not very great and the ground clearance is moderate, the simplest solution to the ground simulation problem is also the best.

APPENDIX C

WAKES OF THREE-DIMENSIONAL PLATES.

Although the study of two-dimensional bluff body wake flows has been extensive over the years, the same is not true of either three-dimensional or axisymmetric bodies and plates. However, as early as 1912, photographs taken by Eden (162) of the wake behind flat plates in air and water showed clearly the periodic nature of the flow. Simmons and Dewey (163) later investigated the air flow past circular discs and found that above a Reynolds number of 100 the standing vortex formed on the base of the disc broke away at regular intervals. Stanton and Marshall (164) in a more carefully controlled experiment using circular discs in a water tank found that the wake was comprised of a series of regularly spaced but distorted vortex loops.

Swain (30) extended the theoretical work of Prandtl, using the momentum transfer theory, to the axisymmetric wake but no experimental results of this case were obtained until Goldstein (165) reported some measurements by Schlichting in 1930 when comparing the theoretical method of Swain with Taylor's vorticity transfer theories. This showed poor agreement but subsequent measurements by Hall and Hislop (166) in the wake behind a similar body, using a tunnel with lower turbulence produced results which fitted closely to the momentum transfer theory.

Fail, Owen and Eyre (21) measured the mean flow and turbulence velocities in the near wake of a series of sharp-edged flat plates set at incidence to the airstream. The near wake is taken to mean the wake within a few bodywidths of the plate. At 90° to the free stream direction, contours of mean velocity along the centre line of the plates, were mapped from pitot and static probe measurements. This showed the reverse flow region to be almost identical in shape and extent for triangular, circular and rectangular plates. Static

pressure measurements along the wake centre line showed the distribution to be independent of the shape generating the wake. Contours of mean velocity taken normal to the free stream direction, at a distance of three plate widths downstream of the square plate, show an almost axisymmetric outer wake, becoming increasingly square in shape as the centre is approached. An interesting feature is the rotation of the planes of symmetry through $\pi/4$ radians. A similar effect is noticable in the contours of turbulence intensity. Measurements were taken from a hot wire anemometer with the wire aligned normal to the free stream direction. On reducing the angle of the plate below 50^{o} the wake becomes dominated by vortices springing from the longitudinal edges of the plate. The turbulent energy spectrum showed that under these conditions the wake flow was highly periodic. Decreasing the angle of the plate increased the frequency of the disturbance, but at 40^{o} incidence the nature of the disturbance changed and although the frequency continued to increase the intensity reduced dramatically.

A hot wire anemometer was used by Cooper and Lutzky (167) to investigate the far wakes of a series of flat rectangular plates and a circular disc. Measurements of the longitudinal flow components were obtained at downstream distances of up to one thousand plate widths. Similarity profiles could be plotted for the turbulence data based on peak turbulence intensity although not for the mean velocity deficit. An unexplained feature of most wakes was the occurrence of an offcentre maximum velocity deficit. Further work by Fail, Lawford and Eyre (49) extended the earlier measurements on periodicity in the wake flow behind rectangular plates, relating the results to two-dimensional flows. Base pressure increased on reducing aspect ratio while drag reduced, the aspect ratio being the ratio of width to height of the plate. The bubble length as a ratio of the smaller plate dimension was found to be a maximum for an aspect ratio of ten, while the square and infinite aspect ratio plates were almost identical. The Strouhal number based on the same dimension and the free stream velocity was found to be almost constant.

It was shown by Billerbeck (168) that the data of Cooper and Lutzky for the rate of growth of the wake width could be fitted to a universal expression based on the drag coefficient of the body generating the wake. The limited data presented gave a growth rate identical to that for a two-dimensional wake except that the exponent of the distance downstream was one third for the three-dimensional case and one half in two-dimensions.

Steiger and Bloom (169) used the assumption of Prandtl to derive wake profiles for a body generating an initially elliptical wake. Experimental work by Kuo and Baldwin (47) on the far wake structure of elliptical plates, however, found that the wake rotated through a right angle within a few plate widths downstream. This meant that the major axis of the wake aligned itself with the minor axis of the body. The wake thereafter tended to axi-symmetry. Spectral measurements showed a Strouhal number increasing with eccentricity, with the Strouhal number based on the equivalent diameter. Detailed measurements in the wake of a circular disc had earlier been performed by Carmody (170). Using hot wire anemometer and pressure probe measurements it was found that similarity was established within fifteen diameters. Ninety five per cent of the energy transfer from mean to turbulent motion took place within three diameters; that is the region of the recirculation bubble. Hwang and Baldwin (171) carried out far wake studies on a circular disc at distances up to one thousand plate diameters downstream.

APPENDIX D

Fold out diagram showing the rectangular blocks
and the cambered blocks.

basic block:– 'N' removed from block 'NS':– 'S' added to } block N

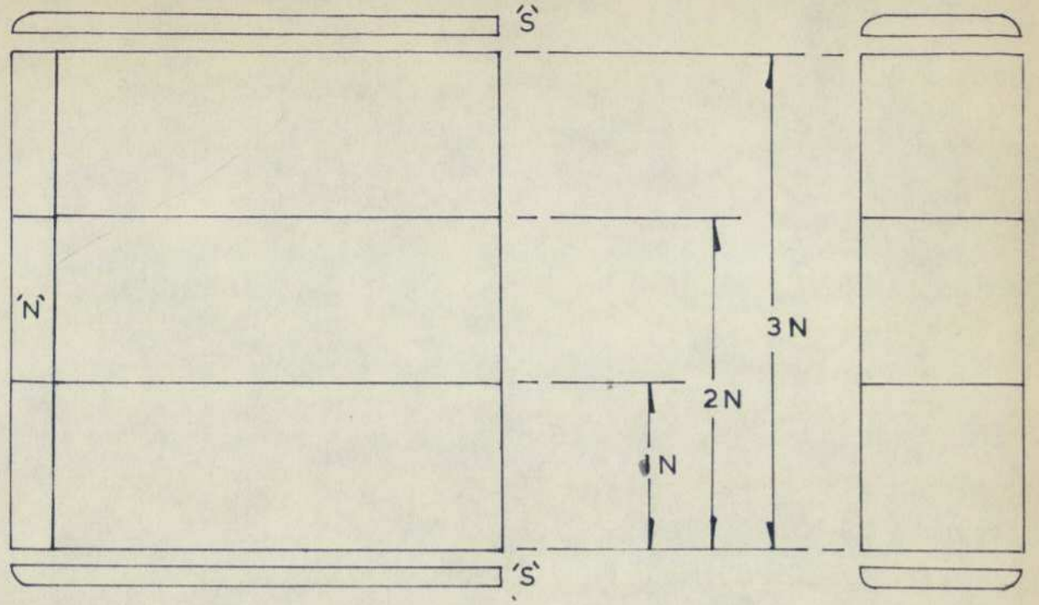

block	span, m
1N	0.1
2N	0.2
3N	0.3
length	0.3 m
thickness	0.1 m

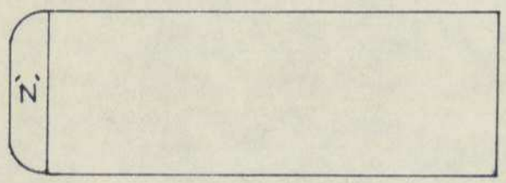

EFFECT OF SPAN

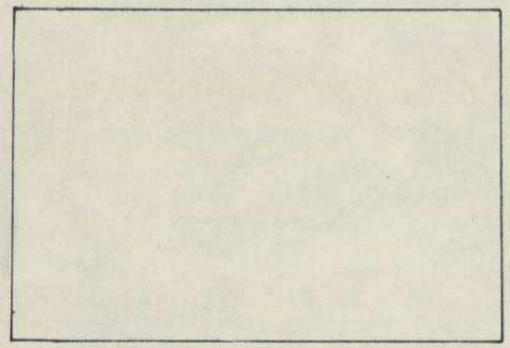

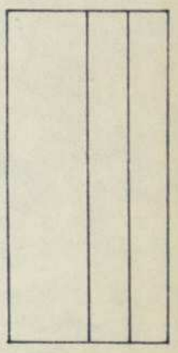

EFFECT OF THICKNESS

nose rad. 0.25 t

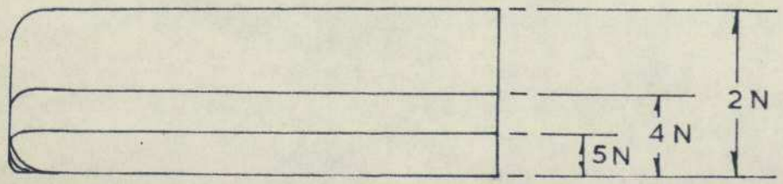

block	thickness
2N	0.1 m
4N	0.05
5N	0.025
length	0.3 m
span	0.2 m

plan

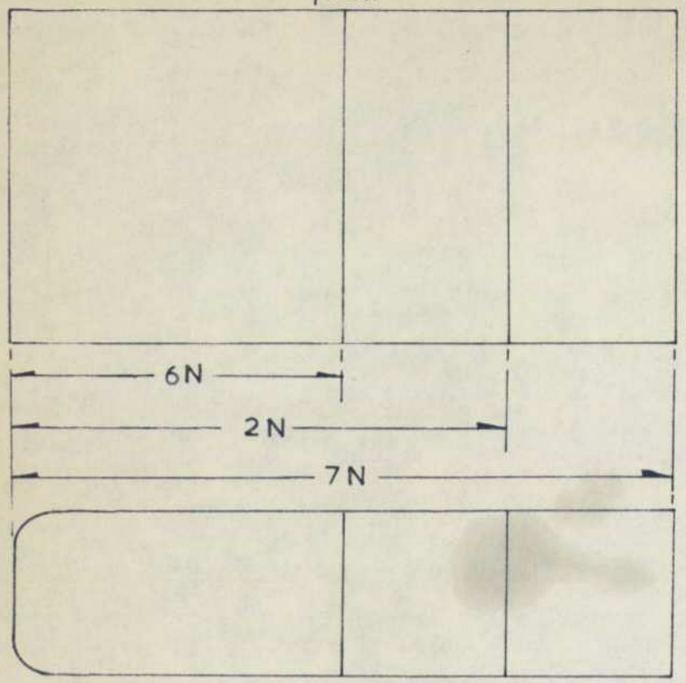

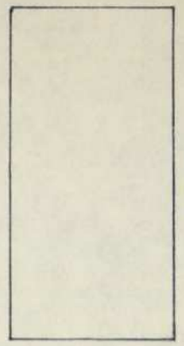

side

block	length, m
6N	0.2
2N	0.3
7N	0.4
span	0.2 m
thickness	0.1 m

EFFECT OF LENGTH

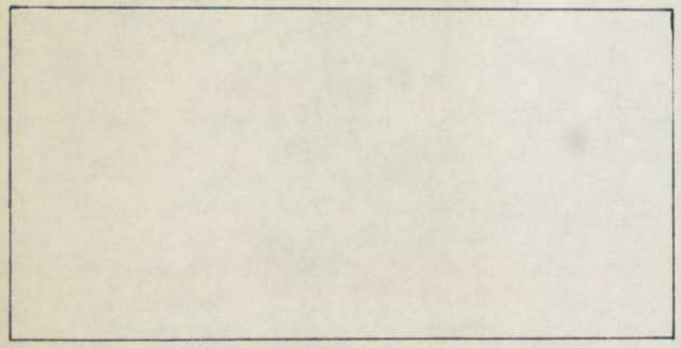

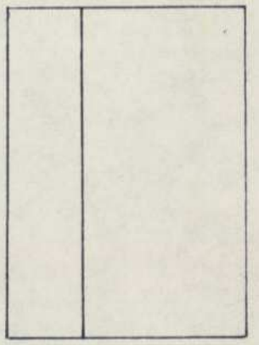

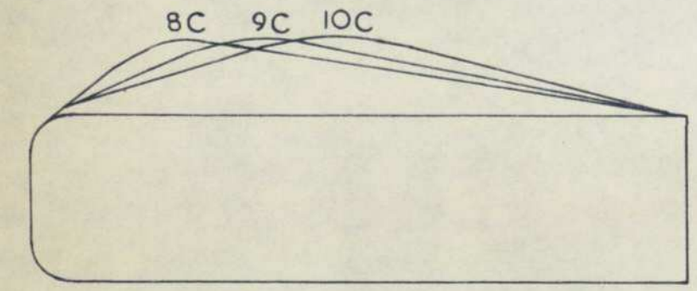

block	max. thickness at % length
8C	25
9C	35
10C	45
11C	60
length	0.4 m
span	0.2 m
thickness	0.15 m

EFFECT OF CAMBER

APPENDIX D

RECTANGULAR BLOCKS (AS FIGURE 8)

[redacted]

[redacted]

[redacted]

[redacted].3. [redacted]

[redacted]

[redacted]

[redacted]

[redacted]

[redacted]

[redacted]

[redacted]

[redacted]

[redacted]

[redacted]

[redacted]

[redacted]

[redacted]

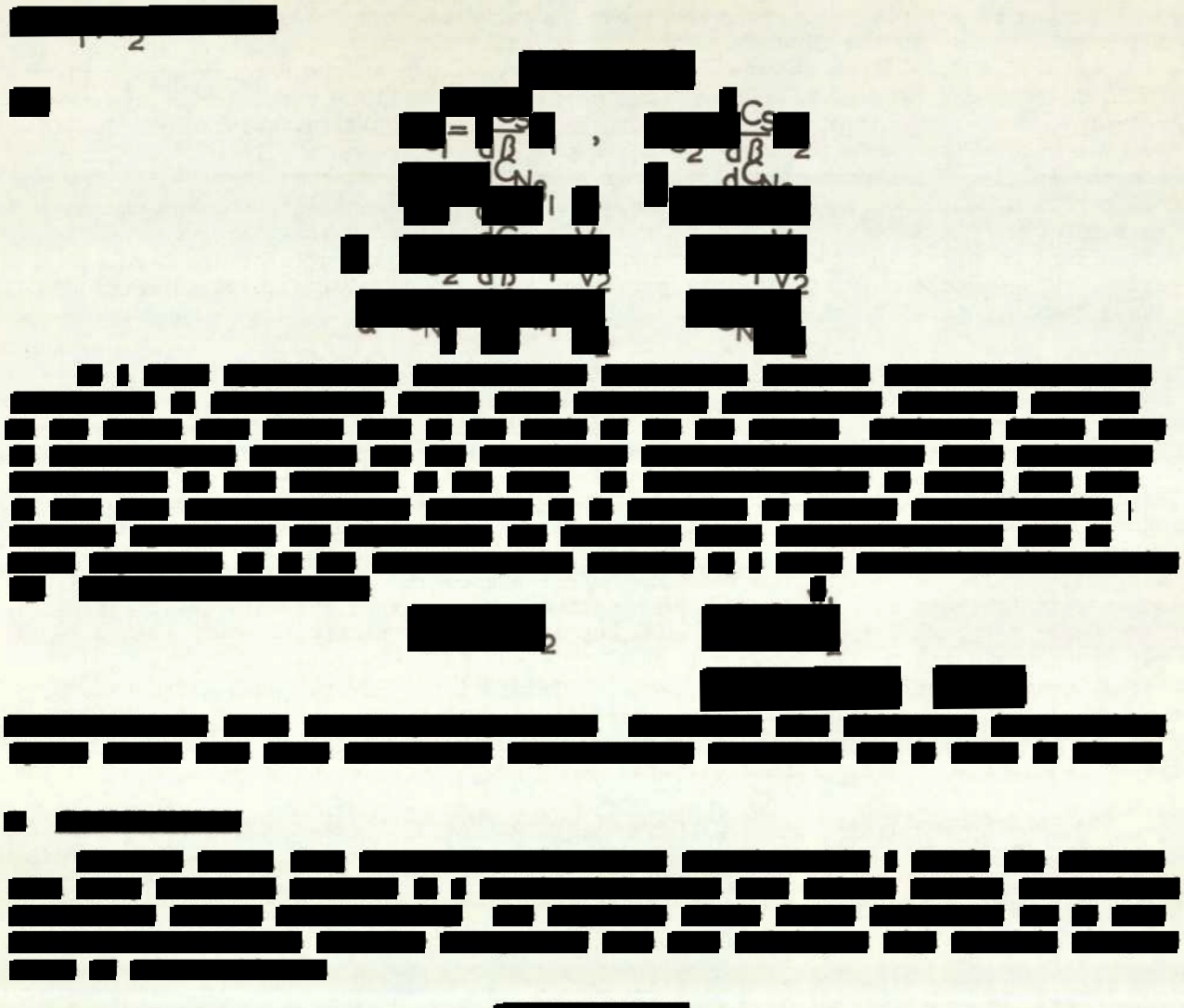

6 Carr, G.W.:

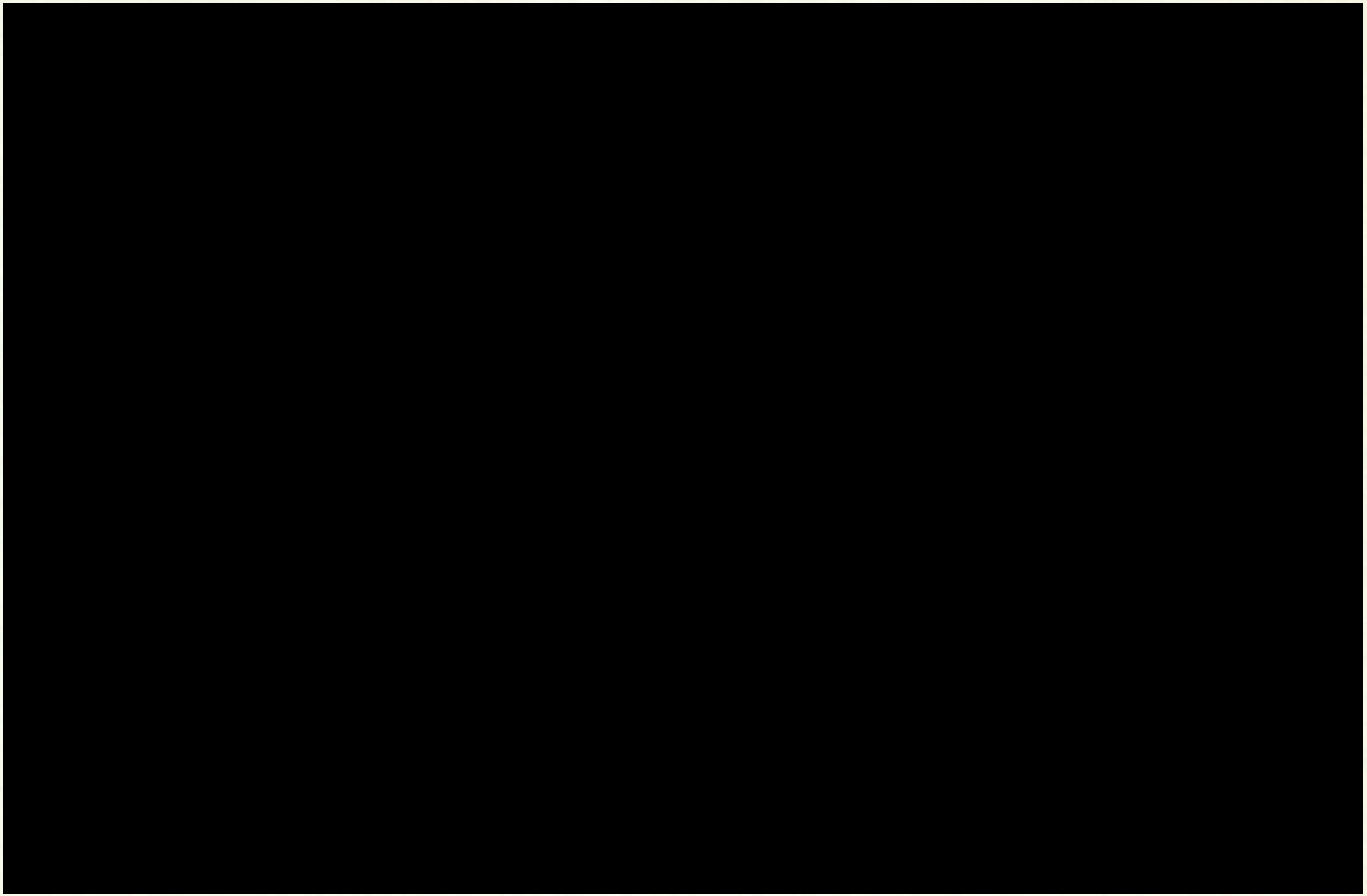

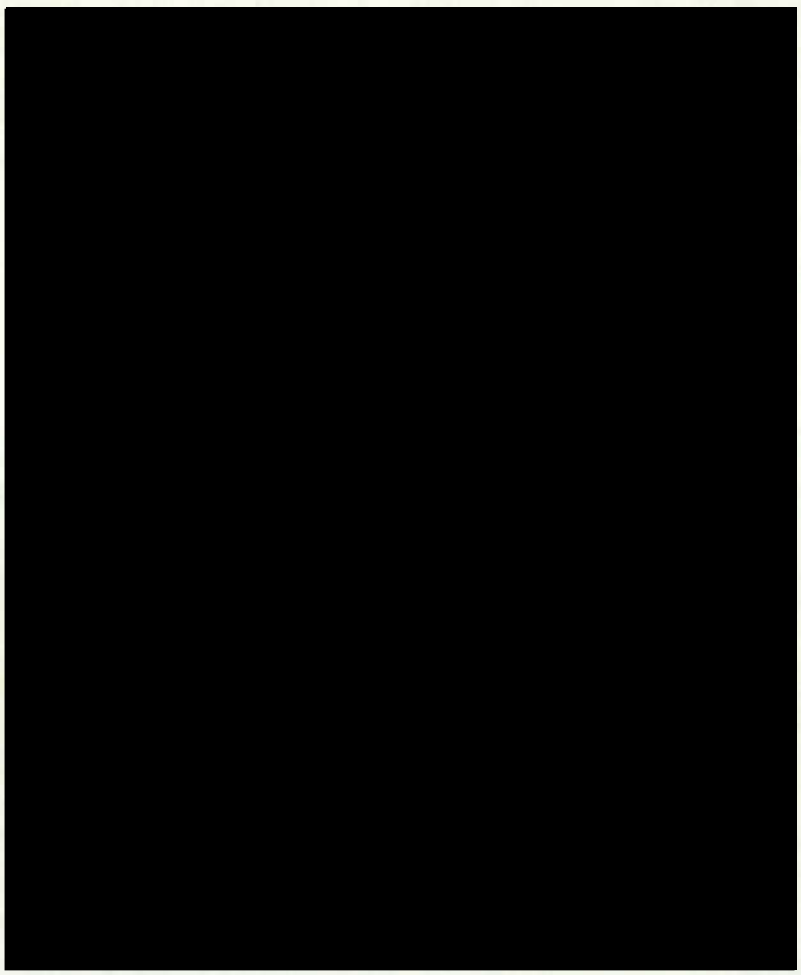

WAKE PROPERTIES OF TYPICAL ROAD VEHICLES

J. P. Howell
Department of Aeronautics, *
The City University
London.

Abstract

A considerable degree of driving discomfort can be experienced when driving a vehicle in the wake of others. This is especially true in either wet or dusty conditions when both forward and rearward vision becomes obscured. This report investigates the wake properties of various vehicle types, principally a saloon car, from a series of wind tunnel tests. Longitudinal and transverse velocity distributions derived from pressure measurements are shown for various downstream positions in the wake. Hot-wire anemometer measurements are used to map the shape of the base flow recirculation bubble for a variety of typical rear end designs; to show the distribution of mean velocity and turbulence intensity in the wake, and the deformation and decay of the trailing vortex sheet. Periodic effects arising from instabilities of the separated shear layer are investigated and a yawed flow is shown to have an influence on the wake.

NOMENCLATURE

B = vehicle width
C_L = lift coefficient (based on frontal area)
e = r.m.s. voltage
e_w = turbulent energy within bandwidth
w = bandwidth/tuned frequency
E = d.c. voltage
f = frequency
H = vehicle height
k = constant
$n\Phi(n) = \left(\frac{e_w}{\frac{e}{w}}\right)^2$
$P_1 P_2$ = pressures in two hole probe
P = total head pressure
R_e = reynolds number
S = static pressure
u, v, w = r.m.s. velocity in X, Y, Z direction
U, V, W = mean velocity in X, Y, Z direction
x = distance from ground board leading edge
β = yaw angle
δ^* = boundary later displacement thickness
ρ = density
ψ = flow angularity
∞ = free stream

* Now Research Fellow, Magnetic Levitation Project, Department of Engineering, University of Warwick, Coventry, England.

[redacted]

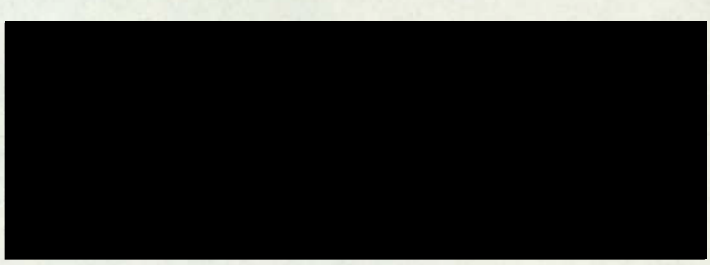

[redacted]

[redacted]

[redacted]

[redacted]

[redacted]

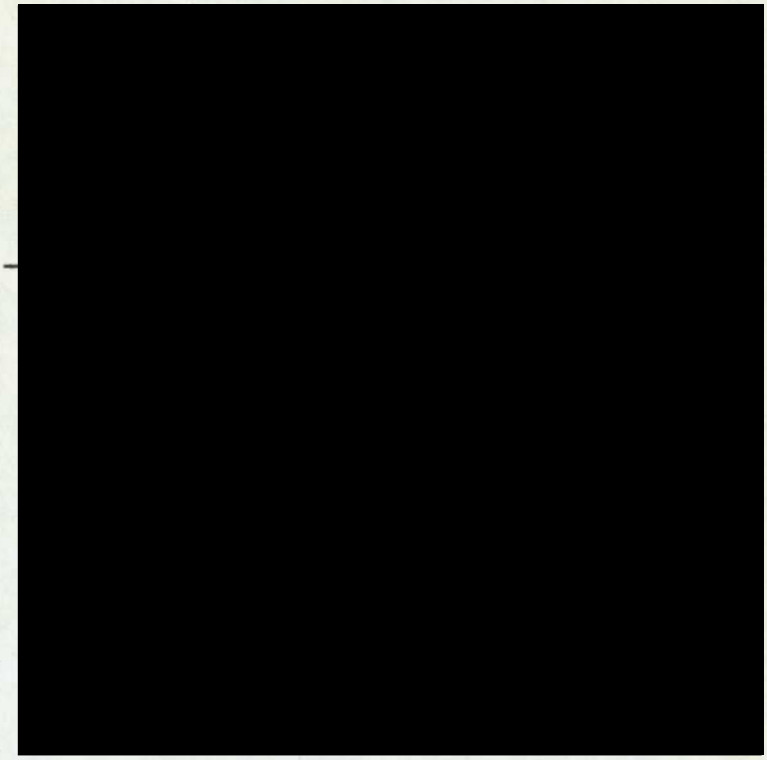

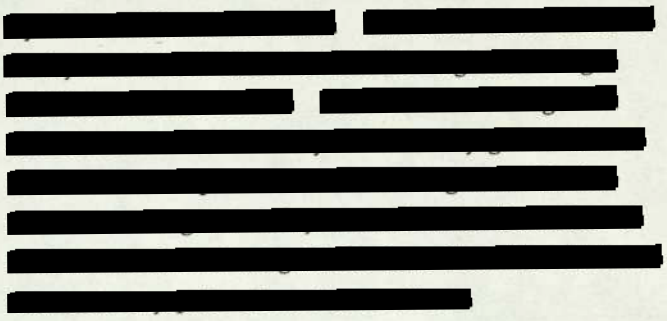

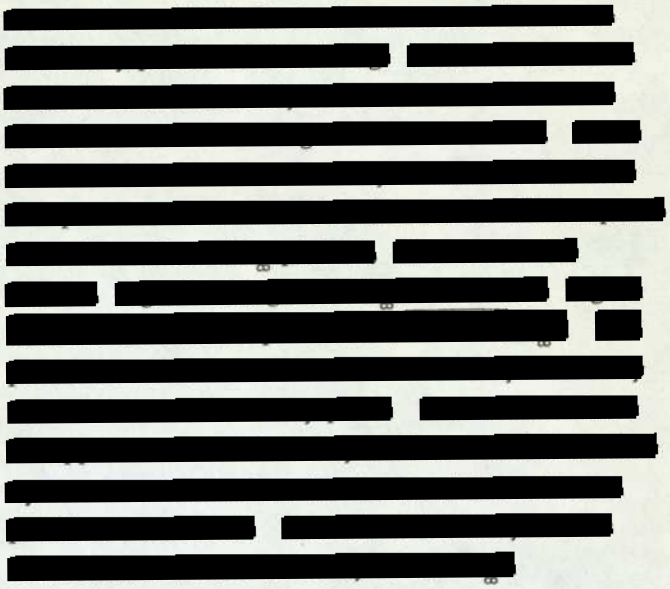

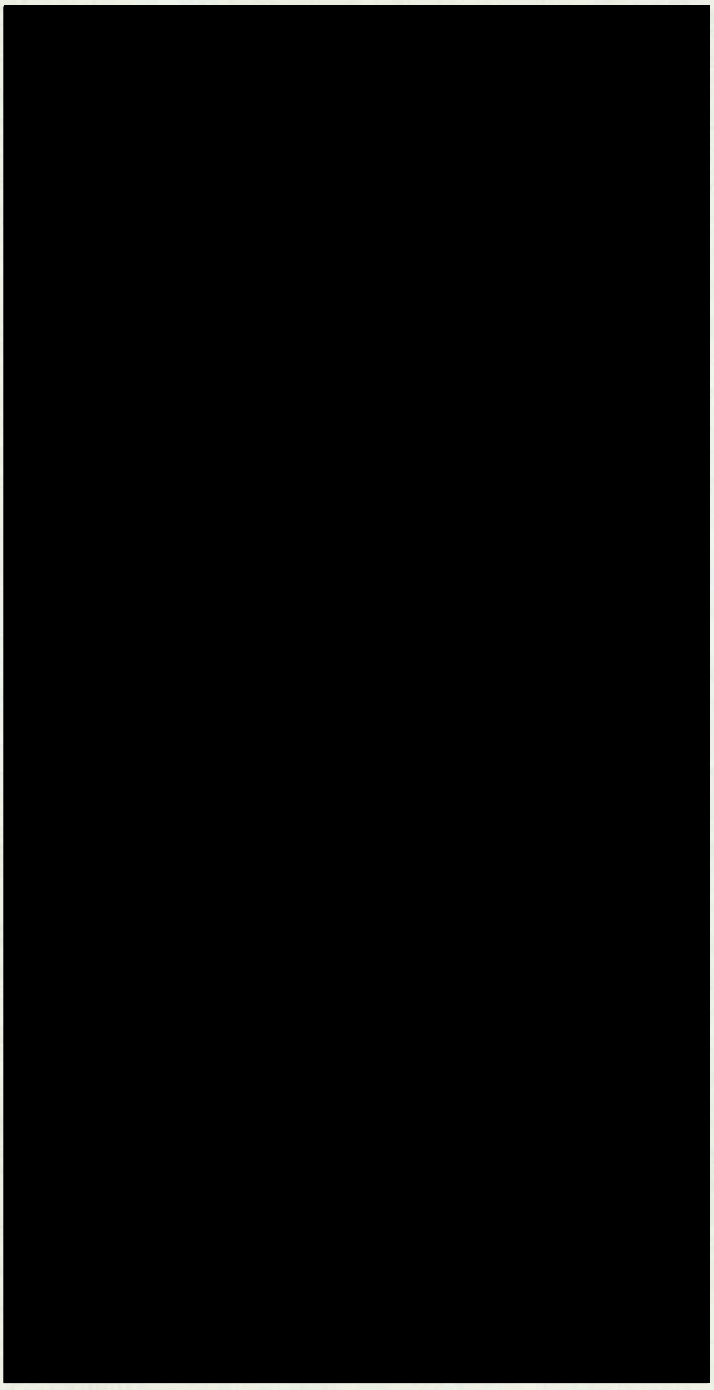

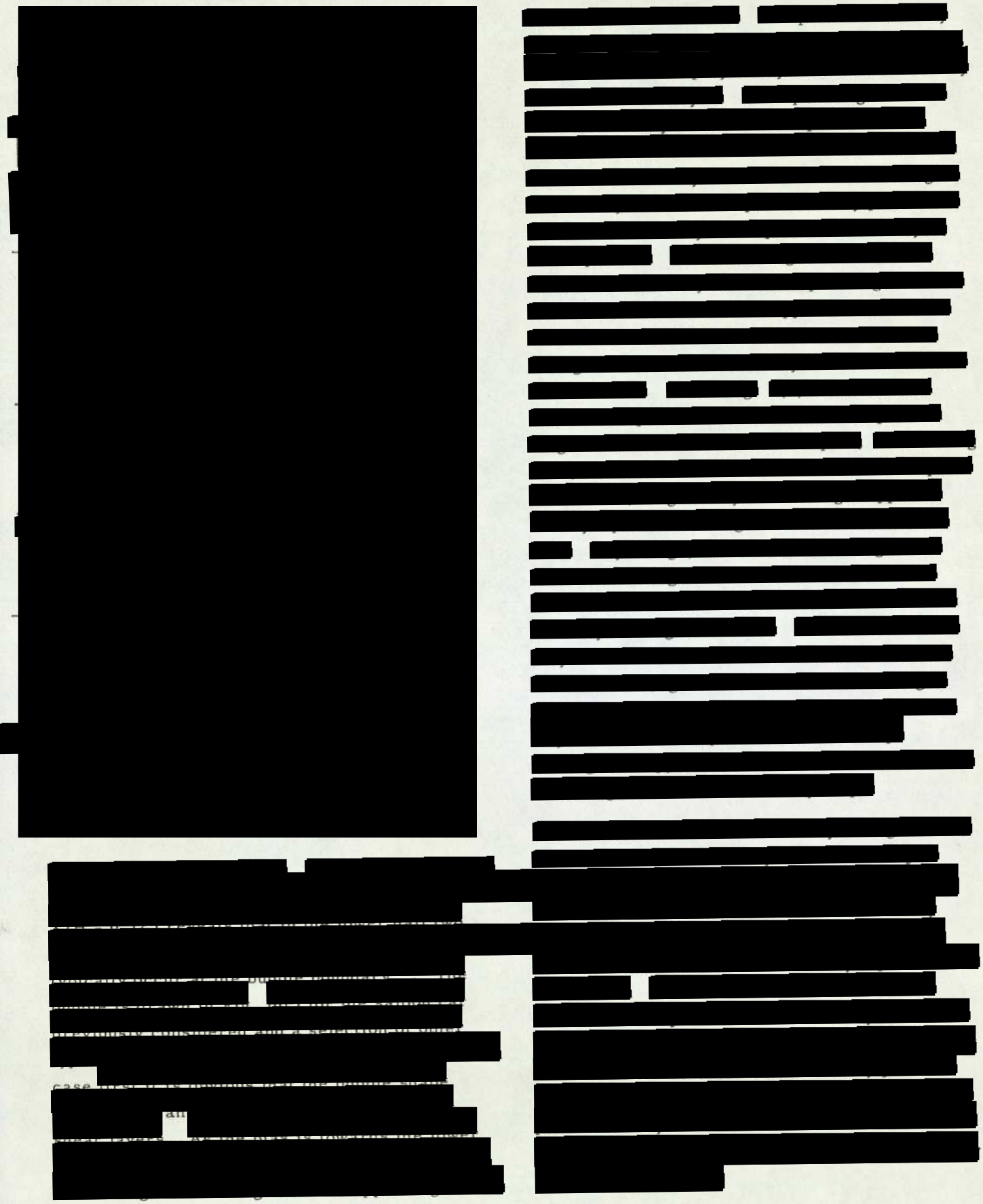

[redacted]

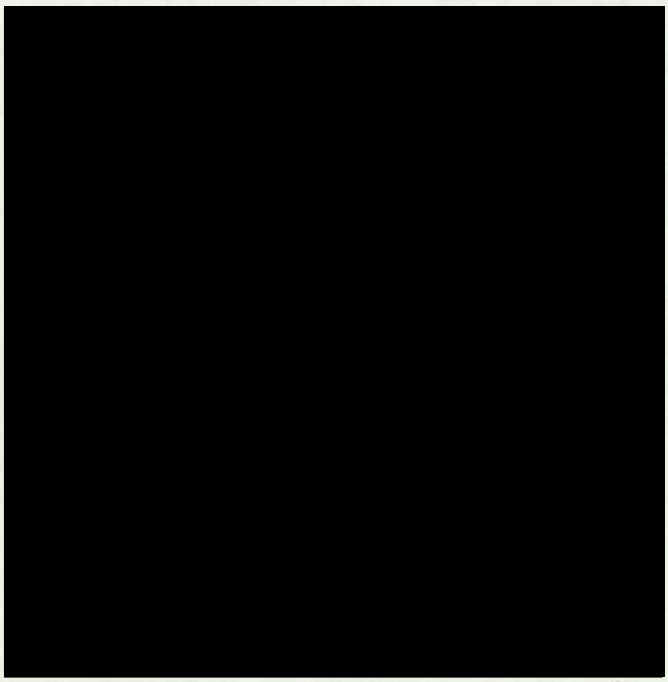

[redacted]

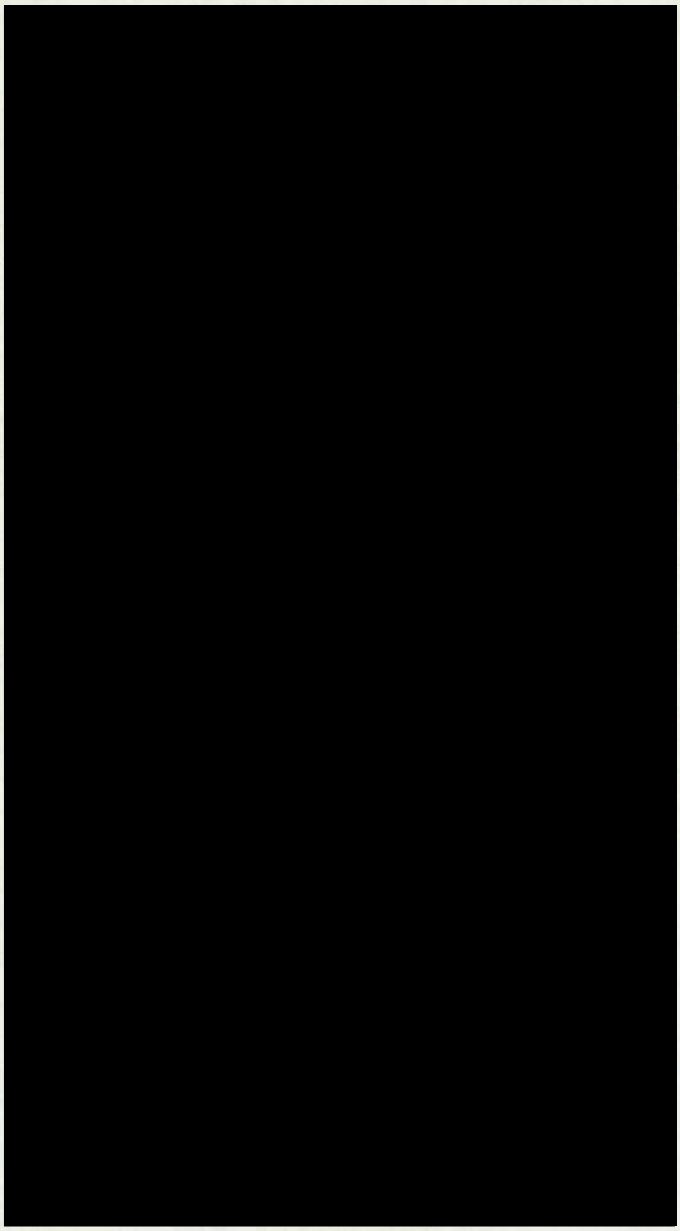

(2) Sherard, T.D., "Suppression of Vehicle Splash and Spray," SAE 730418, 1973

(3) Howell, J.T., "Characteristics of a Typical Car," Advances

(6) [redacted]

[redacted]

[redacted]

[redacted]

[redacted]

(11) [redacted]

[redacted]

[redacted]

[redacted]

REFERENCES

(1) A.Pope, J.J.Harper — Low Speed Wind Tunnel Testing. John Wiley & Sons, Inc. 1966

(2) D.S.Gross, W.S.Sekscienski — Some problems concerning wind tunnel testing of automotive vehicles. SAE 660385 1966

(3) W.H.Bettes, K.B.Kelly — The influence of wind tunnel solid boundaries on automotive test data. Advances in Road Vehicle Aerodynamics. BHRA Cranfield 1973

(4) J.R.Calvert — Blockage corrections for blunt based bodies of revolution. Jnl.Roy.Aero.Soc. Vol 70 1966 pp 532-533

(5) W.A.Mair — Blockage corrections for blunt based bodies of revolution. The Aero. Jnl. Vol 72 p1058 1968

(6) E.C.Maskell — A theory of the blockage effects on bluff bodies and stalled wings in a closed wind tunnel. ARC R&M 3400 1965

(7) G.W.Carr — Wind tunnel blockage corrections for road vehicles. MIRA Report 1971 No4 1971

(8) D.M.Sykes — Blockage corrections for large bluff bodies in wind tunnels. Advances in Road Vehicle Aerodynamics. BHRA Cranfield 1973

(9) J.L.Stollery, W.K.Burns — Forces on bodies in the presence of the ground. Paper 1 Road Vehicle Aerodynamics. The City University 1969

(10) G.W.Carr — The aerodynamics of basic shapes for road vehicles. Pt III streamlined bodies. MIRA Report 1970 No4 1970

(11) D.M.Waters
Thickness and camber effects on bodies in ground proximity
Advances in Road Vehicle Aerodyamics
Paper 12 BHRA Cranfield 1973

(12) K.J.Grunwald
Aerodynamic characteristics of vehicle bodies at crosswind conditions in ground proximity
NASA TND-5935 1970

(13) D.Hulme
'Behind the Wheel'
Autosport July 20 1972

(14) L.J.Janssen
W.H.Hucho
The effect of various parameters on the aerodynamic drag of passenger cars
Advances in Road Vehicle Aerodynamics
Paper 14 BHRA Cranfield 1973

(15) J.R.Ellis
Effect of suspension design on the attitudes of a car during braking and acceleration
Proc.I.Mech.E Vol 187 p787 1973

(16) E.E.Larrabee
Small scale research in automobile aerodynamics
SAE 660384 1966

(17) L.G.Stafford
Calculation of the pressure distribution over the surface of a ground vehicle: PhD thesis
The City University 1972
see also: Advances in Road Vehicle Aerodynamics
Paper 11 BHRA Cranfield 1973

(18) P.G.Wright
'Stability is a drag'
Motor Jan. 5 1974

(19) J.Pothoff
Luftwiderstand und auftrieb moderner kraftfahrzeuge
Paper 12 Road Vehicle Aerodynamics
The City University 1969

(20) W.H.Korff
Aerodynamic design of the Goldenrod to increase stability, traction and speed
The Aerodynamics of Sports and Competition Automobiles
AIAA 1968

(21) R.Fail, T.B.Owen, R.C.W.Eyre
Preliminary low speed wind tunnel tests on flat plates and air brakes
RAE Tech.Note Aero 2356 1955

(22) Tracked Hovercraft Ltd.
A cost comparison of three tracked air cushion vehicle configurations
FRA-RT 71-68 July 1970

(23) G.W.Carr, M.J.Rose
Wind tunnel tests of vehicle models using a moving ground surface
MIRA 1966/13 1966

(24) L.F.East
The measurement of ground effect using a fixed ground board in a wind tunnel
RAE TR 70123 1970

(25) G.J.Brown
The highway aerodynamic test facility
Advances in Road Vehicle Aerodynamics
Paper 19 BHRA Cranfield 1973

(26) F.N.Beauvais, S.C.Tignor, T.R.Turner
Problems of ground simulation in automotive aerodynamics
SAE 680121 1968

(27) W.T.Mason, G.Sovran
Ground plane effects on the aerodynamic characteristics of automobile models - an examination of the wind tunnel test technique
Advances in Road Vehicle Aerodynamics
Paper 17 BHRA Cranfield 1973

(28) R.G.S.White, M.G.Paish
A study of vehicle aerodynamic lift
MIRA Report 1966/16 1966

(29) H.G.Heinrich, D.J.Fekstrom
Velocity distribution in the wake of bodies of revolution based on drag coefficient
ASD-TDR-62-1103 1963

(30) L.M.Swain — On the turbulent wake behind a body of revolution
Proc.Roy.Soc.(London) Ser.A
Vol 125 No 799 1929

(31) J.R.Calvert — Experiments on the low speed flow past cones
J.Fluid Mech. Vol 27 p273-80 1967

(32) J.R.Calvert — Experiments on the flow past an inclined disc
J.Fluid Mech. Vol 29 p691 1967

(33) N.Trentacoste P.M.Sforza — Some remarks on three-dimensional wakes and jets
AIAA Jnl. Vol 6 No 12 p12 1968

(34) C.Verna — Deformation of subsonic wind tunnel wakes 1966
AIAA Student Jnl. Vol 14 No 3 p86

(35) R.Chevray — Turbulent wake of a body revolution
ASME Jnl.Basic Eng.Ser D Vol 90
p 275 1968

(36) D.P.McErlean — Near wake of a blunt based axisymmetric body at Mach 0.14
PhD thesis 1970
University Microfilms Inc. 70-16,944

(37) J.R.Calvert — Some experiments on the flow past a sphere
Aero. Jnl. April 1972 p248 1972

(38) C.Commetta — An investigation of the unsteady flow pattern in the wake of cylinders and spheres, using a hot wire probe
Brown Univ.Eng.Tech.Rep.WT-21 1957

(39) J.M.Kendall — J.Fluid Mech. Vol 21 1965

(40) P.M.Sforza R.F.Mons — Wall-wake: flow behind a leading edge obstacle
AIAA Jnl. Vol 8 Dec. p262 1970

(41) L.R.Wootton — Proc.Symp.Working Committee for tower shaped structures
The Hague 1969

(42) W.A.Mair, D.J.Maull — Aerodynamic behaviour of bodies in the wakes of other bodies 1971 Phil.Trans.Roy.Soc.London A269 p425

(43) D.J.Maull, R.A.Young — The wake of a three-dimensional bluff body in uniform and non-uniform streams 1972 Symposium on External Flows, Bristol

(44) J.C.R.Hunt, G.P.Smith — A theory of wakes behind buildings and some provisional results CERL Lab.Note RD/L/N31 1969

(45) J.C.R.Hunt — Further aspects of the theory of wakes behind buildings and a comparison of the theory with experimental results CERL Lab.Report RD/L/R1665 1970

(46) B.J.Hoole, J.R.Calvert — The use of a hot wire anemometer in turbulent flow The Aero Jnl. Vol 71 July 1967

(47) Y-H.Kuo, L.V.Baldwin — Diffusion and decay of turbulent elliptic wakes AIAA Jnl. Vol 4 Pt 9 1966

(48) J.F.Nash — An analysis of two-dimensional turbulent base flow, including the effect of the approaching boundary layer NPL Aero Rpt. 1036 1962

(49) R.Fail, J.A.Lawford, R.C.W.Eyre — Low speed experiments on the wake characteristics of flat plates normal to an airstream ARC R&M 3120 1959

(50) M.B.Glauert — The wall jet Jnl.Fluid Mech. Vol 1 1956

(51) T.W.Davies — Hot wire anemometry in highly turbulent flows 1972 Symposium on External Flows, Bristol

(52) G.Kiel — A total head meter with small sensitivity to yaw NACA TM 775 1935

(53) D.W.Bryer — Pressure probe methods for determining wind speed and flow direction. H.M.S.O. London 1971

(54) H.Lamb — Hydrodynamics (6th Edition) 1932

(55) F.S.Dee, O.P.Nicholas — Flight measurements of wing tip vortex motion near to ground. ARC CP 1065 1968

(56) J.K.Harvey, F.J.Perry — Flowfield produced by trailing vortices in the vicinity of the ground. AIAA Jnl. Vol 9 No 8 1971

(57) H.Levy, A.G.Fosdyke — The steady motion and stability of a helical vortex. Proc.Roy.Soc. A Vol 120 1928

(58) H.Levy, A.G.Fosdyke — Proc.Roy.Soc. A Vol 116 1927

(59) G.E.LindWalker — Car Aerodynamics. Automobile Engineer 1958. June pp215-221, July pp262-270

(60) W.E.Pringham, W.D.Bowman — Exhaust flow pattern study in a wind tunnel. SAE 730236 1973

(61) C.D.Cone — A theoretical investigation of vortex sheet deformation behind a highly loaded wing and its effect on lift. NASA TN D-657 1961

(62) H.B.Squire — The growth of a vortex in turbulent flow. The Aero. Qtly. Vol 16 1965

(63) P.R.Owen — The decay of a turbulent trailing vortex. The Aero. Qtly. Vol 21 1970

(64) R.Rose — Aircraft vortex wakes and their effects on aircraft. RAE Tech.Note Aero 2934 1963

(65) T.M.Barrows, S.E.Widnall — Optimum lift-drag ratio for a ram wing tube vehicle. AIAA Jnl. Vol 8 No 3 1970

(66) L.U.P.Clarke — 'See-through 1100'. The Motor Jan. 3 1970

(67) R.Choulet, J-L.Favero, L.Romani — A study of the aerodynamic interaction between a lorry and a car. Advances in Road Vehicle Aerodynamics Paper 15 BHRA Cranfield 1973

(68) R.K.Heffley — Aerodynamics of passenger vehicles in close proximity to trucks & buses. SAE 730235 1973

(69) W.S.Johnson, F.H.Speckhart, R.E.Bridwell — Aerodynamic effects of passing vehicles. SAE 730687 1973

(70) G.J.Brown — Aerodynamic disturbances encountered in highway passing situations. SAE 730234 1973

(71) W-H.Hucho, H.J.Emmelman — Theoretical prediction of the aerodynamic derivatives of a vehicle in cross wind gusts. SAE 730232 1973

(72) L.M.Milne-Thompson — Theoretical Hydrodynamics (5th Edn.) Macmillan, London 1968

(73) G.W.Carr — The study of road vehicle aerodynamics using wind tunnel models. Road Vehicle Aerodynamics, Paper 14 The City University 1969

(74) H.Goetz — The influence of wind tunnel tests on body design, ventilation, and surface deposits of sedans and sports cars. SAE 710212 1971

(75) T.D.Sherard — Suppression of vehicle splash and spray. SAE 730718 1973

(76) W.Tempest, M.E.Bryan — Low frequency sound measurements in vehicles. Applied Acoustics Vol 5 1972

(77) K.E.Ludvigsen — The time tunnel - an historical survey of Automotive Aerodynamics. SAE 700035 1970

(78) R.König-Fachsenfeld — 'Aerodynamik des Kraftfahrzeugs' Umschau Verlag, Frankfurt, Germany 1951

(79) G.W.Carr — The aerodynamics of basic shapes for road vehicles Part 2: Saloon car bodies. MIRA 1968/9 1968

(80) R.P.Marcell, G.F.Romberg — Aerodynamic development of the Charger Daytona for stock car competition. SAE 700036 1970

(81) T.R.Turner — Wind tunnel investigation of a 3/8 scale automobile model over a moving belt groundplane. NASA TN-D 4229 1967

(82) G.W.Carr — Aerodynamic effects of underbody details on a typical car model. MIRA 1965/7 1965

(83) W.D.Bowman — Generalisations on the aerodynamic characteristics of sedan type automobile bodies. SAE 660389 1966

(84) R.Barth — Aerodynamic forces on motor vehicles. Deutsche Kraftfahrtforschung und Strassenverkehrstechnik Vol 184 pp 4-14 1966

(85) W.E.Lay, P.W.Lett — Wind effects on car stability. SAE Trans. Vol 61 pp 608-18 1953

(86) R.T.Bundorf, D.E.Pollock, M.C.Hardin — Vehicle handling response to aerodynamic inputs. Paper 716-B SAE 1963

(87) F.N.Beauvais — Transient nature of wind gust effects on an automobile
SAE 670608 1967

(88) R.J.Hawks, E.E.Larrabee — The calculated effect of cross wind gradients on the disturbance of automotive vehicles
The Aerodynamics of Sports and Competition Automobiles
AIAA Ed.B.Pershing 1968

(89) F.D.Hales — Stability problems of road vehicles
Paper 8 Road vehicle aerodynamics
The City University 1969
Ed. A.J.Scibor-Rylski

(90) J.B.Russell, A.J.Scibor-Rylski — Aerodynamic effects on the lateral control and stability of motor vehicles Paper 7 Road vehicle aerodynamics
The City University 1969

(91) F.G.Maccabee — The effect of shear flow on car aerodynamics
Paper 2 Road vehicle aerodynamics
The City University 1969

(92) F.N.Beauvais — Aerodynamic characteristics of a car-trailer combination
SAE 670100 1967

(93) R.Griffiths — 'It's a drag'
Caravan Sept.1967 pp51-53 1967

(94) D.M.Waters — The aerodynamic behaviour of car-caravan combinations
Paper 4 Road Vehicle Aerodynamics
The City University 1969

(95) R.J.Hawks — Reduction of tractor-trailer cross wind response 1971
AIAA Jnl. Aircraft July pp583-5

(96) M.W.Dawley — Aerodynamic effects on automotive components
SAE paper 1965

(97) A.Morelli — Theoretical method for determining the lift distribution on a vehicle Fisita Congress, Tokyo 1964

(98) H.Schlichting — Aerodynamic problems of motor cars Agard Report 307 1960

(99) H.Flynn, P.Kyropoulos — Truck aerodynamics SAE Transactions 1962

(100) J.W.Kirsch, S.K.Garg, W.H.Bettes — Drag reduction of bluff vehicles with airvanes SAE 730686 1973

(101) A.Morelli — Aerodynamic actions on an automobile wheel Paper 5 Road Vehicle Aerodynamics The City University 1969

(102) J.E.Fackrell, J.K.Harvey — The flow field and pressure distribution of an isolated road wheel. Paper 10 Advances in Road Vehicle Aerodynamics BHRA Cranfield 1973

(103) W.R.Stapleford, G.W.Carr — Aerodynamic characteristics of exposed rotating wheels MIRA Report No 1970/2 1970

(104) A.J.Scibor-Rylski — Experimental investigation of the negative aerodynamic lift wings used on racing cars Paper 9 Advances in Road Vehicle Aerodynamics BHRA Cranfield 1973

(105) A.J.Scibor-Rylski — Negative lift devices on racing cars Paper 19 Road Vehicle Aerodynamics The city University 1969

(106) Jim Clark Foundation — The aerodynamic characteristics of racing cars fitted with aerofoils Research Report J.C.F., London 1969

(107) W.D.Bowman — The present status of automobile aerodynamics in automobile engineering and development The Aerodynamics of Sports and Competition Automobiles, AIAA 1968

(108) A.D.Sussex, R.Northcote-Smith — The aerodynamic characteristics of the Piper GTR Group 6 Sports car prototype
Paper 18 Road Vehicle Aerodynamics
The City University 1969

(109) T.R.Boyce, P.J.Lobb — An investigation of the aerodynamics of current Group 6 Sports car designs
Advances in Road Vehicle Aerodynamics
BHRA Cranfield 1973

(110) B.Pershing — Dragster Aerodynamics - Streamlining versus weight; The Aerodynamics of Sports and Competition Automobiles
AIAA 1968

(111) J.S.Irving — The Golden Arrow and the World's Speed Record 1930
Automobile Eng. Vol 24 May pp186-96

(112) T.P.Torda, T.A.Morel — Aerodynamic design of a land speed record car 1971
AIAA Jnl. Aircraft Vol 8 No 12

(113) K.R.Cooper — The wind tunnel development of a low drag, partially streamlined motor cycle 1973
DME/NAE Qtly.Bull. No 1973(4)

(114) W.F.M.Goss — Atmospheric resistance to the motion of railway trains 1898
The Engineer, Aug.12 pp164-166

(115) F.C.Johansen — The air resistance of passenger trains
Proc.I.Mech.E Vol 134 1936

(116) R.G.Gawthorpe — Aerodynamic problems of high speed trains running on conventional tracks: Lecture Series 48 - High Speed Vehicles
Von Karman Institute for Fluid Dynamics, April 10-14 1972

(117) T.Hara, M.Kawaguti, G.Fukuchi, A.Yamamoto — Aerodynamics of high speed train. Monthly Bulletin of the International Railway Congress Association Vol 45 No 2 Feb. 1968

(118) M.Gaillard — Aerodynamics of trains in tunnels. Paper J4 Aerodynamics and ventilation of vehicle tunnels. BHRA Canterbury 1973

(119) T.B.Morrow, F.G.Maccabee — Prediction of the pressure distribution on vehicles moving near the ground; N.P.L. Industrial Aerodynamics Meeting, June30, 1971

(120) H.W.Woolard — Slender body aerodynamics for high speed ground vehicles. AIAA Paper 70-139 1970

(121) T.M.Barrows — The ram air cushion - Advanced fluid suspension for tracked levitated vehicles. ASME Paper No 73-ICT-14 1973

(122) J.E.Davis, G.L.Harris — Non-planar wings in non-planar ground effect 1973. AIAA Jnl. Aircraft Vol 10 No 5

(123) W.J.G.Trebble — Low speed wind tunnel tests on a $^1/_6$th scale model of an air cushion vehicle. ARC CP 983 1968

(124) E.J.Andrews — The external aerodynamics of Hovercraft. The Aeronautical Jnl. Vol 74 June pp 472-482 1970

(125) W.Zeitfuss Jr, E.N.Brooks Jr — Prediction of static aerodynamic characteristics of air cushion vehicles through 180° of yaw. AIAA Jnl. Aircraft Vol 9 No 4 pp 306-310 1972

(126) P.E.Kumar — Stability of Ground Effect Wings. College of Aeronautics, Cranfield. Report Aero 196 1967

(127) S.Ando
Summary of model tests for simple ram wing KAG-3 1964
Hovering Craft & Hydrofoil, Aug-Sep.

(128) R.W.Gallington
M.K.Miller
W.D.Smith
The ram wing surface effect vehicle: comparison of one-dimensional theory with wind tunnel and free flight tests
Hovering Craft & Hydrofoil, Vol 11, No 5, pp 10-19 1972

(129) S.Ando
An idealised ground effect wing
Aeronautical Qtly. Feb. 1966

(130) P.R.Ashill
On the minimum induced drag of ground-effect wings
Aeronautical Qtly. Aug. 1970

(131) S.E.Widnall
T.M.Barrows
An analytic solution for two- and three-dimensional wings in ground effect
Jnl.Fluid Mech. Vol 41 1970

(132) A.Betz
Auftrieb und Widerstand einer tragfläche in der nähe einer horizontal Ebene
ZFM No 12 1912

(133) E.Pistolesi
Ground effect - theory and practice
NACA TM 828 1935

(134) I.Tani
M.Taima
S.Simidu
The effect of ground on the aerodynamic characteristics of a monoplane wing
Rpt. No 156 Aero Research Institute Tokyo University 1937

(135) J.Bagley
The pressure distribution on two-dimensional wings near the ground
ARC R&M 3238 1960

(136) M.P.Fink
J.L.Lastinger
Aerodynamic characteristics of low aspect ratio wings in close proximity to the ground
NASA TN D-926 1961

(137) A.W.Carter — Effect of ground proximity on the aerodynamic characteristics of aspect ratio 1 airfoils with and without endplates
NASA TN D-970 1961

(138) D.L.I.Kirkpatrick — Experimental investigation of the ground effect on the subsonic longitudinal characteristics of a delta wing of aspect ratio 1.616
RAE Tech.Report 66179 1966

(139) C.H.Fox — Prediction of lift and drag for slender sharp edged delta wings in ground proximity
NASA TN D-4891 1968

(140) A.J.Berry — An experimental investigation of ground effect using a moving surface simulation, M.Phil thesis
University of London 1968

(141) T.R.Turner — Endless belt technique for ground simulations
Conf. V STOL Aircraft NASA SP-116
Paper No 25 1966

(142) P.South — Measurement of flow breakdown in rectangular working sections
NRC Aero Rpt. LR-513 1968

(143) R.Barth — Effect of unsymmetrical wind incidence on aerodynamic forces acting on vehicle models and similar bodies
SAE 650136 1965

(144) G.W.Carr — The aerodynamics of basic shapes for road vehicles Pt I: simple rectangular bodies
MIRA Report 1968/2 1968

(145) W.E.Lay — Is 50mpg possible with correct streamlining?
Jnl. SAE Vol 32 1933

(146) J.A.Dunsby
R.L.Wardlaw
D.J.Marsden
An experimental investigation of some methods of reducing the boundary layer thickness on the working section of No3 low-speed wind tunnel with particular reference to half model testing
Lab.Memo AE-106 NAE, Ottawa 1958

(147) W.H.Bettes
Aerodynamic testing of high performance land borne vehicles - a critical review
The Aerodynamics of Sports and Competition Automobiles
AIAA 1968

(148) S.F.J.Butler
B.A.Moy
T.N.Pound
A moving belt rig for ground simulation in low speed wind tunnels
ARC R&M 3451 1963

(149) P.E.Kumar
The College of Aeronautics Whirling Arm - Initial development tests
College of Aeronautics, Aero Note 174
1967

(150) M.C.G.Smith
The use of a runway vehicle for testing lifting rotors in simulated forward flight
The Aeronautical Jnl. Vol 74, July
pp 548-559 1970

(151) H.C.Curtis,Jr
W.F.Putman
A facility for the measurement of VTOL aircraft dynamic characteristics using semi-free flight models
Institute of Aerophysics, University of Toronto, Decennial Symposium Proceedings Pt II 1959

(152) R.H.Heald
Comparison of the ground plane and image methods for representing ground effect in tests on vehicle models
U.S.Nat.Bureau of Standards Jnl. of Research Vol 13 1934

(153) E.A.Stalker — A reflection plate representing the ground
Jnl.Aeronautical Sciences Vol 1 July pp 151-152 1934

(154) M.Ono — On the representation of a ground in a wind tunnel 1935
Jnl.Aeronautical Sciences Vol 3 Nov

(155) C.C.Schmid — Luftwiderstand von Kraftfahrzeugen, Versuche am Fahrzeuge und Modell
Deutsche Kraftfahrtforschung
V.D.I. - Verlag 1938

(156) A.Klemin — A belt method of representing the ground
J.Aero Sciences Vol 1 Oct. 1934

(157) K.Ohtani, M.Takei, H.Sakamoto — Nissan full-scale wind tunnel - Its application to passenger car design
SAE 720100 1972

(158) A.Klemin — Aerodynamics of the railway train
Railway Mechanical Engineer
Vol 108, Aug., pp282-286 1934

(159) G.Volgepohl — Luftwiderstand von Eisenbahn-Fahrzeugen
Z.V.D.I. Feb. 1934

(160) P.R.Ashill — On some aspects of the aerodynamic performance of ground effect wings
PhD thesis, Southampton Uni. 1968

(161) P.E.Kumar — An experimental investigation into the aerodynamic characteristics of a wing with and without endplates in ground effect
College of Aeronautics, Cranfield
Report Aero 201 1968

(162) C.G.Eden — Investigation by visual and photographic methods of the flow past plates and models
Adv. Comm. Aeron. R&M 58 1912

(163) Simmons
Dewey
ARC R&M 1334 1931

(164) T.E.Stanton
D.Marshall
On the eddy current system in the wake of flat circular plates
ARC R&M 1358 1932

(165) S.Goldstein
On the velocity and temperature distribution in the turbulent wake behind a heated body of revolution
Proc.Camb.Phil,Soc. 34 1938

(166) A.A.Hall
G.S.Hislop
Velocity & temperature distributions in the turbulent wake behind a heated body of revolution
Proc.Camb.Phil.Soc. 34 1938

(167) R.D.Cooper
M.Lutzky
Exploratory investigation of turbulent wakes behind bluff bodies 1955
David Taylor Model Basin Report 963

(168) W.J.Billerbeck
Empirical equation for the wake spreading limits behind three-dimensional bodies
J.Ae.Sci. Aug. 1960

(169) M.H.Steiger
M.H.Bloom
Three-dimensional effects in viscous wakes
AIAA Jnl. Vol 1 1963

(170) T.Carmody
Establishment of the wake behind a disc
Trans.A.S.M.E. Jnl. Basic Eng. Ser.D
Vol 86 1964

(171) N.H.C.Hwang
L.V.Baldwin
Decay of turbulence in axisymmetric wakes
Trans. A.S.M.E. Jnl.Basic Eng. Ser.D
Vol 88 1966

PUBLISHED PAPERS

1. The influence of the proximity of a large vehicle on the aerodynamic characteristics of a typical car.
   Advances in Road Vehicle Aerodynamics. B.H.R.A. Cranfield 1973

2. Wake properties of typical road vehicles.
   AIAA 2nd Symposium Aerodynamics and Racing Cars. Los Angeles 1974

3. Wake properties of a saloon car.
   Kolloquium uber Industrieaerodynamik. Aachen 1974

4. The influence of pitch on the lift characteristics of typical road vehicles.
   As 3 above.

5. The aerodynamics of the IBEC club formula racing car.
   'General Engineer' Vol.87, 5, May/June 1976

6. The Wolfson maglev project.
   IEEE Transactions on Magnetics,Vol MagIO No.3 Sept 1974

7. Stability of magnetically levitated vehicles over a split guideway.
   IEEE Transactions on Magnetics,Vol Magll No.5 Sept 1975

8. Performance and stability characteristics of an electrodynamically levitated vehicle over a split guideway.
   ASME Paper 76-Aut-HH, Jnl. of Dyn. Syst. Meas.and Control.

9. Electrodynamic levitation of high speed vehicles.
   IEE 2nd Conference on Advances inMagnetic Materials and their Application. London 1976

10. The application of superconducting magnets to high speed trains.
    'The Indian Engineer' Anniversary Issue 1977

11. Design criteria for rectangular superconducting coils for transport applications.
    6th International Conference on Magnet Technology. Bratislava 1977

THE INFLUENCE OF THE PROXIMITY OF A LARGE VEHICLE ON THE AERODYNAMIC CHARACTERISTICS OF A TYPICAL CAR

J. P. Howell, B.Sc.

The City University, U.K.

Summary

A considerable amount of aerodynamic data is now available for the automobile covering almost every aspect of its environment. Apart from a few examples this data concerns the vehicle in isolation, whereas an actual vehicle is likely to spend much of its time near other vehicles. In this report the influence exerted by a large vehicle on a smaller one is investigated in a series of static wind tunnel tests. The effects of position on the drag and side forces and on the yawing moment are studied along with the effects of basic changes in vehicle geometry. The forces and moments exerted on a typical car by a large commercial type vehicle are found to be considerable depending upon the relative positions of the two vehicles. These results have been extrapolated to show to a first approximation the effect an overtaking manoeuvre by the car would have on the measured forces which only represent the condition where the two vehicles are relatively stationary.

NOMENCLATURE

C_D	$\frac{\text{Drag}}{Q.F}$ Drag coefficient
C_S	$\frac{\text{Side Force}}{Q.F}$ Side force coefficient
C_N	$\frac{\text{Yawing moment}}{Q.F.W}$ Yawing moment coefficient
Q	effective dynamic head. = Qmeas $(1+\epsilon)$
Qmeas	measured dynamic head
ϵ	blockage correction = $\epsilon_S + \epsilon_W$
ϵ_S	Solid blockage
ϵ_W	wake blockage
F	Frontal area
B	Area ratio $\frac{\text{Model Frontal area}}{\text{Working section area}}$
X	Nose to nose distance (+ve car forward)
L	Length of car model
W	Wheelbase of car model
β	Yaw angle
V	Velocity
Y	lateral spacing (℄ car to ℄ lorry)
D	Width of car model
K_1, K_2	Constants

WAKE PROPERTIES OF A SALOON CAR

J. HOWELL

Department of Engineering,
University of Warwick,
Coventry, England.

Summary

A considerable degree of driving discomfort can be experienced when driving a vehicle in the wake of others. This is especially true in either wet or dusty conditions when both forward and rearward vision becomes obscured. This report investigates the wake properties of a typical saloon car from wind tunnel tests. Longitudinal and transverse velocity distributions derived from pressure measurements are shown for various downstream positions in the wake and the decay of turbulence intensity is obtained from hot wire anemometer results. A yawed flow is shown to have a strong influence on the wake.

(NOMENCLATURE)

U, V, W	Mean velocity in X, Y, Z direction.
u, v, w	R.m.s. velocity in X, Y, Z direction.
δ^*	Boundary layer displacement thickness.
x	Distance from ground board leading edge.
Re	Reynolds number.
C_L	Lift coefficient (based on frontal area).
ρ	Density.
P	Total head pressure.
S	Static pressure.
ψ	Flow angularity.
β	Yaw angle.
k	Constant.
$p_1 p_2$	Pressures in two hole probe.
E	D.C. voltage.
e	R.m.s. voltage.
H	Vehicle height.
B	Vehicle width.

1. Introduction

[redacted]

[redacted]

[redacted]

[redacted]

[redacted]

[redacted]

[redacted]

[redacted]

4. [redacted]

[redacted]

[redacted]

[redacted]

[redacted]

[redacted]

[redacted]

[redacted]

[redacted]

[redacted]

[redacted]
2nd [redacted]
May 11 [redacted]

[redacted]

[redacted]

[redacted]

[redacted]

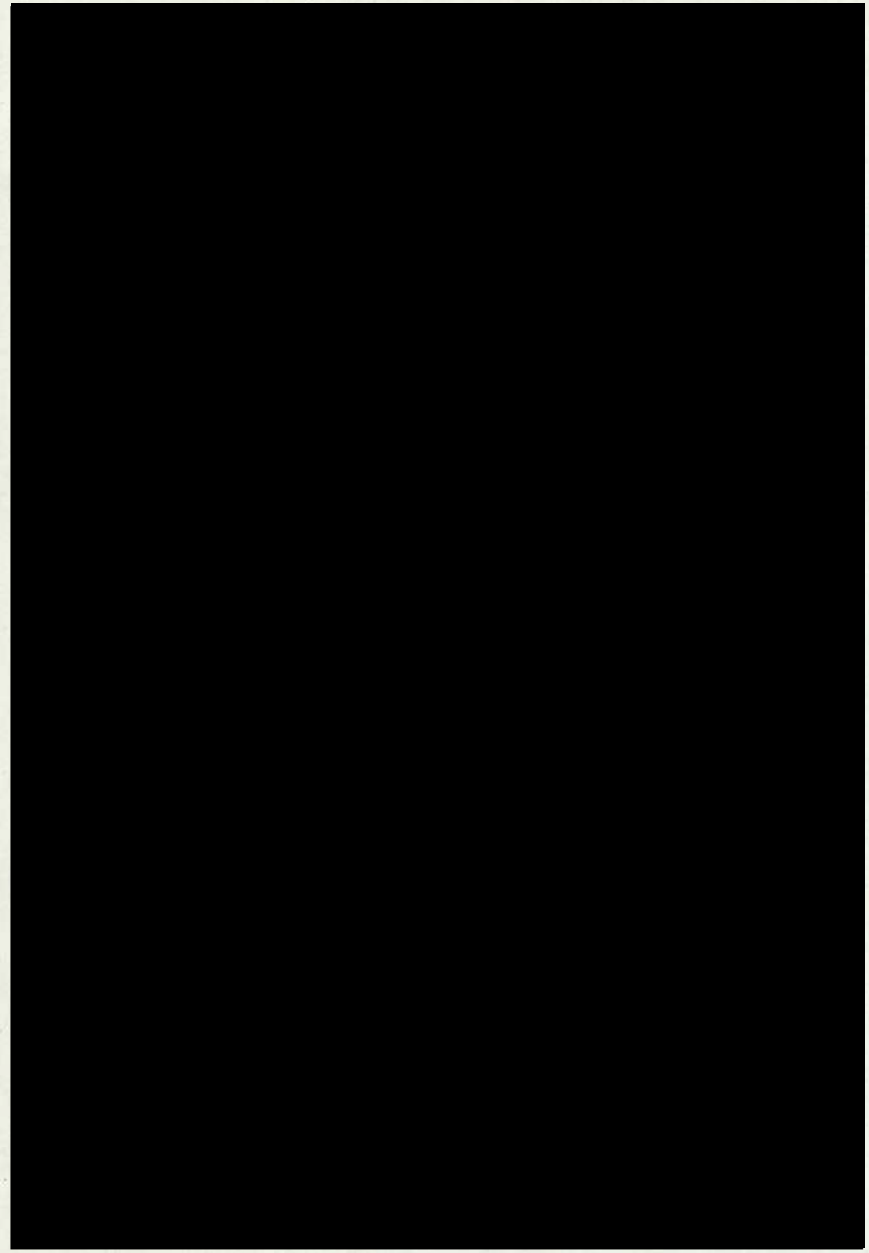

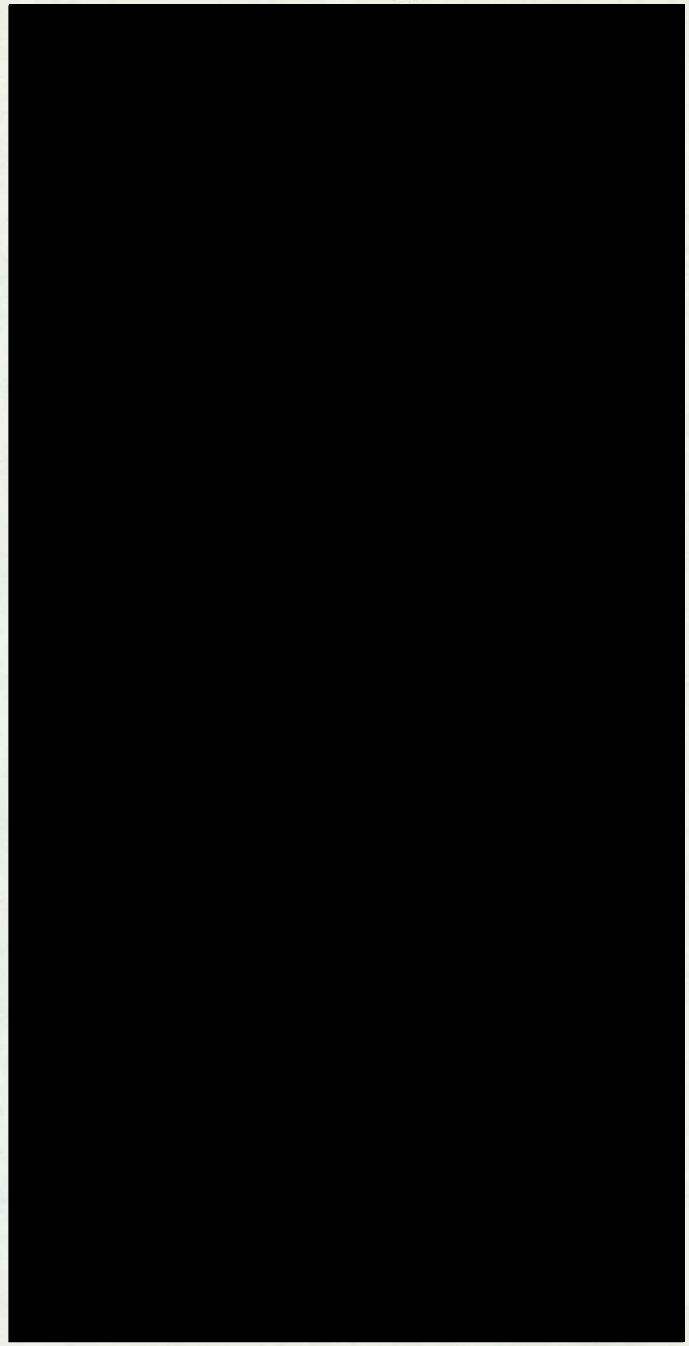

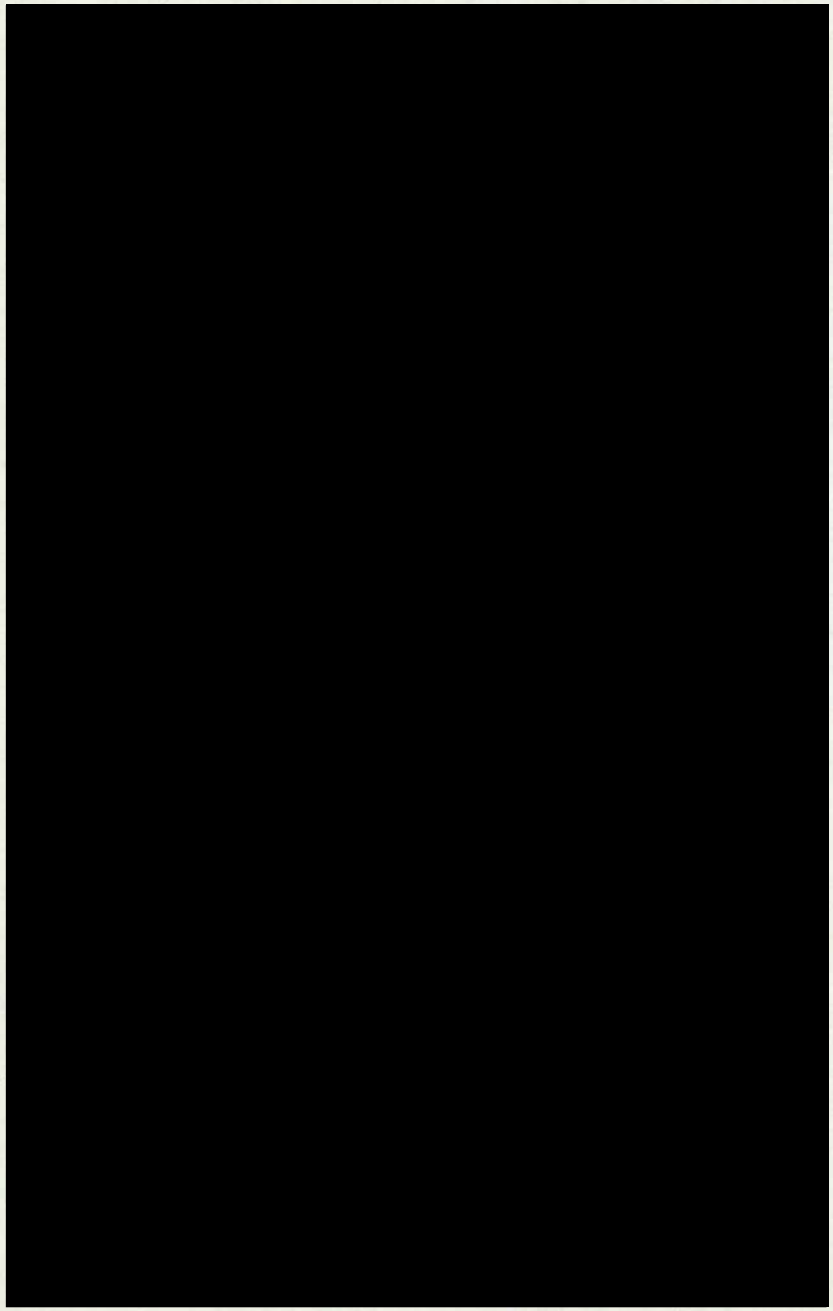

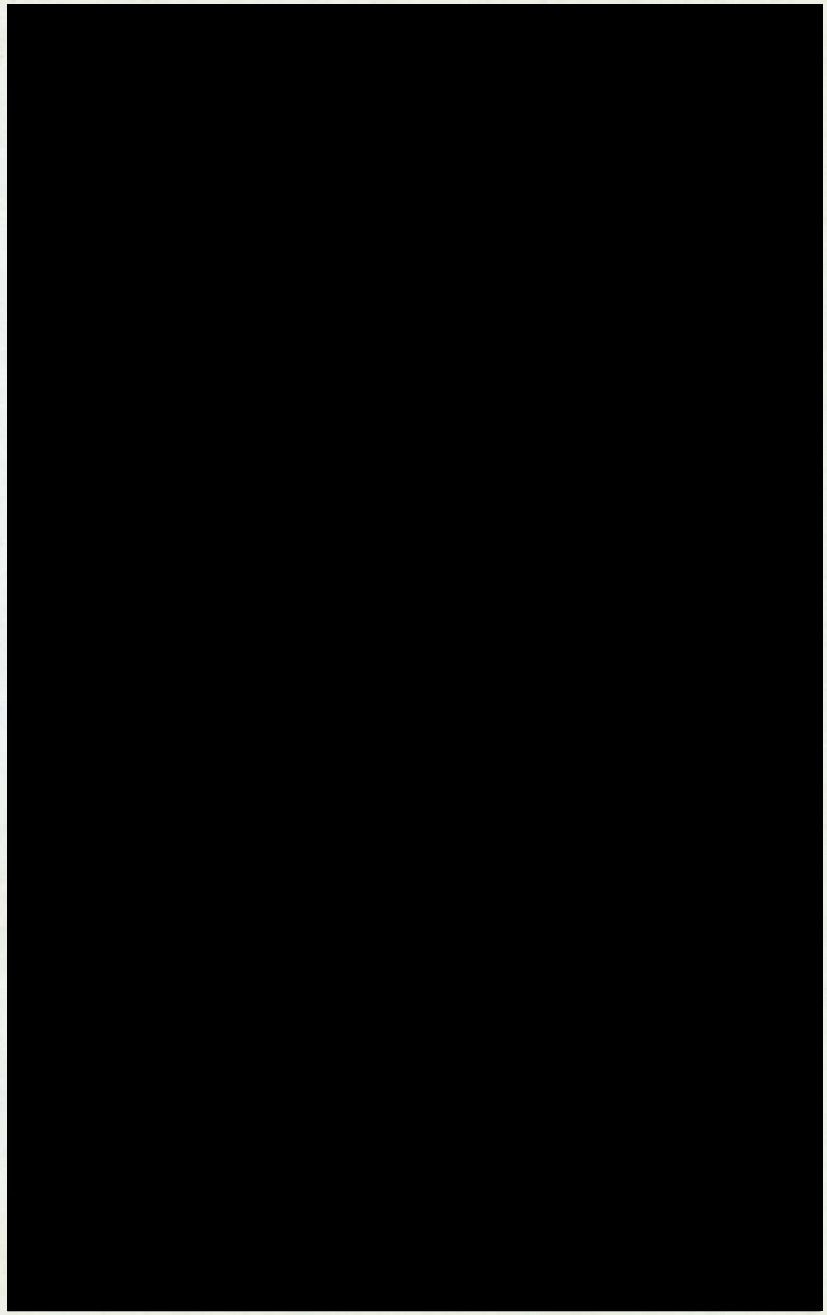

THE INFLUENCE OF PITCH ON THE LIFT CHARACTERISTICS OF TYPICAL ROAD VEHICLES

J. HOWELL

Department of Engineering
University of Warwick
Coventry, England

Summary

The response of a road vehicle to a yawed flow is of great importance to its handling qualities and has naturally received considerable attention. Less interest has been shown in the effects of changes in pitch angle, which occur for a number of reasons. Wind tunnel tests have been performed on a variety of vehicle shapes to determine the effects of pitch and yaw on lift and drag forces. The front wheel lift of a typical vehicle is very sensitive to small changes in incidence. The rear wheel lift and drag are almost independent.

Nomenclature

C_L	Lift coefficient (based on frontal area)
C_{LF}	Front wheel lift coefficient
C_{LR}	Rear wheel lift coefficient
C_{L_0}	Lift coefficient at $\alpha = 0$, wheels on
C_{L_1}	Lift coefficient at α, wheels off
C_D	Drag coefficient
α	Angle of incidence
β	Angle of yaw

1. Introduction

[redacted]

[redacted]

2. [redacted]

2.1 [redacted]

[redacted]

[redacted]

C_L = [redacted]

where C_L i[redacted]
C_{L_0} is [redacted]

3. Results

[redacted]

4. [redacted]

[redacted]

5. [redacted]sions

[redacted]

[redacted]

[redacted] [redacted]

[redacted] [redacted]

[redacted] [redacted]

[redacted] [redacted]

[redacted] [redacted]

[redacted] [redacted]

[redacted] [redacted]

[redacted] [redacted]ear to [redacted]

[redacted] [redacted]

[redacted] [redacted]

[redacted] [redacted]

[redacted] [redacted]

[redacted] [redacted]

[redacted]

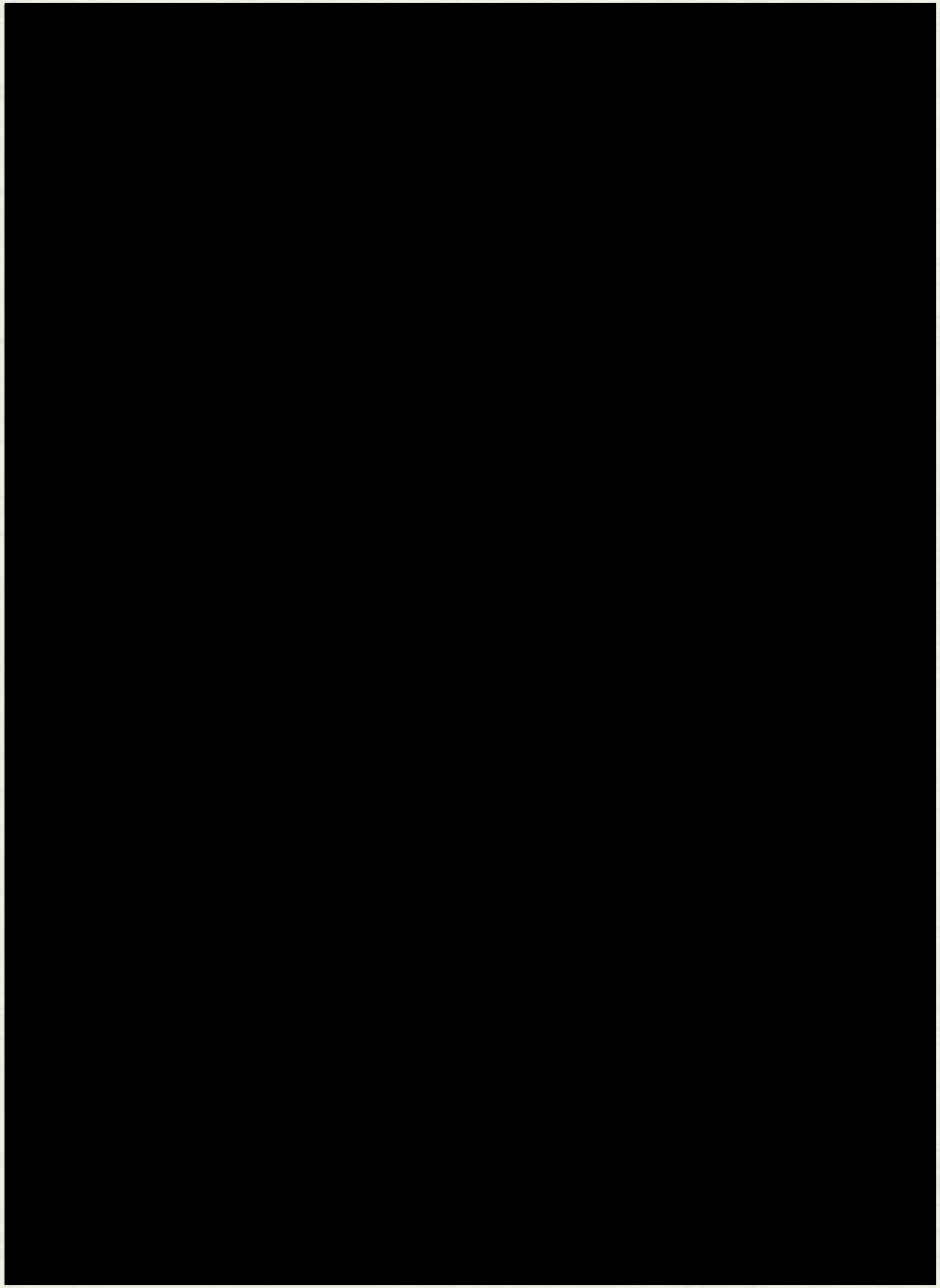

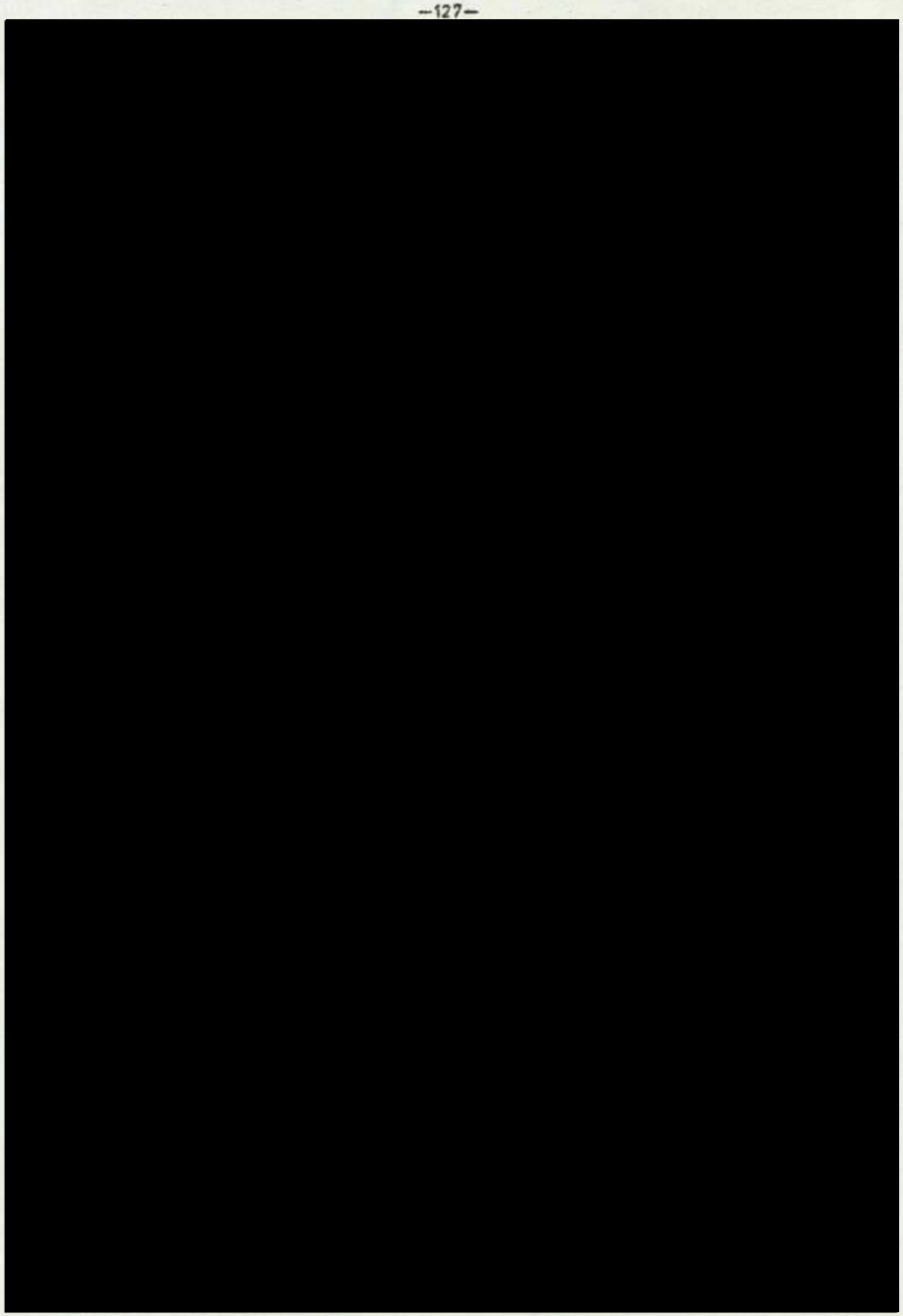

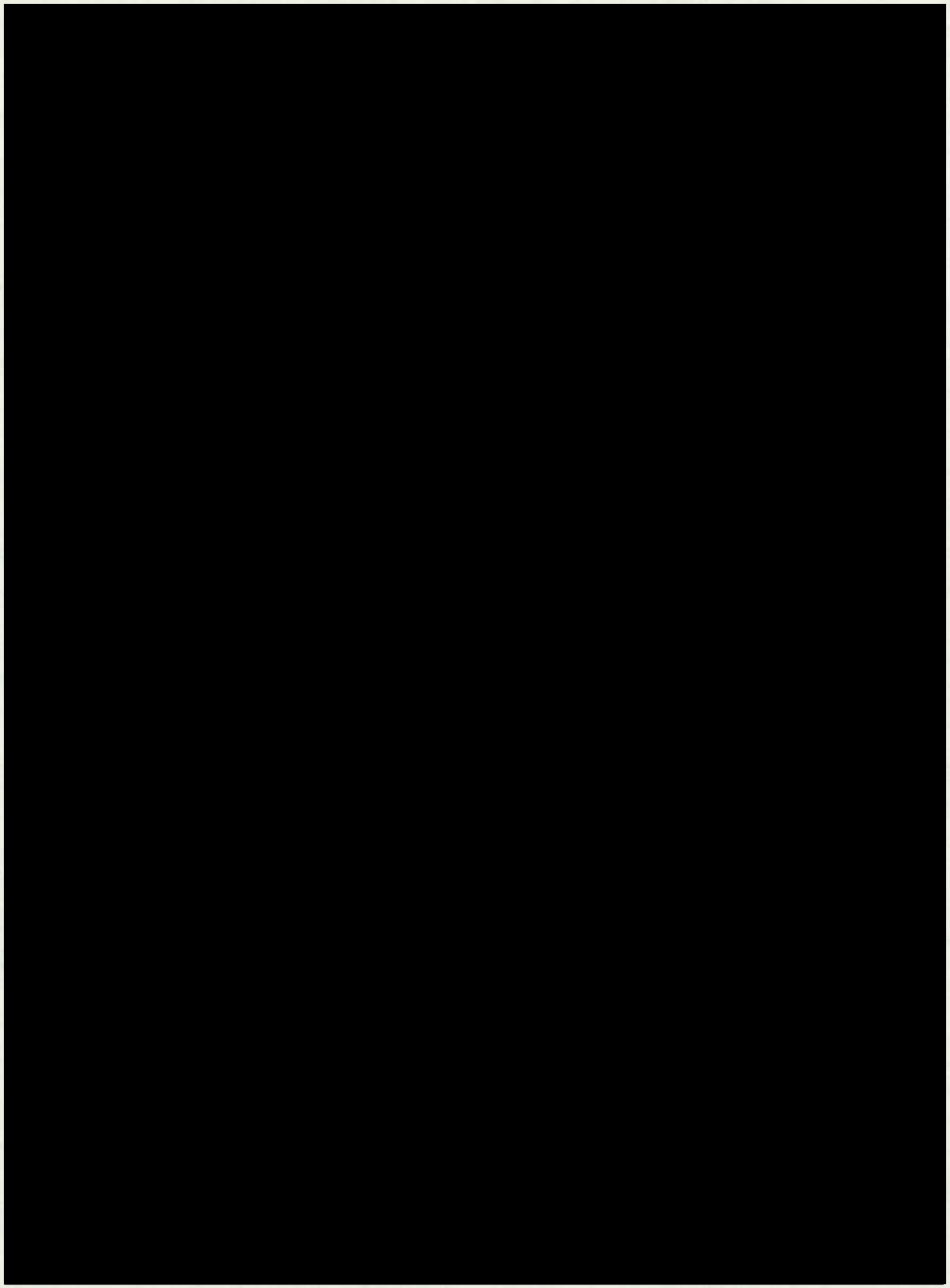

The aerodynamics of the IBEC Club Formula racing car

by J. P. Howell BSc(Eng)

Over the years members have shown some interest in the IBEC Club Formula racing cars. This enterprise of Mr Ian Bracey was first mentioned in the Digest column of the March 1973 Journal and an article was published in May of the same year. This was followed by a paper from Ian Bracey (Managing Director and Driver, IBEC Racing Developments), Brian Main (Mechanical Engineering) and J. P. Howell (Department of Aerodynamics), The City University. It was presented in April, 1974. At the time a copy suitable for publication was not available but Mr Howell (now Research Fellow, Department of Engineering Science University of Warwick on the Magnetic Levitation Project) has sent us this article on the aerodynamics of the P2 car which we are sure will be of special interest to certain of our members. — Editor

Notation

L	=	lift force
D	=	drag force
M	=	pitching moment
F	=	generalised force
V	=	air velocity
P	=	air density
ρ	=	air density
ν	=	air kinematic viscosity
Q	=	$\frac{1}{2}pV^2$ total head
C_L	=	L ÷ QA
C_D	=	D ÷ QA
C_M	=	M ÷ QAW
C_F	=	F ÷ QA
A	=	model frontal area
W	=	model wheelbase
D	=	model overall length
Δ	=	increase over basic case
α	=	incidence angle
β	=	wheel fairing angle
Re	=	Reynolds number = VD ÷ ν

Subscripts

Wing	wing (front or rear)
Body	body
F	front
R	rear

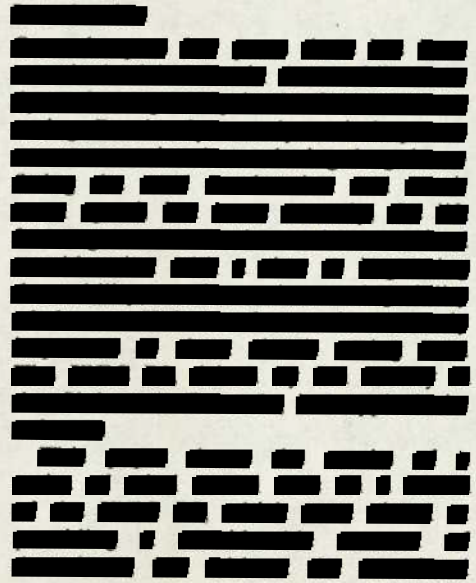

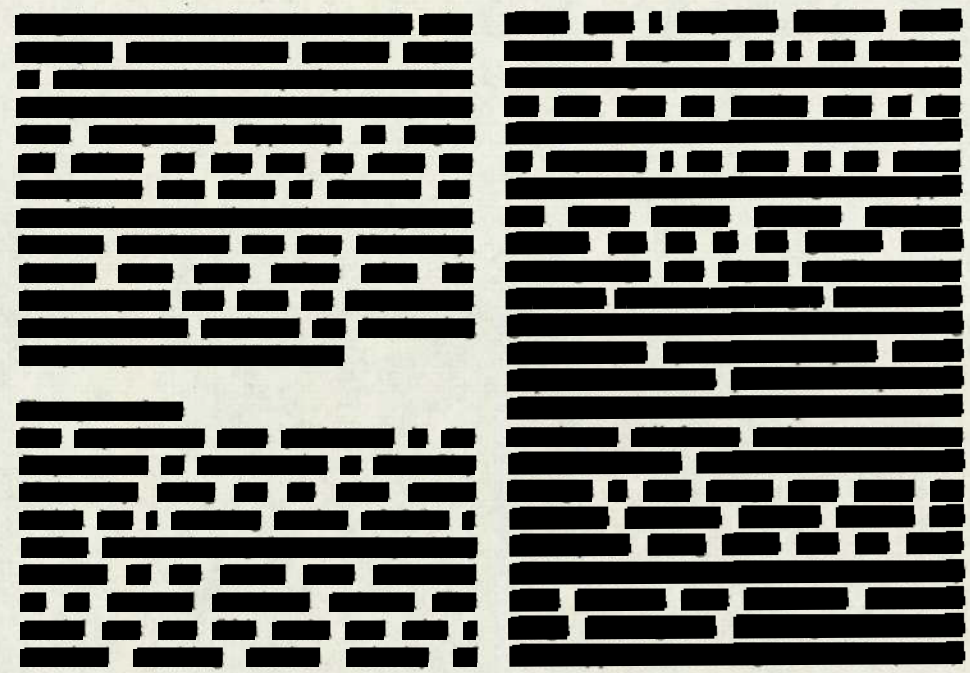

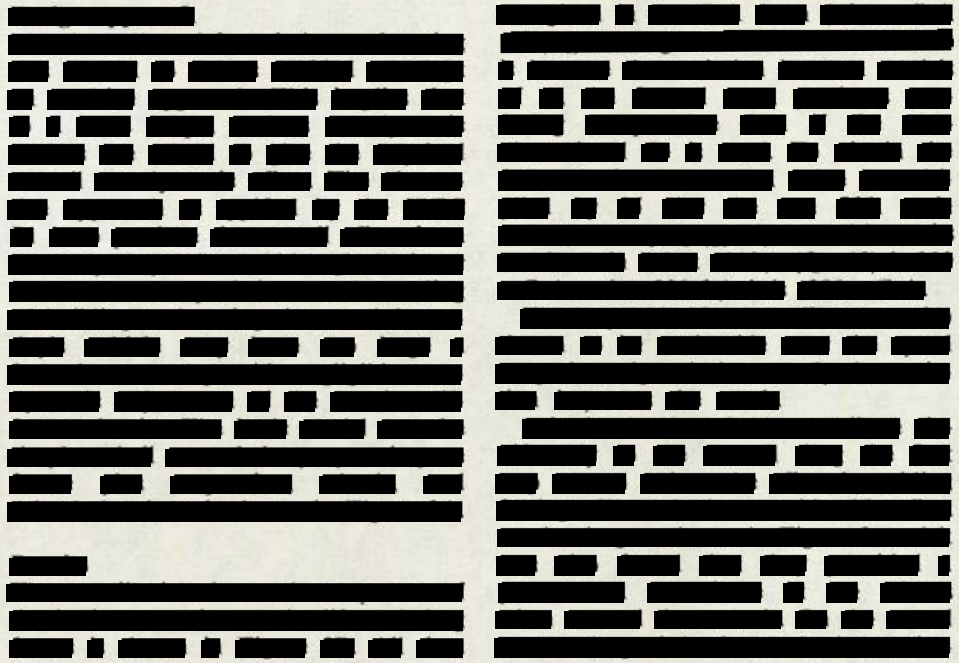

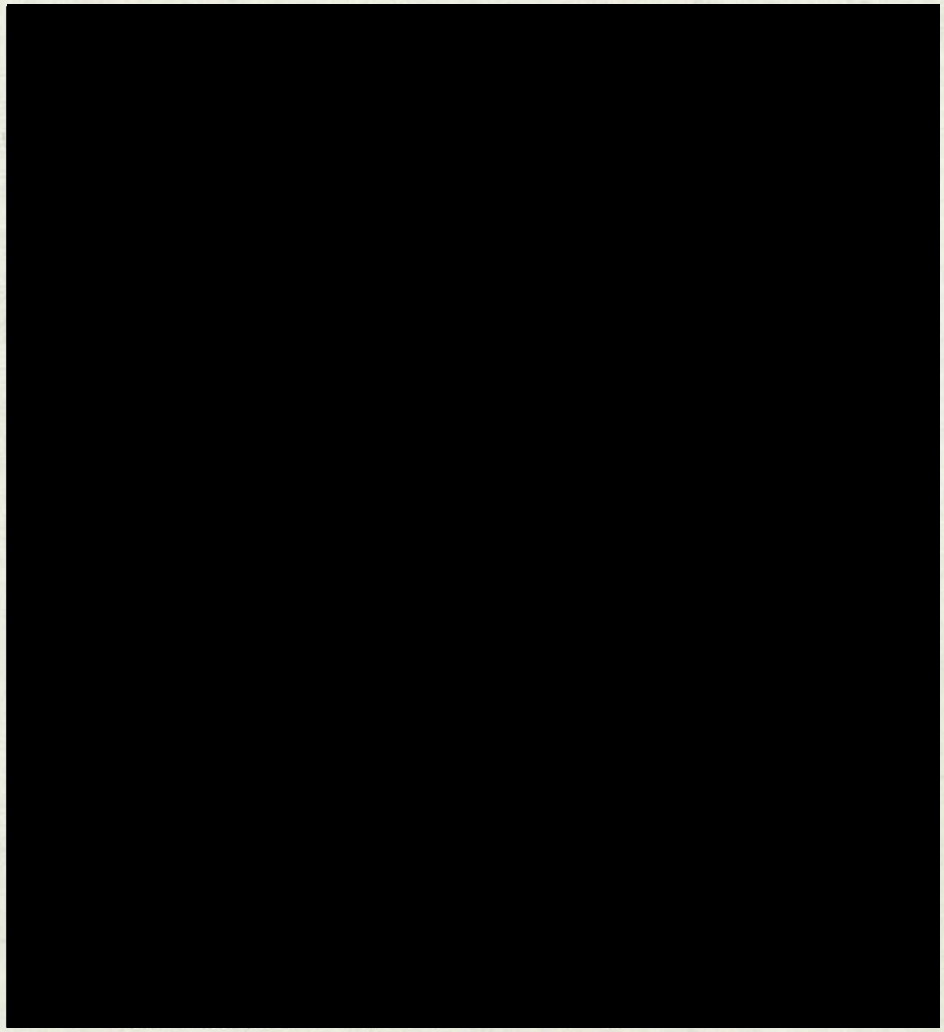

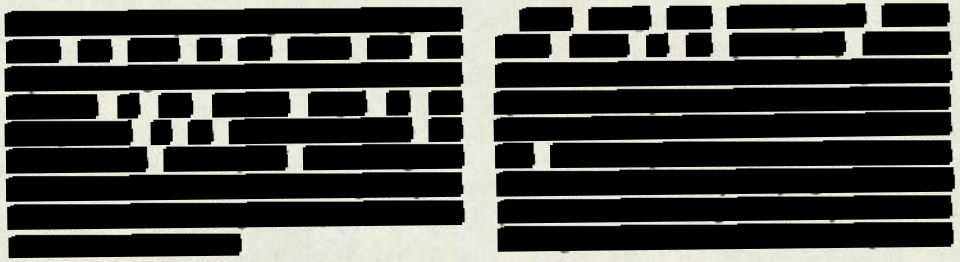

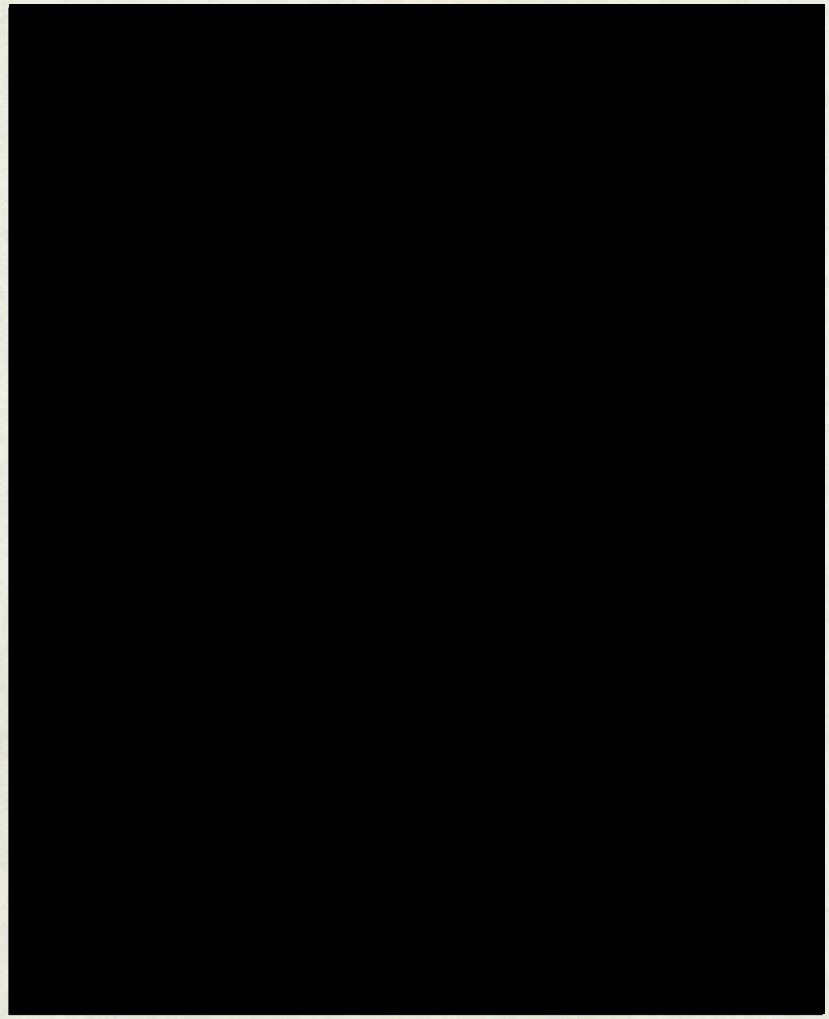

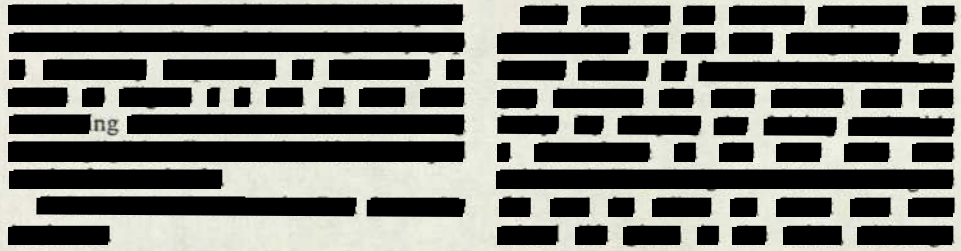
ng